UCLouvain
Institute of Condensed Matter and Nanosciences (IMCN)
Molecular Chemistry, Materials and Catalysis (MOST)

Development and Investigation of Metal-Based Photosensitizers for Solar Fuels Production

Simon De Kreijger

Supervisor – Professor Benjamin Elias

A Thesis Submitted for the Degree of Doctor of Sciences

Louvain-la-Neuve
October 2024

Members of the Jury

Prof. Yann Garcia

UCLouvain, IMCN, President of the Jury

Dr. Murielle Chavarot-Kerlidou

LCBM, Université Grenoble Alpes, CNRS, CEA Grenoble, France

Prof. Yoann Olivier

UNamur

Prof. Sophie Hermans

UCLouvain, IMCN

Prof. Alexandru Vlad

UCLouvain, IMCN

Prof. Benjamin Elias

UCLouvain, IMCN, Supervisor

Acknowledgments

Je souhaite débuter ces remerciements en exprimant ma profonde gratitude à mon "Chef" et promoteur de thèse, le Professeur Benjamin Elias. Merci de m'avoir accueilli dans votre laboratoire dès mon mémoire et de m'avoir donné l'opportunité de poursuivre mes recherches tout au long de ma thèse, dans un environnement à la fois stimulant et équilibré, alliant liberté et encadrement. Cet environnement m'a permis de m'épanouir pleinement au cours de ces sept dernières années. Je vous suis particulièrement reconnaissant pour la confiance que vous m'avez témoignée, pour vos conseils toujours avisés et bienveillants, ainsi que pour la disponibilité dont vous avez fait preuve, malgré vos nombreux engagements. Je tiens également à vous remercier pour m'avoir permis de participer à de nombreuses collaborations et voyages scientifiques, qui m'ont offert l'opportunité de rencontrer des personnes formidables et d'enrichir considérablement mes connaissances en photochimie. Enfin, merci pour vos rappels à l'ordre concernant les tâches administratives, que vous savez être mon domaine de prédilection (ou presque), lorsque cela était nécessaire. Je sais que ces années passées au sein de votre laboratoire resteront gravées dans ma mémoire, tant elles ont été enrichissantes et marquées par le plaisir de travailler avec vous ainsi qu'avec toutes les personnes qui ont contribué à rendre cette aventure si spéciale.

Ensuite, je tenais particulièrement à remercier mon « Sous-Chef » et nouvelle star montante de la photochimie, le Professeur Ludovic Troian-Gautier. Il est difficile de savoir par où commencer tant tu as été présent pour moi au cours de ces dernières années. Tu as toujours été là pour me tirer vers le haut, me poussant à donner le meilleur de moi-même, même dans les moments où je doutais. Ta disponibilité a été exceptionnelle, toujours prêt à discuter de science, même tard le soir. Je suis persuadé que recevoir dix photos (voire plus) par jour sur WhatsApp va cruellement te manquer, mais je suis aussi convaincu que la relève est déjà assurée. Sans ta présence et celle de Benjamin, je n'aurais sans doute jamais réussi à accomplir tout ce que j'ai

réalisé durant cette thèse. Merci pour ton enthousiasme pour la science, tes précieux conseils, ta confiance et ta patience. Je partage avec toi des valeurs communes : l'amour pour la science et un engagement profond dans notre travail, ce qui a rendu notre collaboration encore plus agréable et motivante. Je serai toujours prêt à partager une bonne bière avec toi quand tu le souhaiteras, et tu sais comment me contacter !

Je remercie également les membres de mon jury de thèse, les Professeurs Sophie Hermans, Alexandru Vlad, Yann Garcia, Yoann Olivier, et la Docteure Murielle Chavarot-Kerlidou, pour le temps qu'ils ont consacré à l'évaluation de mon travail et pour leurs retours, qui ont permis d'en améliorer la qualité et la rigueur scientifique.

Mes remerciements s'adressent ensuite aux professeurs qui m'ont accueilli dans leurs laboratoires et qui m'ont permis d'approfondir et de diversifier mes connaissances, notamment dans le domaine de la photoproduction d'hydrogène. Je garderai en mémoire les bons souvenirs de mon séjour chez le Professeur Garry S. Hanan, sous l'encadrement du légendaire Olivier Schott, avec ses appels à 21h pour m'annoncer que mes mesures se sont arrêtées, ainsi que les délicieuses poutines canadiennes et la vue imprenable sur Montréal depuis le Mont Royal. Un merci tout particulier à la Docteure Murielle Chavarot-Kerlidou pour son accueil chaleureux au CEA de Grenoble, ses conseils avisés et son expertise en matière de photoproduction d'hydrogène. J'ai énormément apprécié nos discussions et le temps que tu m'as consacré lors de mon séjour. Merci pour ta rigueur scientifique et ton accompagnement généreux. Je tiens également à souligner l'apport précieux de tous les collaborateurs scientifiques qui ont contribué aux projets de cette thèse. Un grand merci à Emilie Cauët pour les nombreuses heures passées à faire des calculs théoriques en TD-DFT, à la Docteure Dooshaye Moonshiram pour la collaboration fructueuse sur l'absorption transitoire des rayons X, et au Docteur Renato N. Sampaio pour ses mesures d'absorption transitoire et ses tests sur mes composés pour la réduction du CO_2.

Mes remerciements vont aussi à tous les membres du laboratoire Elias, anciens et actuels, avec qui j'ai partagé mes journées lors de ces sept dernières années. J'aimerais tout d'abord exprimer ma gratitude envers les anciens qui m'ont accueilli et transmis leurs connaissances : Guims, l'ancien daron du labo, avec qui j'ai eu l'honneur de partager un bureau pendant la préparation du FRIA ; Justin, alias PP Weynand ou encore "encadrant", qui m'a pris sous son aile lors de mon mémoire et m'a révélé toutes ses astuces au laboratoire ; Simon Cerfontaine, le roi du palladium tetrakis et des couplages, amateur de hardstyle hollandais et de shitty flute ; Robin, alias "Le Beve", avec son optimisme légendaire et ses talents de joueur de fléchettes (une petite flèèèche ?!) ; Akin, alias Fudès, notre b-boy et adepte des micro-siestes sur son bureau, nécessaires pour récupérer de l'énergie en fin de journée ; et enfin Mika, toujours prêt à ouvrir une "légendaaaire dorée", boire un soleil ou jouer une partie de billard.

Je remercie également les membres actuels du laboratoire, avec qui j'ai partagé les dernières années de ma thèse : Alexia, alias "le Pak", experte en cage escape et nouvelle maman du laboratoire, toujours "prête" à ne pas sursauter (Oskrr et Pipou) ; merci pour tous ces bons moments de rires dans le labo ; Noémie, l'ingénieure civile devenue chimiste en moins de temps qu'il ne faut pour le dire, fine connaisseuse de la théorie du champ cristallin et de l'encapsulation (et sûrement plus encore), merci pour ta bonne humeur et nos discussions matinales ou tardives, parfois sérieuses, parfois moins ; et Milan, le poseur fou de petits rappels sous forme de post-it et homme à la gâchette facile dans le triple 17.

Je n'oublie pas non plus la nouvelle génération du laboratoire. Julien, on se connait depuis un moment maintenant, continue de persévérer, et je suis sûr que de belles choses t'attendront durant ta thèse. Merci pour tous les bons moments passés dans le bureau l'année dernière. Joffrey, merci pour toute la bonne humeur que tu as apportée, notamment lors des pauses de midi avec ton fidèle acolyte, je suis persuadé que tu seras un excellent assistant/doctorant. Céline, ce fut un plaisir de t'encadrer pendant deux ans.

Ce qui t'es arrivé m'a profondément affecté, mais je veux te dire à quel point j'admire ton courage, ta détermination et ton optimisme. Je sais que tu feras une thèse extraordinaire, et je serai toujours là si tu en as besoin (même si je suis devenu un vieux ronchon). Merci aussi à Félix, notre nouveau post-doc, pour son aide précieuse et nos discussions scientifiques, ainsi qu'à Katerina, Lakshmi, Karem et Abdullah, les nouvelles recrues du groupe Troian-Gautier.

Un remerciement tout particulier à mes deux briscards du bureau de gauche, sans qui mes journées n'auraient pas été les mêmes. Mon Gillard, merci pour toutes ces belles années passées ensemble, que ce soit pour les corrections, le mundialito, les soupers de thèse ou les barbecues dans le quartier des hommes. Je garde d'excellents souvenirs de tout cela et te souhaite plein de réussite dans ta carrière de professeur à l'IPL. Marty, depuis notre rencontre sur les bancs de l'université et nos aventures en bac 1 (les labos de physique s'en souviennent), nous ne nous sommes jamais vraiment séparés. De partenaire de guindaille à partenaire de padel, la route fût longue mais je ne garde en mémoire que des bons moments passés à tes côtés.

Je remercie également les membres de la plateforme d'analyse, notamment Alain et Gabriella à la RMN, Raoul, Steph et Laurent à la spectrométrie de masse, Laurent à l'HPLC, et Jessica et Christophe au magasin. Merci aussi à Audrey et Jessica pour leur aide précieuse en tant que secrétaires, et enfin Steph, notre intermédiaire de sécurité et future maman, qui veille à ce que les lunettes et blouses soient portées au laboratoire. Merci pour ton aide dans les tâches de tous les jours et de veiller bon fonctionnement du laboratoire.

Je n'oublie pas de remercier mes collègues assistants et nos techniciens de laboratoires didactiques, Édouard, Corentin, Justine et particulièrement Pascale, avec qui j'ai eu beaucoup de plaisir à travailler. Merci aussi à Catherine et Agnès, nos coordinatrices de TP, pour leur bonne humeur, leur confiance et leur collaboration bienveillante.

Je voudrais également remercier mes compagnons d'université, Vincent, François, Benoit, Carole et Axel, avec qui j'ai partagé cinq années de vie étudiante, de soirées en cercle et de longues heures en salle informatique à rédiger des rapports. Vous avez rendu ces années inoubliables, et elles n'auraient pas eu la même saveur sans vous.

Mes derniers mots iront à ma famille, que je remercie du fond du cœur. Papa, maman, vous m'avez toujours soutenu et offert la liberté de suivre ma voie. Vous avez toujours veillé à ce que Nathan et moi grandissions dans les meilleures conditions possibles. Merci pour tout ce que vous avez fait pour nous, je profite de ces quelques lignes pour vous dire des mots que j'ai bien souvent eu du mal à dire de vive voix : je vous aime de tout mon cœur. Nathan, merci pour ces belles années passées à l'appartement, je n'en garde que des bons souvenirs même si je n'ai sans doute pas été le colocataire idéal. Maintenant tu as une nouvelle colocataire (plus au moins chouette que ton frère ?) et je vous souhaite le meilleur pour la suite.

Enfin, je remercie Laurane, mon binôme depuis six ans, c'est-à-dire depuis le début de ma thèse. Merci pour ton oreille attentive, ton soutien et ta présence à mes côtés. Tu as toujours su me remonter le moral ou me changer les idées quand j'en avais besoin. Nous avons traversé ensemble des moments exceptionnels et des défis, et je suis impatient de voir ce que l'avenir nous réserve. Je t'aime et j'ai hâte de vivre nos projets à venir.

Abbreviations

A	Absorbance
a	Distance Between Species
Å	Angström
BIH	1,3-dimethyl-2-phenyl-2,3-dihydro-1H-benzo[d]imidazole
bpph	benzo[a]pyrazino[2,3-h]phenazine
bpy	2,2'-bipyridine
C	Coulomb
CCD	Charge-Coupled Device
CE	Cage Escape
CH_2Cl_2	Dichloromethane
CH_3CN	Acetonitrile
cm	Centimetre
Co	Cobalt
CT	Charge Transfer
CV	Cyclic Voltammetry
D	Diffusion Coefficient
^{dFCF3}ppy	2-(2,4-difluorophenyl)-5-(trifluoromethyl)-pyridine
DMF	Dimethylformamide
$dmgH_2$	Dimethylglyoxime
DPV	Differential Pulse Voltammetry
DSPEC	Dye-Sensitized PhotoElectrochemical Cell
DSSC	Dye-Sensitized Solar Cell
e	Elementary Charge (1.602×10^{-19} C)
E	Energy or Einstein
E_{00}	Energy of the 0–0 Transition
EA	Electron Acceptor
ED	Electron Donor
E_{EA/EA^-}	Reduction Potential of the Electron Acceptor
$E_{ED^+/ED}$	Oxidation Potential of the Electron Donor
EnA	Energy Acceptor
E_{ox}*	Excited-State Oxidation Potential

EPR	Electron Paramagnetic Resonance
E_{red}*	Excited-State Reduction Potential
ES	Excited-State
ESI	Electrospray Ionization
eV	Electron Volt
EXAFS	X-ray Absorption Fine Structure
F	Integrated Emission Spectra Intensity or Total Photon Flux
FC	Franck-Condon
Fe	Iron
fliq	1-(9,9-dimethyl-9H-fluoren-2-yl)isoquinoline)
FRET	Förster Resonance Energy Transfer
fs	Femtosecond
FT	Fourier Transform
GMP	Guanosine 5'-MonoPhosphate
GS	Ground-State
h	Planck Constant (6.626 10^{-34} J.s) or hour
HEC	Hydrogen Evolution Catalyst
HER	Hydrogen Evolution Reaction
HOMO	Highest Occupied Molecular Orbital
HRMS	High Resolution Mass Spectrometry
HX	Hydrohalic Acid
$\hbar\omega_M$	Vibrational Mode
I	Intensity of the Transmitted Light or Luminescence Intensity
I_0	Intensity of the Incident Light
IC	Internal Conversion
IR	Infrared
Ir	Iridium
ISC	InterSystem Crossing
J	Joule
K	Kelvin
k	Kinetic Rate Constant
K_{ass}	Equilibrium Constant of Association

k_{BET}	Kinetic Rate Constant for Back-Electron Transfer
k_{diff}	Kinetic Rate Constant for Diffusional Encounters
k_{et}	Kinetic Rate Constant for Electron Transfer
k_{FRET}	FRET Kinetic Rate Constant
k_{GCR}	Kinetic Rate Constant for Geminate Charge Recombination
kJ/mol	Kilojoule per mole
k_{nr}	Non-Radiative Rate Constant
k_q	Quenching Rate Constant
k_r	Radiative Rate Constant
K_{SV}	Stern-Volmer Constant
l	Optical Path Length or Orbital Quantum Number
LC	Ligand-Centred
LED	Light-Emitting Diode
LLCT	Ligand to Ligand Charge Transfer
LMCT	Ligand to Metal Charge Transfer
LUMO	Lowest Unoccupied Molecular Orbital
m	Metre
M	Molar
MC	Metal Centred
mg	Milligram
MLCT	Metal to Ligand Charge Transfer
MLLCT	Metal-Ligand to Ligand Charge Transfer
mM	Millimolar
MW	Microwave
n	Mole
N_A	Avogadro Constant (6.022×10^{23} mol^{-1})
NHE	Normal Hydrogen Electrode
NIR	Near-Infrared
nm	Nanometer
NMR	Nuclear Magnetic Resonance
ns	Nanosecond
nsTAS	Nanosecond Transient Absorption Spectroscopy
OER	Oxygen Evolution Reaction

Os	Osmium
P	Power of the Irradiation Source
PF_6^-	Hexafluorophosphate Anion
phen	1,10-phenanthroline
piq	1-phenylisoquinoline
PL	Photoluminescence
PLI	Photoluminescence Intensity
ppy	2-phenylpyridine
PS	Photosensitizer
ps	Picosecond
Q	Quencher
r	Distance
R	Ideal Gas Constant
Ru	Ruthenium
s	Second
S	Total Spin Quantum Number
SEC	Spectroelectrochemistry
SED	Sacrificial Electron Donor
s_i	Spin Quantum Number
S_M	Huang Rhys Factor
S_n	Singlet State (n = 0, 1, 2, 3, …)
t	Time
TA	UV-vis Transient Absorption
TAA	Tri-*p*-anisylamine
TAP	1,4,5,8-tetraazaphenanthrene
TD-DFT	Time-Dependent Density-Functional Theory
TEA	Triethylamine
TEOA	Triethanolamine
TLC	Thin Layer Chromatography
T_n	Triplet State (n = 0, 1, 2, 3, …)
TOF	Turnover Frequency
TON	Turnover Number
tpy	2,2’:6’,2”-Terpyridine

v	Vibrational Energy Level
V	Volt
VR	Vibrational Relaxation
w	Electrostatic Work
WOC	Water Oxidation Catalyst
X^-	Halide
X_2	Halogen
XANES	X-ray Absorption Near Edge Structure
XAS	X-ray Absorption Spectroscopy
XTAS	X-Ray Transient Absorption
z	Charge
$\Delta\nu_{1/2}$	Spectral Full-Width at Half-Maximum
$^1O_2$	Singlet Oxygen
ΔA	Absorption Changes
ΔG	Gibbs Free Energy Change
Δx	Average Distance
$\Delta\varepsilon$	Change in Molar Extinction Coefficient
Φ	Luminescence Quantum Yield or Relative Yield of $PS^{\bullet+}$ or $PS^{\bullet-}$ Produced
Φ_{CE}	Cage Escape Yield
α	Amplitude of the Time-Resolved Luminescence
ε_0	Vacuum Permittivity
ε_r	Dielectric Constant of the Medium
ε_λ	Molar Extinction Coefficient
η	Refractive Index
λ	Wavelength
μs	Microsecond
ν	Frequency
τ	Excited State Lifetime

List of publications

1) Lakraychi, A. E.; De Kreijger, S.; Gupta, D.; Elias, B.; Vlad, A., *Phendione–Transition-Metal Complexes with Bipolar Redox Activity for Lithium Batteries*. ChemSusChem 2020, **13** (9), 2225-2231.

2) Aydogan, A.; Bangle, R. E.; De Kreijger, S.; Dickenson, J. C.; Singleton, M. L.; Cauët, E.; Cadranel, A.; Meyer, G. J.; Elias, B.; Sampaio, R. N.; Troian-Gautier, L., *Mechanistic investigation of a visible light mediated dehalogenation/cyclisation reaction using iron(III), iridium(III) and ruthenium(II) photosensitizers*. Catalysis Science & Technology 2021, **11** (24), 8037-8051.

3) Mahy, J. G.; Lejeune, L.; Haynes, T.; Body, N.; De Kreijger, S.; Elias, B.; Marcilli, R. H. M.; Fustin, C.-A.; Hermans, S., *Crystalline ZnO Photocatalysts Prepared at Ambient Temperature: Influence of Morphology on p-Nitrophenol Degradation in Water*. Catalysts 2021, **11** (10), 1182.

4) Zhao, J.; De Kreijger, S.; Troian-Gautier, L.; Yu, J.; Hu, W.; Zhang, X.; Elias, B.; Moonshiram, D., *Deciphering the photophysical kinetics, electronic configurations and structural conformations of iridium–cobalt hydrogen evolution photocatalysts.* Chemical Communications 2022, **58** (58), 8057-8060.

5) De Kreijger, S.; Schott, O.; Troian-Gautier, L.; Cauët, E.; Hanan, G. S.; Elias, B., *Red Absorbing Cyclometalated Ir(III) Diimine Photosensitizers Competent for Hydrogen Photocatalysis*. Inorganic Chemistry 2022, **61** (13), 5245-5254.

6) Gupta, D.; Lakraychi, A. E.; Boruah, B. D.; De Kreijger, S.; Troian-Gautier, L.; Elias, B.; De Volder, M.; Vlad, A., *Visible-Light Augmented Lithium Storage Capacity in a Ruthenium(II) Photosensitizer Conjugated with a Dione-Catechol Redox Couple.* Chemistry – A European Journal 2022, **28** (42), e202201220.

7) Wodon, M.; De Kreijger, S.; Sampaio, R. N.; Elias, B.; Troian-Gautier, L., *Accumulation of mono-reduced [Ir(piq)2(LL)] photosensitizers relevant for solar fuels production.* Photochemical & Photobiological Sciences 2022, **21** (8), 1433-1444. (Co-first author).

8) De Kreijger, S.; Troian-Gautier, L., *Sulfonylation enabled through the photoactivation of EDA complexes.* Chem Catalysis 2022, **2** (4), 653-656. (Perspective paper).

9) Ripak, A.; De Kreijger, S.; Sampaio, R. N.; Vincent, C. A.; Cauët, É.; Jabin, I.; Tambar, U. K.; Elias, B.; Troian-Gautier, L., *Photosensitized activation of diazonium derivatives for C–B bond formation*. Chem Catalysis 2023, **3** (2), 100490.

10) Ripak, A.; De Kreijger, S.; Elias, B.; Troian-Gautier, L., *A protocol for determining cage escape yields using nanosecond transient absorption spectroscopy.* STAR Protocols 2023, **4** (2), 102312. (Co-first author).

11) De Kreijger, S.; Elias, B.; Troian-Gautier, L., *Chloride, Bromide, and Iodide Photooxidation in Acetonitrile/Water Mixtures Using Binuclear Iridium(III) Photosensitizers.* Inorganic Chemistry 2023, **62** (39), 16196-16202.

12) De Kreijger, S.; Gillard, M.; Elias, B.; Troian-Gautier, L., *Spectroscopic Techniques to Unravel Mechanistic Details in Light-Induced Transformations and Photoredox Catalysis.* ChemCatChem 2024, **16** (1), e202301100.

13) Bourgois, C.; De Kreijger, S.; Xu, B.; Tambar, U. K.; Troian-Gautier, L., *Spectroscopic Investigation of the Remote C–H Allylation of Amides* via *Photoredox and Nickel Dual Catalysis.* Synlett 2024.

14) De Kreijger, S.; Ripak, A.; Elias, B.; Troian-Gautier, L., *Investigation of the Excited-State Electron Transfer and Cage Escape Yields Between Halides and a Fe(III) Photosensitizer*. Journal of the American Chemical Society 2024, 146, 10286−10292.

15) De Kreijger, S.; Cauët, E.; Elias, B.; Troian-Gautier, L*., Synthesis of Ru(II) and Os(II) photosensitizers bearing one 9,10-diamino-1,4,5,8-tetraazaphenanthrene scaffold*. Dalton Trans. 2024, **53** (24), 10270-10284.

16) Glaser, F.; De Kreijger, S.; Achilleos, K.; Narayan Satheesh, L.; Ripak, A.; Chantry, N.; Bourgois, C.; Quiquempoix, S.; Scriven, J.; Rubens, J.; Vander Wee-Léonard, M.; Daenen, M.; Gillard, M.; Elias, B.; Troian-Gautier, L., *A Compendium of Methodically Determined Ground- and Excited-State Properties of Homoleptic Ruthenium(II) and Osmium(II) Photosensitizers*. Manuscript submitted (ChemPhotoChem).

17) De Kreijger, S.; Glaser, F.; Troian-Gautier, L., *From Photons to Reactions: Key Concepts in Photoredox Catalysis*. Manuscript accepted for publication (ChemCatalysis).

18) De Kreijger, S.; Elias, B.; Troian-Gautier, L., *Increasing Cage Escape Yields for Halide Oxidation in Aqueous Solutions Using Ir(III) Photosensitizers with π-Extended Aromatic Ligands*. Manuscript in preparation.

Abstract

Due to the diurnal cycle of solar energy, a key for successful solar utilization is the development of an inexpensive storage mechanism, which represents a significant challenge. The smallest-volume in which electrons can be stored is in a chemical bond. Among them, hydrogen gas possesses a high energy density of 140 MJ/kg (9.17 MJ/L at 700 bar), making it a promising target for large scale energy storage and distribution. Therefore, the sunlight-triggered hydrogen evolution reaction (HER) represents a promising solution to worldwide consumption of fossil fuels. Current challenges in the field are related to the regeneration of the photosensitizer after the photoinduced electron transfer event. Indeed, most of reported HER rely on the use of sacrificial electron donors (triethylamine, triethanolamine…) which, after regenerating the photosensitizer, will be degraded and do not lead to any valuable products. With the idea of taking advantage of the photosensitizer regeneration event, researchers have developed systems using halides (X^-) as the electron donor that will ultimately yield a covalent X-X bond after X^- oxidation.

During this Ph.D. thesis, we first explored the potential of new Ir(III) photosensitizers towards solar fuels production applications. Our objective was to develop Ir(III) photosensitizers that absorb a wider range of the solar spectrum, allowing hydrogen production upon blue to red light irradiation. Then, we focused on photoinduced halide oxidation by modifying the chemical structure of the ligands chelated not only onto Ir(III) but also with Ru(II) and Os(II) metal centers in order to increase their photo-oxidizing power while keeping convenient light absorption properties. Finally, photosensitizers based on Fe(III), a first row abundant transition metal, were investigated for halide oxidation applications.

Résumé

En raison du cycle diurne de l'énergie solaire, l'une des clés pour l'utilisation efficace et continue de l'énergie solaire est la mise au point de moyens de stockage peu coûteux, ce qui représente un défi de taille. Le plus petit volume dans lequel des électrons peuvent être stockés est une liaison chimique. L'hydrogène gazeux possède une densité énergétique élevée de 140 MJ/kg (9,17 MJ/L à 700 bars), ce qui en fait une cible prometteuse pour le stockage et la distribution d'énergie à grande échelle. Par conséquent, la production d'hydrogène (appelée *hydrogen evolution reaction* en anglais - HER) initiée par la lumière du soleil à l'aide d'un photosensibilisateur représente une alternative prometteuse pour le stockage de l'énergie solaire et une réponse à la consommation mondiale de combustibles fossiles. Les défis actuels dans ce domaine sont liés à la régénération du photosensibilisateur après le transfert d'électrons photoinduit nécessaire à la production d'hydrogène. En effet, la plupart des HER rapportées reposent sur l'utilisation de donneurs d'électrons sacrificiels (triéthylamine, triéthanolamine...) qui, après avoir régénéré le photosensibilisateur, sont dégradés et ne conduisent pas à la formation de produits à plus haute valeur ajoutée. Dans l'idée de tirer profit de de la régénération du photosensibilisateur, les chercheurs ont développé des systèmes utilisant les halogénures (X^-) comme donneurs d'électrons, qui pourront mener à la formation du composé covalent X-X après l'oxydation de X^-, qui représente donc également un réservoir d'énergie.

Durant cette thèse de doctorat, nous avons d'abord exploré le potentiel de nouveaux photosensibilisateurs à base d'Ir(III) à des visées de production de carburants solaires. Notre objectif était de développer des composés d'Ir(III) qui absorbent une plus large gamme du spectre solaire, permettant la production d'hydrogène sous irradiation de lumière de couleur bleue à rouge. Ensuite, nous nous sommes concentrés sur l'oxydation photoinduite des halogénures en modifiant la structure chimique des ligands chélatés, non seulement sur l'Ir(III) mais aussi avec les centres métalliques à base de Ru(II) et d'Os(II), afin d'augmenter leur pouvoir photo-oxydant tout en conservant

des propriétés d'absorption de la lumière intéressantes. Enfin, un photosensibilisateur basé sur le Fe(III), un métal de transition abondant, a été étudié pour des applications d'oxydation des halogénures.

Table of contents

Chapter I – Prologue and General Introduction

Chapter II – Objectives and Strategies

Chapter III – [Ir(piq)$_2$(LL)] Photosensitizers for Solar Fuels Production

Chapter VI – Development of Ru(II) and Os(II) Photosensitizers for Photo-Oxidation Applications

Chapter VII – Ir(III) Photosensitizers with π-Extended Aromatic Ligands for Halide Oxidation

Chapter VIII – Investigation of the Electron Transfer and Cage Escape Yields Between Halides and a Fe(III) Photosensitizer

Chapter I – Prologue and General Introduction

1.1 Prologue

In the midst of escalating concerns surrounding climate change, dwindling fossil fuel reserves, and geopolitical instability, the imperative for a global energy transition has never been more pressing. The journey towards a sustainable and resilient energy future necessitates a paradigm shift away from carbon-intensive fuels towards renewable and cleaner alternatives. In the view of developing novel sustainable energy supply as an alternative to fossil fuels, different technologies have been explored such as wind energy, hydropower, geothermal energy, biomass energy, tidal/wave energy and solar energy. Each technology brings its own advantages and disadvantages contributing to the complexity of the renewable energy landscape.[1]

Wind energy represents an abundant resource, particularly in coastal and high-altitude regions, coupled with mature technology and proven scalability. Its low greenhouse gas emissions during operation make it an attractive option for reducing carbon footprints.[2] However, the intermittent nature of wind necessitates backup power sources to ensure a reliable supply. Additionally, concerns persist regarding the visual and noise impacts in densely populated areas, alongside land use conflicts.[3] Hydropower, on the other hand, offers reliable and consistent power generation with a long operational lifespan and low operating costs.[4] However, the significant environmental impact on aquatic ecosystems and habitats, limited availability of suitable development sites, and vulnerability to climate changes poses challenges to its widespread adoption.[5] Geothermal energy stands as a reliable source of continuous power generation with low greenhouse gas emissions. It is suitable for both electricity and direct heating applications. Nevertheless, its limited availability to regions with accessible geothermal resources, coupled with high upfront costs for exploration and drilling, and potential subsurface resource depletion over time, represent obstacles to widespread deployment.[6] Biomass is defined as biological material which is directly or indirectly produced by photosynthesis. Examples are wood and wood residues, energy crops, crop residues, and organic waste/residues from industry, agriculture, landscape management and households, which can be used for energy production and

offers flexibility for various applications such as heat, electricity and biofuels. Yet, concerns about carbon neutrality dependent on sustainable sourcing practice, competition with food production for land use, and issues regarding air quality and deforestation warrant careful considerations in its implementation.[7] Finally, tidal and wave energy sources promise predictable and consistent energy generation with low environmental impact.[8] However, their limited deployment locations with strong tidal or wave resources, high upfront costs, and potential impacts on marine ecosystems pose challenges to their widespread adoption.[9, 10]

In comparison to these renewable energy technologies, solar energy emerges as a convincing contender. The sun represents one of the most abundant and widespread sources of renewable energy as it could provide in two hours (8.6×10^{20} J)[11] the energy consumed on earth in 2023 (6.6×10^{20} J)[12]. Moreover, it can be harvested efficiently through chemical engineered solutions. For example, solar cells, first developed in 1954 by the Bell's laboratory,[13] that convert sunlight into electricity are now part of our daily landscape due to their scalable installations suitable for various scales and locations. Yet, intermittency of solar energy creates a dichotomy between the moment when the energy is most needed and when sunlight reaching earth is the most intense. Hence, current developments are focused on novel routes to store solar energy. An interesting approach involves harnessing solar energy to creates chemical bonds, known as solar fuels.[14, 15] Typical examples include the production of hydrogen gas (H_2) from water splitting which is considered worldwide as a promising target for large scale energy storage and distribution.[16] Alternative solar fuels include liquid fuels from CO_2 reduction,[17-19] as well as halogen (X_2), a value added product, that could be concomitantly formed with H_2 upon hydrohalic acid (HX) splitting.[20, 21] With the aim of developing solar fuels productions, researcher have been inspired from photosynthesis, for the design of artificial photosynthetic systems based on photoredox catalysis.[22, 23] Moreover, the use of sunlight mediated chemical reactions had also been reported in 1908 by Ciamician and Sibler using prolonged exposure to sunlight.[24] More than a century later; the use of light-

harvesting molecules, also termed photosensitizers (PS), to initiate chemical transformations using visible light is amongst the most prominent research area in photochemistry and organic chemistry. In conclusion, the pursuit of sustainable energy solutions requires strategic use of photoredox catalysis to fully handle the potential of solar energy. Through the application of photoredox catalysis, future generation will be able to drive the development of highly efficient and scalable methods for solar fuels production. This approach holds one of the keys to overcome the challenge of solar energy intermittency, thereby establishing the foundation for a sustainable energy future.

1.2 Research context

1.2.1 Light induced water and hydrohalic splitting

As stated above, H_2 appears to be a potential solution for moving towards sustainable energy supply. Nowadays, 99% of the H_2 production relies on natural gas steam reforming, as this is currently the most economical production pathway (**Equation 1.1**).[25]

$$C_xH_{y(g)} + x\,H_2O_{(g)} \rightarrow x\,CO_{(g)} + (x+y)\,H_{2(g)}$$

Equation 1.1

Unfortunately, this procedure leads inevitably to the concomitant production of CO, nitrogen oxides (such as N_2O or NO_2), sulphur oxides (such as SO_2) and CO_2.[26] It is therefore of great interest to develop a new carbon free production pathway. In this context, solar energy conversion into chemical fuels, more specifically light-driven water splitting into molecular H_2 and O_2 (E^0 = –1.23 V *vs* NHE for the global water splitting process), represents a promising way for solar energy conversion (**Equation 1.2**).[27]

$$H_2O \rightarrow 2\,H_2 + {}^1\!/_2\,O_2$$

Equation 1.2

This redox process can be divided into two half reactions: the two electrons reduction of protons (**Equation 1.3**) and the four electrons oxidation of water into molecular oxygen (**Equation 1.4**), with an electron flow connecting both processes.

$$2\,H^+ + 2\,e^- \rightarrow H_2$$

$$2\,H_2O \rightarrow O_2 + 4\,H^+ + 4\,e^-$$

Equations 1.3 and 1.4

Up to now, each half equation has been mostly studied separately because the overall process of water splitting is challenging to be carried out in one step. This is due to i) the uphill energy nature of these consecutive reactions (more than 1.23 V *vs* NHE or 285.55 kJ/mol)[28] and ii) the complexity of the water oxidation process, involving the simultaneous loss of 4 electrons, 4 protons and the formation of an oxygen-oxygen bond which is kinetically demanding. The four steps mechanism for the anodic electrocatalytic oxygen evolution reaction (OER) in the presence of a heterogeneous catalyst and absorbed intermediates is described by **Equations 1.5-1.8**.[29]

$$2\,H_2O \rightarrow OH_{(ad)} + H^+ + e^- + H_2O$$

$$OH_{(ad)} \rightarrow O_{(ad)} + H^+ + e^-$$

$$O_{(ad)} + H_2O \rightarrow OOH_{(ad)} + H^+ + e^-$$

$$OOH_{(ad)} \rightarrow O_2 + H^+ + e^-$$

Equations 1.5, 1.6,1.7 and 1.8

Due to the energy input required to split water, this process should benefit from external energy source such as sunlight. As the natural photosynthesis is an efficient system to convert light into chemical energy (the combination of a light triggered reaction and a dark reaction drives the consumption of CO_2 and H_2O to produce O_2 and fixed carbon in the form of carbohydrates)[30], scientists have focused on the development of so-called "artificial photosynthesis" in order to perform efficient solar fuels production. To quote Vincent Artero and Phong D. Tran "*Nature is both beautiful and powerful. She has always been an inexhaustible source of inspiration for us humans on our way to solve our problems and improve ourselves. One of our current most pressing matters concern the unsustainable nature of the fossil fuels and their negative effects on the environment. Luckily, if one looks hard enough, a solution can be found hidden inside the ever-so familiar leaves dancing happily in the sun. Learning the basic structure and function of the natural leaf has led scientists to the creation of its artificial version*".[31]

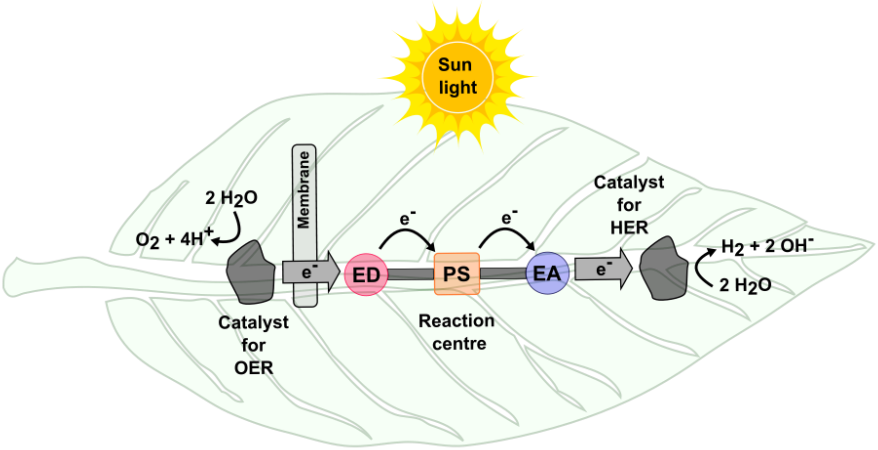

Figure 1.1. Schematic representation of an artificial photosynthetic system for water splitting.

The construction of such artificial systems for solar fuels production is based on mimicking the molecular and supramolecular organization of the natural photosynthesis process. In this ideal case, light-harvesting should lead to charge separation, that must be followed by charge transport to deliver the oxidizing and reducing agents to the catalytic site, where O_2 and H_2 evolution

should separately occur. Therefore, these systems should include the following features: 1) an antenna or photosensitizer (PS) for light-harvesting and funnelling, 2) a charge separation triad composed of an electron donor (ED), the PS and the electron acceptor (EA), 3) a catalyst for hydrogen evolution reaction (HER), one for oxygen evolution reaction (OER) and 4) a membrane separating the reductive and oxidative process (**Figure 1.1**).[32]

As mentioned in this section and due to the complexity of the whole artificial photosynthetic system presented in **Figure 1.1**, considerable attention has been devoted to the development of simplified photocatalytic system for the proton reduction part of the water splitting process. One of the key challenges in the development of efficient systems relies on a mandatory charge separation process, *i.e.* when light is absorbed, it has to be converted into a directional electron flow.[33] Consequently, the design of efficient photocatalytic systems necessitates several essentials components (**Figure 1.2**): a photosensitizer (PS), a catalytic centre for HER, with the possibility of both entities being connected or not by a bridging electronic relay.[34] In addition to these building blocks, a sacrificial electron donor (SED) (such as triethanolamine (TEOA) or triethylamine (TEA))[35] has to reduce the excited photosensitizer or regenerate the ground-state following excited-state electron transfer. It is important to mention that systems consisting of non-covalently bound units PS and HER catalyst are also well described in the literature.[36-38]

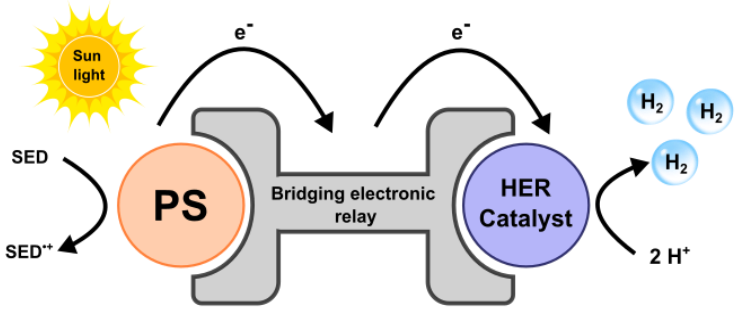

Figure 1.2. Simplified scheme of a photocatalytic system for hydrogen production.

Unfortunately, using a SED in artificial photosynthesis has limitations, primarily because it is consumed in the reaction without yielding any valuable products and the overall process only results in the formation of a hydrogen-hydrogen bond (436 kJ/mol). This represents a significant drawback as it leads to inefficient resource utilization and limits the overall sustainability of the process. This inefficiency underscores the need for alternative approaches that can streamline the process and optimize the production of valuable products.

Table 1.1. Rate Constants for Common Halides Reactions in Aqueous Solution at 298K.[a]

Halide Species	Rate Constant (*k*)[a 39, 40]
$X^{\bullet} + X^{-} \rightarrow X_2^{\bullet-}$ [b]	8.5 x 10^9, 1.6–2.8 x 10^9, 0.1–1.2 x 10^{10}
$X_2^{\bullet-} + X_2^{\bullet-} \rightarrow X^{-} + X_3^{-}$ [b]	1.9–9.0 x 10^9, 0.9–1.2 x 10^{10}, 3.2–3.9 x 10^{10}
$X_2^{\bullet-} \rightarrow X^{\bullet} + X^{-}$ [c]	6 x 10^4, 2 x 10^4, 9 x 10^4

[a] Color code is green (Cl species), Orange (Br species), and purple (I species). [b] *k* in M^{-1} s^{-1}. [c] *k* in s^{-1}.

An alternative to the use of sacrificial electron donors and kinetically demanding water oxidation relies on the thermodynamically uphill conversion of hydrohalic acids (HX) to yield H_2 and the corresponding halogen (X_2), simultaneously providing the reductant (X−) and the oxidant (H^+) to the photocatalytic system. HX splitting is a mechanistically simpler alternative, as halides (X^-) are oxidized to X_2 by a two-electron transfer process that does not involve proton-coupled electron transfer steps.[41] Moreover, using hydrohalic acid (HX) splitting offers a more attractive opportunity, as it generates halogen molecules (X_2) concomitantly with H_2.[20, 21], providing a valuable product alongside the desired H_2 gas; I-I (151 kJ/mol); Br-Br (193 kJ/mol); Cl-Cl (243 kJ/mol). HX splitting would operate according to a mechanism where the light-excited PS oxidizes the halide (X^-), forming the corresponding $X^{\bullet}$ that further reacts with X^- to form $X_2^{\bullet-}$. Then, disproportionation of $X_2^{\bullet-}$ rapidly occurs to form the trihalide (X_3^-) and the

corresponding halide (X^-) (**Table 1.1**). The trihalide anion can then undergoes dissociation to produce X_2 and X^-.

The reduced PS can activate a HER catalyst that in turn generates H_2 from a proton source. The main drawback of hydrohalic splitting is the thermodynamic demand associated with halide oxidation. Aqueous halide oxidation occurs at potentials $E^0(X^{\bullet/-})$ of 1.33, 1.93 and ~ 2.1-2.3V *vs* NHE for iodide, bromide and chloride, respectively.[41] This wide range of potentials was shown to be narrower in organic solvents where E^0 $(X^{\bullet/-})$ of 1.23, 1.35 and 1.46 V *vs* NHE have been roughly estimated in acetonitrile for iodide, bromide and chloride, respectively.[42, 43] Hence, such oxidations are thermodynamically very demanding in water and often requires strong photo-oxidant photosensitizers.

1.3 Photocatalysis and elements of photophysics

1.3.1 Photoredox catalysis

Understanding photoredox catalysis is crucial for the development of artificial photosynthetic systems aimed at sustainable energy production. Photoredox catalysis involves light-induced chemical reactions that proceed via electron or energy transfer processes, mimicking the energy conversion mechanisms found in natural photosynthesis.

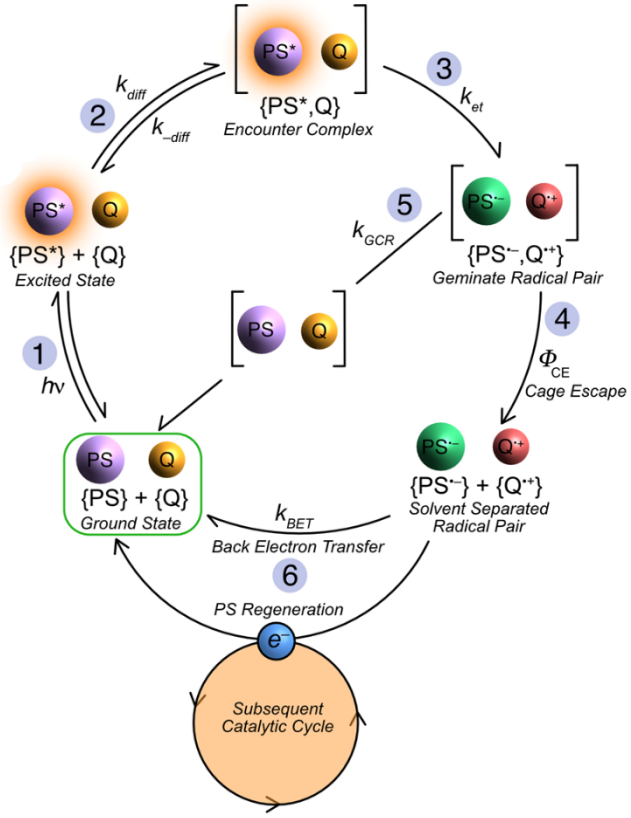

Figure 1.3. Photophysical and photochemical scheme describing the elementary steps between a PS and a Q under light irradiation. The scheme is described for reductive excited-state quenching. The scheme is separated according to steps that will be further described in this chapter: 1) light absorption and excited-state lifetime, 2) formation of the encounter complex via diffusion, 3) energy or electron transfer (represented here for clarity), 4) cage escape (including cage escape yields), 5) geminate charge recombination and 6) back electron transfer These steps are associated with the corresponding rate constants for diffusional encounters (k_{diff}), electron transfer (k_{et}), geminate charge recombination (k_{GCR}) and back-electron transfer (k_{BET}).

In a typical photophysical scheme for photoreactions depicted in **Figure 1.3**, 1) photon absorption by a photosensitizer (PS) leads to the formation of an excited-state (PS*), 2) this PS* can diffuse to form an encounter complex with a quencher (Q), 3) from which an excited-state reaction by electron (or energy transfer) could occur to form a “geminate radical pair” if the thermodynamics are favorable, 4) immediately after electron transfer, the oxidized/reduced PS and the oxidized/reduced Q must undergo a process called “cage escape” in order to perform efficient subsequent reactivity. Unproductive reaction pathways can occur from the geminate radical pair through 5) geminate charge recombination. Additionally, 6) back electron transfer from the escaped products can also lead to ineffective reaction pathways. These different elementary steps will be described hereafter, in the different sections of this chapter.

1.3.2 Absorption of light and formation of the excited state

Beer-Lambert law

In the quantum model, light-induced processes stem from the interaction between molecules and particles known as photons. The energy (E, Joule) carried by a photon correlates directly with its frequency (ν, Hertz) and the Planck constant (h = 6.626 10^{-34} J.s) as expressed in **Equation 1.9**:

$$E = h\nu$$

Equation 1.9

Typically, in UV-visible spectroscopy, a molecule absorbs one photon to generate an electronic excited state with an energy equal to $h\nu$.[44] The absorption of light at a given wavelength (λ) is described by the Beer-Lambert law (**Equation 1.10**), where A is the absorbance, I_0 and I are respectively the intensity of the incident and the transmitted light, ε_λ (M^{-1} cm^{-1}) the molar extinction coefficient, C (M) the concentration of the absorbing molecule and l

(cm) the optical path length.[44] This law provides a macroscopic depiction of electronic transitions taking place at the molecular scale upon photon absorption.

$$A(\lambda) = \log\frac{I_0}{I} = \varepsilon_\lambda\, C\, l$$

Equation 1.10

States multiplicity

From the ground state of a molecule, different excited states may be reached. They are characterized by a multiplicity, depending on their total spin quantum number, which is itself defined as the sum of the spin quantum number (s_i) of each electron (**Equation 1.11**).[44]

$$Multiplicity = 2S + 1 \qquad where\ S = \sum_i s_i$$

Equation 1.11

When all the electrons are paired, the value of S is equal to zero, resulting in a singlet multiplicity denoted as S_0. Upon electron excitation by visible light, singlet state with higher energy (S_1, S_2, S_3…) can be generated, along with triplet states (T_1, T_2, T_3…) if the electron's spin flips after the transition. According to the Hund's rule, the energy of these triplet states is often lower than the energy of the corresponding singlet states.[44]

Selection rules

Electronic transitions between molecular orbitals are governed by specific rules dictating their probability of occurrence. These rules are reflected in the molar extinction coefficient of the Beer-Lambert law (**Equation 1.10**). Firstly, the spin selection rule dictates that transitions between states of different multiplicities are forbidden. However, spin-orbit coupling can enable spin

inversion and allow singlet-triplet transitions, particularly in the presence of heavy atoms. Secondly, the symmetry selection rule (Laporte rule) states that transitions between orbitals of the same parity are prohibited (a change of polarity is required; $\Delta l = \pm 1$ where l is the orbital quantum number), such as d-d transitions. Nevertheless, symmetry-disrupting molecular vibrations can induce symmetry-forbidden transition, albeit with low molar extinction coefficients, through a phenomenon known as vibronic coupling.

Lowest-energy excited state

Among all the allowed transitions, the light-induced promotion of an electron from the Highest Occupied Molecular Orbital (HOMO) to the Lowest Unoccupied Molecular Orbital (LUMO) holds particular significance in photochemistry. This transition results in the formation of the lowest-energy excited state, which is typically populated in solution regardless of the absorbed light's energy. Known as Kasha's rule,[45] this phenomenon underscores that all subsequent photochemical and photochemical processes, which will be described in the following sections, occur via this lowest-energy excited state.

1.3.3 Intramolecular deactivation pathways

As discussed in the previous section, the absorption of a photon in the UV-Visible region leads to the formation of an electronic excited state. The latter can undergo different possible deactivation pathways corresponding to intramolecular relaxation processes through different electronic states of a given molecule. The Jablonski-Perrin diagram[46] (**Figure 1.4**) provides a visual representation of the electronic states and their energy levels within a molecule.

Typically, these states include singlet (S_1, S_2…) and triplet (T_1, T_2…) electronic states of increasing energy. The fundamental vibrational level (v = 0) of each electronic state is represented by a thick horizontal line, while higher vibrational levels (v= 1, 2…) are depicted with thin lines.[47] Radiative

transitions, involving both absorption and emission of photons (*i.e.* fluorescence or phosphorescence), are represented with vertical straight arrows, while non-radiative transitions are shown with wavy arrows.

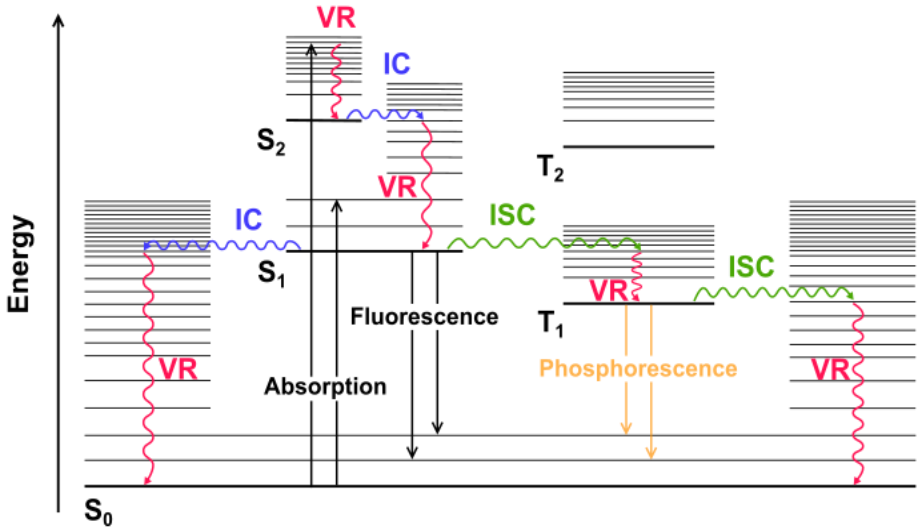

Figure 1.4. Jablonski-Perrin diagram and intramolecular deactivation pathways for a hypothetic molecule; VR = vibrational relaxation, IC = internal conversion, ISC = intersystem crossing.

Franck-Condon principle

The absorption of a photon leads to an electronic transition, typically occurring within a very short timescale (10^{-15} s). According to the Born-Oppenheimer approximation, this transition is commonly considered to occur without significant movement of the nuclei. This implies that the electronic transition is vertical, a concept known as the Franck-Condon transition. Consequently, the excited state S_n resulting from this transition possesses a geometry similar to the ground state, and is often found in a vibrationally hot excited state

Radiative and non-radiative transitions

Following the formation of an S_n excited state (**Figure 1.4**), there is a rapid (10^{-13}-10^{-11} s) deactivation to the lowest-energy excited state in accordance

with Kasha's rule.[45] This relaxation process typically involves internal conversion (IC) between states of the same multiplicity. Since electronic transition are always vertical (Franck-Condon principle), IC is often accompanied by vibrational relaxation (VR), resulting in the S_1 with a vibrational energy level of 0.[48] From this lowest excited state, energy can be dissipated through either radiative or non-radiative deactivation (respectively characterized by a radiative rate constant (k_r) and a non-radiative rate constant (k_{nr})). Since the energy gap between S_1 and S_0 is usually higher that between other S_n and S_{n-1} states, IC and VR are therefore slower, competing with a radiative process known as fluorescence ($S_1 \rightarrow S_0$).[48]

Another pathway involves the inversion of electron spin through an intersystem crossing (ISC) process. This non-radiative process occurs between isoenergetic vibrational levels of electronic states with different multiplicities. Although typically forbidden, the presence of heavy atoms increases the probability of spin-orbit coupling, allowing the lowest-energy triplet states in its 0 vibrational level (T_1) to be reached after VR. Its non-radiative deactivation to the ground state S_0 thus requires a second ISC followed by VR. Alternatively, photon emission may take place during a radiative process called phosphorescence ($T_1 \rightarrow S_0$).[48]

1.3.4 Excited state lifetime and quantum yields

Excited state lifetime

As stated in the previous section, the excited state PS* can be deactivated to the ground state (PS) by a radiative or non-radiative physical process, this being related to the photophysics of the PS. In photoredox catalysis, the magnitude of the excited-state lifetime is a critical factor influenced by the chemical properties of the PS, the temperature and the solvent. Upon light excitation, the decay in the population of the excited state PS* is governed by **Equation 1.12**, where k_r and k_{nr} represent the sum of the rate constants of radiative and non-radiative processes, respectively.[48]

$$-\frac{d[PS^*]}{dt} = (k_r + k_{nr})[PS^*]$$

Equation 1.12

Integration of this equation as a function of time results in the following expression, with τ defined as the excited-state lifetime.[48]

$$[PS^*](t) = [PS^*]_0 \, exp\left(-\frac{t}{\tau}\right) \qquad where \, \tau = \frac{1}{k_r + k_{nr}}$$

Equation 1.13 and 1.14

The excited-state lifetime of a PS can be experimentally measured. Indeed, the time-dependent luminescent intensity (I(t)) is directly connected to the population decay of the luminescent excited states (**Equation 1.15**).[49]

$$I(t) = k_r \, [PS^*]_0 \exp\left(-\frac{t}{\tau}\right)$$

Equation 1.15

To experimentally determine the excited-state lifetime of a PS, time-resolved spectroscopic techniques such as transient absorption spectroscopy or fluorescence spectroscopy can be employed. In transient absorption spectroscopy, the absorption of a short laser pulse excites the PS, and subsequent probing by UV-visible spectroscopy allows to track the decay of the excited state over time. Fluorescence spectroscopy involves exciting the PS with a light source and monitoring the luminescence intensity as the excited state returns to the ground state.

Photoluminescence quantum yield

The luminescence quantum yield (Φ) is defined as the number of excited PS that return to the ground state S_0 via photons emission over the total number of photons absorbed by the PS during the same time range. The luminescence quantum yield is related to the different deactivation rate constants (k_r and k_{nr}) and the lifetime (τ) and given by the **Equation 1.16**.

$$\Phi = \frac{k_r}{k_r + k_{nr}} = k_r \tau$$

Equation 1.16

The luminescence quantum yield of a PS can be readily assessed by actinometry measurement. The latter consists in the comparison between the emission intensity at a known absorbance (at a specific irradiation wavelength) of an actinometer with well-known quantum yield and the PS of interest. For a given PS and actinometer, the quantum yield can be obtained from **Equation 1.17**:[50]

$$\Phi_{PS} = \frac{F_{PS}\left(1 - 10^{-A_{Ref}}\right)\eta_{PS}^2}{F_{Ref}\left(1 - 10^{-A_{PS}}\right)\eta_{Ref}^2}\,\Phi_{Ref}$$

Equation 1.17

Where Φ_{PS} and Φ_{Ref} are the luminescence quantum yield of the studied photosensitizer and the reference actinometer, respectively. F_{PS} and F_{Ref} are the integrated intensities (areas) of the photosensitizer and reference actinometer emission spectra, respectively. A_{PS} and A_{ref} are the absorbance of the photosensitizer and reference actinometer (at λ_{exc}), and η_{PS} and η_{Ref} are the refractive indices of the photosensitizer and the reference actinometer solution.[50]

1.3.5 Excited state deactivation by quenching processes

The importance of excited state lifetime

In diffusional bimolecular reactivity, the excited-state lifetime is probably the most critical parameter to consider. The excited-state lifetime is solvent dependent and sometimes concentration dependent and as such, it is thus necessary to measure the excited-state lifetime of the photosensitizers in controlled conditions. Importantly, τ controls the distance that an excited-state is able to migrate in solution before undergoing deactivation. Thus, excited-state lifetimes play a crucial role in the quenching efficiency. The Einstein equation can be used to determine an average distance (Δx) that an excited molecule can travel within its excited-state lifetime (**Equation 1.18**).

$$\Delta x = \sqrt{2D\tau}$$

Equation 1.18

The average distance that an excited state can travel as a function of the excited-state lifetime is given in **Figure 1.5 A** assuming diffusion coefficients (D) that range from 1 to 5 x10^{-5} cm^2 s^{-1}. In this example, it is straightforward to understand why Ru(II) photosensitizers with microsecond excited-state lifetimes have encountered their success in photoredox catalysis. Indeed, a photosensitizer with an excited-state lifetime of 1 μs can migrate up to an average distance of 630 Å, assuming a diffusion coefficient (D) of 2 x10^{-5} cm^2 s^{-1}. Under similar conditions, an iron photosensitizer with an excited-state lifetime of 2 ns would only be capable of travelling over an average distance of 28 Å, thus limiting the number of potential encounters with a quencher. Fluorescent organic photosensitizers, with excited-state lifetimes that typically range between 3 and 20 ns are thus capable of travelling between 35 and 89 Å, assuming a diffusion coefficient of 2 x10^{-5} cm^2 s^{-1}.

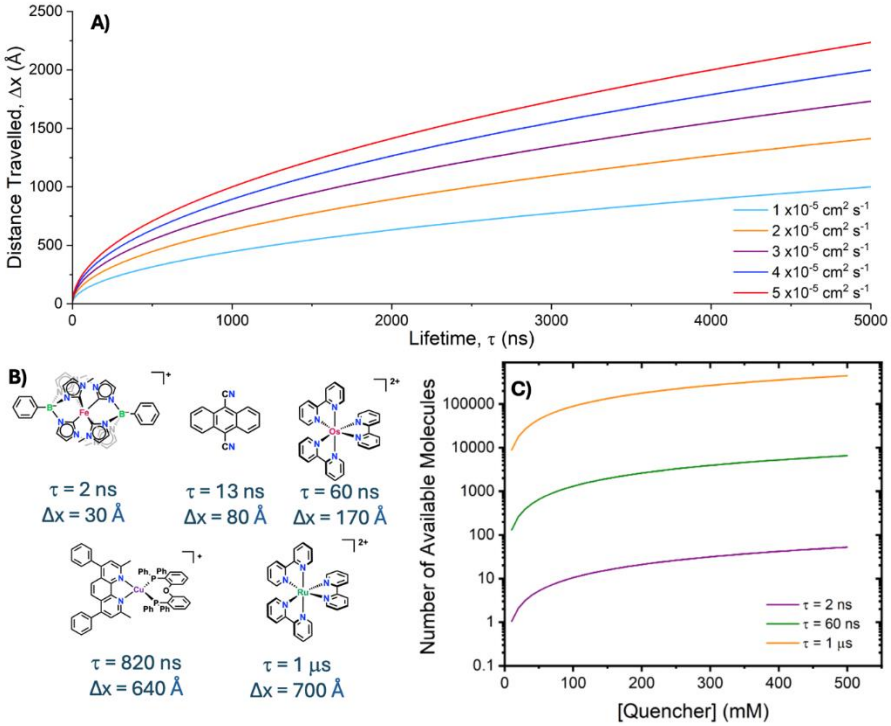

Figure 1.5. Lifetime and concentration effects on possible encounters. A) Average distance travelled according to the excited-state lifetime of the indicated photosensitizer using **Equation 1.18** with diffusion coefficients that ranged from 1 to 5 x10^{-5} cm^2 s^{-1}. B) Structure of representative photosensitizers alongside their excited-state lifetime and distance travelled assuming a diffusion coefficient of 2.5 x10^{-5} cm^2 s^{-1}. C) Number of quencher molecules encompassed within the volume that an excited state can potentially travel through for a diffusion coefficient of 2.5 x10^{-5} cm^2 s^{-1}.

The number of quencher molecules contained within the volume that an excited state can potentially travel through can be crudely estimated assuming an even distribution of quencher molecules at a fixed concentration within the solution. With an excited-state lifetime of around 1 μs, $[Ru(bpy)_3]^{2+}$ (where bpy = 2,2'-bipyridine) can diffuse over a distance of 700 Å in acetonitrile (assuming D = 2.5 x10^{-5} cm^2 s^{-1}). Taking this distance as the maximal radius of a sphere, the corresponding theoretical volume the excited state could potentially explore can be determined. Finally, the number of quencher molecules within that sphere can also be roughly estimated based on Avogadro's number and the concentration of quencher. For the case of $[Ru(bpy)_3]^{2+}$ the excited

complex can potentially diffuse in a volume of 1.44 $x10^{-21}$ m^3 (1.44 $x10^6$ nm^3) and encounter potentially 865 molecules of the quencher for the case of a 1 mM quencher solution (with consequently 6.022 $x10^{23}$ molecules m^{-3}). Unsurprisingly, for an iron photosensitizer with an excited-state lifetime of 2.2 ns, the number of encounters decreases drastically and a concentration of 10 mM is needed to statistically have 1 encounter. A concentration of 250 mM would lead to 26 potential encounters. These theoretical considerations clearly highlight the importance of the excited-state lifetime of the photocatalyst as one key parameter for an efficient catalysis and reasonable long lifetimes are needed to allow efficient diffusional excited-state quenching. In addition, not all encounters introduce excited state deactivation pathways.

Dynamic and static quenching

In the realm of emissive species, “quenching” denotes any process that reduces the radiative quantum yield of a PS. This encompasses various processes, but only a selected few are relevant. Dynamic (or collisional) quenching involves a bimolecular reaction between PS* and Q, while static quenching refers to processes that do not rely on the diffusion of reactants (*e.g.*, pre-association between PS and Q in the ground state). Dynamic quenching can be quantified through time resolved spectroscopic methods, while steady-state techniques (*e.g.*, emission quantum yields) are best suited for detecting static quenching. Employing both methods is essential for a comprehensive understanding of all quenching contributions in a given system. When investigating the interactions between PS* and Q, the Stern-Volmer quenching study, as developed by Otto Stern and Max Volmer in 1919,[51] emerges as a simple and efficient experiment. The latter allows to determine whether a reaction is occurring between PS* and Q. However, it is crucial to emphasize that Stern-Volmer studies offer limited mechanistic insights, except for discerning static versus dynamic quenching contributions (see below). Both energy and electron transfer can involve PS* and yield experimentally indistinguishable results from a Stern-Volmer quenching study. It is only through additional experiments (most notably transient absorption

spectroscopy) that further insight into the exact nature of the reaction mechanism can be studied.[52]

The Stern-Volmer equation is defined as the ratio of the lifetime in the absence (τ_0) and at a given concentration of Q (τ) and is expressed by the **Equation 1.19**.[44] The Stern-Volmer equation can also be formulated in terms of the ratio of emission intensities in the absence (I_0) and at a given concentration of Q (I) (**Equation 1.19**). This equation allows to determine the quenching rate constant (k_q in M^{-1} s^{-1}) of PS* in the presence of Q from the slope of the Stern-Volmer plot (also known as the Stern-Volmer constant (K_{SV} in M^{-1})) (**Figure 1.6**) in the case of pure dynamic quenching.

$$\frac{\tau_0}{\tau} = \frac{I_0}{I} = 1 + \tau_0 k_q [Q] = 1 + K_{SV}[Q]$$

Equation 1.19

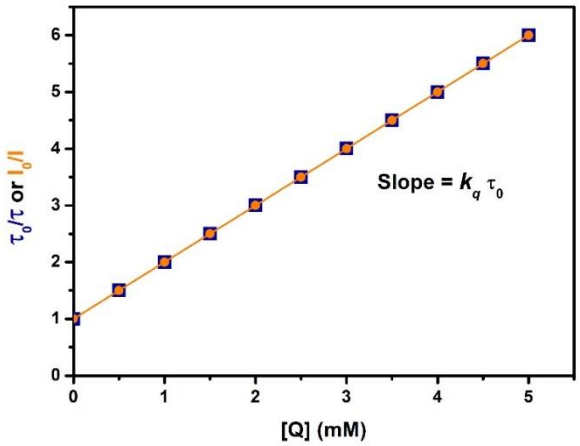

Figure 1.6. Simulated Stern-Volmer plots for τ_0 = 1 μs and k_q = 10^9 M^{-1} s^{-1} for the case of pure dynamic quenching (orange and blue).

However, for a given concentration of Q, a fraction of PS in its ground state can be associated to Q and results in the formation of a PS–Q adduct, which is not luminescent in solution.[53] A quenching in steady-state

photoluminescence, that is larger than the quenching recorded using time-resolved photoluminescence, is thus evidence of static quenching. This process can be characterized by **Equation 1.20**, where K_{ass} is the equilibrium constant of association between PS and Q and is given by **Equation 1.21**. Information about this non-emissive adduct can sometimes be investigated by UV-Visible absorption changes during titrations experiments, or by monitoring the initial amplitude (α) loss of the time-resolved photoluminescence.[41, 54-56] Plots of α_0/α and I_0/I versus the concentration of quencher can provide information about K_{ass}.

$$\frac{\alpha_0}{\alpha} = \frac{I_0}{I} = 1 + K_{ass}[Q]$$

$$PS + Q \rightleftharpoons PS\text{–}Q \qquad\qquad K_{ass} = \frac{[PS\text{–}Q]}{[PS][Q]}$$

Equation 1.20 and 1.21

Interestingly, in the case of a pure static quenching, the relationship between the ratio I_0/I and the quencher concentration [Q] is linear, as in dynamic quenching scenario. However, the ratio τ_0/τ remains constant as a function of [Q] and is equal to one. This constancy arises from the fact that the adduct PS–Q is not luminescent and the unbound PS* in solution has its initial lifetime. Often, a combination of both processes, *i.e.*, static and dynamic quenching takes place. Consequently, a deviation from linearity is observed and the overall process described by **Equation 1.22**[57] and simulated in **Figure 1.7.**

$$\frac{I_0}{I} = (1 + K_{ass}[Q])\left(1 + \tau_0 k_q[Q]\right)$$

Equation 1.22

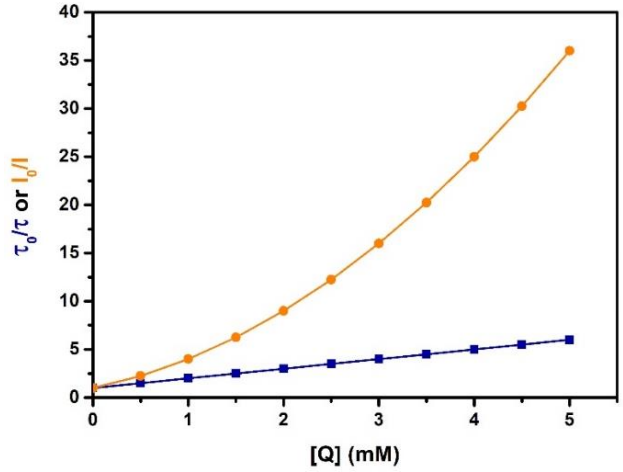

Figure 1.7. Simulated Stern-Volmer plots with K_{ass} = 10^3 M^{-1}, τ_0 = 1 μs and k_q = 10^9 M^{-1} s^{-1} for the combination of a dynamic and static quenching process (orange curve: steady-state luminescence response upon increased quencher concentration and blue curve: luminescence lifetime response upon increased quencher concentration).

Importantly, as previously mentioned in this section, whereas a decrease in photoluminescence indicates an excited-state quenching process, it does not inform on the exact nature of the quenching mechanism, *i.e.*, electron and/or proton transfer, energy transfer, change in non-radiative rate constants, etc., which can only be investigated by more sophisticated time-resolved techniques such as transient absorption spectroscopy.[52, 58]

1.3.6. Excited state reaction and mechanism, energy and electron transfer

As described in the previous section, the lifetime of the lowest-energy excited state controls the distance that an excited state is able to travel before undergoing deactivation. Thus, excited-state lifetimes play a crucial role in the quenching efficiency. Amongst the different excited-state quenching mechanism, two main deactivation process are often proposed, *i.e.* electron transfer and energy transfer. Each process can be divided into an additional two subcategories, i.e. Förster or Dexter energy transfer (**Figure 1.8**) as well as oxidative or reductive electron transfer (**Figure 1.9**). These two processes will be further described in the following sections.

Energy transfer

Energy transfer is a process in which the excited state of a photosensitizer (PS*) is deactivated to the ground state by transferring its energy to a second molecular entity called the energy acceptor (EnA). The energy transfer processes are classified into two categories: the radiative and the non-radiative energy transfer.

In radiative energy transfer, a photosensitizer in its excited state (PS*) can return to its ground state by emitting a photon, which may then be absorbed by surrounding EnA molecules. This process is then occurring without direct interaction between the molecules involved and maintains the lifetime of PS* unaltered. The efficiency of this energy transfer rely on the overlap between the emission spectrum of PS* and the absorption spectrum of EnA, the concentration of EnA, and the optical path of the emitted photons.[59]

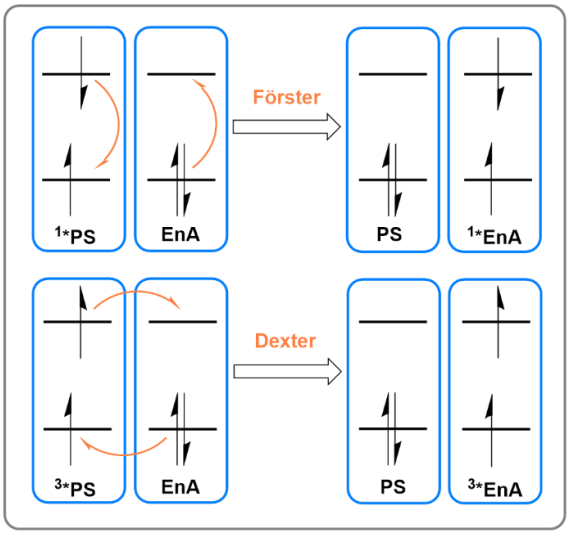

Figure 1.8. Excited-state quenching of an excited photosensitizer (PS*) via energy transfer to an energy acceptor (EnA).

In contrast to radiative energy transfer, non-radiative energy transfer involves interaction between the two components and results in a decrease of the PS* lifetime. These interactions, which may arise from coulombic forces or

intermolecular orbital overlap, correspond to two distinct mechanisms known as Förster Resonance Energy Transfer (FRET) and Dexter energy transfer, respectively (**Figure 1.8**).

FRET involves energy transfer through a coulombic mechanism. This process is driven by the interaction between the transition dipole moments of the excited-state of the PS and the EnA. Important feature for efficient Förster energy transfer includes a degree of spectral overlap between the emission of the energy donor and absorbance of the energy acceptor as well as a marked distance dependence in r^{-6} for the FRET rate constant k_{FRET}.[60] In contrast to the second energy transfer process discussed hereafter, it is important to notice that FRET does not include any exchange of electrons between the donor and acceptor and leads to spin-allowed transitions.

On the other hand, in a Dexter energy transfer (bottom part in **Figure 1.8**) the mechanism operates by the concomitant exchange of two electrons between the excited-state PS and the EnA.[61] It is worth emphasizing that an energy donor in a triplet state can only undergo energy transfer with singlet state ground state by Dexter energy transfer due to Wigners' spin conservation rule. Consequently, for processes relying on sensitized energy transfer from triplet state, Dexter energy transfer is the only relevant process.[62-65]

Electron transfer

Overall, upon irradiation, a photosensitizer becomes a better electron donor (reductant) and acceptor (oxidant). This phenomenon, depicted in **Figure 1.9**, results from the excess energy stored in the excited state due to the energy difference between the ground state and the excited state (E_{00}), both being in their 0th vibrational energy level. The excited-state oxidation and reduction potential can be estimated by the Rehm-Weller equations[66, 67], in which E_{red}* and E_{ox}* stand for the excited-state reduction and oxidation potentials, respectively, while $E_{1/2}$ ($PS^{(n/n-1)}$) and $E_{1/2}$ ($PS^{(n+1/n)}$) are the ground-state reduction and oxidation potentials.

$$E^*_{Red} \; or \; E_{1/2}(PS^{*(n/n-1)}) = E_{1/2}(PS^{(n/n-1)}) + E_{00}$$

$$E^*_{Ox} \; or \; E_{1/2}(PS^{*(n+1/n)}) = E_{1/2}(PS^{(n+1/n)}) - E_{00}$$

Equations 1.23 and 1.24

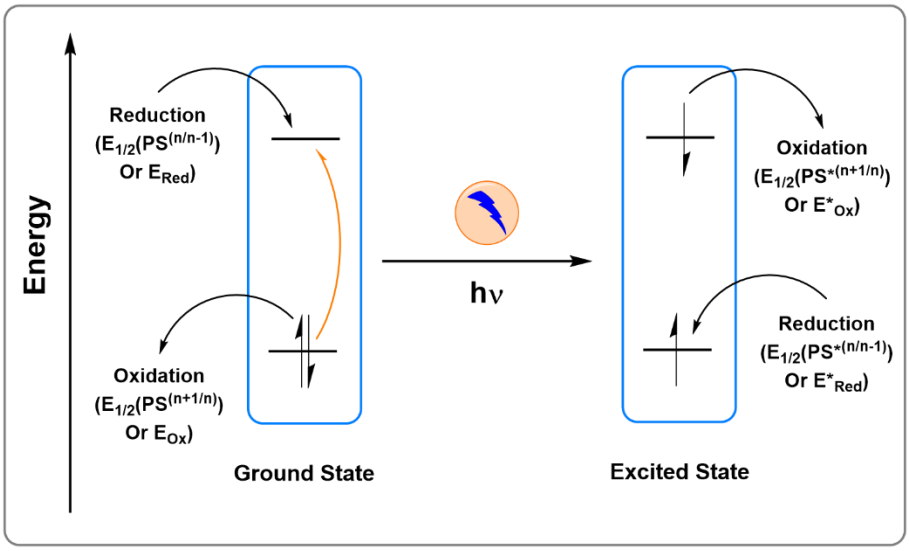

Figure 1.9. Illustration of the oxidizing and reducing power enhancement for a given photosensitizer upon light excitation.

As mentioned previously, excited-state quenching via electron transfer can operate according to two mechanisms: reductive or oxidative excited-state quenching.[68] In an oxidative quenching cycle, a suitable electron acceptor (EA) accepts an electron from the excited photocatalyst, which yields a reduced electron acceptor and an oxidized photocatalyst (top part of **Figure 1.10**). In contrast, with a suitable electron donor (ED) that can provide an electron to the photocatalyst in its excited state, a reductive quenching pathway is possible which results in an oxidized electron donor and a reduced photocatalyst (bottom part in **Figure 1.10**).

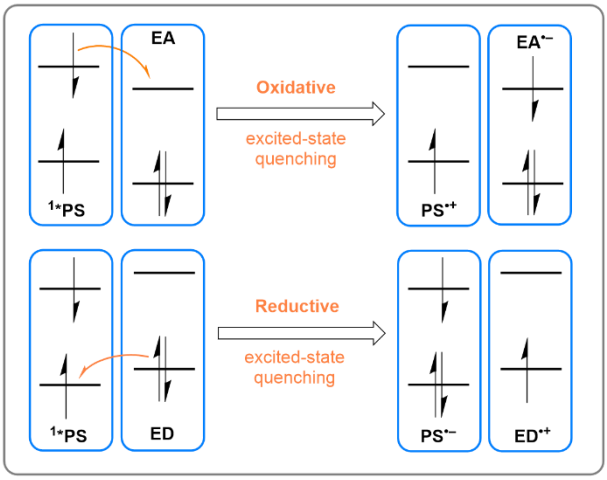

Figure 1.10. Excited-state quenching of an excited photosensitizer (PS*) via electron transfer to an electron donor (ED) or electron acceptor (EA).

The estimated excited-state potentials of the photosensitizer can be utilized in a given polar solvent to evaluate the change in standard Gibbs energy for a photoinduced electron transfer between an electron acceptor and an electron donor (either one of them may be electronically excited) of any charge type, *z*(EA) and *z*(ED) using **Equation 1.25**[69]:

$$\Delta G^0_{et} = N_A \left(e \left(E^0_{ED^{\bullet+}/ED} - E^0_{EA/EA^{\bullet-}} \right) + w(ED^{\bullet+}\, EA^{\bullet-}) - w(ED\, EA) \right) - E_{00}$$

Equation 1.25

Where e is the elementary charge, N_A the Avogadro constant, $E^0(ED^{\bullet+}/ED)$ is the standard electrode potential of the oxidized electron donor resulting from the electron transfer, $E^0(EA/EA^{\bullet-})$ is the standard electrode potential of the acceptor (both in V *vs* the same reference electrode) and E_{00} is the energy associated to the 0–0 transition. *w* ($ED^{\bullet+}$ $EA^{\bullet-}$) (**Equation 1.26**) and *w* (ED EA) (**Equation 1.27**) are the electrostatic work terms that account for the potential Coulombic attraction/repulsion between the two charged species (geminate radical pair) formed during the photoredox reaction[69]:

$$w(ED^{\bullet+}\ EA^{\bullet-})/J = \frac{z(ED^{\bullet+})\ z(EA^{\bullet-})\ e^2}{4\ \pi\ \varepsilon_0\ \varepsilon_r\ a}$$

$$w(ED\ EA)/J = \frac{z(ED)\ z(EA)\ e^2}{4\ \pi\ \varepsilon_0\ \varepsilon_r\ a}$$

Equations 1.26 and 1.27

The term a represents the distance between the charged species after electron transfer, ε_r is the relative medium dielectric constant, ε_0 is the electric constant (vacuum permittivity), and *z*(X) is the charge of the species X. For the case of neutral species EA and AD, z(EA) = z(ED) = 0. In polar solvents such as water or acetonitrile, which have high dielectric constant, the electrostatic work terms are significantly smaller than *E* and can therefore be neglected.[70]

1.3.7 Experimental identification of the excited state reaction mechanism

As detailed in the previous section, the two dominant operative quenching mechanisms in photoredox catalysis are electron and energy transfer. In the case of energy transfer, the photosensitizer PS will return to its ground state while producing an excited energy acceptor, which could subsequently emit a photon. Therefore, the energy transfer mechanism can be experimentally observed using steady-state or time-resolved photoluminescence spectroscopy. This is indicated by a decrease in the initial photoluminescence intensity or excited-state lifetime of the photosensitizer, as well as the appearance of a new emission band belonging to the energy acceptor.[71, 72] Although the observation of energy transfer mechanisms may seem straightforward, it is often challenging to detect them depending on the analysed system.[73]

In the case of electron transfer, oxidative and reductive quenching are both possible, resulting in the formation of the oxidized or reduced photosensitizer (concomitantly with the reduced or oxidized substrate). The direct observation of these products is then of paramount interest in the field of photochemistry as it allows to decipher the mechanistic pathways in photo-induced catalytic reactions.

Transient absorption spectroscopy

A typical transient absorption set-up is composed of two main components (**Figure 1.11**). An excitation part that contains the excitation laser and the optics required to convey light to the sample and a detection unit composed of a light source that probes the sample and is collected by a detector. The wavelength of the excitation laser can be tuned to finely excite the system of interest, while the light probe is usually a broad-band spectrum source. While transient absorption probing is commonly performed by UV-Visible light, other region of the electromagnetic spectrum can be used including infrared radiation[74, 75] and X-rays[76-78]. It is also important to mention that other more specific spectroscopic techniques (such as laser pulse radiolysis[79], photo-

induced dynamic nuclear polarization[80], time-resolved Raman spectroscopy[81] and time-resolved dielectric loss spectroscopy[82]) can also be employed for the investigation of light-induced transformations and photoredox catalysis applications.

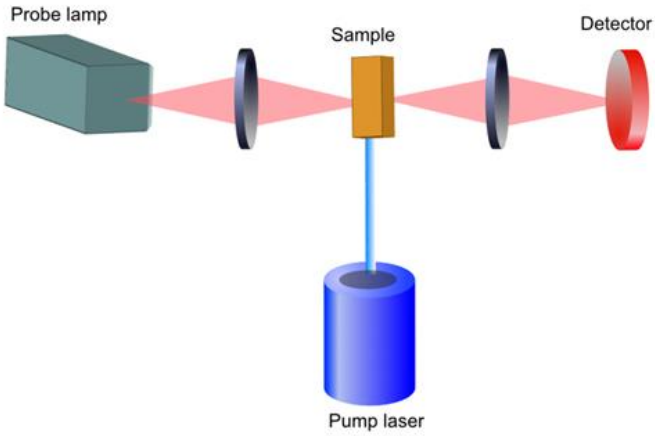

Figure 1.11. General representation of a transient absorption experimental set-up.

UV-Visible transient absorption spectroscopy likely represents the most prominent technique to study reaction intermediates and unravel important mechanistic details. It is part of the pump-probe techniques, in which a sample is illuminated with a laser pulse (the pump) leading to the formation of an excited state. An analytical lamp (the probe) then records an absorption spectrum as a function of time, usually from the fs up to seconds time range, depending on the apparatus. The absorption signal is then compared to a signal without laser illumination and a difference spectrum allows to obtain the changes in absorption before and after pulsed light irradiation (**Figure 1.12**).[83-88] This technique provides UV-Visible absorption spectra of the excited state and the UV-Visible absorption spectra of key intermediates if the excited photosensitizer reacts with a quencher. If the UV-Visible absorption spectra of the oxidized and reduced species are known, it is also possible to determine the nature of the operative quenching mechanism, *i.e.,* whether the light-induced reaction proceeds via oxidative or reductive quenching or via energy transfer. In the case of an energy transfer mechanism, the formation of the

excited state of the EnA can be monitored and then demonstrate the consumption of the EnD excited state leading to the excitation of the EnA.[89]

The direct observation of photoproducts and their evolution over time is a clear advantage of UV-Visible nanosecond transient absorption spectroscopy. Even more importantly, if the formation or consumption of products/reactants can be monitored at specific wavelengths, it is possible to gain access to the kinetic rate constants for any given process. Single wavelength absorption changes can be fitted to obtain the corresponding observed rate at a given concentration. By plotting the observed rates obtained at different concentration as a function of quencher concentration, one can obtain the corresponding kinetic rate constants.

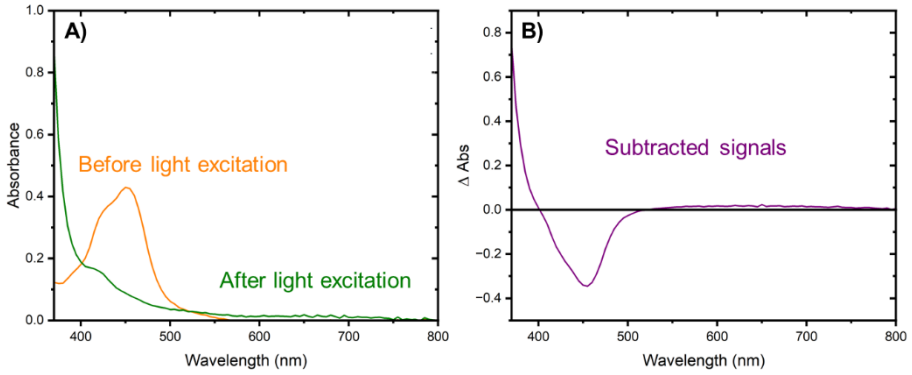

Figure 1.12. A) Absorption spectra of $[Ru(bpy)_3]^{2+}$ (bpy = 2,2'-bipyridine) before and after light excitation. B) Representation of the transient absorption signal.

Transient absorption spectroscopy is often combined with spectroelectrochemistry (SEC) or photolysis experiments in the presence of a sacrificial electron donor or acceptor[90] to identify the species involved in light-induced reaction mechanism. This technique combines advantages of both electrochemistry and steady-state spectroscopy to provide simultaneous characterization of redox potential and the corresponding spectroscopic spectra of the oxidized and reduced species. This approach can be combined to several spectroscopic techniques (UV-vis, NIR, IR, Raman, EPR…) although most examples are reported using UV-Vis and NIR spectroscopy. [91-

[110] SEC is often used as one of the first step in mechanistic investigations as it can be performed on photosensitizers or reactants in solution. SEC can therefore provide essential information on the spectroscopic properties of reaction intermediates produced during photoredox catalysis. For example, SEC can be used to determine the absorption spectra and the corresponding molar absorption coefficient of any reduced or oxidized species (photocatalyst/electron donor/reagents) that could be formed during the reaction, if they are electrochemically stable. These spectra can then be correlated to transient absorption data to determine the nature of key intermediates involved in a photoredox catalytic process.

1.3.8 Cage escape following excited state electron transfer

Immediately after electron transfer, the charge-separated state, *i.e.* the reduced/oxidized photosensitizer and the oxidized/reduced quencher are still intimately enclosed within a solvent cage. For any photoredox catalytic reaction to be efficient, these species must undergo a process called "cage escape", *i.e.* they must escape the solvent cage and create at least one new solvation layer around them. This process was first introduced in 1934 by Franck and Rabinowitsch[111, 112] but was only experimentally verified several years later by Lyon and Levy that performed crossover experiments using mixtures of azomethane and per-deuterated azomethane in the gas phase and in isooctane solution (**Figure 1.14**).[113]

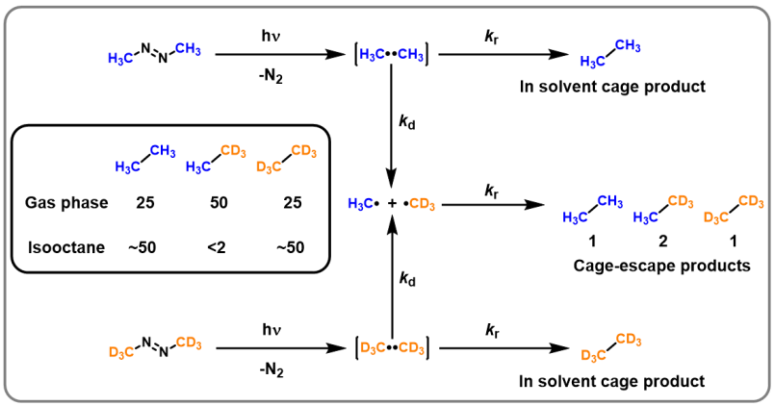

Figure 1.14. Experimental evidence of the cage escape effect through crossover experiments in which equal concentrations of azomethane and perdeutero azomethane were photoexcited.

Photolysis of the azomethane derivatives in the gas phase generated an almost perfect 1:2:1 statistical distribution of CH_3CH_3, CH_3CD_3 and CD_3CD_3, respectively. This result pointed towards that a statistical number of $CH_3^{\bullet}$ radicals "crossed over" and reacted with $CD_3^{\bullet}$ radicals generated from a different azomethane molecule. On the other hand, photolysis in isooctane solutions produced almost exclusively the in-cage recombination products, CH_3CH_3 and CD_3CD_3. These results highlighted that the isooctane solvent molecules trapped the photogenerated methyl radicals, therefore preventing their escape and making bimolecular reactivity nearly impossible.

As of today, there is no clear theory that allows to describe the cage escape process and to predict the corresponding yields (Φ_{CE}). In addition, the factors that impact Φ_{CE} are not well-defined and correlations have been established with parameters such as solvent polarity and viscosity,[114-118] the driving force for electron transfer,[119, 120] the spin states[115, 116, 121-124] as well as ionic strength effects.[117, 118, 121, 125] and all the possible impacts of these factors have recently been reviewed.[126] We believe it is however of paramount importance to first understand and subsequently ideally control these cage escape yields as they have been shown to ultimately impact the overall yields of photoredox catalysis reactions.[74, 75, 127]

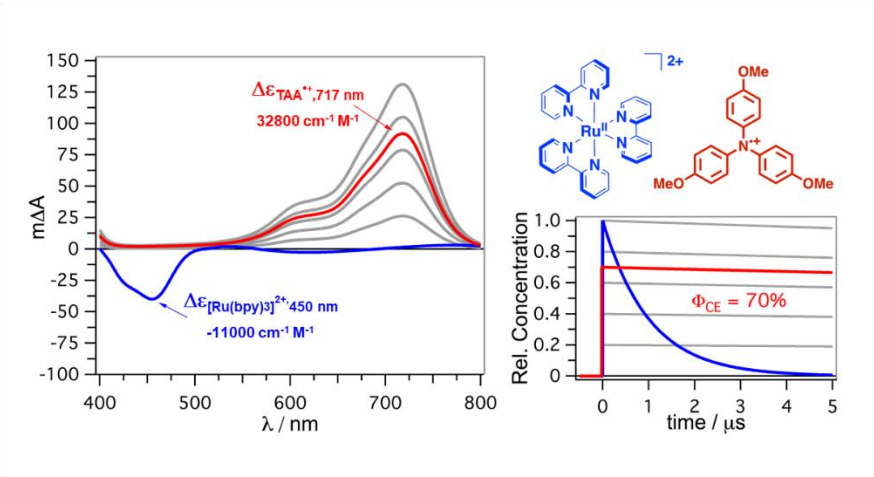

Figure 1.15. Left: Simulated transient absorption spectra showing the changes in absorption corresponding to the absorption of oxidized tri-*p*-anisylamine ($TAA^{\bullet+}$) alongside the changes of absorption of the $[Ru(bpy)_3]^{2+}$ actinometer (blue). Right: Relative concentration of $TTA^{\bullet+}$ based on the ΔA changes recorded at 717 nm and the bleach caused by the excited-state of $^{3*}[Ru(bpy)_3]^{2+}$ (blue) at 450 nm. The traces for the relative concentrations with a cage escape yield calculated based on the respective extinction coefficients[128-132] for the formation of $TAA^{\bullet+}$ between 0 and 100% are provided in gray and the simulated spectrum and kinetic trace for isoabsorptive solutions with 70% is highlighted in red.

Nowadays, these cage escape yields are straightforwardly measured by comparative actinometry techniques using **Equations 1.28** and **1.29**, developed for a reductive quenching process in the present case. In these equations, the absorption changes (ΔA_{PS}) generated from the oxidized PS ($PS^{\bullet+}$) or reduced PS ($PS^{\bullet-}$) are compared with the absorption changes of the

excited state of a reference actinometer (ES_{Ref}) and normalized by their relative absorptances ($1\text{-}10^{-A_{Ref}}$ and $1\text{-}10^{-A_{PS}}$, where A is the ground-state absorbance at the excitation wavelength (λ_{exc})). The change in molar extinction coefficient ($\Delta\varepsilon$) for the actinometer are known from the literature in some cases or can be determined by variable power excitation measurements using transient absorption measurements, whereas the $\Delta\varepsilon$ values of the oxidized or reduced photosensitizers can be determined by photolysis,[90] spectroelectrochemistry[133] or using transient absorption spectroscopy with reference electron acceptor/donors.[134, 135] It is important to determine the changes in extinction coefficient in the same solvent in which the reaction is performed as some species can undergo large changes in molar extinction coefficient depending on the solvent.

$$\Phi_{CE} = \frac{\Phi}{\%\ PL\ Quenched}$$

$$\Phi = \left(\frac{\frac{\Delta A_{PS^-}}{\Delta\varepsilon_{PS^-}}}{\frac{\Delta A_{ES_{Ref}}}{\Delta\varepsilon_{ES_{Ref}}}}\right)\left(\frac{1-10^{-A_{Ref}(\lambda_{exc})}}{1-10^{-A_{PS}(\lambda_{exc})}}\right) = \left(\frac{\Delta[PS^-]}{\Delta[ES]_{Ref}}\right)\left(\frac{1-10^{-A_{Ref}(\lambda_{exc})}}{1-10^{-A_{PS}(\lambda_{exc})}}\right)$$

$$\Phi = \left(\frac{\frac{\Delta A_{PS^-}}{\Delta\varepsilon_{PS^-}}}{\frac{\Delta A_{ES_{Ref}}}{\Delta\varepsilon_{ES_{Ref}}}}\right) = \left(\frac{\Delta[PS^-]}{\Delta[ES]_{Ref}}\right) \text{ for isoabsorptive solutions}$$

Equations 1.28, 1.29 and 1.30

Final Φ_{CE} values are obtained by comparing the relative yield of $PS^{\bullet+}$ or $PS^{\bullet-}$ produced (Φ) to the percentage of quenched photoluminescence (%PL), determined via time-resolved or steady-state measurements. A linear regression of all data points by constraining the Y-intercept at 0 provides a slope that corresponds to the cage escape yield value.[75, 97] Alternative methods consist in using isoabsorptive solutions of photosensitizer and

actinometer, thereby simplifying **Equation 1.29** into **Equation 1.30**, or determining Φ_{CE} at high concentration of quencher where almost all of the excited states are quenched. Whereas this approach is appropriate, there are some instances where cage escape yields decrease at high quencher concentration, either due to kinetic salt effects or due to the fact that the quencher becomes part of the cage.[136] **Figure 1.15** illustrates a possible spectroscopic measurement for the determination of relative concentrations of an oxidized triarylamine derivative with a high extinction coefficient ($\Delta\varepsilon$ = 32800 $M^{-1}cm^{-1}$ in acetonitrile) and $[Ru(bpy)_3]^{2+}$ as reference actinometer ($\Delta\varepsilon$ = –11000 $M^{-1}cm^{-1}$ in acetonitrile).[128-132] For isoabsorptive solutions the relative concentration of both spectroscopic signals can be calculated to determine the cage escape yield using **Equations 1.28** and **1.30**.

1.4 Transition metal-based photosensitizers

1.4.1 Ruthenium and Osmium polypyridine complexes

Photoredox catalysis has become increasingly important in recent years in various fields of chemistry and research applications that take advantage of light as an energy source. In this context, ruthenium (II) and osmium (II) polypyridine complexes attracted attention in the 1950s, both for their chemical stability, redox properties, excited-state reactivity and lifetime.[137-139] Among these luminescent complexes, the most famous example is probably the prototypical $[Ru(bpy)_3]^{2+}$ photosensitizer (**Figure 1.16**), where bpy is 2,2'-bipyridine, that was initially reported by F. H. Burstall in 1936.[140] Their success as photosensitizers in the field of light-induced transformation originated from their relatively easy preparation, the possibility to efficiently tune the ground and excited-state properties,[141-143] and the possibility to access homoleptic and heteroleptic complexes with different scaffolds in a comparably small number of steps.[144]

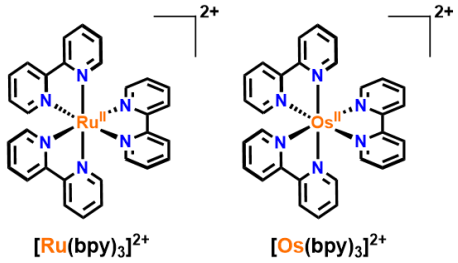

Figure 1.16. Structures of the prototypical $[Ru(bpy)_3]^{2+}$ and $[Os(bpy)_3]^{2+}$.

This is also reflected by recent reports of ruthenium-based polypyridyl complexes, among others, for light-driven catalysis,[145] multi-photon catalysis,[146, 147] solar cells,[148] anticancer treatement[149] like photodynamic therapy.[150] Osmium-based derivatives have also been investigated in the 70s and 90s as well as in recent years, for example in sensitized triplet-triplet annihilation upconversion,[151, 152] (metallo)photoredox catalysis,[153, 154] multi-photon catalysis,[155, 156] energy harvesting and storage[157, 158] or photodynamic therapy.[159, 160] This versatility in the use of Ru(II) and Os(II) photosensitizers is also strengthened by findings gained using novel spectroscopic techniques

or new reaction concepts and methodologies that have allowed to further broaden the scope of light-induced reactivities.[58, 156, 161, 162]

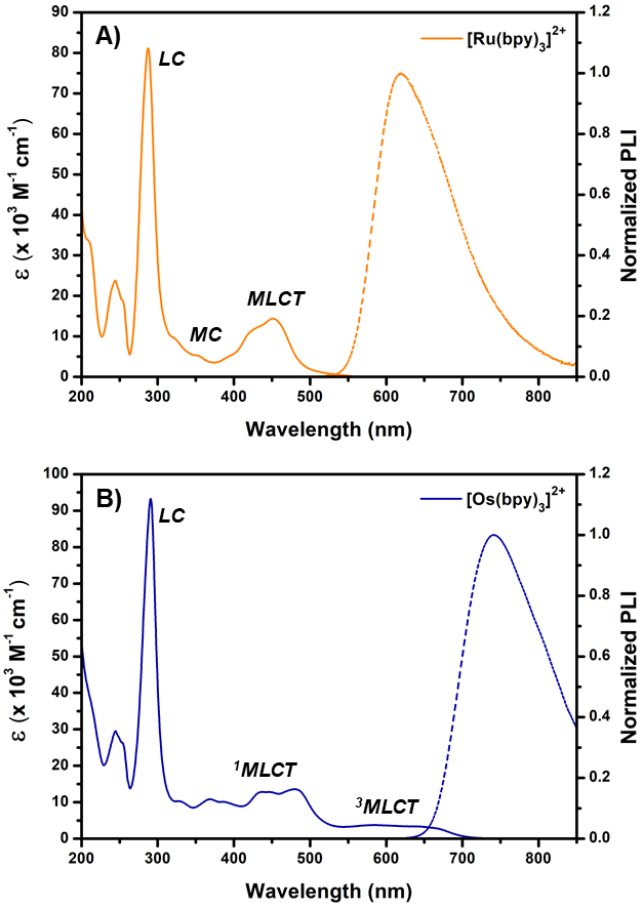

Figure 1.17. UV-visible absorption and photoluminescence spectra of A) $[Ru(bpy)_3]^{2+}$ and B) $[Os(bpy)_3]^{2+}$ recorded at room temperature in argon purged acetonitrile.

$[Ru(bpy)_3]^{2+}$ and $[Os(bpy)_3]^{2+}$ exhibit strong absorption spectra that span over a broad range of visible light (**Figure 1.17**). Moreover, these photosensitizers display absorption features that are typical for these transition metal complexes, namely absorption bands in the UV region attributed to ligand centred (LC) transitions, slightly less energetic transition associated to metal centred (MC) transitions and broad absorption bands in the visible part of the spectra attributed to metal-to-ligand charge transfer (MLCT) transitions

(**Figure 1.18 A**).[52] $[Ru(bpy)_3]^{2+}$ absorbs light intensively around 450 nm ($\varepsilon_{450\ nm} \approx 14500\ M^{-1}\ cm^{-1}$) corresponding to the MLCT transition. $[Os(bpy)_3]^{2+}$ also absorbs light intensively in the visible range around 480 nm ($\varepsilon_{480\ nm} \approx 13500\ M^{-1}\ cm^{-1}$). This transition corresponds to ^{1}MLCT transition, whereas transitions assigned to the direct excitation of the broad ^{3}MLCT band occur at around 590 nm ($\varepsilon_{590\ nm} \approx 3700\ M^{-1}\ cm^{-1}$).[163] These transitions are observable for Os(II) photosensitizers, but not for the Ru(II) analogues, due to the increased spin-orbit coupling afforded by the Os(II) metal center.[164] Visible light excitation of these Ru(II) and Os(II) photosensitizers led to photoluminescence with maxima centered at 620 nm for $[Ru(bpy)_3]^{2+}$ and was further red-shifted to 742 nm for $[Os(bpy)_3]^{2+}$ with associated excited-state lifetime of 884 ns and 54 ns, respectively.[163] This is in line with the smaller HOMO-LUMO gap in $[Os(bpy)_3]^{2+}$ compared to $[Ru(bpy)_3]^{2+}$ (**Figure 1.18 B**).

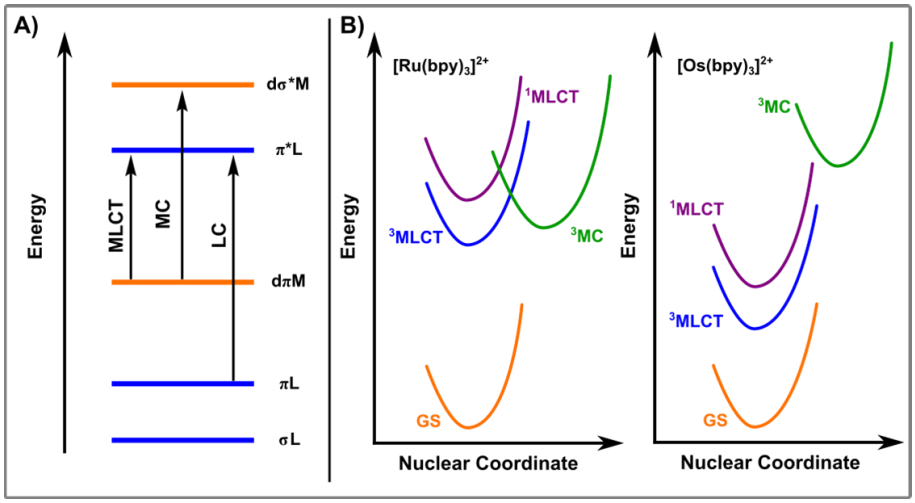

Figure 1.18. A) Simplified molecular orbital diagram for $[Ru(bpy)_3]^{2+}$ and $[Os(bpy)_3]^{2+}$, dσ*, π*, dπ, π and σ stand for the nature of the molecular orbital involved. B) Potential-well diagram of $[Ru(bpy)_3]^{2+}$ and $[Os(bpy)_3]^{2+}$.

Interestingly, as depicted in **Figure 1.18 B** Os(II) photosensitizers, unlike certain Ru(II) analogues, do not cross to the ^{3}MC state, which is often considered too high in energy to be reached at room temperature.[165, 166] This ^{3}MC excited state is often associated with ligand-loss chemistry, which occurs

via non-radiative process accounting for the overall greater photostability of Os(II) photosensitizers compared to Ru(II) photosensitizers.[155, 167]

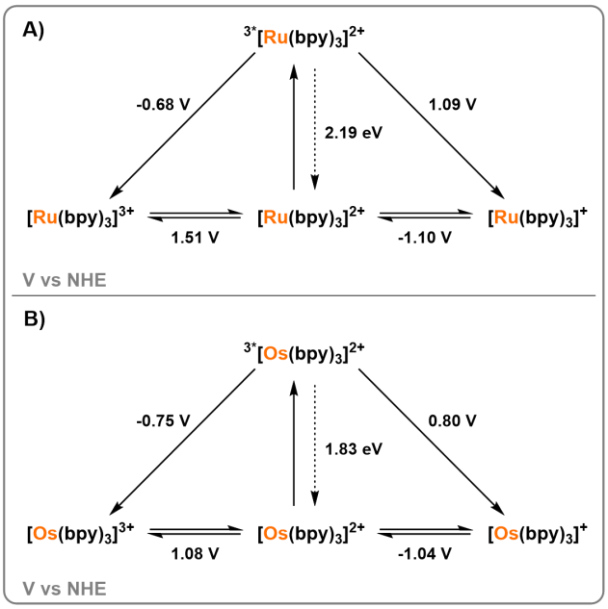

Figure 1.19. Latimer diagram for A) $[Ru(bpy)_3]^{2+}$ and B) $[Os(bpy)_3]^{2+}$.

The lowest ^{3}MLCT excited state of $[Ru(bpy)_3]^{2+}$ and $[Os(bpy)_3]^{2+}$ lives long enough to perform diffusional bimolecular reactivity and possesses suitable properties to act as either an energy or an electron donor or acceptor. As depicted in **Figure 1.19** the energy available to $*[Ru(bpy)_3]^{2+}$ and $*[Os(bpy)_3]^{2+}$ are 2.19 eV and 1.83 eV, respectively. Moreover, as mentioned in **Section 1.3.6**, upon light excitation, the photosensitizers will become a better electron donor (reductant) and acceptor (oxidant). For $*[Ru(bpy)_3]^{2+}$, the reduction and oxidation potentials are +1.09 V and –0.68 V *vs* NHE. In the case of $*[Os(bpy)_3]^{2+}$ the reduction and oxidation potentials are +0.80 V and –0.75 V *vs* NHE.[163] Interestingly, the ground and excited-state oxidation and reduction potential of Ru(II) and Os(II) photosensitizers can be tuned by adding electron withdrawing or donating substituents on the bpy ligand or by altering its π-conjugation. This molecular design allows to control the frontier orbital energy and optimize the properties of the photosensitizer for a given photocatalytic process. **Figure 1.20** illustrates in a simplified way the separate effects on the

HOMO and LUMO energy levels and their relationship to the excited-state reducing and oxidizing power. However, it is rarely feasible to independently control the HOMO or LUMO energy levels.

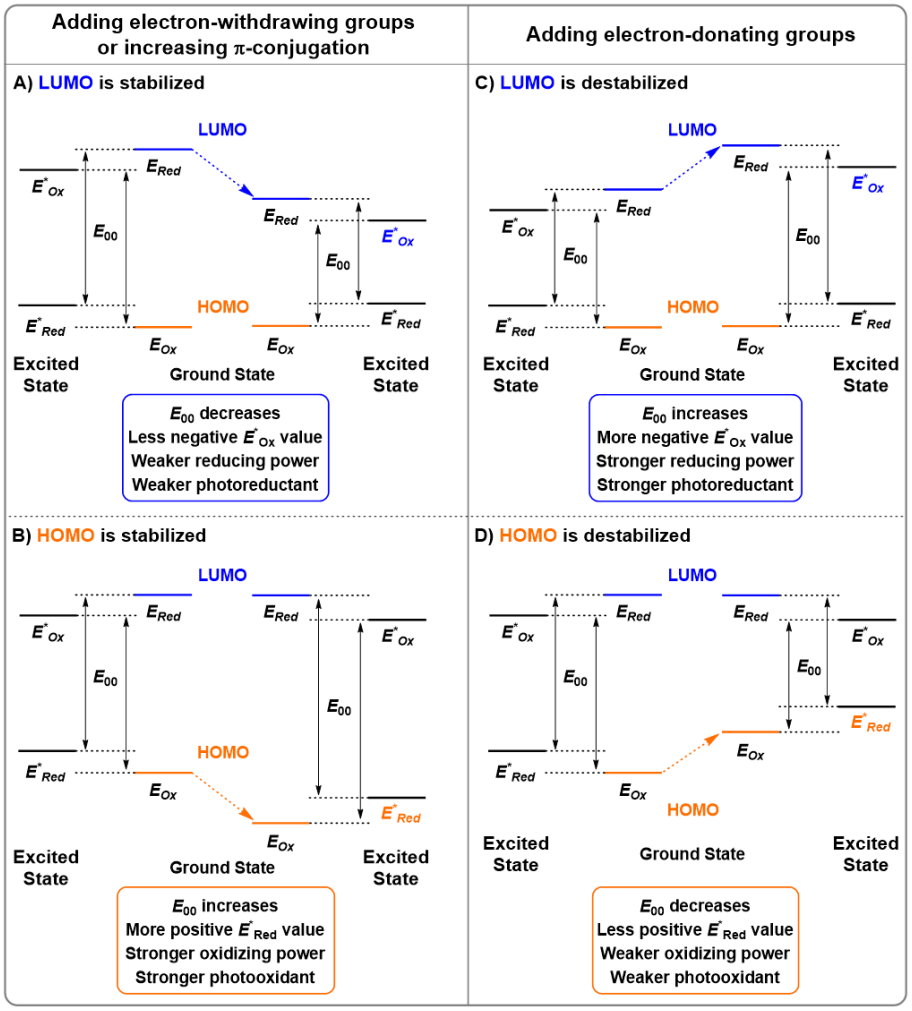

Figure 1.20. Possible strategies to control ground- and excited-state redox properties of metal-based photosensitizers.

Introducing electron-withdrawing groups or extending the π-conjugation stabilizes the HOMO and/or LUMO energy levels (**Figure 1.20 A and B**). If the LUMO is stabilized, E_{00} is decreased, resulting in a less negative E_{ox}*. Conversely, stabilizing the HOMO results in a more positive E_{red}*, enhancing

the excited-state oxidizing power. Introducing electron-donating group generally destabilizes the HOMO and/or the LUMO levels (**Figure 1.20 C and D**). Destabilizing the LUMO increases the HOMO-LUMO gap and E_{00}, leading to a more negative E_{ox}* making the photosensitizer a stronger photoreductant. If the HOMO is destabilized, E_{00} decreases, resulting in a less positive E_{red}* indicating weaker oxidizing power in the excited state. Typically, both the HOMO and LUMO are affected by the addition of substituent or alteration of the conjugation, so the observed effects on E_{00} and excited-state potential depend on which frontier orbital is more significantly influenced by the chemical modification.[168]

1.4.2 Cyclometalated Iridium complexes

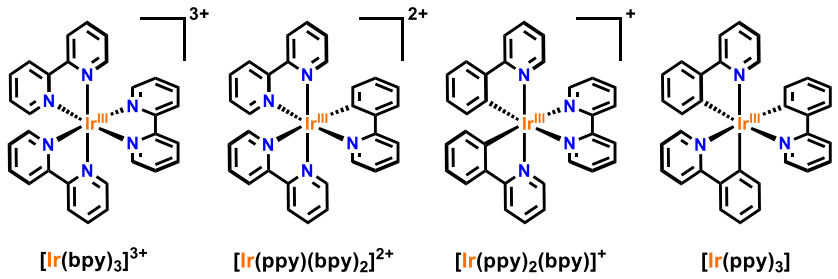

Figure 1.21. Structures of the Ir(III) complexes with different C/N ratio.

Alongside the Ru(II) and Os(II) photosensitizers, Ir(III)-based compounds have emerged as promising candidates for applications in lighting devices,[169, 170] life sciences[171-173], photoredox catalysis[89, 174-178] and solar fuels production.[36, 37, 42, 179-183] As for Ru(II) and Os(II) complexes, Ir(III) photosensitizers success relies on key features such as a relatively long-lived excited states and extraordinary photo- and redox stability. Moreover, what makes Ir(III) complexes particularly noteworthy is their ability to accommodate up to three cyclometalated bonds (Ir–C), which significantly enhances the tunability of their optoelectronic properties. This versatility is especially evident in the $[Ir(ppy)_x(bpy)_{3-x}]^{(3-x)+}$ series (ppy = 2-phenylpyridine, bpy = 2,2'-bipyridine), where x ranges from 0 to 3 (**Figure 1.21 and Table 1.2**).

Table 1.2. Electrochemical and spectroscopic data for $[Ir(ppy)_x(bpy)_{3-x}]^{(3-x)+}$.

	$E(Ir^{IV/III})$[a]	$E(L^{n/n-1})$ [a]	λ_{abs} [nm][b] (ε [$M^{-1}cm^{-1}$])	λ_{PL} [nm] RT[c]	Ref.
fac-$[Ir(ppy)_3]$	+1.01	–1.95	375 (7200)	517	184, 185
$[Ir(ppy)_2(bpy)]^+$	+1.56	–1.16	410 (2800)	587	184, 186
$[Ir(ppy)(bpy)_2]^{2+}$	+2.29	–0.96	390 (2800)	507	184, 186
$[Ir(bpy)_3]^{3+}$	+2.34	–0.86	344 (3300)	452	184, 187

[a] V *vs* NHE in acetonitrile (adapted from the original work where necessary, $V_{NHE} = V_{SCE} + 0.24$ V, $V_{NHE} = V_{Fc+/0} + 0.64$ V). [b] In MeOH at room temperature. [c] In acetonitrile at room temperature.

In this Ph.D. thesis, we will specifically focus on bis-cyclometalated Ir(III) complexes (IrC_2N_4). Depending on the arrangement and the chemical structure of the three bidentate ligands, several optical isomers (Λ and Δ enantiomers; *fac* and *mer* diastereoisomers) can be formed. However, because the electrochemical and photophysical properties of these stereoisomers are identical, racemic mixtures have been used throughout this Ph.D. work**.** As for the Ru(II) and Os(II) complexes, spectroscopic and electrochemical properties of these complexes can be further controlled by the same strategies developed in **Figure 1.20.** IrC_2N_4 complexes probably represent the most extensively studied class of iridium complexes because of their broad range of accessible ground- and excited-state redox potentials. These complexes have been utilized in various applications, including CO_2 and proton reduction,[37, 180, 183, 188, 189] halide oxidation,[42, 179] dye-sensitized solar cells,[190] and bio sensing.[191]

Upon photon absorption by an IrC_2N_4 complex, an electron is promoted from a filled molecular orbital to an empty one. Depending on the nature of the involved molecular orbitals, various electronic transitions can be identified (**Figure 1.22**).

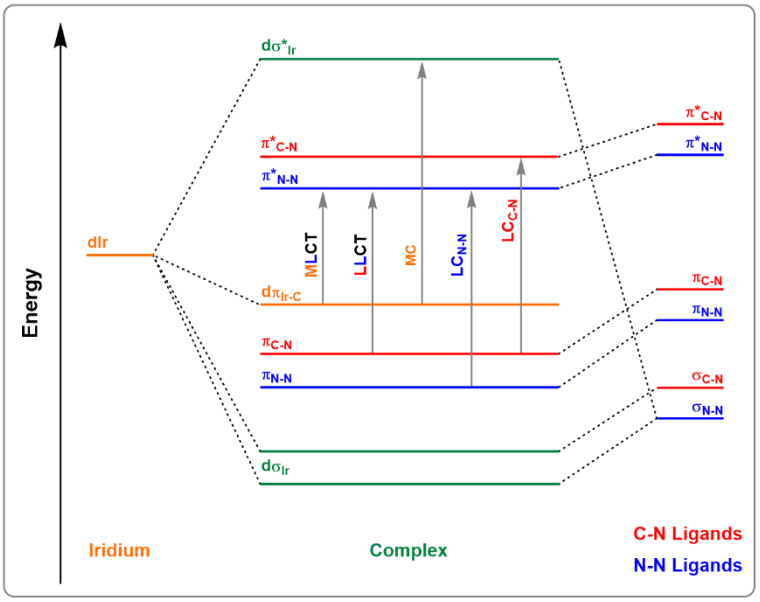

Figure 1.22. Simplified energy diagram for a bis-cyclometalated IrC_2N_4 complex.

Metal centred (MC) transitions occur when an electron moves between two molecular orbitals centred on the metal. They are characterized by small molar extinction coefficient ($\varepsilon < 1000\ M^{-1}\ cm^{-1}$) due to their symmetry-forbidden d-d transitions nature. In Ir(III) cyclometalated complexes, MC transitions are high in energy due to the large ligand field splitting.[192, 193]

Ligand centred transitions typically occur in the UV region and are highly probable (~ $60000\ M^{-1}\ cm^{-1}$). These transitions take place between a bonding molecular orbital ($\pi_{N\text{-}N}$ or $\pi_{C\text{-}N}$) and an anti-bonding ($\pi^*_{N\text{-}N}$ or $\pi^*_{C\text{-}N}$), both located on the same ligand.

Metal to ligand charge transfer (MLCT) transitions involve electron transfer from metal centred molecular orbitals to ligand centred molecular orbitals resulting in a charge-separated state where the metal is oxidized, and the ligand reduced. These transitions are typically observed at the boundary between the UV and the visible region (~ $10000\ M^{-1}\ cm^{-1}$).[192] Nevertheless, the particular nature of the Ir–C bonds implies a strong contribution of each cyclometalated ligand to the oxidation of the complex. Therefore, this process

extends over the entire Ir–C fragment, meaning that the lowest-energy excited state of an IrC_2N_4 complex cannot be a pure MLCT state, as described for Ru(II) and Os(II) polypyridyl complexes.

Ligand to ligand charge transfer (LLCT) transitions involve molecular orbitals localized on two different ligands. Similar to MLCT transitions, they are characterized by absorption in the UV-visible range (~ 5000 M^{-1} cm^{-1}) and can produce an excited state with a strong dipole moment.[192]

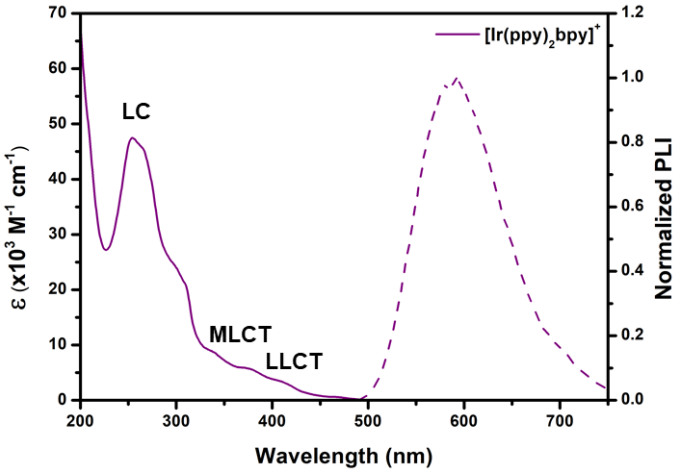

Figure 1.23. UV-visible (solid line) and photoluminescence spectra (dashed line) of $[Ir(ppy)2(bpy)]^+$ recorded in argon purged acetonitrile at room temperature.

The success of heteroleptic complexes with the $[Ir(C–N)_2(N–N)]^+$ architecture relies on their spatially-separated frontier orbitals, enabling independent tuning of HOMO (Ir–C fragment) and LUMO (N–N ligand) levels. Compared to traditional Ru(II) and Os(II) based chromophores, bis-cyclometalated Ir(III) complexes exhibit greater versatility in their electrochemical and photophysical properties. By altering the chemical structures of the different ligands, it is possible to fine-tune their absorption and emission characteristics. Additionally, the oxidation and reduction potentials are significantly affected by, allowing for the design of compounds with desired electrochemical and photophysical properties. The disadvantage of Ir(III) complexes is that they exhibit lower molar extinction coefficient in the visible

light region than Ru(II) and Os(II) complexes. This drawback can be addressed by ligand tuning strategies and will be investigated in this Ph.D. thesis.

For these Ir(III) complexes, the strategies to control the ground and excited state of the complexes (**Figure 1.20**) can independently be applied to the C–N and/or N–N ligands in order to finely tune the HOMO and LUMO energy levels. For cyclometalated ligands, functionalizing the phenyl moiety is particularly effective due to its substantial contribution to the $d_{\pi C\text{-}N}$ molecular orbital. Typically, electron-withdrawing groups stabilize both the HOMO and LUMO, whereas electron-donating groups increase their energy. Consequently, complexes exhibit higher redox potentials with electron-withdrawing substituents on their ligands, while electron-donating groups reduce both oxidation and reduction potentials.

This ability to fine-tune the electrochemical and photophysical properties of bis-cyclometalated Ir(III) complexes is a key factor in their widespread use in solar fuels production, a theme that will be explored throughout this manuscript.

1.4.3 Applications of transition metal complexes in solar fuels production

As described in the previous sections, Ir(III), Ru(II) and Os(II) based photosensitizers offer several advantages in solar fuel photoproduction applications due to their broad absorption spectra, tuneable properties, high photostability, efficient excited-state dynamics and redox versatility. In addition to these precious metal-based photosensitizers, iron complexes will also be investigated in this PhD thesis (**Chapter VIII**), as they represent a more earth-abundant and sustainable alternative. Their photophysical and electrochemical properties, along with their potential in photocatalysis, will be discussed in **Sections 8.1.1** and **8.1.2**.

From the potential scale represented in **Figure 1.24** it can be noticed that Ir(III) complexes are covering a wider ground- and excited-state potential window

than Ru(II) and Os(II) based photosensitizers. This behaviour arises from their ability to accommodate up to three cyclometalated bonds (Ir–C), which significantly enhances the tunability of their optoelectronic properties. IrN_6 complexes usually are the more potent photooxidizing complexes ($[Ir(tpy)_2]^{3+}$, E_{red}* = +2.18 V *vs* NHE) while IrN_2C_2LX are the more potent photoreducing complexes ($[Ir(ppy)_2(NacNac^{Me})]$, E_{ox}* = –1.81 V *vs* NHE).

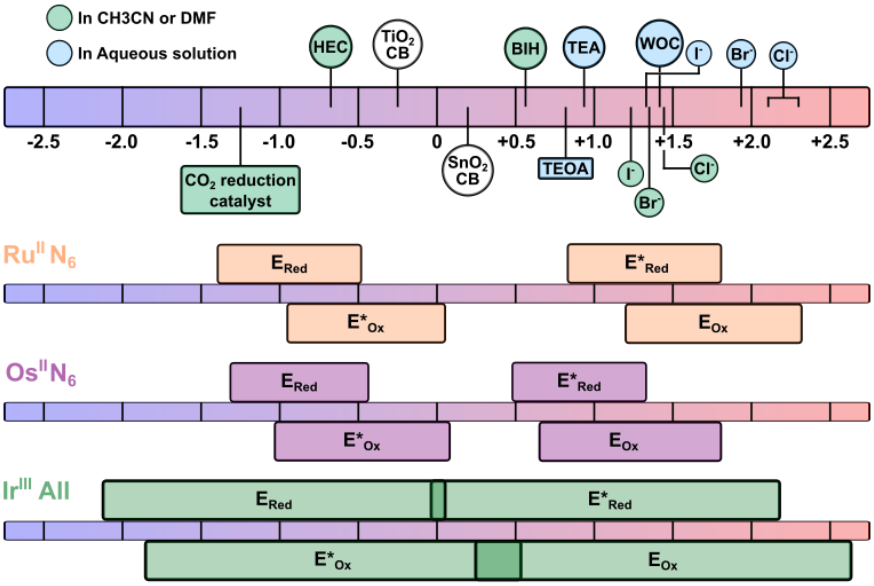

Figure 1.24. Graphical representation of relevant ground and excited-state redox potential for solar fuel production applications. The potentials represented are standing for: i) potentials for the activation of a selected hydrogen evolution catalyst (HEC)[194], water oxidation catalyst (WOC)[195] and CO_2 reduction catalyst[196], ii) potentials for electron injection in the conduction band (CB) of TiO_2 and SnO_2, iii) potentials for the oxidation of different sacrificial electron donors (BIH, TEA and TEOA)[35] as well as halides in CH_3CN[42, 43] (green) and water[41] (blue) and iv) ground and excited-state oxidation and reduction potentials for selected Ir(III) N_6, C_2N_4, C_3N_3 and C_2N_2LX complexes as well as prototypical Ru(II) N_6 and Os(II) N_6 complexes. Potentials are given *vs* NHE and reported in **Table 1.3** while the structures of the corresponding molecules are presented in **Figure 1.25.**

This range of accessible redox potentials makes Ir(III) complexes competent photosensitizers to activate catalyst for proton and CO_2 reduction as well as water oxidation catalyst, while the range of potentials covered by Os(II) and Ru(II) complexes is more limited and would not always be capable of

activating water oxidation or CO_2 reduction catalysts. Moreover, the regeneration of Os(II), Ru(II) and Ir(III) photosensitizers can be performed using prototypical SED such as BIH (1,3-dimethyl-2-phenyl-2,3-dihydro-1H-benzo[d]imidazole, E = +0.57 V *vs* NHE), TEA (triethylamine, E = +0.94 V *vs* NHE) and TEOA (triethanolamine, E = +0.81 V *vs* NHE). Interestingly, these photosensitizers can also react with Guanine, *i.e.* the DNA base with the highest reducing power, to form the corresponding mono-reduced complex and the oxidized guanine via photo-induced electron transfer.[80, 166, 197-202] Therefore, the investigation of photo-induced electron transfer between a prototypical biological substrate, *i.e.* guanosine-5'-monophosphate (GMP), $E(GMP^{\bullet+}/GMP)$ = 1.27 V *vs* NHE[203] and a photosensitizer is a typical "test reaction" to gauge the photoreactivity of a given compound and represent the first step towards the development of Type I photodynamic therapy, i.e. where oxidative damages are triggered via direct electron transfer.[172, 204] Nevertheless, for halides oxidation applications, Ru(II) and Os(II) complexes are limited to halides in acetonitrile and iodide in water while aqueous bromide and chloride oxidation can only be accessed by Ir(III) complexes. However, in the case of Ru(II) complexes, even if the excited-state reduction potential (E_{red}*) does not allow halide oxidation in water, strategies leveraging the ground-state oxidation potential (E_{ox}) can be explored. After photoinduced electron transfer to a proton reduction catalyst, the starting Ru(II) photosensitizers can be regenerated from the Ru(III) photosensitizers through subsequent halide oxidation, either in organic solvents or in water.

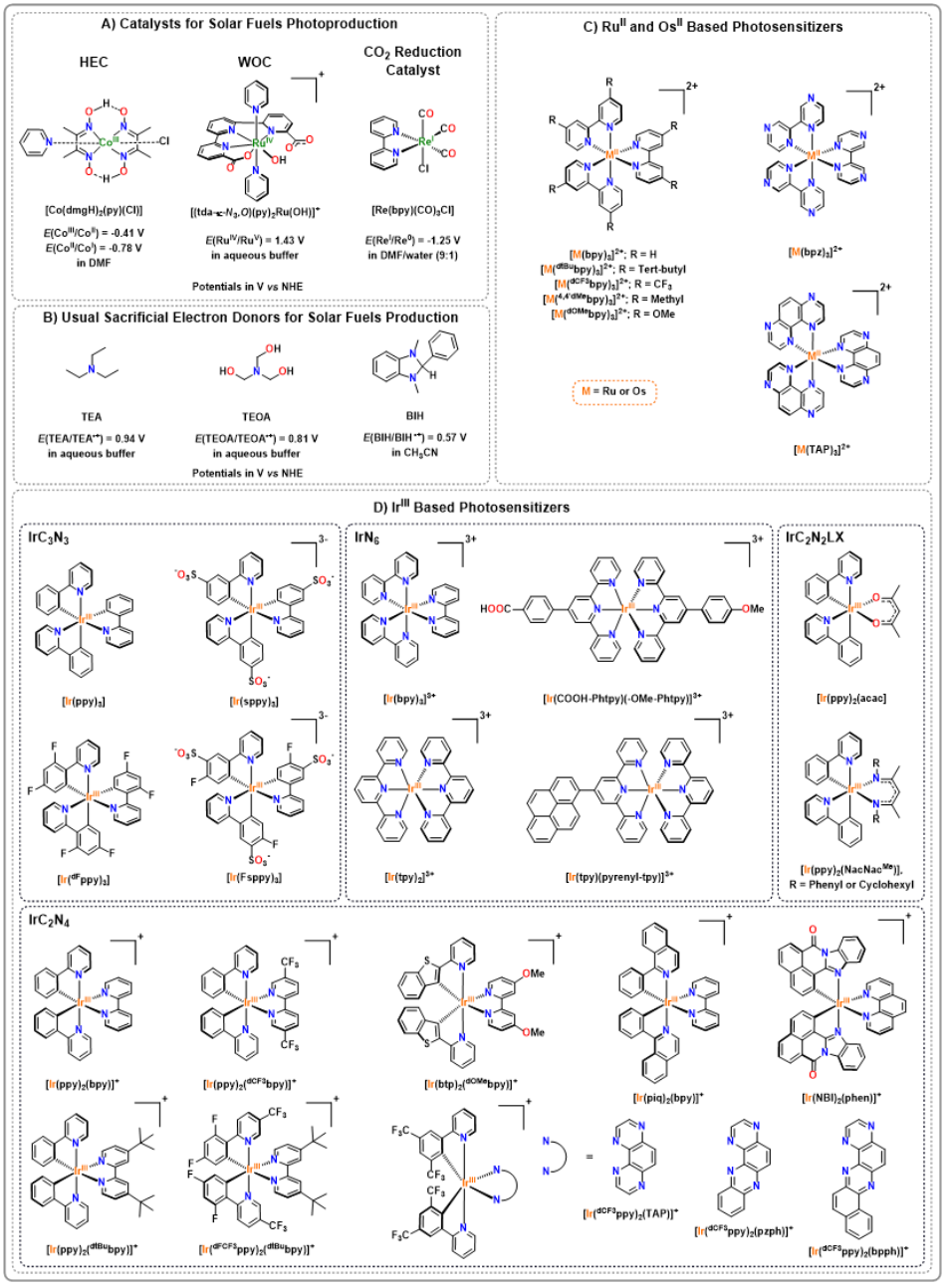

Figure 1.25. Molecular structure of the different complexes used to design **Figure 1.24.** A) Catalysts for solar fuels photoproduction and activation potentials, B) usual sacrificial electron donors for solar fuels production and oxidation potentials, C) Ru(II) and Os(II) based photosensitizers and D) Ir(III) based photosensitizers.

Table 1.3. Electrochemical and spectroscopic data for various Ru(II), Os(II) and Ir(III) based photosensitizers.

Photosensitizers	E_{Ox} / V *vs* NHE	E_{Red} / V *vs* NHE	E_{00} / eV	E_{Ox}* / V *vs* NHE	E_{Red}* / V *vs* NHE	Ref.
Ruthenium						
$[Ru(bpy)_3]^{2+}$	+1.51	–1.10	2.19	–0.68	+1.09	163
$[Ru(bpz)_3]^{2+}$	+2.21	–0.50	2.24	–0.03	+1.75	163
$[Ru(TAP)_3]^{2+}$	> +2.3	–0.52	2.30	>–0.4	+1.78	163
$[Ru(^{dtBu}bpy)_3]^{2+}$	+1.36	–1.21	2.17	–0.81	+0.97	163
$[Ru(^{4,4'dMe}bpy)_3]^{2+}$	+1.35	–1.22	2.16	–0.81	+0.94	163
$[Ru(^{dMeO}bpy)_3]^{2+}$	+1.16	–1.26	2.05	–0.89	+0.79	163
$[Ru(^{dCF3}bpy)_3]^{2+}$	+1.94	–0.62	2.15	–0.21	+1.54	163
Osmium						
$[Os(bpy)_3]^{2+}$	+1.08	–1.04	1.83	–0.75	+0.80	163
$[Os(bpz)_3]^{2+}$	+1.78	–0.57	1.71	+0.07	+1.14	163
$[Os(TAP)_3]^{2+}$	+1.77	–0.43	1.74	+0.04	+1.31	163
$[Os(^{dtBu}bpy)_3]^{2+}$	+0.93	–1.13	1.81	–0.88	+0.68	163
$[Os(^{4,4'dMe}bpy)_3]^{2+}$	+0.91	–1.15	1.79	–0.88	+0.65	163
$[Os(^{dMeO}bpy)_3]^{2+}$	+0.63	–1.20	1.67	–1.04	+0.47	163
$[Os(^{dCF3}bpy)_3]^{2+}$	+1.53	–0.50	1.80	–0.27	+1.31	163
Iridium						
$[Ir(ppy)_3]$	+1.01	–1.95	2.39	–1.38	+0.34	185
$[Ir(^{dF}ppy)_3]$	+1.18	–1.63	2.22	–1.04	+0.50	205
$[Ir(sppy)_3]$	+1.00	nr	2.65	–1.65	nr	178
$[Ir(Fsppy)_3]$	+1.15	nr	2.76	–1.61	nr	178
$[Ir(bpy)_3]^{3+}$	+2.34	–0.86	2.75	–0.41	+1.89	184
$[Ir(tpy)_2]^{3+}$	>+2.6	–0.53	2.71	>–0.11	+2.18	206
[Ir(COOH-Phtpy)(OMe-Phtpy)]$^{3+}$	>+2.4	–0.61	2.19	>+0.21	+1.58	207
$[Ir(tpy)(pyrenyl\text{-}tpy)]^{3+}$	+2.28	+0.04	1.75	+0.53	+1.79	208
$[Ir(ppy)_2(acac)]$	+1.10	nr	2.40	–1.30	nr	209
$[Ir(ppy)_2(NacNac^{Me})]$ R = Phenyl	+0.57	–1.56	2.38	–1.81	+0.82	209
$[Ir(ppy)_2(NacNac^{Me})]$ R = Cyclohexyl	+0.25	< –2.00	2.04	–1.79	< +0.04	210
$[Ir(ppy)_2(bpy)]^+$	+1.49	–1.17	2.10	–0.61	+0.93	211
$[Ir(ppy)_2(^{dtBu}bpy)]^+$	+1.45	–1.27	2.17	–0.72	+0.80	212
$[Ir(ppy)_2(^{dCF3}bpy)]^+$	nr	–0.53	2.03	nr	+1.50	213
$[Ir(^{dFCF3}ppy)_2(^{dtBu}bpy)]^+$	+1.93	–1.77	2.90	–0.97	+1.13	214
$[Ir(btp)_2(^{dOMe}bpy)]^+$	+1.27	–1.19	2.13	–0.86	+0.94	215
$[Ir(piq)_2(bpy)]^+$	+1.50	–1.11	2.10	–0.60	+0.99	180
$[Ir(NBI)_2(phen)]^+$	+1.74	–0.92	2.05	–0.31	+1.13	37
$[Ir(^{dCF3}ppy)_2(TAP)]^+$	> +2.2	–0.41	2.19	nr	+1.78	42
$[Ir(^{dCF3}ppy)_2(pzph)]^+$	> +2.2	–0.13	1.90	nr	+1.77	42
$[Ir(^{dCF3}ppy)_2(bpph)]^+$	> +2.2	–0.25	2.01	nr	+1.76	42

Chapter II – Objectives and Strategies

2.1 Objectives

This Ph.D. thesis focuses on the design of novel light-sensitive molecules based on Fe(III), Ru(II), Os(II), Ir(III) for applications in solar energy conversion.

The first objective is to develop photosensitizers for hydrogen evolution reaction (HER). HER appears to be an interesting solution to worldwide consumption of fossil fuels as hydrogen is an energy-dense and carbon-free fuel.[216,16] Recently, different Ir(III) bis-cyclometalated have been explored to develop stable and robust photosensitizers for HER.[36, 37, 183, 217]

In literature, cobalt macrocyclic complexes represent popular catalyst for homogeneous proton reduction.[218] Cobaloxime complexes (**Figure 1.25 A left**), initially developed as a mimic of vitamin B_{12}, use the self-assembling macrocycle dimethylglyoxime ($dmgH_2$) ligand. Currently, they have a long history in proton reduction catalysis and are particularly attractive due to their ease of synthesis and fairly high catalytic activity.[219] It is worth mentioning that alongside the use of cobaloximes as HEC, a whole series of dyads systems have been designed with more expensive transition metal such as Pt(II)[220-222] and Pd(II).[221, 223, 224]

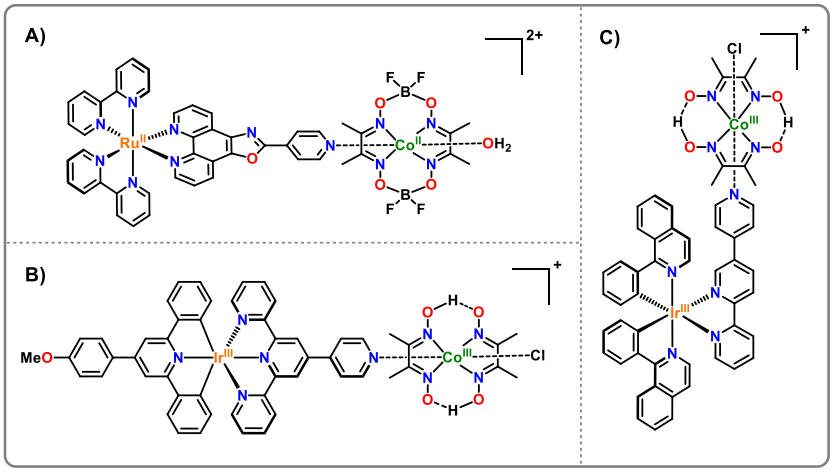

Figure 2.1. Supramolecular Ir(III)-Co(III) and Ru(II)-Co(III) dyads for photocatalytic hydrogen production.[183, 217, 225]

Recently, the coordination of cobaloximes has been successfully achieved on Ir(III)[183, 184, 217] and Ru(II)[225] complexes by the use of bridging ligands (**Figure 2.1**). In these supramolecular systems, the photosensitizer is tethered through the axial C–N bond via a pyridyl moiety. The first example of cobaloxime based photocatalytic devices for hydrogen production were reported by V. Artero and co-workers in 2008.[225] This system was based on a Ru(II) polypyridyl photosensitizer connected by a bridging ligand to the cobaloxime catalytic center (**Figure 2.1 A**). When a white light source was used to irradiate the complex (0.43 mM) in acetone and in the presence of 300 eq. of TEA as the SED and 300 eq. of Et_3NHBF_4 as the proton source, molecular hydrogen was produced with turnover number (TON) of 85 over 8 hours.

Inspired by these supramolecular dyads, our laboratory developed systems based on Ir(III) photosensitizers (**Figure 2.1 B and C**). The first research article published by A. Jacques *et al.* proposed a system based on an Ir(III) bis-tridentate ligands allowing a wider range of visible light to be harvested with significant molar extinction coefficient (**Figure 2.1 B**). Under green-light irradiation (525 nm, LED), this supramolecular dyad (0.1 mM) produced hydrogen over 10 hours (TON = 113) in the presence of 1 M TEOA as the SED, 0.1 M HBF_4 as the proton source in acetonitrile. Interestingly, the rate of activity for this photocatalytic system remained constant over the irradiation time.[217] More recently, C. Lentz *et al.* reported a new supramolecular system that photoproduced hydrogen in a range extending from the blue region of the spectrum to the red region. This system was based on an Ir(III) complex bearing two cyclometalated piq (1-phenylisoquinoline) ligands, which exhibit enhanced conjugation compared to ppy ligands, resulting in increased and red-shifted molar absorption.[183] Furthermore, the cobaloxime moiety was connected to the Ir(III) center by a terpyridine bridging ligand. Under red-light irradiation (630 nm, LED), this supramolecular dyad (0.1 M) produced hydrogen over 110 hours (TON = 80) in the presence of 0.5 M TEOA as the SED and 0.05 M HBF_4 as the proton source in acetonitrile. It is important to mention that multicomponent systems where the cobaloxime/catalytic center moiety is not directly bound to the light-harvesting unit are also well described

in the literature and offers more flexibility in terms of N–N ligand functionalization.[36, 37]

Event thought it has been shown that Ir(III) complexes are outperforming archetypal PS such as $[Ru(bpy)_3]^{2+}$ and $[Os(bpy)_3]^{2+}$, they are still suffering from poor visible light absorption properties as prototypical complexes absorb mainly in the UV region, with limited absorption extending into the blue part of the spectra (**Figure 2.2**). This latter feature is limiting their photons absorption reaching the earth compared to $[Ru(bpy)_3]^{2+}$ and $[Os(bpy)_3]^{2+}$ (**Figure 2.2**). Although our group has reported systems that exploit most of the solar spectrum, there remains significant interest in developing new stable systems based on iridium complexes with extended absorption properties. Additionally, gaining key insights into the photo-induced electron transfer dynamics, photogenerated intermediates, and the influence of cyclometalating ligands on the activity of Ir(III)-based systems are still missing and are therefore of crucial importance.

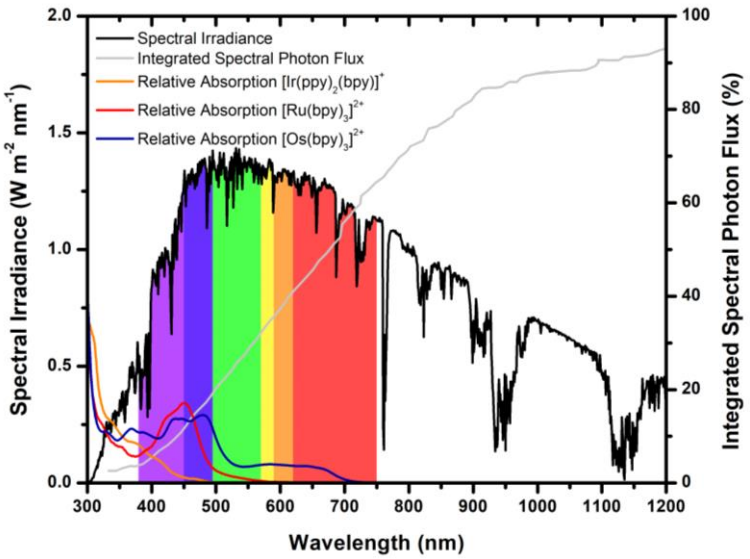

Figure 2.2. Relative absorption spectrum of $[Ru(bpy)_3]^{2+}$ (red), $[Os(bpy)_3]^{2+}$ (blue) and $[Ir(ppy)_2(bpy)]^{+}$ (orange) presented along the solar spectral irradiance (black) and the integrated spectral photon flux (grey).

Fortunately, cyclometalated Ir(III) photosensitizers are an outstanding class of compounds, possessing spatially separated frontier orbitals, meaning that the Ir–C–N centred HOMO and N–N centred LUMO levels can be independently tuned, leading to easily change their absorption and emission properties by altering the chemical structures of the different ligands.[226] Additionally, the oxidation and reduction potentials can be significantly altered, allowing for the design of compounds with desired electrochemical and photophysical properties. Then, their low molar extinction coefficient in the visible light region can be addressed by ligand tuning strategies (presented in **Figure 1.20**) and will be investigated throughout this Ph.D. thesis.

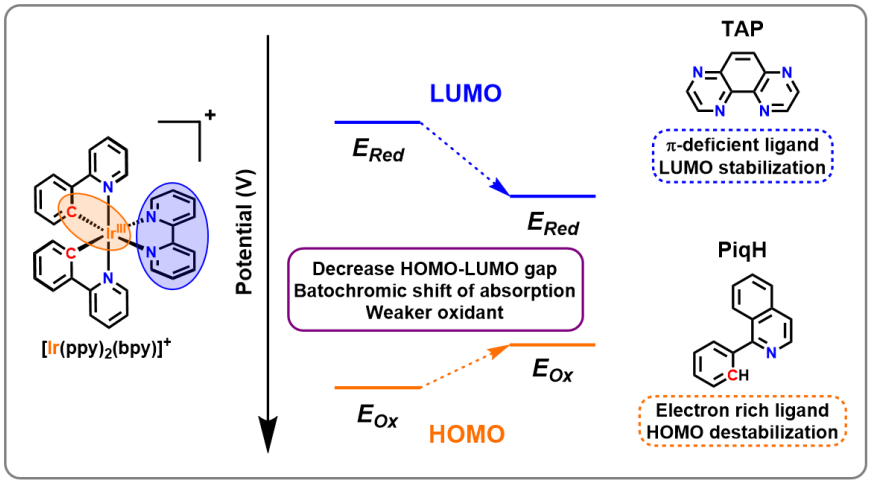

Figure 2.3. Ligand tuning strategy investigated during this Ph.D. thesis to improve visible light absorption of Ir(III)-based photosensitizers for solar fuels photoproduction.

Our approach to address their limited light absorption properties involved the fine-tuning of the spatially separated HOMO and LUMO in bis-cyclometalated Ir(III) complexes (**Figure 2.3**). By employing electron-rich cyclometalated ligands such as **piqH** (1-phenylisoquinoline), we aimed to destabilize the HOMO. Concurrently, the use of π-deficient diimine ligands like the **TAP** (1,4,5,8-tetraazaphenanthrene) was intended to stabilize the LUMO. These modifications collectively decreased the HOMO-LUMO gap in Ir(III) photosensitizer, inducing a bathochromic shift in its absorption properties. However, as this strategy results in the destabilization of the HOMO, this led

to a weaker oxidizing power in both the ground and excited states. Consequently, the regeneration of these photosensitizers after electron transfer is only possible by using sacrificial electron donors such as triethylamine, triethanolamine, and BIH, which, after regenerating the photosensitizer, will be degraded and does not lead to any valuable product.

Moreover, understanding the mechanism of the photo-induced electron transfer process, the photogenerated intermediates and the influence of the cyclometalating ligands is crucial for the development of efficient photocatalytic systems for HER applications. For this purpose, we have used transient absorption techniques such as X-Ray transient absorption (XTAS) and UV-visible transient absorption (TA) spectroscopies as they represent a powerful tool to decipher the reaction pathways, electronic and structural conformations of hydrogen evolution photocatalysts.

However, these systems rely on the use of SEDs, which implies significant limitations. The SED is consumed in the reaction without generating any valuable side-products, resulting only in the formation of a hydrogen-hydrogen bond (436 kJ/mol). This somewhat inefficiency highlights the need for alternative approaches to improve resource utilization and enhance the sustainability of the process by optimizing the production of valuable products. In this context, HX splitting represent an interesting alternative as it involves the thermodynamically challenging process of converting HX into H_2 and the corresponding halogen (X_2). The reverse reaction releases free energy, making this approach particularly advantageous. While both HX splitting and water splitting are significant for producing hydrogen, the kinetic barriers and the complexity of water oxidation pose substantial challenges.[29] This makes HX splitting (where X = Cl^-, Br^-, or I^-) a highly desirable reaction for solar fuel production.[227] Therefore, developing strong photo-oxidant photosensitizers capable of performing halide oxidation is of paramount importance. This aspect will be explored in the second part of this Ph.D. thesis, focusing on the creation and optimization of such photosensitizers for solar fuel production.

Regenerative solar cells converting light into electricity are one of the first reported example using halide oxidation for solar energy conversion applications. These solar cells are generally composed of one dye-sensitized photoelectrode and one metal electrode immersed in an electrolyte with solvated mediators that shuttle redox equivalents between them. In this context, mixture of halogens and halides have long been utilized, particularly I_3^- / I_2^-/ I^- as in the dye-sensitized solar cell (DSSC) introduced by O'Regan and Grätzel in 1991.[228] Since then, various strategies involving both homogeneous and heterogeneous catalysts have been investigated for halide oxidation and HX splitting. Notably, the pioneering work of D. G. Nocera's group on dirhodium catalysts have made significant contributions to the field.[229]

Halide oxidation has already been reported in organic solvents by pioneers such as G. J. Meyer using photosensitizers based on Ru(II)[54-56, 135, 230, 231], Os(II)[158] or Ir(III)[179] (**Figure 2.4 A,B and C**) and D. G. Nocera that performed HX splitting with Rh_2 complexes[229, 232] and halogen atom photoelimination from Ni(III)[233, 234] or Fe(III) complexes.[235] Most of the time, these photosensitizers were designed by using the combination of oxidizing power conferred by ligands bearing electron withdrawing groups or electron-poor ligands such as 2,2'-bipyrazine (bpz) for Ru(II); 4,4'-bis(trifluoromethyl)-2,2'-bipyridine (^{dCF3}bpy) for Os(II); 2-(2,4-difluorophenyl)-5-(trifluoromethyl)-pyridine (^{dFCF3}ppy)) for Ir(III) with ligands capable of halide-pairing. These ligands include the 4,4'-diethylester-2,2'-bipyridine (deeb)[135, 236-241], the dicationic 4,4'-trimethylamino-methyl-2,2'-bipyridine (tmam)[135, 158, 241, 242] or the 4,4′-diethanolamide-2,2′-bipyridine (dea)[241, 243]. This led to ground-state adduct formation with different halides in solvents that included acetonitrile, acetone or dichloromethane. $[Ru(bpz)_2(tmam)]^{4+}$ was found to photo-oxidize chloride in acetone with quenching rate constant greater than 10^{10} M^{-1} s^{-1} and the formation of the monoreduced ruthenium photosensitizer was confirmed by transient absorption spectroscopy.[135] Upon light excitation, $[Os(^{dCF3}bpy)_2(tmam)]^{4+}$ was quenched by iodide in acetone through a combination of static and dynamic excited-state quenching with quenching

rate constant greater than 10^{11} M^{-1} s^{-1}.[158] Unfortunately, due to its moderate excited-state reduction potential, this photosensitizer could only be used for iodide oxidation and unambiguous evidence for excited-state electron transfer was not reported.[158] This could potentially stem from low cage escape yields that are often observed with Os(II) photosensitizers.[126, 244] Finally, $[Ir(^{dFCF3}ppy)_2(tmam)]^{3+}$ was found to be quenched by chloride in acetonitrile with quenching rate constant greater than 10^{10} M^{-1} s^{-1}.[179] The ion pair formation with the tmam ligand enabled rapid excited-state electron transfer at extremely low concentration of chloride. Nevertheless, transient absorption evidence for excited-state chloride oxidation in acetonitrile was not reported.[179] These photosensitizers rely on the pre-association of the photosensitizer and halide in the ground state, which further shifts the one-electron oxidation potential of the halides to more positive value.[243] This shift complicates halide oxidation and could also reduce cage escape yields by increasing back-electron transfer within the pre-associated species. This is exemplified when comparing $[Ru(bpy)_3]^{2+}$ (bpy= 2,2'-bipyridine) with photosensitizers competent for halide-pairing. $[Ru(bpy)_3]^{2+}$ exhibited cage escape yield of 0.50 in CH_2Cl_2,[54] whereas photosensitizers bearing ion-pairing ligands showed lower cage escape yields, *i.e.* 0.34 for $[Ru(^{dtb}bpy)_2(dea)]^{2+}$ (^{dtb}bpy= 4,4'di-*tert*-butyl-2,2'-bipyridine) in CH_2Cl_2,[243] 0.25 for $[Ru(bpy)_2(deeb)]^{2+}$ in CH_2Cl_2, and 0.042 for $[Ru(bpz)(deeb)]^{2+}$ in acetonitrile.[54, 231] Thus, it seems that ground-state ion-pairing of the photosensitizer and the halide could improve excited-state reactivity but could lead to smaller cage escape yields. Strategies to prevent this fast back-electron transfer using secondary coordination effects were proposed by Nocera *et al.* who used aryl substituents to form a Cl•|arene adducts that could be experimentally observed.[233-235, 245] So far, excited-state halide oxidation has almost exclusively been carried out in organic solvent, where the estimated potential are 1.23, 1.35 and 1.46 V *vs* NHE for iodide, bromide and chloride, respectively.[42, 43] Whereas most examples of halide oxidation involved iodide, *i.e.* the most easily oxidized stable halide, there are a few reports of bromide and chloride oxidation that have appeared in recent years. These include bromide and chloride photo-oxidation in acetone using Ru(II)

photosensitizers[135, 238, 239] as well as by one- or two-photon excitation of *N*-phenylphenothiazine in acetonitrile.[246]

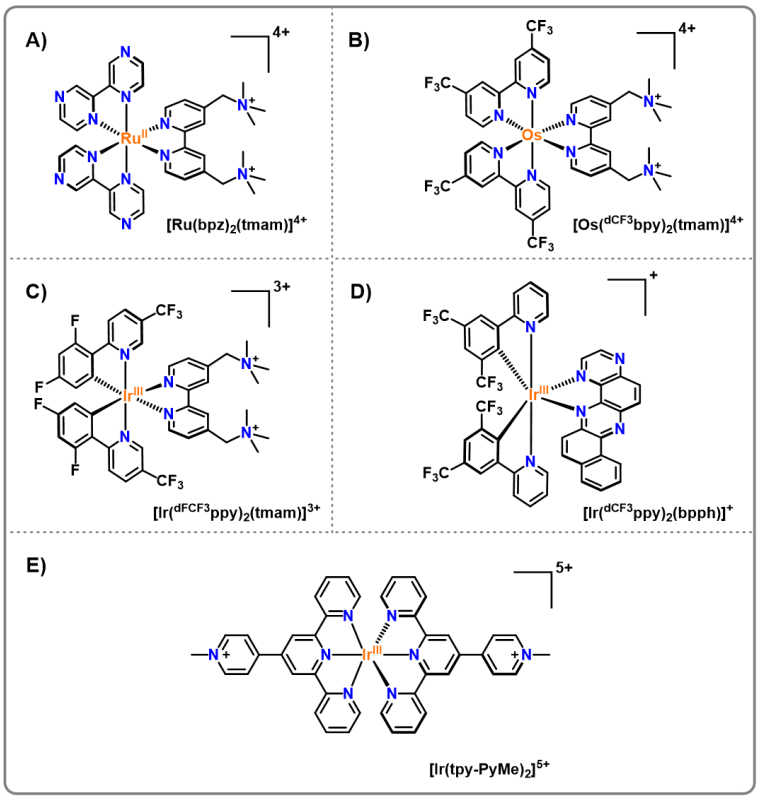

Figure 2.4. Structure of the photosensitizers investigated for halide oxidation.

Recently, our group reported a new Ir(III) photosensitizer, $[Ir(^{dCF3}ppy)_2(bpph)]^+$ (bpph = benzo[a]pyrazino[2,3-h]phenazine) (**Figure 1.25 D bottom right**), that exhibited interesting properties for halide photo-oxidation applications.[42] Indeed, the combination of the ^{dCF3}ppy and the bpph ligands were found to enhance light absorption in the visible region (ε_{450nm} = 9800 M^{-1} cm^{-1}) and to exhibit an excited-state reduction potential, E_{red}* = 1.76 V *vs* NHE (**Table 1.3**) capable of photo-oxidizing iodide, bromide and chloride in acetonitrile. As for the complexes previously described, quenching rate constant were greater than 10^{10} M^{-1} s^{-1} for all the halides in acetonitrile. Additional transient absorption spectroscopy experiments were conducted with

$[Ir(^{dCF3}ppy)_2(bpph)]^+$ in the presence of iodide, bromide, and chloride. For iodide and bromide, the transient absorption changes indicated the formation of the monoreduced iridium complex along with either $I_2^{\bullet -}$ or $Br_2^{\bullet -}$. However, in the case of chloride, excited-state quenching was observed only as a significant decrease in the excited-state lifetime and no photoproducts resulting from electron transfer were detected. In summary, there are few examples in the literature reporting experimental evidence for the photo-oxidation of halides and, more importantly, chloride in organic solvents. Furthermore, this process has never been investigated in water or water enriched conditions. Although aqueous chloride oxidation presents greater challenges ($E_{1/2}(Cl^{\bullet/-})$ = ~2.1-2.3V *vs* NHE) compared to bromide and iodide (1.93 and 1.33 V *vs* NHE, respectively)[41], its abundance and availability make it a promising candidate for HX splitting.

Finally, our group recently reported novel pentacationic IrN_6 photosensitizer ($[Ir(tpy\text{-}PyMe)_2]^{5+}$ (tpy-PyMe = 4′-(4-methyl-pyridinio)-2,2′:6′,2″-terpyridine) (**Figure 2.4 D**), a highly photo-oxidizing and water soluble complex.[182] Even if the latter suffers from low absorption in the visible light region, nanosecond transient absorption spectroscopy (λ_{exc} = 355 nm) experiments in the presence of hydrochloric acid, chloride, bromide and iodide confirmed the occurrence of a photoinduced electron transfer in aqueous solution. Although the cage escape yields were low (0.04), the photo-oxidation of chloride and bromide in water is a noteworthy innovation in the realm of solar fuel photoproduction.

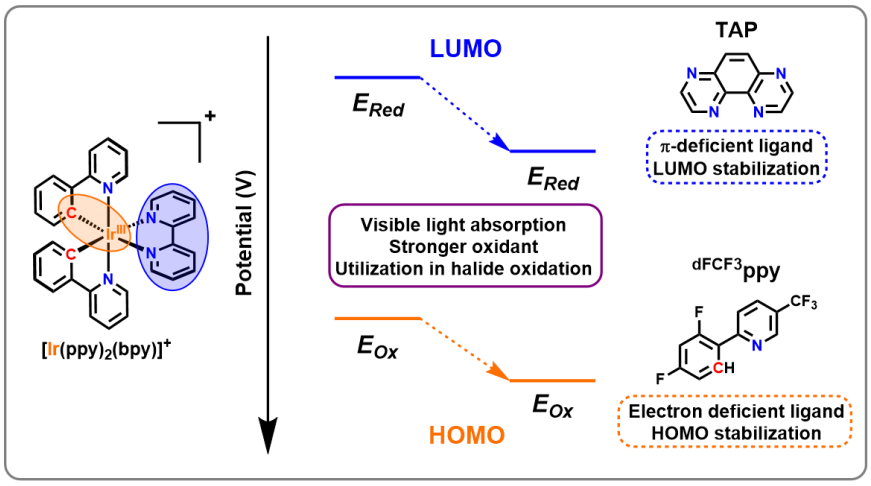

Figure 2.5. Ligand tuning strategy investigated during this Ph.D. thesis to increase oxidizing power of Ir(III)-based photosensitizers while conserving appreciable visible light absorption properties.

With the aim of leveraging the photosensitizer regeneration event, our second objective was to develop systems using halides (X^-) as the electron donor, which would yield a covalent X-X bond after X^- oxidation. Aqueous halide oxidation occurs at potentials $E_{1/2}(X^{\bullet/-})$ of 1.33, 1.93, and ~2.1-2.3V *vs* NHE for iodide, bromide, and chloride, respectively.[41] This makes bromide and chloride photo-oxidation extremely challenging in water with visible light, as it requires an exceptionally strong oxidizing power, which often comes at the cost of visible light absorption. To address this challenge, our ligand tuning strategy involved the use of the electron-deficient **^{dFCF3}ppy** (2-(2,4-difluorophenyl)-5-(trifluoromethyl)pyridine) cyclometalated ligand to stabilize the HOMO, while maintaining appreciable visible light absorption properties by stabilizing the LUMO with a π-deficient diimine ligand. This synthetic approach is expected to lead to strong photo-oxidizing complexes capable of performing halide oxidation in organic solvents and/or water-like conditions by absorbing visible light photons.

Building on this approach, similar strategies can be applied to Os(II) and Ru(II) complexes, which also exhibit promising photophysical and electrochemical properties. This fine ligand tuning allows the resulting complexes to absorb

visible light efficiently while keeping the high oxidizing power to facilitate halide oxidation. Investigating alternative metal centers beyond iridium, such as osmium and ruthenium, is of great interest. It can provide valuable insights into the parameters influencing halide oxidation, such as the intrinsic electronic properties of the metal center, the nature of the ligands, and the overall complex stability. This broader understanding could lead to the design of more efficient and versatile photosensitizers for various applications, including hydrohalic acid splitting and other photocatalytic processes.

Additionally, exploring more abundant metals like Fe(III) for the development of photosensitizers represents a promising alternative that will be pursued in this Ph.D. thesis. Investigating iron complexes will enable a comparison between the “traditional” ^{3}MLCT (metal-to-ligand charge transfer) and the unconventional ^{2}LMCT (ligand-to-metal charge transfer) present in Fe(III) complexes, for halide oxidation. Developing iron-based photosensitizers not only aligns with the goal of using earth-abundant compounds but also offers a cost-effective and sustainable approach to photoredox catalysis.

Chapter III – [Ir(piq)$_2$(LL)] Photosensitizers for Solar Fuels Production

Researchers involved in this project are listed hereafter: Martin Wodon (in the context of his master thesis project, UCLouvain, June 2023) and Dr. Renato N. Sampaio (University of North Carolina at Chapel Hill).

Preface – This chapter focuses on the synthesis and characterization of a novel series of 1-phenylisoquinoline-substitued Ir(III) complexes. Their photophysical and electrochemical properties as well as their reactivity for electron transfer with prototypical sacrificial electrons donors for solar fuels production were thoroughly investigated. The results presented in this chapter have been published in Photochemical & Photobiological Sciences (Wodon, M.; De Kreijger, S.; Sampaio, R. N.; Elias, B.; Troian-Gautier, L., Accumulation of mono-reduced [Ir(piq)2(LL)] photosensitizers relevant for solar fuels production. Photochemical & Photobiological Sciences 2022, 21 (8), 1433-1444. (Co-first author)).

3.1. Introduction

Both natural and artificial photosynthesis aim to generate high-energy fuels using sunlight to initiate a series of light-induced electron transfer events.[102, 104, 247-251] Visible light induced electron transfer chemistry represents a powerful approach towards the development of sustainable energy supplies. In this context, the reduction of protons into molecular hydrogen (H_2) or of CO_2 into valuable chemicals such as CO, HCOOH, CH_3OH or CH_4 are both considered as promising strategies towards sustainability.[219, 225, 229, 252-259] Research has been dedicated to the development of transition metal complexes that function either as photosensitizers or as catalytic centres where these reduction processes can take place. Prototypical photosensitizers such as $[Ru(bpy)_3]^{2+}$ (bpy = 2,2'-bipyridine), $[Ir(ppy)_3]$ (ppy = 2-phenylpyridine) and $[Ir(ppy)_2(bpy)]^+$ have been used in concert with Ni, Ru, Re, Fe and Co based molecular catalysts for proton or CO_2 reduction.[219, 225, 229, 252-259] Typically, visible light excitation of the photosensitizer leads to an excited-state that undergoes direct electron transfer with a sacrificial electron donor. Commonly used sacrificial electron donor include triethanolamine (TEOA) or 1,3-dimethyl-2-phenyl-2,3-dihydro-1*H*-benzo[*d*]imidazole (BIH) with formal reduction potentials of 0.82 V *vs* NHE and 0.57 V *vs* NHE,

respectively.[35] The monoreduced photosensitizer is then able to transfer an electron to a molecular catalysts, commonly $[Co(dmgH)_2(py)(Cl)]$ ($E_{Co(III)/Co(II)}$ = –0.41 V and $E_{Co(II)/Co(I)}$ = –0.78 V *vs* NHE)[194] for proton reduction or [*fac*-$Re(bpy)(CO)_3Cl$] ($E_{Re(I)/Re(0)}$ = –1.25 V *vs* NHE)[196, 260] for CO_2 reduction.

This sequence of reductive electron transfer events relies on a delicate balance of thermodynamics, and fine-tuning the ground- and excited-state energy levels of the photosensitizers is essential for an efficient process to take place. In this context, bis-cyclometalated Ir(III) complexes are particularly useful, as the significant spatial separation of each frontier orbital enables independent tuning of either the HOMO or the LUMO of the complex (or both).[226, 261] In addition, Ir(III) photosensitizer are often very robust under irradiation and their (photo)-redox potentials can be tuned over a far greater range than their Ru(II), Os(II) or Cu(I) counterparts.[175, 226]

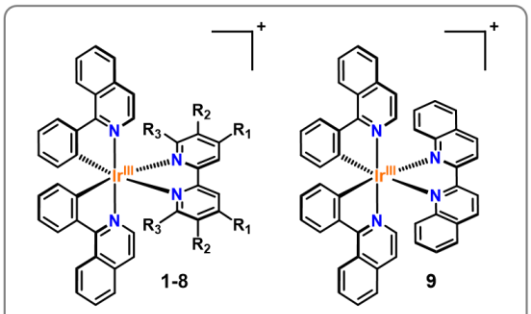

$[Ir(piq)_2(bpy)]^+$ (**1**): $R_1 = R_2 = R_3 = H$
$[Ir(piq)_2(4,4'\text{-}(CH3)_2\text{-}bpy)]^+$ (**2**): $R_1 = CH_3$, $R_2 = R_3 = H$
$[Ir(piq)_2(5,5'\text{-}(CH3)_2\text{-}bpy)]^+$ (**3**): $R_1 = H$, $R_2 = CH_3$, $R_3 = H$
$[Ir(piq)_2(6,6'\text{-}(CH3)_2\text{-}bpy)]^+$ (**4**): $R_1 = R_2 = H$, $R_3 = CH_3$
$[Ir(piq)_2(4,4'\text{-}(^tBu)_2\text{-}bpy)]^+$ (**5**): $R_1 = {}^tBu$, $R_2 = R_3 = H$
$[Ir(piq)_2(4,4'\text{-}(C_9H_{19})_2\text{-}bpy)]^+$ (**6**): $R_1 = (CH2)_8CH_3$, $R_2 = R_3 = H$
$[Ir(piq)_2(4,4'\text{-}(OCH_3)_2\text{-}bpy)]^+$ (**7**): $R_1 = OCH_3$, $R_2 = R_3 = H$
$[Ir(piq)_2(4,4'\text{-}(Br)_2\text{-}bpy)]^+$ (**8**): $R_1 = Br$, $R_2 = R_3 = H$
$[Ir(piq)_2(biq)]^+$ (**9**): biq = 2,2'-biquinoline

Figure 3.1. The series of $[Ir(piq)_2(LL)]^+.PF_6^-$ photosensitizers investigated in this chapter.

In this chapter, we report a series of nine $[Ir(piq)_2(LL)]^+$ photosensitizers, where piqH = 1-phenylisoquinoline and LL is a N^N diimine ligand (**Figure 3.1**). These photosensitizers absorbed visible light with molar absorption

coefficients in the 5400-7900 $M^{-1}cm^{-1}$ range, and exhibit excited-state lifetimes in the microsecond time scales that were competent for efficient reductive excited-state electron transfers with BIH. Steady-state photolysis in the presence of BIH showed that most of the photosensitizers were stable in their reduced form, which is a paramount criterion for efficient and long-term light-driven reduction of protons or CO_2 to solar fuel products.

3.2 Results and discussion

3.2.1 Synthetic approach

The synthetic approach to produce the series of Ir(III) photosensitizers relied on the use of iridium complexes with two cyclometalating piq ligands (piqH = 1-phenylisoquinoline). These ligands are relatively electron-rich, and cyclometalating ligands that are also known to increase the molar absorption coefficient of the resulting photosensitizers in the visible range.[226] The synthesis proceeded via the chelation of the cyclometalated ligands (providing an Ir(III) dichloro-bridged dimer), as described by Nonoyama,[262] followed by the addition of the N^N ligand (**Figure 3.2**). The N^N ligands were systematically varied over a wide range of ligand substitutions, which included 2,2'-bipyridine (bpy), 4,4'-, 5,5', and 6,6'-$(CH_3)_2$-2,2'-bipyridine, 4,4'-$(OCH_3)_2$-2,2'-bipyridine, 4,4'-$(^tBu)_2$-2,2'-bipyridine, 4,4'-$(C_9H_{19})_2$-2,2'-bipyridine, 4,4'-$(Br)_2$-2,2'-bipyridine as well as 2,2'-biquinoline (biq). The modifications of the N^N diimine ligands influenced the LUMO energy level of each complex, which in turn affected the visible light absorption properties, as well as the ground-state and excited-state reduction potentials.

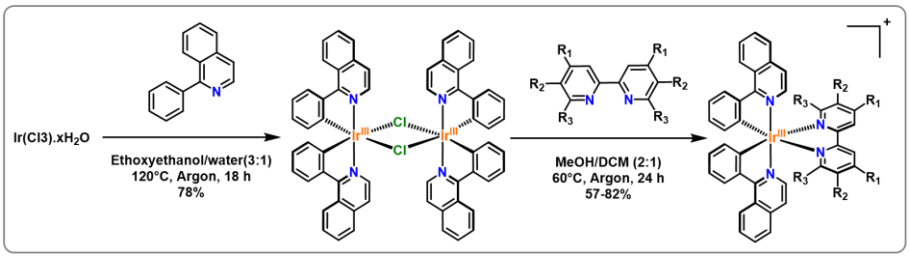

Figure 3.2. Synthetic route for the synthesis of $[Ir(piq)_2(LL)]^+.PF_6^-$ photosensitizers.

The following general procedure was used to synthesize the different Ir(III) photosensitizers: Ir(III) chloro-bridged dimer $[Ir(piq)_2\mu\text{-}Cl]_2$ (75 mg, 58.9 μmol) and the corresponding diimine ligand (147.25 μmol, 2.5 eq.) were placed in a sealed tube under argon atmosphere with 9 mL of MeOH/DCM 2:1 mixture. The reaction was heated at 60 °C for 24 hours. After reaction, the orange-red mixture was brought to room temperature. The DCM fraction was evaporated, and the resulting solution was treated with 10 mL of milliQ water and an excess of NH_4PF_6 was then added. The complex was isolated by centrifugation and was washed 3 times with milliQ water and 3 times with diethyl ether to give the desired complexes with yields that ranged from 57 to 82 %.

3.2.2 Photophysical and electrochemical properties

The UV-visible absorption features of all complexes were characterized by strong ligand-centred (LC) absorption bands in the UV region (**Figure 3.3**). The transitions observed at wavelengths greater than 350 nm are often assigned to mixed metal-to-ligand (MLCT) and ligand-to-ligand (LLCT) charge transfer bands as well as metal-ligand-to-ligand charge transfer (MLLCT) from the cyclometalating ligand to the N^N ligand.[226, 263, 264] These transitions were determined to have molar absorption coefficients in the 5400-7900 $M^{-1}cm^{-1}$ range at 427-442 nm (**Table 3.1**).

Blue light excitation yielded photoluminescence (PL) decays that were in all cases well described using a bi-exponential decay. Irrespective of the nature of the photosensitizer, a short excited-state lifetime (15 ± 2 ns) was determined in all cases, which probably arose from a piq-centred deactivation. The second component of the excited-state lifetime, tabulated in **Table 3.1**, was strongly influenced by the nature of the N^N ligand, where electron withdrawing groups such as in $4,4'\text{-}(Br)_2\text{-}2,2'$-bipyridine and 2,2'-biquinoline exhibited shorter excited-state lifetimes (τ) of 250 and 313 ns, respectively, while photosensitizers bearing more electron-rich ligands exhibited lifetimes values between 1.41 μs and 3.35 μs, (**Table 3.1**). The photoluminescence quantum yields (Φ_{PL}), under air and in argon-purged solutions, were

determined by comparative actinometry (**Equation 1.17**) using $[Ru(bpy)_3]^{2+}$ as the actinometer.[50] $[Ir(piq)_2(4,4'\text{-}(Br)_2\text{-}bpy)]^+$ and $[Ir(piq)_2(biq)]^+$ each exhibited a moderate Φ_{PL} of 0.029 and 0.063 under argon, respectively. All other photosensitizers exhibited a Φ_{PL} between 0.108 and 0.161 under argon. For the photosensitizers with τ greater than 1 μs, Φ_{PL} was always 4 to 6 times greater under argon than under air, indicating the possibility of $^1O_2$ photosensitization. Quenching rate constant by triplet oxygen of (2-7) x 10^8 $M^{-1}s^{-1}$ for those photosensitizers were estimated using an oxygen concentration of 2.4 mM for the air-saturated acetonitrile.[265]

Table 3.1. Photophysical properties of photosensitizers **1-9** recorded in argon purged acetonitrile.

Complex	Abs ε (M^{-1} cm^{-1})	PL_{max}	τ ns	Φ^a	k_r (x$10^4$$s^{-1}$)	k_{nr} (x$10^6$$s^{-1}$)
(1)	438 (6300)	630, 594	2580	0.108 (0.024)	4.84	0.34
(2)	440 (6500)	631, 593	3210	0.143(0.025)	4.76	0.26
(3)	440 (6000)	629, 594	3160	0.151(0.024)	4.83	0.27
(4)	434 (6000)	637, 601	3350	0.143(0.027)	4.20	0.26
(5)	441 (5900)	630, 594	1410	0.145 (0.022)	10.6	0.60
(6)	441 (6200)	630, 592	3180	0.137 (0.053)	4.31	0.27
(7)	442 (5900)	630, 596	2960	0.161 (0.030)	5.52	0.28
(8)	436 (5400)	635	250	0.029 (0.020)	12.1	3.88
(9)	427 (7900)	669	313	0.063 (0.044)	20.4	2.99

[a]Values for air-equilibrated solution in parenthesis

The iridium photosensitizers were also characterized by differential pulse voltammetry (DPV) (**Figure 3.4**), as well as by cyclic voltammetry (**Figure S3.1-9**) in 0.1M $TBAPF_6$ CH_3CN electrolytes. The nine photosensitizers exhibited reversible or quasi-reversible $Ir^{IV/III}$ oxidation waves at potentials centred between 1.41 and 1.53 V *vs* NHE. The introduction of electron-withdrawing derivatives, such as 4,4'-$(Br)_2$-2,2'-bipyridine and 2,2'-biquinoline had little influence on the $Ir^{IV/III}$ redox couple. On the other hand, the ligand-centred reductions were strongly influenced by the nature of the substituents on the 2,2'-bipyridine backbone. Compared to $[Ir(piq)_2(bpy)]^+$, which displayed a first one-electron ligand-centred reduction at –1.15 V *vs* NHE, derivatives with electron donating substituents in the 4,4', 5,5' or 6,6' position shifted the reduction potentials 60-120 mV more negative. The introduction of 4,4'-$(C_9H_{19})_2$-2,2'-bipyridine resulted in a 10 mV anodic shift compared to the

prototypical $[Ir(piq)_2(bpy)]^+$. The most drastic shifts were observed for the photosensitizers bearing 4,4'-$(Br)_2$-2,2'-bipyridine and 2,2'-biquinoline ligands, where the ligand-centred reductions were shifted by +320 mV and +410 mV, respectively. The corresponding excited state reduction (E_{red}*) and oxidation (E_{ox}*) potentials were determined using **Equations 1.23** and **1.24**, where E_{00} corresponds to the free energy stored in the excited state.[266, 267] As expected based on ground-state reduction potentials, $[Ir(piq)_2(4,4'-(Br)_2-bpy)]^+$ and $[Ir(piq)_2(biq)]^+$ were the most potent photo-oxidants, with E_{red}* of 1.41 and 1.37 V *vs* NHE, respectively. The other 7 photosensitizers had very similar E_{red}* (**Table 3.2**).

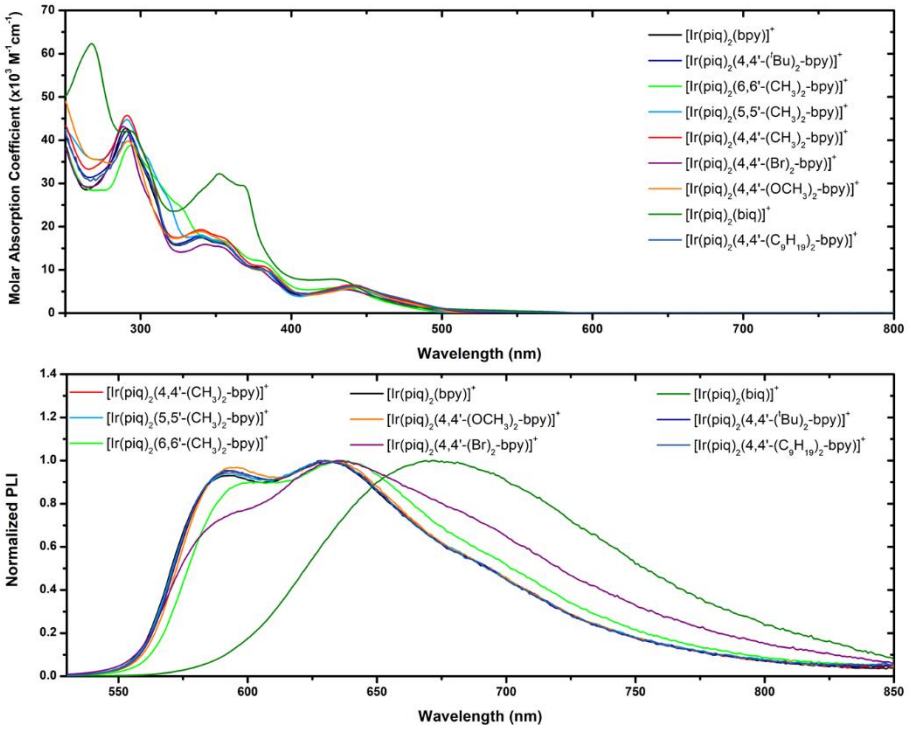

Figure 3.3. UV-Visible absorption (top) and photoluminescence (bottom) spectra of $[Ir(piq)_2(bpy)]^+$ (black), $[Ir(piq)_2(4,4'-(^tBu)_2-bpy)]^+$ (blue), $[Ir(piq)_2(6,6'-(CH_3)_2-bpy)]^+$ (green), $[Ir(piq)_2(5,5'-(CH_3)_2-bpy)]^+$ (light blue), $[Ir(piq)_2(4,4'-(CH_3)_2-bpy)]^+$ (red), $[Ir(piq)_2(4,4'-(Br)_2-bpy)]^+$ (purple), $[Ir(piq)_2(4,4'-(OCH_3)_2-bpy)]^+$ (orange), $[Ir(piq)_2(biq)]^+$ (olive) and $[Ir(piq)_2(4,4'-(C_9H_{19})_2-bpy)]^+$ (pale blue) recorded in acetonitrile at room temperature under argon.

Table 3.2. Ground and excited-state reduction and oxidation potentials for photosensitizers **1-9**.

Complex	$E_{1/2}(Ir^{IV/III})$ V *vs* NHE[a]	$E_{1/2}(L^{n/n-1})$ V *vs* NHE[a]	E_{00} (eV)[b]	*Eox** V *vs* NHE	*Ered** V *vs* NHE
(1)	1.48	–1.15	2.23	–0.75	1.08
(2)	1.45	–1.24	2.23	–0.78	0.99
(3)	1.48	–1.27	2.23	–0.75	0.96
(4)	1.45	–1.22	2.21	–0.77	0.99
(5)	1.46	–1.21	2.23	–0.77	1.02
(6)	1.47	–1.22	2.23	–0.76	1.01
(7)	1.44	–1.26	2.22	–0.78	0.96
(8)	1.53	–0.83	2.24	–0.71	1.41
(9)	1.41	–0.74	2.11	–0.70	1.37

[a] Electrochemical data (in V *vs* NHE, converted from V *vs* Ag/AgCl reference electrode by adding 0.205 V to the measured value) of the indicated Ir(III) photosensitizers (1 mM) recorded in argon purged acetonitrile with tetrabutylammonium hexafluorophosphate (0.1 M) as supporting electrolyte (scan rate : 0.1 V/s). [b]The E_{00} was determined using the generalizable method of extrapolating a tangent line on the blue edge of the corrected PL spectrum to the emission baseline.

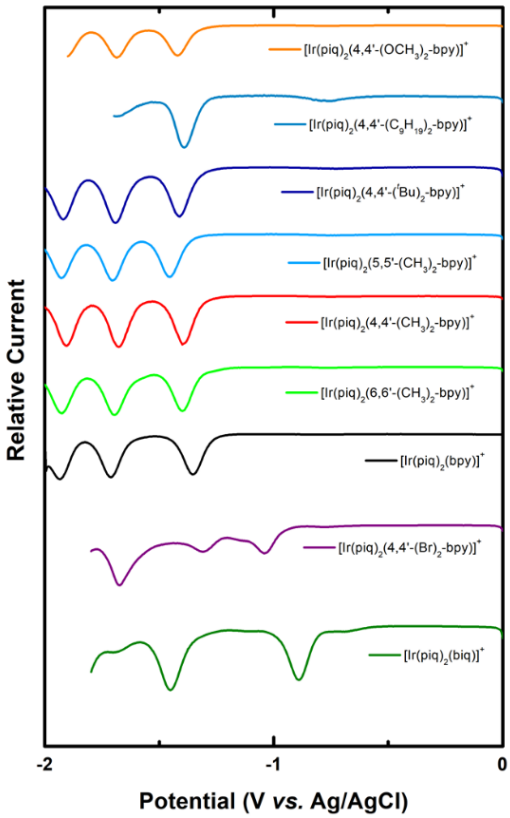

Figure 3.4. Differential pulse voltammetry of the indicated Ir(III) photosensitizers (1 mM) recorded in argon purged acetonitrile with 0.1 M $TBAPF_6$ as supporting electrolyte (scan rate : 0.05 V/s).

Excited-state reactivity of all $[Ir(piq)_2(LL)]^+$ photosensitizers towards triethylamine (TEA), triethanolamine (TEOA) and 1,3-dimethyl-2-phenyl-2,3-dihydro-1*H*-benzo[*d*]imidazole (BIH) as sacrificial electron donors was investigated in argon-purged acetonitrile. The driving force for electron transfer with BIH, TEOA and TEA was estimated based on available ground and excited-state reduction potentials.[35] With BIH as sacrificial electron donor, the driving force for electron transfer from all complexes was exergonic, with the Gibbs free energy for electron transfer, ΔG_{et}, ranging from –0.39 V for $[Ir(piq)_2(4,4'\text{-}(OCH_3)_2\text{-}bpy)]^+$ to –0.83 V with $[Ir(piq)_2(4,4'\text{-}(Br)_2\text{-}bpy)]^+$. With TEA and TEOA as the electron donors, ΔG_{et} was almost always ergoneutral or slightly endergonic. From the tabulated values in **Table 3.3**, ΔG_{et} became more exergonic with more potent photo-oxidants, *i.e.* $[Ir(piq)_2(4,4'\text{-}(Br)_2\text{-}bpy)]^+$ and $[Ir(piq)_2(biq)]^+$. This observation in driving force was also evident from Stern-Volmer measurements (**Figure 3.5** and **Figures S3.10-17**). A representative result of a Stern-Volmer titration using $[Ir(piq)_2(6,6'\text{-}(CH_3)_2\text{-}bpy)]^+$ with BIH, TEA and TEOA as the electron donors is shown in **Figure 3.5**. With BIH, drastic quenching of the steady-state photoluminescence was observed. The corresponding Stern-Volmer plot was linear within the quencher concentration range examined. From the slope, and taking the initial value of τ, a quenching rate constant (k_q) of 5.3 x10^9 $M^{-1}s^{-1}$ was determined. With TEA and TEOA, only moderate excited-state quenching was observed and the corresponding Stern-Volmer plots exhibited a downward curvature. This downward curvature was observed for almost all of the Ir(III) photosensitizers investigated in this study. Although a corresponding quenching rate constant could not be unambiguously determined, **Figure 3.5-D** indicates that the excited-state quenching was approximately three orders of magnitude smaller (10^6 $M^{-1}s^{-1}$) than with BIH (10^9 $M^{-1}s^{-1}$). For $[Ir(piq)_2(bpy)]^+$ an important decrease in PLI was observed upon the first addition of TEOA (**Figure S3.12-B**). This behaviour can be attributed to the formation of a pre-associated encounter complex by hydrogen bonding in alcohol environment between the ground-state photosensitizer and TEOA or to the photosensitizer partial degradation.

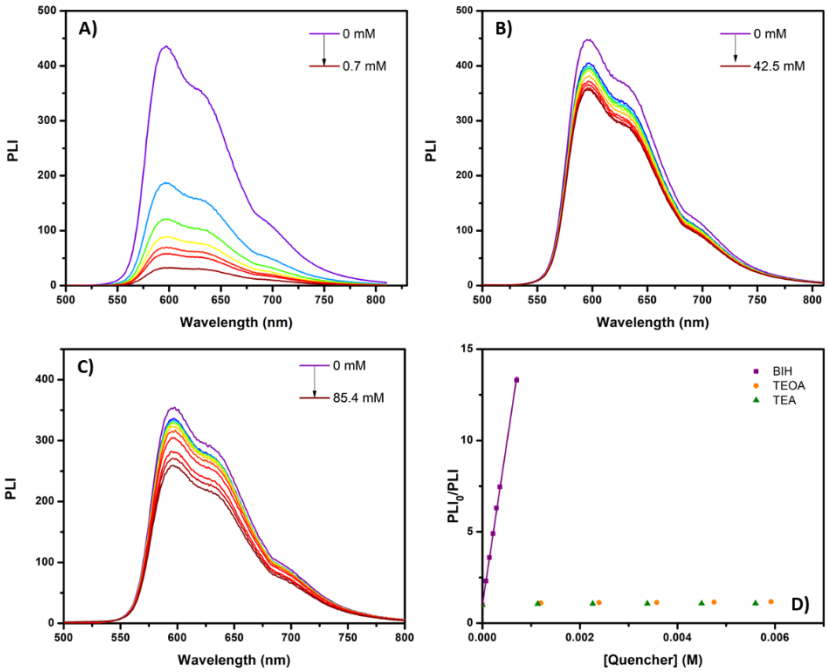

Figure 3.5. Excited-state quenching of [Ir(piq)$_2$(6,6'-(CH$_3$)$_2$-bpy)]$^+$ with BIH (A), TEOA (B) and TEA (C) in argon purged acetonitrile. The corresponding Stern-Volmer plots is shown in panel D, with the corresponding linear fit for the excited-state quenching in the presence of BIH.

To gain additional information of this peculiar behaviour, we performed time-resolved quenching experiments using [Ir(piq)$_2$(bpy)]$^+$ and TEA. Excited-state quenching was unambiguously observed when the concentration of TEA was gradually increased to 1.32 M. The corresponding Stern-Volmer plot was linear and the corresponding quenching rate constant of 7.1 x10^5 M^{-1}s^{-1} was determined from the slope. (**Figure S3.18**) This experiment confirmed the greater excited-state quenching conferred by BIH compared to TEA. The Stern-Volmer plots for the excited-state quenching of the nine Ir(III) photosensitizers with BIH are shown in **Figure 3.6**. The Stern-Volmer plots were all linear and the corresponding quenching rate constants were determined in the range of 1.6 x10^9 M^{-1}s^{-1} to 7.1 x10^9 M^{-1}s^{-1} (**Table 3.3**). These quenching rate constants were in line with other reports using Ir(III) PS and BIH electron donor.[180, 268] A rather counterintuitive quenching behavior was noted for photosensitizers [Ir(piq)$_2$(4,4'-(Br)$_2$-bpy)]$^+$ and [Ir(piq)$_2$(biq)]$^+$

where a smaller k_q was obtained despite having larger ΔG_{et} compared to other photosensitizers in the series studied, while [Ir(piq)$_2$(bpy)]$^+$ exhibited the larger quenching rate constant.

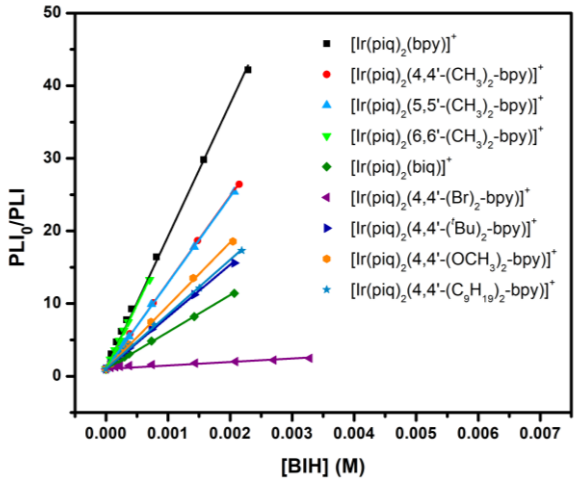

Figure 3.6. Stern-Volmer plots and corresponding linear fit for the excited-state quenching of all Ir(III) photosensitizers in the presence of BIH.

Although such behaviour could be attributed to a "Marcus inverted region behaviour", *i.e.* decreasing rate constant upon increased exergonicity, this is rarely observed in the case of diffusion controlled bimolecular electron transfer reactions.[42, 269-271] Instead, it was found that the decrease in k_q could likely result from reduced stability of both complexes upon illumination. Indeed, with [Ir(piq)$_2$(4,4'-(Br)$_2$-bpy)]$^+$ it was observed that allowing more light to excite the photosensitizer, by using wider excitation slits, resulted in some degradation that was detected as an increase in photoluminescence upon titration with BIH (see later photostability experiments). To observe genuine quenching, the opening of the excitation slit had to be kept minimal. With [Ir(piq)$_2$(biq)]$^+$, degradation was not observed with BIH, but with TEA as a quencher, a novel, more energetic photoluminescent band appeared (**Figure S3.16**). This was evidenced by the presence of an isosbestic point, indicating the formation of a new species in solution. Such an observation has already been recorded with [Ir(ppy)$_2$(4,4'-(^{t}Bu)$_2$-bpy)]$^+$ and [Ir(ppy)$_2$(bpy)]$^+$ and is more in line with an irreversible reduction of the N^N ligand.[74, 272] To further investigate whether

the changes in k_q could originate from degradation processes, we performed time-resolved photoluminescence measurements with [Ir(piq)$_2$(biq)]$^+$, [Ir(piq)$_2$(4,4'-(^{t}Bu)$_2$-bpy)]$^+$ and [Ir(piq)$_2$(bpy)]$^+$ in the presence of increasing amounts of BIH (**Figure 3.7**).

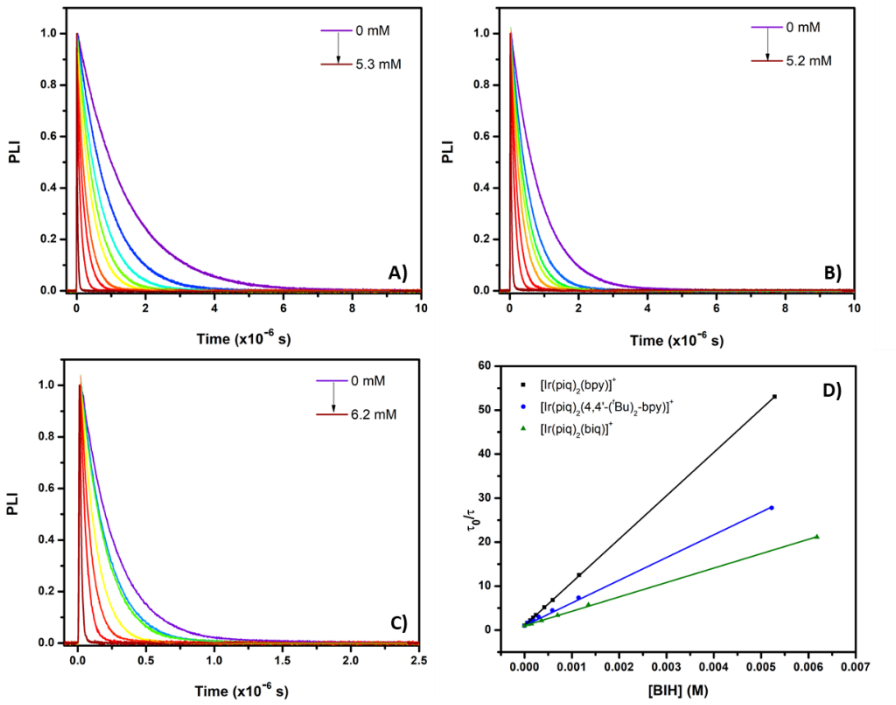

Figure 3.7. Time-resolved photoluminescence quenching of [Ir(piq)$_2$(bpy)]$^+$ (A), [Ir(piq)$_2$(4,4'-(^{t}Bu)$_2$-bpy)]$^+$ (B) and [Ir(piq)$_2$(biq)]$^+$ (C), with increasing amounts of BIH, with the corresponding Stern-Volmer plots shown in panel D.

The corresponding Stern-Volmer plot were all linear, with quenching rate constants of 7.1 x10^9 M^{-1}s^{-1}, 6.2 x10^9 M^{-1}s^{-1} and 1.3 x10^{10} M^{-1}s^{-1} for [Ir(piq)$_2$(bpy)]$^+$, [Ir(piq)$_2$(4,4'-(^{t}Bu)$_2$-bpy)]$^+$ and [Ir(piq)$_2$(biq)]$^+$, respectively. The values determined via steady-state or time-resolved photoluminescence measurements where the same for [Ir(piq)$_2$(bpy)]$^+$ and [Ir(piq)$_2$(4,4'-(^{t}Bu)$_2$-bpy)]$^+$ within experimental errors. However, for [Ir(piq)$_2$(biq)]$^+$, the quenching rate constant was almost one order of magnitude greater using time-resolved spectroscopy than by using steady-state techniques. This change in magnitude could originate from a degradation pathway occurring during steady-state photolysis. Hence, we hypothesized that neither [Ir(piq)$_2$(4,4'-

$(Br)_2$-bpy)]$^+$ nor $[Ir(piq)_2(biq)]^+$ would exhibit reversible behavior upon steady-state illumination and/or photoreduction catalysis, but that the other seven photosensitizers would be attractive candidates.

Table 3.3. Driving force (ΔG) and quenching rate constants (k_q) for electron transfer between BIH, TEOA or TEA and excited photosensitizers **1-9**.[a]

Compound	ΔG_{BIH} (eV)	ΔG_{TEOA} (eV)	ΔG_{TEA} (eV)	k_q (BIH) ($M^{-1}s^{-1}$)
(1)	–0.51	0.00	–0.06	7.1×10^9
(2)	–0.42	0.09	0.03	3.7×10^9
(3)	–0.39	0.12	0.06	3.8×10^9
(4)	–0.42	0.09	0.03	5.3×10^9
(5)	–0.44	0.06	0.00	5.1×10^9
(6)	–0.44	0.07	0.01	2.4×10^9
(7)	–0.39	0.12	0.06	2.9×10^9
(8)	–0.83	–0.33	–0.39	1.9×10^9
(9)	–0.79	–0.29	–0.35	1.6×10^9

[a] k_q with TEA and TEOA were in the 10^6 $M^{-1}s^{-1}$ range.

3.2.3 Transient absorption spectroscopy

Nanosecond transient absorption spectroscopy was then used to further confirm that the large quenching rate constant observed with BIH were originating from efficient excited-state electron transfer. Argon-purged solutions of $[Ir(piq)_2(bpy)]^+$, $[Ir(piq)_2(4,4'\text{-}(^t\text{Bu})_2\text{-bpy})]^+$ and $[Ir(piq)_2(biq)]^+$ were exposed to 420 nm pulsed-light excitation to determine their excited-state absorption features (**Figure 3.8**). Both $[Ir(piq)_2(bpy)]^+$ and $[Ir(piq)_2(4,4'\text{-}(^t\text{Bu})_2\text{-bpy})]^+$ exhibited positive absorption features centred around 520 nm. The excited state of $[Ir(piq)_2(biq)]^+$ presented positive absorption features around 460 nm accompanied by large absorption profile at wavelength greater than 600 nm, consistent with the population of a 2,2'-biquinoline-centered excited-state. In the presence of 5.2-6.2 mM of BIH, pulsed-light excitation led to the formation of the corresponding mono-reduced PS that could easily be observed (**Figure 3.8**). The spectral profile of the mono-reduced PS was in line with other reported spectra of related reduced iridium PS.[42, 43, 177, 273, 274] The efficiency of charge separation after electron transfer (cage escape yield) seems to be in the same range for the three PS, assuming similar molar absorption coefficient for the three mono-reduced PS.

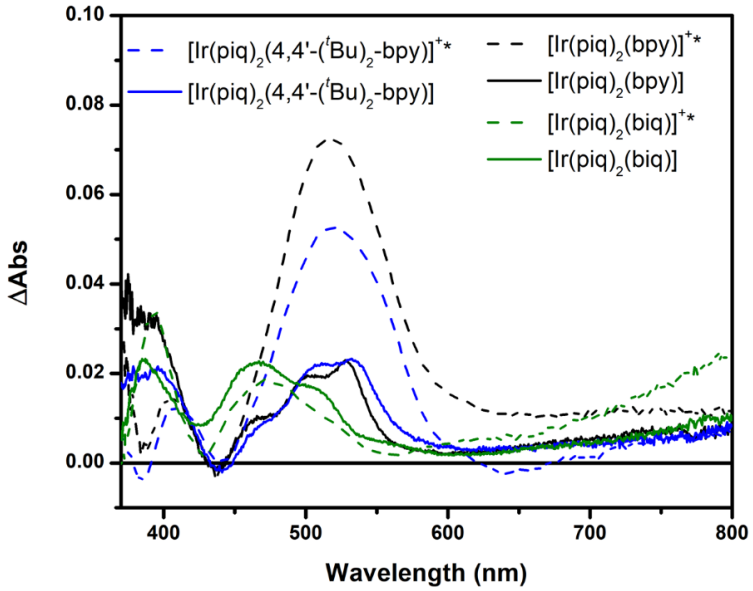

Figure 3.8. Transient absorption spectroscopy of [Ir(piq)$_2$(bpy)]$^+$ (black), [Ir(piq)$_2$(4,4'-(^{t}Bu)$_2$-bpy)]$^+$ (blue) and [Ir(piq)$_2$(biq)]$^+$ (olive) recorded 20 ns after the laser pulse in argon purged acetonitrile (dashed) and in the presence of 5.2-6.2 mM BIH (solid).

3.2.4 Steady-state illumination

Finally, steady-state illumination was performed to investigate the possibility of reversible accumulation of the mono-reduced photosensitizers. Consequently, solutions of the Ir(III) photosensitizers with an absorbance around 0.5 in the visible region were prepared in argon-purged acetonitrile. BIH was added to reach a concentration of 1 mM. The solutions were then irradiated with commercial blue LED strips for 15 minutes and absorption spectra were recorded at specific time intervals. **Figure 3.9** shows representative data for [Ir(piq)$_2$(bpy)]$^+$, [Ir(piq)$_2$(4,4'-(CH$_3$)$_2$-bpy)]$^+$, [Ir(piq)$_2$(biq)]$^+$ and [Ir(piq)$_2$(4,4'-(Br)$_2$-bpy)]$^+$. Steady-state illuminations with the other photosensitizers are gathered in the experimental section (**Figures S3.19-23**). With [Ir(piq)$_2$(bpy)]$^+$ and [Ir(piq)$_2$(4,4'-(CH$_3$)$_2$-bpy)]$^+$, blue light excitation led to changes in absorbance that agreed with excited-state electron transfer from BIH to the excited photosensitizers and subsequent mono-reduced complex formation. Indeed, the double absorption peaks at 500 and 530 nm, coupled with the increased absorbance beyond 700 nm were in line with absorption changes observed in transient absorption spectroscopy

with related photosensitizers. After 15 minutes of irradiation, an excess of potassium persulfate ($K_2S_2O_8$) was added as an irreversible electron acceptor to oxidize the monoreduced Ir photosensitizer and recover the ground-state Ir(III) products. [Ir(piq)$_2$(bpy)]$^+$ and [Ir(piq)$_2$(4,4'-(CH$_3$)$_2$-bpy)]$^+$ showed full reversibility upon the addition of $K_2S_2O_8$, highlighting their great photostability when storing high energy electrons and hence their promise as efficient photosensitizers for applications in reductive catalysis. When [Ir(piq)$_2$(4,4'-(Br)$_2$-bpy)]$^+$ was used, an increase of the absorbance around 400 nm was rapidly observed with irradiation. Upon addition of $K_2S_2O_8$, this absorption band decreased, but the original spectrum was never recovered, suggesting the instability of this photosensitizer upon prolonged illumination in the presence of electron donors. Finally, [Ir(piq)$_2$(biq)]$^+$ was also irradiated in the presence of BIH and showed the irreversibility of the photoreduction event (**Figure 3.9-C**). As mentioned previously, the irreversibility observed with [Ir(piq)$_2$(biq)]$^+$ and [Ir(piq)$_2$(4,4'-(Br)$_2$-bpy)]$^+$ could originate from partial/complete reduction of the N^N diimine ligand under prolonged irradiation, as has already been reported for [Ir(ppy)$_2$(4,4'-(^{t}Bu)$_2$-bpy)]$^+$ and [Ir(ppy)$_2$(bpy)]$^+$ using TEA as sacrificial electron donor.[74, 272] The complete reversibility observed for the other photosensitizers speaks towards their robustness and the possibility to use them for solar fuel production such as hydrogen or carbon dioxide reduction.

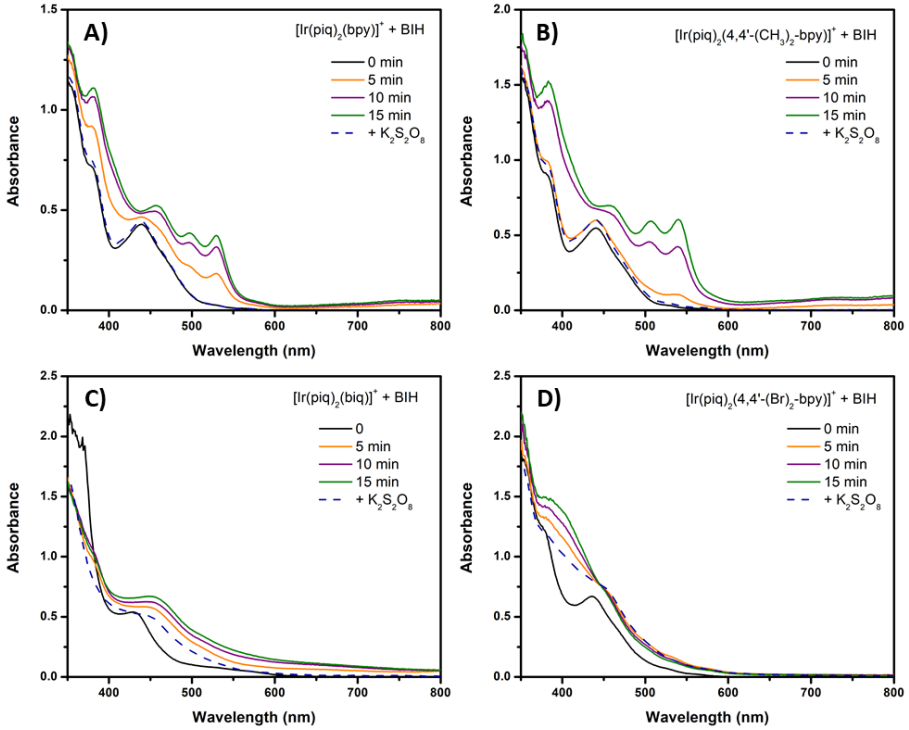

Figure 3.9. Absorption spectra of $[Ir(piq)_2(bpy)]^+$ (A), $[Ir(piq)_2(4,4'\text{-}(CH_3)_2\text{-}bpy)]^+$ (B), $[Ir(piq)_2(biq)]^+$ (C) and $[Ir(piq)_2(4,4'\text{-}(Br)_2\text{-}bpy)]^+$ (D) in argon-purged acetonitrile at room temperature at t= 0 minutes (black) and following 5 minutes (orange), 10 minutes (purple) and 15 minutes (olive) irradiation with blue LED light in the presence of 1 mM BIH. After the irradiation, an excess of $K_2S_2O_8$ was added to oxidize the photo-reduced photosensitizer and investigate reversibility.

3.3 Conclusions

A series of nine $[Ir(piq)_2(LL)]^+$ photosensitizers, including two newly reported complexes, $[Ir(piq)_2(4,4'\text{-}(Br)_2\text{-}bpy)]^+$ and $[Ir(piq)_2(6,6'\text{-}(CH3)_2\text{-}bpy)]^+$, was synthesized via one common route that involved the synthesis of the $[Ir(piq)_2(\mu\text{-}Cl)]_2$ dimer that further reacted with the N^N ligand. All photosensitizers exhibited appreciable visible light absorption with molar absorption coefficients in the 5400-7900 $M^{-1}cm^{-1}$ range at 427-442 nm. Excited-state electron transfer with classical electron donors such as TEA, TEOA and BIH was methodically investigated by steady-state excited-state quenching experiments in acetonitrile at ambient temperature. With TEA and TEOA, the quenching rate constants were low (~10^6 $M^{-1}s^{-1}$), but they reached

diffusion limited values (1.9-7.1 $x10^9$ $M^{-1}s^{-1}$) when BIH was used. Steady-state illumination in the presence of BIH confirmed that excited-state electron transfer occurred. Compounds with electron withdrawing 2,2'-bipyridine analogues were less stable upon irradiation in the presence of BIH, but the other seven photosensitizers exhibited exceptional dark- and photostability. This stability is vital for photoreduction catalysis, such as solar fuel formation via proton or CO_2 reduction, as reductants with $E_{1/2}(L^{n/n-1})$ between –1.34V and –1.47 V *vs* NHE can be reversibly accumulated. Altogether, the results presented herein show that comparisons between photosensitizers with different LL ligands highlight the significant impact of ligand modifications on both photophysical properties and excited-state quenching efficiency, providing valuable insights for the development of robust photosensitizers for solar fuel production.

3.4. Experimental section

The materials and methods used in this chapter are described in ***Chapter X****.*

Ethanol (≥99.9%, VWR), dichloromethane (≥99.9%, VWR), methanol (≥99.9%, VWR), tetrahydrofuran (≥99.9%, VWR), diethyl ether (≥99%, VWR), acetone (≥99.9%, VWR), ethyl acetate (≥99.9%, VWR), 2-ethoxyethanol (≥99%, Acros Organics), acetonitrile (≥99.9%, VWR), acetonitrile anhydrous (99.8%, Sigma Aldrich), [NH_4][PF_6] (99%, Fluorochem), $NaBH_4$ powder (98+%, Acros Organics), KOH (≥98% p.a., Roth), CH_3I (99% stab. with copper, ThermoFischer), 2-phenylbenzimidazole (>98.0%, TCI), tetra-*n*-butylammonium hexafluorophosphate (97%, Fluorochem), triethanolamine (99+%, Acros Organics), triethylamine (99%, Acros Organics), $K_2S_2O_8$ (99+%, Acros Organics), iridium trichloride hydrate (53% Ir, Pressure Chemical), 1-phenylisoquinoline (98%, TCI), 2,2'-bipyridine (97%, Ambeed), 4,4'-(CH3)2-2,2'-bipyridine (98%, ArkPharm), 5,5'-$(CH3)_2$-2,2'-bipyridine (98%, Sigma Aldrich), 6,6'-$(CH3)_2$-2,2'-bipyridine (99%, Ambeed), 4,4'-(^{t}Bu)$_2$-2,2'-bipyridine (98%, ArkPharm), 4,4'-$(C9H19)_2$-2,2'-bipyridine (97%, Alfa Aesar), 4,4'-$(OCH3)_2$-2,2'-bipyridine (97%, Sigma Aldrich), 4,4'-$(Br)_2$-2,2'-bipyridine (97%, TCI), 2,2'-biquinoline (98%, Ambeed), were purchased from commercial sources and used as received. [Ir(piq)$_2$(μ-Cl)]$_2$ and BIH were synthesized according to published procedures.[254, 262] Water was purified by a Millipore Milli-Q system. The precipitates were isolated by centrifugation at 4000 rpm for 3 min in a Hettich Universal 320 centrifuge.

3.4.1 Synthesis of the Ir(III) photosensitizers

Ir(III) chloro-bridged dimer [Ir(piq)$_2$μ-Cl]$_2$ (75 mg, 58.9 μmol) and the corresponding diimine ligand (147.25 μmol, 2.5 eq.) were placed in a sealed tube under argon atmosphere with 9 mL of MeOH/DCM 2:1 mixture. The reaction was heated at 60 °C for 24 hours. After reaction, the orange-red mixture was brought to room temperature. The DCM fraction was evaporated, and the resulting solution was treated with 10 mL of milliQ water and an excess of NH_4PF_6 was then added. The complex was isolated by centrifugation and was washed 3 times with milliQ water and 3 times with

diethyl ether to give the desired complexes with yields that ranged from 57 to 82 %.

[Ir(piq)$_2$(bpy)]$^+$.PF$_6^-$ was obtained by using the synthetic procedure described above with 2,2'-bipyridine as diimine ligand (23 mg), to give an orange powder (84.8 mg, 80% yield). ^{1}H NMR (500 MHz, CD_3CN) δ 9.04 – 8.99 (m, 2H), 8.54 (d, *J* = 8.2 Hz, 2H), 8.38 (d, *J* = 8.1 Hz, 2H), 8.11 (td, *J* = 7.9, 1.6 Hz, 2H), 8.04 – 7.92 (m, 2H), 7.87 (ddd, *J* = 5.5, 1.6, 0.8 Hz, 2H), 7.85 – 7.78 (m, 4H), 7.51 (d, *J* = 6.4 Hz, 2H), 7.46 (ddd, *J* = 7.7, 5.5, 1.2 Hz, 2H), 7.42 (dd, *J* = 6.5, 0.9 Hz, 2H), 7.18 – 7.05 (m, 2H), 6.88 (td, *J* = 7.4, 1.3 Hz, 2H), 6.31 (dd, *J* = 7.6, 1.3 Hz, 2H). HRMS (ESI) m/z calculated for $[C_{40}H_{28}N_4Ir - PF_6]^+$ = 755.19144; found 755.19152. NMR data are consistent with literature values.[183]

[Ir(piq)$_2$(4,4'-(CH$_3$)$_2$-bpy)]$^+$.PF$_6^-$ was obtained by using the synthetic procedure described above with 4,4'-dimethyl-2,2'-bipyridine as diimine ligand (27.1 mg), to give an orange powder (88.1 mg, 80% yield). ^{1}H NMR (500 MHz, CD_3CN) δ 9.06 – 8.95 (m, 2H), 8.44 – 8.27 (m, 4H), 8.06 – 7.92 (m, 2H), 7.91 – 7.74 (m, 4H), 7.68 (d, *J* = 5.7 Hz, 2H), 7.50 (d, *J* = 6.4 Hz, 2H), 7.42 (dd, *J* = 6.5, 0.9 Hz, 2H), 7.28 (ddd, *J* = 5.6, 1.8, 0.8 Hz, 2H), 7.12 (ddd, *J* = 8.2, 7.3, 1.3 Hz, 2H), 6.87 (td, *J* = 7.4, 1.3 Hz, 2H), 6.32 – 6.30 (m, 2H), 2.51 (s, 6H). HRMS (ESI) m/z calculated for $[C_{42}H_{32}N_4Ir - PF_6]^+$ = 783.22274; found 783.22266. NMR data are consistent with literature values.[275]

[Ir(piq)$_2$(5,5'-(CH$_3$)$_2$-bpy))]$^+$.PF$_6^-$ was obtained by using the synthetic procedure described above with 5,5'-dimethyl-2,2'-bipyridine as diimine ligand (27.1 mg), to give an orange powder (78.1 mg, 71% yield). ^{1}H NMR (500 MHz, CD_3CN) δ 9.08 – 8.98 (m, 2H), 8.37 (t, *J* = 8.1 Hz, 4H), 8.04 – 7.96 (m, 2H), 7.93 – 7.88 (m, 2H), 7.87 – 7.77 (m, 4H), 7.60 (d, *J* = 2.0 Hz, 2H), 7.51 (d, *J* = 6.4 Hz, 2H), 7.42 (d, *J* = 6.4 Hz, 2H), 7.13 (ddd, *J* = 8.3, 7.2, 1.4 Hz, 2H), 6.88 (td, *J* = 7.4, 1.3 Hz, 2H), 6.30 (dd, *J* = 7.7, 1.3 Hz, 2H), 2.14 (s, 6H). HRMS (ESI) m/z calculated for $[C_{42}H_{32}N_4Ir - PF_6]^+$ = 783.22274; found 783.22251. NMR data are consistent with literature values.[276]

[Ir(piq)$_2$(6,6'-(CH$_3$)$_2$-bpy))]$^+$.PF$_6^-$ was obtained by using the synthetic procedure described above with 6,6'-dimethyl-2,2'-bipyridine as diimine ligand (27.1 mg), to give an orange powder (84.3 mg, 77% yield). ^{1}H NMR (500 MHz, CD_3CN) δ 9.01 – 8.89 (m, 2H), 8.29 (d, *J* = 7.5 Hz, 2H), 8.19 (d, *J* = 8.0 Hz, 2H), 8.04 – 7.97 (m, 2H), 7.91 (t, *J* = 7.9 Hz, 2H), 7.88 – 7.75 (m, 6H), 7.45 (d, *J* = 6.2 Hz, 2H), 7.29 (dd, *J* = 7.7, 1.2 Hz, 2H), 7.03 (ddd, *J* = 8.3, 7.2, 1.3 Hz, 2H), 6.81 – 6.61 (m, 2H), 6.30 (dd, *J* = 7.7, 1.3 Hz, 2H), 1.81 (s, 6H). HRMS (ESI) m/z calculated for $[C_{42}H_{32}N_4Ir - PF_6]^+$ = 783.22274; found 783.22256.

[Ir(piq)$_2$(4,4'-(^{t}Bu)$_2$-bpy))]$^+$.PF$_6^-$ was obtained by using the synthetic procedure described above with 4,4'-^{t}Bu-2,2'-bipyridine as diimine ligand (39.5 mg), to give an orange powder (68.6 mg, 57% yield). ^{1}H NMR (500 MHz, CD_3CN) δ 9.07 – 8.95 (m, 2H), 8.52 (dd, *J* = 2.1, 0.7 Hz, 2H), 8.37 (d, *J* = 8.0 Hz, 2H), 8.08 – 7.93 (m, 2H), 7.89 – 7.79 (m, 4H), 7.73 (dd, *J* = 5.9, 0.6 Hz, 2H), 7.55 – 7.36 (m, 6H), 7.12 (ddd, *J* = 8.1, 7.2, 1.3 Hz, 2H), 6.87 (td, *J* = 7.4, 1.2 Hz, 2H), 6.30 (dd, *J* = 8.0, 1.3 Hz, 2H), 1.39 (s, 18H). HRMS (ESI) m/z calculated for $[C_{48}H_{44}N_4Ir - PF_6]^+$ = 867.31664; found 867.31621. NMR data are consistent with literature values.[277]

[Ir(piq)$_2$(4,4'-(C$_9$H$_{19}$)$_2$-bpy))]$^+$.PF$_6^-$ was obtained by using the synthetic procedure described above with 4,4'-$CH_3(CH_2)_8$-2,2'-bipyridine as diimine ligand (60.1 mg), to give an orange powder (81.3 mg, 60% yield). ^{1}H NMR (500 MHz, CD_3CN) δ 9.01 (dd, *J* = 6.4, 3.4 Hz, 2H), 8.48 – 8.30 (m, 4H), 8.07 – 7.93 (m, 2H), 7.90 – 7.74 (m, 4H), 7.69 (d, *J* = 5.9 Hz, 2H), 7.49 (d, *J* = 6.5 Hz, 2H), 7.42 (d, *J* = 5.9 Hz, 2H), 7.28 (dd, *J* = 5.7, 1.9 Hz, 2H), 7.17 – 7.05 (m, 2H), 6.87 (td, *J* = 7.4, 1.3 Hz, 2H), 6.31 (dd, *J* = 7.7, 1.4 Hz, 2H), 2.78 (t, *J* = 7.7 Hz, 4H), 1.69 (q, *J* = 7.2 Hz, 4H), 1.45 – 1.09 (m, 24H), 0.99 – 0.68 (m, 6H). HRMS (ESI) m/z calculated for $[C_{58}H_{64}N_4Ir - PF_6]^+$ = 1007.47314; found 1007.47317. NMR data are consistent with literature values.[278]

[Ir(piq)$_2$(4,4'-(OCH$_3$)$_2$-bpy)MeO-bpy)]$^+$.PF$_6^-$ was obtained by using the synthetic procedure described above with 4,4'-MeO-2,2'-bipyridine as diimine

ligand (31.8 mg), to give an orange powder (93.4 mg, 82% yield). ^{1}H NMR (500 MHz, CD_3CN) δ 9.07 – 8.92 (m, 2H), 8.36 (d, *J* = 8.0 Hz, 2H), 8.00 (dd, *J* = 6.8, 2.7 Hz, 4H), 7.92 – 7.72 (m, 4H), 7.61 (d, *J* = 6.4 Hz, 2H), 7.56 (d, *J* = 6.5 Hz, 2H), 7.45 (d, *J* = 6.3 Hz, 2H), 7.16 – 7.06 (m, 2H), 6.98 (dd, *J* = 6.4, 2.7 Hz, 2H), 6.86 (td, *J* = 7.4, 1.3 Hz, 2H), 6.31 (dd, *J* = 7.9, 1.1 Hz, 2H), 3.97 (s, 6H). HRMS (ESI) m/z calculated for $[C_{42}H_{32}O_2N_4Ir - PF_6]^+$ = 815.21257; found 815.21250. NMR data are consistent with literature values.[279]

$[Ir(piq)_2(4,4'\text{-}(Br)_2\text{-}bpy)]^+.PF_6^-$ was obtained by using the synthetic procedure described above with 4,4'-Br-2,2'-bipyridine as diimine ligand (45.9 mg), to give a red powder (86.3 mg, 70% yield). ^{1}H NMR (500 MHz, CD_3CN) δ 9.08 – 8.95 (m, 2H), 8.79 (dd, *J* = 1.7, 0.9 Hz, 2H), 8.52 – 8.29 (m, 2H), 8.04 – 7.97 (m, 2H), 7.90 – 7.79 (m, 4H), 7.66 (t, *J* = 1.1 Hz, 4H), 7.51 (d, *J* = 6.4 Hz, 2H), 7.48 – 7.42 (m, 2H), 7.13 (ddd, *J* = 8.2, 7.3, 1.3 Hz, 2H), 6.88 (td, *J* = 7.5, 1.3 Hz, 2H), 6.26 (dd, *J* = 7.7, 1.3 Hz, 2H). HRMS (ESI) m/z calculated for $[C_{40}H_{26}N_4Br_2Ir - PF_6]^+$ = 911.01246; found 911.01276.

$[Ir(piq)_2(biq)]^+.PF_6^-$ was obtained by using the synthetic procedure described above with 2,2'-biquinoline as diimine ligand (37.7 mg), to give a dark purple powder (96.2 mg, 81% yield). ^{1}H NMR (500 MHz, CD_3CN) δ 8.82 (d, *J* = 8.8 Hz, 2H), 8.65 (d, *J* = 8.7 Hz, 2H), 8.56 (d, *J* = 8.8 Hz, 2H), 8.27 (d, *J* = 7.4 Hz, 2H), 8.00 – 7.89 (m, 4H), 7.86 – 7.70 (m, 8H), 7.53 (ddd, *J* = 8.1, 6.8, 1.1 Hz, 2H), 7.31 (d, *J* = 6.5 Hz, 2H), 7.14 (ddd, *J* = 8.7, 6.8, 1.5 Hz, 2H), 7.10 (ddd, *J* = 8.2, 7.2, 1.3 Hz, 2H), 6.87 (td, *J* = 7.4, 1.3 Hz, 2H), 6.47 (dd, *J* = 7.8, 1.4 Hz, 2H). HRMS (ESI) m/z calculated for $[C_{48}H_{32}N_4Ir - PF_6]^+$ = 855.22274; found 855.22281. NMR data are consistent with literature values.[280]

3.4.2 Electrochemistry

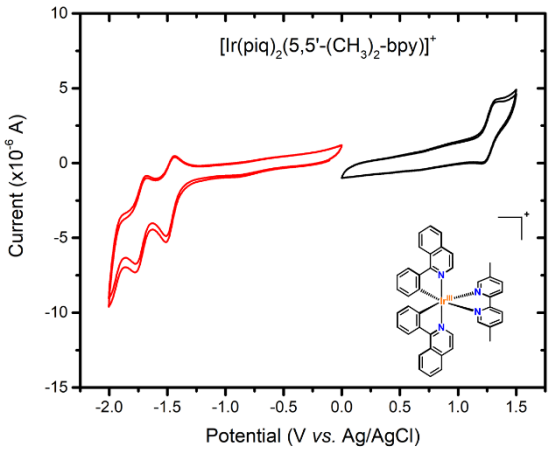

Figure S3.1. Cyclic voltammetry of [Ir(piq)$_2$(5,5'-(CH$_3$)$_2$-bpy]$^+$.PF$_6^-$ (1 mM) recorded at 100 mV/s in argon purged acetonitrile with 0.1M TBAPF$_6$ electrolyte.

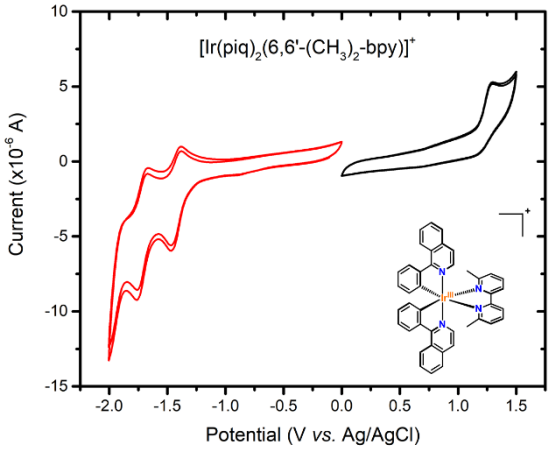

Figure S3.2. Cyclic voltammetry of [Ir(piq)$_2$(6,6'-(CH$_3$)$_2$-bpy]$^+$.PF$_6^-$ (1 mM) recorded at 100 mV/s in argon purged acetonitrile with 0.1M TBAPF$_6$ electrolyte. It is important to note that the photosensitizer exhibited a quasi-reversible Ir$^{IV/III}$ oxidation wave.

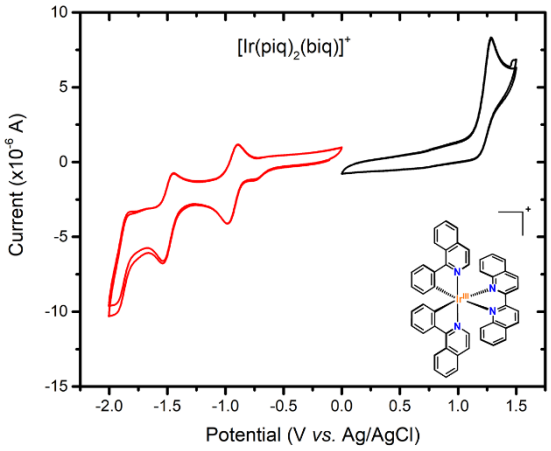

Figure S3.3. Cyclic voltammetry of [Ir(piq)$_2$(biq)]$^+$.PF_6^- (1 mM) recorded at 100 mV/s in argon purged acetonitrile with 0.1M $TBAPF_6$ electrolyte. It is important to note that the photosensitizer exhibited a quasi-reversible $Ir^{IV/III}$ oxidation wave.

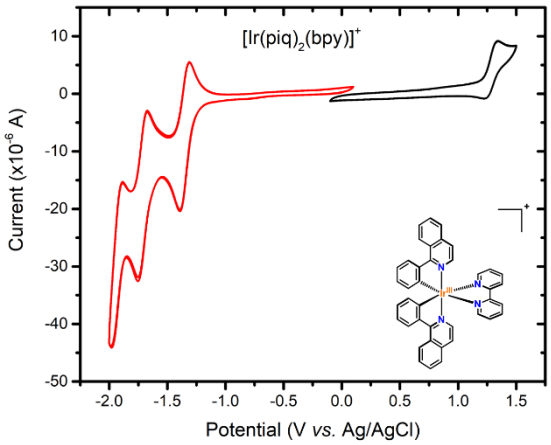

Figure S3.4. Cyclic voltammetry of [Ir(piq)$_2$(bpy)]$^+$.PF_6^- (1 mM) recorded at 100 mV/s in argon purged acetonitrile with 0.1M $TBAPF_6$ electrolyte.

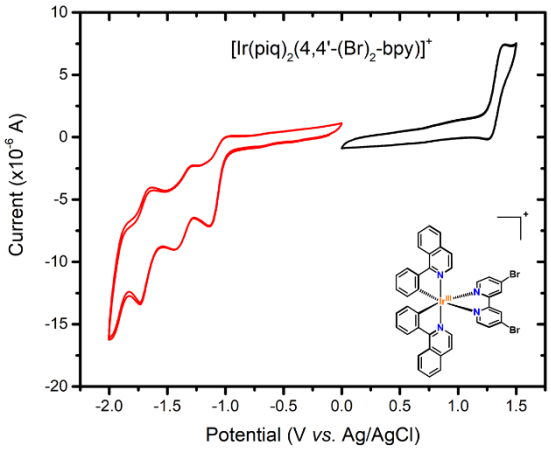

Figure S3.5. Cyclic voltammetry of [Ir(piq)$_2$(4,4'-(Br)$_2$-bpy)]$^+$.PF_6^- (1 mM) recorded at 100 mV/s in argon purged acetonitrile with 0.1M $TBAPF_6$ electrolyte.

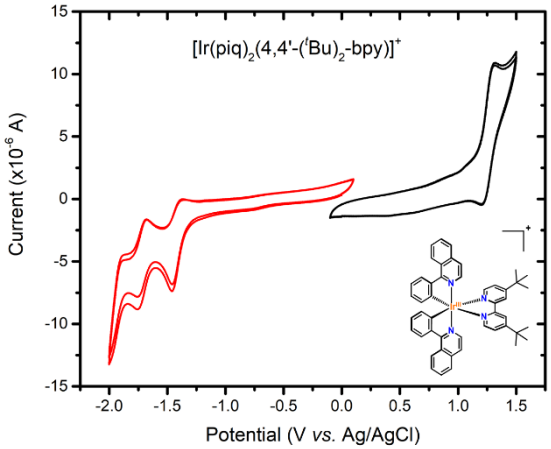

Figure S3.6. Cyclic voltammetry of [Ir(piq)$_2$(4,4'-(^{t}Bu)$_2$-bpy)]$^+$.PF_6^- (1 mM) recorded at 100 mV/s in argon purged acetonitrile with 0.1M $TBAPF_6$ electrolyte.

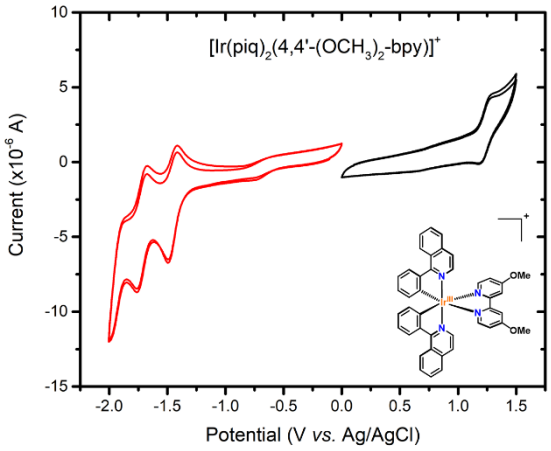

Figure S3.7. Cyclic voltammetry of [Ir(piq)$_2$(4,4'-(OCH$_3$)$_2$-bpy)]$^+$.PF$_6^-$ (1 mM) recorded at 100 mV/s in argon purged acetonitrile with 0.1M TBAPF$_6$ electrolyte.

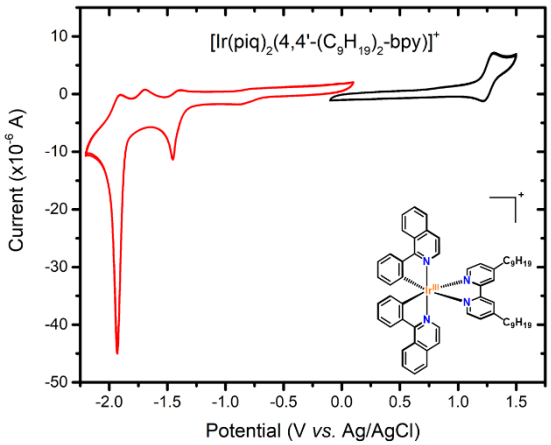

Figure S3.8. Cyclic voltammetry of [Ir(piq)$_2$(4,4'-(C$_9$H$_{19}$)$_2$-bpy)]$^+$.PF$_6^-$ (1 mM) recorded at 100 mV/s in argon purged acetonitrile with 0.1M TBAPF$_6$ electrolyte.

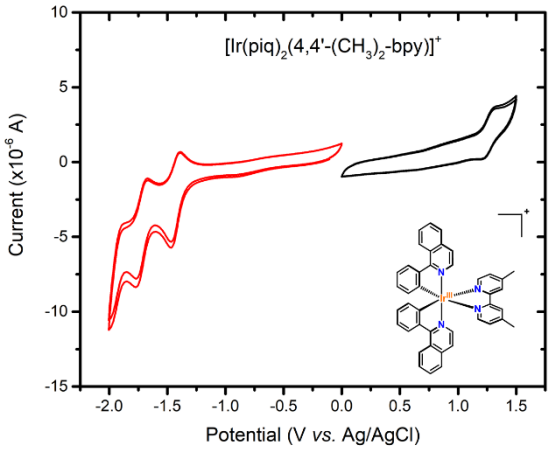

Figure S3.9. Cyclic voltammetry of [Ir(piq)$_2$(4,4'-(CH$_3$)$_2$-bpy]$^+$.PF$_6^-$ (1 mM) recorded at 100 mV/s in argon purged acetonitrile with 0.1M TBAPF$_6$ electrolyte.

3.4.3 Stern-Volmer

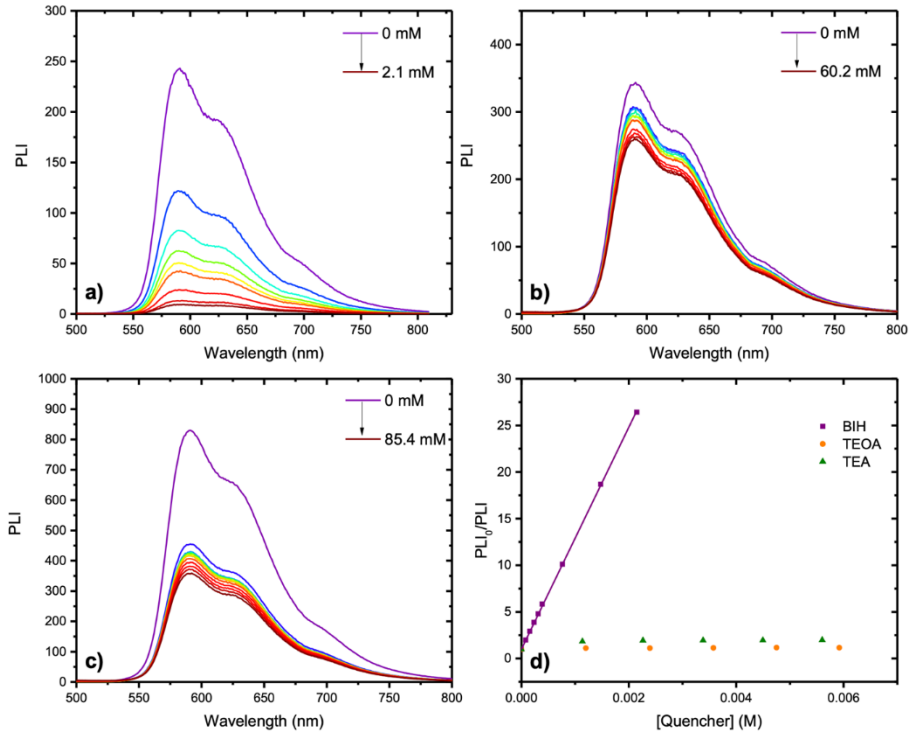

Figure S3.10. Excited-state quenching of [Ir(piq)$_2$(4,4'-(CH$_3$)$_2$-bpy)]$^+$ with BIH (a), TEOA (b) and TEA (c) in argon purged acetonitrile. The corresponding Stern-Volmer plots is shown in panel d, with the corresponding linear fit for the excited-state quenching in the presence of BIH.

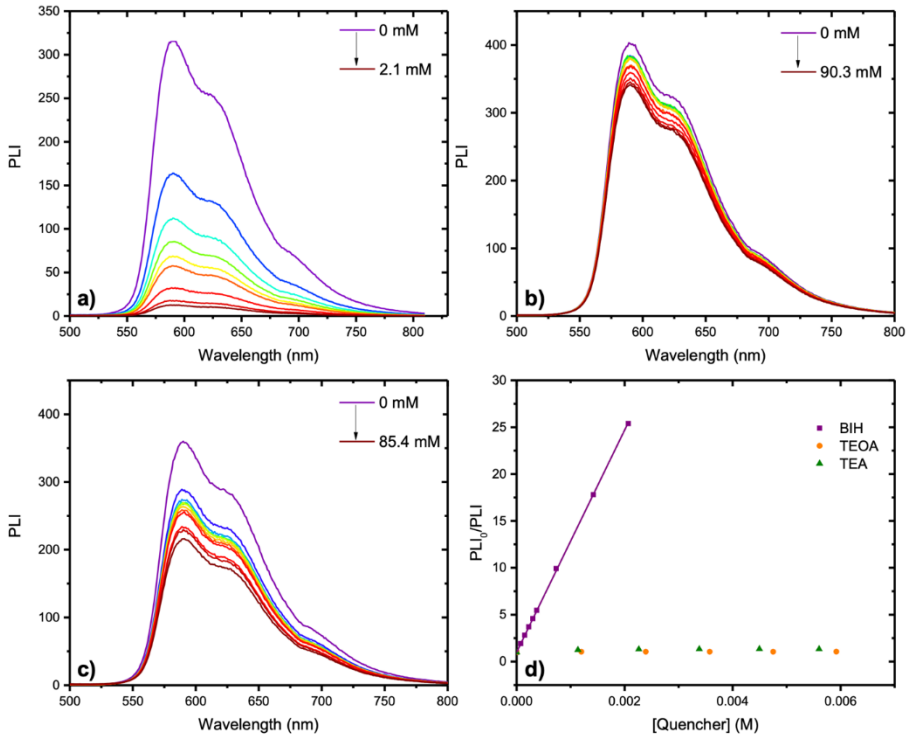

Figure S3.11. Excited-state quenching of [Ir(piq)$_2$(5,5'-(CH$_3$)$_2$-bpy)]$^+$ with BIH (a), TEOA (b) and TEA (c) in argon purged acetonitrile. The corresponding Stern-Volmer plots is shown in panel d, with the corresponding linear fit for the excited-state quenching in the presence of BIH.

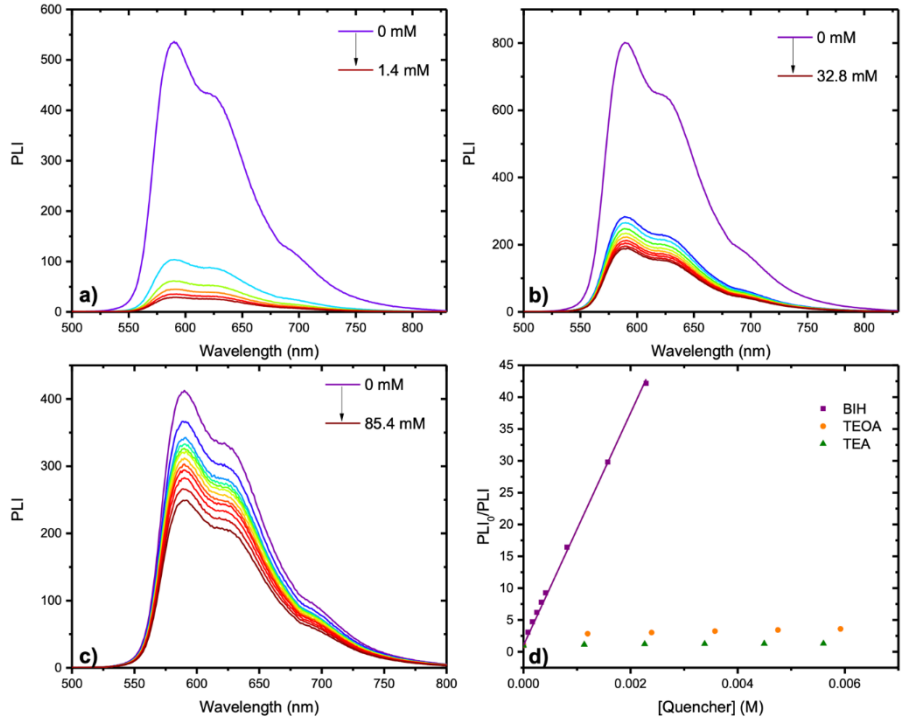

Figure S3.12. Excited-state quenching of [Ir(piq)$_2$(bpy)]$^+$ with BIH (a), TEOA (b) and TEA (c) in argon purged acetonitrile. The corresponding Stern-Volmer plots is shown in panel d, with the corresponding linear fit for the excited-state quenching in the presence of BIH.

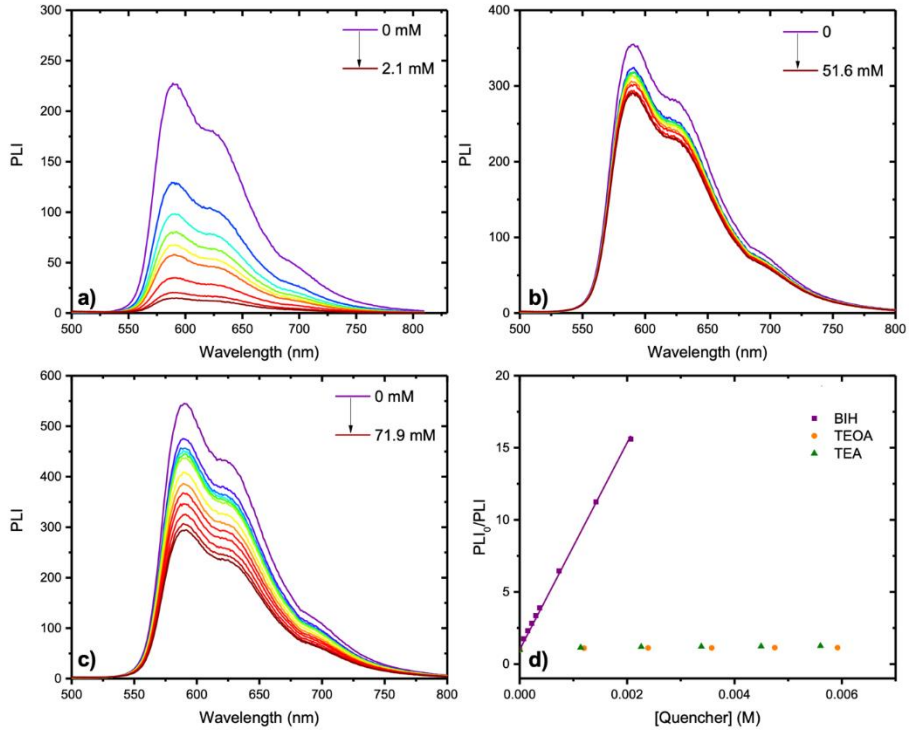

Figure S3.13. Excited-state quenching of [Ir(piq)$_2$(4,4'-(^{t}Bu)$_2$-bpy)]$^+$ with BIH (a), TEOA (b) and TEA (c) in argon purged acetonitrile. The corresponding Stern-Volmer plots is shown in panel d, with the corresponding linear fit for the excited-state quenching in the presence of BIH.

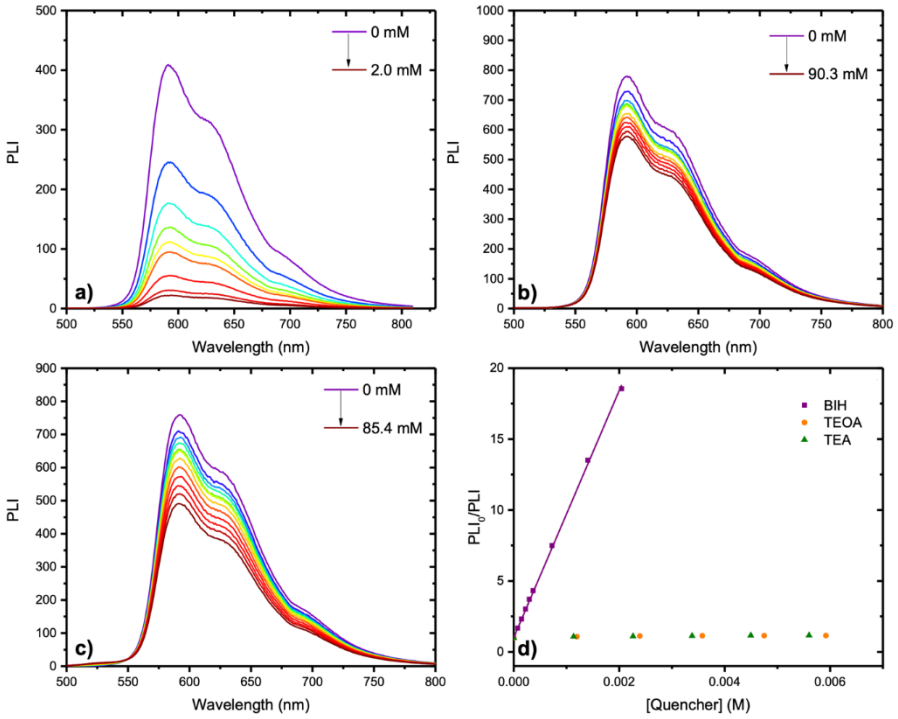

Figure S3.14. Excited-state quenching of [Ir(piq)$_2$(4,4'-(OCH$_3$)$_2$-bpy)]$^+$ with BIH (a), TEOA (b) and TEA (c) in argon purged acetonitrile. The corresponding Stern-Volmer plots is shown in panel d, with the corresponding linear fit for the excited-state quenching in the presence of BIH.

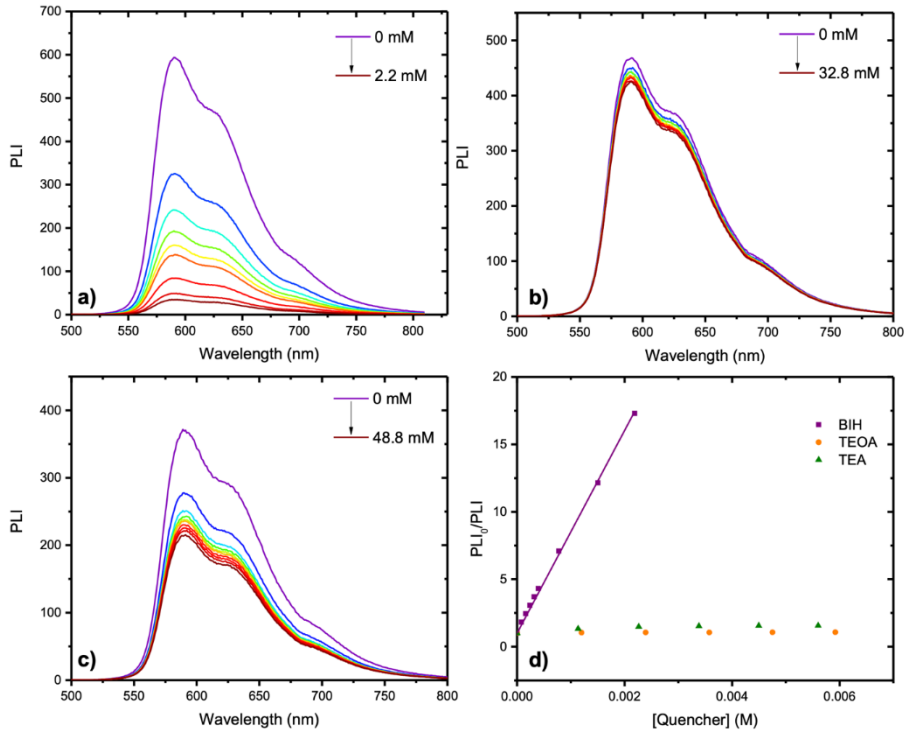

Figure S3.15. Excited-state quenching of [Ir(piq)$_2$(4,4'-(C$_9$H$_{19}$)$_2$-bpy)]$^+$ with BIH (a), TEOA (b) and TEA (c) in argon purged acetonitrile. The corresponding Stern-Volmer plots is shown in panel d, with the corresponding linear fit for the excited-state quenching in the presence of BIH.

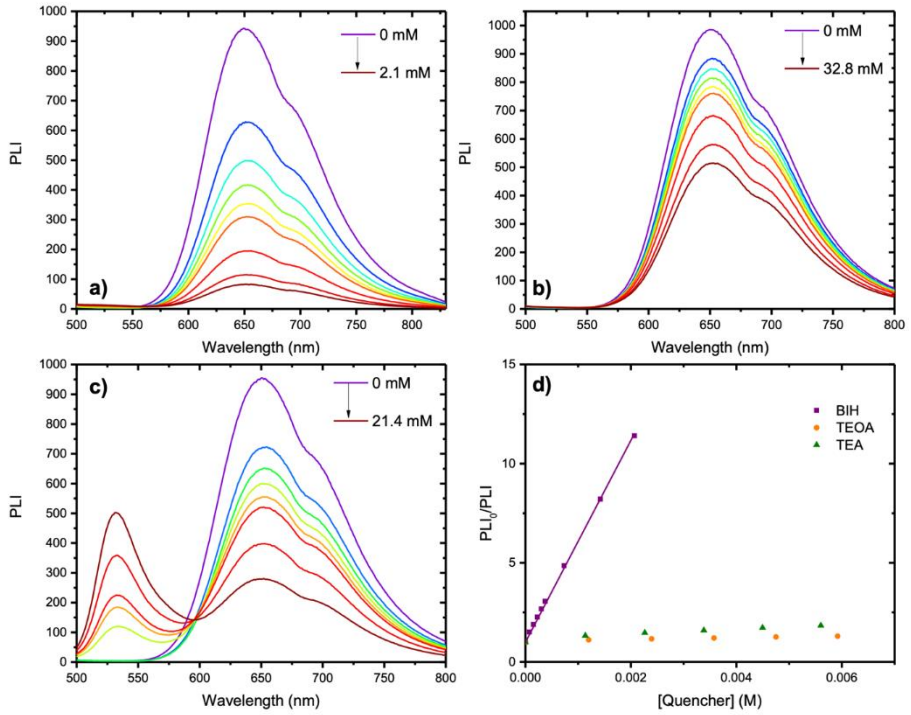

Figure S3.16. Excited-state quenching of [Ir(piq)$_2$(biq)]$^+$ with BIH (a), TEOA (b) and TEA (c) in argon purged acetonitrile. The corresponding Stern-Volmer plots is shown in panel d, with the corresponding linear fit for the excited-state quenching in the presence of BIH.

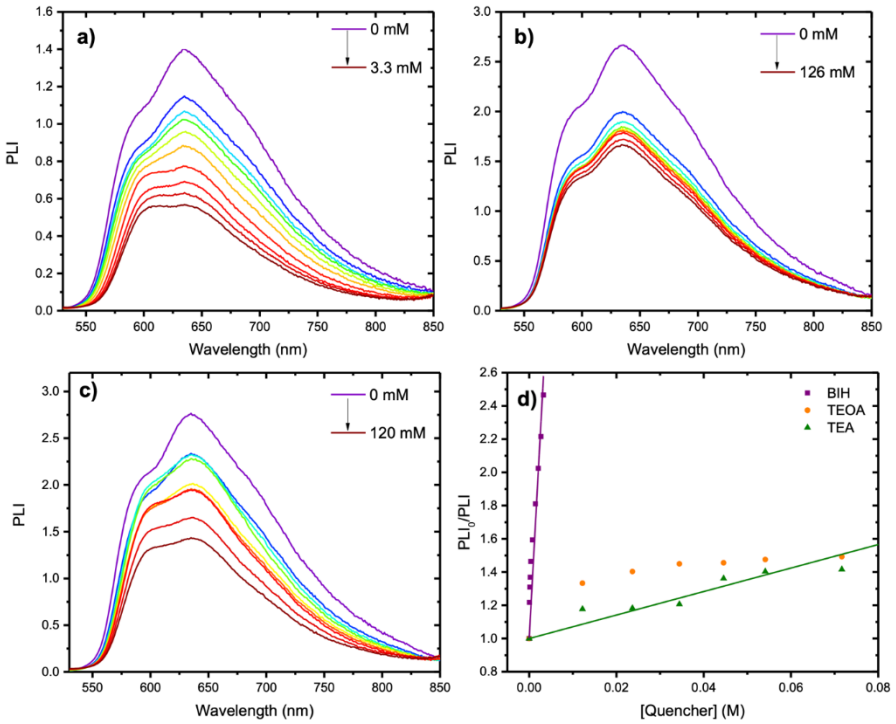

Figure S3.17. Excited-state quenching of [Ir(piq)$_2$(4,4'-(Br)$_2$-bpy)]$^+$ with BIH (a), TEOA (b) and TEA (c) in argon purged acetonitrile. The corresponding Stern-Volmer plots is shown in panel d, with the corresponding linear fit for the excited-state quenching in the presence of BIH.

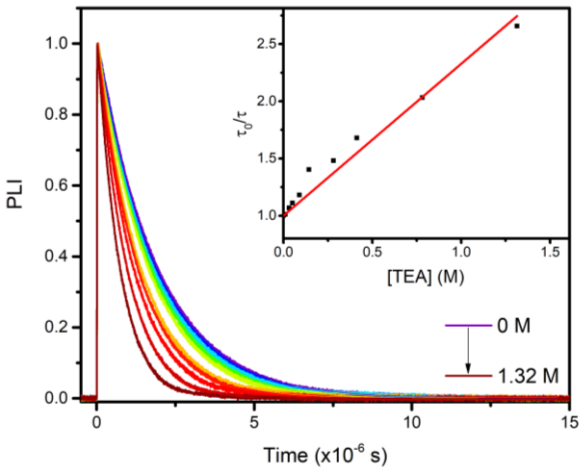

Figure S3.18. Excited-state quenching of [Ir(piq)$_2$(bpy)]$^+$ with TEA in argon purged acetonitrile. The corresponding Stern-Volmer plot is shown in the inset, with the corresponding linear fit.

3.4.4 Steady-state photolysis

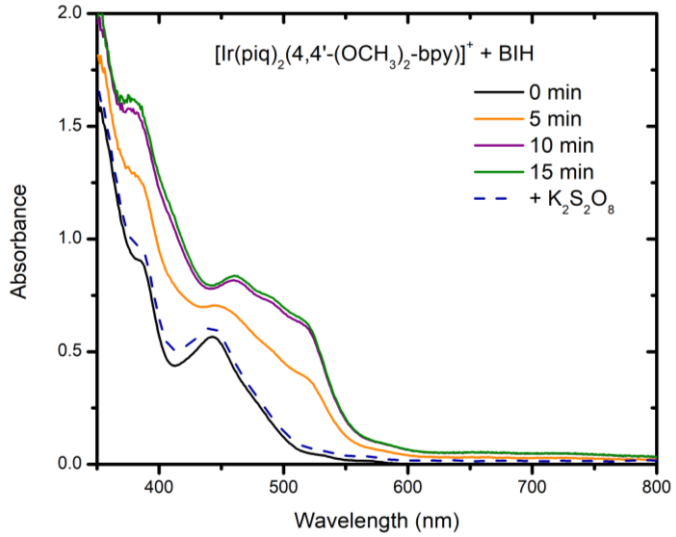

Figure S3.19. Absorption spectra of [Ir(piq)$_2$(4,4'-(OCH$_3$)$_2$-bpy)]$^+$ in argon-purged acetonitrile at room temperature at t = 0 minutes (black) and following 5 minutes (orange), 10 minutes (purple) and 15 minutes (olive) irradiation with blue-light in the presence of 1 mM BIH. After the experiment, $K_2S_2O_8$ was added to oxidize the photo-reduced photosensitizer and investigate reversibility.

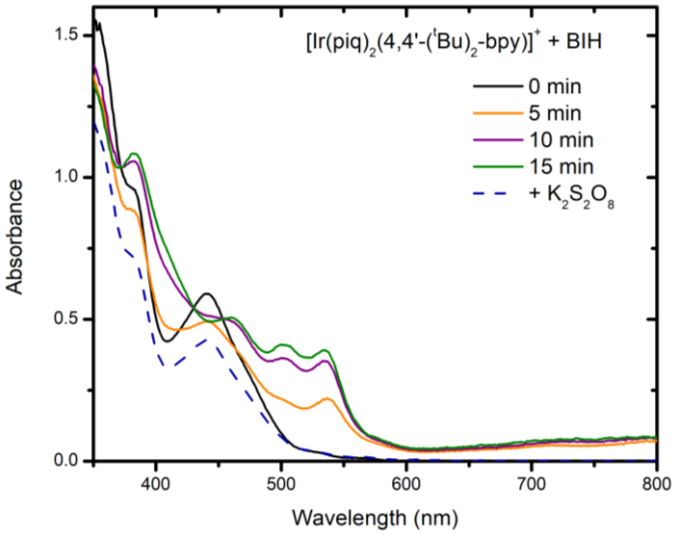

Figure S3.20. Absorption spectra of [Ir(piq)$_2$(4,4'-(^{t}Bu)$_2$-bpy)]$^+$ in argon-purged acetonitrile at room temperature at t = 0 minutes (black) and following 5 minutes (orange), 10 minutes (purple) and 15 minutes (olive) irradiation with blue-light in the presence of 1 mM BIH. After the experiment, $K_2S_2O_8$ was added to oxidize the photo-reduced photosensitizer and investigate reversibility.

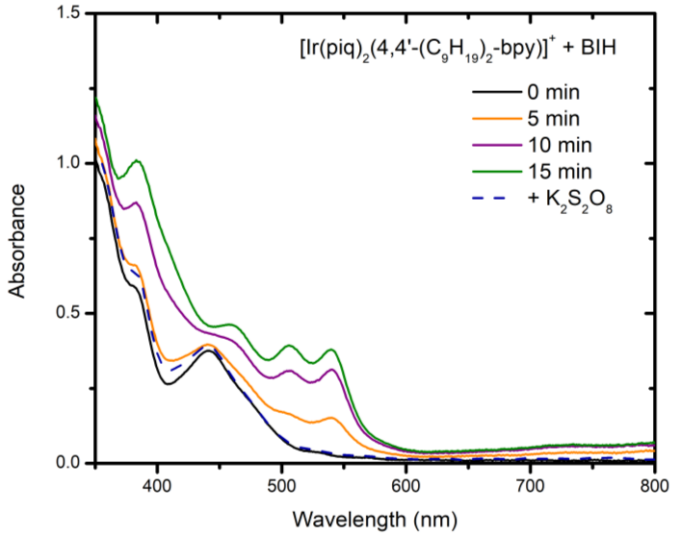

Figure S3.21. Absorption spectra of [Ir(piq)$_2$(4,4'-(C$_9$H$_{19}$)$_2$-bpy)]$^+$ in argon-purged acetonitrile at room temperature at t = 0 minutes (black) and following 5 minutes (orange), 10 minutes (purple) and 15 minutes (olive) irradiation with blue-light in the presence of 1 mM BIH. After the experiment, $K_2S_2O_8$ was added to oxidize the photo-reduced photosensitizer and investigate reversibility.

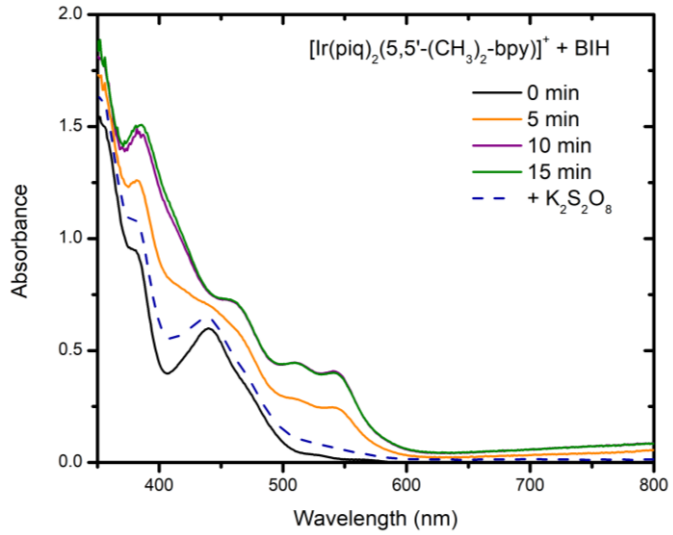

Figure S3.22. Absorption spectra of [Ir(piq)$_2$(5,5'-(CH$_3$)$_2$-bpy)]$^+$ in argon-purged acetonitrile at room temperature at t = 0 minutes (black) and following 5 minutes (orange), 10 minutes (purple) and 15 minutes (olive) irradiation with blue-light in the presence of 1 mM BIH. After the experiment, $K_2S_2O_8$ was added to oxidize the photo-reduced photosensitizer and investigate reversibility.

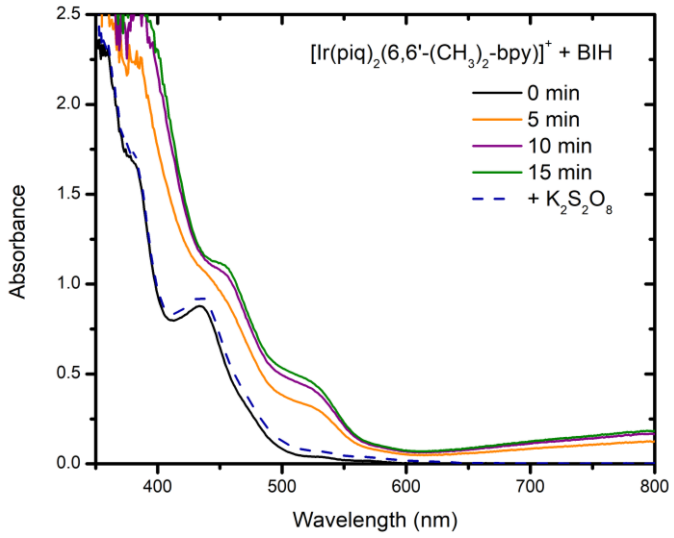

Figure S3.23. Absorption spectra of [Ir(piq)$_2$(6,6'-(CH$_3$)$_2$-bpy)]$^+$ in argon-purged acetonitrile at room temperature at t = 0 minutes (black) and following 5 minutes (orange), 10 minutes (purple) and 15 minutes (olive) irradiation with blue-light in the presence of 1 mM BIH. After the experiment, $K_2S_2O_8$ was added to oxidize the photo-reduced photosensitizer and investigate reversibility.

Chapter IV – Red Absorbing Cyclometalated Ir(III) Diimine Photosensitizers Competent for Hydrogen Photocatalysis

Researchers involved in this project are listed hereafter: Dr. Olivier Schott (Université de Montréal), Prof. Emilie Cauët (Université Libre de Bruxelles) and Prof. Garry S. Hanan (Université de Montréal). Hydrogen photo-evolution measurements were performed during a research internship at Université de Montréal in Prof. Garry S. Hanan's laboratory.

Preface – This chapter focuses on the synthesis and characterization of two new cyclometalated Ir(III) diimine complexes. Their spectroelectrochemical properties were characterized and their performances as photosensitizers for homogeneous hydrogen evolution reaction investigated. The results presented hereafter have been published in Inorganic Chemistry (De Kreijger, S.; Schott, O.; Troian-Gautier, L.; Cauët, E.; Hanan, G. S.; Elias, B., Red Absorbing Cyclometalated Ir(III) Diimine Photosensitizers Competent for Hydrogen Photocatalysis. Inorganic Chemistry 2022, 61 (13), 5245-5254.)

4.1 Introduction

In the view of developing a new sustainable energy supply as an alternative or complement to fossil fuels, different technologies have been explored for the conversion of sunlight into useful energy sources.[281, 282] Among them, a sunlight-triggered hydrogen evolution reaction (HER) appears to be an interesting solution to worldwide consumption of fossil fuels as hydrogen is an energy-dense and carbon-free fuel.[216, 16] From a molecular approach, this HER is typically based on photoinduced electron transfer from a photosensitizer (PS) to a catalytic centre, where hydrogen is produced.[220, 257, 283-286] In this context, cobalt macrocyclic complexes represent popular catalysts for homogeneous proton reduction. Cobaloximes are amongst the most studied molecular catalysts due to their ease of synthesis and fairly high activity.[219, 287, 256] While the development of such efficient homogeneous molecular catalysts has experienced great progress, the elaboration of photostable photosensitizers with increased visible light absorption properties still remains a challenging part of the HER advancement.[226] Cobaloximes have been associated to various transition metal-based PSs such as Zn(II),[288] Pt(II),[289, 290] Ru (II)[225, 291, 292] and Re (I)[293, 294] complexes. More recently, different Ir(III) bis-cyclometalated complexes have been explored as potential

candidates to develop stable and robust PSs for HER.[37, 183, 217, 295] These complexes are excellent candidates due to their inherent photophysical and electrochemical tunability coupled to a high photostability.[226] Even though it has been shown that Ir(III) complexes are outperforming archetypal PS such as $[Ru(bpy)_3]^{2+}$ (bpy = 2,2'-bipyridine), they are still suffering from poor visible light absorption properties that typically do not exceed 450 nm.

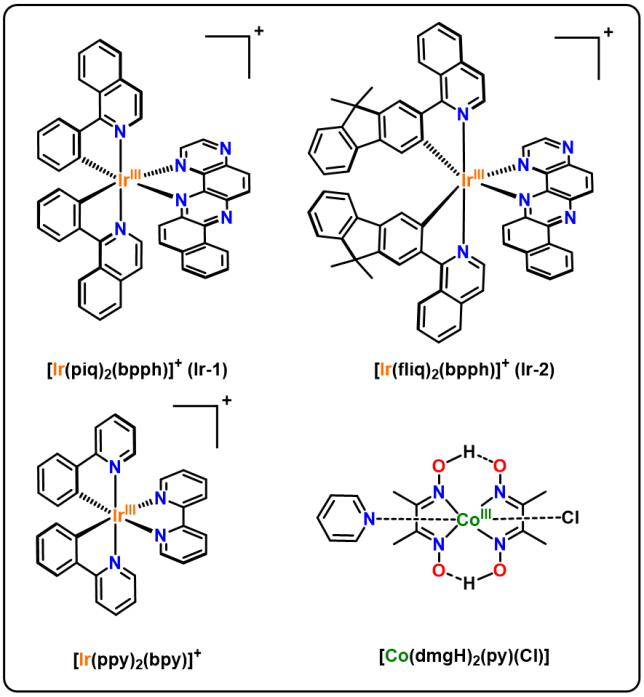

Figure 4.1. Structures of $[Ir(piq)_2bpph]^+$ (**Ir-1**), $[Ir(fliq)_2bpph]^+$ (**Ir-2**), $[Ir(ppy)_2bpy]^+$ and the precatalyst $[Co(dmgH)_2(py)(Cl)]$ used in this chapter.

The results of the previous chapter (see **Chapter III**) showed us that electron transfer was possible with triethylamine, triethanolamine and 1,3-dimethyl-2-phenyl-2,3-dihydro-1*H*-benzo[*d*]imidazole. We therefore used the excited-state of Ir(III) photosensitizers to achieve HER. The choice of the ligands, *i.e.* having extended π-delocalisation, has been governed by the desire to develop Ir(III) complexes able to absorb more visible light for solar fuels production. In this chapter, we report two novel Ir(III) based cyclometalated photosensitizers for HER that are efficiently working with $[Co(dmgH)_2(py)(Cl)]$ ($dmgH_2$ =

dimethylglyoxime) even when red light irradiation is used. These complexes display two cyclometalated **piq** (**Figure 4.1**, **Ir-1**) or **fliq** (**Figure 4.1**, **Ir-2**) ligands (**piqH** = 1-phenylisoquinoline; **fliqH** = 1-(9,9-dimethyl-9H-fluoren-2-yl)isoquinoline). In the previous chapter, the **piq** ligand was demonstrated to increase visible light absorption and to form Ir(III) photosensitizers that were competent for efficient reductive excited-state electron transfers with a prototypical sacrificial electron donor. We also investigated the **fliq** ligand, which exhibited increased conjugation compared to the **piq** ligand and, therefore, increased the HOMO stabilization as explained in our ligand design strategy (**Chapter II**, **Figure 2.3)**. These two cyclometalating ligands were combined with a recently reported N^N diamine π-extended heteroaromatic ligand, *i.e.* the bpph ligand (bpph = benzo[a]pyrazino[2,3-h]phenazine), which was shown to exhibit increased electronic conjugation to stabilize the Ir(III) LUMO and resulted in a redshift of the lowest energy absorption feature.[42] Strikingly, **Ir-1** and **Ir-2** exhibit a red-shifted absorption up to 620 nm, thus covering most of the visible spectrum. Consequently, both complexes were shown to efficiently evolve hydrogen under blue, green and low energy red-light irradiation, with turn-over numbers up to 11650, 10600 and 174 mol_{H2} mol_{PS}^{-1}, respectively.

4.2 Results and discussion

4.2.1 Synthetic approach

First, **fliqH** was obtained from a reported Suzuki coupling reaction between 1-chloroisoquinoline and 2-(9,9-dimethylfluorenyl)boronic acid in the presence of tetrakis(triphenylphosphine)palladium and aqueous sodium carbonate.[296] Second, the iridium dimers ($[Ir(piq)_2(\mu\text{-}Cl)]_2$ and $[Ir(fliq)_2(\mu\text{-}Cl)]_2$) were synthesized according to literature procedures, in which **piqH** or **fliqH** were refluxed in 2-ethoxyethanol/water (3:1) in the presence of iridium trichloride hydrate.[262] The **bpph** ligand was synthesized through a previously described condensation of quinoxaline-5,6-diamine with naphthalene-1,2-dione in acetic acid at 60 °C under microwave irradiation.[42] Finally, **bpph** was chelated onto the Ir(III) dimer precursors ($[Ir(piq)_2(\mu\text{-}Cl)]_2$ for **Ir-1** and $[Ir(fliq)_2(\mu\text{-}Cl)]_2$ for **Ir-2**)

in ethylene glycol at 110°C (see experimental section). The resulting complexes were further purified by several washing steps with water, ethanol and diethyl ether and were typically obtained with yields greater than 75%. The purity of the photosensitizers was assessed by HPLC.

4.2.2 X-Ray diffraction structures

The slow diffusion of diisopropylether into acetonitrile solutions of **Ir-1** and **Ir-2** at room temperature led to the growth of crystalline plates suitable for X-Ray diffraction. Both crystals shared the same space group P^{-1}. Crystals were measured at 100 K. Crystallographic and refinement parameters are given in **Table S4.1**. The quality of data diffraction was good for both structures. The unit cell of **Ir-1** and **Ir-2** included a racemic mixture of the two Λ and Δ enantiomers. The Ir coordination sphere of both photosensitizers exhibited widely similar near octahedral geometries to parent complexes previously reported such as the reference $[Ir(ppy)_2(bpy)]^+$ or Irpiq-2254tpy (2254tpy = 2,2',5',4"-terpyridine) or $[Ir(^{dCF3}ppy)_2(bbph)]^+$ (see **Table S4.3**).[42, 297] Deeper in details, the Ir(1)-N(14) bond of the extended conjugated side of **bpph** was 0.1 Å longer than the Ir(1)-N(11) that corresponded to N-bidentate bond lengths in the reference complexes (see **Figure 4.2** and **Tables S4.2 and S4.3**). In the 1-phenylisoquinoline derivatives, a higher typical torsion angle between the cyclometalated ligand and the N-cycle was observed: N(21)-C(29)-C(210)-C(224)= 15.7°(4) for **Ir-2** *vs* 1.5°(6) in $[Ir(ppy)_2(bpy)]^+$. The hindered fliq cyclometalated derivative **Ir-2** showed weakly more angular distortions in the coordination sphere than **Ir-1** (see **Table S4.2**).

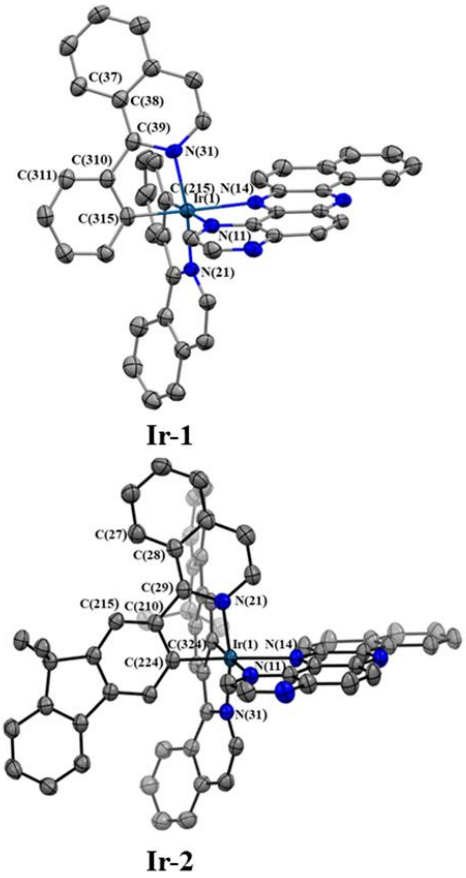

Figure 4.2. X-Ray structures of the Ir-1 (top) and Ir-2 (bottom). Ellipsoids are at the 50 % probability level. H atoms, PF_6^- counter anions, and co-crystallized solvent molecules are omitted for clarity.

4.2.3 Electrochemistry

The electrochemical data for **Ir-1** and **Ir-2** were measured by cyclic voltammetry in dry deoxygenated acetonitrile, a suitable solvent for photocatalytic H_2 production, using 0.1M $TBAPF_6$ as supporting electrolyte (**Figure 4.3**). The half-wave electrochemical potentials are gathered in **Table 4.1**.

Ir-2 displayed a reversible one-electron oxidation wave, $E_{ox,\,\mathbf{Ir\text{-}2}}$ = + 1.51 V *vs* NHE, that, in agreement with the literature, was assigned to the oxidation of the Ir(III)-cyclometalated ligand fragment.[298] **Ir-1** exhibited an irreversible

Ir(III)-cyclometalated ligand oxidation wave at scan rates comprised between 0.05 and 1 V/s. When the scan rate was increased to values larger than 1V/s, reversibility was observed which allowed to determine an oxidation potential, $E_{ox,\ \mathbf{Ir\text{-}1}}$ = + 1.61 V *vs* NHE. In both cases, the dependence of the peak current versus the square root of the scan rate was linear, in agreement with the Randles-Sevcik equation.[299]

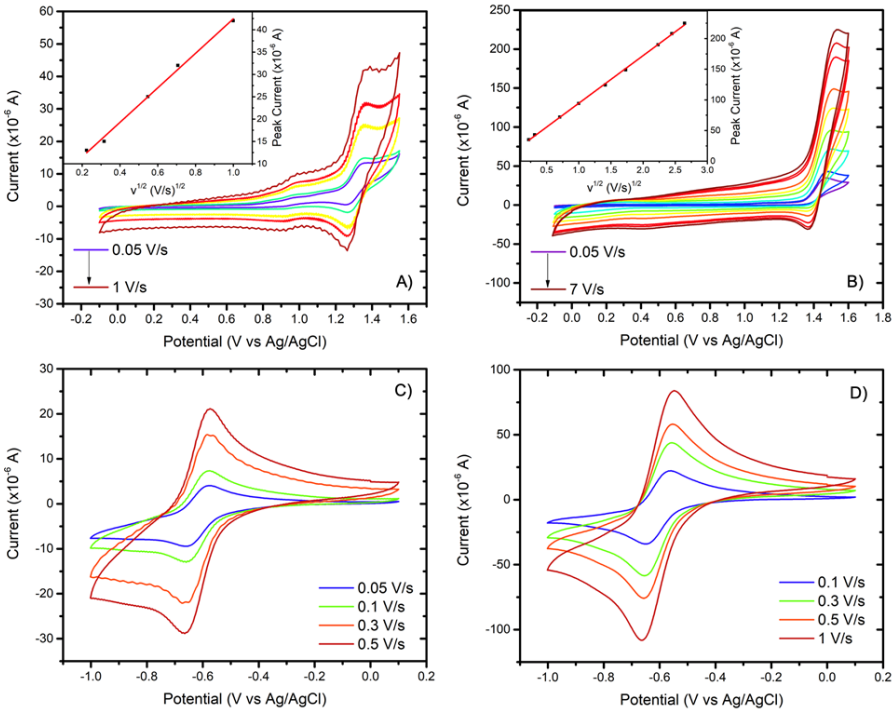

Figure 4.3. Cyclic voltammograms of **Ir-2** (A-C) and **Ir-1** (B-D) recorded at the indicated scan rate in argon purged acetonitrile containing 0.1 M $TBAPF_6$. The concentration of **Ir-1** was 1 mM whereas a concentration of 0.5 mM was used for **Ir-2**. The inset of panel A and B shows the dependence of the peak current versus the square root of the scan rate, according to the Randles-Sevcik equation.[299]

This implies that the electrochemical reaction is a reversible electron transfer process involving freely diffusing redox species. The slightly less anodic oxidation for **Ir-2** likely originates from the extended π-conjugation on the **fliq** compared to its homologue **Ir-1** containing the **piq** ligand. Furthermore, an additional oxidation process was observed at 1.89 V *vs* NHE for **Ir-2**. This

latter was ascribed to the oxidation of the **fliq** moieties. Indeed, an irreversible oxidation process at 1.96 V *vs* NHE was observed for the ligand alone in acetonitrile (**Figure S4.5**). **Ir-1** and **Ir-2** displayed a similar reversible one-electron reduction pattern, with waves at –0.40 V and –1.13 V *vs* NHE corresponding to a reduction process taking place on the **bpph** ligand as shown for related complexes.[42] Further cathodic electrochemical processes involve both the **bpph** and **fliq** or **piq** ligands.

Table 4.1. Electrochemical and photophysical properties of **Ir-1**, **Ir-2** and $[Ir(ppy)_2(bpy)]^+$ in acetonitrile at room temperature.

	Ir-1	**Ir-2**	**$[Ir(ppy)_2(bpy)]^+$**
E_{ox}[a]	+ 1.61	+ 1.51; + 1.89	+ 1.57
E_{red}[a]	–0.40; –1.13; –1.57	–0.41; –1.13; –1.54	–1.10
λ_{abs}[b], [c]	428 (140); 455 (109); 560 (11.7); 620 (9.4)	365 (412); 430 (183); 500 (36.6); 560 (10.1); 620 (9.2)	310 (227); 376 (64); 412 (36)
λ_{em}[b], [d]	776	667, 778	599
Φ_{PL}	0.001 [e]	0.002[e]	0.022 [f]
τ (ns)	τ_1 = 19 ns τ_2 = 410 ns	τ_1 = 450 ns τ_2 = 1300 ns	365 ns [g]

[a] Electrochemical data (in V *vs* NHE, converted from V *vs* Ag/AgCl by adding 0.205 V) were measured with tetrabutylammonium hexafluorophosphate (0.1 M) as supporting electrolyte with a sweep rate of 0.3 V/s and a photosensitizer concentration of 1mM (**Ir-1**) and 0.5 mM (**Ir-2**). [b] In nm, recorded in argon purged acetonitrile. [c] Values in parenthesis indicate the molar absorption coefficient, ε x 10^2 $M^{-1}cm^{-1}$. [d] excitation at 450 nm. [e] Measured *vs* $[Os(bpy)_3]^{2+}$ (Φ_{ref} = 0.005 in argon-saturated acetonitrile) (λ_{exc} = 450 nm), $[Os(bpy)_3]^{2+}$ was chosen because it possesses the same emission spectral range (λ_{em} = 742 nm) as the investigated Ir(III) complexes.[300] [f] Measured under air-equilibrated solution *vs* Quinine in 0.5M H_2SO_4 in water (Φ_{ref} = 0.546 - λ_{exc} = 365 nm).[300] [g] from ref [74]

4.2.4 Theoretical studies

The excited state of bis-cyclometalated Ir(III) complexes is usually dominated by a mixture of Ligand-Centred (LC), Ligand-to-Ligand Charge Transfer (LLCT), Metal-to-Ligand Charge Transfer (MLCT) and Metal-Ligand-to-Ligand Charge Transfer (MLLCT) transitions.[226] For **Ir-1** and **Ir-2**, time-dependent density functional theory (TD-DFT) calculations, performed in collaboration

with Prof. E. Cauët, showed that each of these molecular orbital transition contributes to the absorption features (**Figures 4.4-D and 4.5** and **Figure S4.6**), with moderate to strong oscillator strength, confirming the CT nature of the lowest excited states. The theoretically determined transitions matched well with the experimentally recorded electronic absorption spectra (**Figure 4.4-D**). Among the most intense transitions of **Ir-1**, the one centred at 328 and 375 nm involved an electronical transition centred on the **bpph** moieties combined with contributions from the Ir(III) centre (**Figure 4.5**). These transitions are hence ascribed to MLLCT transitions. The less energetic contribution to the absorption (457 nm) involved a transition from the metallic centre and both ligands towards the **bpph** N^N diimine ligand and is ascribed to a mixture of MLLCT and LLCT transitions. For **Ir-2**, the transitions at 323 and 412 nm are centred on the **bpph** and **fliq** moieties of the complex, respectively, with some contribution from the Ir(III) centre. The most bathochromic transition at 467 nm exhibits contributions from both the Ir(III) centre and the **bpph** moiety (**Figure 4.5**). In addition, a clear shift to lower energetical transitions is observed from **Ir-1** to **Ir-2**, confirming the higher stabilization induced by the **fliq** ligand.

4.2.5 Photophysical properties

The absorption spectra of ppyH, fliqH, piqH, bbph as well as the absorption and steady-state photoluminescence spectra for **Ir-1** and **Ir-2** were recorded in argon purged acetonitrile at room temperature and are displayed in **Figures 4.4-A and C**. The corresponding photophysical data are gathered in **Table 4.1** along with those of $[Ir(ppy)_2(bpy)]^+$, (ppyH = 2-phenylpyridine) for comparison purposes. Both ppyH and piqH exhibited absorption features in the UV region with molar absorption coefficients that ranged from 5000 $M^{-1}cm^{-1}$ (piqH) to 15,000-20,000 $M^{-1}cm^{-1}$ (ppyH). The 1-phenylisoquinoline ligand also presented absorption features between 300 and 350 nm, with moderate molar absorption coefficients. The use of fliqH allowed to drastically increase the molar absorption coefficient to reach values around 20,000 $M^{-1}cm^{-1}$ at 350 nm. The donor-acceptor structure of the bpph ligand enabled absorption in the visible region with molar absorption coefficients that reached 10,000 $M^{-1}cm^{-1}$

at 410 nm. Regarding the iridium photosensitizers, both **Ir-1** and **Ir-2** are characterized by strong ligand-centred (LC) absorption bands in the UV region ($\varepsilon > 10^4$ M^{-1} cm^{-1} at wavelengths < 340 nm). In good agreement with the theoretical studies, lower energy (> 350 nm) Metal-Ligand to Ligand Charge Transfer (MLLCT) transitions are observed with a strong intensity ($\varepsilon > 10^4$ M^{-1} cm^{-1}). As expected, in **Ir-1** and **Ir-2**, the higher electronic conjugation within the π-system of the N^N diimine as well as the use of piq and fliq cyclometalated ligands led to a red-shifted absorption accompanied by an important increase in the molar absorption coefficient compared to the reference photosensitizer $[Ir(ppy)_2(bpy)]^+$. In line with the TD-DFT analysis, **Ir-2** shows a bathochromic shift compared to **Ir-1**, due the presence of π-conjugated **fliq** ligands.[296]

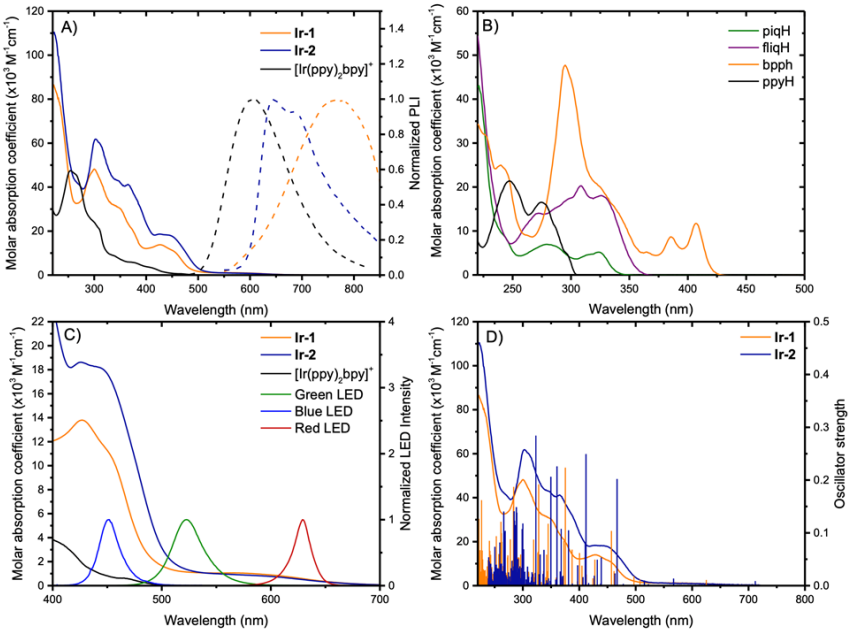

Figure 4.4. A) Absorption spectra of **Ir-1** (orange), **Ir-2** (blue) and $[Ir(ppy)_2(bpy)]^+$ (black) recorded in acetonitrile at room temperature as well as the corresponding photoluminescence in argon purged acetonitrile at room temperature. B) Absorption spectra of piqH (green), ppyH (black), fliqH (purple) and bpph (orange) recorded in acetonitrile at room temperature. C) Overlap between the absorption spectra of **Ir-1** (orange), **Ir-2** (blue) and $[Ir(ppy)_2(bpy)]^+$ (black) and the irradiation source used in this HER study. (D) Absorption spectra of **Ir-1** (orange) and **Ir-2** (blue) recorded in acetonitrile at room temperature with their corresponding calculated TD-DFT transitions in their ground-state singlet geometries. See **Chapter X** and experimental section for additional details on the theoretical calculations.

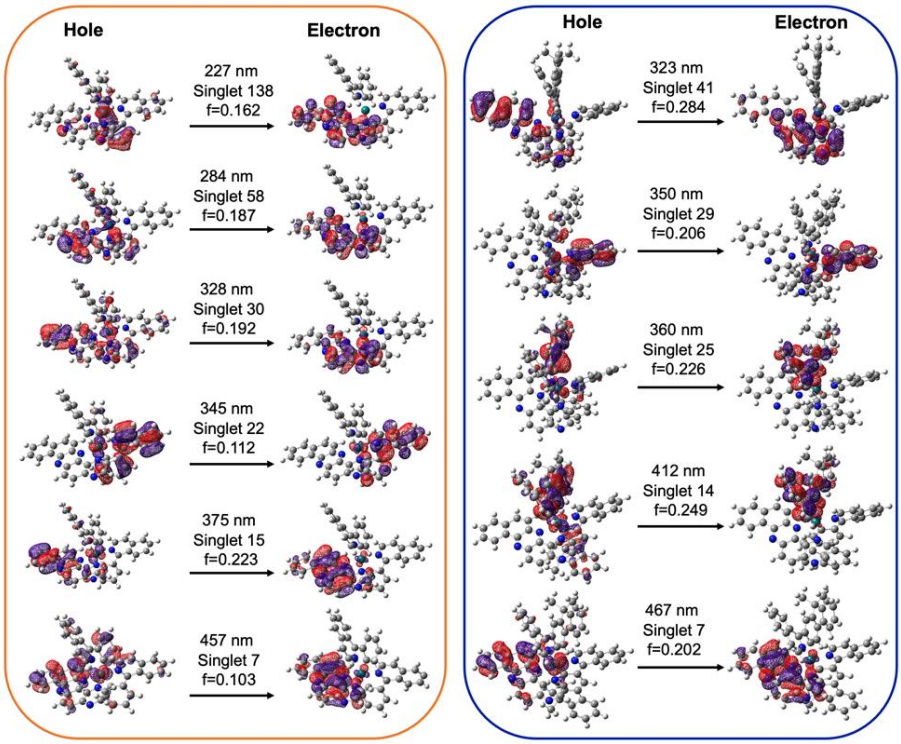

Figure 4.5. NTOs representation of the indicated transition for **Ir-1** (orange) and **Ir-2** (blue) computed at the B3LYP level of theory. See **Chapter X** and experimental section for additional details on the theoretical calculations.

Luminescence quantum yields and excited-state lifetimes for the different Ir(III)-based photosensitizers were measured at room temperature in acetonitrile under inert atmosphere (**Table 4.1**). In air-equilibrated solvents, a decrease in the luminescence intensity with respect to degassed solution is consistently observed for each photosensitizer, indicating a quenching by molecular oxygen.[301] Whereas **Ir-1** and $[Ir(ppy)_2(bpy)]^+$ exhibit a broad unstructured photoluminescence (**Figure 4.4-A**), as expected for charge transfer (CT) type excited states, a more structured photoluminescence with blue-shifted bands is observed for **Ir-2**. This blue-shifted photoluminescence arises from a ligand-centred (LC) contribution to the excited state of **Ir-2** in addition to the expected CT-type excited state, as suggested by TD-DFT calculations. The difference between the photoluminescence of $[Ir(ppy)_2(bpy)]^+$ and the lower-energy lying emission of **Ir-1** and **Ir-2** can be

explained by both HOMO and LUMO stabilization due to the π-extended network of the N^N diimine ligand as well as the cyclometalated piq and fliq ligands.

4.2.6 Hydrogen photo-evolution

Driven by their promising photophysical and electrochemical properties, **Ir-1** and **Ir-2** were tested for photocatalytic hydrogen evolution and compared to the prototypical $[Ir(ppy)_2(bpy)]^+$. $[Co(dmgH)_2(py)(Cl)]$ was used as the pre-catalyst for H_2 production using LED irradiation at different wavelengths, *i.e.* from blue (λ_{max} = 446 nm) to green (λ_{max} = 518 nm) and red (λ_{max} = 634 nm). The duplicated photocatalyzed reactions were carried out in degassed acetonitrile in order to solubilize the Ir(III) complexes with 1M TEOA as sacrificial electron donor and 0.1 M of HBF_4 as proton source. The cobalt catalyst was used in large excess (1 $x10^{-3}$ M) compared to the photosensitizers (5 $x10^{-6}$ M under blue and green light irradiation, and 1 $x10^{-4}$ M under red light irradiation) in order to assess the efficiency and durability of the Ir(III) complexes *vs* HERs. In addition, four equivalents of $dmgH_2$ (4 $x10^{-3}$ M) were also introduced at the start of the photocatalytic experiments to ensure Co catalyst recovery. Control experiments in the absence of cobalt catalysts did not show any sign of hydrogen photoproduction. Hydrogen evolution was monitored for 12 hours before affirming that no hydrogen was detected. We determined the limit of detection of the instrument at around 0.05 μL_{H2} min^{-1}, that corresponds to 82 $mmol_{H2}.mol^{-1}{}_{PS}.min^{-1}$ of TOF for a photosensitizer at 0.005 mM in the usual experimental condition of this study. The TON (the number of catalytic cycles that can be achieved by the catalyst before deactivation) and the TOF (the number of reaction products generated per active site per unit time) were determined for the iridium (III) photosensitizers.

Under blue irradiation (**Figure 4.6-A**), all photosensitizers efficiently achieved the photo-redox process for hydrogen evolution. The reference system $[Ir(ppy)_2(bpy)]^+/[Co(dmgH)_2(py)(Cl)]$ slowly reached a TOF_{max} of 2480 $mmol_{H2}$ mol^{-1} min^{-1}, followed by a slow decrease to reach a TON of 4850 in 52.9h

(**Figure 4.6-D** and **Table 4.2**). Interestingly, both **Ir-1** and **Ir-2** behaved very differently than the reference system. Indeed, they reacted slowly under blue irradiation to reach a $TOFs_{max}$ of 4250 and 2850 $mmol_{H2}$ mol^{-1} min^{-1}, respectively, followed by a slower decrease compared to $[Ir(ppy)_2(bpy)]^+$, with TONs of 11650 and 8370 in 92.6h, respectively. These systems are clearly outperforming the $[Ir(ppy)_2(bpy)]^+$ based system and most of the systems described in the literature (**Table 4.2,** entries 9 to 14) due to their higher TON and longer operating time. Moreover, after 92h of blue light irradiation of **Ir-2** alone in acetonitrile (λ_{max} = 446 nm), its absorption spectrum displays only minor changes, suggesting a high photostability for this photosensitizer. Although this strongly suggests a photo-dechelation of the **bpph** ligand (**Figures S4.9** and **S4.10**)., inducing a higher absorbance in the LC region, HER for **Ir-1** is monitored with a higher efficiency compared to **Ir-2**, clearly demonstrating the great potential of this photosensitizer.

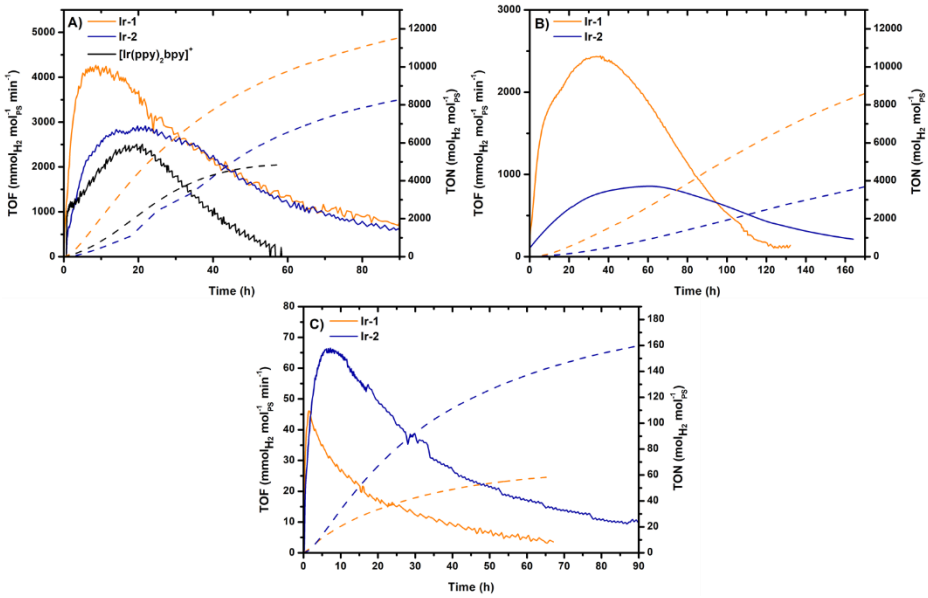

Figure 4.6. HER at (A) 446 nm with 5 $x10^{-6}$ M Ir(III) photosensitizers and $[Ir(ppy)_2(bpy)]^+$, (B) 518 nm with 5 $x10^{-6}$ M Ir(III) photosensitizers, (C) 634 nm of 1 $x10^{-4}$ M Ir(III) photosensitizers. All experiments were carried out with 1 $x10^{-3}$ M of $[Co(dmgH)_2(py)(Cl)]$ and 4 $x10^{-3}$ M $dmgH_2$ in CH_3CN with 1 M TEOA as the electron source and 0.1 M HBF_4 as the proton source: solid lines, TOF; dashed lines, TON.

Control experiments highlighted that the **bpph** ligand was unable to produce hydrogen catalytically (**Table 4.2,** entry 8). We also observed that the TOF, and to a lesser extend the TON, decreased when the amount of photosensitizer was doubled ($1x10^{-5}$ M). This suggests that a lower photosensitizer-to-cobalt catalyst ratio promotes more efficient hydrogen production, probably by preventing side reactions between photosensitizers in their reduced or excited states. In these conditions, doubling the concentration of HBF_4 (0.2 M) did not significantly impact the TOF or TON, indicating that the proton source is not the limiting factor (**Figure S4.8**). Some catalytic activity could be recovered when a fresh aliquot of photosensitizer was added after 90-114 hours of illumination, indicating that some photosensitizer degradation occurred after such prolonged irradiation and catalysis. Importantly, these results indicate that the four additional $dmgH_2$ equivalents that are added at the start of the experiment help ensure the integrity of the cobaloxime catalyst over time.

Under green light irradiation, the reference system $[Ir(ppy)_2bpy]^+/[Co(dmgH)_2(py)(Cl)]$ did not lead to any hydrogen photoproduction. This can be explained by the limited overlap of the absorption spectrum of $[Ir(ppy)_2bpy]^+$ with the spectral profile of the green LED (**Figure 4.4-C**). **Ir-1** and **Ir-2** are less efficient under green light than under blue light irradiation but still exhibit a remarkably high activity (**Figure 4.4-B**) compared to other molecular PSs described in the literature (**Table 4.2,** entries 10 to 12). Indeed, **Ir-1** and **Ir-2** gradually achieve $TOFs_{max}$ of 2450 and 850 $mmol_{H2}$ mol^{-1} min^{-1}, respectively. This was followed by a slower decrease than under blue light irradiation, meaning that systems are deactivated at a slower rate under less energetic irradiation. The final TONs obtained were 10600 and 5550 in 132.1 and 164.0h, respectively, showing the good efficiency of these novel photosensitizers to photo-evolve H_2 under less energetic irradiation.

Finally, both photosensitizers were also able to perform HER under red light irradiation (**Figure 4.4-C**). In this case, the concentration of both

photosensitizers was increased to 10^{-4} M to maximize absorption at these less energetic wavelengths. As the overlap of the absorption spectrum and the emission spectrum of the LED is smaller than for green light, the activity of the complexes was lower than for the previous measurements. Yet, considerable H_2 photoproduction could be detected, with $TOFs_{max}$ of 46 and 66 $mmol_{H2}$ mol^{-1} min^{-1} for **Ir-1** and **Ir-2**, respectively. Then, the activity decreased until the photosensitizers reached a TON of 58 and 173 after 67.0 and 133.1 hours. It is worth mentioning that the **fliq** based photosensitizer showed a better activity under red light irradiation than the **piq** homologue. These results were in the same range of TON and TOF_{max} than a previously reported system (**Table 4.2,** entries 10 and 11). It is important to note that the concentration used for hydrogen production using red light irradiation are higher than when blue or green light is used, *i.e.* $1x10^{-4}$ M compared to $5x10^{-6}$ M. This may lead to additional side reaction that could account for the different trend observed between **Ir-1** and **Ir-2** under red light irradiation. The absolute quantum yields for hydrogen production were 0.087 for the reference $[Ir(ppy)_2(bpy)]^+$ under blue irradiation, 0.13, 0.086 and 0.018 % for **Ir-1**, and 0.097, 0.036 and 0.028 % for **Ir-2** under blue, green and red light irradiation, respectively (**Table S4.7**). Again, under red light irradiation, the reference system $[Ir(ppy)_2(bpy)]^+$/$[Co(dmgH)_2(py)(Cl)]$ did not lead to any hydrogen photoproduction, most probably due to the lack of overlap between the absorption spectrum of $[Ir(ppy)_2(bpy)]^+$ with the spectral profile of the red LED (**Figure 4.4-C**).

Table 4.2. Performances for HER of photocatalytic systems under various irradiation wavelengths and comparison of HER efficiency using metal-based complexes as photosensitizer and cobaloxime as the proton reduction catalyst.

	PS[a]	Catalysts	SED/H$^+$	Irr. (nm)	TON (*vs* PS)[b]
1[c]	**Ir-1** (5 x10^{-6} M and 10^{-4} M for 634 nm irradiation)	[Co(dmgH)$_2$(py)(Cl)] (10^{-3} M) dmgH$_2$ (4 x10^{-3}M)	TEOA (1 M) HBF_4 (0.1 M)	446 518 634	11650 (92.6h) 10600 (132.1h) 58 (67.0h)
2[c]	**Ir-2** (5 x10^{-6} M and 10^{-4} M for 634 nm irradiation)	[Co(dmgH)$_2$(py)(Cl)] (10^{-3} M) dmgH$_2$ (4 x10^{-3}M)	TEOA (1 M) HBF_4 (0.1 M)	446 518 634	8370 (92.6h) 5550 (164.0h) 174 (133.1h)
3[c]	[Ir(ppy)$_2$bpy]$^+$ (5 x10^{-6} M)	[Co(dmgH)$_2$(py)(Cl)] (10^{-3} M) dmgH$_2$ (4 x10^{-3}M)	TEOA (1 M) HBF_4 (0.10 M)	446 518 634	4850 (52.9h) / [f] / [f]
4[c]	**Ir-1** (1 x10^{-5} M)	No catalyst	TEOA (1 M) HBF_4 (0.1 M)	446	/ [f]
5[c]	**Ir-2** (1 x10^{-5} M)	No catalyst	TEOA (1 M) HBF_4 (0.1 M)	446	/ [f]
6[c]	**Ir-1** (1 x10^{-5} M), **bpph** (1x10^{-4} M)	$Co(BF_4)_2.6H_2O$ (1x10^{-3} M)	TEOA (1 M) HBF_4 (0.1 M)	446	/ [f]
7[c]	**Ir-1** (1 x10^{-5} M),	$Co(BF_4)_2.6H_2O$ (1x10^{-3} M)	TEOA (1 M) HBF_4 (0.1 M)	446	/ [f]
8[c]	**bpph** (1 x10^{-4} M),	[Co(dmgH)$_2$(py)(Cl)] (10^{-3} M) dmgH$_2$ (4 x10^{-3}M)	TEOA (1 M) HBF_4 (0.1 M)	446	/ [f]
9[c][295]	[Ir(ttbutpy)(btfp)Cl]$^+$ (20 mM)	[Co(dmgH$_2$)(4-COOMe-py)Cl] (335 mM)	AscNa (100 mM) Acetate buffer	>390	670 (3h)
10[c][183]	[Ir(piq)$_2$-L(tpy)-Co] (0.1 M)	Dyad	TEOA (0.5 M) HBF_4 (0.05 M)	452 525 630	180 (2.3h) 251 (3h) 80 (110h)
11[d][302]	[Ru(Tolyltpy)(L1)]$^{2+}$ (0.1 mM)	[Co(H_2O)$_6$](BF$_4$)$_2$ (1 mM) dmgH$_2$ (6 mM)	TEOA (1.0 M) HBF_4 (0.1M)	445 630	269 (24h) 135 (60h)
12[c][217]	[Ir(4'-Py-tpy)(4'-MeO-tppy)-Co]$^+$ (0.1 mM)	Dyad	TEOA (1.0 M) HBF_4(0.1 M)	452 525	440 (66h) 113 (25h)
13[e][288]	[ZnTMPyP]$^{4+}$ (4.0 x10^{-5} M)	[Co(dmgH)$_2$(py)(Cl)] (4.9 x10^{-4} M)	TEOA (5% (v/v) H_2O	> 440	280 (20h)
14[e][37]	[Ir(NBI)$_2$phen]$^+$ (2.2 x10^{-4} M)	[Co(dmgH)$_2$(py)(Cl)] (3.7 x10^{-4} M)	DMT (0.07 M) H_2O	452	372 (20h)

[a] The abbreviations used for the different ligands correspond to: ttbutpy = 4,4',4"-tri-*tert*-butyl-2,2':6',2"-terpyridine, btfp = 2-(benzo[b]thiophen-2-yl)-5-trifluoromethylpyridine, L(tpy) = 2,2';5',4"-terpyridine, Tolyltpy = 4'-tolyl-2,2':6',2"-terpyridine, L1 = 6-(4-Bromophenyl)-2,4-di(pyridin-2-yl) pyrimidine, 4'-Py-tpy = 4'-(4-pyridinyl)-2,2';6',2"-terpyridine, 4'-MeO), tppy = 2,6-diphenyl-4-(4'-methoxyphenyl)pyridine, [ZnTMPyP]$^{4+}$ = zinc *meso*-tetrakis(1-methyl-pyridinium-4-yl)porphyrin, NBI = 1,8-naphthalenebenzimidazole, phen = 1,10-phenanthroline. [b] TON in mol_{H2} mol_{PS}^{-1}. For **Ir-1**, **Ir-2** and [Ir(ppy)$_2$(bpy)]$^+$ the error associated for the

TON values is estimated to be 10%. [c] In CH_3CN. [d] In DMF. [e] In CH_3CN and H_2O. [f] No H_2 production detected under these experimental conditions.

4.2.7 Mechanistic considerations

The results presented herein point toward a mechanism that involves electron transfer from triethanolamine to the excited-state photosensitizers. Stern-Volmer experiments were carried out in argon purged acetonitrile with $[Ir(ppy)_2(bpy)]^+$, **Ir-1** and **Ir-2**. The addition of triethanolamine to argon-purged solutions of Ir(III) photosensitizers led to a decrease in steady-state photoluminescence (**Figure S4.11**). However, the corresponding Stern-Volmer plots were non-linear, with downward curvature, preventing the accurate determination of quenching rate constants.

From the excited-state PL spectra and the electrochemical measurements, excited-state reduction potential $E_{1/2}Ir^{(III*/II)}$ of 1.67 and 1.66 V *vs* NHE were calculated for **Ir-1** and **Ir-2**, respectively. With those potential, a driving force for electron transfer from TEOA (E^0 = 0.82 V *vs* NHE) to the photosensitizers' excited state of –0.85 and –0.84 eV was estimated for **Ir-1** and **Ir-2**, respectively. The driving force for electron transfer from the excited photosensitizer to the cobalt pre-catalyst was only slightly exothermic. Hence, giving the large concentration of TEOA used herein as well as the favourable driving force for electron transfer, the proposed mechanism would be more consistent with electron transfer from TEOA to the excited-state PS, which would then transfer an electron to the cobaloxime.[194] The second electron transfer event to generate the active Co(I) catalyst would in all cases be energetically uphill, pointing towards an alternative mechanism for H_2 evolution via disproportionation of Co(II) to Co(III) and Co(I).[217, 219, 256]

To gain additional mechanistic information and assess if excited-state electron transfer is occurring between the excited photosensitizers and triethanolamine, photolysis experiments with **Ir-1** and **Ir-2** in the presence of 0.1 M TEOA were performed in argon-purged acetonitrile. In both cases, photolysis using blue LED irradiation led to spectral changes with novel absorption features centred around 370 nm and 470 nm. These spectral

changes were in agreement with the formation of the monoreduced Ir(III) photosensitizers, as observed by transient absorption spectroscopy for related photosensitizers.[42, 177, 273] Interestingly, the reaction proceeded faster for **Ir-1** compared to **Ir-2**, that was still undergoing reaction after 20 minutes of irradiation (**Figure 4.7**). The initial state of the photosensitizers could then be recovered by the addition of potassium persulfate, a known sacrificial oxidant. However, as indicated by the dashed lines in **Figure 4.7**, the initial photosensitizer was not fully regenerated, presumably indicating some degradation of the accumulated reduced photosensitizer over time. This degradation could also occur during the hydrogen evolution reaction, although we hypothesize that the monoreduced photosensitizer is not accumulated over long periods of time as it would react with the cobalt catalyst.

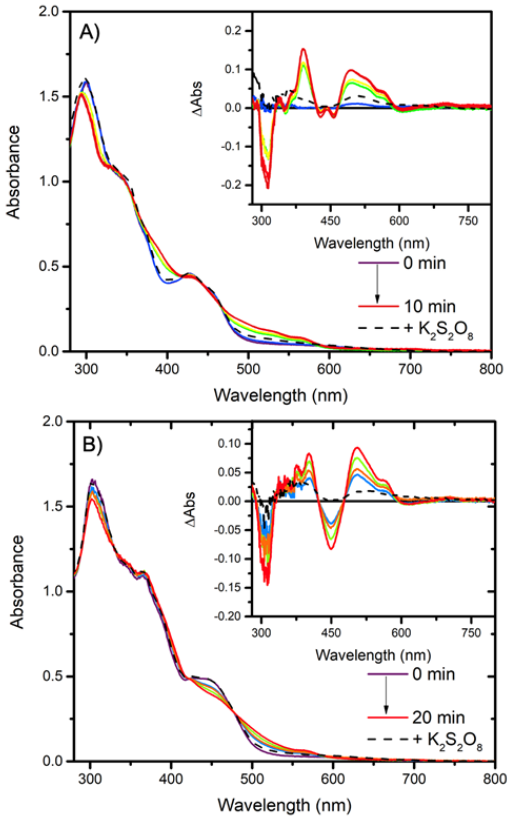

Figure 4.7. Absorption spectra of **Ir-1** (A) and **Ir-2** (B) recorded in argon-purged acetonitrile at room temperature over time following irradiation with blue LED light in the presence of 0.1 M TEOA. After the irradiation, an excess of $K_2S_2O_8$ was added to oxidize the photo-reduced photosensitizer and investigate reversibility.

4.3 Conclusions

The synthesis of two novel Ir(III) photosensitizers and their efficiency for the visible light mediated hydrogen production reaction was reported. The ground and excited-state behaviour of both photosensitizers were fully characterized. Red-shifted absorption properties were obtained by the judicious use of cyclometalating **piq** and **fliq** ligand in combination with the recently reported **bpph** N^N diimine ligand. The absorption properties were fully in line with theoretical calculations and ascribed the red-shifted transitions from both the Ir(III) centre and the **bpph** moiety. In acetonitrile, in the presence of a cobalt catalyst, a sacrificial electron donor and a proton source, both Ir(III) photosensitizers were able to utilize blue, green and red photons to generate hydrogen with turn-over numbers up to 11650, 10600 and 174 mol_{H2} mol_{PS}^{-1}, respectively, outperforming most the parent compounds described in the literature (see **Table 4.2**). Moreover, our systems demonstrated extended hydrogen production over a longer time period (67 to 164 h), highlighting their improved stability under photocatalytic conditions.

4.4 Experimental section

The materials and methods used in this chapter are described in ***Chapter X****.*

Ethanol (≥99.9%, VWR), dichloromethane (≥99.9%, VWR), methanol (≥99.9%, VWR), tetrahydrofuran (≥99.9%, VWR), diethyl ether (≥99%, VWR), n-hexane (≥97%, VWR), ethyl acetate (≥99.9%, VWR), petroleum ether 40-60°C (VWR), 2-ethoxyethanol (≥99%, Acros Organics), ethylene glycol (≥99%, Roth), acetonitrile (≥99.9%, VWR), acetic acid glacial (≥99.9%, VWR), $[NH_4][PF_6]$ (99%, Fluorochem), SiO_2 (40-63 mm, Rocc), Celite (Roth), 4-nitro-*o*-phenylenediamine (98%, Acros Organics), glyoxal 40 wt. % solution in water (Acros Organics), hydroxylamine hydrochloride (≥99%, Acros Organics), palladium (10%) on activated carbon (Chimet), hydrazine monohydrate (hydrazine 64%) (≥99.9%, Acros Organics), 2-naphtoquinone (97% Sigma Aldrich), 2-iodo-9,9-dimetylfluorene ((≥98%, TCI), *n*-butyllithium 1.6M solution in hexanes (Acros Organics), Trimethyl borate (99%, Acros Organics), 1-chloroisoquinoline (97%, Fluorochem), Triphenylphosphine (99%, Sigma Aldrich), sodium carbonate (99.5%, Acros Organics), iridium trichloride hydrate (53% Ir, Pressure Chemical), 1-phenylisoquinoline (98% TCI) were purchased from commercial sources and used as received. $[Pd(PPh_3)_4]$,[303] $[Os(bpy)_3](PF_6)_2$,[304] $[Co(dmgH)_2(py)(Cl)]$,[194] (9,9-dimethyl-9*H*-fluoren-2-yl)boronic acid, 1-(9,9-dimethyl-9H-fluoren-2-yl)isoquinoline (**FliqH**),[296] benzo[*a*]pyrazino[2,3-*h*]phenazine (**bpph**)[42] and $[Ir(piq)_2(\mu\text{-}Cl)]_2$,[262] were synthesized according to published procedures. Water was purified by a Millipore Milli-Q system. The precipitates were isolated by centrifugation at 4000 rpm for 3 min in a Hettich Universal 320 centrifuge.

4.4.1 Synthesis of the Ir(III) photosensitizers

$[Ir(fliq)_2(\mu\text{-}Cl)]_2$. Iridium trichloride hydrate (75 mg, 0.214 mmol, 1 eq.) and 1-(9,9-dimethyl-9H-fluoren-2-yl)isoquinoline (150 mg, 0.467 mmol, 2.2 eq.) were suspended in a mixture of 2-ethoxyethanol (3 ml) and water (1 ml). The mixture was then heated at reflux overnight under argon atmosphere. The solution was allowed to cool down at room temperature, and water (10 ml)

was added. The deep red precipitate was centrifugated, washed with water and diethyl ether, and then dried under vacuum. The dimeric precursor **$[Ir(fliq)_2(\mu\text{-}Cl)]_2$** was isolated as a red powder (119 mg, 0.068 mmol, 64%). ^{1}H NMR (500 MHz, $CDCl_3$) δ 9.10 (d, *J* = 6.3 Hz, 4H), 9.02 (d, *J* = 8.4 Hz, 4H), 8.18 (s, 4H), 7.96 (d, *J* = 7.6 Hz, 4H), 7.92 – 7.88 (m, 4H), 7.83 (ddd, *J* = 8.3, 6.9, 1.4 Hz, 4H), 7.22 (d, *J* = 7.3 Hz, 4H), 7.08 (td, *J* = 7.3, 1.1 Hz, 4H), 6.97 (td, *J* = 7.5, 0.9 Hz, 4H), 6.89 (d, *J* = 7.5 Hz, 4H) 6.62 (d, *J* = 6.2 Hz, 4H), 6.46 (s, 4H), 1.39 (s, 12 H), 1.38 (s, 12 H).

$[Ir(piq)_2(bpph)]^+$. $[Ir(piq)_2(\mu\text{-}Cl)]_2$ (40 mg, 0.031 mmol, 1 eq.) and **bpph** (18.6 mg, 0.066 mmol, 2.1 eq.) were dissolved in 4 mL of ethylene glycol. The mixture was then heated at 110°C for 18 hours under argon atmosphere. The solution was then allowed to cool down at room temperature and 5 mL of a NH_4PF_6 saturated aqueous solution were added. The dark precipitate was centrifugated and washed with water (three times), ethanol (two times) and sorely with diethyl ether (five to eight times). The iridium complex was isolated as a dark green powder (49 mg, 0.047 mmol, 76%). ^{1}H NMR (500 MHz, CD_3CN) δ 9.53 – 9.46 (m, 1H), 9.12 (d, *J* = 2.6 Hz, 1H), 9.10 – 9.04 (m, 1H), 9.01 – 8.96 (m, 1H), 8.83 (d, *J* = 9.4 Hz, 1H), 8.63 (d, *J* = 9.4 Hz, 1H), 8.52 – 8.44 (m, 2H), 8.04 (d, *J* = 2.6 Hz, 1H), 7.99 – 7.74 (m, 11H), 7.54 (d, *J* = 6.5 Hz, 1H), 7.31 – 7.23 (m, 2H), 7.23 – 7.13 (m, 3H), 7.02 (qd, *J* = 7.5, 1.3 Hz, 2H), 6.39 (dd, *J* = 7.7, 1.3 Hz, 1H), 6.32 (dd, *J* = 7.7, 1.3 Hz, 1H). HRMS(ESI) m/z calculated for $[C_{48}H_{30}N_6{}^{191}Ir\text{-}PF_6]^+$ = 881.21324; found 881.21326.

$[Ir(fliq)_2(bpph)]^+$. $[Ir(fliq)_2(\mu\text{-}Cl)]_2$ (48 mg, 0.027 mmol, 1 eq.) and **bpph** (18.6 mg, 0.058 mmol, 2.1 eq.) were dissolved in 4 mL of ethylene glycol. The mixture was then heated at 110°C for 18 hours under argon atmosphere. The solution was then allowed to cool down at room temperature and 5 mL of a NH_4PF_6 saturated aqueous solution were added. The dark precipitate was centrifugated and washed with water (three times), ethanol (two times) and sorely with diethyl ether (five to eight times). The iridium complex was isolated as a dark green powder (55mg, 0.043 mmol, 79%). ^{1}H NMR (500 MHz, CD_3CN) δ 9.49 (d, *J* = 8.1 Hz, 1H), 9.14 – 9.09 (m, 2H), 9.02 (d, *J* = 8.4 Hz,

1H), 8.84 (d, *J* = 9.4 Hz, 1H), 8.64 (d, *J* = 9.4 Hz, 1H), 8.60 (s, 1H), 8.55 (s, 1H) 8.15 (d, *J* = 2.7 Hz, 1H), 8.00 – 7.80 (m, 10H), 7.77 (d, *J* = 9.6 Hz, 1H), 7.63 (d, *J* = 9.6 Hz, 1H), 7.56 (d, *J* = 6.5 Hz, 1H), 7.55 – 7.50 (m, 2H), 7.32 – 7.27 (m, 3H), 7.25 – 7.19 (m, 2H), 7.13 (td, *J* = 7.5, 1.1 Hz, 1H), 7.10 (td, *J* = 7.5, 1.1 Hz 1H) 7.03 – 6.99 (m, 1H), 6.87 – 6.84 (m, 1H), 6.70 – 6.65 (m, 2H), 1.72 (s, 3H), 1.63 (s, 3H), 1.57 (s, 6H). HRMS(ESI) m/z calculated for $[C_{66}H_{46}N_6{}^{191}Ir\text{-}PF_6]^+$ = 1113.33844; found 1113.33862.

4.4.2 X-ray diffraction of crystal structures

Table S4.1. X-ray diffraction information of crystal structures.

Identification	Ir-1	Ir-2
CCDC Number	2117219	2117221
Empirical formula	$C_{54}H_{44}F_6IrN_6OP$	$C_{69.5}H_{51.25}F_6IrN_{7.75}P$
Formula weight	1130.12	1332.10
Temperature/K	100	100
Crystal system	triclinic	triclinic
Space group	P-1	P-1
a/Å	9.9089(9)	11.8481(3)
b/Å	13.9799(12)	12.2896(3)
c/Å	17.2051(15)	21.0729(5)
α/°	103.196(2)	97.6860(10)
β/°	91.060(2)	93.4600(10)
γ/°	99.007(2)	100.2650(10)
Volume/Å^3	2288.1(3)	2980.98(13)
Z	2	2
ρ_{calc}g/cm^3	1.640	1.484
μ/mm^{-1}	6.599	5.159
F(000)	1128.0	1337.0
Crystal size/mm^3	0.19 × 0.06 × 0.02	0.23 × 0.07 × 0.03
Radiation	CuKα (λ = 1.54178)	CuKα (λ = 1.54178)
2Θ range for data collection/°	5.284 to 136.562	7,39 to 144.04
Index ranges	-10 ≤ h ≤ 11, -16 ≤ k ≤ 16, -20 ≤ l ≤ 20	-14 ≤ h ≤ 14, -14 ≤ k ≤ 13, -25 ≤ l ≤ 25
Reflections collected	92870	82788
Independent reflections	8171 [R_{int} = 0.0366, R_{sigma} = 0.0152]	11374 [R_{int} = 0.0452, R_{sigma} = 0.0239]
Data/restraints/parameters	8171/165/645	11374/24/769
Goodness-of-fit on F^2	1.056	1.062
Final R indexes [I>=2σ (I)]	R_1 = 0.0267, wR_2 = 0.0696	R_1 = 0.0343, wR_2 = 0.0879
Final R indexes [all data]	R_1 = 0.0277, wR_2 = 0.0705	R_1 = 0.0362, wR_2 = 0.0895
Largest diff. peak/hole / e Å^{-3}	1.28/-0.55	2.71/-0.80

Crystals suitable for X-Ray diffraction analysis were grown by slow diffusion of diisopropylether in an acetonitrile solution of Ir photosensitizers. The morphology of the crystal for Ir-1 and Ir-2 is the shape of plate. Both share the same space group triclinic P^{-1}.

Crystallographic data of both structures Ir-1, Ir-2 were collected at 100 K using a Bruker Platform diffractometer, equipped with a Bruker SMART 4 K Charged-Coupled Device (CCD) Area Detector using the program APEX2 and a Nonius FR591 rotating anode equipped with a Montel 200 optics. The crystal-to-detector distance was 5.0 cm, and the data collection was carried out in 512 x 512-pixel mode.

For data collection, determination of cell parameters, cell refinement, and data reduction APEX2 and SAINT (Bruker, 2007) were used. Absorption and corrections were applied using SADABS and TWINABS (Bruker 2001)[305]. Structure solutions were performed using direct methods with SHELXT (Sheldrick, (2008 and 2015)[306, 307] and refined on F2 by fullmatrix least squares using SHELXL2014 (Sheldrick, 2008 and 2015)[307]. OLEX2 (Dolomanov et al., 2009). The material was prepared for publication using OLEX2 (Dolomanov et al., 2009), PLATON (Spek, 2009)[308], and Mercury [309].

Ir-1: The quality of the data set is good. A solvent molecule of diisopropylether is well modelized anisotropically. The occupation factor of two PF_6^- localisations are defined by anisotropic refinement with a free variable of occupation 40/60. The R1 factor reaches 2.67 %.

Ir-2: The Ir complex and his PF_6^- counter anion are well described. Two molecules of acetonitrile are modelized anisotropically. A residual electron density attributed to solvent disorder is treated with the olex mask. This residual electron density is distributed around one volume. The total solvent accessible volume is 205 $Å^3$ also 6,9 % of the cell that corresponds at 38 electrons. Two molecules of acetonitrile or one diisopropylether that doesn't exist in all unit cells of the crystal could occupy the void with different positions.

The electron density is weak in the volume of the void: 5,4 Å^3/e, probably due to the evaporation. The R1 factor goes from 4,32 % to 3,43 % after the olex-mask processing.

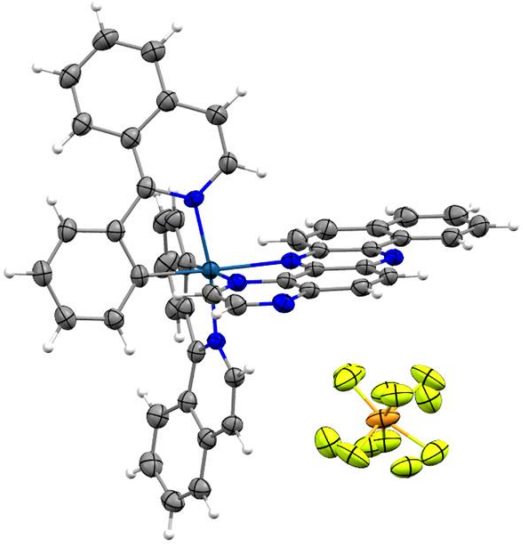

Figure S4.1. X-ray crystal structure of **Ir-1**, atoms are represented at the 50% probability level. The co-crystallised solvent is omitted.

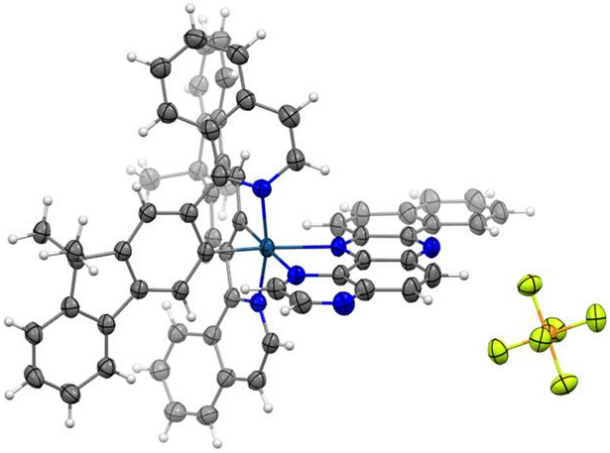

Figure S4.2. X-ray crystal structure of **Ir-2**, atoms are represented at the 50% probability level. The co-crystallised solvent is omitted.

Table S4.2. Selected angles (°) and bond length (Å) of crystal structures.

Ir-1		Ir-2	
Bond lengths in Å			
Ir(1)–C(315)	2.012 (3)	Ir(1)–C(224)	2.001 (3)
Ir(1)–C(215)	2.017 (3)	Ir(1)–C(324)	2.015 (3)
Ir(1)–N(31)	2.042 (8)	Ir(1)–N(21)	2.055 (3)
Ir(1)–N(21)	2.049 (3)	Ir(1)–N(31)	2.041 (3)
Ir(1)–N(11)	2.130 (3)	Ir(1)–N(11)	2.134 (3)
Ir(1)–N(14)	2.235 (2)	Ir(1)–N(14)	2.225 (2)
Angles in °			
N(11)–Ir(1)–N(21)	95.75 (10)	N(11)–Ir(1)–N(31)	100.73(10)
N(14)–Ir(1)–N(21)	89.93 (9)	N(14)–Ir(1)–N(31)	91.39(10)
C(215)–Ir(1)–N(21)	79.77 (12)	C(324)–Ir(1)–N(31)	79.70(12)
C(315)–Ir(1)–N(21)	94.29 (11)	C(224)–Ir(1)–N(31)	91.14(11)
N(11)–Ir(1)–N(31)	92.43 (10)	N(11)–Ir(1)–N(21)	89.44 (10)
N(14)–Ir(1)–N(31)	97.44 (9)	N(14)–Ir(1)–N(21)	99.17 (10)
C(215)–Ir(1)–N(31)	92.11 (12)	C(324)–Ir(1)–N(21)	90.22 (12)
C(315)–Ir(1)–N(31)	79.32 (12)	C(224)–Ir(1)–N(21)	79.65(12)
N(11)–Ir(1)N(14)	76.74 (9)	N(11)–Ir(1)–N(14)	76.67 (10)
N(14)–Ir(1)–C(215)	102.36 (11)	N(14)–Ir(1)–C(324)	102.76 (10)
C(215)–Ir(1)–C(315)	85.88 (12)	C(324)–Ir(1)–C(224)	86.26 (12)
N(11)–Ir(1)–N(315)	95.26 (11)	C(224)–Ir(1)–N(11)	94.30 (11)
N(21)–Ir(1)–N(31)	170.07 (10)	N(21)–Ir(1)–N(31)	166.82 (11)
N(11)–Ir(1)–C(215)	175.45 (11)	N(11)–Ir(1)–C(324)	179.29 (10)
N(14)–Ir(1)–C(315)	171.32 (11)	N(14)–Ir(1)–C(224)	170.93 (11)
Dihedral angles between cyclometalated and N-cycle moieties			
N(21)-C(29)-C(210)-C(215)	13.5 (3)	N(21)-C(29)-C(210)-C(224)	15.7 (4)
N(31)-C(39)-C(310)-C(315)	12,0 (4)	N(31)-C(39)-C(310)-C(324)	13.8 (3)
Dihedral angles in isoquinoline moiety			
N(21)-C(29)-C(28)-C(27)	166.2 (3)	N(21)-C(29)-C(28)-C(27)	160.9 (4)
N(31)-C(39)-C(38)-C(37)	163.1 (3)	N(31)-C(39)-C(38)-C(37)	166.1 (3)

Table S4.3. Selected angles (°) and bond length (Å) of crystal structures.

$[Ir(^{dCF3}ppy)_2(bbph)]^{+}$ a 42	$[Ir(^{dCF3}ppy)_2(bpz)]^{+}$ b 264	$[Ir(ppy)_2(bpy)]^{+}$ c 310
Bond lengths in Å		
2.043 (4)	2.058 (3)	2.024 (5)
2.066 (4)	2.063 (3)	2.004 (5)
2.054 (3)	2.048 (3)	2.048 (3)
2.074 (3)	2.063 (2)	2.042 (3)
2.117 (4)	2.145 (2)	2.129 (3)
2.203 (3)	2.127 (2)	2.136 (3)
Angles in °		
90.14 (13)	91.41 (10)	95.77 (14)
80.7(12)	81.99 (10)	90.45 (13)
80.14 (13)	80.46 (11)	80.66 (15)
104.88 (14)	104.68 (11)	92.97 (15)
93.03(12)	86.01 (10)	89.16 (13)
96.72 (13)	92.51 (10)	96.72 (13)
103.75(14)	101.63 (12)	95.22 (15)
80.75 (14)	80.51 (11)	80.09 (15)
77.61 (13)	77.06 (10)	76.21 (13)
98.39 (13)	96.61 (11)	96.36 (15)
92.35 (15)	94.27 (12)	87.90 (16)
92.37 (15)	92.73 (10)	99.70 (14)
173.13 (15)	174.33 (10)	172.11 (13)
170.02 (13)	170.39 (11)	171.80 (14)
168.64 (14)	168.08 (11)	174.93 (15)
Dihedral angles between cyclometalated and N-cycle moieties		
2.1 (5)	0.7 (4)	1.5 (6)
10.5 (5)	1.6 (4)	6.0 (4)

The geometry of coordination sphere and the cyclometalated ligand are compared between the similar complexes and the reference $[Ir(ppy)_2(bpy)]^{+}$. In these archetype complexes, the near octahedral geometry is observed as expected for the reference complexes $[Ir(ppy)_2(bpy)]^{+}$[310] or $[Ir(piq)_2(bpy)]^{+}$.[311] The coordination sphere of **Ir-1** and **Ir-2** shows weak differences of structural parameters. The extended N-chelate bpph derivatives **Ir-1**, **Ir-2** and $[Ir(^{dCF3}ppy)_2(bbph)]^{+}$ show a common particularity in the coordination sphere. The Ir-N length bond around 2,23 Å on the side of benzene extension in bpph is longer by 0.1 Å than the Ir-N bond on the other side 2.13 Å. The latter is around 0.09 Å longer than the Ir-N cyclometalated ligand around 2.05 Å. This length bond is familiar to the reference complexes. The shortest bond around 2.01 Å is the cyclometalated bond to the Ir that should favour the σ orbital

overlap. Otherwise, a *trans* effect of Ir σ-C could accentuate the longer Ir-N(bpy) and promotes the cis-arrangement of the cyclometalated ligand. The bite angle of N-chelate is around 76-77° and around 80° for the cyclometalated ligand. The hindered fliq cyclometalated derivative **Ir-2** shows weakly more angular distortions in the coordination sphere than **Ir-1**. For **Ir-1** and **Ir-2**, torsion angles in the phenylisoquinoline ligand are in the same range of other phenylisoquinoline derivatives.[297]

4.4.3 Electrochemistry

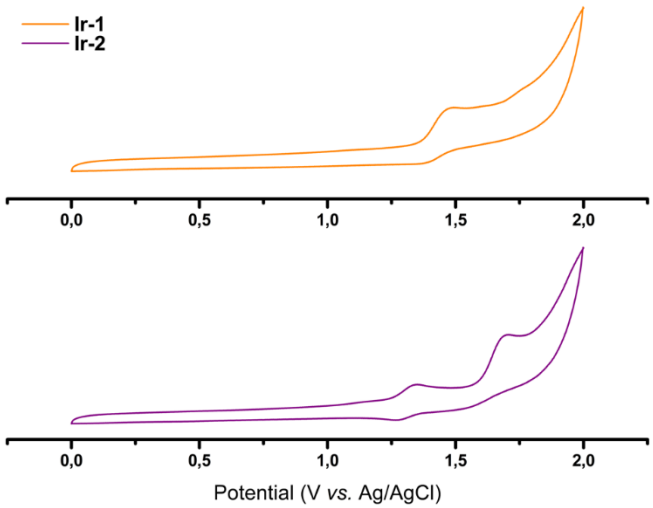

Figure S4.3. Cyclic voltammograms for the oxidation of **Ir-1** (1 mM) and **Ir-2** (0.5 mM) in argon purged acetonitrile (0.3 V/s) with tetrabutylammonium perchlorate (0.1M) as supporting electrolyte.

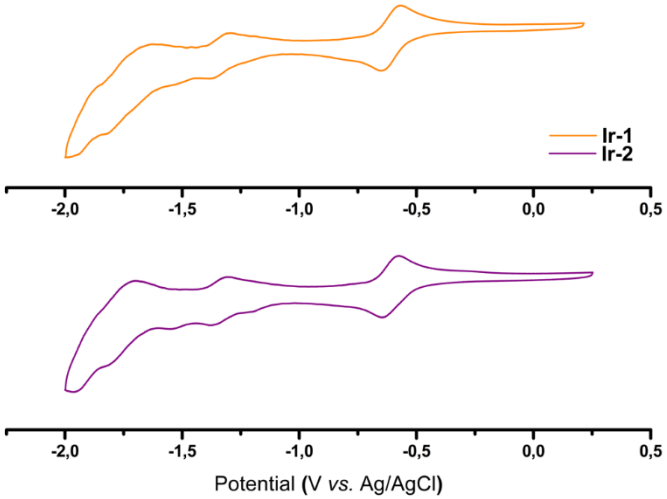

Figure S4.4. Cyclic voltammograms for the reduction of **Ir-1** (1 mM) and **Ir-2** (0.5 mM) in argon purged acetonitrile (0.3 V/s) with tetrabutylammonium perchlorate (0.1M) as supporting electrolyte.

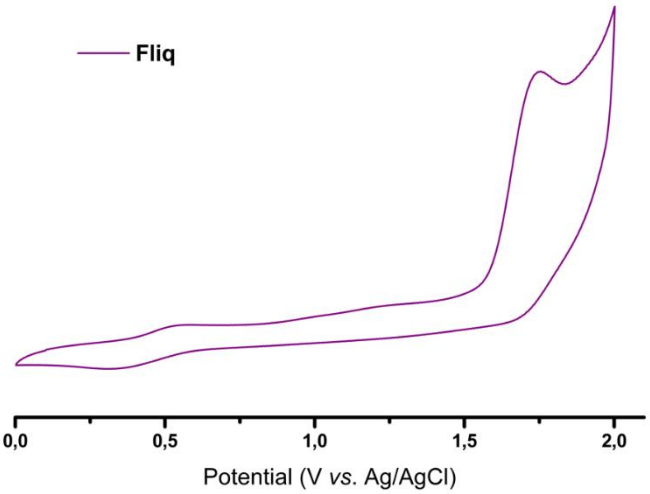

Figure S4.5. Cyclic voltammogram for the oxidation of **Fliq** (2 mM) in argon purged acetonitrile (0.3 V/s) with tetrabutylammonium perchlorate (0.1M) as supporting electrolyte.

4.4.4 Theoretical studies

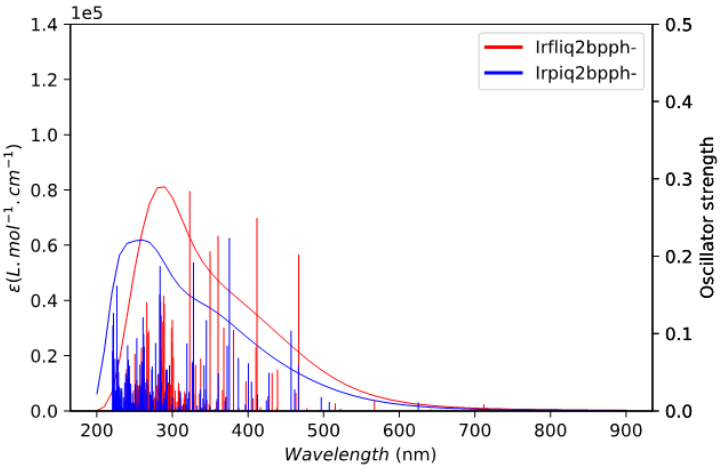

Figure S4.6. The simulated TD-DFT absorption spectra of **Ir-1** and **Ir-2** in their ground-state singlet geometries.

Table S4.4. Cartesian Coordinates (in Å) of the equilibrium geometry of the singlet state of the $[Ir(piq)_2(bpph)]^+$ (**Ir-1**) complex.

Ir	0.636316	-0.237875	0.117671	C	-3.285787	0.201196	-2.807523
C	-2.406825	-0.811143	-0.785112	H	-3.128250	0.787849	-3.708094
C	3.064558	1.245169	1.119367	N	0.305906	-3.478540	3.864335
C	-0.525603	1.342443	2.638788	C	1.483542	-2.929338	3.601407
C	-1.605321	-1.882648	1.106820	C	1.465044	-1.630427	-1.105078
C	3.495634	-0.403481	-0.534143	H	2.660297	-1.578020	2.358007
C	-0.583842	2.487551	0.578075	H	-4.057384	-3.770847	2.591465
C	-0.529690	-2.229101	1.983326	H	-2.155914	-4.375214	4.102568
C	0.015686	2.516503	-0.770150	C	-1.494084	3.457035	1.133205
C	2.885693	-1.558157	-1.211267	C	-1.779754	3.388294	2.537254
C	1.689035	-2.019534	2.544829	C	-2.185104	4.434025	0.362419
C	1.151788	1.291373	-2.522188	C	-2.628896	4.357421	3.132582
C	0.809331	-2.692415	-1.744908	H	-2.813571	4.302231	4.201247
C	-3.706104	-1.390549	-0.507812	C	-3.231095	5.326680	2.362687
C	-1.240585	2.312439	3.286689	C	-3.029692	5.343106	0.962867
C	-2.881804	-2.461672	1.339443	H	-0.148384	4.650623	-1.123668
C	-0.723206	-3.135250	3.053488	C	-4.823159	-1.107149	-1.397588
C	3.596212	-2.599198	-1.843149	C	-4.604920	-0.304415	-2.549099
C	0.159829	3.695197	-1.529324	C	-5.683500	-0.032194	-3.417692
C	1.230810	2.453795	-3.293916	C	-6.112120	-1.618180	-1.144605
C	1.520804	-3.681000	-2.429004	H	-6.268514	-2.231186	-0.264891
H	-0.154964	0.469884	3.162524	C	-7.157951	-1.335177	-2.008976
H	2.301152	1.698535	1.736354	C	-6.944349	-0.539534	-3.150337
H	1.564797	0.370252	-2.920810	C	4.375692	1.622562	1.187219
H	-0.273033	-2.766245	-1.697408	H	-3.556391	6.069826	0.352532
H	1.690920	2.417703	-4.278016	H	-2.087196	4.439510	-0.714093
H	0.986189	-4.493880	-2.913485	H	-3.887368	6.059531	2.821787
H	2.319374	-3.200526	4.240245	H	-1.432041	2.233542	4.351310
N	-0.207371	1.425098	1.315790	H	-7.769620	-0.324744	-3.822017
C	0.756149	3.665228	-2.786819	H	-5.510264	0.580213	-4.297638
H	0.861482	4.582817	-3.357366	H	-8.148129	-1.730126	-1.804386
C	2.917892	-3.649219	-2.455019	C	5.308130	1.064079	0.277084

H	3.478062	-4.444157	-2.937364	C	4.851594	0.069502	-0.650008
H	4.677460	-2.627378	-1.822711	C	6.654935	1.507914	0.232146
C	0.565860	1.288839	-1.246091	H	6.984828	2.244405	0.958644
N	-1.371391	-1.036204	0.067671	C	5.750890	-0.341096	-1.673747
N	2.636724	0.255720	0.279675	C	7.514580	1.037567	-0.734733
N	0.682930	-1.668765	1.747259	C	7.045844	0.130383	-1.712427
C	-3.063665	-3.360950	2.448834	H	8.541590	1.387283	-0.770448
C	-2.030027	-3.690797	3.271235	H	5.408432	-0.988507	-2.467469
N	-3.920519	-2.185263	0.539811	H	4.686220	2.381318	1.896896
C	-2.236225	-0.032547	-1.970775	H	7.706734	-0.186767	-2.512794
H	-1.254123	0.355364	-2.193042				

Table S4.5. Cartesian Coordinates (in Å) of the equilibrium geometry of the singlet state of the $[Ir(fliq)_2(bpph)]^+$ (**Ir-2**) complex.

Ir	0.157944	-0.312296	-1.051346	C	-3.395902	-2.449108	3.571313
C	1.789988	-2.036521	1.132608	H	-3.616435	-1.422351	3.877966
C	-0.422993	1.777387	-3.144721	H	-3.865931	-3.129413	4.288947
C	2.726894	-0.496245	-2.940023	H	-2.312493	-2.598134	3.624196
C	1.124204	-3.090427	-0.820866	C	-3.588416	-4.183826	1.738281
C	-2.238068	1.251751	-1.706078	H	-3.942530	-4.401814	0.726329
C	2.850079	1.049793	-1.162437	H	-2.508591	-4.361796	1.770470
C	0.380482	-3.099556	-2.042407	H	-4.065854	-4.888052	2.427332
C	2.028393	1.829607	-0.222052	C	3.190136	-2.189052	3.625821
C	-2.698299	0.251249	-0.732410	C	3.221547	-3.310306	2.754077
C	-0.979049	-1.981289	-3.520251	C	3.948718	-4.458080	3.128907
C	-0.091367	2.024489	0.952465	C	3.889394	-2.244813	4.850570
C	-2.007949	-1.550138	0.759116	C	4.602371	-3.379848	5.199882
C	2.492646	-3.251220	1.495146	C	4.631279	-4.489794	4.334689
C	-1.136162	2.730397	-3.814811	H	3.859953	-1.385691	5.514211
C	4.036390	-0.315034	-3.292810	H	5.139134	-3.415092	6.142758
C	1.797510	-4.278468	-0.428632	H	5.191499	-5.376716	4.613640
C	0.302360	-4.266032	-2.840308	H	3.964775	-5.309325	2.458618
C	-4.047720	0.016571	-0.393762	C	4.864688	0.493958	-2.474045
C	2.427572	3.085806	0.291714	C	6.257509	0.618042	-2.717223
C	0.343352	3.232088	1.506655	C	7.061614	1.312630	-1.841793
C	-3.333168	-1.728397	1.141271	C	4.277416	1.153236	-1.343738
H	2.080162	-1.162357	-3.497806	C	5.150809	1.805729	-0.429050
H	0.598692	1.534284	-3.401784	C	6.505625	1.882783	-0.673357
H	-1.078356	1.645381	1.198301	H	6.679065	0.131986	-3.592032
H	-1.235311	-2.181980	1.188087	H	8.127933	1.395588	-2.027981
H	-0.690712	3.252441	-4.654357	H	7.153274	2.373489	0.046241
H	-1.651690	-3.149879	-5.207959	H	4.446377	-0.823364	-4.158740
N	2.147219	0.165808	-1.899267	H	4.760241	2.208130	0.495172
C	1.595580	3.775279	1.157075	H	3.361254	3.535668	-0.024106
C	-4.355965	-0.961316	0.545859	C	-0.322527	4.158577	2.428841
H	-4.850646	0.548261	-0.887388	C	-1.564724	4.078749	3.065792
C	0.728617	1.306812	0.068735	C	-1.957354	5.122740	3.907096
N	1.144026	-1.961447	-0.061976	C	0.521240	5.271405	2.630069
N	-0.962002	1.056535	-2.116774	C	0.123704	6.307349	3.469834
N	-0.256325	-1.957114	-2.402690	C	-1.121080	6.228100	4.107842
C	1.729170	-5.445264	-1.269102	H	0.763714	7.170442	3.633706
C	1.009175	-5.445706	-2.424604	H	-1.440718	7.031796	4.764962
N	2.493877	-4.331042	0.714629	H	-2.918836	5.077116	4.410354
C	1.769537	-0.947497	2.057229	C	-2.432645	3.077476	-3.357756
H	1.204776	-0.065070	1.798439	C	-2.979644	2.367464	-2.238121
C	2.434748	-1.028839	3.243571	C	-4.193224	2.854919	-1.677098
H	2.395276	-0.191446	3.934322	C	-3.163840	4.140840	-3.946935
N	-0.428086	-4.276542	-3.980865	H	-2.740472	4.648452	-4.808390
C	-1.056254	-3.153219	-4.299288	C	-4.368829	4.540856	-3.414779

C	-1.664112	-0.578245	-0.196403	C	-4.867693	3.911509	-2.251532
H	-1.493724	-1.073102	-3.809517	H	-4.571739	2.433933	-0.757248
H	2.267000	-6.325049	-0.933594	H	-5.783125	4.273564	-1.794511
H	0.943234	-6.323513	-3.057436	H	-4.919767	5.361252	-3.863969
C	-5.648229	-1.404642	1.085299	H	-2.215494	3.222182	2.913281
C	-5.409897	-2.433807	2.019956	C	1.816863	5.129936	1.830124
C	-6.950361	-0.973296	0.817789	C	1.961983	6.263032	0.788652
C	-6.472713	-3.033490	2.688332	H	2.857931	6.112032	0.177449
C	-8.013661	-1.581120	1.491739	H	1.094967	6.300312	0.122466
C	-7.778757	-2.602536	2.419642	H	2.054773	7.234086	1.285939
H	-7.139431	-0.179352	0.100343	C	3.052465	5.109552	2.758545
H	-9.031491	-1.257080	1.294076	H	3.154569	6.063625	3.286053
H	-8.615365	-3.064546	2.935853	H	2.973011	4.312738	3.504061
H	-6.300942	-3.827318	3.410802	H	3.967130	4.946899	2.178825
C	-3.913749	-2.727621	2.141165				

4.4.5 Hydrogen photoproduction quantum yield

The hydrogen quantum yield at different irradiation wavelength were determined using **Equation 4.1**, where n_{H2} is the total amount of H_2 in mol and F the total photon flux in E s^{-1}.

$$\Phi_{H2} = 2\,\frac{n_{H2}}{F}$$

Equation 4.1

The total photon flux irradiating the bottom of the vial was determined using **Equation 4.2**, where P is the power of the irradiation source measured with a power-meter, h is Planck's constant (6.626 x10^{-34} J s^{-1}), c is the speed of light (3.00 x10^{8} m s^{-1}) and λ is the irradiation wavelength, taken as the maximum of the LED emission spectra.

$$F = \frac{P \times \lambda}{c \times h}$$

Equation 4.2

Table S4.6. Maxima, width band of emission spectra and photon flux of used LEDs.

	Blue	**Green**	**Red**
λ_{max}(nm)	446	518	634
$\Delta\lambda$ (nm)	190	150	110
F in E.s^{-1} [a]	1.3 x10^{-6}	1.3 x10^{-6}	1.3 x10^{-6}
P in Watt [a]	0.346	0.300	0.245

[a] An analog power-meter PM100A (THORLABS) associated with a compact photodiode power head with silicon detector S120C is used to evaluate the photon flux for each LEDs. Photo-diode detector is placed at the same distance from the LED surface than the bottom of the illuminated vial (3.8 cm^2)

Table S4.7. Absolute QY for hydrogen production at different irradiation wavelength.

	$[Ir(ppy)_2(bpy)]^+$	**Ir-1**	**Ir-2**
Absorbed Flux at 446 nm (E s^{-1})[a]	2.57 x10^{-8}	3.03 x10^{-7}	4.29 x10^{-7}
Absorbed Flux at 518 nm (E s^{-1})[a]	4.24 x10^{-10}	4.67 x10^{-8}	6.68 x10^{-8}
Absorbed Flux at 634 nm (E s^{-1})[a]	No overlap	3.84 x10^{-7}	3.5 x10^{-7}
Absolute QY at 446 nm (%)	0.087	0.13	0.097
Absolute QY at 518 nm (%)	No H_2 detected	0.086	0.036
Absolute QY at 634 nm (%)	No H_2 detected	0.018	0.028

[a]The absorbed photon flux by the Ir photosensitizers is deduced from the multiplication of normalized LED spectrum by the calculated absorbance of Ir complexes at the respective concentration for the optical path of the photoreactions 1.8 cm.

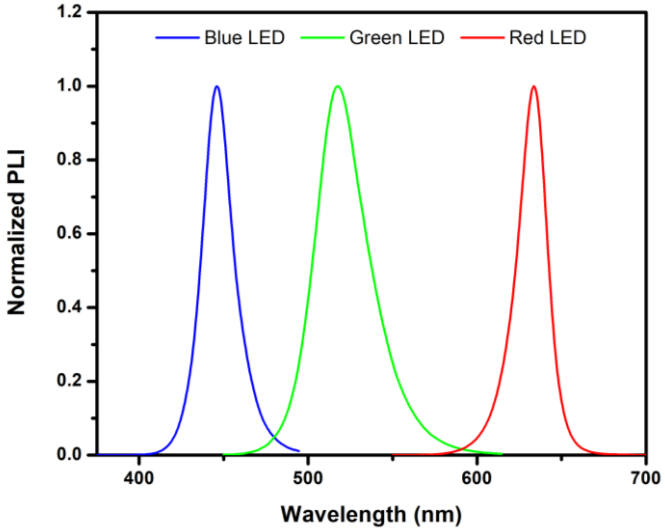

Figure S4.7. Emission spectra of light-emitting diodes used as irradiation sources for HER experiments (blue, green and red).

4.4.6 Control experiments

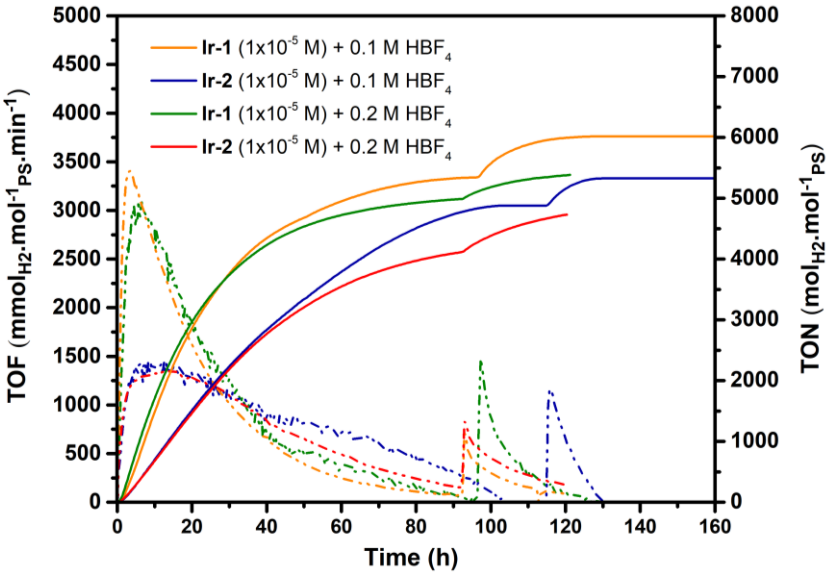

Figure S4.8. TON (solid) and TOF (dashed) recorded with 1 $x10^{-5}$ M Ir(III) photosensitizers with 1 $x10^{-3}$ M of $[Co(dmgH)_2(py)(Cl)]$, 4 $x10^{-3}$ M $dmgH_2$ in CH_3CN with 1 M TEOA as the electron source and 0.1 M or 0.2M HBF_4 as the proton source.

4.4.7 Photostability experiments

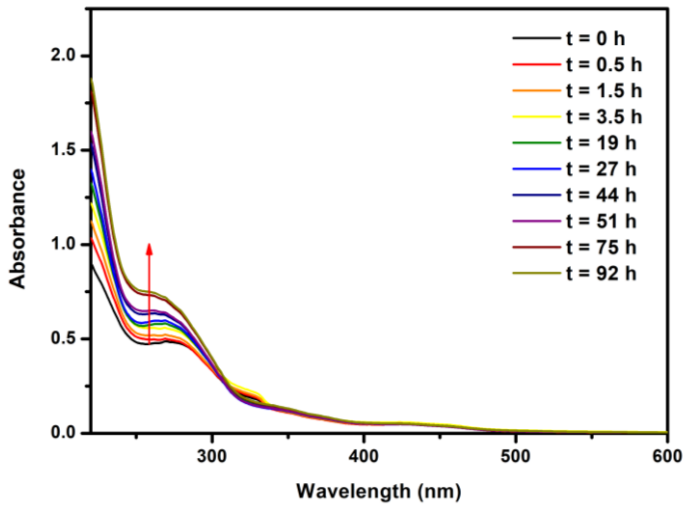

Figure S4.9. Absorption spectra of 5 10^{-6} M **Ir-1** in acetonitrile over time under blue light irradiation (452 nm).

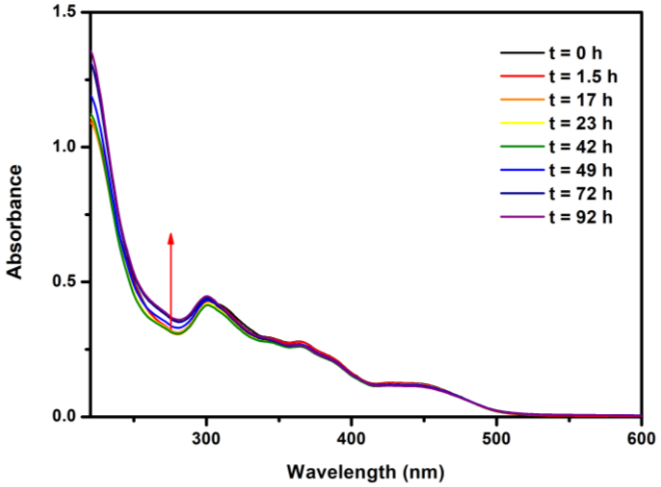

Figure S4.10. Absorption spectra of 5 10^{-6} M **Ir-2** in acetonitrile over time under blue light irradiation (452 nm).

4.4.8 Excited-state quenching experiments

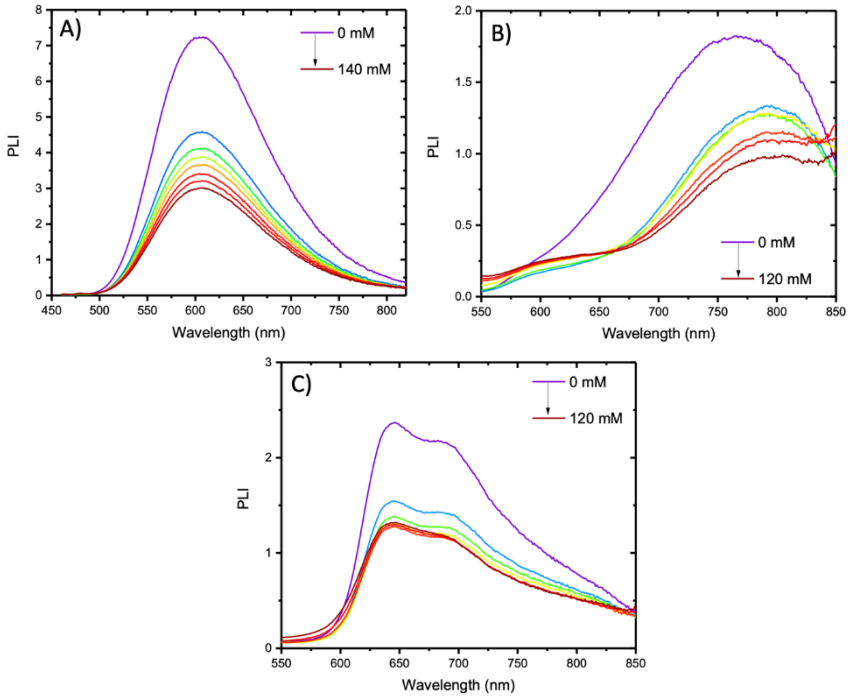

Figure S4.11. Excited-state quenching of $[Ir(ppy)_2(bpy)]^+$ (A), **Ir-1** (B) and **Ir-2** (C) in argon-purged acetonitrile with the indicated concentration of TEOA. The corresponding Stern-Volmer plots were non-linear with downward curvature, preventing the determination of the corresponding quenching rate constants.

Chapter V – Deciphering the Photophysical Kinetics of Iridium-Cobalt Hydrogen Evolution Photocatalysts

Researchers involved in this project are listed hereafter: Jiang Zhao and Dr. Dooshaye Moonshiram (Instituto de Ciencia de Materiales de Madrid), Dr. Jin Yu and Dr. Xiaoyi Zhang (Argonne National Laboratory) and Dr. Wenhui Hu (Marquette University). Time dependent density functional theory calculations, X-ray and optical transient absorption spectroscopy experiments were carried out by laboratory of Dr. Dooshaye Moonshiram.

Preface – This chapter focuses on the utilization of picosecond optical and X-ray spectroscopies with time-dependent density functional theory to decipher the reaction pathways, electronic and structural conformations of Ir-Co hydrogen evolution photocatalysts. The results presented in this chapter have been published in Chemical Communications (Zhao, J.; De Kreijger, S.; Troian-Gautier, L.; Yu, J.; Hu, W.; Zhang, X.; Elias, B.; Moonshiram, D., Deciphering the photophysical kinetics, electronic configurations and structural conformations of iridium–cobalt hydrogen evolution photocatalysts. Chemical Communications 2022, 58 (58), 8057-8060.)

5.1 Introduction

In the previous chapter, we demonstrated that by our proposed ligand design strategy, we developed Ir(III) photosensitizers that were able to generate hydrogen under blue, green and red irradiation with high to moderate turn-over numbers. However, understanding the mechanistic of the photo-induced electron transfer process, the photogenerated intermediates and the influence of the cyclometalating ligands is crucial for the development of efficient photocatalytic systems. In this context, it is interesting to study binuclear systems, particularly those consisting of a photosensitizer and a hydrogen evolution catalyst connected by a bridging electronic relay, as these systems can provide superior electron transfer capabilities compared to mononuclear counterparts.[34, 220, 222, 223] To this aim we used two previously reported by our group Ir(III)-Co(III) dyads (**Figure 5.1**) consisting of cobaloxime hydrogen evolution catalysts $[Co(dmgH)(dmgH_2)]Cl_2$[256] ($dmgH_2$ = dimethylglyoxime) chelated to Ir(III)-based photosensitizers with 2-phenylpyridine ($[Ir(ppy)_2$-L]) or 1-phenylisoquinoline ($[Ir(piq)_2$-L]) ligands and found to display larger than 200 turnover rates of hydrogen generation upon light irradiation in acetonitrile with

0.5 M triethanolamine as the sacrificial electron donor and 0.05 M tetrafluoroboric acid as the proton source.[183, 297] To get a better picture of the photo-induced electron transfer dynamics, we decide to use X-ray transient absorption (XTAS) and UV-vis transient absorption (TA) spectroscopies in the pico-microsecond time regime coupled with time-dependent density functional theoretical calculations (TD-DFT) as powerful tools at both Co and Ir K and L-edges. Indeed, this one of a kind study will help us to extract valuable information about the coordination sphere around the cobalt catalytic centre and resolve the kinetics, electronic and structure scheme of these Ir(III)-based photosensitizers, hence providing a global mechanistic study on the photo-induced electron transfer processes at stake in these two Ir(III)-Co(III) dyads. This would allow us to determine which one of the two possible electron-transfer pathways occurs in these systems: either (1) oxidative quenching of the Ir photosensitizer ^{3}MLLCT state by the Co(III) catalyst or (2) reductive quenching of the Ir photosensitizer by TEOA followed by electron transfer to the Co(III)-based complex.

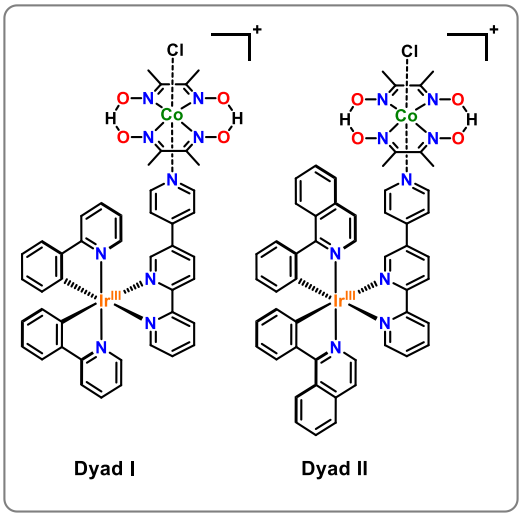

Figure 5.1. Structure of the Ir-Co based dyads I and II obtained respectively through chelation of the Ir(III)-based photosensitizers [Ir(ppy)$_2$-L] and [Ir(piq)$_2$-L] with the Co(III)-based catalyst.

X-ray transient absorption spectroscopy follows the same pump-probe scheme than classical transient absorption spectroscopy described in the previous chapters, using a laser pulse to trigger the formation of a transient species and a time delayed X-ray pulse to probe the transient electronic and geometric structures around X-ray absorbing atoms. XTAS is based on the steady-state X-ray absorption spectroscopy (XAS), including X-ray absorption near edge structure (XANES) and extended X-ray absorption fine structure (EXAFS). The main difference between classical transient absorption spectroscopy and XTAS lies in the fact that the pump and the probe pulse induce two different absorption processes that are not coupled coherently due to their high photon energy difference (~2 eV for the laser pulse and ~7 keV for the X-ray probe).[312] The inner shell to valence orbital transitions induced by highly energetic X-ray photons provides a new sets of electronic transitions correlated with electronic configurations of X-ray absorbing atoms. During photoredox catalysis, transition metals centers undergo oxidation, spin state and chemical environment changes in which electronic configurations of frontier orbitals are altered. Such changes frequently lack distinct features in the visible light region or are masked by strong electronic transitions such as ligands centered π to π^* transition. Moreover, as the atomic ionization energy (energy required to remove an electron from an atom) depends on the atomic number, XTAS allows the specific analysis of an element, which renders XTAS a powerful method to identify electronic configurational changes at specific metal centers induced by visible-light excitation.[313] This powerful technique allowed to study the excited state structure of light-absorbing molecules[314, 315] as well as to decipher the mechanisms and kinetics of photoinduced CO_2 reduction[316], water oxidation[317, 318] and reduction[77, 319, 320] as well as organic synthetic[321] processes.

5.2 Results and discussion

5.2.1 X-ray absorption spectroscopy

Prior to conducting time-resolved measurements, the cobaloxime-based Co(III) catalyst and Ir(III)-based photosensitizers were analysed by XANES and EXAFS techniques. The XANES, EXAFS, and Fourier-transform (FT) of the k^2-weighted Co(III) EXAFS spectra are illustrated in **Figure 5.2-A**, **Figure S5.1-A**, and **Figure 5.2-B**, respectively. The Co(III) FT EXAFS spectrum displays a prominent peak and shoulder, labelled as Peaks I and II (**Figure 5.2-B**), which correspond to the characteristic Co-N and Co-Cl bond distances. EXAFS fits for both the first coordination sphere and the complete spectrum are presented in **Figure S5.2** and **Table S5.1** in the experimental section. Analysis of the first peak in the cobaloxime Co(III) complex clearly identifies four Co-N distances at 1.85 Å, and including a Co-Cl distance at 2.16 Å enhances the fit quality, as evidenced by the reduced R-factors and χ^2 value (**Table S5.1, Fits 1 and 3**). The fitted Co-N and Co-Cl bond distances align with the reported XRD structure[297] and relaxed structures from DFT geometry optimization. Variations detected in the experimental FT of the Co(III) EXAFS correlate well with data from X-ray diffraction (XRD) analysis and EXAFS simulations of DFT-optimized coordinates (**Figure S5.3**). These results demonstrate that theoretical methods, including geometry optimization for the Co(III) complex, accurately reproduce experimental data and can thus be reliably utilized for analysing the Co(II) intermediate.

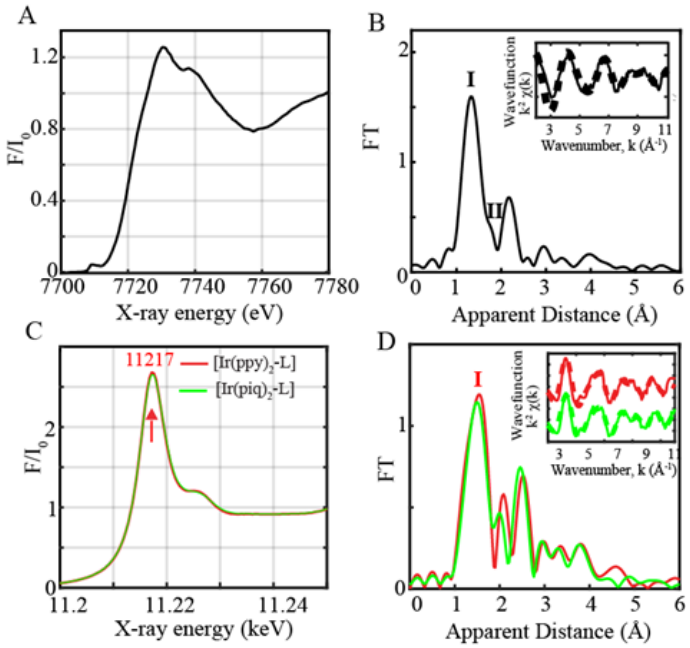

Figure 5.2. A) Normalized Co K-edge XANES for Co^{III} complex in **dyads I** and **II** (black). B) Fourier transforms of k^2-weighted Co EXAFS for the Co(III) catalyst (black). *Inset*: Back Fourier transformed experimental (solid lines) and fitted (dashed lines) $k_2[\chi(k)]$. C) Normalized Ir L-edge XANES for $Ir(ppy)_2$-L (red) and $Ir(piq)_2$-L (green). D) Fourier transforms of k^2-weighted Ir EXAFS Inset. Back Fourier transformed experimental (solid lines) and fitted (dashed lines) $k_2[\chi(k)]$ for Ir complexes in dyads I and II. Experimental spectra were calculated for k values of 2-11 $Å^{-1}$.

The two Ir-based photosensitizers, $[Ir(ppy)_2$-L] and $[Ir(piq)_2$-L], were further evaluated using steady-state L-edge XANES and EXAFS spectroscopy, as shown in **Figure 5.2-C, D,** and **Figure S5.1-B**. Ir(III) complexes exhibit a formal d^6 electronic configuration, characterized by filled t_{2g} and empty e_g levels. As a result, an intense peak at 11217 eV is observed, corresponding to the Ir 2p to unoccupied 5d states with e_g symmetry (**Figure 5.2-C**). The lower energy region below 11217 eV shows no features, due to the absence of vacancies in the t_{2g} states. The FT of the k^2-weighted EXAFS spectra for $[Ir(ppy)_2$-L] and $[Ir(piq)_2$-L] reveals a prominent peak (**Peak I, Figure 5.1-D**), which corresponds to the averaged Ir-N/C distances of 2.00 Å and 2.01 Å, respectively. These values are in close agreement with the reported XRD structures, which exhibit Ir-N distances of 2.06 Å (**Table S5.1, Figure S5.3**).

5.2.2 Time resolved X-ray and optical spectroscopic investigations

Following the steady-state measurements, X-ray transient absorption spectroscopy (XTAS) was employed to directly monitor the electronic configurations, kinetics, and structural dynamics of the photo-generated Co(II) and Ir triplet states within the supramolecular assemblies under similar photocatalytic conditions[297], using triethanolamine (TEOA) as the sacrificial electron donor and aqueous tetrafluoro boric acid as the proton source in argon purged acetonitrile (**Figures 5.3 and 5.4**). The Ir-Co binuclear dyads were optically excited at 400 nm in the mixed Metal-Ligand-to-Ligand Charge Transfer (MLLCT) range with a 10 kHz repetition-rate laser and probed with X-ray pulses at various time delays ranging from 100 ps to ~25 μs. XAS spectra of the supramolecular assemblies were recorded before and after laser excitation. By subtracting the laser-off spectrum from the laser-on spectrum, a transient signal was obtained for each pump-probe delay, providing insights into the photo-induced dynamics and the electronic and structural states of the catalyst and photosensitizer excited states.

Upon light excitation, mixed Metal-to-Ligand-Ligand Charge Transfer (MLLCT) occurs from the 5d orbital of Ir(III) to the π^* orbital of the ligand, followed by intersystem crossing (ISC) to a triplet excited state.[226] This process is followed by electron transfer from the TEOA to the excited photosensitizer, generating the reduced photosensitizer. The latter can in turn transfer an electron to the Co(III) complex, generating a Co(II) species. **Figure 5.3-A** illustrates the Co XTAS spectrum of both supramolecular assemblies with an averaged time delay of 11.3 μs between laser and X-ray pulses.

A prominent peak at 7720 eV and a broad dip at 7735 eV are observed, corresponding to the formation of the reduced Co(II) species[78] and ground state bleaching of Co(III), respectively. These energy transitions indicate a shift of the Co centre K-edge to lower energy, confirming the reduction of Co(III) and the formation of Co(II) via electron transfer from the Ir(III)-based photosensitizers. Notably, changes are observed not only in the oxidation

state of the Co catalytic metal site but also in its electronic configuration and coordination environment, as indicated by the pre-edge region of the absorption spectrum at lower photon energies around 7710 eV (**Figure 5.3-B, red trace**).

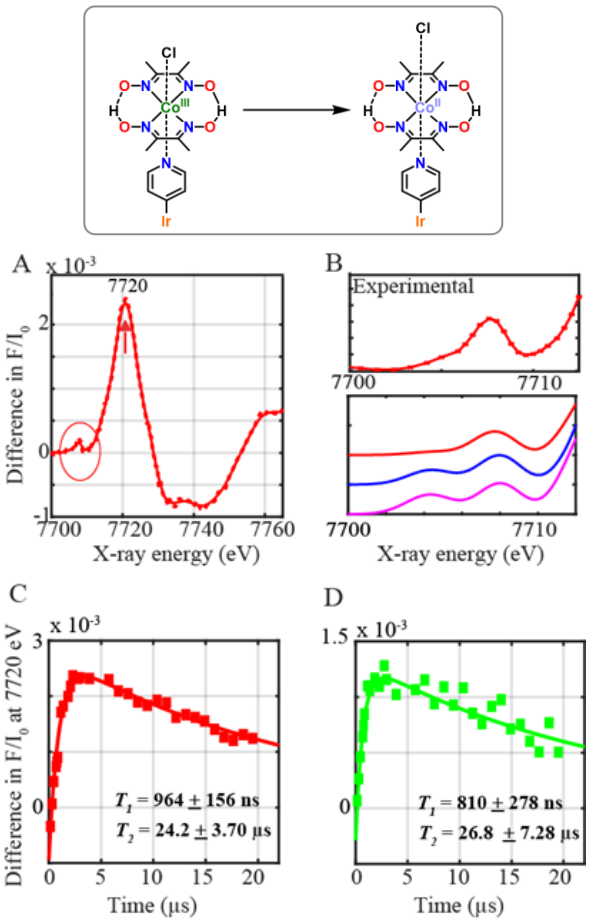

Figure 5.3. A) Experimental difference spectrum (laser on-laser off) corresponding to the Co(III) transient signal at a time delay of ~11.3 µs between laser and X-ray pulses (red) in 1 mM **dyads I** and **II** with 1 M TEOA and 10 mM tetrafluoro boric acid. B) Zoom-in of the pre-edge Co(II) transient experimental spectrum (red) (top) together with the simulated difference spectra for $[Ir^{III}\text{-L-}Co^{II}Cl]$ octahedral (red), $[Ir^{III}\text{-L-}Co^{II}CH_3CN]^+$ octahedral (blue) and $[Ir^{III}\text{-L-}Co^{II}]^+$ square pyramidal (magenta) geometries (bottom). Pump-probe time delay scans recorded at 7720 eV for C) **dyad I** and D) **dyad II**, reflecting the formation and decay of the Co(II) photo-induced species. Kinetic fits T_1 and T_2 of the Co(II) formation and decay processes are shown.

Upon laser excitation, the Co d shell occupation changes from d^6 to d^7. This transition is accompanied by structural relaxation and hybridization of the valence 3d states with N/O ligand p-orbitals.[322] Notably, the fraction of the Co(II) excited state between the laser pump and X-ray probing was too low (less than 3%) to reconstruct the EXAFS and structural conformations of the excited states. Therefore, transient XANES spectra were combined with TD-DFT XANES simulations to extract electronic and geometric information about the photo-generated Co(II) (**Figure 5.3-B**). Various possible geometries of the intermediate Co(II) structure were theoretically explored. As shown in **Figure 5.3-B**, there is poor agreement between the experimental spectrum and theoretical simulations for a Co(II) square bipyramidal structure without coordinated solvent molecules and an octahedral complex with a bonded acetonitrile molecule (compare red, blue, and magenta traces). In contrast, simulations for a distorted octahedral geometry with an elongated chlorido ligand at 2.4 Å accurately resolve the pre-edge feature (red trace), confirming the formation of a Co(II) derivative with a loosely coordinated chloride in both supramolecular assemblies upon photoexcitation.

The kinetics of the formation and decay of the Co(II) species were further investigated in both supramolecular assemblies by setting the photon energy to 7720 eV, which corresponds to the formation of Co(II), and varying the time delays between the laser and X-ray pulses (**Figure 5.3-C** and **-D, Figure S5.4**). The formation and decay kinetics for the Co(II) species are similar in both dyads, appearing promptly within 964 ± 154 ns and 810 ± 278 ns, respectively (**Figures 5.3-C** and **-D**), and decaying within 24.20 ± 3.70 μs and 26.80 ± 7.28 μs (**Figures 5.3-C** and **-D**). Notably, the transient signal of Co in **dyad I** is approximately twice as large as that in **dyad II**, indicating more efficient formation of the reduced Co(II) species in **dyad I** (**Figures 5.3-C and -D**)

To further investigate this process, transient XANES was conducted to elucidate the photo-induced electron transfer dynamics of the supramolecular assemblies at the Ir L-edge site. Three prominent features, I, II, and III, at

energies of 11213, 11216, and 11220 eV, respectively, are observed (**Figures 5.4-A** and **-B**). Feature I (**Figures 5.4-A** and **-B**) corresponds to a 2p to Ir unoccupied t_{2g} state, which arises after electron transfer to the ligand.[323] Features II and III (**Figures 5.4-A** and **-B**), in contrast, result from an increase in the energy of the XANES white line upon photoexcitation. As previously corroborated through DFT calculations,[323] both the Ir 5d e_g and 2p states shift towards lower energies in the photo-excited configuration of the triplet state. The shift of the 2p levels is more significant than that of the 5d states, resulting in an increase in the XANES white line[323] of the Ir-^{3}MLLCT state compared to the ground state. This leads to a more positive feature III and a lower minimum at feature II (**Figures 5.4-A** and **-B**).

In the Ir-Co **dyad I**, the ^{3}MLLCT state of the [Ir(ppy)2-L] appears promptly within the 100 ps pulse duration of the X-ray and decays within 6.03 ± 0.66 ns (**Figure 5.4-C**). Conversely, in the Ir-Co **dyad II**, the transient spectrum of [Ir(piq)2-L] persists within the 100 ps to 459 ns time scales (**Figure 5.4-B**) and shows two decay lifetimes of 4.48 ± 2.62 ns and 170 ± 65 ns (**Figure 5.4-D**). The Ir-based photosensitizers were also studied with TEOA in the absence of the Co-based catalyst and tetrafluoro boric acid, and similar time scales were obtained within error bars (**Figure S5.5**). There are two possible electron-transfer pathways in the photocatalytic cycle of the Ir-Co supramolecular assemblies: (1) oxidative quenching of the Ir photosensitizer ^{3}MLLCT state by the Co(III) catalyst, or (2) reductive quenching of the Ir photosensitizer by TEOA followed by electron transfer to the Co(III)-based complex (**Figure 5.5**). However, the oxidative quenching pathway can be excluded because the formation of the reduced Co-based catalyst occurs on much longer time scales (810-960 ns) than the decay of the Ir-based ^{3}MLLCT states, as shown in **Figures 5.4-C** and **-D**. In the presence of excess TEOA, which serves as a sacrificial electron donor, the predominant pathway is the reductive quenching of the Ir ^{3}MLLCT state. The decay lifetime T_1 of 4.48-6.02 ns observed in both dyads corresponds to the formation of the reduced ^{3}MLLCT state (**Figure 5.5**). Importantly, the second decay lifetime T_2 of 170 ± 65 ns for the [Ir(piq)2-L] photosensitizer, observed in both the absence and presence of the Co(III)-

based catalyst, corresponds to the decay to the Ir(III) ground-state due to inefficient quenching. This is further corroborated by the low excited state fraction obtained for the Ir-Co **dyad II**. Approximately 50% of the [Ir(piq)2-L] recombines back to the ground state, while the other 50% participates in the efficient electron transfer reaction to the Co(III) catalyst to generate the photo-reduced Co(II) species (**Figure 5.3-D, Figure 5.5**).

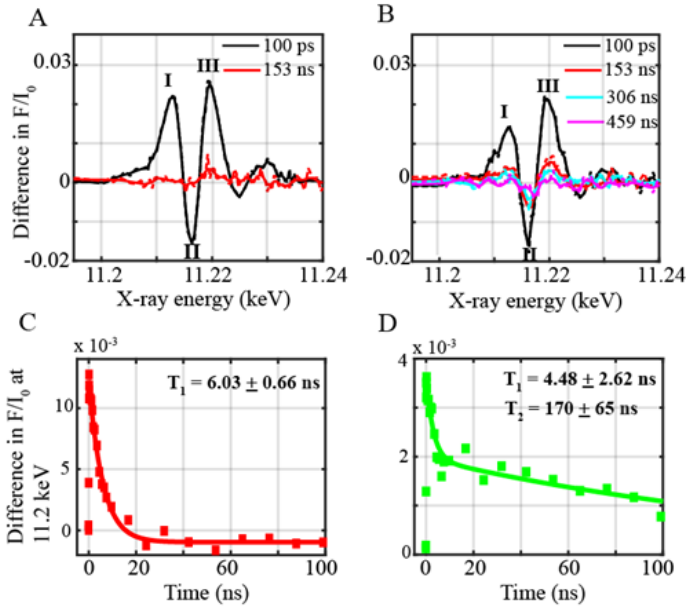

Figure 5.4. Experimental difference spectra (laser on-laser off) corresponding to the ^{3}MLLCT signals of A) [Ir(ppy)$_2$-L] and B) [Ir(piq)$_2$-L] in **dyad I** and **II** respectively. Pump-probe time delay scans recorded at 11.2 keV of C) [Ir(ppy)$_2$-L] in **dyad I** and D) [Ir(piq)$_2$-L] in **dyad II** corresponding to the decay of the triplet excited states formation. Kinetic fits of the ^{3}MLLCT state reaction with TEOA (T_1) with the excited-state relaxation time (T_2) for complex [Ir(piq)$_2$-L] due to inefficient quenching are indicated.

Limited by the 100 ps pulse duration of the X-rays, the intersystem crossing (ISC) timeframe from the singlet to the triplet excited states, as well as the decay of the ^{3}MLLCT states of the Ir(III)-based photosensitizers within both dyads, were determined using TA from 1 ps to 2 ns timescales (**Figure S5.8**). Interestingly, [Ir(ppy)$_2$-L] and [Ir(piq)$_2$-L] exhibit similar ISC times within experimental error, at 10.7 ± 3.1 ps and 9.89 ± 0.82 ps respectively (**Figures S5.8-A** and **-B**). Likewise, the ^{3}MLLCT states for [Ir(ppy)$_2$-L] and [Ir(piq)$_2$-L] in **dyads I** and **II** decay within 7.74 ± 1.71 ns and 6.68 ± 0.19 ns, respectively

(**Figures S5.8-A** and **-B**) consistent with the decay lifetimes of the ^{3}MLLCT states of the Ir-based photosensitizers obtained through XTAS (**Figure 5.4-C** and **-D**). Despite their similarities, [Ir(ppy)$_2$-L] and [Ir(piq)$_2$-L] exhibit different electron densities, leading to varying photophysical properties.

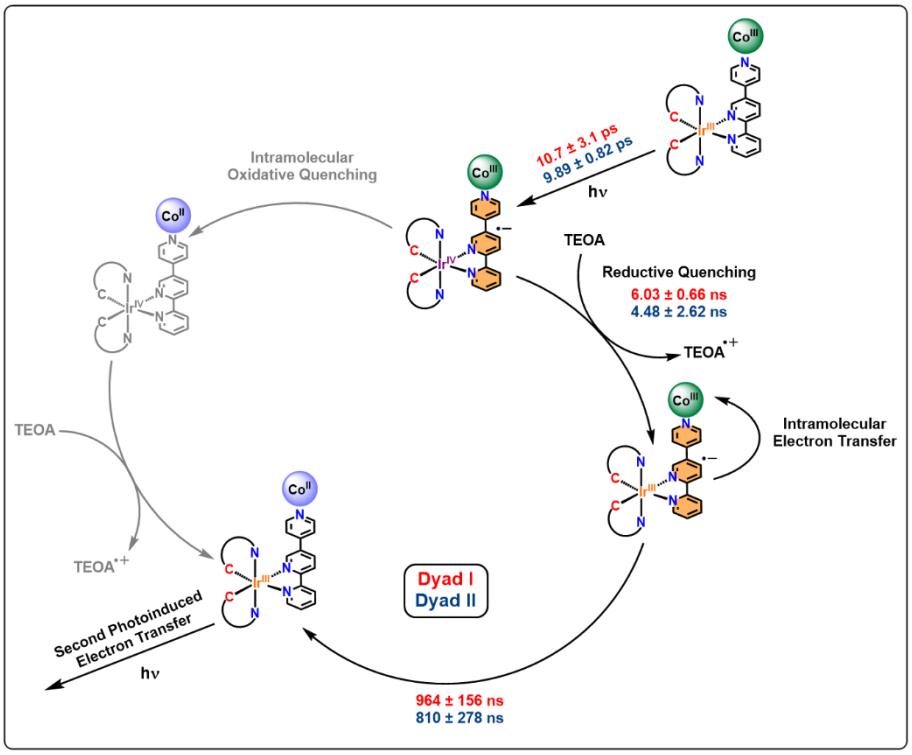

Figure 5.5. Mechanistic pathways of Ir–Co **dyads I** and **II**. Rate constants for **dyads I** and **II** are respectively shown in red and blue.

Previous TD-DFT calculations have shown that the lowest triplet excited state for [Ir(ppy)$_2$-L] is a ^{3}MLLCT state, while that for [Ir(piq)$_2$-L] consists of a combination of C^N centred and ^{3}LC characters.[297] The increased contribution of the ^{3}LC transition in the excited state of [Ir(piq)$_2$-L] results in a less efficient ^{3}MLLCT state and lower electron density in the excited state of the pendant pyridine moiety, causing rapid decay to the ground state as revealed by XTAS measurements conducted in the presence and absence of the Co(III) catalyst (**Figure 5.4-D and Figure S5.5-B**). Hydrogen evolution measurements previously carried out under similar experimental conditions as XTAS, using

triethanolamine as a sacrificial electron donor and tetrafluoro boric acid as the proton source[297], further demonstrated that **dyads I** and **II** displayed maximum turnover frequencies of 180 and 58 under green light excitation, corroborating the lower efficiency of [Ir(piq)$_2$-L].

5.3 Conclusions

In summary, we used combined TA and XTAS measurements at the Co K-edge and Ir L-edge energies, along with DFT calculations, to evaluate the impact of 2-phenylpyridine and 1-phenylisoquinoline ligands on Ir(III)-based photosensitizers when chelated to a Co(III)-based hydrogen evolution catalyst. Time-resolved XANES with TD-DFT simulations at the Co K-edge demonstrated that upon photoexcitation, the Co(III) octahedral catalyst is reduced to a Co(II) species, accompanied by a Co–Cl bond elongation. We also tracked the kinetics of the rise and decay of the Co(II) intermediate in both dyads, with formation times between 810–964 ns and decay back to the Co(III) complex within 24.2–26.8 μs. Analysis of the supramolecular assemblies at the Ir L-edge revealed the rapid formation of an Ir ^{3}MLLCT state within the 100 ps pulse duration of the X-rays in both dyads. Additionally, combined kinetics studies using TA and Ir L-edge XTAS showed that both Ir(III)-based photosensitizers in **dyads I** and **II** exhibited similar ISC times of 9.89–10.7 ps and were reductively quenched by TEOA within 4.48–7.74 ns. Notably, [Ir(piq)$_2$-L] in **dyad II** was found to be less efficient than its [Ir(ppy)$_2$-L] counterpart in **dyad I**, as it exhibited decay to the Ir(III) ground state within 170 ± 65 ns and showed 50% less electron transfer efficiency to the Co(III) catalyst to produce the photoreduced species. This mechanistic study provides significant insights into the reaction pathways and efficiencies of a versatile previously reported family of supramolecular Ir–Co dyads, highlighting future potential for developing Ir(III)-based photosensitizers with less conjugated cyclometalated ligand derivatives for HER applications. However, as depicted in **Chapter IV** Ir(III) complexes are suffering from poor visible light absorption properties that could be overcome by the use of highly conjugated cyclometalated ligands such as **piq** or **fliq**.

In the literature, the mechanisms for light-driven H_2 evolution catalyzed by cobalt systems are reported to begin with the absorption of a photon by the photosensitizer (PS), creating an excited PS* state. This excited-state can undergo an oxidative quenching process where the cobalt complex acts as an electron acceptor, generating the active Co(I) species. Subsequently, a second electron transfer occurs from the sacrificial electron donor to the oxidized photosensitizer (PS^+), regenerating the PS. Alternatively, the PS* can be reductively quenched by the sacrificial electron donor, forming a reduced PS^-, which then reduces the cobalt catalyst to the Co(I) state. For Co(III) catalysts specifically, an initial photoinduced electron transfer generates the Co(II) complex, which is further reduced to the Co(I) state, potentially causing an induction period.[219, 324, 325] This study, which combines TA and XTAS measurements, unequivocally proves a mechanism operating via a reductive quenching of the PS* by the sacrificial electron donor to form a reduced PS^-, [293] which is then able to reduce the Co(III) catalyst to the Co(II) species. Unfortunately, these techniques are not providing mechanistic insights on the reduction of this Co(II) catalyst to the active Co(I) species. Nevertheless, this could arise from a second electron transfer event from the reduced PS^-. Alternatively, some electrons entering the cobalt catalytic cycle might originate from a thermal (dark) process involving the SED, typically an amine like triethanolamine (TEOA) or triethylamine (TEA). After electron transfer to PS* or PS^+, a radical cation of the SED is formed, which is known to decompose in the reaction medium to give one equivalent of proton and one equivalent of electron, together with aldehyde and secondary amine byproducts.[326, 327]

5.4 Experimental section

The materials and methods used in this chapter are described in ***Chapter X***

5.4.1 EXAFS analysis

Table S5.1. EXAFS Fits parameters for Co and Ir-based complexes

Complex	Fit	Region	Shell, N	R, Å	E_0	ss.^{2} (10^{-3})	R-factor	Reduced Chi^2
Co(III) chlorido complex	1	I	Co-N,5	1.87	-8.6	4.9	0.0594	1954
	2	I	Co, N-5 Co-Cl, 1	1.84 2.15	-13	0.55 1.5	0.0221	515
	3	I,II	Co-N,5 Co-Cl,1 Co-C, 10	1.85 2.16 2.73	-9.4	1.8 0.50 9.3	0.0135	246
Ir(ppy)$_2$-L	4	I	Ir-C/N,6	2.00	-0.74	5.9	0.0145	132
	5	I,II	Ir-C/N,6 Ir-C, 4 IrC, 8	2.00 2.75 3.02	-3.0	6.5 5.5 2.9	0.0202	136
Ir(piq)$_2$-L	6	I	Ir-C/N,6	2.01	-1.2	7.5	0.0165	147
	7	I,II	Ir-C/N,6 Ir-C, 4 IrC, 8	1.98 2.67 2.95	-4.8	7.8 3.5 2.6	0.0157	108

* The amplitude reduction factor S_0^2 was fixed to 0.8

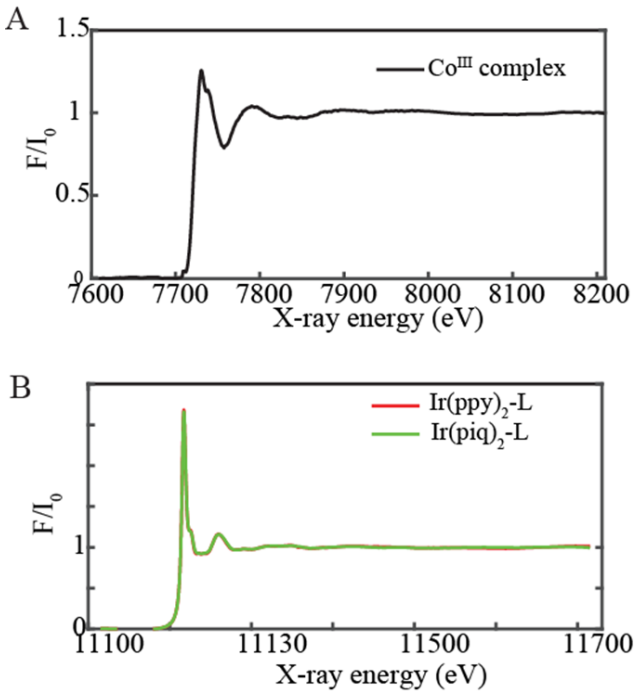

Figure S5.1. A) Normalized Co K-edge EXAFS for Co(III) complex in **dyads I** and **II** (black), B) Normalized Ir L_3-edge EXAFS for $Ir(ppy)_2$-L (red) and $Ir(piq)_2$-L (green) in **dyads I** and **II** respectively.

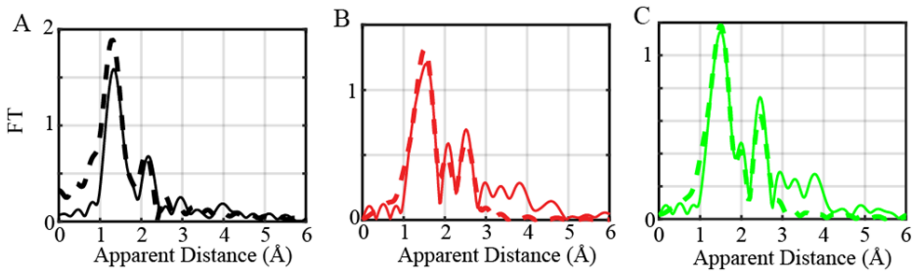

Figure S5.2. Fourier transforms of k^2-weighted EXAFS for A) 1 mM Co(III) complex in **dyads I** and **II** (solid black line) and its corresponding fit (**Fit 3, Table S5.1**), for B) 1 mM $Ir(ppy)_2$-L complex (**dyad I**) (red solid line), and its corresponding fit (**Fit 5, Table S5.1**) and C) 1 mM $Ir(piq)_2$-L complex (**dyad II**) (green solid line) and its corresponding fit (**Fit 7, Table S5.1**).

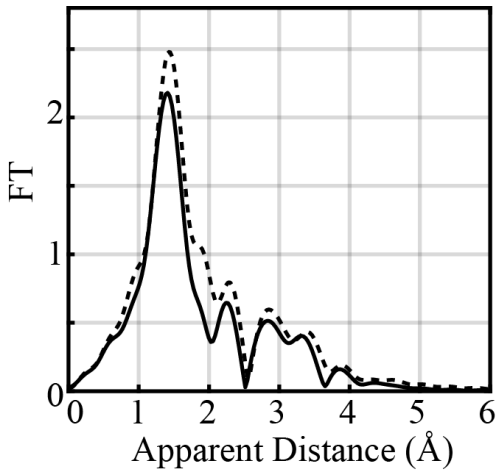

Figure S5.3. Simulated EXAFS spectra for Co(III) chloro complex in **dyads I** and **II**. Atomic coordinates were obtained from single crystal X-ray diffraction structure of $[LCo^{III}Cl]^{+}$ (solid black line)[297] and from DFT simulations (dashed black line).

5.4.2 XTAS analysis

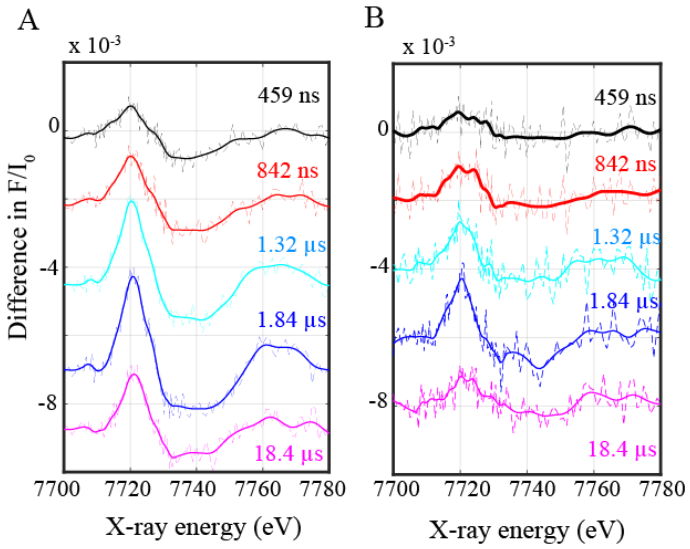

Figure S5.4. Stacked spectra corresponding to a series of time delays between laser and X-ray pulses of A) **dyad I** and B) **dyad II**. These measurements were carried out for a range of averaged time delays from 0 to 18.4 µs. The dotted lines represent the raw data and the solid lines represent a smoothening of the spectrum.

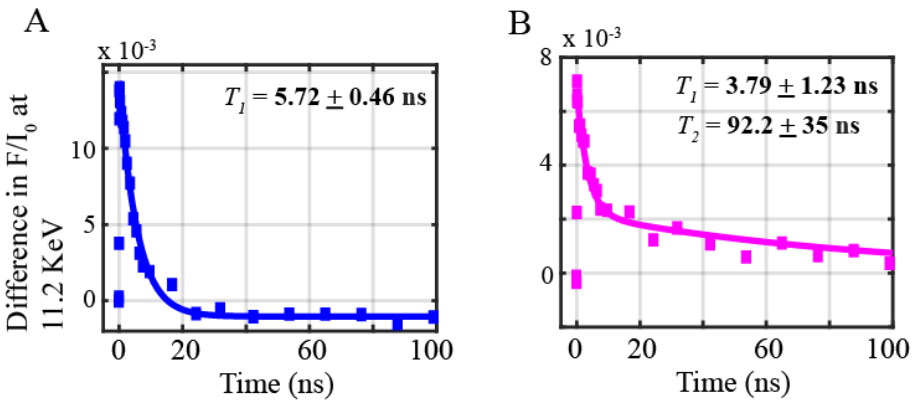

Figure S5.5. Pump-probe time delay scans recorded at 11.2 keV of A) $Ir(ppy)_2$-L and B) $Ir(piq)_2$-L complexes with triethanolamine in the absence of the Co(III) catalyst and tetrafluoro boric acid proton source. Kinetic fittings of the Ir ^{3}MLLCT state with the electron donor triethanolamine (T_1) together with the back-electron transfer times (T_2) in the case of complex $Ir(piq)_2$-L are indicated.

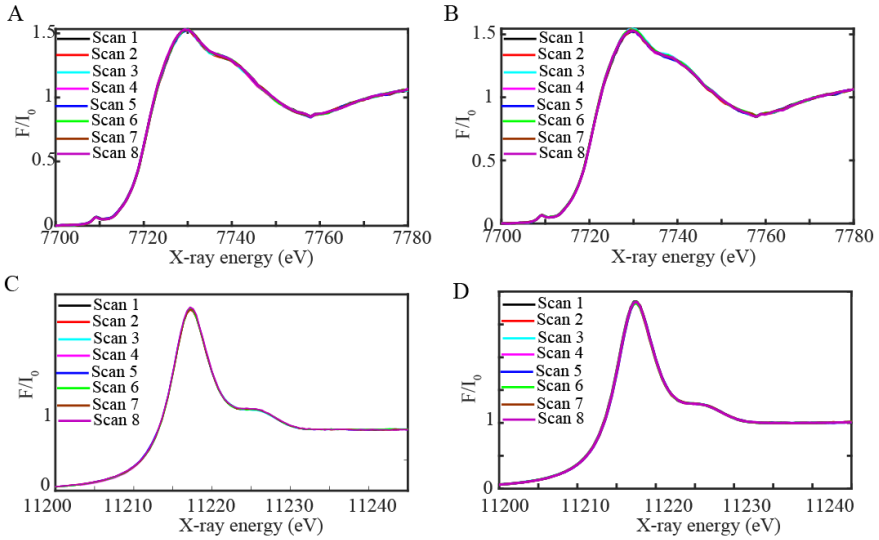

Figure S5.6. "Laser-on" scans of **dyads I** and **II** at Co K-edge energy of A) **Dyad I** B) **Dyad II** and at Ir L-edge of C) **Dyad I**, D) **Dyad II**. No change is hereby observed in the XANES spectra of one batch of sample over the course of 2.7 hrs indicating their intact nature and lack of decomposition.

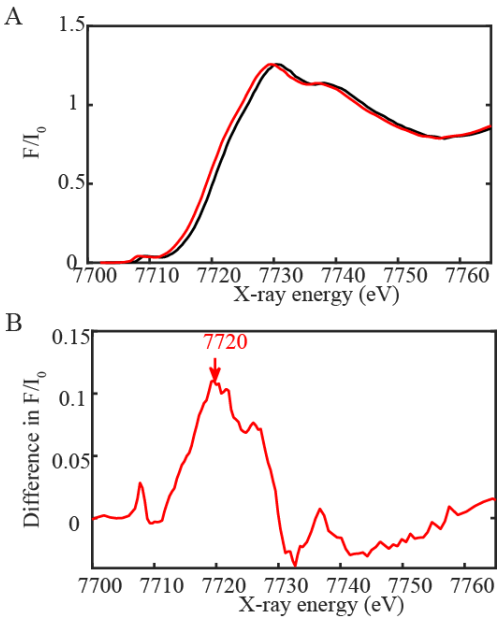

Figure S5.7. A) Normalized Co K-edge XANES for Co(III) complex (black) and Co(III) complex shifted by -1 eV (in red), B) Experimental difference spectrum between black and red spectrum shown in **Figure S5.4-A**. A difference spectrum with a peak energy of 7720 eV is observed showing that the K-edge of the Co centre shifts to lower energy and confirming the formation of Co(II) from Co(III).

5.4.3 Transient absorption

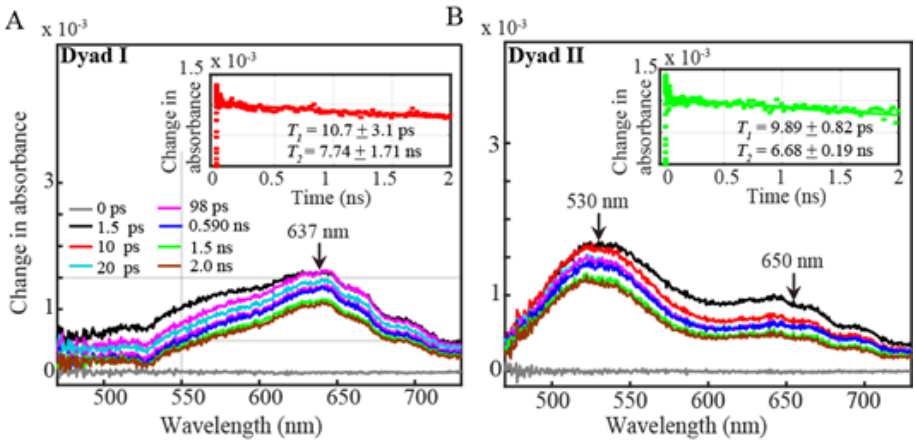

Figure S5.8. TA spectra of a solution of 0.3 mM A) **dyad I** and B) **dyad II** with 0.3 M TEOA and 3 mM tetrafluoroboric acid at pump-probe delays between 1.5 ps to 2 ns. Inset) Kinetic decay profiles at λ= 630 nm and λ= 530 nm after excitation at λ_{exc} = 410 nm. *T1* and *T2* are the resulting decay lifetimes. Upon light excitation, a broad emission at 637 nm as expected from the triplet charge transfer-type excited state (^{3}CT) is observed in the Ir-Co **dyad I**. By contrast, two more structured emission bands at 530 nm and 650 nm arising from the ligand-centred (^{3}LC) contribution to the excited state of the [Ir(piq)2-L] photosensitizer in addition to the expected ^{3}CT-type excited state are noticeable in the Ir-Co **dyad II**.

5.4.4 Theoretical studies

Table S5.2. DFT optimized coordinates of Co(III) complexes using the BP-86[328] functional, and the atom-pairwise Grimme dispersion correction with the Becke-Johnson damping scheme (D3BJ)[329].

[LCo^{III}Cl]$^{2+}$ octahedral complex				**[LCo^{III}CH$_3$CN]$^{3+}$ octahedral complex**			
Co	23.056504	7.777308	17.785380	Co	23.209160	7.662558	17.811237
O	21.133961	8.210469	19.810294	O	21.427138	8.356376	19.872275
O	23.359639	9.050204	15.284206	O	23.634264	8.884637	15.308775
O	22.812090	6.480054	20.333957	O	22.872109	6.399391	20.380403
O	25.108790	7.392870	15.815900	O	25.127261	6.950838	15.776988
N	21.902887	6.436150	16.947589	N	21.859009	6.506693	17.017620
N	21.555748	8.581747	18.620658	N	21.827362	8.660040	18.666501
N	22.656127	9.001953	16.392380	N	22.931241	8.915470	16.408959
N	23.518457	6.571442	19.200757	N	23.527251	6.369104	19.211788
N	24.627794	7.009856	17.007008	N	24.616028	6.635684	16.975468
C	19.820890	10.317188	18.423281	C	20.261928	10.546052	18.447863
H	19.397455	9.819195	19.301944	H	19.956000	10.230143	19.450029
H	19.045502	10.422881	17.650909	H	19.387816	10.510746	17.780630
H	20.130728	11.331388	18.720904	H	20.598341	11.592558	18.492481
C	20.987018	9.534782	17.917094	C	21.349039	9.654296	17.948005
C	21.622254	9.777969	16.630309	C	21.986678	9.800103	16.644212
C	21.173937	10.829240	15.669665	C	21.647048	10.843877	15.633174

H	21.948427	10.980694	14.909620
H	20.983734	11.780016	16.187477
H	20.241322	10.539036	15.159357
C	25.133050	4.891740	20.019472
H	24.528566	4.929730	20.931035
H	26.173872	5.142692	20.271547
H	25.128932	3.860497	19.633611
C	24.590359	5.847928	19.010084
C	25.240906	6.106094	17.724700
C	26.511084	5.441622	17.309719
H	26.779066	5.747364	16.293952
H	26.414999	4.346007	17.345256
H	27.332228	5.720268	17.987955
C	20.268495	4.511895	15.758818
C	20.079548	4.886312	17.088908
H	19.294087	4.442421	17.699410
C	20.910781	5.849472	17.650896
H	20.790076	6.175730	18.682735
C	22.084927	6.083308	15.657505
H	22.883832	6.593261	15.122560
C	21.289361	5.127506	15.035058
H	21.479054	4.877809	13.991904
H	22.040704	7.282057	20.200533
H	24.392369	8.197634	15.517943
H	19.631416	3.758476	15.294681
Cl	24.359544	9.333316	18.738533
H	22.557475	11.368496	15.310284
H	20.930616	11.571552	16.028710
H	21.217913	10.380250	14.732040
C	24.810056	4.390316	19.936109
H	24.435347	4.634221	20.935443
H	25.899948	4.261653	19.974465
H	24.376286	3.423963	19.634326
C	24.433986	5.460782	18.968401
C	25.067231	5.612343	17.650348
C	26.144865	4.710858	17.151757
H	26.226189	4.783376	16.061714
H	25.947667	3.669269	17.437419
H	27.119581	4.992289	17.581236
C	19.952719	4.816423	15.891079
C	19.914365	5.129337	17.249455
H	19.144537	4.726137	17.905965
C	20.879445	5.976467	17.781630
H	20.872794	6.250246	18.834129
C	21.895687	6.217902	15.698679
H	22.686318	6.683466	15.114373
C	20.960767	5.376291	15.107149
H	21.034098	5.171389	14.039902
H	22.220952	7.274606	20.266528
H	24.544320	7.831700	15.489189
N	24.472861	8.817529	18.568415
H	19.208669	4.152251	15.450877
C	25.240123	9.547350	19.032536
C	26.198353	10.464727	19.609813
H	25.694990	11.397550	19.899076
H	26.984482	10.694064	18.877104
H	26.657079	10.016628	20.501827

$[LCo^{II}Cl]^{+}$ octahedral complex

Co	23.296993	7.549305	17.902322
O	21.366522	8.017348	19.948352
O	23.385691	8.673771	15.256319
O	23.139046	6.333749	20.510952
O	25.137596	6.964176	15.799993
N	21.884407	5.936952	17.000704
N	21.770725	8.316997	18.730574
N	22.743466	8.623672	16.453642
N	23.782410	6.394144	19.315340
N	24.766335	6.700041	17.038792
C	19.869236	9.865036	18.467640
H	19.372496	9.225454	19.210077
H	19.173846	10.083264	17.644815
H	20.109478	10.817982	18.970728
C	21.099373	9.173056	17.977176
C	21.679203	9.361392	16.658360
C	21.129042	10.302071	15.633934
H	21.894353	10.502432	14.875120
H	20.817864	11.250387	16.094981
H	20.248107	9.874186	15.125678
C	25.411713	4.752265	20.160331
H	25.197076	5.167125	21.153920
H	26.497281	4.639104	20.038227
H	24.960273	3.746277	20.119284

$[LCo^{II}CH_3CN]^{2+}$ octahedral complex

Co	23.079043	7.571296	17.739524
O	21.126045	8.016721	19.757972
O	23.521485	9.108183	15.332716
O	22.800996	6.232351	20.269414
O	25.160346	7.257449	15.807763
N	21.874422	6.222000	16.770713
N	21.649019	8.445479	18.632398
N	22.814276	8.975761	16.494413
N	23.550691	6.415428	19.157992
N	24.698955	6.893045	16.996454
C	20.071794	10.328464	18.628795
H	19.267742	9.660161	18.968499
H	19.662639	11.051488	17.913005
H	20.419385	10.876676	19.519377
C	21.181440	9.527885	18.033088
C	21.864561	9.833990	16.784329
C	21.522900	11.002731	15.919600
H	22.261389	11.105772	15.117948
H	21.495802	11.930725	16.509374
H	20.529355	10.878632	15.460280
C	25.179132	4.803437	20.055328
H	24.915395	5.178678	21.052504
H	26.267184	4.686290	19.983304
H	24.721416	3.806085	19.952685

C	24.844632	5.656142	19.112005
C	25.411833	5.818383	17.782519
C	26.618454	5.085994	17.290861
H	26.657743	5.166954	16.196866
H	26.596150	4.024020	17.579439
H	27.549546	5.521628	17.692718
C	19.734284	5.373665	15.277233
C	19.517742	5.659080	16.629801
H	18.510983	5.671065	17.051411
C	20.610024	5.929861	17.450165
H	20.480805	6.169155	18.507873
C	22.088712	5.647788	15.696916
H	23.128358	5.680345	15.363476
C	21.053304	5.365675	14.809719
H	21.283803	5.146321	13.765999
H	22.355422	7.067947	20.368444
H	24.201006	7.976818	15.419218
H	18.899095	5.165641	14.606418
Cl	24.715271	9.279903	18.747326
C	24.667262	5.742456	19.013591
C	25.336776	6.011292	17.747426
C	26.617201	5.369951	17.324461
H	26.754384	5.519126	16.246878
H	26.617724	4.293409	17.547926
H	27.483459	5.813662	17.841965
C	20.223189	4.407796	15.440103
C	19.892846	4.871336	16.714217
H	18.986634	4.539871	17.220465
C	20.740440	5.776857	17.347239
H	20.522770	6.169430	18.342010
C	22.197692	5.773085	15.541700
H	23.127935	6.158216	15.120868
C	21.398561	4.869518	14.846502
H	21.701557	4.537975	13.853896
H	22.037528	6.992781	20.152433
H	24.254007	8.330691	15.436913
H	19.576568	3.700192	14.919623
N	24.712185	9.452813	19.363899
C	25.378537	9.684889	18.438255
C	26.199338	9.956041	17.271841
H	25.720371	10.724583	16.650046
H	26.292191	9.038459	16.669022
H	27.194674	10.304495	17.577716

$[LCo^{II}]^{2+}$ square bypiramidal complex

Co	22.928691	7.628737	17.699868
O	21.026385	8.221884	19.780234
O	23.281172	8.965761	15.213150
O	22.656252	6.380248	20.242438
O	25.051520	7.290665	15.779682
N	21.750943	6.218998	16.826902
N	21.526215	8.561253	18.563610
N	22.620605	8.938496	16.352557
N	23.408109	6.521535	19.170829
N	24.559070	6.963158	17.002087
C	19.886347	10.405137	18.422541
H	19.407561	9.904782	19.270632
H	19.138909	10.593805	17.639053
H	20.254272	11.385041	18.766452
C	21.007601	9.568471	17.899998
C	21.644428	9.793490	16.609083
C	21.254277	10.868971	15.649953
H	22.111774	11.109571	15.009283
H	20.921699	11.774449	16.174684
H	20.431784	10.546432	14.989250
C	25.042749	4.924652	20.086826
H	24.754305	5.314133	21.072223
H	26.133497	4.817392	20.037593
H	24.598659	3.919224	19.999293
C	24.535767	5.845430	19.026875
C	25.199642	6.098956	17.755374
C	26.481406	5.451071	17.345362
H	26.616311	5.540284	16.261775
H	26.492764	4.389917	17.630026
H	27.342476	5.933662	17.834828
C	20.175581	4.255907	15.619575

C	20.250990	4.355124	17.009444
H	19.701168	3.673186	17.657919
C	21.047442	5.346567	17.576496
H	21.142497	5.457577	18.658606
C	21.677524	6.127913	15.483615
H	22.259100	6.860550	14.920787
C	20.903427	5.161711	14.846972
H	20.877808	5.127973	13.757492
H	21.686639	7.417304	20.077933
H	24.346061	8.041098	15.447872
H	19.561889	3.487759	15.147408

Chapter VI – Development of Ru(II) and Os(II) Photosensitizers for Photo-Oxidation Applications

People involved in this project are listed hereafter: Skander Ben Guiza (Institut Paul Lambin, in the frame of his bachelor dissertation, June 2022) and Prof. Emilie Cauët (Université Libre de Bruxelles).

Preface – This chapter focuses on the synthesis and characterization of eight novel Ru(II) and Os(II) photosensitizers bearing a common 9,10-disubstituted-1,4,5,8-tetraazaphenanthrene backbone. Their photophysical and electrochemical properties were characterized and the most promising photosensitizers were investigated for guanosine-5'-monophosphate photo-oxidation in aqueous buffer. This application was chosen instead of halides photo-oxidation as their excited-state reduction potentials were only allowing iodide oxidation in pure water. The results presented hereafter have been published in Dalton Transactions (De Kreijger, S.; Cauët, E.; Elias, B.; Troian-Gautier, L., Synthesis of Ru(II) and Os(II) photosensitizers bearing one 9,10-diamino-1,4,5,8-tetraazaphenanthrene scaffold. Dalton Trans. 2024, 53 (24), 10270-10284.)

6.1 Introduction

With the aim of leveraging the photosensitizer regeneration event, the second part of this Ph.D. thesis is dedicated to the development of systems using halides (X^-) as the electron donor, which would yield a covalent X-X bond after X^- oxidation. As mentioned previously, bromide and chloride photo-oxidation are extremely challenging in water with visible light, as it requires an exceptionally strong oxidizing power, which often comes at the cost of visible light absorption. To address this challenge, we initially chose to investigate Ru(II) and Os(II) photosensitizers, which are known for their good visible light absorption properties. To grant access to strong oxidizing power, we chose to work with the strong π-accepting 1,4,5,8-tetraazaphenanthrene (TAP). The latter can stabilize the HOMO and LUMO of the photosensitizers, allowing access to good visible light absorption properties while increasing the oxidizing power of the photosensitizers. Transition metal complexes based on Ru(II) and Os(II) photosensitizers have numerous applications in fields that include halide oxidation,[20, 21, 135, 158] photoredox

catalysis,[174, 330, 331] luminescence cellular imaging,[332-335] photodynamic therapy and other biomedical applications,[336-340] as well as solar energy conversion.[102, 104, 252, 341-344] A common interest however, for many photosensitizers, earth abundant and rare, is the development of ligands with extended π-systems or with the ability to bridge a second metal center.[136, 222, 345-355] For example, in biomedical applications, intercalation within DNA or photoreaction with DNA bases was made possible with transition metal complexes (Ru, Rh, Os) carrying extended ligands such as TPPHZ (tetrapyrido[3,2-a:2',3'-c:3'',2''-h:2''',3'''-j]phenazine), dppz (dipyrido[3,2-a:2',3'-c]phenazine), PHEHAT (1,10-phenanthrolino[5,6-b]-1,4,5,8,9,12-hexaazatriphenylene) or TAPHAT (1,4,5,8-tetraazaphenanthrene[9,10-b]-1,4,5,8,9,12-hexaazatriphenylene).[346, 356-360] The structure of these ligands are presented in **Figure 6.1**. Such complexes were also used in artificial photosynthesis[361-368] and several binuclear photosensitizers based on the bridging TPPHZ ligand have also been developed for bio-imaging purposes.[332-334] The photoreactivity of such complexes could be further tuned by the use of different ancillary ligands that, for example, possess a strong π-accepting character, such as 1,4,5,8-tetraazaphenanthrene (TAP) or 1,4,5,8,9,12-hexaazatriphenylene (HAT). Such photosensitizers can react with Guanine, *i.e.* the DNA base with the most reducing power, to form the corresponding mono-reduced complex and the oxidized guanine via photo-induced electron transfer.[80, 166, 197-202] Therefore, the investigation of photo-induced electron transfer between a prototypical biological substrate, *i.e.* guanosine-5'-monophosphate (GMP), $E(GMP^{\bullet+}/GMP)$ = 1.27 V *vs* NHE[203] and a photosensitizer is of paramount importance for the development of Type I photodynamic therapy and represent a first step towards the investigation of challenging oxidation processes.[172, 204]

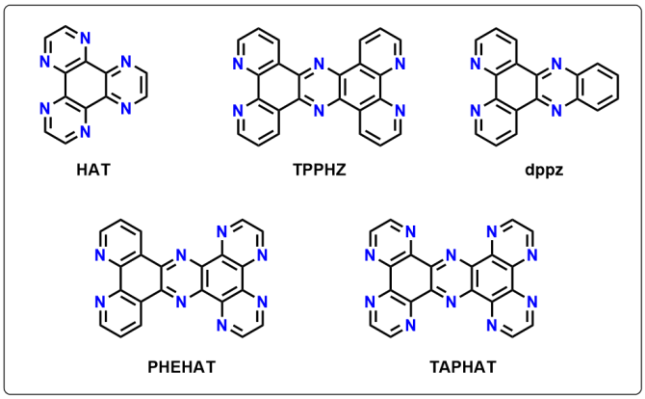

Figure 6.1. Structure of 1,4,5,8,9,12-hexaazatriphenylene (HAT), dipyrido[3,2-a:2',3'-c]phenazine (dppz), tetrapyrido[3,2-a:2',3'-c:3'',2''-h:2''',3'''-j]phenazine (TPPHZ), 1,10-phenanthrolino[5,6-b]-1,4,5,8,9,12-hexaazatriphenylene (PHEHAT) and 1,4,5,8-tetraazaphenanthrene[9,10-b]-1,4,5,8,9,12-hexaazatriphenylene (TAPHAT).

The TPPHZ ligand has been extensively used in the field of hydrogen photoproduction with the development of photosensitizers such as $[Ru(dtb)_2(TPPHZ)MX_2]^{2+}$, where M is either Pt or Pd, X is Cl or I, and dtb is 4,4'-^{t}Bu-2,2'-bipyridine.[222, 353, 354] Light excitation of these photosensitizers leads to an initial electron transfer from the Ru(II) centre to the bridging ligand, followed by the activation of the catalytic centre (M). The Ru(II) centre is usually regenerated by electron transfer from a sacrificial electron donor reagent present in solution such as triethylamine or triethanolamine. This light-activated process is repeated a second time to fully activate the secondary metal centre, which can then perform proton reduction to form molecular hydrogen. Similar approaches are used for CO_2 reduction, as well as for the development of photocathode or photoanode materials.[219, 252, 369-374] A general pattern in the photocatalysis approach is to connect a photosensitizer and catalytic centre via a bridging ligand. This allows for efficient electron or hole transfer and subsequent long-lived charge separated state, as well as the modification of the associated redox potential, which can tune the range and efficiency of possible transformations.[101] Hence, the development of new bridging structures to funnel electrons between metal centres is still highly relevant.

Here, we focused on the development of a series of photosensitizers bearing a common ligand scaffold, 9,10-diNH_2-1,4,5,8-tetraazaphenanthrene (**Figure 6.2**).[375-380] The 1,4,5,8-tetraazaphenanthrene (TAP) offers similar redox potential as the prototypical 2,2'-bipyrazine ligand while the inclusion of the diamino functionality would allow for the straightforward development of a series of bridging ligands (**Figure 6.1**), through condensation with *o*-diones, such as 1,10-phenanthroline-5,6-dione, for example. This could lead to the development of strong photo-oxidant photosensitizers capable of bridging a proton reduction catalyst to perform homogeneous HX splitting. We found that 9,10-diNH_2-1,4,5,8-tetraazaphenanthrene could be directly chelated onto Os(II) centres but that, with Ru(II), the chelation efficiency strongly depended on the ancillary ligands. When 1,10-phenanthroline ancillary ligands were used, chelation of 9,10-diNH_2-1,4,5,8-tetraazaphenanthrene led to the formation of two photosensitizers; one where the diamine ligand is chelated via the polypyridyl-type backbone and a second one where the ligand is coordinated as an *o*-quinonediimine. Such coordination scaffold has already been reported in the literature, amongst others by A. B. P. Lever.[381-385] This led to drastically different ground and excited-state properties, as described hereafter.

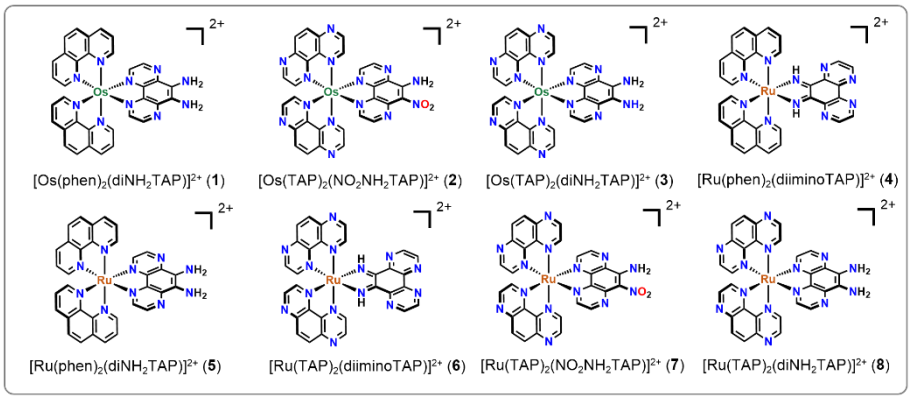

Figure 6.2. The structures of the eight photosensitizers reported in the present study : $[Os(phen)_2(diNH_2TAP)]^{2+}$ (1), $[Os(TAP)_2(NO_2NH_2TAP)]^{2+}$ (2), $[Os(TAP)_2(diNH_2TAP)]^{2+}$ (3) $[Ru(phen)_2(diiminoTAP)]^{2+}$ (4), $[Ru(phen)_2(diNH_2TAP)]^{2+}$ (5), $[Ru(TAP)_2(diiminoTAP)]^{2+}$ (6), $[Ru(TAP)_2(NO_2NH_2TAP)]^{2+}$ (7), and $[Ru(TAP)_2(diNH_2TAP)]^{2+}$ (8).

6.2 Results and discussion

6.2.1 Synthesis

The ligands of interest, *i.e.* 1,4,5,8-tetraazaphenanthrene (TAP), 9-amino-10-nitro-1,4,5,8-tetraazaphenanthrene (NO_2NH_2TAP) and 9,10-diamino-1,4,5,8-tetraazaphenanthrene ($diNH_2TAP$) were synthesized following a combination of reported procedures but were optimized for larger scale production (~100 g of starting material) during the internship of Skander Ben Guiza at UCLouvain (**Scheme 6.1**).[375-380] First a condensation of 4-nitro-1,2-diaminobenzene and glyoxal in refluxing ethanol was performed to obtain the corresponding 6-nitroquinoxaline in 80% yield. Vicarious nucleophilic substitution with hydroxylamine using sodium methanolate yielded 5-amino-6-nitroquinoxaline in a 56% yield, which was then reduced using hydrazine hydrate with 10% Pd/C to yield 5,6-diamino-quinoxaline in 98% yield. This derivative was pivotal for the synthesis, as it not only allowed for the desired 1,4,5,8-tetraazaphenanthrene to be obtained in an 80% yield following condensation with glyoxal, but it is also a central fragment for the synthesis of 9-amino-10-nitro-1,4,5,8-tetraazaphenanthrene and 9,10-diamino-1,4,5,8-tetraazaphenanthrene. As such, 5,6-diamino-quinoxaline was protected using *p*-toluenesulfonyl chloride in pyridine. The subsequent nitration was not optimized for large scale synthesis and was therefore carried out several times on 7 grams of starting material (72% of average yield). Deprotection was performed using sulfuric acid and water, leading to the corresponding diamino derivative (96% yield) that was condensed with glyoxal to yield 9-nitro-1,4,5,8-tetraazaphenanthrene in a 52% yield. Amination led to the formation of the 9-amino-10-nitro-1,4,5,8-tetraazaphenanthrene in 98% yield that could be further reduced, using hydrazine hydrate with 10% Pd/C, to form the final product 9,10-diamino-1,4,5,8-tetraazaphenanthrene in 71% yield.

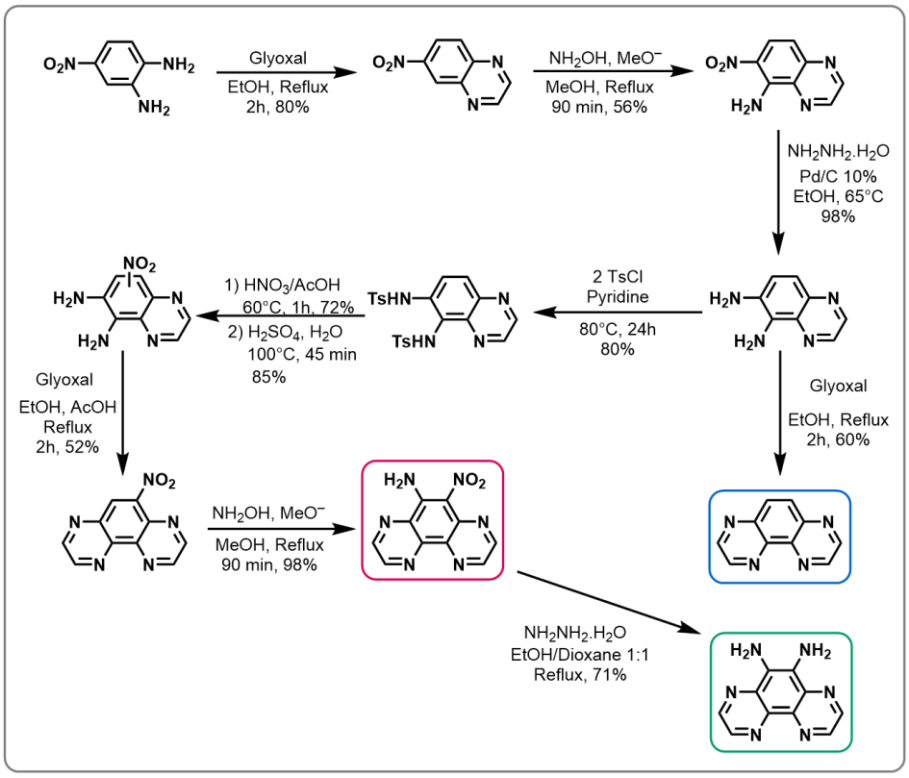

Scheme 6.1. Synthesis scheme of 1,4,5,8-tetraazaphenanthrene (TAP), 9-amino-10-nitro-1,4,5,8-tetraazaphenanthrene (NO_2NH_2TAP) and 9,10-diamino-1,4,5,8-tetraazaphenanthrene ($diNH_2TAP$).

The synthesis of the Os(II) photosensitizers was straightforward. $[Os(phen)_2Cl_2]$ and $[Os(TAP)_2Cl_2]$ precursors were prepared according to reported procedures using $(NH_4)_2OsCl_6$ freshly prepared from OsO_4. $[Os(phen)_2Cl_2]$ and $[Os(TAP)_2Cl_2]$ were then respectively reacted with 1,4,5,8-tetraazaphenanthrene-9,10-diamine in ethylene glycol at 160°C under microwave irradiation for 2 hours to yield $[Os(phen)_2(diNH_2TAP)]^{2+}$ (**1**) and $[Os(TAP)_2(diNH_2TAP)]^{2+}$ (**3**) in 39% and 44% isolated yields, respectively. $[Os(TAP)_2(NO_2NH_2TAP)]^{2+}$ (**2**) was also synthesized in 36% yield for comparison purposes.

The synthesis of $[Ru(phen)_2(diNH_2TAP)]^{2+}$ (**5**) was already reported and was thus performed according to a previously published procedure through the reaction between $[Ru(phen)_2Cl_2]$ and 9,10-diamino-1,4,5,8-

tetraazaphenanthrene in EtOH/Water mixtures.[349] Although not reported, this reaction resulted in the formation of two products: $[Ru(phen)_2(diNH_2TAP)]^{2+}$ (**5**) and $[Ru(phen)_2(diiminoTAP)]^{2+}$ (**4**) that could be separated by column chromatography on alumina. $[Ru(phen)_2(diNH_2TAP)]^{2+}$ (**5**) was isolated in 68% yield as an orange solid, whereas $[Ru(phen)_2(diiminoTAP)]^{2+}$ (**4**) was isolated in 23% yield as a pink solid. It should be noted that Ishow *et al.* reported in 1999 that "*Attempts to prepare the precursor diamino complex* $[Ru(bpy)_2(diNH_2phen)]^{2+}$ *by reaction of 5,6-diamino-1,10-phenanthroline with* $[Ru(bpy)_2Cl_2]$ *in the presence of* $AgCF_3SO_3$ *mostly gave the phenanthrolinediimido complex and the dinuclear* $[(bpy)_2Ru(tpphz)Ru(bpy)_2]^{4+}$ *arising from the auto-condensation of the phendiamine in oxidizing conditions*".[386] Note that similar phenanthrolinediimido complexes have also been reported using different approaches.[387-390] When similar reaction conditions were applied using $[Ru(TAP)_2Cl_2]$ with 9,10-diamino-1,4,5,8-tetraazaphenanthrene in EtOH/Water mixtures or in pure water, the reaction exclusively led to the formation of $[Ru(TAP)_2(diiminoTAP)]^{2+}$ (**6**) with no formation of the desired $[Ru(TAP)_2(diNH_2TAP)]^{2+}$ (**8**). This difference in reactivity is probably a direct consequence of the redox potential of the ruthenium centre (*vide infra*) that is a stronger oxidant when chelated to π-accepting ligands such as 1,4,5,8-tetraazaphenanthrene compared to 1,10-phenanthroline. Hence, an alternative approach proceeding via the synthesis of the precursor complex $[Ru(TAP)_2(9\text{-}NH_2\text{-}10\text{-}NO_2\text{-}TAP)]^{2+}$ (**7**) was developed. This complex was synthesized from the reaction between $[Ru(TAP)_2Cl_2]$ and 9-NH_2-10-NO_2-1,4,5,8-tetraazaphenanthrene in moderate yields of 33%. This resulted from the very low solubility of 9-NH_2-10-NO_2-1,4,5,8-tetraazaphenanthrene in most common organic solvents which prevented any efficient reaction, but facilitated the purification procedure. The chemical reduction of $[Ru(TAP)_2(9\text{-}NH_2\text{-}10\text{-}NO_2\text{-}TAP)]^{2+}$ (**7**) to the corresponding $[Ru(TAP)_2(diNH_2TAP)]^{2+}$ (**8**) was then investigated. Procedures using hydrazine hydrate and Pd/C, Raney

Nickel, or H_2 on Pd/C have been reported for reduction of nitro groups on ruthenium complexes. Hydrazine hydrate in EtOH/MeOH mixture in combination with Pd/C 10% was found to be optimal to reduce the nitro group of **7** to obtain $[Ru(TAP)_2(diNH_2TAP)]^{2+}$ (**8**) as an orange solid in 78% yield.

6.2.2 Electrochemistry

All photosensitizers were electrochemically characterized by differential pulse voltammetry and cyclic voltammetry in acetonitrile containing 0.1M $TBAPF_6$ and the electrochemical data are tabulated in **Table 6.1**. The electrochemical data of $[Os(phen)_2(diNH_2TAP)]^{2+}$ (**1**) showed three reduction peaks at –0.71V, –1.14 V and –1.42V *vs* NHE. The first peak was attributed to the one-electron reduction of the 1,4,5,8-tetraazaphenanthrene backbone of 1,4,5,8-tetraazaphenanthrene-9,10-diamine. The peak at –1.14V and –1.42V *vs* Ag/AgCl corresponds well to reported reduction potentials of the ancillary 1,10-phenanthroline ligands. Oxidation waves at +1.02 V and +1.49V *vs* NHE were measured. The first peak was attributed to an oxidation of the amine functional group, as this potential is too cathodic to correspond to the Os(II/III) oxidation, which is instead well matched to the +1.49 V *vs* NHE peak. Conversely, with $[Os(TAP)_2(diNH_2TAP)]^{2+}$ (**3**), the first reduction was measured at –0.44 V *vs* NHE and can safely be attributed to the reduction of one of the ancillary 1,4,5,8-tetraazaphenanthrene ligands. Indeed, the reduction of 1,4,5,8-tetraazaphenanthrene-9,10-diamine typically occurs at more negative potentials due to the increased electron density afforded by the two amino groups. An oxidation peak was recorded at +1.08 V *vs* NHE corresponding to the oxidation of the amine, whereas the metal centre oxidation was recorded at +1.94V *vs* NHE. This value is more positive than typically observed with Os(II) complexes, but it in agreement with the electron-withdrawing nature of 1,4,5,8-tetraazaphenanthrene-type ligands. $[Os(TAP)_2(NO_2NH_2TAP)]^{2+}$ (**2**) exhibited a first reduction peak at –0.33V *vs* NHE attributed to the reduction of the 9-amino-10-nitro-1,4,5,8-tetraazaphenanthrene ligand.

The metal-centred oxidation potential of $[Os(TAP)_2(NO_2NH_2TAP)]^{2+}$ was recorded at +1.82 V *vs* NHE, in line with the introduction of two electron-withdrawing 1,4,5,8-tetraazaphenanthrene ancillary ligands. The electrochemical data suggested interesting excited state properties of the Os(II) complexes that could drive several reactions (*vide infra*). Interestingly, none of the electrochemical results for the photosensitizers bearing the 9-amino-10-nitro-1,4,5,8-tetraazaphenanthrene ligand showed a wave that could correspond to the oxidation of the amine group. This likely suggests the role of the nitro group in stabilizing the amine functionality and preventing its oxidation.

The electrochemical data obtained with the Os(II) photosensitizers facilitated the interpretation of the data for the Ru(II) photosensitizers. $[Ru(phen)_2(diNH_2TAP)]^{2+}$ (**5**) exhibited two oxidation waves centred at +1.02 V and +1.91 V *vs* NHE. The first wave was attributed to the oxidation of the amine functional group, while the second peak was attributed to the Ru(II/III) oxidation. Similar conclusions were drawn for $[Ru(TAP)_2(diNH_2TAP)]^{2+}$ (**7**) where the first oxidation, centred at +1.08 V *vs* NHE, was attributed to the oxidation of the amine moiety. However, in this photosensitizer, oxidation of the Ru(II) centre occurred at potentials greater than 2.2V *vs* NHE, in line with other Ru(II) complexes carrying the 1,4,5,8-tetraazaphenantrene ligand such as $[Ru(TAP)_3]^{2+}$.[391]

Finally, with $[Ru(phen)_2(diiminoTAP)]^{2+}$ (**4**) and $[Ru(TAP)_2(diiminoTAP)]^{2+}$ (**6**) the metal-centred oxidations occurred at potentials of +1.77 V and +2.04 V *vs* NHE, respectively. Comparison of $[Ru(phen)_2(diiminoTAP)]^{2+}$ (**4**) with $[Ru(phen)_3]^{2+}$ supported the theory that the diimino scaffold decreased the electron density around the metal centre and rendered the Ru(II) harder to oxidize. Compounds bearing an *o*-quinonediimine scaffold have been scarcely reported in the literature, but this observation is in line with these reports.[392] Most representative examples include work by Barton,[392] focusing of

$[Ru(phi)_3]^{2+}$ (phi = *o*-phenanthrenequinone-diimine) and by Zehnder,[390] who developed three diimino complexes, namely $[Ru(bpy)(diiminobenzene)_2]^{2+}$, $[Ru(bpy)_2(diiminonaphthalene)]^{2+}$ and $[Ru(bpy)_2(phi)]^{2+}$ where the diimino ligands were shown to increase the oxidation potential of the ruthenium complex compared to classical polypyridyl Ru(II) complexes.

Table 6.1. Electrochemical properties of complexes **1-8** and reference complexes in acetonitrile at room temperature.

Complexes	E_{ox}[a]	E_{red}[a]	Ref
$[Os(phen)_2(diNH_2TAP)]^{2+}$ (1)	+1.02 ; +1.49	–0.70 ; –1.14, –1.39	[b]
$[Os(TAP)_2(NO_2NH_2TAP)]^{2+}$ (2)	+1.83	–0.34 ; –0.55 ; –0.79 ; –0.97 ; –1.34	[b]
$[Os(TAP)_2(diNH_2TAP)]^{2+}$ (3)	+1.08 ; +1.94	–0.44 ; –0.61 ; –0.94 ; –1.31	[b]
$[Ru(phen)_2(diiminoTAP)]^{2+}$ (4)	+1.77	–0.12 ; –0.54 ; –1.34	[b]
$[Ru(phen)_2(diNH_2TAP)]^{2+}$ (5)	+1.02 ; +1.91	–0.73 ; –1.22 ; –1.45	[b]
$[Ru(TAP)_2(diiminoTAP)]^{2+}$ (6)	+2.04	+0.12 ; –0.54 ; –0.74 ; –0.88 ; –0.92	[b]
$[Ru(TAP)_2(NO_2NH_2TAP)]^{2+}$ (7)	> +2.2	–0.40 ; –0.62 ; –0.79 ; –0.92	[b]
$[Ru(TAP)_2(diNH_2TAP)]^{2+}$ (8)	+1.08, > +2.2	–0.53 ; –0.69 ; –0.93	[b]
$[Ru(phi)_3]^{2+}$	+ 1.47 ; +1.66	–0.14 ; –0.36 ; –0.51 ; –0.71 ; –0.87	392
$[Ru(bpy)(diiminobenzene)_2]^{2+}$	+ 1.44	–0.19 ; –0.63 ; –1.36 ; –1.72	390
$[Ru(bpy)_2(diiminonaphthalene)]^{2+}$	+ 1.28	–0.60 ; –1.22 ; –1.74	390
$[Ru(bpy)_2(phi)]^{2+}$	+ 1.22	–0.66 ; –1.28 ; –1.77	390
$[Ru(phen)_3]^{2+}$	+1.53	–1.11; –1.28	393
$[Ru(TAP)_3]^{2+}$	+2.18	–0.51 ; –0.64 ; –0.86 ; –1.36 ; –1.56	391

[a] Electrochemical data of the indicated Ru(II) or Os(II) photosensitizers (1 mM) (in V *vs* NHE, converted from V *vs* Ag/AgCl reference electrode by adding 0.205 V to the measured value) were recorded in argon purged acetonitrile with tetrabutylammonium hexafluorophosphate (0.1 M) as supporting electrolyte (scan rate : 0.1 V/s). [b] Data of this work.

Regarding the reduction potentials, from Zehnder's and Barton's work, it is concluded that the addition of diimino ligands shifts the reduction potentials to more positive values. Reduction potentials centred around –0.60 V *vs* NHE were reported for $[Ru(bpy)_2(diiminonaphthalene)]^{2+}$ and $Ru(bpy)_2(phi)]^{2+}$, whereas for $[Ru(bpy)(diiminobenzene)_2]^{2+}$ and $[Ru(phi)_3]^{2+}$ reduction waves at –0.19 V and –0.14 V *vs* NHE were

reported respectively. Furthermore, a second reduction wave of $[Ru(bpy)(diiminobenzene)_2]^{2+}$ was centred at –0.63 V *vs* Ag/AgCl, a value too anodic to be attributed to a reduction of the 2,2'-bipyridine ligand, that was therefore attributed to the reduction of the second diiminobenzene ligand. For complexes bearing only one "diimino-type" ligand, the second reduction has been reported at potentials more negative than –1.36 V *vs* Ag/AgCl and have therefore be attributed to reduction of one of the ancillary 2,2'-bipyridine ligands. For $[Ru(phi)_3]^{2+}$, six successive reductions were recorded, with the first three being centred at –0.14 V, –0.36 V and –0.51 V *vs* NHE, respectively, and corresponding to the successive reductions of each "phi" ligand. For $[Ru(phen)_2(diiminoTAP)]^{2+}$ (**4**), several reduction waves were recorded at –0.12 V, –0.54 V and –1.34 V *vs* NHE. Reduction potentials for $[Ru(phen)_3]^{2+}$ indicated that the first reduction centred on 1,10-phenanthroline only occurs at potentials more negative than –1.11 V *vs* NHE. Therefore, the first and second reductions of complex **4** were attributed to the reduction of the diiminoTAP ligand and the third reduction wave attributed to an ancillary 1,10-phenanthroline reduction. Regarding $[Ru(TAP)_2(diiminoTAP)]^{2+}$ (**6**), reduction events at +0.12, –0.54, –0.74, –0.88 and –0.92 V *vs* NHE were obtained. By comparison with the parent compound $[Ru(TAP)_3]^{2+}$, the first reduction wave was attributed to a reduction of the diiminoTAP ligand, whereas subsequent reduction events could be unambiguously attributed. Notably, the first reduction wave for $[Ru(TAP)_2(diiminoTAP)]^{2+}$ (**6**) was exceptionally positive compared to other classical complexes, an observation that probably resulted from the ancillary 1,4,5,8-tetraazaphenanthrene ligands that, due to their highly π-accepting character, drained the ruthenium centre of its electron density. As a result, more electron density was donated from the diiminoTAP ligand, making it easier to reduce than in $[Ru(phen)_2(diiminoTAP)]^{2+}$ (**4**), where the 1,10-phenanthroline ligands are less π-accepting.

6.2.3 Photophysical properties and theoretical studies

The ground-state properties of the eight photosensitizers were first characterized by UV-Visible absorption measurements in acetonitrile (**Figure 6.3**). Most of the photosensitizers exhibited absorption features that are typical for these classes of compounds. Indeed, the three osmium complexes absorbed intensely in the visible range with molar extinction coefficients in the 16100-21300 $M^{-1}cm^{-1}$ range between 456 and 484 nm. $[Ru(phen)_2(diNH_2TAP)]^{2+}$ (**5**) and $[Ru(TAP)_2(diNH_2TAP)]^{2+}$ (**7**) also exhibited classical features, namely absorption bands in the UV region attributed to ligand centred (LC) transitions and a broad absorption band between 400 nm and 480 nm attributed to metal-to-ligand charge transfer (MLCT) transitions. The molar absorption coefficients were in the 14700-17600 $M^{-1}cm^{-1}$ range between 437 and 467 nm. Interestingly, in $[Ru(phen)_2(diiminoTAP)]^{2+}$ (**4**) and $[Ru(TAP)_2(diiminoTAP)]^{2+}$ (**6**), the visible absorption features were red-shifted to 535 nm and 520 nm with molar absorption coefficients of 19700 $M^{-1}cm^{-1}$ and 25300 $M^{-1}cm^{-1}$, respectively.

Table 6.2. Photophysical properties of photosensitizers **1-8** in acetonitrile.

[2]	λ_{Abs} (nm), (ε, $10^3 M^{-1}cm^{-1}$)	λ_{em}[a] (nm)	Φ_{PL}[c] air	Φ_{PL}[c] argon	τ (ns)
(1)	263 (89.4), 419 (21.0), 484(19.1)	717	0.00008	0.00018	67[b], 228[a]
(2)	279 (56.7), 411 (18.4), 467 (16.1)	718	0.01801	0.02283	217[b], 280[a]
(3)	282 (74.7), 420 (22.1),456 (21.3)	709	0.00128	0.00174	238[b], 340[a]
(4)	263 (70.7), 535 (19.7)	---	---	---	---
(5)	261 (92.1), 416 (20.7), 467 (14.7)	699	0.00271	0.00560	292[b], 644[a]
(6)	277 (58.2), 520 (25.3)	---	---	---	---
(7)	268 (68.8), 405 (21.8)	612	0.00949	0.01125	220[b], 250[a]
(8)	278 (61.4), 412 (17.0), 439 (17.6)	623	0.00172	0.00205	158[b], 245[a]

[a]Recorded in argon purged acetonitrile. [b]Recorded in air equilibrated acetonitrile. [c]Measured *vs* $[Ru(bpy)_3]^{2+}$ (Φ_{ref} = 0.018 in air equilibrated acetonitrile).

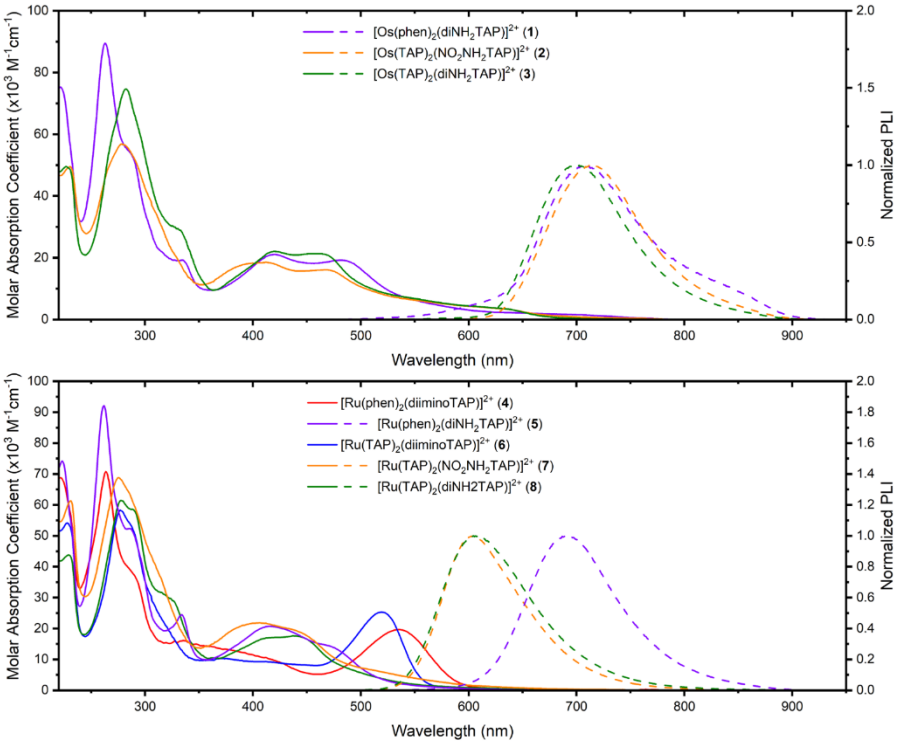

Figure 6.3. Absorption (solid) and photoluminescence (dashed) spectra of Os(II) (top) and Ru(II) (bottom) photosensitizers recorded in acetonitrile at room temperature under argon.

Time-dependent density functional theory (TD-DFT) calculations agreed with the classical depiction of metal-to-ligand charge transfer bands for $[Ru(phen)_2(diNH_2TAP)]^{2+}$ (**5**) and $[Ru(TAP)_2(diNH_2TAP)]^{2+}$ (**7**) where electron density is transferred from the metal centre to the most electron accepting ligand(s) (**Figure 6.4 a** and **b**). For $[Ru(phen)_2(diNH_2TAP)]^{2+}$ (**5**), the transition with the highest probability in the visible range appeared at 409 and 418 nm and involved an electronic transition from the Ru(II) centre to the ancillary ligands. For $[Ru(TAP)_2(diNH_2TAP)]^{2+}$ (**7**), the excitation at 403 nm was consistent with a transition transferring electron density from Ru(II) to the ancillary 1,4,5,8-tetraazaphenanthrene ligands whereas the one at 416 nm additionally transferred electron density on the 9,10-diamino-1,4,5,8-tetraazaphenanthrene ligand. For $[Ru(phen)_2(diiminoTAP)]^{2+}$ (**4**) and $[Ru(TAP)_2(diiminoTAP)]^{2+}$ (**6**) the most probable excitation in the visible part

of the spectrum seems to heavily involve the *o*-quinonediimine ligand which could warrant a mixed metal-ligand-to-ligand charge transfer complex, similar to what is observed in prototypical Ir(III) photosensitizers.[226]

The excited-state properties of the photosensitizers were then investigated by steady-state and time-resolved spectroscopic techniques in argon-purged and air-equilibrated acetonitrile. Visible light excitation of all Os(II) photosensitizers led to appreciable photoluminescence centred between 709 and 718 nm. Photoluminescence decay of these excited states was well described by first-order kinetics from which excited-state lifetimes that spanned 228-340 ns under argon were determined.

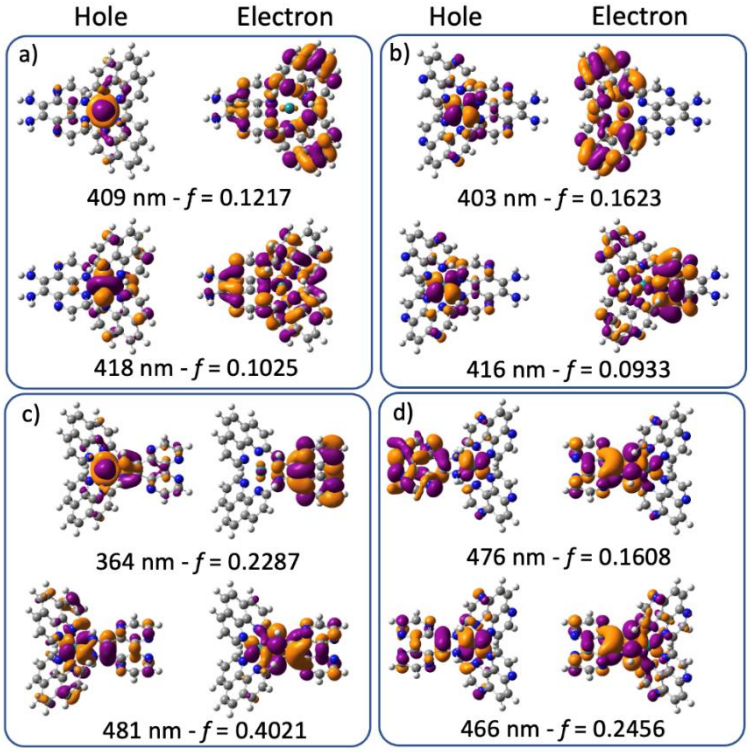

Figure 6.4. Natural Transition Orbitals (NTOs) for $[Ru(phen)_2(diNH_2TAP)]^{2+}$ (a), $[Ru(TAP)_2(diNH_2TAP)]^{2+}$ (b), $[Ru(phen)_2(diiminoTAP)]^{2+}$ (c) and $[Ru(TAP)_2(diiminoTAP)]^{2+}$ (d) involved in each excited state according to the TD-DFT calculations. For each excited state, absorption wavelengths (in nm) and calculated oscillator strengths (f) are listed. See **Chapter X** and experimental section for additional details on the theoretical calculations.

The photoluminescence quantum yields for these Os(II) photosensitizers were unsurprisingly small (**Table 6.2**), as expected based on the energy gap law,[394] as well as by the introduction of amine groups that favour non-radiative decay by increasing interactions with the solvent. The exception was $[Os(TAP)_2(NO_2NH_2TAP)]^{2+}$ (**2**) that exhibited an appreciable photoluminescence quantum yield of 0.023 under argon. Considering the electrochemical data gathered for this complex, it is probable that this originates from a stabilization of the amino group by the vicinal nitro group through hydrogen bonding, thus decreasing interactions with the solvent.

$[Ru(phen)_2(diNH_2TAP)]^{2+}$ (**5**), $[Ru(TAP)_2(diNH_2TAP)]^{2+}$ (**7**) and $[Ru(TAP)_2(NO_2NH_2TAP)]^{2+}$ (**8**) were luminescent in acetonitrile with steady-state photoluminescence maxima centred at 699, 623 and 612 nm, respectively. This agrees with an excited-state localized on the 9,10-diamino-1,4,5,8-tetraazaphenanthrene ligand for $[Ru(phen)_2(diNH_2TAP)]^{2+}$ (**5**). In contrast, the higher energy luminescence indicated excited-state localization on the ancillary 1,4,5,8-tetraazaphenanthrenes, which is consistent with literature for $[Ru(TAP)_2(diNH_2TAP)]^{2+}$ (**7**) and $[Ru(TAP)_2(NO_2NH_2TAP)]^{2+}$ (**8**). Both Ru(II) photosensitizers bearing *o*-quinonediimine moieties, *i.e.* $[Ru(phen)_2(diiminoTAP)]^{2+}$ (**4**) and $[Ru(TAP)_2(diiminoTAP)]^{2+}$ (**6**), were non-luminescent between 600 and 900 nm. Such behaviour is consistent with a small energy gap between the LUMO and the HOMO that may favour fast non-radiative decay through strong inter-state coupling.

6.2.4 Excited-state reactivity

The ground-state electrochemical data and the steady-state photoluminescence spectra allowed to determine the corresponding excited-state reduction (E_{red}^*) and oxidation (E_{ox}^*) potentials in acetonitrile (**Table 6.3**). The photosensitizers exhibited excited-state reduction potentials that are between 1.24 V and 1.86 V *vs* NHE.

$[Ru(TAP)_2(diNH_2TAP)]^{2+}$ (**8**) and $[Ru(TAP)_2(NO_2NH_2TAP)]^{2+}$ (**7**) presented the most positive excited-state reduction potentials, 1.75 V and 1.86 V *vs* NHE, respectively. Given these excited-state reduction potentials, these photosensitizers would be suitable for halides oxidation in organic solvents. Nevertheless, their application in aqueous solution are limited to iodide (1.33 V *vs* NHE) oxidation as bromide and chloride are thermodynamically not favourable for electron transfer (1.93 and ~2.1-2.3 V *vs* NHE, respectively). For this reason and due to their large use in the field of photodynamic therapy, we decided to investigate the bimolecular reactivity of these photosensitizers with a prototypical biological substrate, *i.e.* guanosine-5'-monophosphate (GMP).

Table 6.3. Excited-state reduction and oxidation potential of the emissive photosensitizers.

Complexes	E_{red}^* (V *vs* NHE)	E_{ox}^* (V *vs* NHE)	E_{00} (eV)
$[Os(phen)_2(diNH_2TAP)]^{2+}$(1)	1.24	-0.46	1.95
$[Os(TAP)_2(NO_2NH_2TAP)]^{2+}$(2)	1.61	-0.12	1.95
$[Os(TAP)_2(diNH_2TAP)]^{2+}$(3)	1.53	-0.03	1.97
$[Ru(phen)_2(diNH_2TAP)]^{2+}$(5)	1.30	-0.13	2.03
$[Ru(TAP)_2(NO_2NH_2TAP)]^{2+}$(7)	1.86	>–0.07	2.27
$[Ru(TAP)_2(diNH_2TAP)]^{2+}$(8)	1.75	>–0.08	2.28

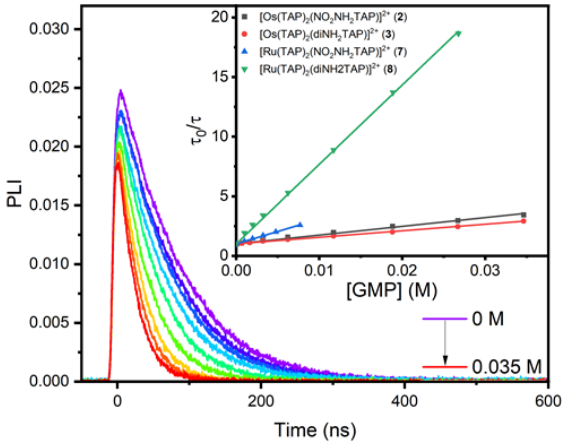

Figure 6.5. Time-resolved excited-state quenching of $[Os(TAP)_2(NO_2NH_2TAP)]^{2+}$ by GMP and the corresponding Stern-Volmer plots of all photosensitizers undergoing excited-state quenching (inset). Experiments were performed in air-equilibrated tris HCl buffer (50 mM, pH = 7.4) at room temperature using 440 nm light excitation.

Excited-state quenching experiments were performed in air-equilibrated Tris-HCl aqueous buffer at pH 7.4 with all emissive photosensitizers and GMP. A representative example for the excited-state quenching of $[Os(TAP)_2(NO_2NH_2TAP)]^{2+}$ with GMP is presented in **Figure 6.5**. Overall, appreciable excited-state quenching was only observed for Ru(II) and Os(II) photosensitizers bearing ancillary 1,4,5,8-tetraazaphenanthrene ligands. The quenching rate constants were close to the diffusion limit and were determined for $[Os(TAP)_2(NO_2NH_2TAP)]^{2+}$ and $[Os(TAP)_2(diNH_2TAP)]^{2+}$ as k_q = 8.9 x10^8 $M^{-1}s^{-1}$ and 6.1 x10^8 $M^{-1}s^{-1}$, respectively. For the corresponding Ru(II) photosensitizers, meanwhile, the quenching rate constants were determined to be slightly larger with k_q = 1.7 x10^9 $M^{-1}s^{-1}$ and 1.3 x10^9 $M^{-1}s^{-1}$ for $[Ru(TAP)_2(diNH_2TAP)]^{2+}$ and $[Ru(TAP)_2(NO_2NH_2TAP)]^{2+}$, respectively. These quenching rate constants agree with the favourable driving force for GMP oxidation by these four photosensitizers in aqueous conditions.

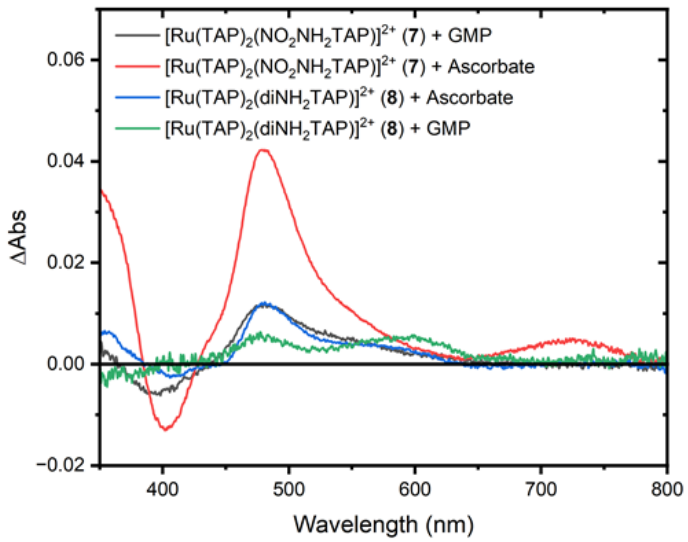

Figure 6.6. Transient absorption spectra of $[Ru(TAP)_2(diNH_2TAP)]^{2+}$ and $[Ru(TAP)_2(NO_2NH_2TAP)]^{2+}$ recorded in the presence of 20 mM of sodium ascorbate or with 10 mM of GMP. Spectra were recorded in argon purged tris-HCl buffer (50,mM, pH = 7.4) 1 μs after the laser pulse and integrated for 50 ns. Samples were excited at 440 nm with a laser fluence of 10 mJ/pulse.

Finally, we sought to investigate whether the excited-state quenching proceeded via electron transfer. Using transient absorption spectroscopy, changes in absorption of $[Ru(TAP)_2(diNH_2TAP)]^{2+}$ and $[Ru(TAP)_2(NO_2NH_2TAP)]^{2+}$ using sodium ascorbate as electron donor were initially determined. In both cases, pulsed light excitation led to absorption changes with a novel transition appearing between 490 and 500 nm that was assigned to the formation of the monoreduced ruthenium photosensitizer. When similar experiments were carried out in the presence GMP in Tris HCl buffer at pH 7.4, the nanosecond transient absorption changes were similar to those obtained with sodium ascorbate, thus confirming excited-state electron transfer from GMP to the ruthenium photosensitizers. While the transient absorption spectra with $[Ru(TAP)_2(NO_2NH_2TAP)]^{2+}$ and GMP matched well with those obtained with sodium ascorbate, the one of obtained with $[Ru(TAP)_2(diNH_2TAP)]^{2+}$ and GMP presented an additional signal at 600 nm that we are currently unable to assign. Unfortunately, such electron transfer products were not observed with the osmium photosensitizers, preventing a confirmation that excited-state electron transfer from GMP occurred. It is however highly probable, given the similar quenching rate constants and excited-state redox potentials, that excited-state electron transfer is the operative quenching pathway but the associated cage escape yields are probably lower, as already reported for Os(II) photosensitizers.[124, 158]

6.3 Conclusions

The synthesis of eight photosensitizers with Os(II) and Ru(II) metal centres and polyazaaromatic ancillary ligands is reported. All photosensitizers carry one ligand with a 1,4,5,8-tetraazaphenanthrene backbone bearing one (NO_2NH_2TAP) or two ($diNH_2TAP$) amine functions. The isolated complexes represent a series of photosensitizers that can also serve as precursors for the development of bridged compounds, useful for solar fuel production or photodynamic and bioimaging applications. For the Ru(II) photosensitizers, a particular

chelating behaviour was observed. Indeed, when 1,10-phenanthroline ancillary ligands were used, the reaction between $[Ru(phen)_2Cl_2]$ and 9,10-diamino-1,4,5,8-tetraazaphenanthrene led to the formation of $[Ru(phen)_2(diNH_2TAP)]^{2+}$ (**5**) as the major product and $[Ru(phen)_2(diiminoTAP)]^{2+}$ (**4**) as minor product. However the reaction only yielded $[Ru(TAP)_2(diiminoTAP)]^{2+}$ (**6**) when $[Ru(TAP)_2Cl_2]$ was used as precursor. This difference in reactivity is probably a direct consequence of the redox potential of the ruthenium centre that is a stronger oxidant when chelated to π-accepting ligands such as 1,4,5,8-tetraazaphenanthrene compared to 1,10-phenanthroline. This hypothesis was strengthened by the results of the reactions with Os(II) complexes, where the *o*-quinonediimine complexes were not obtained under similar conditions. Hence, for Ru(II) complexes, to obtain $[Ru(TAP)_2(diNH_2TAP)]^{2+}$, a synthetic methodology involving the ligand 9-NH_2-10-NO_2-1,4,5,8-tetraazaphenanthrene was developed. This led to a precursor complex bearing one amino and one nitro group that could be further reduced using hydrazine hydrate on Pd/C with high reaction yields to yield the desired complex.

The coordination pattern was shown to strongly impact the redox, as well as the optical properties. Whereas complexes bearing unchelated amine functional groups were almost all luminescent with typical excited-state lifetimes, photosensitizers bearing *o*-quinonediimine scaffolds were non-luminescent in acetonitrile with very short excited-state lifetimes, *i.e* below the instrument response of our transient absorption spectroscopy apparatus (~2 ns). The short excited-state lifetimes, unusual redox properties and red-shifted absorbance all pointed towards a decreased energy gap between the HOMO and LUMO levels, with strongly coupled excited and ground states, allowing for fast non-radiative decay.

Nevertheless, excited-state electron transfer was not thermodynamically favourable for reductive quenching with bromide and chloride in water

(1.93 and ~2.1-2.3 V *vs* NHE, respectively). For this reason and due to their large use in the field of photodynamic therapy, we decided to investigate their potential use in photodynamic therapy as Type I photosensitizers. Time-resolved quenching experiments and nanosecond transient absorption spectroscopy confirmed that these photosensitizers were competent for excited-state electron transfer, as clearly observed for both $[Ru(TAP)_2(diNH_2TAP)]^{2+}$ and $[Ru(TAP)_2(NO_2NH_2TAP)]^{2+}$. Hence, these novel photosensitizers could find applications as potential photo drugs in photodynamic therapy or as building blocks for larger complexes with π-extended ligands or dyads for bio-imaging applications or solar fuels formation.

6.4 Experimental section

The materials and methods used in this chapter are described in ***Chapter X***

Acetonitrile 99.9% (VWR), dichloromethane 99.9% (stabilized with about 0.002% of 2-methylbut-2-ene, VWR), diethyl ether 99.9% (VWR), ethanol absolute 99.9% (VWR), methanol 99.9% (VWR), ethylene glycol ≥ 99.5% (Roth), cyclohexane 99.9% (VWR), acetone 99.9% (VWR), chloroform ≥ 99.8% (VWR), 1,4-dioxane 99.8% (Sigma-Aldrich), hydrochloric acid 37% (VWR), acetic acid glacial ≥ 99.7% (Fischer Chemical), celite (Roth) aluminium oxide, for chromatography, neutral, Brockmann I, 40-300 μm, 60 Å (Thermo Fischer), silica gel 60 Å for flash column chromatography, 40-63 μm (ROCC), sephadex LH-20 (GE Healthcare), sodium hydroxide ≥ 98.0% (Roth), pyridine ≥ 99% (VWR), *p*-toluenesulfonyl chloride ≥ 99.0% (Acros Organics), hydrazine hydrate 50-60% (Sigma-Aldrich), palladium (10%) on activated carbon (Chimet), (+)-sodium L-ascorbate 99.0% (Acros Organics), guanosine 5'-monophosphate disodium salt hydrate ≥ 99.0% (TCI), tris-(hydroxymethyl)-aminomethane hydrochloride ≥ 99.5% (VWR), glyoxal 40 wt. % in water (Acros Organics), sodium in kerosene ≥ 99.8% (Sigma Aldrich), hydroxylamine hydrochloride ≥ 99.0% (Acros Organics), ammonia 25% solution (Roth) and 4-nitro-*o*-phenylenediamine 98% (Acros Organics) were purchased from commercial suppliers and used as received. Water was purified by a Millipore Milli-Q system.

6.4.1 Synthesis

6-Nitroquinoxaline. 128 mL of 40% glyoxal was added in a dropwise fashion to a hot solution of 4-nitro-1,2-diaminobenzene (92.2 g, 602 mmol) in 800 mL of absolute ethanol. The thick solution was mechanically stirred at refluxed for two hours. The progress of the reaction was monitored by TLC (SiO_2, cyclohexane/acetone 7:3). Once the reaction was complete, the solution was cooled down to room temperature then in an ice bath. The precipitate was collected by filtration and the solid was subsequently rinsed with cold methanol to

afford 6-nitroquinoxaline as a yellow solid (84.4 g, 80%). **^{1}H NMR** (300 MHz, $CDCl_3$) δ 9.08 – 8.99 (m, 3H), 8.57 (dd, J = 9.2, 2.5 Hz, 1H), 8.29 (d, J = 9.2 Hz, 1H). NMR shifts agreed with the reported values.[395]

5-Amino-6-nitroquinoxaline. A sodium methanolate solution was prepared by adding small portions of sodium (29.2g, 1,27 mol) to 1.2 L of methanol. After reaction of the metallic sodium, hydroxylamine hydrochloride (37.6g, 540 mmol) previously dissolved in 600 mL of methanol was added. After settling, the sodium chloride was filtered off and the filtrate poured into a suspension of 6-nitroquinoxaline (60.0g, 344 mmol) in 1.2 L of methanol, which was then refluxed and stirred. The reaction medium quickly turned black. Reflux was maintained and the progress of the reaction monitored by TLC (10 mL $CHCl_3$ with 2 to 5 drops of ammonia). Once the starting product disappeared, the reaction medium was cooled down to room temperature. The solution was filtered, and the precipitate washed with cold methanol to yield 5-amino-6-nitroquinoxaline as a brown powder (36.4 g, 56%). **^{1}H NMR** (300 MHz, $CDCl_3$) δ 8.97 (d, J = 1.9 Hz, 1H), 8.75 (d, J = 1.9 Hz, 1H), 8.40 (d, J = 9.7 Hz, 1H), 7.27 (d, J = 9.7 Hz, 3H). NMR shifts agreed with the reported values.[395]

5,6-Diaminoquinoxaline. 122 mL of 98% hydrazine hydrate were added dropwise to a suspension of 5-amino-6-nitroquinoxaline (92.5 g, 485 mmol) and 8.9 g of 10% Pd/C in 3.6 L of ethanol. The reaction medium was heated to 65°C and the reduction was monitored by TLC (SiO_2, $CHCl_3$/acetone 8:2). After reaction, the catalyst was removed by filtration through celite. The red solution was evaporated under reduced pressure. The recovered solid was dried under vacuum to yield 5,6-diaminoquinoxaline as a red powder (76.1 g, 98%).**^{1}H NMR** (300 MHz, $CDCl_3$) δ 8.62 (dd, J = 1.9 Hz, 2H), 7.50 (d, J = 8.8 Hz, 1H), 7.32 – 7.22 (m, 1H), 4.39 (s, 2H), 3.77 (s, 2H). NMR shifts agreed with the reported values.[395]

1,4,5,8-Tetraazaphenanthrene. 44 mL of a 40% aqueous glyoxal solution was added dropwise to a hot solution of 5,6-diaminoquinoxaline (33.1 g, 206 mmol) in 350 mL of ethanol. The solution was then refluxed and monitored by TLC (SiO_2, $CHCl_3$/Acetone 9:1). After reaction, the reaction medium was cooled down to room temperature and filtered. The precipitate was purified by silica gel column chromatography (eluent CH_2Cl_2/acetone 80:20 to 50:50). The solvents were removed to recover 1,4,5,8-tetraazaphenanthrene as a white cotton-like solid (22.8 g, 60%). **^{1}H NMR** (300 MHz, DMSO-d_6) δ 9.23 (d, J = 2.0 Hz, 2H), 9.20 (d, J = 2.0 Hz, 2H), 8.37 (s, 2H). NMR shifts agreed with the reported values.[395]

5,6-bis(N-*p*-toluenesulfonamido)quinoxaline. To a stirred solution of 5,6-diaminoquinoxaline (55.5 g, 345 mmol) in 200 mL pyridine, *p*-toluenesulfonyl chloride (132.4 g, 696 mmol) was added in portions. The mixture was then refluxed for 24 hours. After reaction, the reaction medium was cooled down to room temperature and poured over 2.8 L of ice-cold water containing 106 mL of hydrochloric acid (37%), allowing the compound of interest to precipitate as a brown powder. The solid was then washed four times with 800 mL of a water/HCl solution (28:1), with ethanol (800 mL) and diethyl ether (800 mL). The final product was dried under vacuum to yield 5,6-bis(N-*p*-toluenesulfonamido)quinoxaline as a beige solid (129.1 g, 80%). **^{1}H NMR** (300 MHz, $CDCl_3$) δ 9.15 (s, 1H), 8.61 (d, J = 1.9 Hz, 1H), 8.34 (d, J = 1.9 Hz, 1H), 8.24 (d, J = 9.4 Hz, 1H), 7.89 (d, J = 9.4 Hz, 1H), 7.85 – 7.76 (m, 2H), 7.55 (s, 1H), 7.37 – 7.28 (m, 2H), 7.33 – 7.18 (m, 2H), 6.94 – 6.85 (m, 2H), 2.36 (s, 3H), 2.19 (s, 3H). NMR shifts agreed with the reported values.[376]

5,6-bis(N-*p*-toluenesulfonamido)-8(7)-nitroquinoxaline. To a suspension of 5,6-bis(N-*p*-toluenesulfonamido)quinoxaline (7.0 g, 15.2 mmol) in 60 mL of acetic acid maintained at 60°C, approximately one third of a nitrating mixture prepared from fuming nitric acid (1mL) and glacial acetic acid (10mL) was added. Shortly after the first addition, the

dissolution of the product was observed. Over time, a brown precipitate began to appear. Finally, the rest of the nitrating mixture was added, and the reaction was refluxed for 1 hour. After reaction, the medium was brought to 0°C and the precipitate was collected by filtration and washed with acetic acid and water. 5,6-bis(N-*p*-toluenesulfonamido)-8(7)-nitroquinoxaline was obtained as a beige solid (5.56g, 72%). **^{1}H NMR** (300 MHz, $CDCl_3$) δ 9.35 (s, 1H), 8.80 (d, J = 1.8 Hz, 1H), 8.74 (s, 1H), 8.51 (d, J = 1.8 Hz, 1H), 7.90 – 7.83 (m, 2H), 7.80 (s, 1H), 7.41 – 7.35 (m, 2H), 7.31 – 7.27(m, 2H), 7.01 – 6.95 (m, 2H), 2.39 (s, 3H), 2.23 (s, 3H). NMR shifts agreed with the reported values.[376]

5,6-diamino-8(7)-nitroquinoxaline. The nitro compound (50.0 g, 97.4 mmol) was dissolved in 155 mL of concentrated sulphuric acid, containing 8 mL of water, and heated to 100°C. The mixture was stirred for 50 minutes at this temperature before being poured onto ice. The solution was then brought to a pH of 9 by addition of NaOH (12 M). The dark red precipitate was filtered, washed with water and dried under vacuum to afford 5,6-diamino-8(7)nitroquinoxaline (17.0g, 85%). **^{1}H NMR** (300 MHz, $CDCl_3$) δ 8.90 (d, J = 1.9 Hz, 1H), 8.80 (d, J = 1.9 Hz, 1H), 7.62 (s, 1H), 7.50 (s, 2H), 4.51 (s, 2H). NMR shifts agreed with the reported values.[376]

9-nitro-1,4,5,8-tetraazaphenanthrene. 5,6-diamino-8(7)nitroquinoxaline (35.8 g, 174 mmol) was added to a mixture of 3.5 L ethanol and 130 mL acetic acid and refluxed. Glyoxal (79 mL glyoxal 40%) was then added dropwise, and reflux was maintained for 3 hours. The mixture was concentrated to a volume of approximately 150 mL. Water was then added and neutralisation with ammonia resulted in the recovery of a brown precipitate, which was recovered by filtration. The solid was washed with acetone at room temperature and then with 1 L of hot acetone. The filtrate was recovered, and the acetone evaporated. The product obtained was then purified by a silica gel chromatography column ($CHCl_3$/acetone, 8:2) to yield the title compound as a beige solid

(20.5g, 52%). **^{1}H NMR** (300 MHz, DMSO-d_6) δ 9.39 (d, J = 2.0 Hz, 1H), 9.36 (d, J = 2.0 Hz, 1H), 9.32 (d, J = 2.0 Hz, 1H), 9.28 (d, J = 2.0 Hz, 1H), 9.06 (s, 1H). NMR shifts agreed with the reported values.[376]

9-amino-10-nitro-1,4,5,8-tetraazaphenanthrene. Sodium methanolate was prepared by dissolving metallic sodium (1.42 g, 62 mmol) in 80 mL of methanol. After reaction of the sodium, hydroxylamine hydrochloride (2.05g, 29.5 mmol), previously dissolved in 30 mL of methanol, was added. After settling, the salt formed was filtered off and the filtrate was poured onto a suspension of 9-nitro-1,4,5,8-tetraazaphenanthrene (1.00 g, 4.32 mmol) in 35 mL of methanol kept at reflux. The progress of the reaction was monitored by TLC (SiO_2, eluent $CHCl_3$/acetone, 8:2). After about 2 hours, the reaction was stopped, and the reaction medium cooled down to room temperature. The yellow precipitate was recovered by filtration, rinsed with cold methanol and with diethylether. This reaction yielded 9-amino-10-nitro-1,4,5,8-tetraazaphenanthrene in the form of a yellow powder (1.03 g, 98%). **^{1}H NMR** (300 MHz, DMSO-d_6) δ 9.34 (d, J = 2.1 Hz, 1H), 9.20 (d, J = 2.1 Hz, 1H), 8.94 (d, J = 2.1 Hz, 1H), 8.88 (d, J = 2.1 Hz, 1H), 7.91 (s, 2H). NMR shifts agreed with the reported values.[376]

9,10-diamino-1,4,5,8-tetraazaphenanthrene. Hydrazine hydrate 98% (2.2 mL, 44.9 mmol) in 10 mL of 1:1 ethanol/dioxane is added dropwise to a hot suspension of 9-amino-10-nitro-1,4,5,8-tetraazaphenanthrene (0.85g, 3.4 mmol) in 130 mL of 1:1 ethanol/dioxane, containing 0.7g Pd/C 10%. The mixture was heated under reflux and monitored by TLC until the starting material disappeared (Al_2O_3, $CHCl_3$/EtOH 98:2). Hot filtration on celite removed the catalyst, and the appearance of red needles was noted as the medium cooled. The needles were collected by filtration and the filtrate was evaporated to dryness before being triturated in water at room temperature, filtered and washed with water and diethylether. The dark-red powder was then dried under vacuum, yielding 9,10-diamino-1,4,5,8-tetraazaphenanthrene (0.51 g, 71%). **^{1}H**

NMR (300 MHz, DMSO-d_6) δ 8.96 (d, J = 2.1 Hz, 2H), 8.88 (d, J = 2.1 Hz, 2H), 5.77 (s, 4H). NMR shifts agreed with the reported values.[376]

$[Os(phen)_2(diNH_2TAP)]^{2+}.2PF_6^-$ (1). 1,4,5,8-tetraazaphenanthrene-9,10-diamine (11.2 mg, 0.053 mmol) and $[Os(phen)_2Cl_2]$ (30.0 mg, 0.048 mmol) were suspended in ethylene glycol (3 mL) in a microwave tube. The solution was degassed by three vacuum/argon cycles. The mixture was heated for 2h at 160 °C under microwave irradiation (maximum power = 600W). After reaction, the mixture was brought to room temperature and a saturate NH_4PF_6 aqueous solution was added to induce precipitation of the complex. The precipitate was collected by centrifugation and washed three times with cold water and Et_2O. The crude product was then purified by column chromatography (Al_2O_3, CH_3CN/H_2O 100:0 to 93:7) to yield $[Os(phen)_2(diNH_2TAP)]^{2+}$ as a dark-red powder (23.0 mg, 39%). **^{1}H NMR** (500 MHz, CD_3CN) δ 8.48 (dd, *J* = 8.3, 1.2 Hz, 2H), 8.43 (dd, *J* = 8.3, 1.2 Hz, 2H), 8.41 (d, *J* = 3.0 Hz, 2H), 8.25 (s, 4H), 7.95 (dd, *J* = 5.4, 1.2 Hz, 2H), 7.88 (dd, *J* = 5.4, 1.2 Hz, 2H), 7.81 (d, *J* = 3.0 Hz, 2H), 7.60 (td, *J* = 8.4, 5.4 Hz, 4H), 5.35 (s, 4H). HRMS(ESI) m/z calculated for $[C_{34}H_{24}N_{10}{}^{184}Os]^{2+}$ = 378.08497; found 378.08524.

$[Os(TAP)_2(NO_2NH_2TAP)]^{2+}.2PF_6^-$ (2). 9-NH_2-10-NO_2-1,4,5,8-tetraazaphenanthrene (12.7 mg, 0.0525 mmol) and $[Os(TAP)_2Cl_2]$ (30.0 mg, 0.048 mmol) were suspended in ethylene glycol (3 mL) in a microwave tube. The solution was degassed by three vacuum/argon cycles. The mixture was heated for 2h at 160 °C under microwave irradiation (maximum power = 600W). After reaction, the mixture was brought to room temperature and the complex was precipitated from by the gradual addition of a 3:1 Et_2O/EtOH mixture. The precipitate was collected by centrifugation and washed three times with Et_2O. The crude product was purified by size exclusion chromatography (Sephadex LH-20, conditioned in MeOH). The desired fraction was collected, and the solvent was removed under vacuum. The dark solid was dissolved in

water and isolated as a PF_6^- salt after ion metathesis. The precipitate was collected by centrifugation and washed three times with cold water and Et_2O to yield $[Os(TAP)_2(NO_2NH_2TAP)]^{2+}$ as a dark-brown solid (18.7 mg, 36%). **^{1}H NMR** (500 MHz, CD_3CN) δ 8.94 (d, *J* = 2.9 Hz, 1H), 8.92 (d, *J* = 2.9 Hz, 1H), 8.85 (dd, *J* = 2.9, 1.1 Hz, 2H), 8.73 (d, *J* = 3.0 Hz, 1H), 8.63 (dt, *J* = 3.0, 1.6 Hz, 4H), 8.27 (t, *J* = 2.9 Hz, 2H), 8.20 (d, *J* = 2.9 Hz, 1H), 8.13 (d, *J* = 2.9 Hz, 1H), 8.11 (d, *J* = 2.9 Hz, 1H), 7.81 (d, *J* = 3.0 Hz, 2H). HRMS(ESI) m/z calculated for $[C_{30}H_{18}O_2N_{14}{}^{184}Os]^{2+}$ = 395.06255; found 395.06271.

$[Os(TAP)_2(diNH_2TAP)]^{2+}.2PF_6^-$ (3). $[Os(TAP)_2(diNH_2TAP)]^{2+}$ was obtained using the synthetic procedure described for $[Os(TAP)_2(NO_2NH_2TAP)]^{2+}$ with 1,4,5,8-tetraazaphenanthrene-9,10-diamine (11.2 mg, 0.053 mmol) to yield $[Os(TAP)_2(diNH_2TAP)]^{2+}$ a dark-brown solid (22.5 mg, 44%). **^{1}H NMR** (500 MHz, CD_3CN) δ 8.83 (dd, *J* = 9.4, 2.9 Hz, 4H), 8.63 (d, *J* = 2.9 Hz, 2H), 8.61 (s, 4H), 8.16 (dd, *J* = 5.7, 2.9 Hz, 4H), 7.84 (d, *J* = 2.9 Hz, 2H), 5.46 (s, 4H). HRMS(ESI) m/z calculated for $[C_{30}H_{20}N_{14}{}^{184}Os]^{2+}$ = 380.07547; found 380.07557.

$[Ru(phen)_2(diiminoTAP)]^{2+}.2PF_6^-$ (4) and $[Ru(phen)_2(diNH_2TAP)]^{2+}.2PF_6^-$ (5). $[Ru(phen)_2Cl_2]$ (300 mg, 0.56 mmol) and 9,10-diamino-1,4,5,8-tetraazaphenanthrene (130 mg, 0.61 mmol) were placed in 20 mL of an argon purged $EtOH/H_2O$ (1:1) mixture. The mixture was heated at reflux under argon and protection from ambient light. After 6h, the reaction was cooled down to room temperature and evaporated to dryness. The residue was purified by column chromatography (Al_2O_3, CH_3CN/H_2O 99:1 to 90:10), yielding $[Ru(phen)_2(diNH_2TAP)]^{2+}$ as an orange solid and $[Ru(phen)_2(diiminoTAP)]^{2+}$ as a pink solid. The solids were dissolved in water and isolated as PF_6^- salts after ion metathesis. The precipitates were collected by centrifugation and washed three times with cold water and Et_2O to yield $[Ru(phen)_2(diNH_2TAP)]^{2+}$ (367 mg, 68%) and $[Ru(phen)_2(diiminoTAP)]^{2+}$ (124 mg, 23%). Characterization for

$[Ru(phen)_2(diNH_2TAP)]^{2+}$ matched those previously reported in the literature.[349] **$[Ru(phen)_2(diiminoTAP)]^{2+}$**, **^{1}H NMR** (300 MHz, CD_3CN) δ 13.39 (s, 2H), 9.10 (d, *J* = 2.3 Hz, 2H), 8.86 (d, *J* = 2.3 Hz, 2H), 8.73 (dd, *J* = 8.3, 1.3 Hz, 2H), 8.63 (dd, *J* = 8.3, 1.3 Hz, 2H), 8.30 (dd, *J* = 5.3, 1.3 Hz, 2H), 8.26 (s, 4H), 7.91 (dd, *J* = 5.2, 1.3 Hz, 2H), 7.83 (dd, *J* = 8.3, 5.2 Hz, 2H), 7.67 (dd, *J* = 8.3, 5.2 Hz, 2H). HRMS(ESI) m/z calculated for $[C_{34}H_{22}N_{10}{}^{96}Ru]^{2+}$ = 333.05470; found 333.05504. **$[Ru(phen)_2(diNH_2TAP)]^{2+}$**, **^{1}H NMR** (300 MHz, CD_3CN) δ 8.73 – 8.52 (m, 6H), 8.25 (s, 4H), 8.07 (dd, *J* = 5.2, 1.3 Hz, 2H), 7.99 (dd, *J* = 5.3, 1.3 Hz, 2H), 7.81 (d, *J* = 2.8 Hz, 2H), 7.69 – 7.60 (m, 4H). HRMS(ESI) m/z calculated for $[C_{34}H_{24}N_{10}{}^{96}Ru]^{2+}$ = 334.06252; found 334.06296.

$[Ru(TAP)_2(diiminoTAP)]^{2+}.2PF_6^-$ (6). $[Ru(TAP)_2Cl_2]$ (300 mg, 0.55 mmol) and 9,10-diamino-1,4,5,8-tetraazaphenanthrene (233 mg, 1.1 mmol) were suspended in 30 mL of water. The mixture was refluxed for 6h, allowing the solution to adopt a burgundy coloration. After reaction, the mixture was cooled down to room temperature and the solvent removed under reduced pressure. The crude product was purified by column chromatography (Al_2O_3, CH_3CN/H_2O 100:0 to 90:10) yielding $[Ru(TAP)_2(diiminoTAP)]^{2+}$ as a pink solid. The solid was dissolved in water and isolated as a PF_6^- salt after ion metathesis. The precipitate was collected by centrifugation and washed three times with cold water and Et_2O to yield $[Ru(TAP)_2(diiminoTAP)]^{2+}$ (420 mg, 79%). **^{1}H NMR** (300 MHz, CD_3CN) δ 13.27 (s, 2H), 9.22 (d, *J* = 2.7 Hz, 2H), 9.12 (d, *J* = 2.2 Hz, 2H), 9.01 (d, *J* = 2.8 Hz, 2H), 8.88 (d, *J* = 2.3 Hz, 2H), 8.63 (s, 4H), 8.58 (d, *J* = 2.8 Hz, 2H), 8.21 (d, *J* = 2.8 Hz, 2H). HRMS(ESI) m/z calculated for $[C_{30}H_{18}N_{14}{}^{96}Ru]^{2+}$ = 335.04519; found 334.04564.

$[Ru(TAP)_2(NO_2NH_2TAP)]^{2+}.2PF_6^-$ (7). $[Ru(TAP)_2Cl_2]$ (200 mg, 0.38 mmol) and 9-NH_2-10-NO_2-1,4,5,8-tetraazaphenanthrene (110 mg, 0.45 mmol) were suspended in 6 mL of water. The suspension was heated for 1h at 120°C under microwave irradiation (maximum power = 200W). After reaction, the mixture was centrifuged to remove insoluble materials

and the filtrate was evaporated under reduced pressure. The residue was purified by column chromatography (Al_2O_3, CH_3CN/H_2O 98:2 to 90:10), yielding $[Ru(TAP)_2(NO_2NH_2TAP)]^{2+}$ as an orange solid. The solid was dissolved in water and isolated as a PF_6^- salt after ion metathesis. The precipitate was collected by centrifugation and washed three times with cold water and Et_2O to yield $[Ru(TAP)_2(NO_2NH_2TAP)]^{2+}$ (125 mg, 33%). **^{1}H NMR** (300 MHz, CD_3CN) δ 9.06 (dd, *J* = 4.6, 2.8 Hz, 2H), 8.98 (dd, *J* = 2.8, 1.9 Hz, 2H), 8.90 (d, *J* = 2.8 Hz, 1H), 8.77 (d, *J* = 2.8 Hz, 1H), 8.68 – 8.56 (m, 4H), 8.33 (dd, *J* = 3.6, 2.8 Hz, 2H), 8.27 (d, *J* = 2.8 Hz, 1H), 8.23 – 8.13 (m, 2H), 7.86 (d, *J* = 2.9 Hz, 1H), 7.76 (s, 2H). HRMS(ESI) m/z calculated for $[C_{30}H_{18}O_2N_{14}{}^{96}Ru]^{2+}$ = 351.04011; found 351.04050.

$[Ru(TAP)_2(diNH_2TAP)]^{2+}.2PF_6^-$ (8). $[Ru(TAP)_2(9\text{-}NH_2\text{-}10\text{-}NO_2TAP)]^{2+}.2PF_6^-$ (100 mg, 0.10 mmol) and 40 mg of Pd/C 10% were suspended in 15 mL of argon purged EtOH/MeOH (1:1) mixture. Hydrazine hydrate (85 µL, 87.5 mg; 1.75 mmol) was added and the mixture was heated at reflux under argon for 8h. After reaction, the mixture was brought to room temperature and filtered through a celite pad to remove the palladium catalyst. The celite pad was washed with 50 mL of MeOH to recover all the complex. After evaporation of the filtrate, the residue was purified by column chromatography (Al_2O_3, CH_3CN/H_2O 95:5 to 85:15) to yield $[Ru(TAP)_2(diNH_2TAP)]^{2+}$ as an orange powder (76 mg, 78%). **^{1}H NMR** (300 MHz, CD_3CN) δ 8.98 (dd, *J* = 5.0, 2.8 Hz, 1H), 8.75 (d, *J* = 2.8 Hz, 1H), 8.62 (s, 1H), 8.22 (dd, *J* = 2.8, 1.7 Hz, 1H), 7.89 (d, *J* = 2.8 Hz, 1H). HRMS(ESI) m/z calculated for $[C_{30}H_{20}N_{14}{}^{96}Ru]^{2+}$ = 336.05302; found 334.05341.

6.4.2 Electrochemistry

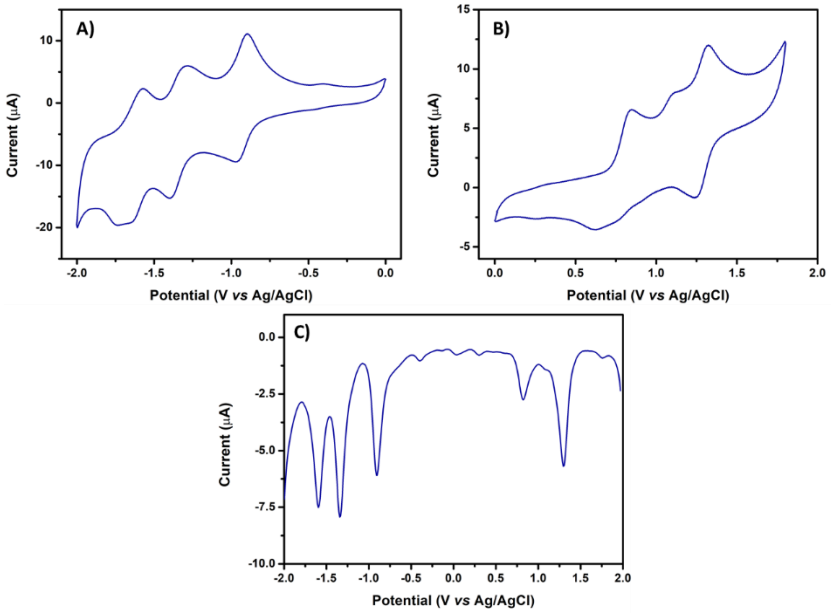

Figure S6.1. Cyclic voltammograms (A, B) and differential pulse voltammogram (C) of $[Os(phen)_2(diNH_2TAP)]^{2+}$ (1 mM) in argon purged acetonitrile (0.1 V/s) with tetrabutylammonium hexafluorophosphate (0.1M) as supporting electrolyte.

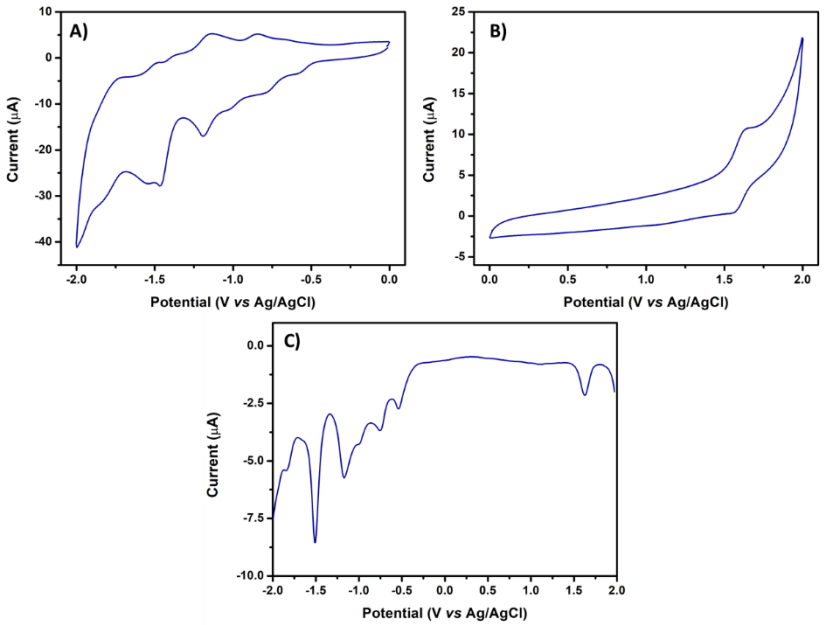

Figure S6.2. Cyclic voltammograms (A, B) and differential pulse voltammogram (C) of $[Os(TAP)_2(NO_2NH_2TAP)]^{2+}$ (1 mM) in argon purged acetonitrile (0.1 V/s) with tetrabutylammonium hexafluorophosphate (0.1 M) as supporting electrolyte.

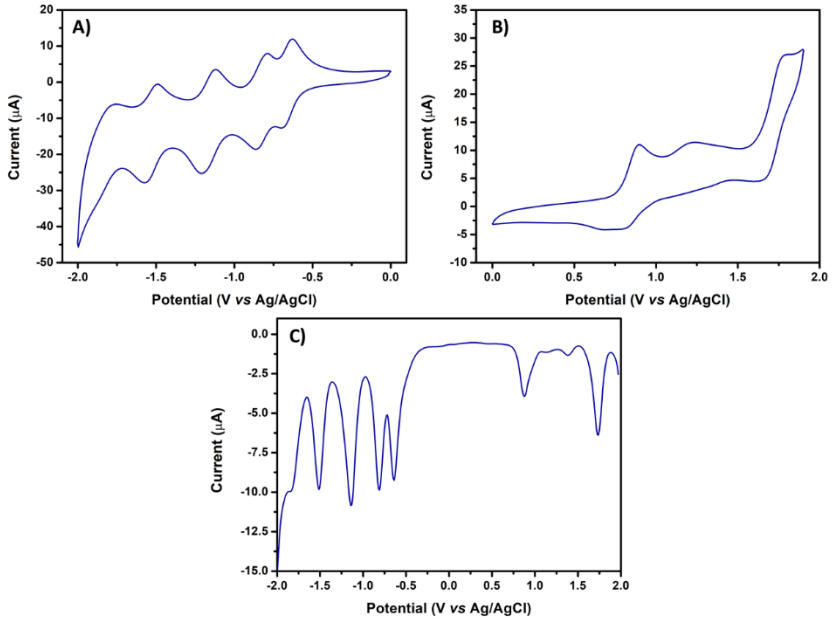

Figure S6.3. Cyclic voltammograms (A, B) and differential pulse voltammogram (C) of $[Os(TAP)_2(diNH_2TAP)]^{2+}$ (1 mM) in argon purged acetonitrile (0.1 V/s) with tetrabutylammonium hexafluorophosphate (0.1 M) as supporting electrolyte.

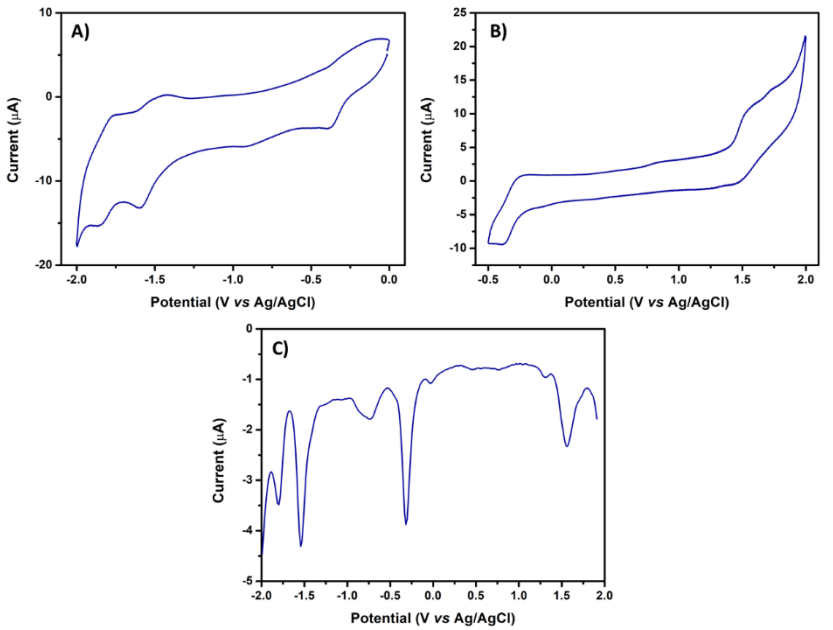

Figure S6.4. Cyclic voltammograms (A, B) and differential pulse voltammogram (C) of $[Ru(phen)_2(diiminoTAP)]^{2+}$ (1 mM) in argon purged acetonitrile (0.1 V/s) with tetrabutylammonium hexafluorophosphate (0.1 M) as supporting electrolyte.

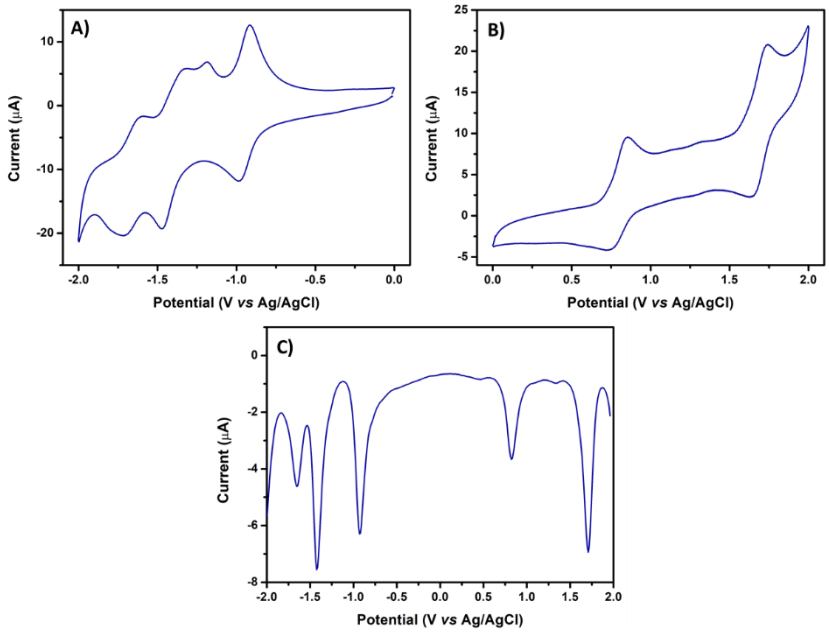

Figure S6.5. Cyclic voltammograms (A, B) and differential pulse voltammogram (C) of $[Ru(phen)_2(diNH_2TAP)]^{2+}$ (1 mM) in argon purged acetonitrile (0.1 V/s) with tetrabutylammonium hexafluorophosphate (0.1 M) as supporting electrolyte.

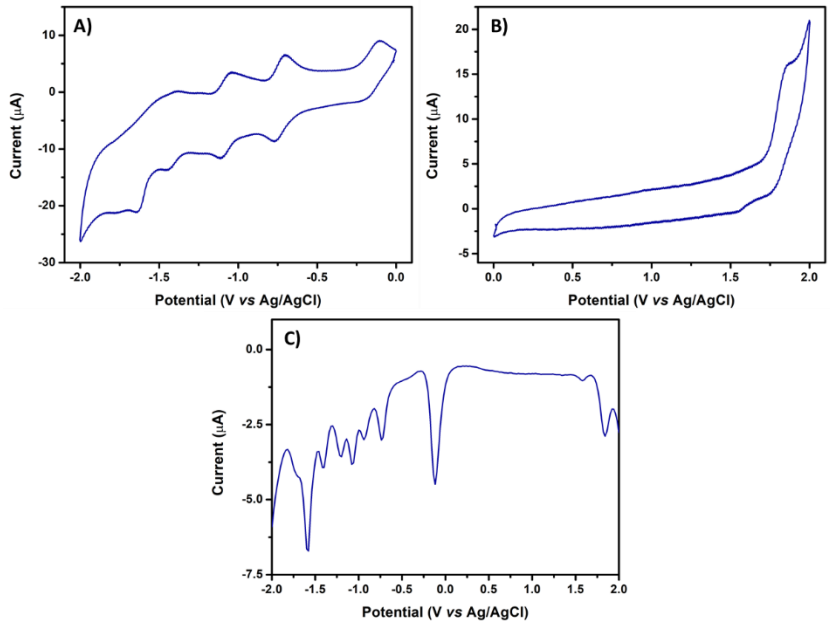

Figure S6.6. Cyclic voltammograms (A, B) and differential pulse voltammogram (C) of $[Ru(TAP)_2(diiminoTAP)]^{2+}$ (1 mM) in argon purged acetonitrile (0.1 V/s) with tetrabutylammonium hexafluorophosphate (0.1 M) as supporting electrolyte.

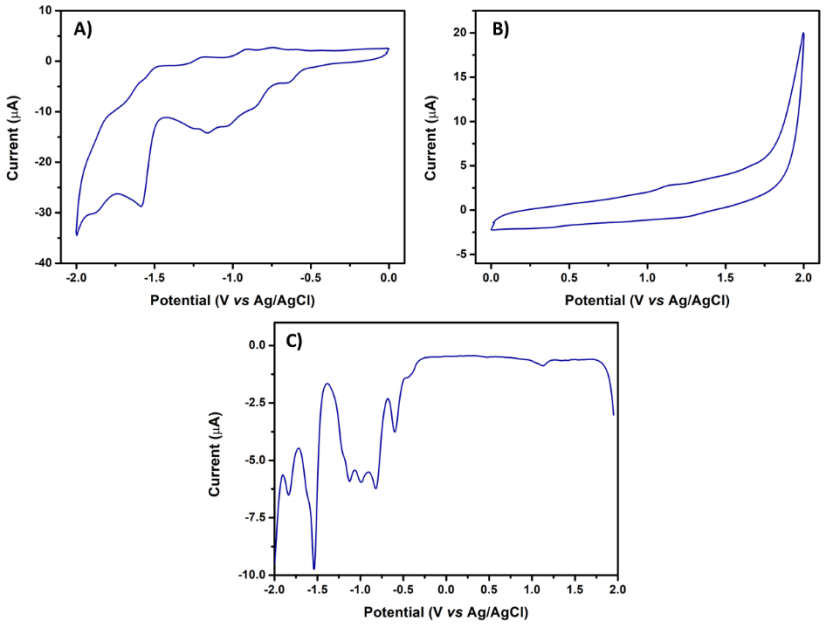

Figure S6.7. Cyclic voltammograms (A, B) and differential pulse voltammogram (C) of $[Ru(TAP)_2(NO_2NH_2TAP)]^{2+}$ (1 mM) in argon purged acetonitrile (0.1 V/s) with tetrabutylammonium hexafluorophosphate (0.1 M) as supporting electrolyte.

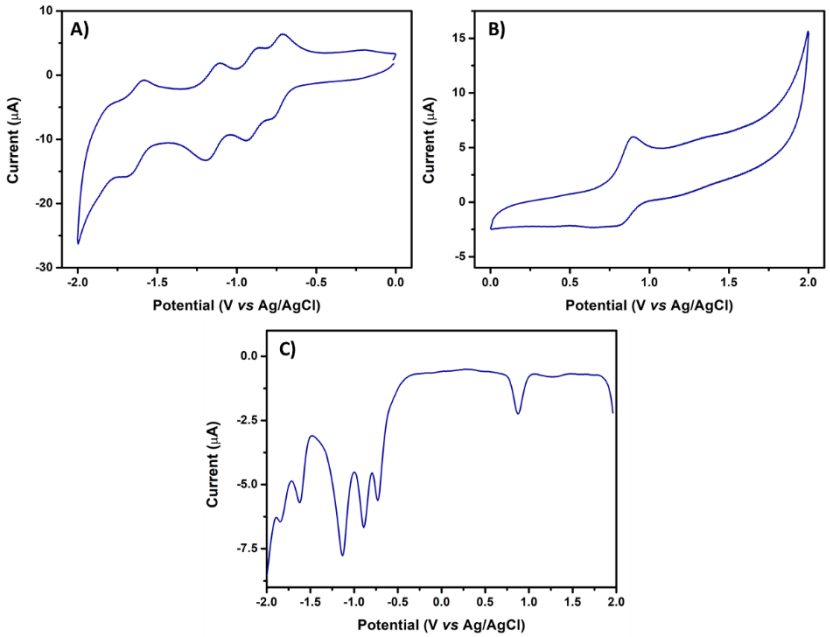

Figure S6.8. Cyclic voltammograms (A, B) and differential pulse voltammogram (C) of $[Ru(TAP)_2(diNH_2TAP)]^{2+}$ (1 mM) in argon purged acetonitrile (0.1 V/s) with tetrabutylammonium hexafluorophosphate (0.1 M) as supporting electrolyte.

6.4.3 Theoretical Studies

Table S6.1. Cartesian Coordinates (in Å) of the equilibrium geometry of the singlet state of the $Ru(phen)_2(diNH_2TAP)]^{2+}$ complex.

Ru	-0.30625	0.00001	-0.00003	N	1.29017	-0.8244	-1.06166
C	-2.45636	-0.60559	-2.16445	N	-0.43873	1.76808	-1.11572
C	1.30569	1.6717	2.10848	C	-3.75354	-2.64625	-2.2579
C	-2.45627	0.60519	2.16457	C	-0.85299	-4.26114	2.35637
C	-2.08952	-2.25419	-0.54335	C	-0.85409	4.26096	-2.35649
C	2.50489	0.43593	0.55223	C	-3.75374	2.64566	2.25822
C	-2.08991	2.25387	0.54343	C	-3.06769	3.10767	1.1091
C	-1.36398	-2.65822	0.6154	C	-1.60987	3.91993	-1.20889
C	-1.36457	2.65801	-0.6154	C	3.72997	0.88856	1.09747
C	2.50495	-0.43552	-0.55231	C	3.73011	-0.88801	-1.09752
C	0.26651	-2.12112	2.2078	C	-1.60897	-3.92021	1.20888
C	0.26586	2.12118	-2.20795	C	-3.06724	-3.10815	-1.10889
C	1.30594	-1.67142	-2.10859	H	-1.01086	5.21836	-2.83982
C	-3.4444	-1.39815	-2.77726	H	-4.51104	3.2685	2.72035
C	2.53314	2.128	2.64142	H	-4.51083	-3.26919	-2.7199
C	-3.44434	1.39761	2.77753	H	-1.0095	-5.21859	2.83968
C	0.07992	-3.36037	2.84764	N	3.72365	1.75498	2.15957
C	0.07894	3.36036	-2.84782	N	3.72391	-1.75442	-2.15962
C	2.53346	-2.12757	-2.64151	C	4.9785	-0.4522	-0.53863
H	-2.19793	-0.36729	2.55835	C	4.97843	0.45292	0.53858
H	0.35984	1.98498	2.52416	N	6.14479	-0.92864	-1.0882
H	-2.19819	0.36692	-2.55829	N	6.14464	0.92952	1.08813
H	0.9842	1.40501	-2.58059	H	7.00167	-0.94036	-0.55855
H	0.36013	-1.9848	-2.5243	H	6.06435	-1.58063	-1.85455
H	0.98473	-1.40482	2.58041	H	7.00158	0.94112	0.55859
H	2.52803	2.81292	3.48042	H	6.06416	1.5815	1.85448
H	-3.95129	1.01686	3.65486	C	-3.30409	-4.3857	-0.49077
H	-3.95154	-1.01748	-3.65452	C	-2.60397	-4.7757	0.61866
H	0.67125	3.59276	-3.72346	C	-2.60495	4.77525	-0.61856
H	2.52845	-2.8125	-3.4805	C	-3.30485	4.38516	0.49098
H	0.67238	-3.5927	3.72319	H	-2.78898	-5.74147	1.07523
N	-1.78614	-1.01802	-1.07164	H	-4.05338	5.03715	0.92672
N	-1.78626	1.01775	1.07167	H	-4.05257	-5.03781	-0.92643
N	1.29004	0.82467	1.06154	H	-2.79021	5.74097	-1.07514
N	-0.43826	-1.76813	1.11566				

Table S6.2. Cartesian Coordinates (in Å) of the equilibrium geometry of the singlet state of the $Ru(TAP)_2(diNH_2TAP)]^{2+}$ complex.

Ru	-0.31824	0.00000	0.0000	N	-0.4308	1.75345	-1.12983
C	-2.49309	0.67312	2.16127	N	1.28688	0.81174	1.07763
C	1.30081	-1.63585	-2.13984	N	-0.4308	-1.75344	1.12983
C	-2.49309	-0.67312	-2.16127	C	-3.04952	-3.12112	-1.0739
C	-2.0796	2.25769	0.51998	C	-1.58572	-3.90035	1.23272
C	2.49745	-0.42614	-0.55962	C	3.72436	-0.86626	-1.11307
C	-2.0796	-2.25769	-0.51998	C	3.72436	0.86625	1.11307
C	-1.35327	2.64482	-0.63082	C	-1.58572	3.90035	-1.23272
C	-1.35327	-2.64482	0.63082	C	-3.04952	3.12112	1.07389
C	2.49745	0.42614	0.55962	N	3.71742	-1.71232	-2.19183
C	0.25699	2.13504	-2.21953	N	3.71742	1.71232	2.19183
C	0.25699	-2.13504	2.21953	C	4.97315	0.44229	0.54833
C	1.30081	1.63585	2.13984	C	4.97315	-0.44229	-0.54833
C	-3.46758	1.54156	2.70642	N	6.13598	0.90823	1.10783

C	2.5311	-2.07902	-2.68279	N	6.13598	-0.90824	-1.10783
C	-3.46758	-1.54156	-2.70642	H	7.00127	0.91175	0.59255
C	0.02248	3.39752	-2.81301	H	6.05844	1.54025	1.89091
C	0.02248	-3.39752	2.81301	H	7.00127	-0.91174	-0.59255
C	2.5311	2.07902	2.68279	H	6.05844	-1.54025	-1.89091
H	-2.28618	0.28604	-2.61207	C	-3.28097	4.39464	0.45178
H	0.35708	-1.94351	-2.56369	C	-2.57332	4.77153	-0.65999
H	-2.28618	-0.28604	2.61207	C	-2.57332	-4.77153	0.65999
H	0.98528	-1.45116	2.62907	C	-3.28097	-4.39464	-0.45178
H	0.35708	1.94351	2.56369	H	-2.73473	5.72914	-1.13874
H	0.98528	1.45116	-2.62907	H	-4.02925	-5.0398	-0.89457
H	2.52732	-2.74654	-3.53534	H	-4.02925	5.0398	0.89456
H	-4.01947	-1.23638	-3.5862	H	-2.73473	-5.72914	1.13874
H	-4.01947	1.23638	3.5862	N	-0.87565	-4.27081	2.3436
H	0.58776	-3.6859	3.68995	N	-3.75058	-2.74144	-2.18722
H	2.52732	2.74654	3.53534	N	-3.75058	2.74144	2.18722
H	0.58776	3.6859	-3.68995	N	-0.87565	4.27081	-2.3436
N	-1.79554	1.02726	1.0683				
N	-1.79554	-1.02726	-1.0683				
N	1.28688	-0.81174	-1.07763				

Table S6.3. Cartesian Coordinates (in Å) of the equilibrium geometry of the singlet state of the $Ru(phen)_2(diiminoTAP)]^{2+}$ complex.

Ru	0.51642	-0.00011	0.00002	C	1.9202	3.8588	1.30073
C	2.58119	-0.69173	2.24967	C	-3.51683	0.89459	-1.13493
C	2.58175	0.69272	-2.24889	C	-3.51658	-0.89631	1.13444
C	2.31563	-2.26297	0.53792	C	1.92359	-3.85773	-1.30075
C	-2.25753	0.44628	-0.56775	C	3.2694	-3.13721	1.11239
C	2.31429	2.26393	-0.53741	H	1.3906	5.09453	3.00261
C	1.64276	-2.62463	-0.66461	H	4.62183	3.37007	-2.79056
C	1.6407	2.62527	0.66483	H	4.62366	-3.36722	2.79146
C	-2.25742	-0.44769	0.56718	H	1.39583	-5.09331	-3.00331
C	0.04968	-2.04583	-2.28448	C	-4.7401	0.45422	-0.57702
C	0.04728	2.04575	2.2841	C	3.54971	-4.38207	0.4476
C	3.53724	-1.5096	2.88058	C	2.9048	-4.72762	-0.70905
C	3.53714	1.51142	-2.87971	C	2.90083	4.72944	0.70918
C	0.27699	-3.25364	-2.96873	C	3.54642	4.38423	-0.44718
C	0.27333	3.25391	2.96814	H	3.12104	-5.6694	-1.20029
H	2.29965	-0.25923	-2.67412	H	4.28154	5.04891	-0.88636
H	2.29798	0.25986	2.67498	H	4.28533	-5.04616	0.88685
H	-0.67561	1.32622	2.64087	H	3.11603	5.67155	1.20024
H	-0.67349	-1.32674	-2.6415	C	-4.73999	-0.45614	0.57663
H	3.98971	1.17204	-3.80247	C	-4.65119	2.13537	-2.71152
H	3.98929	-1.16992	3.80349	C	-5.8714	1.70149	-2.16005
H	-0.28991	3.45907	3.86919	C	-4.65063	-2.13754	2.71102
H	-0.28568	-3.45901	-3.87009	C	-5.87093	-1.70385	2.15965
N	1.98169	-1.05157	1.10047	H	-1.02866	1.41249	-1.79784
N	1.98158	1.05215	-1.0999	H	-1.02842	-1.41315	1.79766
N	-1.0525	0.77572	-0.99723	N	-5.91763	-0.87243	1.10488
N	0.72004	-1.73064	-1.15919	N	-3.4774	-1.73454	2.19946
N	-1.05233	-0.77652	0.99694	N	-3.47786	1.73262	-2.20006
N	0.71844	1.73072	1.15926	N	-5.91788	0.87013	-1.10529
C	3.8877	-2.72732	2.31843	H	-6.81659	2.02862	-2.57561
C	1.2099	-4.15923	-2.48586	H	-4.6247	2.80447	-3.56238
C	1.20575	4.16007	2.48543	H	-6.81603	-2.03107	2.57534
C	3.88638	2.72951	-2.31761	H	-4.62391	-2.8066	3.56191
C	3.26742	3.13898	-1.11178				

Table S6.4. Cartesian Coordinates (in Å) of the equilibrium geometry of the singlet state of the $Ru(TAP)_2(diiminoTAP)]^{2+}$ complex.

Ru	-0.54025	0.00000	0.00000	C	3.5017	-0.89579	-1.13747
C	-2.63732	-0.76429	-2.22808	C	-1.87222	-3.85435	1.32261
C	-2.63731	0.76432	2.22808	C	-3.24296	-3.16621	-1.06771
C	-2.30234	-2.27644	-0.50568	C	4.72194	0.45536	0.57803
C	2.23956	0.44861	0.57132	C	-3.50127	-4.4141	-0.40518
C	-2.30231	2.27646	0.50568	C	-2.83951	-4.74666	0.74819
C	-1.61972	-2.62064	0.68423	C	-2.83945	4.74669	-0.7482
C	-1.61969	2.62065	-0.68423	C	-3.50121	4.41413	0.40518
C	2.23955	-0.44864	-0.57131	H	-3.01945	-5.68534	1.25677
C	-0.04619	-2.06251	2.2966	H	-4.23006	5.07747	0.85342
C	-0.04617	2.0625	-2.29661	H	-4.23012	-5.07743	-0.85342
C	-3.58011	-1.66042	-2.786	H	-3.01938	5.68536	-1.25678
C	-3.58008	1.66046	2.786	C	4.72194	-0.45539	-0.57803
C	-0.30462	-3.30186	2.92897	C	4.63322	2.13536	2.71427
C	-0.30459	3.30184	-2.92898	C	5.85313	1.70104	2.16123
H	-2.41241	-0.17607	2.70828	C	4.63321	-2.13538	-2.71427
H	-2.41241	0.17609	-2.70828	C	5.85312	-1.70107	-2.16123
H	0.67986	1.36885	-2.69364	H	1.01746	1.41328	1.80346
H	0.67985	-1.36888	2.69364	H	1.01745	-1.41329	-1.80345
H	-4.08565	1.39584	3.70578	N	5.89962	-0.87035	-1.10553
H	-4.08567	-1.39579	-3.70577	N	3.4604	-1.73215	-2.20199
H	0.23492	3.56127	-3.83069	N	3.46041	1.73213	2.202
H	0.23488	-3.56129	3.83068	N	5.89962	0.87032	1.10553
N	-2.00059	-1.06631	-1.08564	H	6.79854	2.0277	2.57628
N	-2.00058	1.06633	1.08564	H	4.60673	2.80378	3.56532
N	1.04161	0.77739	1.00152	H	6.79853	-2.02773	-2.57628
N	-0.70671	-1.71937	1.17838	H	4.60672	-2.8038	-3.56532
N	1.0416	-0.77741	-1.00152	N	-1.1948	4.18592	-2.46567
N	-0.70669	1.71937	-1.17838	N	-3.8888	2.83634	2.22923
C	-3.24292	3.16624	1.06771	N	-1.19485	-4.18592	2.46566
C	-1.87218	3.85435	-1.32261	N	-3.88884	-2.8363	-2.22923
C	3.5017	0.89576	1.13747				

Chapter VII – Ir(III) Photosensitizers with π-Extended Aromatic Ligands for Halide Oxidation

Preface – This chapter focuses on the detailed investigation of five novel Ir(III) photosensitizers bearing ligands with π-extended aromatic systems and exhibiting optimal photo-oxidizing abilities for halide oxidation in acetonitrile/water (50:50) mixtures. For comparison purpose, they will be described alongside an Ir(III) photosensitizer that does not possess a π-extended planar ligand. Manuscript in preparation (De Kreijger, S.; Elias, B.; Troian-Gautier, L., Increasing Cage Escape Yields for Halide Oxidation in Aqueous Solutions Using Ir(III) Photosensitizers with π-Extended Aromatic Ligands).

7.1 Introduction

Building on our previous work with Ru(II) and Os(II) photosensitizers, which demonstrated the ability for excited-state electron transfer in GMP oxidation, we turned our attention to the development of Ir(III) photosensitizers for more demanding applications. As explained in **Chapter I** – **Section 1.4.3**, the range of accessible redox potentials of Ir(III) photosensitizers is wider than the range of potentials covered by Os(II) and Ru(II) complexes. Therefore, the fine-tuning of the spatially separated HOMO and LUMO in bis-cyclometalated Ir(III) complexes (**Chapter II, Figure 2.5**) is expected to afford strong photo-oxidizing complexes capable of performing halide oxidation in organic solvents and/or water-like conditions by absorbing visible light photons. In this chapter, we investigate Ir(III) photosensitizers capable of oxidizing halides in water-enriched conditions. To achieve this, we employed ligand tuning strategies, incorporating π-extended ligands, designed to stabilize the LUMO, improve light absorption and presenting a second coordination site that could, for instance, accommodate a catalyst for HER. This ligand was combined with the electron-deficient ^{dFCF3}ppy (2-(2,4-difluorophenyl)-5-(trifluoromethyl)pyridine) cyclometalated ligand to stabilize the HOMO. This approach aimed to create multifunctional complexes capable of both efficient halide oxidation and proton reduction, paving the way for advanced applications in solar fuel generation.

Halide oxidation has already been reported in organic solvents by pioneers such as G. J. Meyer using photosensitizers based on Ru(II)[54-56, 135, 230, 231], Os(II)[158] or Ir(III)[179] and D. G. Nocera that performed HX splitting with Rh_2 complexes[229, 232] and halogen atom photoelimination from Ni(III)[233, 234] or Fe(III) complexes.[235] Most of the time, these photosensitizers were designed by using the combination of oxidizing power conferred by ligands bearing electron withdrawing groups or electron-poor ligands such as 2,2'-bipyrazine (bpz) for Ru(II); 4,4'-bis(trifluoromethyl)-2,2'-bipyridine (^{dCF3}bpy) for Os(II); 2-(2,4-difluorophenyl)-5-(trifluoromethyl)-pyridine (^{dFCF3}ppy)) for Ir(III) with ligands capable of halide-pairing. These ligands include the 4,4'-diethylester-2,2'-bipyridine (deeb)[135, 236-241], the dicationic 4,4'-trimethylamino-methyl-2,2'-bipyridine (tmam)[135, 158, 241, 242] or the 4,4′-diethanolamide-2,2′-bipyridine (dea)[241, 243]. This led to ground-state adduct formation with different halides in solvents that included acetonitrile, acetone or dichloromethane. $[Ru(bpz)_2(tmam)]^{4+}$ was found to photo-oxidize chloride in acetone with quenching rate constant greater than 10^{10} M^{-1} s^{-1} and the formation of the monoreduced ruthenium photosensitizer was confirmed by transient absorption spectroscopy.[135] Upon light excitation, $[Os(^{dCF3}bpy)_2(tmam)]^{4+}$ was quenched by iodide in acetone through a combination of static and dynamic excited-state quenching with quenching rate constant greater than 10^{11} M^{-1} s^{-1}.[158] Unfortunately, due to its moderate excited-state reduction potential, this photosensitizer could only be used for iodide oxidation and unambiguous evidence for excited-state electron transfer was not reported.[158] This could potentially stem from low cage escape yields that are often observed with Os(II) photosensitizers.[126, 244] Finally, $[Ir(^{dFCF3}ppy)_2(tmam)]^{3+}$ was found to be quenched by chloride in acetonitrile with quenching rate constant greater than 10^{10} M^{-1} s^{-1}.[179] The ion pair formation with the tmam ligand enabled rapid excited-state electron transfer at extremely low concentration of chloride. Nevertheless, transient absorption evidence for excited-state chloride oxidation in acetonitrile was not reported.[179] These photosensitizers rely on the pre-association of the photosensitizer and halide in the ground state, which further shifts the one-electron oxidation potential of the halides to more positive value.[243] This shift complicates halide oxidation and could also reduce

cage escape yields by increasing back-electron transfer within the pre-associated species. This is exemplified when comparing $[Ru(bpy)_3]^{2+}$ (bpy= 2,2'-bipyridine) with photosensitizers competent for halide-pairing. $[Ru(bpy)_3]^{2+}$ exhibited cage escape yield of 0.50 in CH_2Cl_2,[54] whereas photosensitizers bearing ion-pairing ligands showed lower cage escape yields, *i.e.* 0.34 for $[Ru(^{dtb}bpy)_2(dea)]^{2+}$ (^{dtb}bpy= 4,4'di-*tert*-butyl-2,2'-bipyridine) in CH_2Cl_2,[243] 0.25 for $[Ru(bpy)_2(deeb)]^{2+}$ in CH_2Cl_2, and 0.042 for $[Ru(bpz)(deeb)]^{2+}$ in acetonitrile.[54, 231] Thus, it seems that ground-state ion-pairing of the photosensitizer and the halide could improve excited-state reactivity but could lead to smaller cage escape yields. Recent work carried out by Nocera and co-workers showed that halide oxidation (through bond homolysis of Nickel complexes) could be favored using secondary coordination effects. As such, it appears that stabilizing the halogen atom further from the reaction center could help in increasing product formation.

So far, excited-state halide oxidation has almost exclusively been carried out in organic solvent, where the estimated potential are 1.23, 1.35 and 1.46 V *vs* NHE for iodide, bromide and chloride, respectively.[42, 43] Whereas most examples of halide oxidation involved iodide, *i.e.* the most easily oxidized stable halide, there are a few reports of bromide and chloride oxidation that have appeared in recent years. These include bromide and chloride photo-oxidation in acetone using Ru(II) photosensitizers[135, 238, 239] as well as by one- or two-photon excitation of N-phenylphenothiazine in acetonitrile.[246] Recently, $[Ir(^{dCF3}ppy)_2(bpph)]^+$ (^{dCF3}ppy = 2-(3,5-bis(trifluoromethyl-phenyl)pyridine) and bpph = benzo[a]pyrazino[2,3-h]phenazine) was reported by our group for halide photo-oxidation applications.[42] Quenching rate constant in the 10^{10} M^{-1} s^{-1} range were reported for iodide, bromide and chloride in acetonitrile. For iodide and bromide, transient absorption spectroscopy experiments confirmed the formation of both the monoreduced iridium complex alongside $I_2^{\bullet-}$ or $Br_2^{\bullet-}$. In the case of chloride, excited-state quenching was observed only as a significant decrease in the excited-state lifetime and no photoproducts resulting from electron transfer were detected.

Finally, a pentacationic IrN_6 photosensitizer ($[Ir(tpy\text{-}PyMe)_2]^{5+}$ (tpy-PyMe = 4′-(4-methyl-pyridinio)-2,2′:6′,2″-terpyridine) was recently reported for hydrochloric acid, chloride, bromide and iodide oxidation in water by our group. Efficient excited-state electron transfer was confirmed by nanosecond transient absorption spectroscopy.[182] Despite low cage escape yields (0.04) and limited visible light absorption properties, the successful photo-oxidation of halides in water marks a significant step forward.

In this chapter, we provide a detailed investigation of a series of five novel Ir(III) photosensitizers bearing ligands with π-extended aromatic systems and exhibiting optimal photo-oxidizing abilities for halide oxidation in acetonitrile/water (50:50) mixtures. The series includes novel Ir(III) photosensitizers featuring the ^{dFCF3}**ppy** (2-(2,4-difluorophenyl)-5-(trifluoromethyl)pyridine) cyclometalating ligand in combination with the π-extended ligand **TPPHZ** (tetrapyrido[3,2-a:2',3'-c:3'',2''-h:2''',3'''-j]phenazine) and **PHEHAT** (1,10- phenanthrolino[5,6-b]1,4,5,8,9,12-hexaazatriphenylene) (**Figure 7.1**). This ligand can either be chelated via the 1,10-phenanthroline scaffold (**PHEHAT**) or via the 1,4,5,8,9,12-hexaazatriphenylene scaffold (**HATPHE**).[349, 352, 357] For comparison purpose, binuclear Ir(III) photosensitizers (**Ir_2-TPPHZ** and **Ir_2-TAPHAT**, **TAPHAT** = 1,4,5,8-tetraazaphenanthrene[9,10-b]1,4,5,8,9,12-hexaazatriphenylene) will also be described, alongside the mononuclear, **Ir-TAP**, which features 1,4,5,8-tetraazaphenanthrene (**TAP**) as its ancillary ligand and does not possess a π-extended planar ligand. In this chapter, we will demonstrate the efficiency of these photosensitizers in oxidizing iodide, bromide, and chloride. We will explore their excited-state reactivity and investigate the electron transfer processes using transient absorption spectroscopy. Additionally, we will examine the cage escape yields in both acetonitrile and acetonitrile/water mixtures, providing insights into their potential applications for halide oxidation.

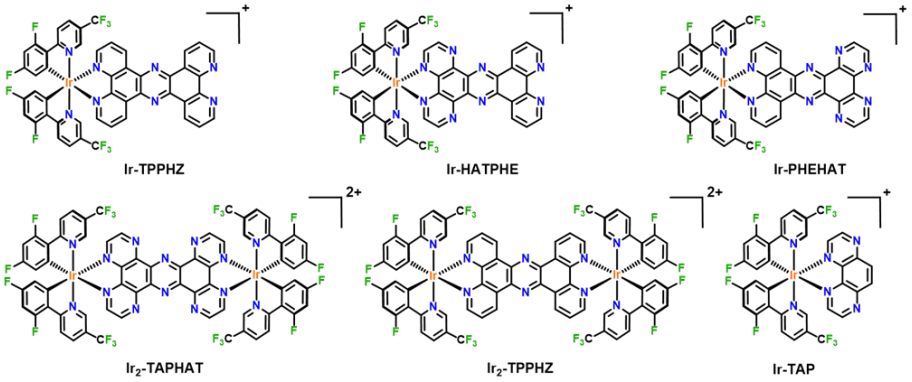

Figure 7.1. Structures of the six Ir(III) photosensitizers reported in the present study.

7.2 Results and discussion

7.2.1 Synthesis

$[Ir(^{dFCF3}ppy)_2(\mu\text{-}Cl)]_2$ was prepared according to literature procedure, in which **^{dFCF3}ppy** was refluxed in 2-ethoxyethanol/water (3:1) mixture in the presence of iridium trichloride hydrate.[396] For **Ir-TPPHZ** and **Ir-PHEHAT**, a first synthetic step consisted in the reaction between $[Ir(^{dFCF3}ppy)_2(\mu\text{-}Cl)]_2$ and 1,10-phenanthroline-5,6-dione (phd) in a MeOH/CH_2Cl_2 (2:1) mixture to yield $[Ir(^{dFCF3}ppy)_2(phd)]^+$ in 89% yield. Condensation of the *o*-dione ligand with 1,10-phenanthroline-5,6-diamine (diNH_2phen) or 1,4,5,8-tetraazaphenantrene-9,10-diamine (diNH_2TAP) resulted in the formation of **Ir-TPPHZ** and **Ir-PHEHAT** with 41% and 73% yield, respectively. For **Ir-HATPHE**, the reaction between $[Ir(^{dFCF3}ppy)_2(\mu\text{-}Cl)]_2$ and diNH_2TAP in ethylene glycol yielded the precursor $[Ir(^{dFCF3}ppy)_2(diNH_2TAP)]^+$ in 84% yield that was then condensed with phd to form **Ir-HATPHE** in 57% yield. Finally, direct reaction of $[Ir(^{dFCF3}ppy)_2(\mu\text{-}Cl)]_2$ with 1,4,5,8-tetraazaphenantrene (TAP) in a MeOH/CH_2Cl_2 (2:1) mixture yielded **Ir-TAP** in 86% yield. **Ir_2-TAPHAT** and **Ir_2-TPPHZ** were were obtained via the reaction between $[Ir(^{dFCF3}ppy)_2(\mu\text{-}Cl)]_2$ and the corresponding TPPHZ or TAPHAT ligand, which were synthesized using literature procedures.[346, 347] This yielded **Ir_2-TPPHZ** and **Ir_2-TAPHAT** in 70% and 68% yield, respectively. Further details about the synthesis and purification are reported in the experimental section of this chapter. From ^{1}H

NMR spectra, the number of observed signals and their integration confirm the presence of a C_2 symmetry axis in the final mononuclear and binuclear complexes, which simplifies their interpretation. This symmetry axis makes the protons of the two ^{dFCF3}ppy ligands equivalent, as well as those of the TAP, TPPHZ, PHEHAT, HATPHE and TAPHAT ligands located on either side of the axis. In the case of the binuclear complexes this symmetry axis allows the observation of only three stereoisomers instead of four by ^{1}H NMR spectroscopy. Although a pair of diastereoisomers is still present, the distance between the metal centers is sufficient that the chemical environment of one center does not influence the other, causing the protons to appear chemically equivalent.

7.2.2 Photophysical characterization

The UV-visible absorption features of all complexes were characterized by strong ligand-centred (LC) absorption bands in the UV region (**Figure 7.2-A**). The transitions observed at wavelengths greater than 350 nm are often assigned to mixed metal-ligand-to-ligand charge transfer (MLLCT) from the Ir-cyclometalating ligand fragment to the diimine ligand.[226, 263] All the complexes absorbed in the visible range with molar absorption coefficient in the 4300-6400 $M^{-1}cm^{-1}$ range between 410 and 450 nm (**Table 7.1**). The steady-state photoluminescence was recorded in acetonitrile and is presented in **Figure 7.2-B**. Large shifts of the photoluminescence were observed for the series of photosensitizers, where **Ir-TPPHZ** displayed a photoluminescence maximum (PL_{max}) centered at 522 nm that was red-shifted to 653 nm for **Ir_2-TAPHAT**. The most blue-shifted photoluminescence spectra were observed for photosensitizers that were chelated via the 1,10-phenanthroline scaffold, *i.e.* **Ir-TPPHZ** and **Ir-PHEHAT**, respectively. When the photosensitizers were chelated via the **TAP** moiety, the photoluminescence was red-shifted to values of 625 nm, 645 nm and 653 nm for **Ir-TAP**, **Ir-HATPHE** and **Ir-TAPHAT**, respectively.

In contrast to the well-known $[Ru(bpy)_2(dppz)]^{2+}$ (dppz = dipyrido[3,2-a:2',3'-c]phenazine), whose luminescence is fully quenched in pure water but

gradually reappears as the organic solvent content increases, becoming noticeable at ratios between 90:10 and 50:50 acetonitrile/water,[397] all Ir(III) complexes based on these π-extended ligands remained luminescent in a 50:50 acetonitrile/water mixture, exhibiting a behavior similar to the previously reported Ir(III) DPPZ derivatives.[398] Investigations in pure water were not possible due to the limited solubility of our systems. Ru(II) complexes based on the **HATPHE** and **TAPHAT** ligands have been reported to exhibit luminescence in both organic solvents and pure water.[349, 399] In contrast, those based on the **TPPHZ** and **PHEHAT** were luminescent in organic solvents but showed residual to no-emission in pure water, and are thus categorized as "light-switches", *i.e.* compounds able to sense their solvent micro-environment.[347, 349] For all the Ir(III) photosensitizers, a distinct solvatochromism was observed, *i.e.* a red-shift of the emission maxima ranging between 17 nm and 60 nm for **Ir-TPPHZ** and **Ir-PHEHAT**, respectively, when the solvent was switched from acetonitrile to acetonitrile/water (50:50) mixtures. This solvatochromism confirms the charge transfer character of the excited state for this series of Ir(III) photosensitizers.[400]

Table 7.1. Photophysical properties of the Ir(III) complexes.

	λ_{Abs} (nm), [ε,$10^3 M^{-1}cm^{-1}$][a]	PL_{max} (nm)[a]	PL_{max} (nm)[b]	PL_{max} (nm)[c]	τ (ns)[a]	τ (ns)[b]
Ir-TPPHZ	390 (28.0), 410 (4.9)	522	539	473	5290	655
Ir-PHEHAT	381 (26.5), 410 (5.8)	586	646	473	1520	46
Ir-HATPHE	388 (25.8), 410 (4.8)	645	681	572	240	40
Ir_2-TAPHAT	385 (23.8), 450 (5.2)	653	689	583	150	17
Ir_2-TPPHZ	386 (38.5), 420 (6.4)	646	658	467	620	125
Ir-TAP	375 (7.6), 400 (4.3)	625	660	520	430	50
$[Ir(^{dFCF3}ppy)_2(dtbbpy)]^{+214}$	310 (33.9), 380 (6.1)	470	/	/	2300	/

[a] In argon-purged acetonitrile. [b] In argon-purged acetonitrile/water 50:50. [c] In EtOH/MeOH (4:1) glass matrix at 77K.

For all six Ir(III) photosensitizer, time-resolved photoluminescence in acetonitrile was well described by single-exponential decay from which excited-state lifetimes ranging from 5290 ns for **Ir-TPPHZ** to 150 ns for **Ir_2-**

TAPHAT were measured. As expected for charge transfer excited states, these excited-state lifetimes were shorter in the presence of water. The ground and excited-state photophysical properties are gathered in **Table 7.1**.

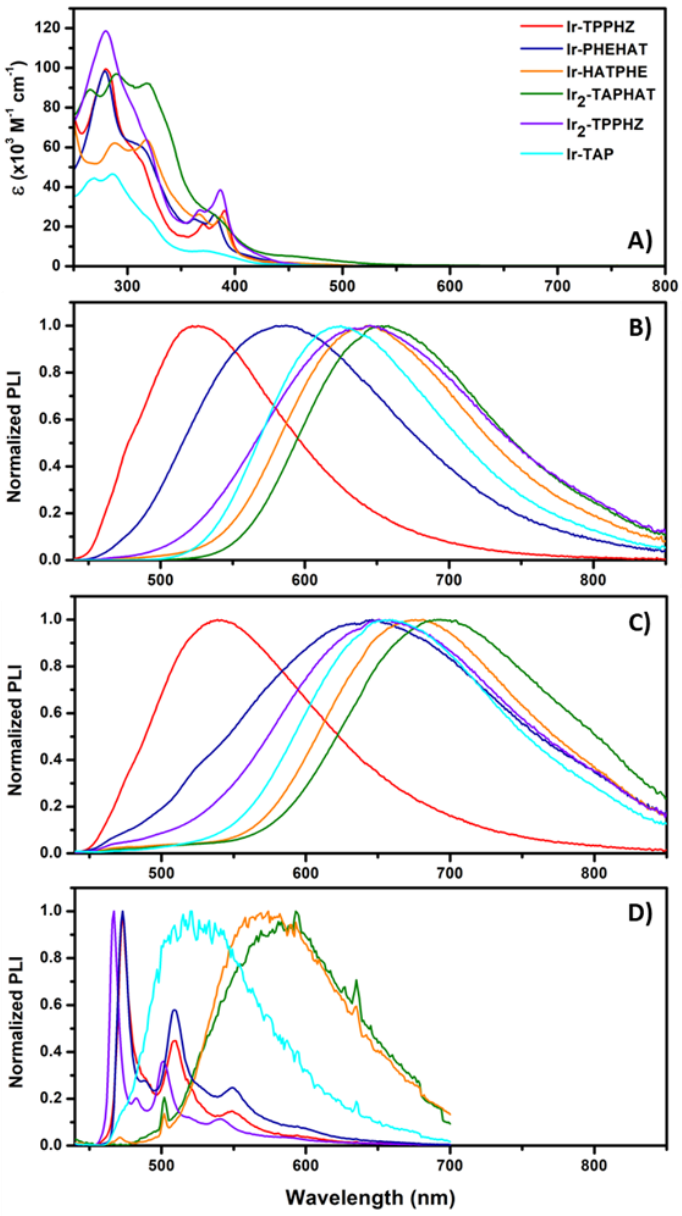

Figure 7.2. UV-visible spectra in acetonitrile (A), steady state photoluminescence in argon purged acetonitrile (B), steady state photoluminescence spectra in argon purged acetonitrile/water (50:50) (C), and steady state luminescence spectra in EtOH/MeOH (4:1) glass matrix at 77K (D) for the different Ir(III) complexes.

The steady-state photoluminescence was further investigated in EtOH/MeOH 4:1 glass at 77K (**Figure 7.2-D**). The spectra were systematically blue-shifted compared to those recorded at room temperature. Interestingly, two main behaviors are observed. Photosensitizers where the Ir core is chelated via a "TAP-like" moieties exhibit a broad, structureless emission whereas those chelated via a "phen-like" moiety exhibit highly blue-shifted and structured emission, reminiscent of ligand-centered emissive states. A double-mode Franck-Condon (FC) lineshape analysis was used to fit the photoluminescence spectra that were used to obtain the energy of the transition between the lowest vibrational levels of the ground and excited states (E_{00}), the energy of the weighted-average, ground-state, acceptor vibrational mode in cm^{-1} ($\hbar\omega_M$), the Huang Rhys factor (S_M) which gauges the geometric distortion between the ground and excited states, and the spectral full-width at half-maximum ($\Delta\nu_{1/2}$). The emission spectral fitting parameters are summarized in **Table S7.1**. Medium-frequency vibrational mode was estimated in the 1200-1700 cm^{-1} range for all photosensitizers, consistent with ring vibrations in the diimine ligand[401] whereas the low-frequency vibrational mode (500-700 $cm^{-1,}$) arises from Ir-N stretching modes. This is in agreement with values previously reported for analogous Ir(III) photosensitizers. For **Ir-TPPHZ**, **Ir_2-TPPHZ** and **Ir-PHEHAT**, the photoluminescence exhibits structural features, with significantly smaller $\Delta\nu_{1/2}$ values, reminiscent of ligand-centered emission. This observation is clearly indicative of the participation of a LC excited state in the steady-state photoluminescence spectra. Thus, similarly to compounds described by by Zanoni *et al.*,[402] we propose that **Ir-TPPHZ**, **Ir_2-TPPHZ** and **Ir-PHEHAT** are characterized by an inversion in excited-state arrangement, with photoluminescence originating from MLLCT at 298 K and LC at 77 K. To summarize, all complexes emit from a ^{3}MLLCT excited state in acetonitrile and acetonitrile/water mixture at room temperature. In frozen medium, **Ir-TAPHAT**, **Ir-HATPHE** and **Ir-TAP** remain emissive from ^{3}MLLCT excited state whereas the nature of the emissive excited state of of **Ir-TPPHZ**, **Ir_2-TPPHZ** and **Ir-PHEHAT** is modified and becomes mainly ^{3}LC in character. Further investigation by theoretical calculations (TD-DFT) or by measuring the evolution of the steady-state

photoluminescence throughout a temperature gradient would be very informative but is beyond the scope of the present study.

7.2.3 Electrochemistry

The photosensitizers were electrochemically characterized by differential pulse voltammetry and cyclic voltammetry in acetonitrile containing 0.1M $TBAPF_6$ and the electrochemical data are tabulated in **Table 7.2**. The combination of the **^{dFCF3}ppy** with the different diimine ligands led to Ir(III/IV) oxidation potential greater than 2.0 V *vs* NHE, a value slightly more positive than the reference complex $[Ir(^{dFCF3}ppy)_2(dtbbpy)]^+$ (dtbbpy = 4,4'-di-*tert*-butyl-2,2'-dipyridyl) of 1.93 V *vs* NHE.[214] The electrochemical data for **Ir-TPPHZ** showed a first reduction wave at –0.70 V *vs* NHE that was attributed to the one-electron reduction of the TPPHZ ligand.[347] This reduction process is facilitated compared to the –1.13 V *vs* NHE reported for $[Ir(^{dFCF3}ppy)_2(dtbbpy)]^+$ due to the better π-accepting character of **TPPHZ** compared to dtbbpy. Two other reduction peaks were observed at –1.26 V and –1.47 V *vs* NHE that were attributed to a second reduction occurring on the **TPPHZ** ligand and the reduction of one of the **^{dFCF3}ppy** ligands, respectively.[347] In comparison, the binuclear complex **Ir_2-TPPHZ** exhibited a more positive first reduction wave at –0.45 V *vs* NHE. This value is more positive than those determined for **Ir-TPPHZ** and is due to the presence of the second electron deficient Ir(III) center. This behavior was also reported by S. Campagna and co-workers using the mononuclear $[Ru(phen)_2(TPPHZ)]^{2+}$. For the latter, they observed that the first reduction of the **TPPHZ** occurred at –0.75 V *vs* NHE, whereas this reduction process occurred at –0.53 V *vs* NHE for the binuclear $[Ru(phen)_2(\mathbf{TPPHZ})Ru(phen)_2]^{4+}$.[368] For **$Ir_2$-TPPHZ** and **$Ir_2$-TAPHAT** the observation of one oxidation wave at a unique potential indicates that the two Ir(III) centers are oxidized simultaneously by a two electron process, which means that they behave independently and are thus weakly coupled.[345] **Ir_2TAPHAT** exhibits the most positive Ir(III/IV) oxidation potential (2.14 V *vs* NHE) due to the presence of the more π-accepting **TAPHAT** ligand. For this binuclear complex, three reduction peaks are observed at –0.21, –0.38 and –0.47 V *vs* NHE with a strong overlap between the second and third reduction

waves. These three reduction processes can be attributed to successive reduction of the **TAPHAT** ligand.[399]

Table 7.2. Ground- and excited-state electrochemical properties of the Ir(III) complexes.

	E_{ox}[a] (V *vs* NHE)	E_{red}[a] (V *vs* NHE)	E_{red}*[b] (V *vs* NHE)
Ir-TPPHZ	2.03	–0.70	2.07
Ir-PHEHAT	2.03	–0.57	2.10
Ir-HATPHE	2.12	–0.39	1.94
Ir_2-TAPHAT	2.14	– 0.21	2.09
Ir_2-TPPHZ	2.03	– 0.45	2.02
Ir-TAP	2.09	–0.48	1.88
$[Ir(^{dFCF3}ppy)_2(dtbbpy)]^{+}$[214]	1.93[e]	–1.13[e]	1.45

[a] Electrochemical data (in V *vs* NHE, converted from V *vs* Ag/AgCl reference electrode by adding 0.205 V to the measured value) of the indicated Ir(III) photosensitizers (1 mM) recorded in argon purged acetonitrile with tetrabutylammonium hexafluorophosphate (0.1 M) as supporting electrolyte (scan rate : 0.1 V/s). [b] The E_{00} were determined by fitting a tangent line on the blue edge of the corrected PL spectra to the emission baseline.[403, 404]

The different chelation site of the planar ligand in the **Ir-PHEHAT** and **Ir-HATPHE** induced a more positive oxidation peak (2.12 V *vs* NHE) for **Ir-HATPHE** compared to **Ir-PHEHAT** (2.03 V *vs* NHE). This is in line with the Ir(III) center chelated to a more π-accepting ligand (**HATPHE**), shifting the Ir(III/IV) potential to more positive value, thus following the same trend as what has been reported for Ru(II) complexes.[349] In contrast, the first ligand-centered reduction is less negative for **Ir-HATPHE** (–0.39 V *vs* NHE) than for **Ir-PHEHAT** (–0.57 V *vs* NHE). Finally, for **Ir-TAP** the two first reduction peaks at –0.48 V and – 1.14 V *vs* NHE can safely be attributed to two successive reduction of the **TAP** ligand.[42, 405]

7.2.4 Excited-state reactivity

The electrochemical data and the steady-state photoluminescence spectra allowed to determine the corresponding excited-state reduction potentials (E_{red}^*) (**Table 7.2**). The photosensitizers exhibited excited-state reduction

potentials that range between 1.88 and 2.10 V *vs* NHE. Given their very positive excited-state reduction potential, these Ir(III) photosensitizers should be capable of oxidizing iodide, bromide, and chloride in acetonitrile as well as in water-like conditions, although for chloride, lower excited-state quenching rate constant are expected based on thermodynamic parameters (estimated ΔG_{et} = 0.00 to 0.42 eV) The excited-state quenching was monitored in argon purged acetonitrile/water (50:50) by time-resolved photoluminescence which showed moderate to drastic decrease of the excited-state lifetime upon addition of tetra-*n*-butylammonium halide salts. Stern-Volmer analysis yielded a linear relationship from which a quenching rate constant (k_q) was determined (**Table 7.3**).

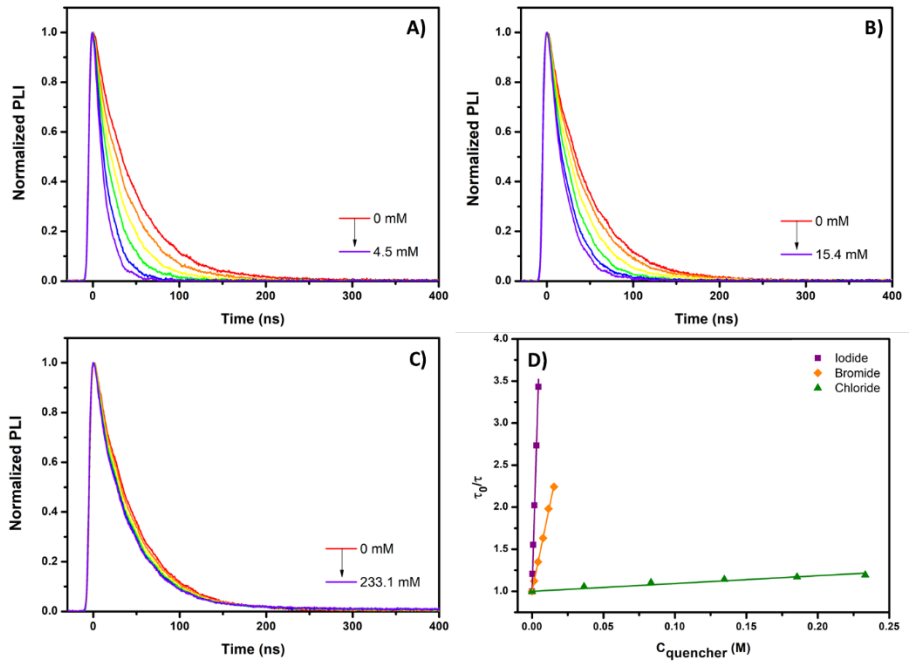

Figure 7.4. Time-resolved photoluminescence of **Ir-PHEHAT** with increasing amount of A) tetra-*n*-butylammonium iodide, B) tetra-*n*-butylammonium bromide and C) tetra-*n*-butylammonium chloride in argon purged acetonitrile/water (50:50). D) The corresponding Stern-Volmer plots obtained with iodide (purple), bromide (orange) and chloride (green). The corresponding quenching rate constants are gathered in **Table 7.3.**

All the photosensitizers were efficiently quenched by iodide and bromide in these conditions, with quenching rate constants in the ~10^{10} $M^{-1}s^{-1}$ and 10^{8}-10^{9} $M^{-1}s^{-1}$ range, respectively (**Table 7.3**). Excited-state quenching was also observed with chloride, although with a lower quenching rate constant (10^{6}-10^{8} $M^{-1}s^{-1}$), as expected from thermodynamic parameters.[41] Aqueous halide oxidation occurs at potentials $E_{1/2}(X^{\bullet/-})$ of 1.33, 1.93 and ~2.1-2.3V *vs* NHE for iodide, bromide and chloride, respectively.[41] Importantly, the steady-state UV absorption spectrum of iodide in a 50/50 acetonitrile/water mixture closely resembles the one obtained in pure water, indicating similar solvation environments for the halide (**Figure 7.4**). Consequently, the one-electron reduction potential of each halides in the acetonitrile/water mixture is likely comparable to that in neat water.[136] Hence, the quenching rate constant determined herein in acetonitrile/water 50:50 mixture followed the expected periodic trend I>Br>Cl according to $E_{1/2}(X^{\bullet/-})$.

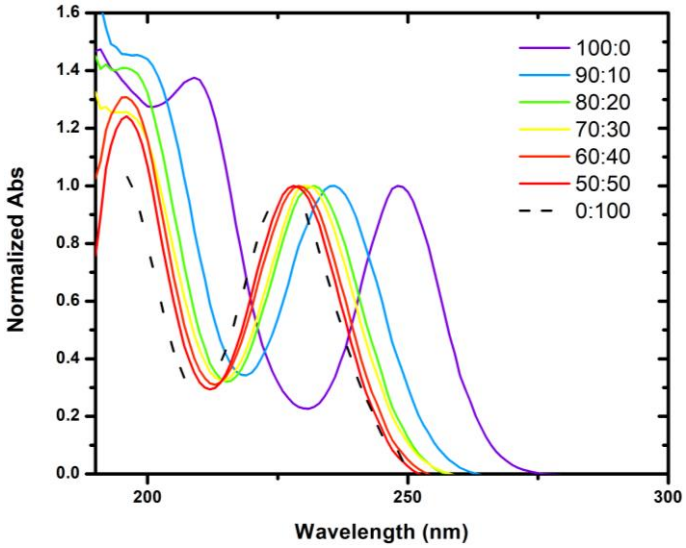

Figure 7.4. UV absorption spectra of *tetra-n*-butyliodide recorded in acetonitrile/water 100/0 → 50/50 mixtures (solid lines) compared to the one of potassium iodide (dashed black line) in water.

Table 7.3. Quenching rate constants for the Ir(III) photosensitizers with I^-, $Br^-$and Cl^- in acetonitrile/water 50:50.

	Iodide k_q (M^{-1} s^{-1})	Bromide k_q (M^{-1} s^{-1})	Chloride k_q (M^{-1} s^{-1})
Ir-TPPHZ	1.4×10^{10}	8.0×10^{8}	4.9×10^{6}
Ir-PHEHAT	1.2×10^{10}	1.8×10^{9}	2.0×10^{7}
Ir-HATPHE	1.5×10^{10}	1.9×10^{9}	1.6×10^{7}
Ir_2-TAPHAT	2.0×10^{10}	4.8×10^{9}	1.3×10^{8}
Ir_2-TPPHZ	2.1×10^{10}	4.3×10^{9}	3.6×10^{7}
Ir-TAP	1.3×10^{10}	8.5×10^{8}	2.0×10^{7}

7.2.5 Nanosecond transient absorption spectroscopy

As Stern-Volmer experiments do not inform on the nature of the excited-state quenching process, nanosecond transient absorption spectroscopy (nsTAS) was performed for all the photosensitizers in acetonitrile and acetonitrile/water 50:50 mixture. The Ir(III) complexes were individually irradiated using pulsed 410 nm light in the presence of iodide, bromide and chloride in argon purged solution. In acetonitrile, transient absorption spectra were consistent with excited-state electron transfer from the halides to the excited photosensitizers.

The appearance of a long-lived transient species absorbing at 410 and 580 nm for **Ir-PHEHAT** (**Figure 7.5-A**) was consistent with the formation of the mono-reduced photosensitizer, as confirmed by control experiments using tri-*p*-tolylamine, a reference electron donor (**Figure S7.17**). For **Ir-TPPHZ** and **Ir-TAP**, pulsed light excitation led to absorption changes similar to those observed for **Ir-PHEHAT** with novel transitions appearing around 415 nm and 590 nm for **Ir-TPPHZ (Figure S7.12)** and around 400 nm and 550 nm for **Ir-TAP (Figure S7.16)**. Under pulsed light excitation **Ir-HATPHE** presented a new absorption feature at 405 nm as well as broad signal centered at 650 nm. In the presence of iodide, the formation of $I_2^{\bullet-}$ was evidenced by a novel weak to moderate absorption feature around 750 nm.[54, 55, 230, 231, 241] For **Ir-HATPHE (Figure S7.13)**, the broad $I_2^{\bullet-}$ absorption overlaps with the broad absorption feature associated with the mono-reduced photosensitizer which accounts for the broad absorption signal from 600 nm to 800 nm. Interestingly, these

absorption changes corresponding to the mono-reduced photosensitizers were also observed in the presence of bromide and chloride, albeit with lower intensities. For **Ir_2-TPPHZ** (**Figure S7.15**) and **Ir_2-TAPHAT** (**Figure S7.14**) transient absorption spectra were consistent with excited-state electron transfer from the halides to the excited photosensitizers. Indeed, the appearance of a long-lived transient species absorbing around 600 nm was consistent with the formation of the mono-reduced photosensitizers.

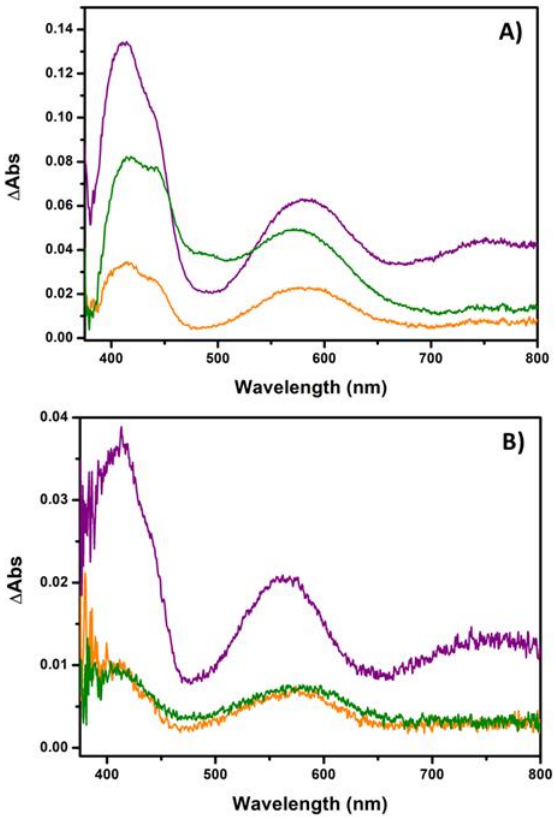

Figure 7.5. Transient absorption spectra of **Ir-PHEHAT** recorded in acetonitrile (A) in the presence of 1 mM iodide (purple), 1 mM bromide (orange) and 1 mM chloride (green) in acetonitrile. Transient absorption spectra of **Ir-PHEHAT** recorded in acetonitrile/water 50:50 mixture (B) in the presence of 5 mM iodide (purple), 15 mM bromide (orange) and 250 mM chloride. Experiments were carried out in argon purged solution at room temperature using 410 nm light irradiation. Spectra were recorded 500 ns after the laser pulse.

Motivated by these results and the encouraging excited-state quenching, nsTAS experiments were also carried out with all the Ir(III) photosensitizers in acetonitrile/water 50:50 mixture. In the presence of iodide, formation of the mono-reduced Ir(III) photosensitizers was observed by nsTAS, demonstrating the efficient iodide oxidation in water-enriched conditions. This was confirmed by the appearance of similar spectral features as those observed in acetonitrile, except for **Ir-HATPHE**, where the absorption signal shifted from 650 nm to 700 nm. With bromide and chloride, **Ir-TPPHZ** and **Ir-PHEHAT** showed similar transient absorption pattern than in acetonitrile. **Ir-HATPHE** exhibited the same absorption signal than with iodide in acetonitrile/water 50:50 mixture. Formation of the monoreduced **Ir_2-TPPHZ** (**Figure S7.15**) and **Ir_2-TAPHAT** (**Figure S7.14**) was also observed by nsTAS, demonstrating that halide oxidation occurred efficiently in water-enriched conditions. The transient absorption around 600 nm point towards excited-state halide oxidation in acetonitrile/water 50:50 mixture. These results are significant as they highlight the potential of these Ir(III) photosensitizers bearing π-extended ligands in the field of halide oxidation applications in water enriched conditions. On the other hand, for **Ir-TAP**, direct evidence for excited-state electron transfer was not observed with bromide and chloride, despite similar quenching rate constants (**Figure S7.16**). The absence of measurable photoproducts could be explained by fast back-electron transfer and/or low cage escape yields. This result underscores the importance of the extended planar ligand in the formation of the mono-reduced Ir(III) photosensitizers and the oxidized halide.

7.2.6 Cage escape yields

The cage escape yields, *i.e.* the efficiency with which the geminate radical pair (*i.e.* the mono-reduced Ir(III) photosensitizers and oxidized halide) separate after excited state electron transfer was quantified using nsTAS.[406] Quantifying this process is important as it has been shown to affect the subsequent reaction that can be carried out using these solvent-separated radicals.[74, 75, 90, 127, 406] Here, cage escape yields were determined by comparative actinometry using $[Ru(bpy)_3]^{2+}$ as the actinometer.[407] The

transient absorption changes corresponding to the singly reduced Ir(III) photosensitizers were compared to the changes in absorption of the reference $[Ru(bpy)_3]^{2+}$ (ES_{ref}) at 450 nm. A $\Delta\varepsilon$ value of –11000 M^{-1} cm^{-1} was used for the actinometer at 450 nm.[131, 132] The transient absorption changes were monitored at 550 nm ($\Delta\varepsilon$ = 2700 M^{-1} cm^{-1}) for **Ir-TAP** and at 430 nm ($\Delta\varepsilon$ = 4500 $M^{-1}cm^{-1}$) for **Ir-HATPHE**. For **Ir-TPPHZ** and **Ir-PHEHAT**, a detection wavelength of 590 nm ($\Delta\varepsilon_{TPPHZ}$ = 5200 M^{-1} cm^{-1} and $\Delta\varepsilon_{PHEHAT}$ = 7800 M^{-1} cm^{-1}) was used in acetonitrile, whereas absorption changes were monitored at 420 nm ($\Delta\varepsilon_{TPPHZ}$ = 12750 M^{-1} cm^{-1} and $\Delta\varepsilon_{PHEHAT}$ = 10800 M^{-1} cm^{-1}) in acetonitrile/water 50:50 in order to improve measurement quality. All the $\Delta\varepsilon$ for the Ir(III) photosensitizers were determined by nsTAS using tri-*p*-tolylamine as reference in acetonitrile and were assumed to remain identical in acetonitrile/water 50:50 mixture (**Figure S7.17**). Cage escape yields (Φ_{CE}) values were obtained by comparing the relative yield of mono-reduced photosensitizer produced (Φ) to the percentage of quenched photoluminescence (%PL) (**Figure 7.6** and **Table 7.4**).

Table 7.4. Cage escape yields (Φ_{CE}) recorded in argon purged acetonitrile and acetonitrile/water 50:50 mixture.

	Iodide		Bromide		Chloride	
	CH_3CN	CH_3CN/H_2O	CH_3CN	CH_3CN/H_2O	CH_3CN	CH_3CN/H_2O
Φ_{CE} **Ir-TPPHZ**	0.63	0.08	0.89	0.10	0.48	0.07
Φ_{CE} **Ir-PHEHAT**	0.81	0.21	0.82	0.03	0.67	0.05
Φ_{CE} **Ir-HATPHE**	0.81	0.19	0.47	0.12	0.86	0.11
Φ_{CE} **Ir_2-TAPHAT**	0.97	0.35	0.74	0.04	0.57	0.05
Φ_{CE} **Ir_2-TPPHZ**	1.00	0.12	0.87	0.02	0.87	0.02
Φ_{CE} **Ir-TAP**	0.95	0.06	1.00	0.00	1.00	0.00

All the reported Ir(III) photosensitizers exhibited large Φ_{CE} in neat acetonitrile. For iodide, **Ir_2-TPPHZ**, **Ir_2-TAPHAT** and **Ir-TAP** exhibited the highest Φ_{CE} of 1.00, 0.97 and 0.95, respectively, whereas the lowest value of 0.63 was obtained with **Ir-TPPHZ**. For bromide, **Ir-TPPHZ** and **Ir-TAP** exhibit the highest Φ_{CE} of 0.89 and 1.00 but the cage escape yields were overall large for

all Ir(III) photosensitizers. Finally, the same general behavior was observed for chloride with Φ_{CE} values from 1.00 and 0.48. These Φ_{CE} values outperform previously reported photosensitizers based on Ru(II)[54, 243] or Fe(III)[408] where values ranged from 0.072 to 0.50 in CH_2Cl_2 are obtained for iodide oxidation. While most halide oxidation studies focus on iodide, only few recent reports have also explored bromide and chloride oxidation. These studies include photo-oxidation of bromide and chloride with Ru(II) photosensitizers in acetone,[135, 238, 239] with Ir(III) photosensitizers in acetonitrile[42] and through the one- or two-photon excitation of *N*-phenylphenothiazine in acetonitrile.[246] Our Ir(III) photosensitizers unambiguously demonstrate their ability to oxidize bromide and chloride in acetonitrile with large Φ_{CE} (0.47-1.00), underscoring their potential for efficient halide oxidation in organic solvents.

Importantly, these Ir(III) photosensitizers were capable of performing halide oxidation in water-enriched conditions. This is particularly noteworthy given the challenging nature of bromide and chloride oxidation in water, which typically requires strong oxidizing species. However, the Φ_{CE} are consistently higher in pure acetonitrile for iodide, bromide and chloride than in acetonitrile/water mixture. For iodide, the larger Φ_{CE} were obtained with **Ir_2-TAPHAT** (0.32) and **Ir-PHEHAT** (0.21). In the case of bromide and chloride, these Φ_{CE} were significantly lower and only reached maximum values of 0.11 for **Ir-HATPHE**. The reactivity of **Ir-TAP**, which exhibited amongst the largest cage escape yields in acetonitrile, is completely turned off in the presence of water, with cage escape yields below 0.06. This observation emphasizes the importance of π-extended diimine ligands to afford large cage escape yields for efficient halide oxidation in water-enriched conditions. In addition, the previously reported $[Ir(tpy\text{-}PyMe)_2]^{5+}$ exhibited low cage escape yields of 0.04 for iodide, bromide and chloride in water using 355 nm light excitation.[182] In our case, the values are slightly larger, notably for iodide oxidation, but visible light excitation could be used, further underscoring the importance of these π-extended diimine ligands.

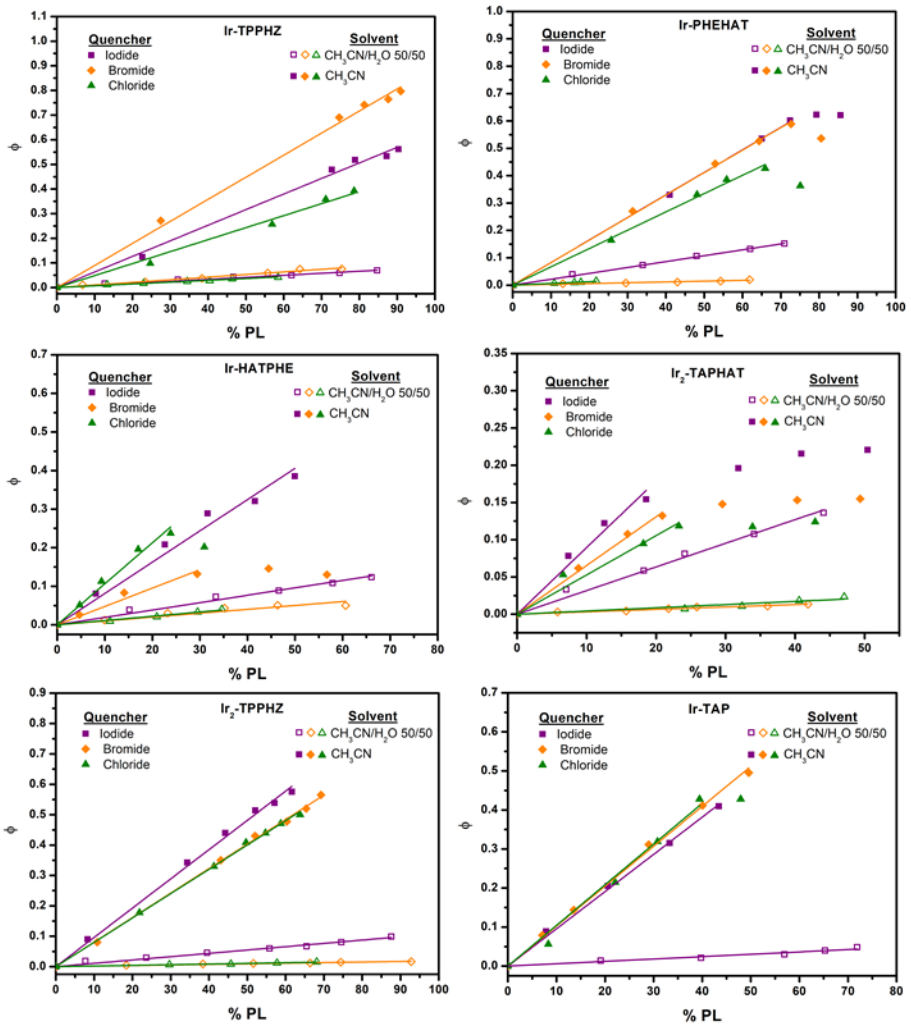

Figure 7.6. Cage escape yields recorded using the six different Ir(III) photosensitizers in argon purged acetonitrile (closed symbols) and acetonitrile/water 50:50 (open symbols) in the presence of iodide (purple), bromide (orange) and chloride (green). Cage escape yields were determined from the initial slope when linear deviation was observed upon increasing halide concentration.

The decrease in cage escape yields between acetonitrile and acetonitrile/water mixture could mostly originate from changes in the nature of the solvent cage as well as from changes in viscosity and dielectric constant (and by extend solvent polarity). Indeed, in acetonitrile/water 50:50 mixture, hydrogen bonding between the acetonitrile and water could contribute to the formation of a more structured solvent. Moreover, increasing solvent polarity

could lead to greater stabilization of the geminate radical pair, favoring geminate charge recombination over the cage escape process. The influence of viscosity on cage escape yields was also reported by Sun *et al.* in a comparative study examining the effect of viscosity on cage escape yields in various solvents, specifically water, acetonitrile, and propylene carbonate.[409] This was also investigated by Wolff *et al*. in mixtures of water/acetonitrile with increased amount of ethylene glycol in thermostatic conditions.[410, 411] As expected, the cage escape yields decreased as the viscosity was increased, in agreement with the viscous drag of the solvent thus decreasing the diffusion limit. Similar effects have been described by other research group.[410-412] In our case, we believe that the addition of water to acetonitrile does not significantly alter the viscosity of the solvent, and we consider this parameter to have little influence on the cage escape process. Several reports have also shown that the cage escape yields increase as the driving force for geminate charge recombination becomes more favourable, further localizing the reaction in the Marcus inverted region.[127, 413-415] In the present case, this does not allow to explain the change in cage escape yields from acetonitrile to water-enriched conditions. Indeed, the one electron reduction potential is expected to be much more positive in these water-enriched conditions, and as such geminate charge recombination should be located further into the Marcus inverted region than in neat acetonitrile. Thus, based on the previously described examples, we believe that the drop-in cage escape yield in most likely due to the increasing viscosity. Nevertheless, we were able to maintain acceptable Φ_{CE} values using π-extended ligands that somehow assist in the cage escape process, thereby limiting the negative impact of the increased viscosity.

7.3 Conclusion

In conclusion, we report a series of Ir(III) photosensitizers that have been fully characterized photophysically and electrochemically. These photosensitizers were shown to exhibit strong absorption in the visible range, with molar absorption coefficients in the 4300-6400 $M^{-1}cm^{-1}$ range between 410 and 450 nm. The electrochemical data and the steady-state photoluminescence spectra allowed to determine the corresponding excited-state reduction

potentials, which ranged between 1.88 and 2.10 V *vs* NHE. All the photosensitizers were shown to be efficiently quenched by iodide, bromide, and chloride in an acetonitrile/water mixture. Importantly, nanosecond transient absorption spectroscopy revealed that excited-state electron transfer of all investigated halides occurred efficiently for all the photosensitizers based on π-extended diimine ligands, with large to moderate cage escape yields. **Ir-TAP** demonstrated a distinct pattern compared to the other complexes. For iodide, bromide, and chloride, this complex exhibited the highest Φ_{CE} value in acetonitrile. However, when the same experiments were conducted in water-enriched conditions, Φ_{CE} was relatively low with iodide compared to the other Ir(III) photosensitizers based on π-extended diimine ligands. This result underscores the importance of the π-extended ligand in the formation of the mono-reduced Ir(III) photosensitizers and the oxidized halides in the investigated series. The comparison between acetonitrile and acetonitrile/water mixtures highlights the critical impact of the solvent environment on the cage-escape yields of these iridium complexes for halide oxidation applications. The experimental verification of excited-state electron transfer in a 50:50 acetonitrile/water mixture, combined with the free chelation site on the π-extended diimine ligand, which could host a catalyst for proton reduction, further expands the applicability of these photosensitizers as candidates for hydrohalic acid splitting.

7.4 Experimental section

The materials and methods used in this chapter are described in ***Chapter X***

Acetonitrile 99.9% (VWR), diethyl ether 99% (VWR), ethylene glycol 99% (Roth), ethanol 99.9% (VWR), NH_4PF_6 99% (Fluorochem), acetic acid glacial ≥ 99.7% (Fischer Chemical), celite (Roth), aluminium oxide, for chromatography, neutral, Brockmann I, 40-300 μm, 60A(Thermo Fischer), silica gel 60 Å for flash column chromatography, 40-63 μm (ROCC), tetra-*n*-butylammonium hexafluorophosphate ≥ 98% (TCI), tri-*p*-tolylamine ≥ 98% (Ambeed) were purchased from commercial suppliers and used as received. Water was purified by a Millipore Milli-Q system. Tetrabutylammonium iodide (TBAI, Sigma-Aldrich, ≥ 99.0 %), tetrabutylammonium bromide (TBABr, Sigma-Aldrich, ≥ 99.0 %), and tetrabutylammonium chloride (TBACl, Sigma-Aldrich, ≥ 97.0 %) were recrystallized from acetone and diethyl ether and stored in a vacuum desiccator. Tetrapyrido[3,2-a:2',3'-c:3'',2''-h:2''',3'''-j]phenazine (TPPHZ),[347] 1,4,5,8-tetraazaphenanthrene[9,10-b]1,4,5,8,9,12-hexaazatriphenylene (TAPHAT),[399] 2-(2,4-difluorophenyl)-5-(trifluoromethyl)pyridine,[416] 1,4,5,8-tretraazaphenanthrene (TAP),[417] 9,10-diamino-1,4,5,8-tetraazaphenanthrene ($diNH_2TAP$),[417] 5,6-diamino-1,10-phenanthroline ($diNH_2phen$),[347] 1,10-phenanthroline-5,6-dione (phd),[418] $[Ir(^{dFCF3}ppy)_2(\mu\text{-}Cl)]_2$.[396]

<u>7.4.1 Synthesis</u>

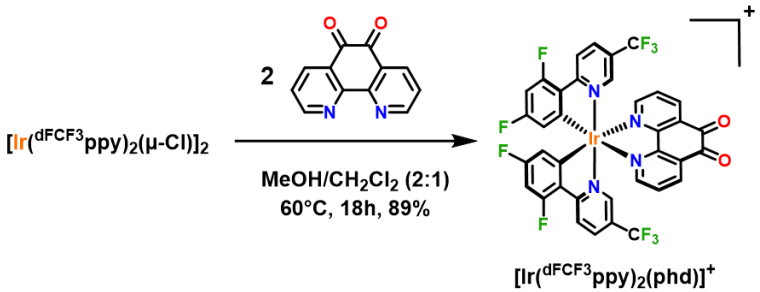

$[Ir(^{dFCF3}ppy)_2(phd)]^+.PF_6^-$: $[Ir(^{dFCF3}ppy)_2(\mu\text{-}Cl)]_2$ (200 mg, 0.134 mmol, 1 eq.) and **phd** (62 mg, 0.295 mmol, 2.2 eq.) were suspended in 18 mL of

MeOH/CH_2Cl_2 (2:1) mixture in a sealed tube. The solution was purged with argon and heated at 60°C for 18 hours under stirring. After reaction, the mixture was brought to room temperature and the solvents were removed under reduced pressure. The solid was dissolved in a minimum amount of MeOH and a saturated solution of NH_4PF_6 was added to induce precipitation of the complex. The precipitate was collected by centrifugation and washed three times with water and Et_2O to yield **[Ir(^{dFCF3}ppy)$_2$(phd)]$^+$. PF_6^-** as an ocher powder (255 mg, 0.240 mmol, 89%). ^{1}H NMR (300 MHz, CD_3CN) δ 8.69 (dd, *J* = 8.0, 1.5 Hz, 2H), 8.52 (dd, *J* = 8.8, 2.9 Hz, 2H), 8.36 – 8.04 (m, 4H), 7.99 – 7.52 (m, 4H), 6.82 (ddd, *J* = 12.8, 9.4, 2.3 Hz, 2H), 6.10 – 5.68 (m, 2H) ppm.

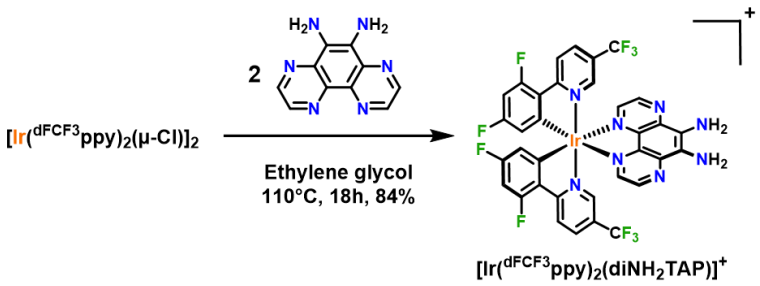

[Ir(^{dFCF3}ppy)$_2$(diNH$_2$TAP)]$^+$.PF_6^-: [Ir(^{dFCF3}ppy)$_2$(μ-Cl)]$_2$ (150 mg; 0.101 mmol, 1 eq.) and **diNH$_2$TAP** (47 mg, 0.221 mmol, 2.2 eq.) were suspended in argon purged ethylene glycol (9 mL) in a sealed tube. The reaction mixture was heated at 110°C for 18 hours under stirring. After reaction, the mixture was brought to room temperature and the complex was precipitated by the addition of a saturated solution of NH_4PF_6. The product was collected by centrifugation and washed three times with water and Et_2O to yield **[Ir(^{dFCF3}ppy)$_2$(diNH$_2$TAP)]$^+$.PF_6^-** as a brown solid that was used without further purifications (181 mg, 0.169 mmol, 84%). The product was stored under argon atmosphere in a freezer as degradation was observed over time at room temperature (5 months). ^{1}H NMR (300 MHz, CD_3CN) δ 8.98 (d, *J* = 2.6 Hz, 1H), 8.46 – 8.35 (m, 2H), 8.11 (d, *J* = 2.4 Hz, 2H), 8.01 (d, *J* = 2.6 Hz,

2H), 7.49 (s, 2H), 6.81 (ddd, *J* = 12.6, 9.3, 2.4 Hz, 2H), 5.87 (dd, *J* = 8.6, 2.6 Hz, 2H), 5.45 (s, 4H) ppm.

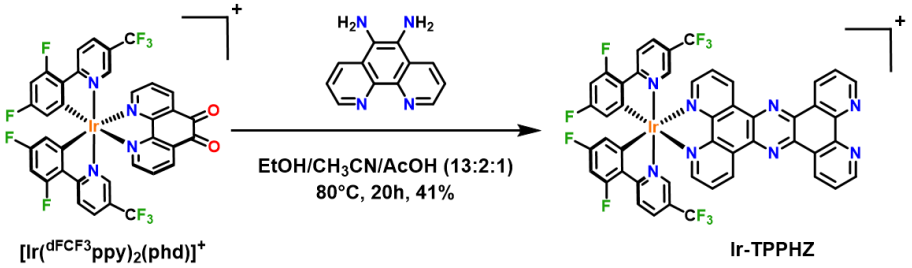

[Ir(^dFCF3ppy)₂(TPPHZ)]⁺.PF₆⁻ (Ir-TPPHZ): [Ir(^dFCF3ppy)₂(phd)]⁺.PF₆⁻ (100 mg, 0.094 mmol, 1eq.) and **diNH₂phen** (23.7 mg, 0.113 mmol, 1.2 eq.) were refluxed in 16 mL of EtOH/CH_3CN/AcOH (13:2:1) mixture for 20h. After reaction, the mixture was brought to room temperature. The green solution was purged with O_2, causing the color to shift from green to brown-yellow. The solvents were removed under reduced pressure and the crude product purified by column chromatography (SiO_2, $CH_3CN/H_2O/KNO_{3(sat.)}$, 7:0.5:0.5) yielding **[Ir(^dFCF3ppy)₂(TPPHZ)]⁺** as an yellow solid. The complex was dissolved in water and isolated as a PF_6^- salt after ion metathesis. The precipitate was collected by centrifugation and washed three times with cold water and Et_2O to yield **[Ir(^dFCF3ppy)₂(TPPHZ)]⁺.PF₆⁻** (47.2 mg, 0.038 mmol, 41%). ^{1}H NMR (300 MHz, CD_3CN) δ 9.84 – 9.50 (m, 4H), 8.86 – 8.71 (m, 2H), 8.54 (dd, *J* = 5.2, 1.4 Hz, 4H), 8.19 – 8.13 (m, 2H), 8.09 (dd, *J* = 8.3, 5.2 Hz, 2H), 8.01 (s, 2H), 7.87 (dd, *J* = 8.1, 4.5 Hz, 2H), 6.89 (ddd, *J* = 11.8, 9.4, 2.4 Hz, 2H), 5.98 (dd, *J* = 8.4, 2.4 Hz, 2H) ppm. HRMS(ESI) m/z calculated for $[C_{48}H_{22}N_8F_{10}{}^{191}Ir]^+ + H^+$ = 546.07405; found 546.07538.

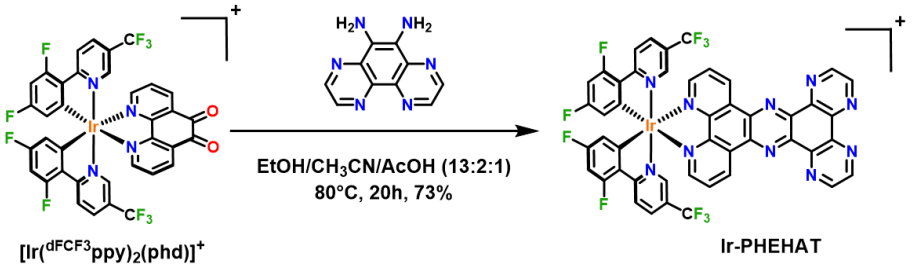

[Ir(^{dFCF3}ppy)$_2$(PHEHAT)]$^+$.PF$_6^-$ (Ir-PHEHAT): [Ir(^{dFCF3}ppy)$_2$(phd)]$^+$.PF$_6^-$ (200 mg, 0.188 mmol, 1eq.) and **diNH$_2$TAP** (47.9 mg, 0.225 mmol, 1.2 eq.) were refluxed in 32 mL of EtOH/CH$_3$CN/AcOH (13:2:1) mixture for 20h. After reaction, the mixture was brought to room temperature. The solvents were removed under reduced pressure and the crude product purified by column chromatography (SiO$_2$, CH$_3$CN/H$_2$O/KNO$_{3(sat.)}$, 9:0.5:0.5) yielding **[Ir(^{dFCF3}ppy)$_2$(PHEHAT)]$^+$** as an ocher solid. The complex was dissolved in water and isolated as a PF$_6^-$ salt after ion metathesis. The precipitate was collected by centrifugation and washed three times with cold water and Et$_2$O to yield **[Ir(^{dFCF3}ppy)$_2$(PHEHAT)]$^+$.PF$_6^-$** (204 mg, 0.164 mmol, 73%). ^{1}H NMR (300 MHz, CD$_3$CN) δ 9.99 (dd, *J* = 8.3, 1.5 Hz, 2H), 9.33 (d, *J* = 0.8 Hz, 4H), 8.64 – 8.41 (m, 4H), 8.27 – 8.06 (m, 4H), 7.83 – 7.58 (m, 2H), 6.87 (ddd, *J* = 12.8, 9.4, 2.3 Hz, 2H), 5.98 (dd, *J* = 8.4, 2.6 Hz, 2H) ppm. HRMS(ESI) m/z calculated for [C$_{46}$H$_{20}$N$_{10}$F$_{10}$^{191}Ir]$^+$ = 1093.13132; found 1093.13193.

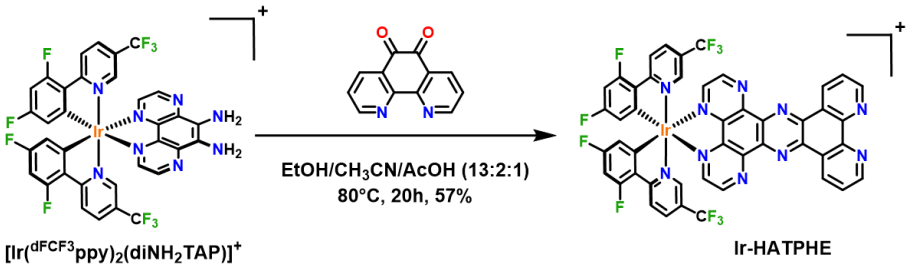

[Ir(^{dFCF3}ppy)$_2$(HATPHE)]$^+$.PF$_6^-$ (Ir-HATPHE): [Ir(^{dFCF3}ppy)$_2$(diNH$_2$TAP)]$^+$.PF$_6^-$ (100 mg, 0.094 mmol, 1eq.) and **phd** (23.6 mg, 0.112 mmol, 1.2 eq.) were refluxed in 16 mL of EtOH/CH$_3$CN/AcOH

(13:2:1) mixture for 20h. After reaction, the mixture was brought to room temperature. The solvents were removed under reduced pressure and the crude product purified by column chromatography (SiO_2, $CH_3CN/H_2O/KNO_{3(sat.)}$, 9:0.5:0.5) yielding **[Ir(^{dFCF3}ppy)$_2$(HATPHE)]$^+$** as an orange solid. The complex was dissolved in water and isolated as a PF_6^- salt after ion metathesis. The precipitate was collected by centrifugation and washed three times with cold water and Et_2O to yield **[Ir(^{dFCF3}ppy)$_2$(HATPHE)]$^+$.PF$_6^-$** (66.2 mg, 0.053 mmol, 57%). ^{1}H NMR (300 MHz, CD_3CN) δ 9.93 (dd, *J* = 8.2, 1.7 Hz, 2H), 9.50 (d, *J* = 2.6 Hz, 2H), 9.28 (dd, *J* = 4.7, 1.7 Hz, 2H), 8.69 – 8.45 (m, 4H), 8.25 – 8.04 (m, 4H), 7.79 (s, 2H), 7.03 – 6.75 (m, 2H), 5.94 (dd, *J* = 8.4, 2.2 Hz, 2H) ppm. HRMS(ESI) m/z calculated for $[C_{46}H_{20}N_{10}F_{10}{}^{191}Ir]^+ + H^+$ = 547.06930; found 547.07050.

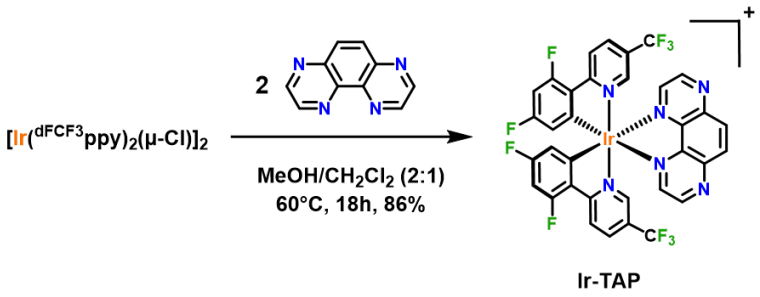

[Ir(^{dFCF3}ppy)$_2$(TAP)]$^+$.PF$_6^-$ (Ir-TAP): [Ir(^{dFCF3}-ppy)$_2$(μ-Cl)]$_2$ (150 mg; 0.101 mmol, 1 eq.) and **TAP** (40.3 mg, 0.221 mmol, 2.2 eq.) were suspended in 12 mL of MeOH/CH_2Cl_2 (2:1) mixture in a sealed tube. The solution was purged with argon and heated at 60°C for 18 hours under stirring. After reaction, the mixture was brought to room temperature and the solvents were removed under reduced pressure. The solid was dissolved in a minimum amount of MeOH and a saturated solution of NH_4PF_6 was added to induce precipitation of the complex. The precipitate was collected by centrifugation and washed three times with water and Et_2O to yield **[Ir(^{dFCF3}ppy)$_2$(TAP)]$^+$. PF$_6^-$** as a yellow powder (180 mg, 0.173 mmol, 86%). ^{1}H NMR (300 MHz, CD_3CN) δ 9.26 (d, *J* = 2.5 Hz, 2H), 8.63 (s, 2H), 8.49 (dd, *J* = 8.9, 2.9 Hz, 2H), 8.37 (d, *J* = 2.6 Hz, 2H), 8.15 (dd, *J* = 8.8, 2.2 Hz, 2H), 7.62 – 7.45 (m, 2H), 6.86 (ddd, *J* = 12.8,

9.4, 2.3 Hz, 2H), 5.91 (dd, *J* = 8.3, 2.7 Hz, 2H). HRMS(ESI) m/z calculated for $[C_{46}H_{20}N_{10}F_{10}{}^{191}Ir]^+$ = 889.08772; found 889.08843.

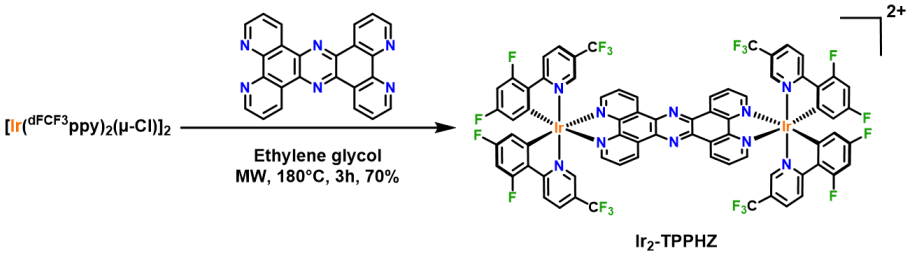

Ir_2-TPPHZ

$[Ir(^{dFCF3}ppy)_2(TPPHZ)\ Ir(^{dFCF3}ppy)_2]^{2+}.2PF_6^-$ (Ir_2-TPPHZ). $[Ir(^{dFCF3}ppy)_2(\mu\text{-}Cl)]_2$ (200 mg, 0.134 mmol, 1 eq.) and **TPPHZ** (43 mg, 0.112 mmol, 0.83 eq.) were suspended in 16 mL of ethylene glycol in a microwave tube. The mixture was then heated at 180°C for 3 hours under microwave irradiation (maximum power = 600W). The solution was then allowed to cool to room temperature and diluted with 10 ml of water. The mixture was filtered on a Millipore syringe filter (0.45 mm) and a NH_4PF_6 saturated aqueous solution was added to induce precipitation. The precipitate was collected by centrifugation and washed with water (three times), ethanol (two times) and diethyl ether (three times). The iridium complex was isolated as a yellow powder (164 mg, 0.078 mmol, 70%). ^{1}H NMR (300 MHz, CD_3CN) δ 10.15 (dd, *J* = 8.3, 1.4 Hz, 4H), 8.66 – 8.43 (m, 8H), 8.28 – 8.02 (m, 8H), 7.69 (s, 4H), 6.87 (ddd, *J* = 12.8, 9.4, 2.3 Hz, 4H), 5.98 (dd, *J* = 8.5, 2.4 Hz, 4H). HRMS(ESI) m/z calculated for $[C_{72}H_{32}F_{20}N_{10}{}^{191}Ir_2]^{2+}$ = 900.08581; found 901.08639.

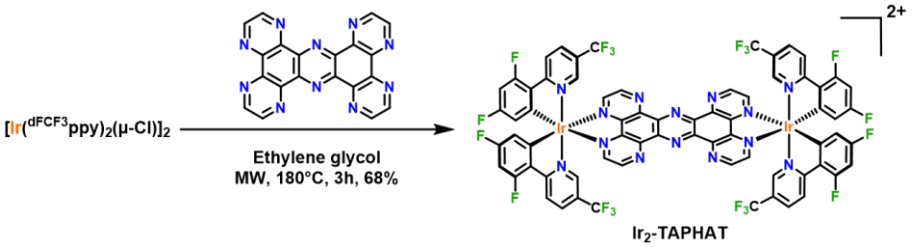

Ir_2-TAPHAT

[Ir(^{dFCF3}ppy)$_2$(TAPHAT) Ir(^{dFCF3}ppy)$_2$]$^{2+}$.2PF$_6^-$ (Ir$_2$-TAPHAT). [Ir(^{dFCF3}ppy)$_2$(μ-Cl)]$_2$ (200 mg, 0.134 mmol, 1 eq.) and **TAPHAT** (43.2 mg, 0.112 mmol, 0.83 eq.) were suspended in 16 mL of ethylene glycol in a microwave tube. The mixture was then heated at 180°C for 3 hours under microwave irradiation (maximum power = 600W). The solution was then allowed to cool down at room temperature and diluted with 10 ml of water. The solution was then allowed to cool to room temperature and diluted with 10 ml of water. The mixture was filtered on a Millipore syringe filter (0.45 mm) and a NH_4PF_6 saturated aqueous solution was added to induce precipitation. The precipitate was collected by centrifugation and washed with water (three times), ethanol (two times) and diethyl ether (three times). The iridium complex was isolated as a dark brown powder (159 mg, 0.076 mmol, 68%). ^{1}H NMR (300 MHz, CD_3CN) δ 9.55 (d, *J* = 2.6 Hz, 4H), 8.61 (d, *J* = 2.6 Hz, 4H), 8.56 (d, *J* = 7.7 Hz, 4H), 8.20 (d, *J* = 9.5 Hz, 4H), 7.73 (s, 4H), 7.16 – 6.62 (m, 4H), 5.94 (dd, *J* = 8.6, 2.5 Hz, 4H). HRMS(ESI) m/z calculated for $[C_{68}H_{28}F_{20}N_{14}{}^{191}Ir_2]^{2+}$ = 902.07631; found 903.07716.

7.4.2 77 K Steady-state photoluminescence

Table S7.1 Emission Parameters for the indicated complexes evaluated by Franck−Condon lineshape analysis of photoluminescence spectra at 77K according to **Equation 10.1 (Chapter X)**.

	E_{00} / cm^{-1}	$\hbar\omega_m$ / cm^{-1}	S_m	$\hbar\omega_m$ / cm^{-1}	S_n	$\nu_{1/2}$ / cm^{-1}
Ir-HATPHE	17820	1720	0.690	500	0.520	2340
Ir-TAP	19760	1460	0.850	630	0.710	1850
Ir_2-TAPHAT	17920	1210	0.440	1290	0.850	2160
Ir-PHEHAT	21100	1440	0.940	690	0.400	510
Ir-TPPHZ	21100	1480	0.690	670	0.430	530
Ir_2-TPPHZ	21380	1470	0.670	680	0.370	550

	E_{00} / cm^{-1}	E_{00} / nm	E_{00} / eV
Ir-HATPHE	17820	561	2.21
Ir-TAP	19760	506	2.45
Ir_2-TAPHAT	17920	558	2 .22
Ir-PHEHAT	21100	474	2.62
Ir-TPPHZ	21100	474	2.62
Ir_2-TPPHZ	21380	468	2.65

7.4.3 Electrochemistry

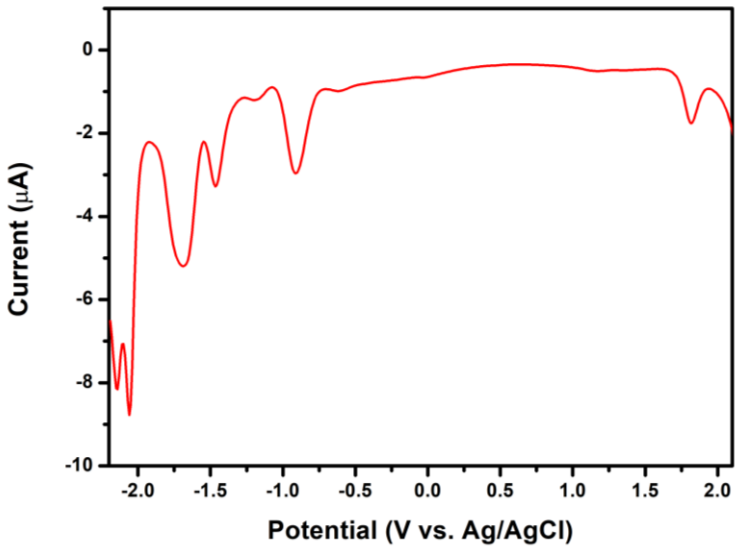

Figure S7.1. Differential pulse voltammogram of **Ir-TPPHZ** (1 mM) in argon purged acetonitrile (0.05 V/s) with tetrabutylammonium hexafluorophosphate (0.1M) as supporting electrolyte.

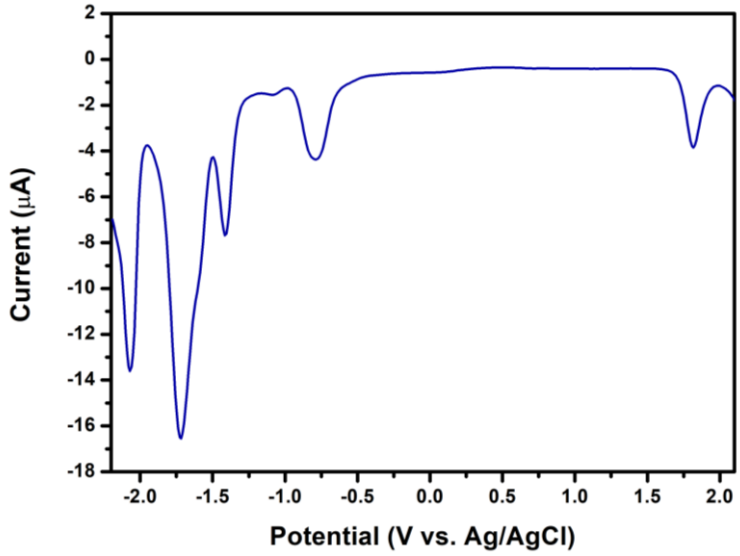

Figure S7.2. Differential pulse voltammogram of **Ir-PHEHAT** (1 mM) in argon purged acetonitrile (0.05 V/s) with tetrabutylammonium hexafluorophosphate (0.1M) as supporting electrolyte.

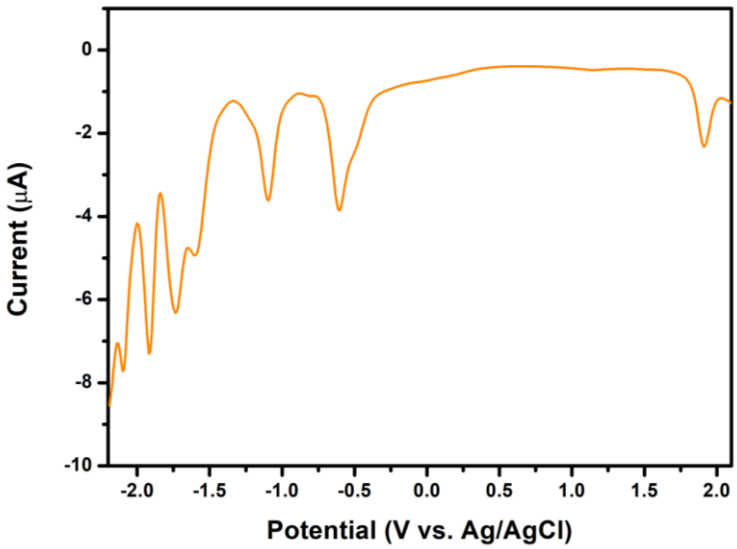

Figure S7.3. Differential pulse voltammogram of **Ir-HAT˙PHE** (1 mM) in argon purged acetonitrile (0.05 V/s) with tetrabutylammonium hexafluorophosphate (0.1M) as supporting electrolyte.

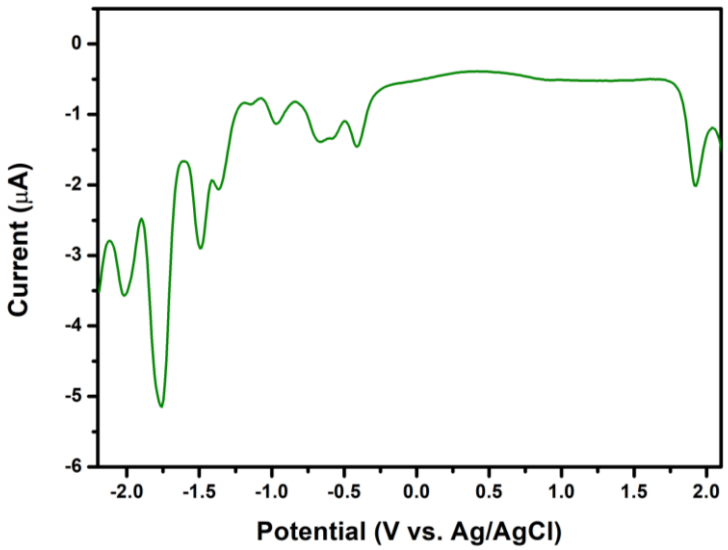

Figure S7.4. Differential pulse voltammogram of **Ir_2-TAPHAT** (1 mM) in argon purged acetonitrile (0.05 V/s) with tetrabutylammonium hexafluorophosphate (0.1M) as supporting electrolyte.

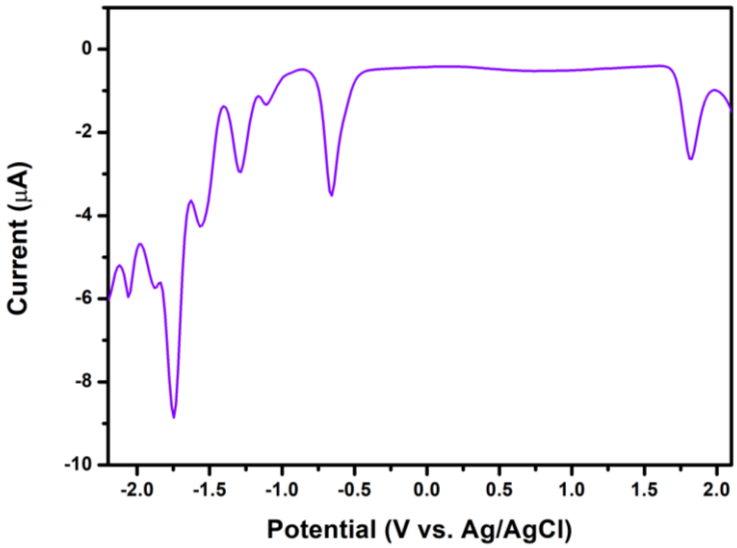

Figure S7.5. Differential pulse voltammogram of **Ir_2-TPPHZ** (1 mM) in argon purged acetonitrile (0.05 V/s) with tetrabutylammonium hexafluorophosphate (0.1M) as supporting electrolyte.

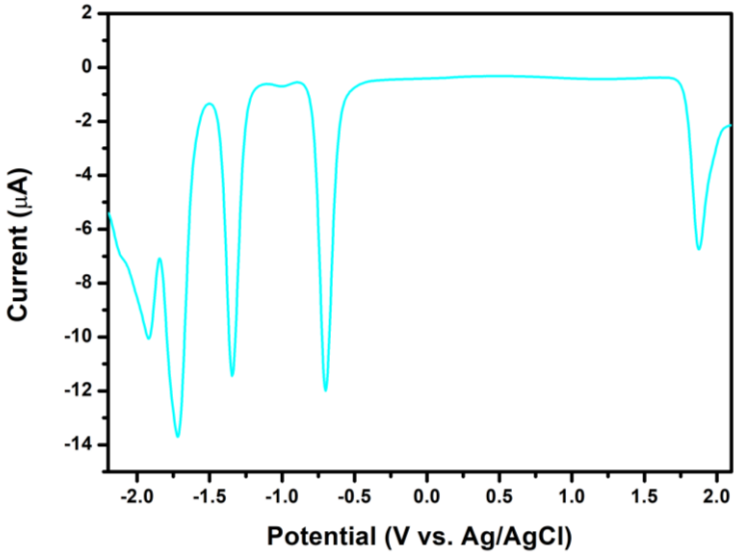

Figure S7.6. Differential pulse voltammogram of **Ir-TAP** (1mM) in argon purged acetonitrile (0.05 V/s) with tetrabutylammonium hexafluorophosphate (0.1M) as supporting electrolyte.

7.4.4 Stern-Volmer Experiments

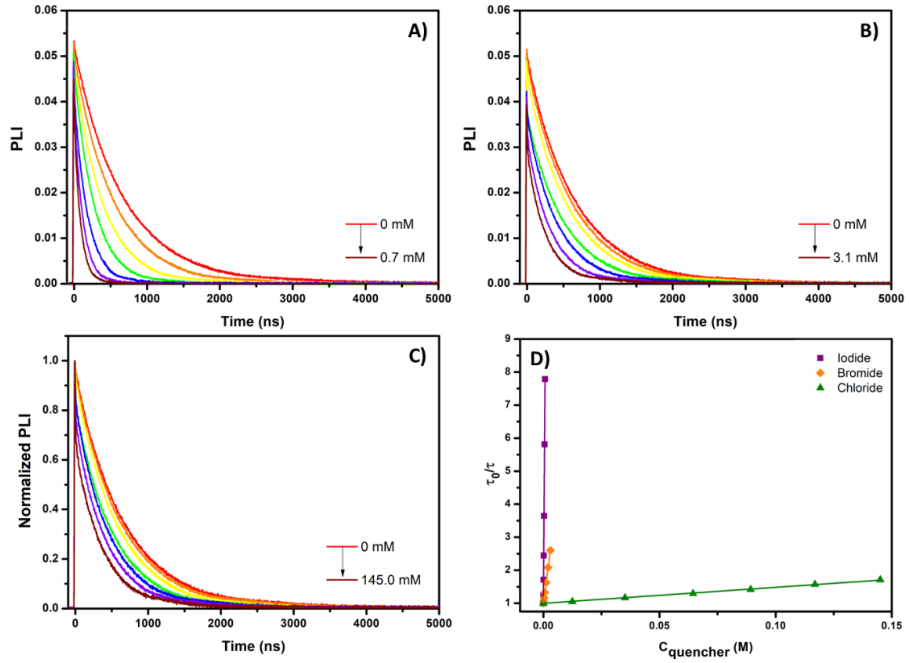

Figure S7.7. Time resolved photoluminescence of **Ir-TPPHZ** with increasing amount of A) tetrabutylammonium iodide, B) tetrabutylammonium bromide and C) tetrabutylammonium chloride in acetonitrile/water (50:50). D) Corresponding Stern-Volmer plots obtained with iodide (purple), bromide (orange) and chloride (green). The corresponding quenching rate constants are gathered in **Table 7.3.**

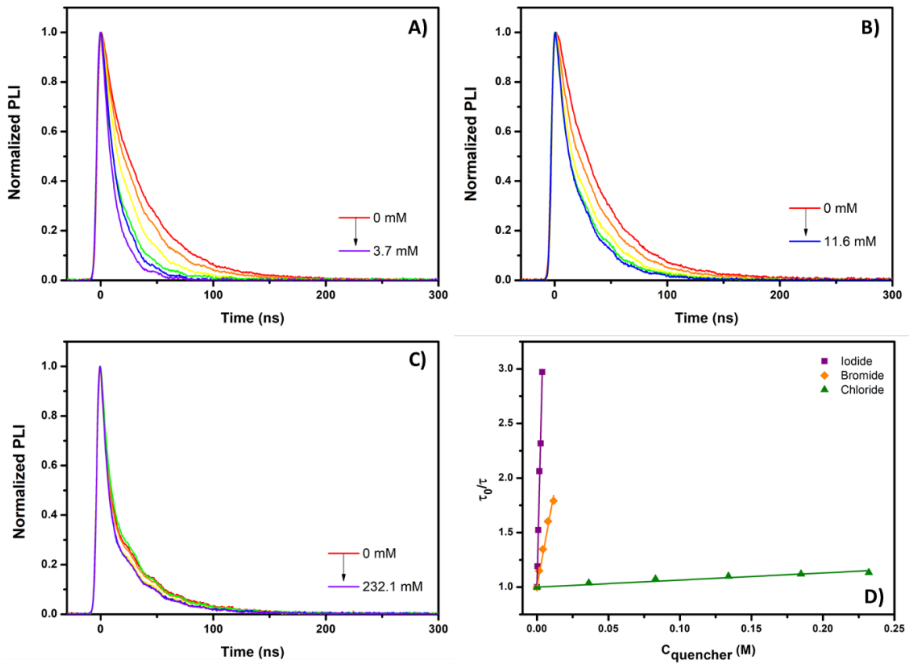

Figure S7.8. Time resolved photoluminescence of **Ir-HATPHE** with increasing amount of A) tetrabutylammonium iodide, B) tetrabutylammonium bromide and C) tetrabutylammonium chloride in acetonitrile/water (50:50). D) Corresponding Stern-Volmer plots obtained with iodide (purple), bromide (orange) and chloride (green). The corresponding quenching rate constants are gathered in **Table 7.3.**

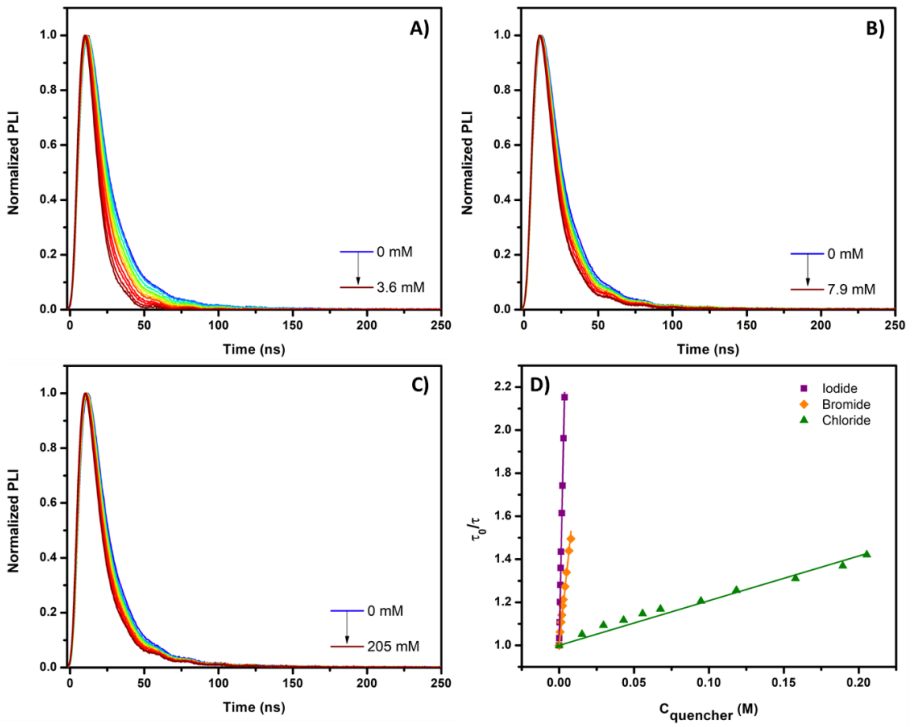

Figure S7.9. Time resolved photoluminescence of **Ir_2-TAPHAT** with increasing amount of A) tetrabutylammonium iodide, B) tetrabutylammonium bromide and C) tetrabutylammonium chloride in acetonitrile/water (50:50). D) Corresponding Stern-Volmer plots obtained with iodide (purple), bromide (orange) and chloride (green). The corresponding quenching rate constants are gathered in **Table 7.3.**

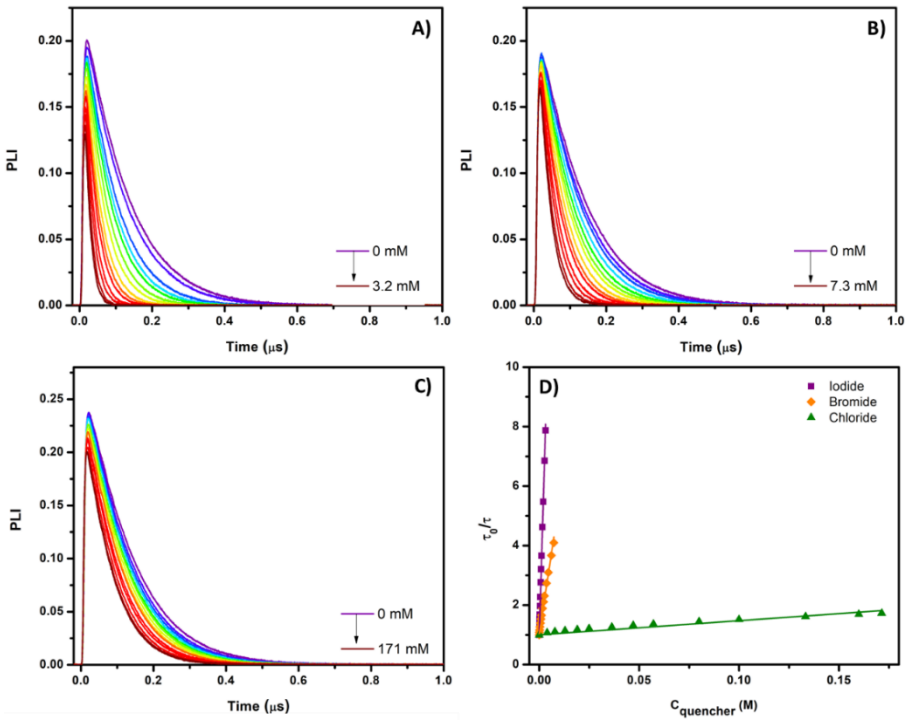

Figure S7.10. Time resolved photoluminescence of **Ir-HATPHE** with increasing amount of A) tetrabutylammonium iodide, B) tetrabutylammonium bromide and C) tetrabutylammonium chloride in acetonitrile/water (50:50). D) Corresponding Stern-Volmer plots obtained with iodide (purple), bromide (orange) and chloride (green). The corresponding quenching rate constants are gathered in **Table 7.3.**

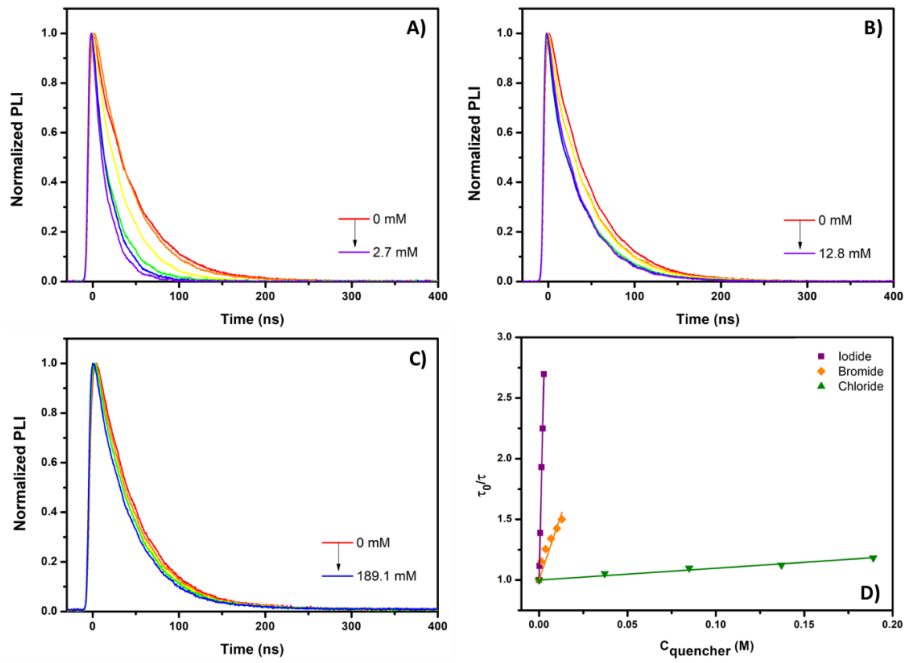

Figure S7.11. Time resolved photoluminescence of **Ir-TAP** with increasing amount of A) tetrabutylammonium iodide, B) tetrabutylammonium bromide and C) tetrabutylammonium chloride in acetonitrile/water (50:50). D) Corresponding Stern-Volmer plots obtained with iodide (purple), bromide (orange) and chloride (green). The corresponding quenching rate constants are gathered in **Table 7.3.**

7.4.5 Nanosecond Transient Absorption Measurements

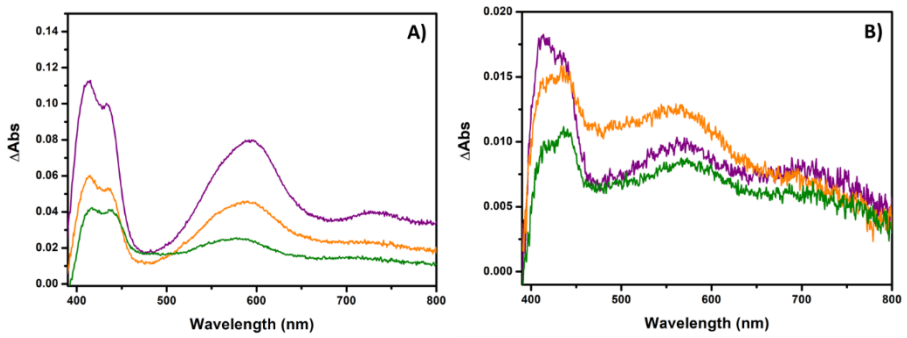

Figure S7.12. Transient absorption spectra of **Ir-TPPHZ** recorded in acetonitrile (A) in the presence of 1 mM iodide (purple), 1 mM bromide (orange) and 1 mM chloride (green) in acetonitrile. Transient absorption spectra of **Ir-TPPHZ** recorded in acetonitrile/water 50:50 mixture (B) in the presence of 1 mM iodide (purple), 5 mM bromide (orange) and 150 mM chloride. Experiments were carried out in argon purged solution at room temperature using 410 nm light irradiation. Spectra were recorded 500 ns after the laser pulse in acetonitrile and 1 μs after the laser pulse in acetonitrile/water 50:50 mixture.

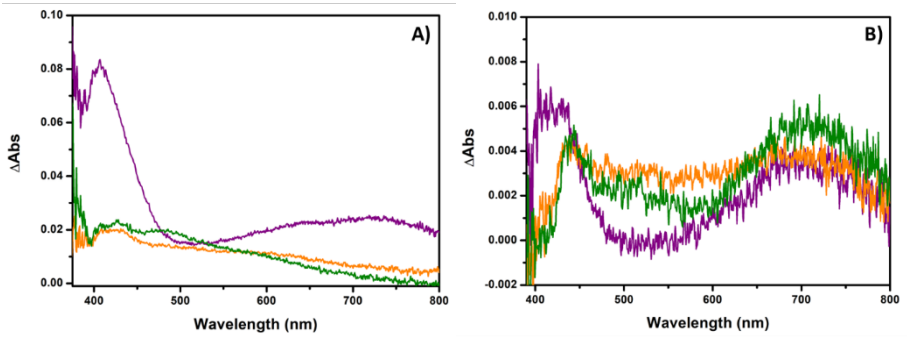

Figure S7.13. Transient absorption spectra of **Ir-HATPHE** recorded in acetonitrile (A) in the presence of 1 mM iodide (purple), 1 mM bromide (orange) and 1 mM chloride (green) in acetonitrile. Transient absorption spectra of **Ir-HATPHE** recorded in acetonitrile/water 50:50 mixture (B) in the presence of 5 mM iodide (purple), 15 mM bromide (orange) and 250 mM chloride. Experiments were carried out in argon purged solution at room temperature using 410 nm light irradiation. Spectra were recorded 500 ns after the laser pulse in acetonitrile and 1 μs after the laser pulse in acetonitrile/water 50:50 mixture.

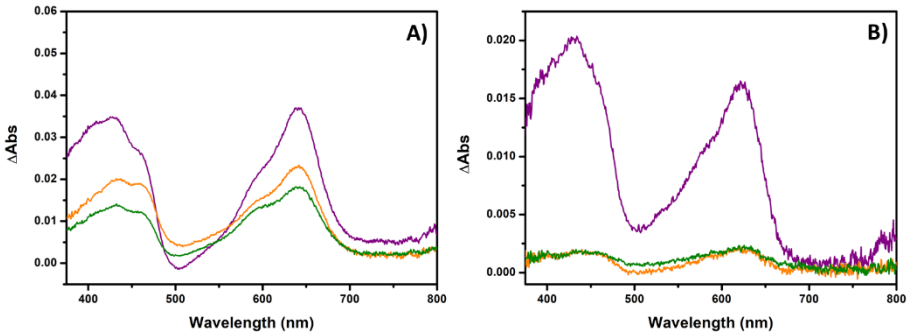

Figure S7.14. Transient absorption spectra of **Ir_2-TAPHAT** recorded in acetonitrile (A) in the presence of 1 mM iodide (purple), 1 mM bromide (orange) and 1 mM chloride (green) in acetonitrile. Transient absorption spectra of **Ir_2-TAPHAT** recorded in acetonitrile/water 50:50 mixture (B) in the presence of 10 mM iodide (purple), 10 mM bromide (orange) and 200 mM chloride. Experiments were carried out in argon purged solution at room temperature using 410 nm light irradiation. Spectra were recorded 500 ns after the laser pulse unless for bromide and chloride in acetonitrile/water 50:50 mixture that were recorded 30 μs after the laser pulse.

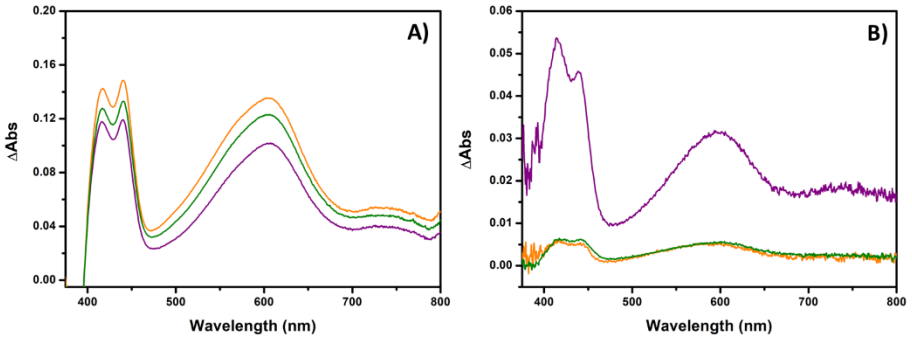

Figure S7.15. Transient absorption spectra of **Ir_2-TPPHZ** recorded in acetonitrile (A) in the presence of 1 mM iodide (purple), 1 mM bromide (orange) and 1 mM chloride (green) in acetonitrile. Transient absorption spectra of **Ir_2-TPPHZ** recorded in acetonitrile/water 50:50 mixture (B) in the presence of 10 mM iodide (purple), 10 mM bromide (orange) and 200 mM chloride. Experiments were carried out in argon purged solution at room temperature using 410 nm light irradiation. Spectra were recorded 500 ns after the laser pulse.

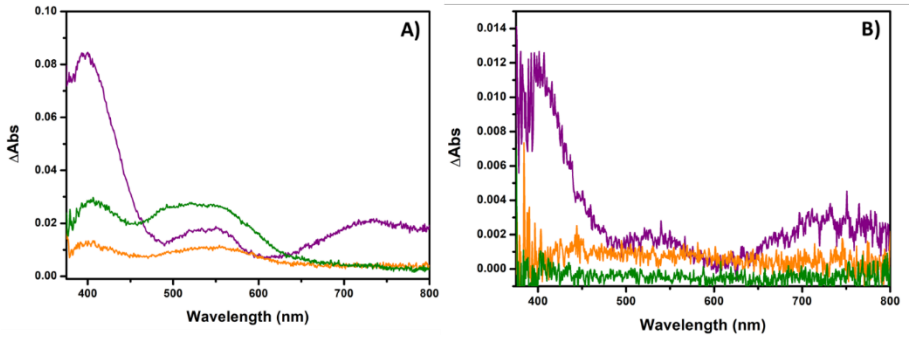

Figure S7.16. Transient absorption spectra of **Ir-TAP** recorded in acetonitrile (A) in the presence of 1 mM iodide (purple), 1 mM bromide (orange) and 1 mM chloride (green) in acetonitrile. Transient absorption spectra of **Ir-TAP** recorded in acetonitrile/water 50:50 mixture (B) in the presence of 5 mM iodide (purple), 15 mM bromide (orange) and 200 mM chloride. Experiments were carried out in argon purged solution at room temperature using 410 nm light irradiation. Spectra were recorded 500 ns after the laser pulse.

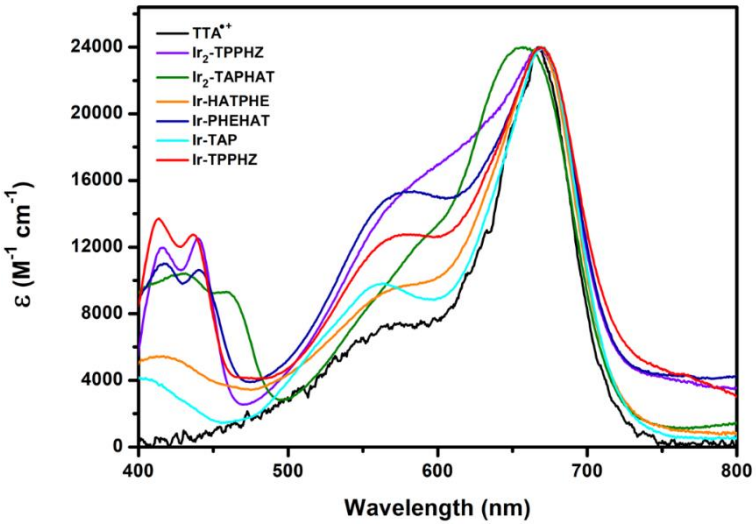

Figure S7.17. Nanosecond transient absorption of Ir(III) complexes recorded 500 ns (integration for 500 ns) after pulsed 410 nm light excitation (10 mJ/pulse) in the presence of 10 mM of tri-*p*-tolylamine. The authentic spectra of oxidized tri-p-tolylamine radical cation ($TTA^{\bullet+}$) recorded by spectroelectrochemistry is also shown. From that, $\Delta\varepsilon$ can be determined by subtracting the $TTA^{\bullet+}$ spectrum.

Chapter VIII – Investigation of the Electron Transfer and Cage Escape Yields Between Halides and a Fe(III) Photosensitizer

Researcher involved in this project are listed hereafter: Alexia Ripak (Ph.D. Student, UCLouvain).

Preface – This chapter focuses on the investigation of the excited-state electron transfer and cage escape yields between halides and a literature reported Fe(III) photosensitizer. The results presented herein represents a first step toward the transition to earth-abundant photosensitizers for halide oxidation, albeit only in organic solvent. The results presented hereafter have been published in the Journal of the American Chemical Society (De Kreijger, S.; Ripak, A.; Elias, B.; Troian-Gautier, L., Investigation of the Excited-State Electron Transfer and Cage Escape Yields Between Halides and a Fe(III) Photosensitizer. Journal of the American Chemical Society 2024, 146, 10286−10292).

8.1 Introduction

8.1.1 Iron-based analogues of $[Ru(bpy)_3]^{2+}$

In the previous chapter, we focussed on the design and study of rare transition metal-based photosensitizers. Despite their interesting properties for hydrogen production and halide oxidation applications as demonstrated throughout this Ph.D. thesis, we wanted to expand our scope by investigation other metal, more abundant, such as iron. Iron, after oxygen, silicon, and aluminum, stands as one of the most abundant elements in the Earth's crust. Its d^6 valence electronic configuration in Fe(II) makes it comparable to Ru(II), Os(II), and Ir(III), highlighting its potential as a substitute for these heavier and less abundant metals.[419] The $[Fe(bpy)_3]^{2+}$ complex, synthesized in the 1960s,[420] exhibits intense visible absorption features with molar absorption coefficients similar to those of $[Ru(bpy)_3]^{2+}$ and $[Os(bpy)_3]^{2+}$.[421] However, despite the ground state spectral similarity, the excited-state behaviors of 3d and 4d/5d metal complexes are markedly different.

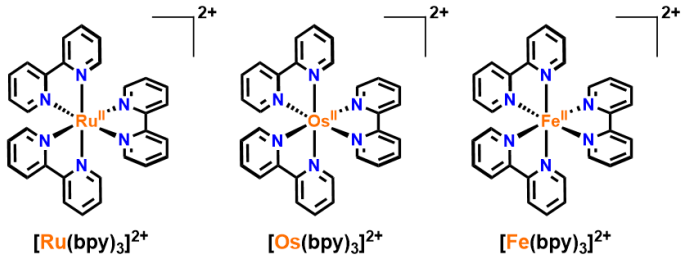

Figure 8.1. Structures of the prototypical $[Ru(bpy)_3]^{2+}$, $[Os(bpy)_3]^{2+}$ and $[Fe(bpy)_3]^{2+}$.

For $[Ru(bpy)_3]^{2+}$, transient absorption spectroscopy reveals a bleach of the metal-to-ligand charge transfer (MLCT) transition and the emergence of new absorption bands in the UV and beyond 550 nm. This bleaching is associated with the oxidation of Ru(II) to Ru(III) and the new absorption bands are attributed to the ligand-centred reduction, often described as $^{3*}[Ru(III)(bpy)_2(bpy^{\bullet-})]^{2+}$. Initially, $[Fe(bpy)_3]^{2+}$ exhibits similar transient absorption signals, indicating a MLCT character, denoted as $*[Fe(III)(bpy)^2(bpy^{\bullet-})]^{2+}$. However, the excited-state of $[Fe(bpy)_3]^{2+}$ evolves rapidly within 100 fs to an overall bleached signal, suggesting a shift to a different excited state compared to the typical MLCT state in $[Ru(bpy)_3]^{2+}$ (**Figure 8.2**). The lack of positive transient absorption around 400 nm for $[Fe(bpy)_3]^{2+}$ indicates that the excited state is not a charge-transfer species but rather a ligand-field state, likely a high-spin $^5T_{2g}$ state as confirmed by McCusker and co-workers.[422-424] Upon ultrafast intersystem crossing from ^{1}MLCT to $^5T_{2g}$, the relaxation of the metal-centred dark excited state was modelled with a single exponential decay with a lifetime of 18 ± 2 ns.[425, 426]

In essence, the ^{1}MLCT state in $[Fe(bpy)_3]^{2+}$ quickly decays (on a ~100 fs time scale) to low-lying metal-centred ligand-field states, populating a high-spin quintet excited state ($^5T_{2g}$). This photophysical pathway is common for Fe(II) complexes with classical polypyridyl ligands.[424, 425, 427-429] Unlike the long-lived ^{3}MLCT excited state in Ru(II) complexes, Fe(II) complexes do not exhibit long-lived net charge separation upon formation of the excited-state. Consequently, the overall remarkable difference between $[Ru(bpy)_3]^{2+}$ and $[Fe (bpy)_3]^{2+}$ in the excited state is caused by a change of the lowest excited state from a MLCT state to a metal-centred state. Because of its ligand-field nature and its lower

energy relative to its ^{1}MLCT state,[394] its reactivity is fundamentally different and less appealing in photoredox catalysis compared to the ^{3}MLCT state of Ru(II) complexes.[430]

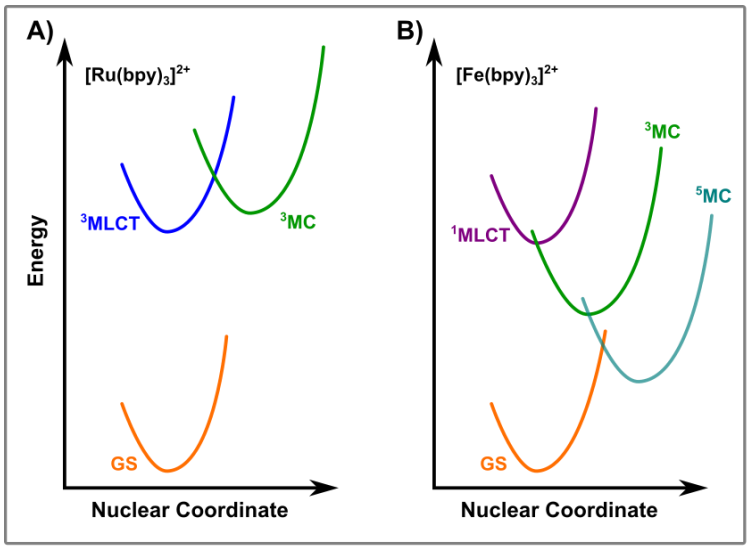

Figure 8.2. Potential-well diagram of A) $[Ru(bpy)_3]^{2+}$ and B) $[Fe(bpy)_3]^{2+}$.

8.1.2 Strategies to extend the excited-state lifetime of iron photosensitizers

The extremely short excited-state lifetimes of Fe(II) polypyridyl (**Figure 8.3** top) and related Fe(III) photosensitizers (**Figure 8.3** bottom) pose a significant challenge for their use in diffusion-based photoredox catalysis. To address this limitation, several groups have developed two main strategies to enhance the viability of iron catalysts in such applications.

One prominent approach involves modifying the excited-state energy landscape to extend the lifetime of charge-separated states and minimize deactivation through metal-centred states. This strategy aims to make iron catalysts more appealing for photoredox catalysis by prolonging their excited-state lifetimes.[419, 431-436] The main rational is to extend the lifetime of the MLCT states, either by stabilizing it or by destabilizing the metal-centred (MC) states involved in the ultrafast deactivation. These strategies include the use of

highly σ-donating ligands to strengthen the ligand field, which increases the separation between t_{2g} and e_g molecular orbitals, and employing ligands with low-energy π* orbitals to stabilize the MLCT states. Additionally, achieving a geometry close to a perfect octahedron enhances ligand field strength, while introducing asymmetry in the first coordination sphere can increase the energy gap between MLCT and metal-centred states.[437] These strategies have significantly extended the lifetimes of iron-based photosensitizers with MLCT excited states from ~10 ps in 2013[438] to 528 ps in 2018 with several gradual steps in between.[439] The current record for iron-based photosensitizers with MLCT excited states is around 1–1.25 ns.[440, 441]

In terms of purely LMCT emitters, an Fe(III) photosensitizer with six carbene ligands exhibited a low-lying luminescent doublet LMCT (^{2}LMCT) state with an excited-state lifetime of ~2.2 ns.[99] Unlike the spin-forbidden phosphorescence of the ^{3}MLCT state in Fe(II) complexes, this emission is a spin-allowed fluorescence from the ^{2}LMCT to the ground state ^{2}GS (**Figure 8.3** bottom). Considering the strategies previously discussed for extending the excited-state lifetimes of d^6 metal complexes with MLCT states, it was found that in the polycarbene Fe(III) complex, deactivation via vibrational modes rather than ^{4}MC states is a limiting factor for the excited-state lifetime.[443] Despite this, the achieved lifetimes are comparable to those of singlet states in short-lived organic chromophores, enabling diffusion-controlled encounters in solution. This suggests that these complexes could potentially be applied in photoredox catalysis.

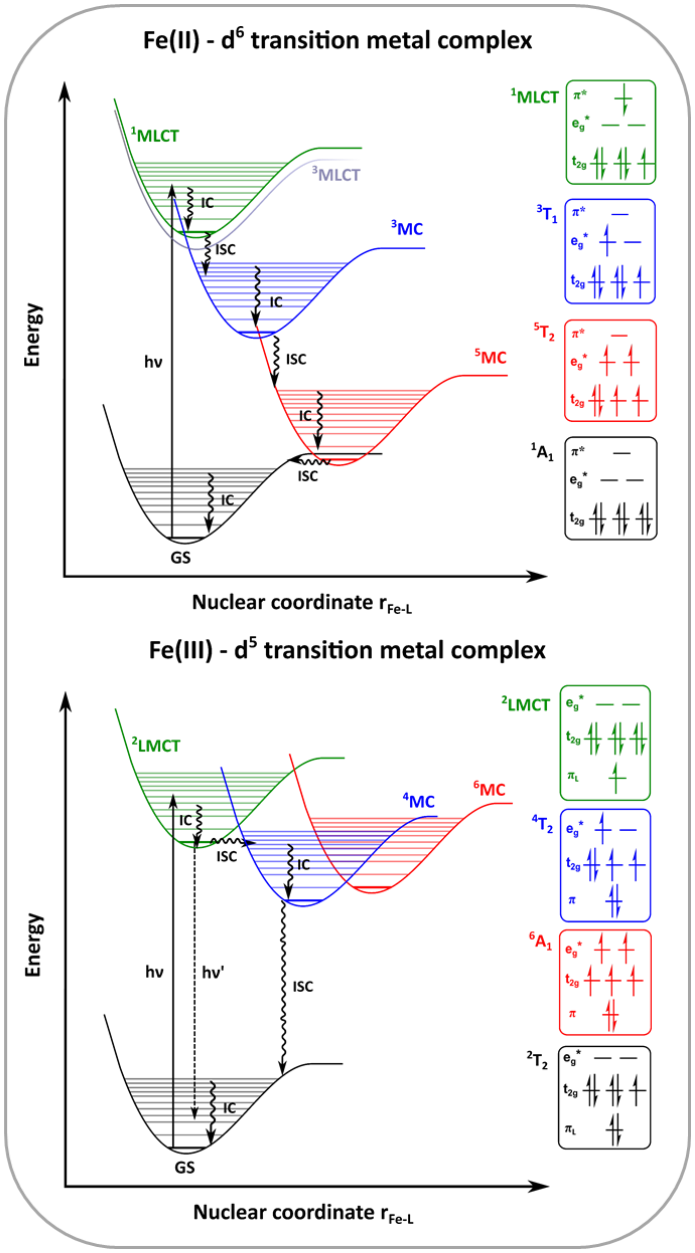

Figure 8.3. Schematic potential energy surfaces and relevant electronic states for the excited-state decay of a) Fe(II) and b) Fe(III) transition metal complexes. Electron configurations are given for *O*h symmetry for simplicity. Radiative decay pathways are denoted as dotted straight lines while non-radiative decay pathways are presented as wavy lines. GS = ground state, IC = internal conversion, ISC = intersystem crossing, MLCT = metal-to-ligand charge transfer, LMCT = ligand-to-metal charge transfer, MC = metal-centered. Adapted from literature.[442]

8.1.3 Towards halides oxidation by Fe(III) photosensitizers?

The current energy landscape requires new approaches to solar fuels formation. Solar energy has long been considered a prime alternative with several technologies that have been developed over the years.[14, 17, 22, 219, 252, 341, 342, 370, 444-451] Solar energy conversion to electricity is commonly efficiently achieved with photovoltaic panels. Yet, a dichotomy exists between the moment when energy is most needed and when sunlight reaching the earth is the most intense. Hence, current developments are focused on novel avenues to store solar energy. As previously mentioned, an interesting approach is to store solar energy in chemical bonds, *i.e.* the so-called *solar fuels*.[14, 15, 41, 93, 102, 344, 355, 452-454] Typical examples include hydrogen gas (H_2) which is considered worldwide as a promising target for large scale energy storage and distribution.[16] Alternative solar fuels include liquid fuels from CO_2 reduction,[17, 455, 456] as well as halogen (X_2), a value added product, that could be concomitantly formed with H_2 upon hydrohalic acid (HX) splitting. The main drawback of hydrohalic splitting is the thermodynamic demand associated with halide oxidation. Aqueous halide oxidation occurs at potentials $E^0(X^{\bullet/-})$ of 1.33, 1.93 and ~2.1-2.3 V *vs* NHE for iodide, bromide and chloride, respectively.[41] This wide range of potentials was shown to be narrower in organic solvents where E^0 $(X^{\bullet/-})$ of 1.23, 1.35 and 1.46 V *vs* NHE have been roughly estimated in acetonitrile for iodide, bromide and chloride, respectively.[42, 43] Hence, such oxidations are thermodynamically very demanding in water and often requires using photosensitizers based on precious ruthenium and iridium metals. Whereas evidence for iodide or bromide oxidation in organic solvent with Ru(II) and Ir(III) photosensitizers was unambiguously confirmed by transient absorption spectroscopy,[42, 43, 136] it is only very recently that evidence for chloride oxidation in water-like conditions was provided using the Ir(III) photosensitizers presented in **Chapter VII** or a pentacationic Ir(III) complex[182] capable to oxidize chloride in pure water. Notably bromide and chloride photo-oxidation have been monitored in acetone using Ru(II) photosensitizers[135, 238, 239] as well as by one- or two-photon excitation of N-phenylphenothiazine in acetonitrile.[246]

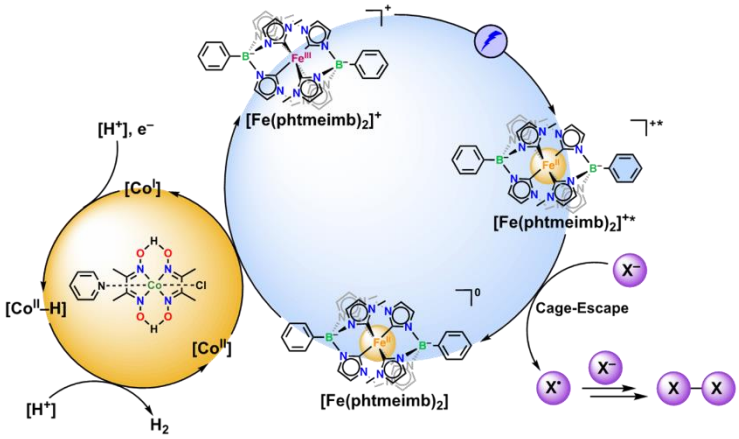

Figure 8.4. Structure of $[Fe(phtmeimb)_2]^+$ alongside the proposed scheme for the HX (X = I, Br, Cl) splitting reaction. Hydrogen production using $[Fe(phtmeimb)_2]^+$ has been reported by Wärnmark and co-workers.[457] Halide oxidation represents the focus of the present chapter.

A luminescent iron(III) photosensitizer $[Fe(phtmeimb)_2]^+$ (**Figure 8.4**), where phtmeimb is phenyl[tris(3-methyl-imidazolin-2-ylidene)]borate, was recently pioneered by Wärnmark and co-workers.[99] This photosensitizer has been thoroughly characterized spectroscopically and its use in photoredox catalysis and hydrogen photoproduction has also been documented,[74, 75, 90, 99, 100, 436, 442, 443, 457-459] but it has yet to be used for halide oxidation, which could open the way to HX splitting. With its 2 ns excited-state lifetime and excited-state reduction and oxidation potential of 1.6 V and –1.3 V *vs* NHE respectively, this photosensitizer shows great promise for excited-state electron transfer and catalysis.[99] In here, we investigated the use of $[Fe(phtmeimb)_2]^+$ as photosensitizer for halide oxidation in dichloromethane (CH_2Cl_2), acetonitrile (CH_3CN) and CH_3CN/H_2O 1:1 mixture. In neat organic solvent, large quenching rate constant close to the diffusion limit were obtained. In CH_3CN/H_2O 1:1 mixture, iodide and to a lesser extend bromide were competent for excited-state quenching. Direct evidence for excited-state electron transfer was only obtained by nanosecond transient absorption spectroscopy for iodide in dichloromethane and acetonitrile. The cage escape yields were also determined and were shown to be larger in dichloromethane (0.079) than in acetonitrile (0.017). Altogether, the results presented herein

represent a first step towards the transition to earth abundant photosensitizers for halide oxidation, albeit only in organic solvent.

8.2 Results and discussion

The ground-state absorption and excited-state photoluminescence spectra (**Figure 8.5**) were only slightly sensitive to the solvent nature or the presence of dioxygen, as expected for the doublet ligand-to-metal charge transfer excited-state character of $[Fe(phtmeimb)_2]^+$.[75, 99] The excited-state lifetime was also not drastically affected and ranged from 1.8 ns in CH_3CN/H_2O 1:1 to 2.4 ns in CH_2Cl_2. Excited-state quenching was then investigated with tetra-*n*-butylammonium iodide, bromide and chloride in CH_2Cl_2, CH_3CN and CH_3CN/H_2O 1:1 mixture (**Figure 8.6** and **Figures S8.1-S8.12**). In CH_3CN, the quenching rate constants (k_q) followed the expected periodic trend with k_q that ranged from 1.49 $x10^{10}$ to 2.06 $x10^{10}$ $M^{-1}s^{-1}$ for chloride and iodide, respectively (**Table 8.1**).[460]

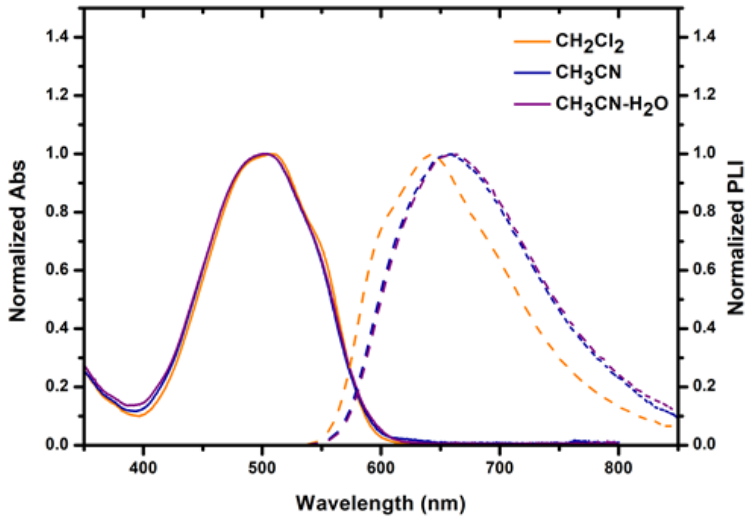

Figure 8.5. UV-Vis (solid lines) and photoluminescence (dashed lines) spectra of $[Fe(phtmeimb)_2]^+$ recorded at room temperature under air in CH_2Cl_2 (orange), CH_3CN (blue) and CH_3CN/H_2O 1:1 (purple).

Table 8.1. Excited-state quenching rate constants for the reaction between $[Fe(phtmeimb)_2]^+$ and tetra-n-butylammonium halide.

Solvent	k_q (x10^{10} $M^{-1}s^{-1}$)		
	Iodide	Bromide	Chloride
CH_3CN	2.06	1.87	1.49
$CH_3CN:H_2O$ 1:1	1.46	0.25	---[d]
CH_2Cl_2	2.03	2.02	1.71
CH_2Cl_2[a]	2.14	2.05	1.63
CH_2Cl_2[b]	0.39	0.31	0.24
CH_2Cl_2[c]	0.39	0.30	0.20

[a]eluted through basic Al_2O_3. [b]with 0.5 M $TBAPF_6$. [c]eluted through basic Al_2O_3 and with 0.5 M $TBAPF_6$. [d]no excited-state quenching observed.

The k_q in CH_3CN/H_2O 1:1 slightly decreased to values of 1.46 x10^{10} and 2.49 x10^9 $M^{-1}s^{-1}$ for iodide and bromide, respectively. Excited-state quenching with chloride could not be observed under these conditions. In dichloromethane, the k_q were on the same order of magnitude as those determined in acetonitrile (**Table 8.1**). Note that, in neat dichloromethane, the downward curvature of the Stern-Volmer plots at higher quencher concentrations was most likely due to the kinetic salt effect and the quenching rate constants with chloride in neat dichloromethane are an estimate.[72, 461-465] The excited-state quenching experiments were thus performed in dichloromethane containing 0.5 M of tetra-*n*-butylammonium hexafluorophosphate ($TBAPF_6$). A ~10-fold excess of $TBAPF_6$ *vs* halide in neat CH_2Cl_2 was used to investigate this kinetic salt effect. In this case, the excited-state quenching rate constant were one order of magnitude smaller, *i.e.* 3.9 x10^9, 3.1 x10^9 and 2.4 x10^9 $M^{-1}s^{-1}$ for iodide, bromide and chloride, respectively. This is in line with a decreased diffusion rate upon the introduction of large concentration of electrolyte. All experiments were also repeated with dichloromethane freshly eluted over basic Al_2O_3 to remove any residual traces of HCl or other impurities, which led to identical results.[466]

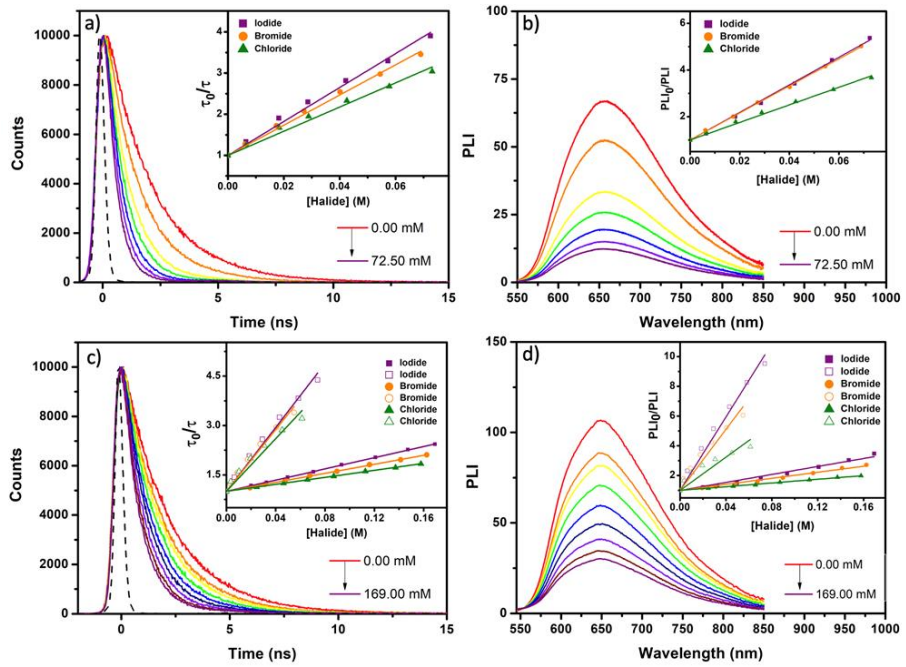

Figure 8.6. Time-resolved (a,c) and steady-state (b,d) excited-state quenching of $[Fe(phtmeimb)_2]^+$ with iodide in argon purged CH_3CN (a, b) and in CH_2Cl_2 with 0.5 M $TBAPF_6$ (c,d). The inset represents the corresponding Stern-Volmer plots with iodide (purple), bromide (orange) and chloride (green) in CH_3CN (a,b) and in CH_2Cl_2 (c,d, open symbols) and CH_2Cl_2 containing 0.5 M $TBAPF_6$ (c, d, closed symbols).

As mentioned before, Stern-Volmer experiments do not inform on the exact nature of the quenching process, nanosecond transient absorption spectroscopy was carried out to gain insight into the mechanism of the photo-induced process.[58] Pulsed 470 nm light excitation of solutions containing $[Fe(phtmeimb)_2]^+$ and iodide showed clear evidence for excited-state electron transfer in CH_2Cl_2 and CH_3CN (**Figure 8.7** and **Figures S8.13-16**). This was evidence by novel absorption features centered at 385 nm and 750 nm, attributed to a combination of a reduced $[Fe(phtmeimb)_2]$ species and $I_2^{\bullet-}$, the latter formed through a reaction between $I^\bullet$ and I^-.[54, 55, 230, 231, 241] The kinetic rate constant for the formation of $I_2^{\bullet-}$ could not be determined as it appeared within the instrument's response. Modelling of the transient absorption spectra using authentic spectra of the reduced photosensitizer and $I_2^{\bullet-}$ highlighted that they were formed in a 1:1 ratio (**Figure 8.7 and Figure S8.19**). Direct evidence

for excited-state electron transfer was not observed with the other halides or in CH_3CN/H_2O 1:1 (**Figures S8.17-S8.18**).

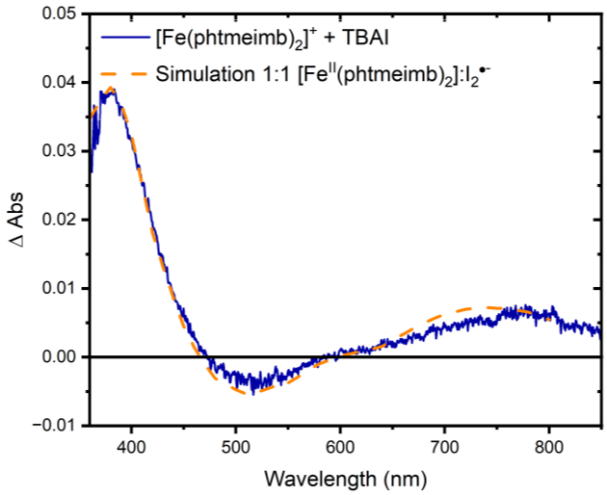

Figure 8.7. Nanosecond transient absorption spectrum (blue) of a solution containing $[Fe(phtmeimb)_2]^+$ and 45 mM of iodide in CH_2Cl_2. Spectrum is shown 25 ns after the laser pulse and was integrated for 50 ns. The spectra were modeled (orange dashed line) using a 1:1 ratio of Fe(II) to $I_2^{\bullet-}$ (2.45 μM of each). Experiments were carried out in argon purged solvents using 470 nm pulsed light excitation at 10 mJ/pulse.

The cage escape yields (Φ_{CE}), *i.e.* the efficiency with which the geminate pair of radicals separate after bimolecular excited-state electron transfer were quantified by comparative actinometry using **Equations 1.28** and **1.29** with $[Ru(bpy)_3]^{2+}$ as actinometer.[406] The transient absorption changes were monitored at 385 nm, *i.e.* at the maximum absorption changes corresponding to a combination of the reduced photosensitizer and $I_2^{\bullet-}$ (**Figure 8.8**). As spectral modelling showed that these were produced in a 1:1 ratio (**Figure 8.6**), the single wavelength absorption changes were analyzed using $\Delta\varepsilon_{385nm}$ = 7200 $M^{-1}cm^{-1}$ and 8600 $M^{-1}cm^{-1}$ for Fe(II) and $I_2^{\bullet-}$, respectively.[41, 99] These signals were compared to the changes in absorption of the reference $[Ru(bpy)_3]^{2+}$ (ES_{ref}) at 450nm. A $\Delta\varepsilon$ value of –11000 $M^{-1}cm^{-1}$ was used for the actinometer at 450 nm.[130-132] Φ_{CE} were obtained by comparing the relative yield of mono-reduced PS produced (Φ) to the percentage of quenched photoluminescence (%PL).

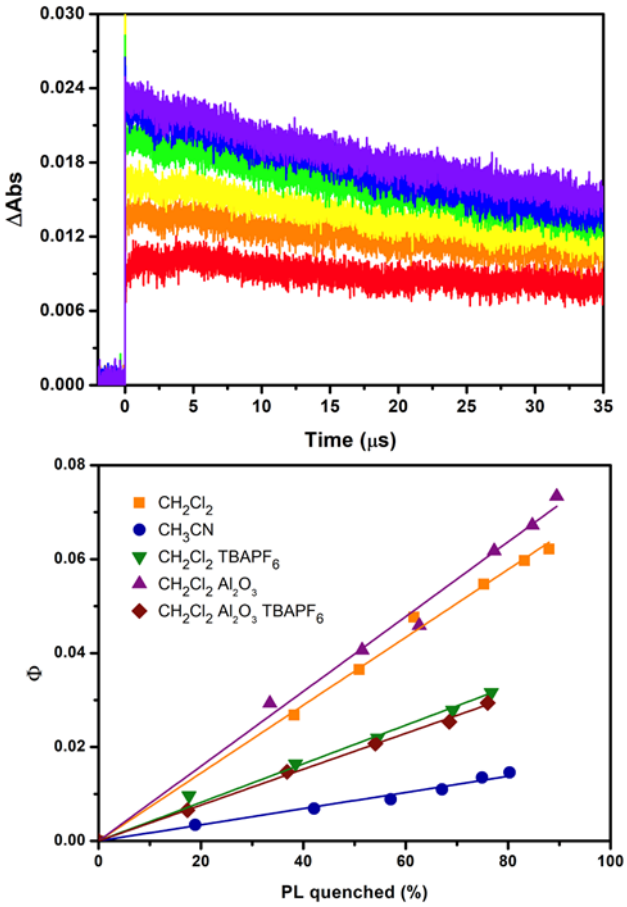

Figure 8.8. Single wavelength absorption changes recorded at 385 nm following pulsed light 470 nm excitation in the presence of increasing amounts of iodide (top). The single wavelength absorption changes were deconvoluted using a 1:1 ratio of reduced [Fe(phtmeimb)$_2$] to $I_2^{\bullet-}$ which was used to determine the cage escape yields (bottom).

Using this procedure, cage escape yields ranged from 0.079 in dichloromethane to 0.017 in acetonitrile (**Table 8.2**). Φ_{CE} could not be determined for bromide and chloride. This could imply that the in-cage geminate charge recombination is much faster than the cage escape process.[458] These Φ_{CE} are small compared to values recorded in organic solvents for photosensitizers where $X_2^{\bullet-}$ was observed, where values ranged

0.25-0.96.[54, 136, 243] In some instances, low Φ_{CE} (~0.04) with observation of $I_2^{\bullet-}$ in acetonitrile have also been reported using Ru(II) photosensitizers.[231]

Table 8.2. Cage escape yields for the reaction between $[Fe(phtmeimb)_2]^+$ and iodide in the indicated solvent.

Solvent	Φ_{CE}
CH_3CN	0.017
CH_2Cl_2	0.072
CH_2Cl_2 – Al_2O_3	0.079
CH_2Cl_2 – 0.5 M $TBAPF_6$	0.041
CH_2Cl_2 – Al_2O_3 – 0.5 M $TBAPF_6$	0.038

The origin of the difference in Φ_{CE} is at this stage not easy to rationalize. Contrary to what has been reported in the literature, there does not seem to be any effect of the driving force for geminate charge recombination on the Φ_{CE}, as larger Φ_{CE} would have otherwise been observed with bromide and chloride.[467-474] An impact of the solvent on the intersystem crossing of the geminate radical pair, as previously hypothesized,[75] may result in state mixing with a higher spin state such as the ^4CS which would convey a partial spin-forbidden character to geminate charge recombination, thus increasing Φ_{CE}. Iodide could also promote such state mixing through heavy atom effect compared to the other halides, hence increasing the spin-forbidden character of the geminate charge recombination. Excited-state electron transfer would yield an overall neutral reduced photosensitizer and a neutral halogen atom and as such, electrostatic repulsion is not expected to be a main contributor to these Φ_{CE}, although the data in CH_2Cl_2 and with added electrolyte could suggest otherwise. As iodide is the most polarizable halide, we propose that the larger Φ_{CE} observed in dichloromethane stems from either a better solvation of the separated iodine atom and the reduced photosensitizer than in acetonitrile or that the geminate radical pair is more stabilized in acetonitrile, decreasing the gap to the ground state product, thus favoring recombination.

8.3 Conclusions

With the aim of broadening our field of investigation to include more abundant metals for halides oxidation applications a known Fe(III) photosensitizer was used for bimolecular excited-state reactivity with iodide, bromide and chloride in CH_2Cl_2, CH_3CN and CH_3CN/H_2O 1:1 mixture. Steady-state and time-resolved excited-state quenching experiments were in line with dynamic quenching with a potentially small static quenching process. Large quenching rate constant were obtained in most conditions. Unambiguous proof for excited-state electron transfer was obtained with iodide, where both the monoreduced photosensitizer and $I_2^{\bullet-}$ were spectroscopically observed. The absence of signals for bromide and chloride suggests that the in-cage geminate charge recombination is faster than the kinetics for the cage escape process.[458] Φ_{CE} for the reaction with iodide were determined and ranged from 0.079 to 0.017 in CH_2Cl_2 and CH_3CN, respectively. The origin of the difference in Φ_{CE} is currently under investigation. These results however highlight the great versatility of $[Fe(phtmeimb)_2]^+$ since its initial report by Wärnmark and co-workers in 2019 and open great opportunity for bimolecular excited-state reactivity of iron complexes in photoredox catalysis and solar fuels formation.

These results highlight the great versatility of this Fe(III) photosensitizer in photoredox catalysis and represents one of the first reported examples of halide oxidation with a 3d metal-based photosensitizer alongside the work of D. G. Nocera and co-workers.[233-235] However, the experimental evidence for reductive electron transfer was only demonstrated for iodide in organic solvents (CH_2Cl_2, 0.079) and (CH_3CN, 0.017) with Φ_{CE} relatively low compared to the Ir(III)-based photosensitizers reported in **Chapter VII** (0.63 to 1.00 in CH_3CN for iodide). This difference could originate from the closed-shell nature of the Ir(III) photosensitizers (d^6) that involves a low rate of triplet–singlet intersystem crossing within the geminate radical pair implying that charge recombination toward the ground state is a spin-forbidden process, favoring larger cage escape yields. Geminate charge recombination in open-shell metal complexes, such as Fe(III) photosensitizers studied in this chapter, is

no longer a spin-forbidden process (doublet for both the ground- and excited-states) and becomes highly sensitive to solvent effects.[244] This demonstrates that, for the moment, photosensitizers based on precious metals are more competent for iodide, bromide and chloride oxidation in organic solvents and water enriched conditions.

8.4 Experimental section

The materials and methods used in this chapter are described in ***Chapter X***

Acetonitrile 99.9% (VWR), dichloromethane 99.9% (stabilized with about 0.002% of 2-methyl-2-butene, VWR), tetra-*n*-butylammonium hexafluorophosphate ≥ 98% (TCI), aluminium oxide, activated, basic for column chromatography, 50-200 micron (Acros Organics) were purchased from commercial suppliers and used as received. Water was purified by a Millipore Milli-Q system. Tetrabutylammonium iodide (TBAI, Sigma-Aldrich, ≥ 99.0 %), tetrabutylammonium bromide (TBABr, Sigma-Aldrich, ≥ 99.0 %), and tetrabutylammonium chloride (TBACl, Sigma-Aldrich, ≥ 97.0 %) were recrystallized from acetone and diethyl ether and stored in a vacuum desiccator. $[Fe(phtmeimb)_2]^+(PF_6^-)$ was synthesized using a modified procedure[75] from the initial reported procedure.[99]

8.4.1 Stern-Volmer experiments

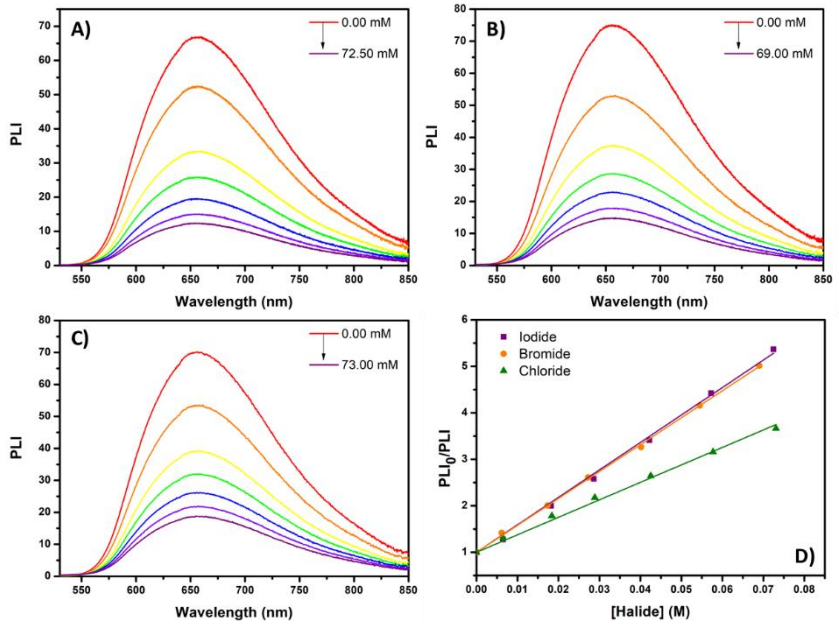

Figure S8.1. Steady-state excited-state quenching of $[Fe(phtmeimb)_2]^+$ with A) iodide, B) bromide and C) chloride in argon purged CH_3CN. The corresponding Stern-Volmer plots, from which the quenching rate constants (k_q) were determined, are gathered in panel D).

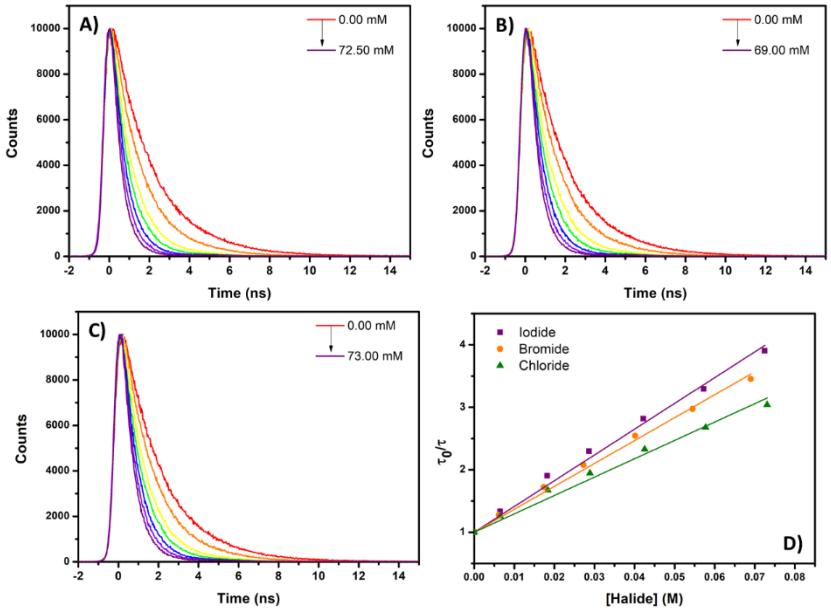

Figure S8.2. Time-resolved excited-state quenching of $[Fe(phtmeimb)_2]^+$ with A) iodide, B) bromide and C) chloride in argon purged CH_3CN. The corresponding Stern-Volmer plots, from which the quenching rate constants (k_q) were determined, are gathered in panel D).

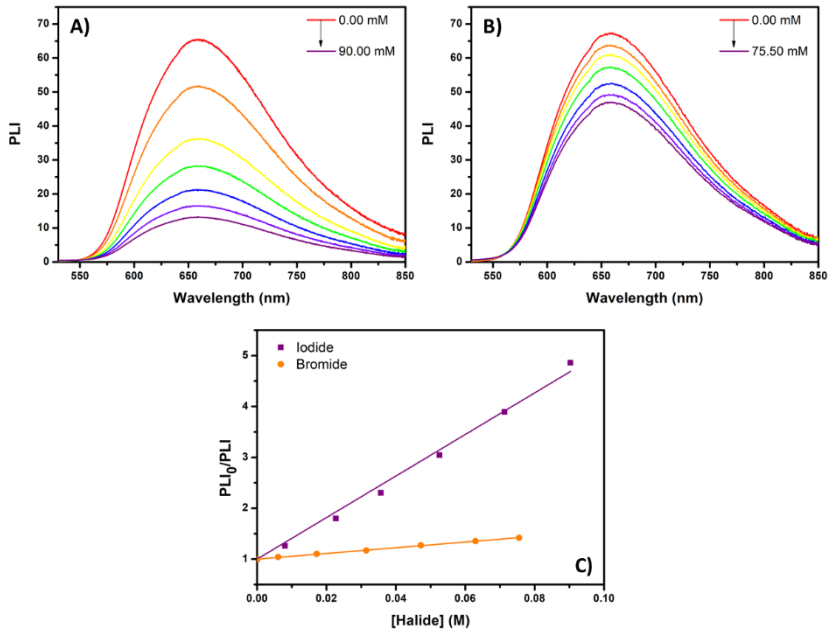

Figure S8.3. Steady-state excited-state quenching of $[Fe(phtmeimb)_2]^+$ with A) iodide and B) bromide in argon purged CH_3CN/H_2O 1:1. The corresponding Stern-Volmer plots, from which the quenching rate constants (k_q) were determined, are gathered in panel C).

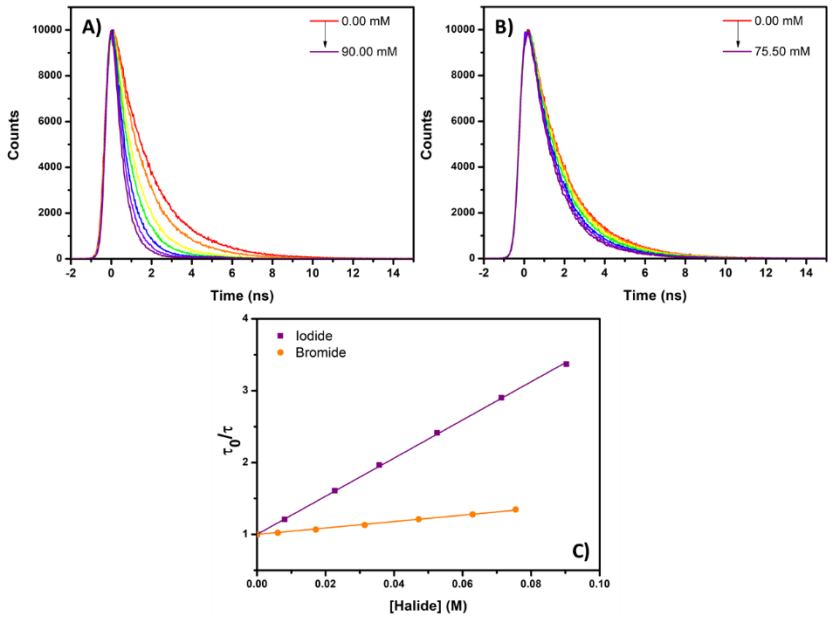

Figure S8.4. Time-resolved excited-state quenching of $[Fe(phtmeimb)_2]^+$ with A) iodide and B) bromide in argon purged CH_3CN/H_2O 1:1. The corresponding Stern-Volmer plots, from which the quenching rate constants (k_q) were determined, are gathered in panel C).

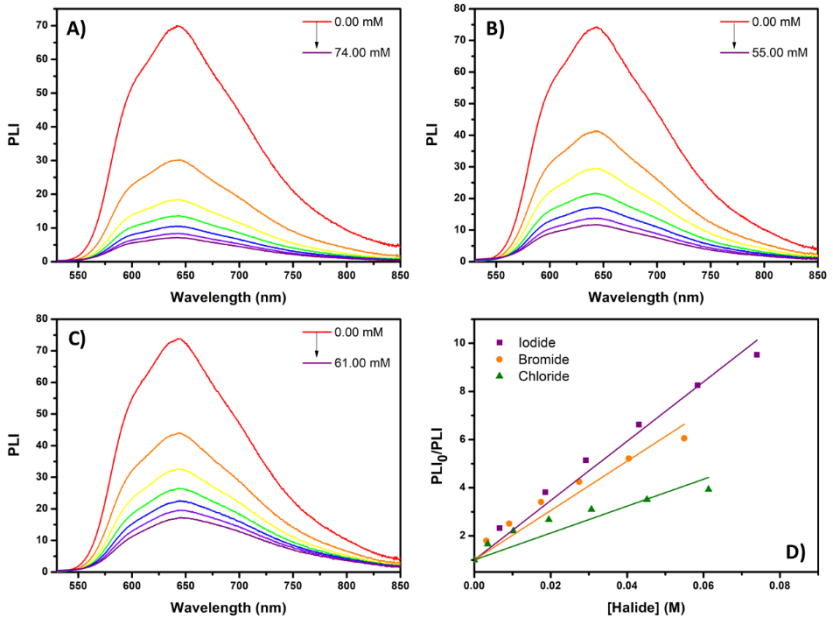

Figure S8.5. Steady-state excited-state quenching of $[Fe(phtmeimb)_2]^+$ with A) iodide, B) bromide and C) chloride in argon purged CH_2Cl_2. The corresponding Stern-Volmer plots, from which the quenching rate constants (k_q) were estimated, are gathered in panel D).

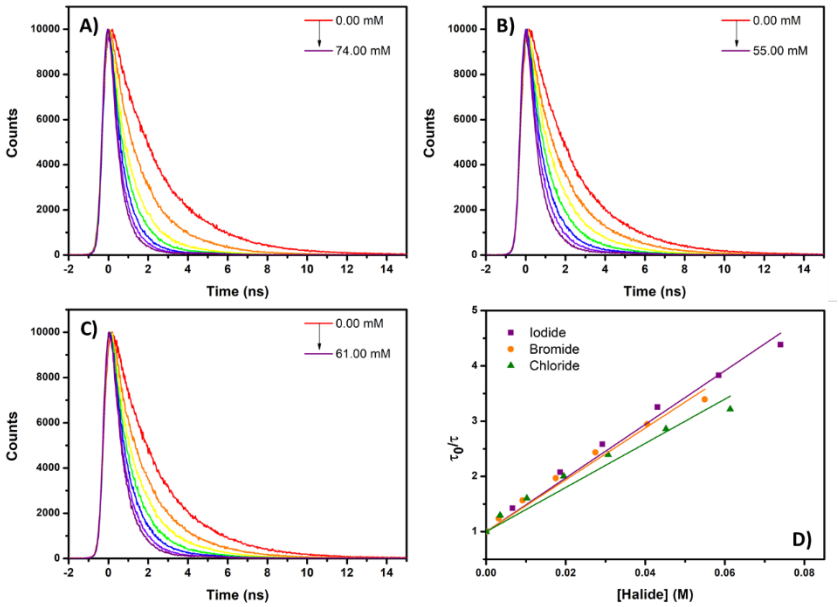

Figure S8.6. Time-resolved excited-state quenching of $[Fe(phtmeimb)_2]^+$ with A) iodide, B) bromide and C) chloride in argon purged CH_2Cl_2. The corresponding Stern-Volmer plots, from which the quenching rate constants (k_q) were determined, are gathered in panel D).

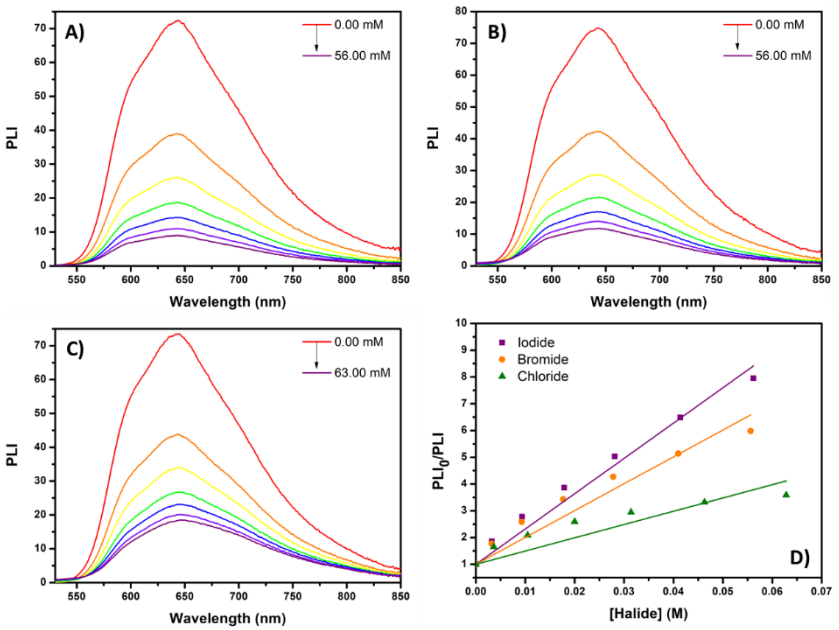

Figure S8.7. Steady-state excited-state quenching of $[Fe(phtmeimb)_2]^+$ with A) iodide, B) bromide and C) chloride in argon purged CH_2Cl_2 eluted through basic Al_2O_3. The corresponding Stern-Volmer plots, from which the quenching rate constants (k_q) were estimated, are gathered in panel D).

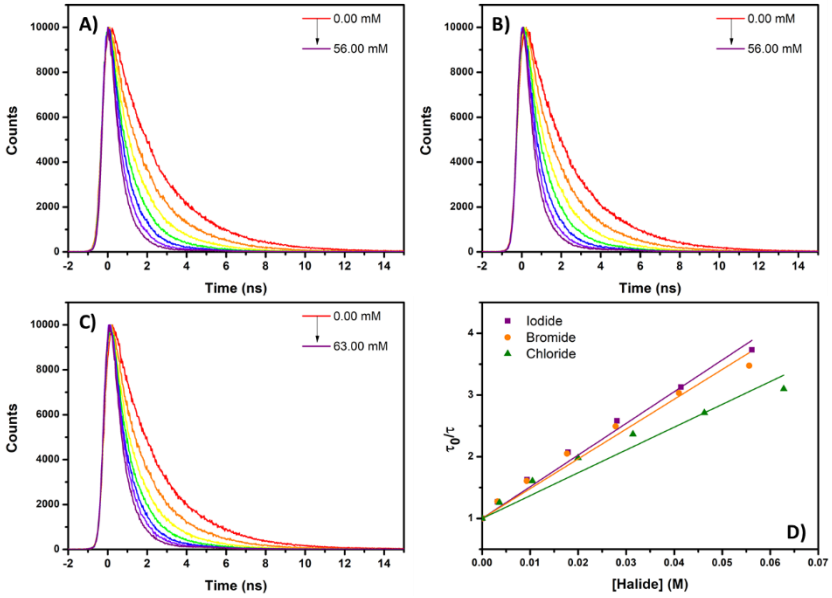

Figure S8.8. Time-resolved excited-state quenching of $[Fe(phtmeimb)_2]^+$ with A) iodide, B) bromide and C) chloride in argon purged CH_2Cl_2 eluted through basic Al_2O_3. The corresponding Stern-Volmer plots, from which the quenching rate constants (k_q) were determined, are gathered in panel D).

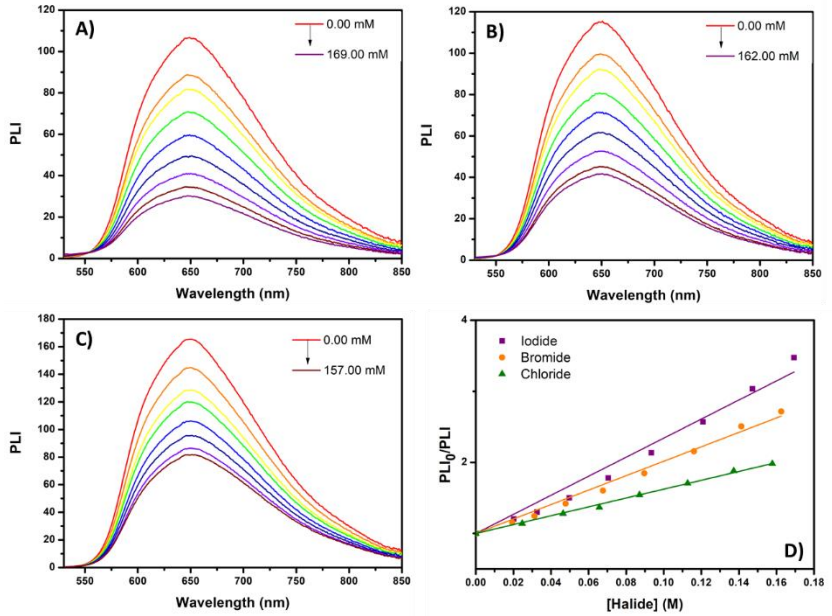

Figure S8.9. Steady-state excited-state quenching of $[Fe(phtmeimb)_2]^+$ with A) iodide, B) bromide and C) chloride in argon purged CH_2Cl_2 with 0.5M $TBAPF_6$. The corresponding Stern-Volmer plots, from which the quenching rate constants (k_q) were determined, are gathered in panel D).

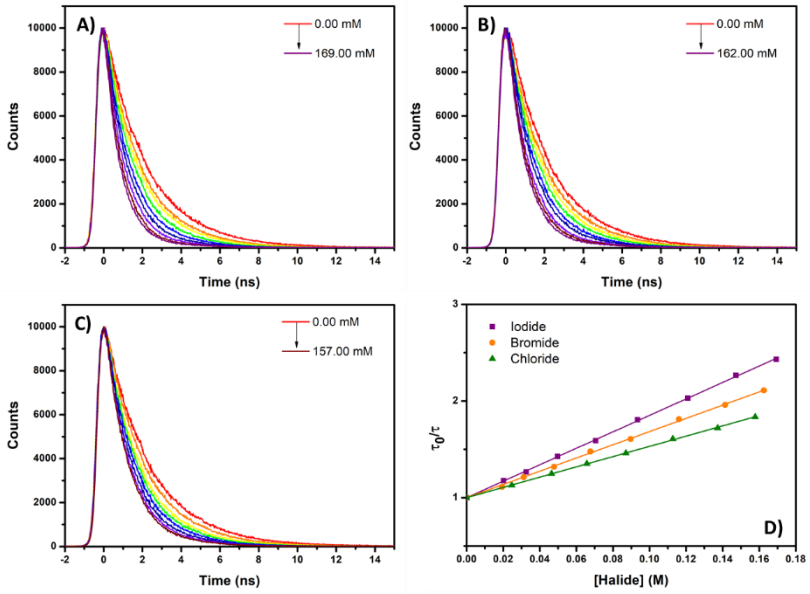

Figure S8.10. Time-resolved excited-state quenching of $[Fe(phtmeimb)_2]^+$ with A) iodide, B) bromide and C) chloride in argon purged CH_2Cl_2 with 0.5M $TBAPF_6$. The corresponding Stern-Volmer plots, from which the quenching rate constants (k_q) were determined, are gathered in panel D).

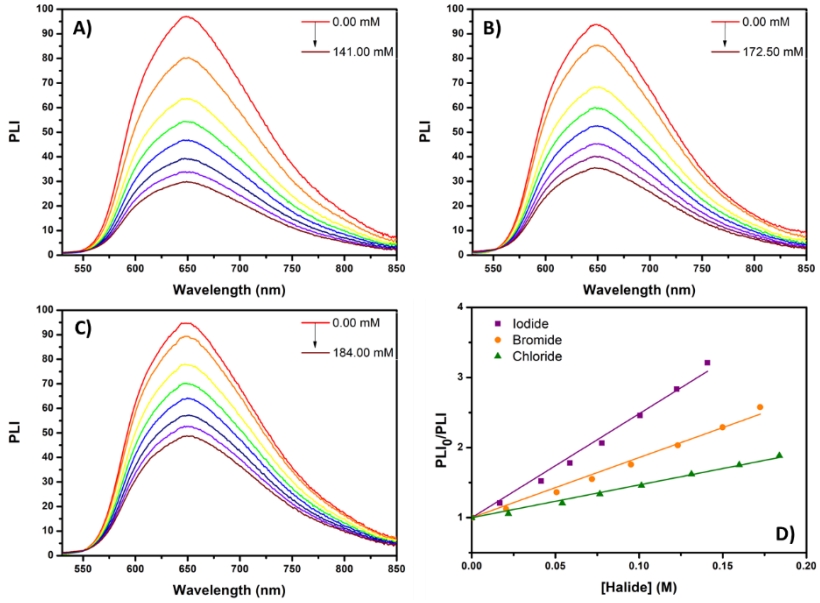

Figure S8.11. Steady-state excited-state quenching of $[Fe(phtmeimb)_2]^+$ with A) iodide, B) bromide and C) chloride in argon purged CH_2Cl_2 eluted through basic Al_2O_3 with 0.5M $TBAPF_6$. The corresponding Stern-Volmer plots, from which the quenching rate constants (k_q) were determined, are gathered in panel D).

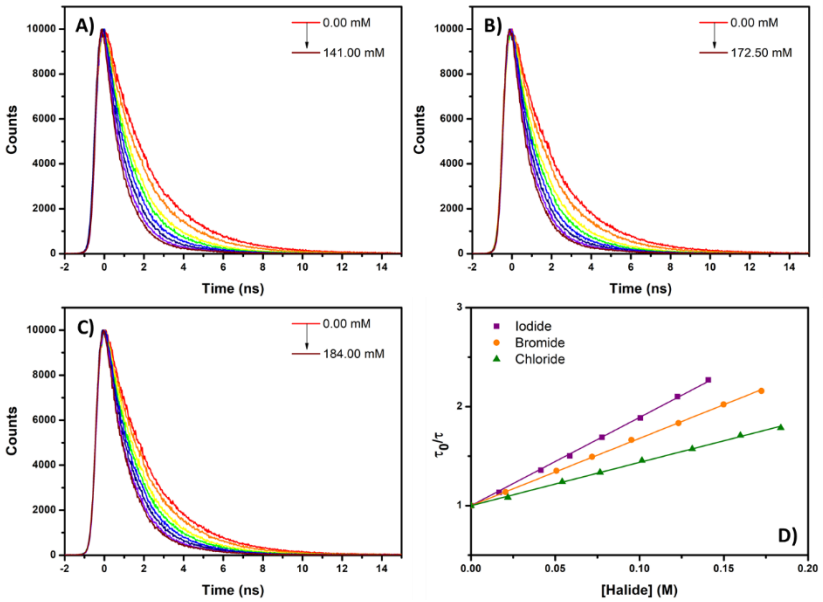

Figure S8.12. Time-resolved excited-state quenching of $[Fe(phtmeimb)_2]^+$ with A) iodide, B) bromide and C) chloride in argon purged CH_2Cl_2 eluted through basic Al_2O_3 with 0.5M $TBAPF_6$. The corresponding Stern-Volmer plots, from which the quenching rate constants (k_q) were determined, are gathered in panel D).

8.4.2 Nanosecond transient absorption and cage escape measurements

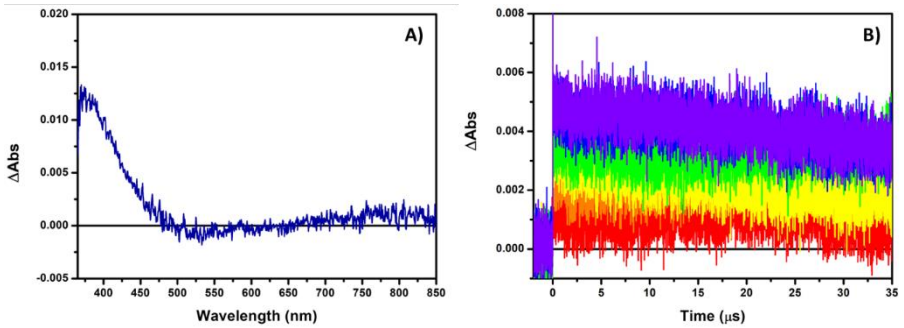

Figure S8.13. A) Nanosecond transient absorption spectrum (blue) of a solution containing $[Fe(phtmeimb)_2]^+$ and 61 mM of iodide. Spectrum is shown 25 ns after the laser pulse and was integrated for 50 ns. B) Single wavelength absorption changes recorded at 385 nm following pulsed light 470 nm excitation in the presence of increasing amounts of iodide. Experiments were carried out in argon purged CH_3CN using 470 nm pulsed light excitation at 10 mJ/pulse.

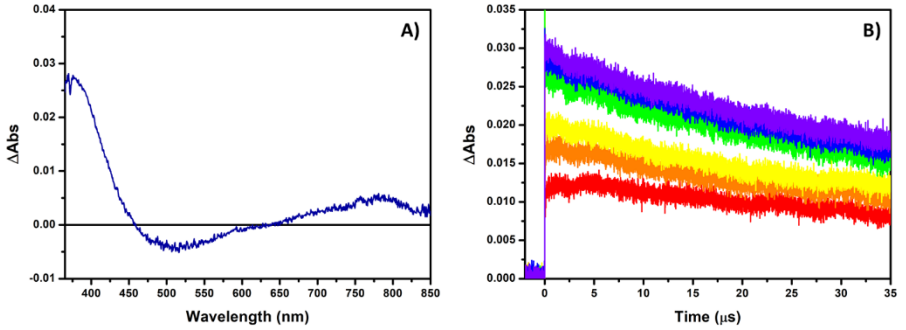

Figure S8.14. A) Nanosecond transient absorption spectrum (blue) of a solution containing $[Fe(phtmeimb)_2]^+$ and 45 mM of iodide. Spectrum is shown 25 ns after the laser pulse and was integrated for 50 ns. B) Single wavelength absorption changes recorded at 385 nm following pulsed light 470 nm excitation in the presence of increasing amounts of iodide. Experiments were carried out in argon purged CH_2Cl_2 eluted through basic Al_2O_3 using 470 nm pulsed light excitation at 10 mJ/pulse.

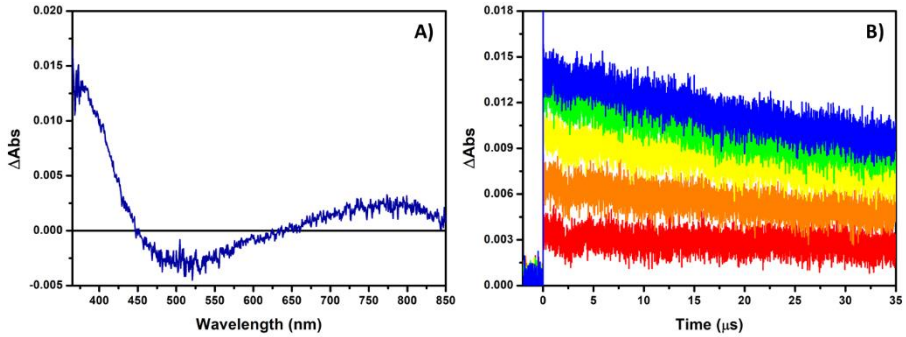

Figure S8.15. A) Nanosecond transient absorption spectrum (blue) of a solution containing $[Fe(phtmeimb)_2]^+$ and 165 mM of iodide. Spectrum is shown 25 ns after the laser pulse and was integrated for 50 ns. B) Single wavelength absorption changes recorded at 385 nm following pulsed light 470 nm excitation in the presence of increasing amounts of iodide. Experiments were carried out in argon purged CH_2Cl_2 with 0.5M $TBAPF_6$ using 470 nm pulsed light excitation at 10 mJ/pulse.

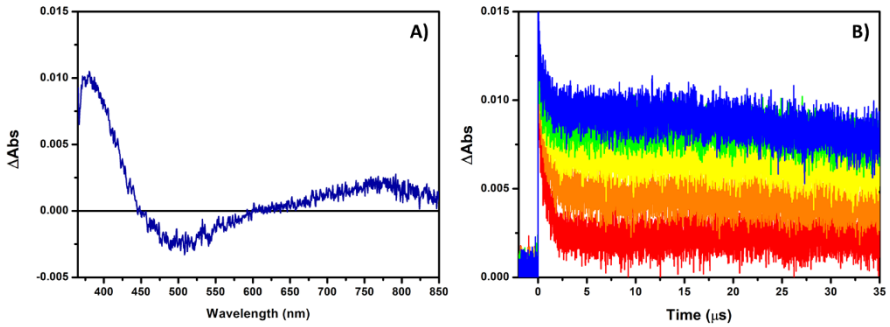

Figure S8.16. A) Nanosecond transient absorption spectrum (blue) of a solution containing $[Fe(phtmeimb)_2]^+$ and 165 mM of iodide. Spectrum is shown 2 μs after the laser pulse and was integrated for 50 ns. B) Single wavelength absorption changes recorded at 385 nm following pulsed light 470 nm excitation in the presence of increasing amounts of iodide. Experiments were carried out in argon purged CH_2Cl_2 with 0.5M $TBAPF_6$ eluted through basic Al_2O_3 using 470 nm pulsed light excitation at 10 mJ/pulse.

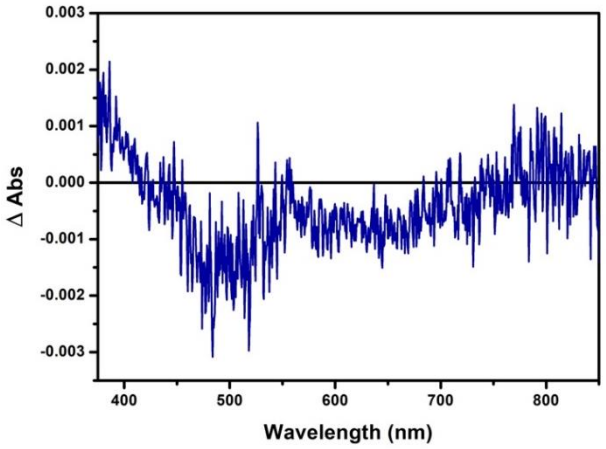

Figure S8.17. Nanosecond transient absorption spectrum of a solution containing $[Fe(phtmeimb)_2]^+$ and 160 mM of iodide. Spectrum is shown 25 ns after the laser pulse and integrated for 50 ns. Experiments were carried out in argon purged CH_3CN/H_2O 1:1 using 470 nm pulsed light excitation at 10 mJ/pulse.

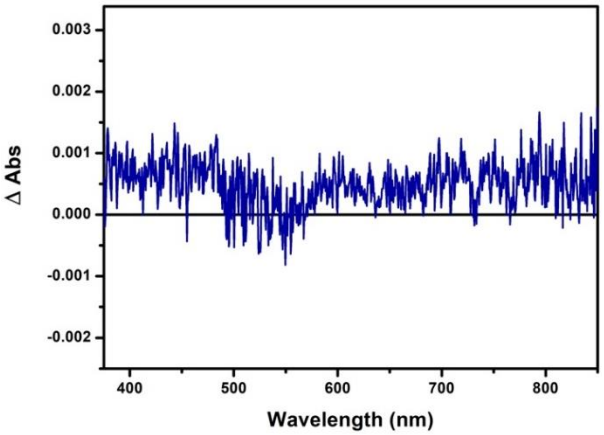

Figure S8.18. Nanosecond transient absorption spectrum of a solution containing $[Fe(phtmeimb)_2]^+$ and 250 mM of bromide. Spectrum is shown 25 ns after the laser pulse and integrated for 50 ns. Experiments were carried out in argon purged CH_2Cl_2 using 470 nm pulsed light excitation at 10 mJ/pulse.

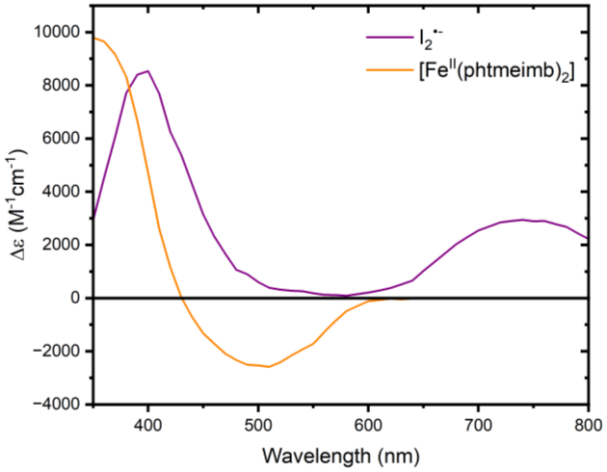

Figure S8.19. Reference spectra of $I_2^{\bullet-}$ and $[Fe^{II}(phtmeimb)_2]$ used for the spectra simulation presented in **Figure 8.7.**

8.4.3 Synthesis

$[Fe(phtmeimb)_2]^+.PF_6^-$: A 50 mL Schlenk, equipped with a stirring bar was charged with phtmeimb (196 mg, 0.315 mmol) and dried under vacuum for 3 hours before being purged under argon. Dry THF (6.3 mL) was then added, and the mixture was cooled to –78°C. A solution of commercial LiHMDS was prepared by adding solid LiHMDS (181 mg, 1.08 mmol) into a heat-dried flask

kept under argon followed by 2.30 mL of dry THF. The entire solution was then added to the cooled mixture, which was stirred at –78°C for 30 minutes. Meanwhile, a solution of $FeBr_2$ was prepared by adding $FeBr_2$ (32 mg, 0.15 mmol) into a heat-dried flask kept under argon followed by 6mL of dry THF. The mixture was sonicated for 20 minutes to ensure solubilization of the iron salt. Afterwards, the cooling bath was removed and the entire solution of $FeBr_2$ was added to the deprotonated ligand solution resulting in a dark-coloured solution. The reaction mixture was then stirred at room temperature under argon for 22h in the dark. After that, the mixture was exposed to air which led to a rapid colour change to yield a dark red solution that was evaporated under reduced pressure. The resulting residue was dissolved in CH_2Cl_2, filtered through a porosity 4 frit, washed with DCM and the filtrate was evaporated under reduced pressure resulting in a dark red solid. The residue was then purified by flash chromatography on neutral alumina, eluted first with pure DCM and then with dichloromethane containing 20% CH_3CN. Notably, the purification procedure employed in this study was optimized compared to the method reported in the literature,[75, 99] resulting in a much cleaner NMR spectrum. The desired fractions were collected and evaporated under reduced pressure to afford bis (tris(3-methylimidazol-1-ylidene) (phenyl)borate) iron (III) hexafluorophosphate (**$[Fe(phtmeimb)_2]^+.PF_6^-$**) as a dark red solid with 42 % yield (0.0548 g, 0.3272 mmol). ^1H NMR (400 MHz, CD_3CN) δ 14.86 (d, *J* = 5.2 Hz, 4H), 10.45 (t, *J* = 5.5 Hz, 4H), 9.78 (t, *J* = 7.3 Hz, 2H), 4.87 (s, 18H), -12.58 (s, 6H) ppm. NMR shifts match those reported in the literature.[99]

Chapter IX – Conclusions and Prospects

9.1 General conclusion

First, this Ph.D. thesis aimed to develop novel bis-cyclometalated Ir(III) photosensitizers for hydrogen evolution reaction. Especially, our objective was to increase their low molar extinction coefficient in the visible light region by ligand tuning strategies to exploit most of the photons reaching the surface of the earth.

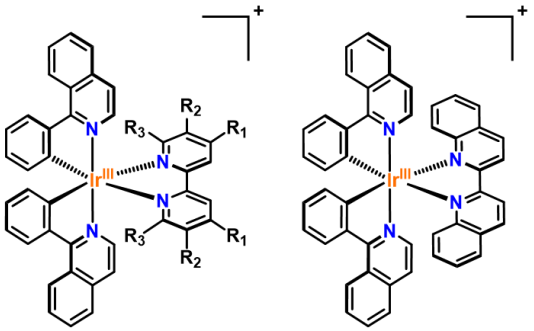

Figure 9.1. Structure of the $[Ir(piq)_2(LL)]^+.PF_6^-$ photosensitizers investigated in **Chapter III**.

To this end, the first part of this Ph.D. thesis was devoted to the synthesis and the study of a series of nine $[Ir(piq)_2(LL)]^+$ photosensitizers based on the electron rich piqH ligand. These photosensitizers absorbed visible light with molar absorption coefficients in the 5400-7900 $M^{-1}cm^{-1}$ range, and the excited-state electron transfer with classical electron donors such as TEA, TEOA and BIH was investigated by steady-state excited-state quenching experiments in acetonitrile. Steady-state photolysis in the presence of BIH showed that most of the photosensitizers were stable in their reduced form, which is a paramount criterion for efficient and long-term light-driven reduction of protons.

In a second time, increased red-shifted absorption properties were obtained by the judicious use of cyclometalating piq and fliq ligands in combination with the recently reported bpph diimine ligand (**Figure 9.2**). These two photosensitizers exhibited a red-shifted absorption up to 620 nm, thus capable of covering most of the visible spectrum. In acetonitrile, in the presence of a cobalt catalyst, a sacrificial electron donor and a proton source, both Ir(III)

photosensitizers were able to utilize blue, green and red photons to generate hydrogen with turn-over numbers up to 11650, 10600 and 174 mol_{H2} mol_{PS}^{-1}, respectively.

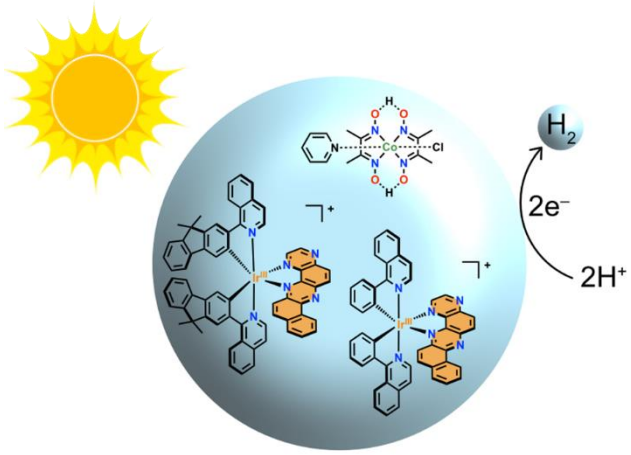

Figure 9.2. Structures of $[Ir(piq)_2bpph]^+$, $[Ir(fliq)_2bpph]^+$, and the precatalyst $[Co(dmgH)_2(py)(Cl)]$ used for HER in **Chapter IV**.

In a collaborative study, two Ir(III)-Co(III) previously reported by our group consisting of cobaloxime hydrogen evolution catalysts chelated to Ir(III)-based photosensitizers with ppy or piq were investigated by XTAS and TA in the picosecond timescale spectroscopies coupled with TD-DFT theoretical calculations. This allowed to investigate the photo-induced electron transfer dynamics, photogenerated intermediates and influence of the cyclometalating ligands on the Ir(III)-based photosensitizers that are responsible for the dyads´ activities. This mechanistic study provided significant insights into the reaction pathways and efficiencies of supramolecular Ir(III)–Co(III) dyads, highlighting the future potential for developing Ir(III)-based photosensitizers with less conjugated cyclometalated ligand derivatives for HER applications. However, as depicted throughout this Ph.D. thesis, this improvement often comes at the expense of visible light absorption.

In an initial effort to advance photosensitizer regeneration via halide oxidation, we developed a series of Ru(II) and Os(II) complexes featuring a common ligand scaffold, 9,10-diNH_2-1,4,5,8-

tetraazaphenanthrene (diNH$_2$TAP) (**Figure 9.3**). The 1,4,5,8-tetraazaphenanthrene (TAP) moiety provides high oxidizing power, while the incorporation of diamino functionalities would facilitate the development of a series of bridging ligands through condensation with *o*-diones, such as 1,10-phenanthroline-5,6-dione. This approach aims to create strong photo-oxidant photosensitizers capable of bridging a proton reduction catalyst for homogeneous HX splitting. However, their excited-state reduction potential is only suitable for halide oxidation in organic solvents and iodide in aqueous solutions, but not for the oxidation of bromide and chloride in water. Consequently, and due to their extensive use in photodynamic therapy, we decided to investigate the bimolecular reactivity of these photosensitizers with a prototypical biological substrate, specifically guanosine-5'-monophosphate (GMP). Time-resolved quenching experiments and nanosecond transient absorption spectroscopy confirmed that these photosensitizers were competent for excited-state electron transfer, as clearly observed for both [Ru(TAP)$_2$(diNH$_2$TAP)]$^{2+}$ and [Ru(TAP)$_2$(NO$_2$NH$_2$TAP)]$^{2+}$.

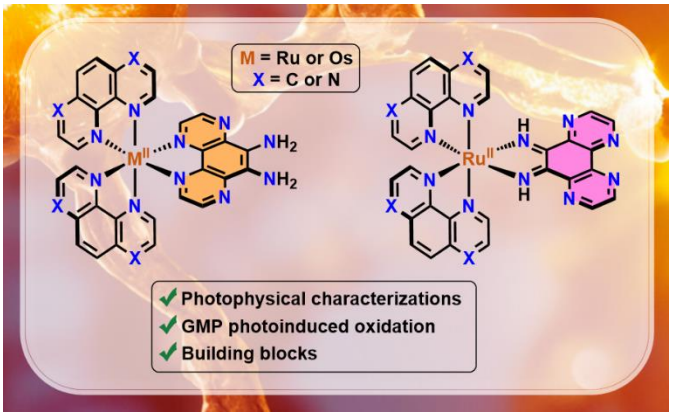

Figure 9.3. Structure of the Ru(II) and Os(II) photosensitizers reported in **Chapter VI**.

Following the results obtained with Ru(II) and Os(II) complexes, which showed some potential in type I photodynamic therapy applications, we shifted back our focus on the utilization of Ir(III) complexes for halide oxidation applications due to their wider accessible excited-state potential range. Hence six new

Ir(III) photosensitizers bearing the ^{dFCF3}ppy cyclometalated ligand in combination with the π-extended diimine ligands were designed (**Figure 9.4**). All photosensitizers showed excellent excited-state reactivity toward iodide, bromide, and chloride in water-enriched conditions, as evidenced by significant excited-state quenching with quenching rate constants (k_q) reaching up to 10^{10} $M^{-1}s^{-1}$, 10^{9} $M^{-1}s^{-1}$ and 10^{8} $M^{-1}s^{-1}$ for iodide, bromide and chloride oxidation, respectively. Further investigation using transient absorption spectroscopy confirmed efficient electron transfer from iodide, bromide, and chloride to the excited photosensitizers in acetonitrile/water mixtures, allowing the investigation of cage escape processes. Cage escape yields were investigated for all halides and were found to be larger in acetonitrile (0.47–1.00) than in 50:50 acetonitrile/water mixture (0–0.35), further expanding the applicability of these photosensitizers as candidates for HX splitting.

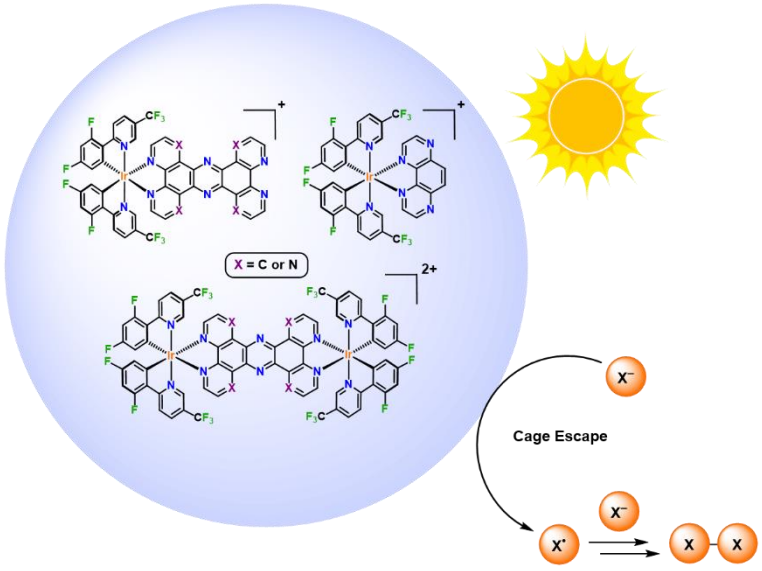

Figure 9.4. Structure of the Ir(III) photosensitizers presented in **Chapter VII** alongside the proposed scheme for the HX (X = I, Br, Cl) splitting reaction.

Finally, we investigated the use of a previously reported Fe(III)-based photosensitizer for halide oxidation in dichloromethane, acetonitrile, and acetonitrile/water mixture. In neat organic solvent, large quenching rate constants close to the diffusion limit were obtained. In CH_3CN/H_2O 1:1

mixture, iodide and to a lesser extend bromide were competent for excited-state quenching. Direct evidence for excited-state electron transfer was only obtained by nanosecond transient absorption spectroscopy for iodide in dichloromethane and acetonitrile. The cage escape yields were also determined and were shown to be larger in dichloromethane (0.079) than in acetonitrile (0.017). However, these values were relatively low compared to those obtained for Ir(III) photosensitizers and evidence for electron transfer was only demonstrated for iodide in organic solvent. The results presented in **Chapter VIII** represent a first step towards the transition to earth abundant photosensitizers for halide oxidation, albeit only in organic solvent.

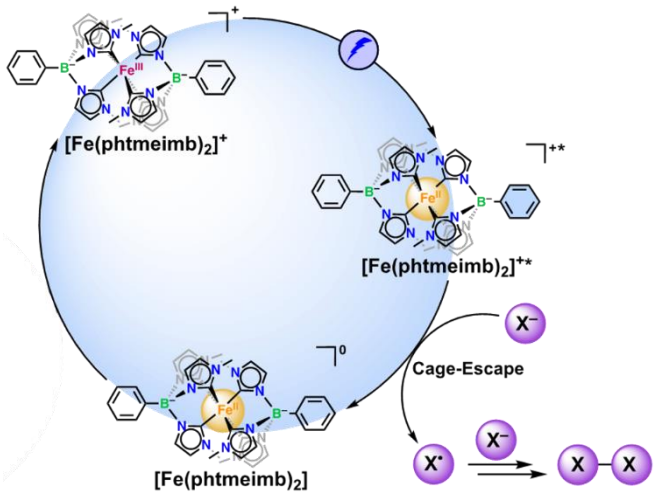

Figure 9.5. Structure of $[Fe(phtmeimb)_2]^+$ alongside the proposed scheme for the HX (X = I, Br, Cl) splitting reaction investigated in **Chapter VIII**.

9.2 Prospects

9.2.1 Towards homogeneous HX splitting

The conclusive and encouraging results of this Ph.D. thesis in the field of halide oxidation encouraged us to take advantage of the chelation site available in the photosensitizers presented in **Chapter VII** for HER. For this purpose, we took inspiration from the Ru-Pt dyads reported by Sven Rau[221, 222, 353] to synthesize Ir-Pt dyads from Ir-TPPHZ, Ir-HATPHE and Ir-PHEHAT(**Figure 9.6**) to regenerate the PS via halide oxidation instead of using prototypical sacrificial electron donors.

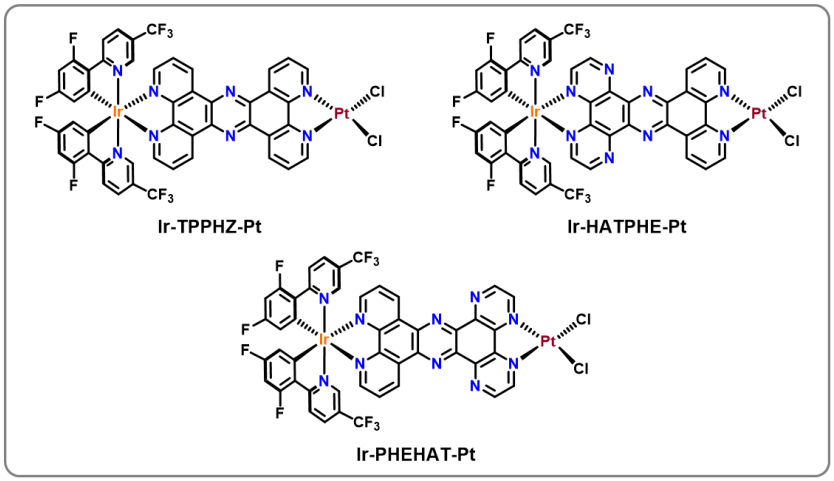

Figure 9.6. Structure of the different Ir-Pt dyads investigated in this perspective section.

The three Ir-Pt dyads were tested for photocatalytic hydrogen evolution during a research stay at CEA-Grenoble under the supervision of Dr. Murielle Chavarot-Kerlidou (Directrice de Recherches au CNRS). The photocatalytic hydrogen evolution was assessed using the following conditions: a schlenk tube was charged with acetonitrile (3.0 mL) containing the photocatalyst in the dark and under argon stream, after adding of degassed triethylamine (1.5 mL) and degassed 2M H_2SO_4 aqueous solution (0.5 mL) the final catalyst concentration in the catalysis solution was 70 μM. Subsequently, the solution was irradiated with a Kessil LED lamp (PR160L, λ_{max} = 440 nm). Under these

conditions, hydrogen evolution was only observed for the Ir-TPPHZ-Pt dyad (**Figure 9.7**). Control experiments highlighted that the dyad was unable to produce hydrogen catalytically without TEA or the Pt catalytic centre. The reasons why the Ir-HATPHE-Pt and Ir-PHEHAT-Pt dyads did not produce hydrogen under these conditions are currently under investigation.

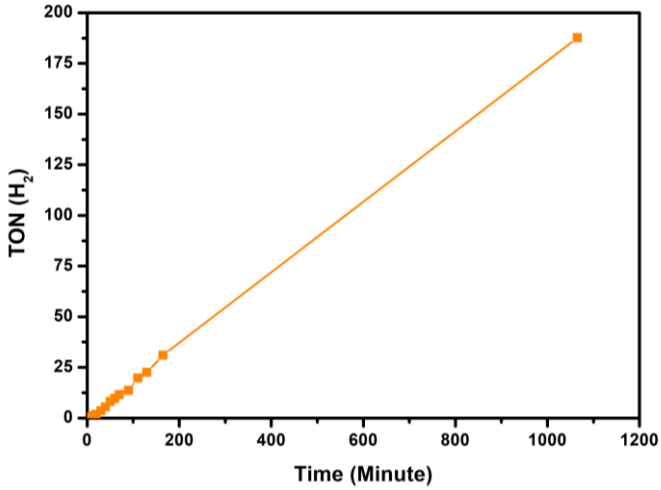

Figure 9.7. HER at 440 nm with 70 x10^{-6} M Ir(III)-TPPHZ-Pt(II) dyad, carried out in CH_3CN (3.0 mL) with 1.5 mL TEA as the electron source and 2M H_2SO_4 (0.5 mL) as the proton source.

The first trials for hydrogen production using halides instead of triethylamine in the same conditions have been carried out on the Ir-TPPHZ-Pt dyad during this research stay. At this stage, hydrogen production is not yet efficient using tetra-*n*-butylammonium iodide or potassium iodide and requires further optimization. This can be due to the low cage escape yields in water enriched conditions observed in **Chapter VII**. Therefore, moving towards conditions similar to **Chapter IV**, *i.e.*, using pure acetonitrile with HBF_4 as the proton source and using non-covalently bound PS and HER catalysts, could be the key parameters to move towards HX splitting.

9.2.2 Photosensitizers heterogenization

The next step in our research focuses on the heterogenization of our systems to investigate their photocatalytic activity through the construction of Dye-Sensitized PhotoElectrochemical Cells (DSPECs) for HX splitting applications. The transition from homogeneous to heterogeneous phase will allow us to get rid of the water solubility drawback of the Ir(III) and Fe(III) complexes and to develop robust system for hydrohalic splitting.

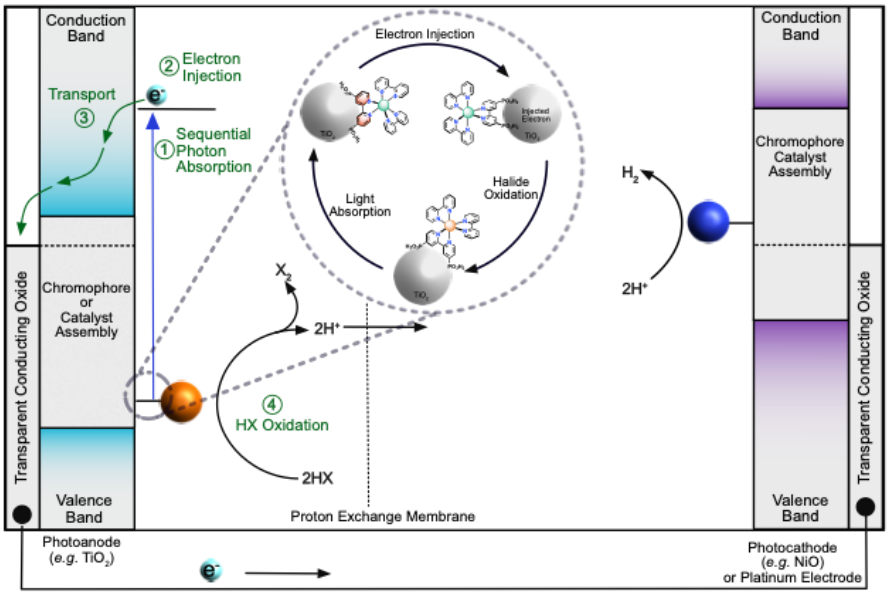

Figure 9.8. General DSPEC architecture where visible light absorption (1) leads to charge injection into the TiO_2 conduction band (2). The electron then diffuses (3) to the (photo)cathode where proton reduction can occur while the oxidized metal complex is regenerated by X^- oxidation (4).

These solar cells consist of three distinct parts. The photoanode comprises a transparent conductive oxide, such as fluorine-doped tin oxide, with a thin film of mesoporous TiO_2 deposited on it, which is then covered by a photosensitizer covalently anchored to the semiconductor surface. The photocathode also consists of fluorine-doped tin oxide coated with NiO, which is covered by a photosensitizer-catalyst assembly covalently anchored to the semiconductor. Alternatively, the photocathode can be replaced by a cathode made of fluorine-doped tin oxide coated with platinum to reduce protons. The

third part is the liquid electrolyte and a proton exchange membrane that allows the diffusion of protons to the cathode or photocathode (**Figure 9.8**).

To this end, phosphonic groups will be introduced on different ligands presented in this Ph.D. thesis (**Figure 9.9**). This can be easily achieved by starting with brominated substituents, which can then be converted into phosphonic acids. At the photocathode, photosensitizers that do not present a coordination site for a HER catalyst can be co-anchored with the catalyst or attached using a layer-by-layer technique, where components are interconnected by Zr(IV) cations.[102] The resulting photosensitizers will be anchored onto thin metal oxide films (TiO_2 or NiO), and their ability to inject electrons (photoanode) or holes (photocathode) into the conduction band of these semiconductors upon light excitation will be investigated.

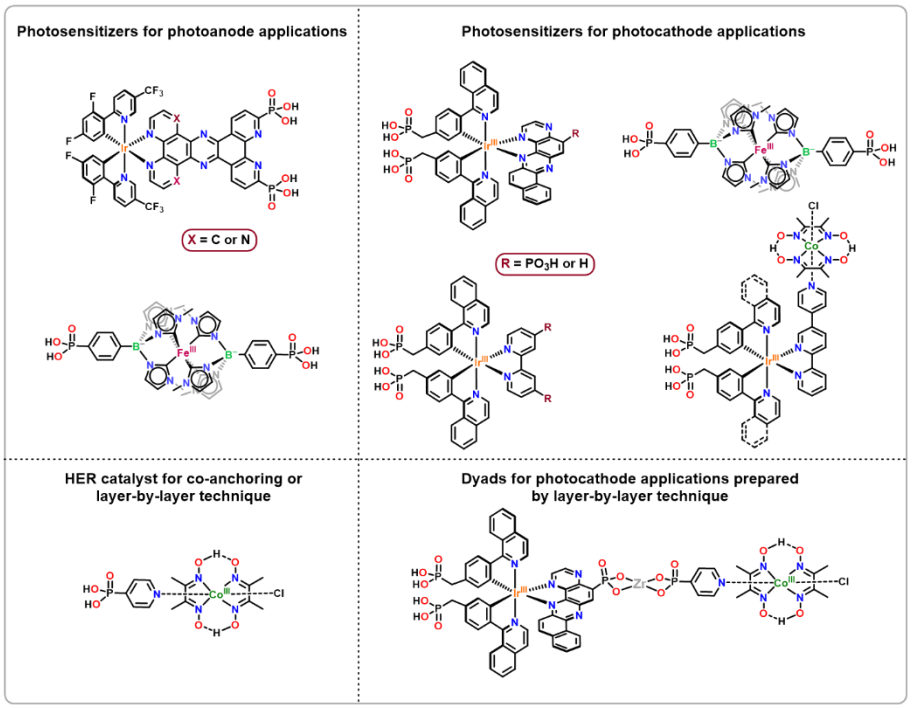

Figure 9.9. Proposed structures for the design of photoanode and photocathode materials.

It is clear that extensive studies will be necessary before achieving an operational Ir(III) or Fe(III)-based dye-sensitized photoelectrosynthesis system for HX splitting applications. While the progress made in this Ph.D. thesis represents a significant step towards the understanding and optimization of photosensitizers for halide oxidation and proton reduction, many challenges remain to be addressed. The foundational work done here offers valuable insights but also highlights the complexity of developing efficient and sustainable systems for solar fuel production. Continued research is essential to overcome these hurdles and make practical advancements. The path ahead is demanding, yet the potential benefits for clean energy and environmental sustainability make this a vital area of ongoing investigation.

Chapter X – Materials and Methods

Nuclear Magnetic Resonance. Characteristic ^{1}H NMR spectra were obtained at room temperature using a Bruker AM-300 (300 MHz) or a Bruker AM-500 (500 MHz) spectrometer at 23 °C. Solvent residual peaks were used as internal standards for ^{1}H (δ =7.26 ppm for $CDCl_3$, δ = 1.94 ppm for CD_3CN and δ = 2.50 ppm for $(CD_3)_2SO$) chemical shift referencing. NMR spectra were processed using MNOVA.

Microwave synthesis. Microwave (MW) syntheses were performed on a Milestone MicroSYNTH labstation under magnetic stirring. Typically, the conditions allowed the vessels to reach the desired temperature in 3 minutes and the vessels were held at the desired temperature for the indicated period of time.

High-resolution mass spectrometry. HRMS spectra were recorded on a Q-Extractive orbitrap from ThermoFisher. Samples were ionized by electrospray ionization (ESI; capillary temperature = 250°C, vaporizer temperature = 250°C, and sheath gas flow rate = 20).

UV−Visible Absorption. UV−vis absorption spectra were recorded on a Shimadzu UV-1700 with 1 cm path length quartz cell.

Steady-State Photoluminescence. Room temperature steady-state photoluminescence (PL) spectra were recorded on a Horiba Scientific-FL-1000 fluorimeter and were corrected by calibration of the instrument's response with a standard tungsten-halogen lamp. The photoluminescence intensity was integrated for 0.1 s at 1 nm resolution and averaged over 3 scans.

Time-Resolved Photoluminescence. Time-resolved PL data were acquired on a nitrogen dye laser with excitation centred at 445 nm. Pulsed light excitation was achieved with a Photon Technology International (PTI) GL-301 dye laser that was pumped by a PTI GL-3300 nitrogen laser. The PL was detected by a Hamamatsu R928 PMT optically coupled to a

ScienceTech Model 9010 monochromator terminated into a LeCroy Waverunner LT322 oscilloscope. Decays were monitored at the PL maximum and averaged over 180 scans. Nonradiative and radiative rate constants were calculated from the quantum yields, $\Phi = k_r/(k_r + k_{nr})$ and lifetimes, $\tau = 1/(k_r + k_{nr})$.

Time-Resolved and Steady-State Photoluminescence (Chapter VIII). Time-resolved and steady-state photoluminescence spectra were recorded on an Edinburgh Instruments FS5 Spectrofluorometer equipped with a time-correlated single photon counting module. The steady-state photoluminescence spectra were recorded using a 150 W Xenon arc lamp as the excitation source. The photoluminescence was detected at a right angle to the excitation beam using a single photon counting PMT-900 in a temperature stabilized housing. The spectra were integrated at 0.1s and three spectra were averaged. Steady-state photoluminescence spectra were corrected for the instrument's spectral response. All room-temperature spectra were obtained from Argon-sparged solutions. Time-resolved photoluminescence data were collected on the FS5 using the time-correlated single photon counting technique (TCSPC). Excitation was achieved with a 510 ± 5 nm diode laser (Edinburgh Instruments EPL-510, 90 ps pulse width at 10 MHz). Photons reaching the detector were accumulated to reach a count of 10,000.

Electrochemistry. Cyclic voltammetry was performed with an Autolab PGSTAT 100 potentiostat using a standard three-electrode-cell, *i.e.* a glassy carbon disk working electrode (approximate area = 0.03 cm^2), a platinum wire counter electrode and an aqueous Ag/AgCl reference electrode (salt bridge: 3M KCl/saturated AgCl). Experiments were performed in dry 0.1 M tetrabutylammonium hexafluorophosphate acetonitrile electrolyte, and the samples were purged with argon before each measurement.

Franck-Condon lineshape analysis of the luminescence spectra. Fitting of the steady-state photoluminescence spectra was made possible through

Franck-Condon lineshape analysis. After converting the wavelength abscissa values to energy, the emission spectral data (multiplied by λ^2) were renormalized and fit to **Equation 10.1**.

$$I(\tilde{\nu}) = \sum_{\nu_m}^{\infty}\sum_{\nu_n}^{\infty}\left(\frac{E_0 - \nu_m\omega_m - \nu_n\hbar\omega_n}{E_0}\right)^4 \frac{S_M^{\nu_m}}{\nu_m!}\frac{S_N^{\nu_n}}{\nu_n!} \times exp\left\{-4\ln 2\left(\frac{\tilde{\nu} - E_0 + \nu_m\hbar\omega_m + \nu_n\hbar\omega_n}{\Delta\tilde{\nu}_{1/2}}\right)^2\right\}$$

Equation 10.1

In this equation, v_m and v_n are the vibrational quantum numbers for the acceptor mode, S_M and S_N are the Huang-Rhys factors, also known as the coupling factor, $\hbar\omega_m$ and $\hbar\omega_n$ correspond to the vibrational energy spacing in the ground-state potential energy surface for the corresponding vibration mode, E_{00} corresponds to the energy difference between the ground and excited state potential surfaces. Luminescence spectra can be modeled using one or two vibration modes, which correspond to the dominant vibration mode or an average of vibration. Usually, transitions implying v=0 to v=0 to 5 are sufficient to fit the experimental data. These transitions are broadened thanks to a Gaussian distribution, which takes solvent effects into account; $\Delta v_{½}$ is the full-width at half-maximum of the broadening for the transition and a normalization factor of 4ln2 is added to ensure that the integrated area corresponds to the intensity of the line that is broadened into a Gaussian distribution.

Stern-Volmer experiments. Excited-state quenching experiments were performed on a Varian Cary Eclipse spectrometer and the photoluminescence spectra were not corrected for the instrument's response. Typically, photosensitizer solution with an absorbance of ~ 0.1 around 420-440 nm was prepared in acetonitrile. Various quencher solutions with concentration ranging from 0.05 to 0.5 M were prepared in the desired solvent also containing the photosensitizer with the same absorbance. The solutions were purged with argon for 15 minutes prior to the experiments. The desired quencher was gradually added to the solution of photosensitizer and the

excited-state quenching was monitored by steady-state photoluminescence. The decrease of photoluminescence was related to the concentration of quencher and the respective Stern-Volmer plots were extrapolated using Equation 1.19. The quenching rate constant (k_q) was then determined by dividing the slope by the initial lifetime without any quencher, determined for each experiment.

Transient absorption. Nanosecond transient absorption measurements were recorded on an LP920-K spectrometer from Edinburgh Instruments equipped with an iCCD detector from Andor. The excitation source was a tunable Nd:YAG Laser NT342 Series from EKSPLA. The third harmonic (355 nm) at 150 mJ was directed into an optical parametric oscillator (OPO) to enable wavelength tuning starting from 410 nm. The laser power was then attenuated to reach appreciable signal/noise and the integrity of the samples were verified by UV-Vis measurements. All samples were recorded in argon-purged acetonitrile at room temperature.

Another transient absorption spectroscopy set-up used during this Ph.D. thesis was a LP980-K spectrometer from Edinburgh Instruments equipped with an iCCD detector from Andor (DH320T). The excitation source was a tuneable Nd:YAG Laser NT342 Series from EKSPLA. The third harmonic (355 nm) at 100 mJ was directed into an optical parametric oscillator (OPO) to enable wavelength tuning starting from 410 nm. The laser power was then attenuated to reach appreciable signal/noise and the integrity of the samples was verified by UV–Vis measurements. The LP980-K is equipped with a symmetrical Czerny-Turner monochromator. For single wavelength absorption changes, an 1800 g mm^{-1} grating, blazed at 500 nm is used, which affords wavelength coverage from 200 to 900 nm. For spectral mode (iCCD), a 150 g mm^{-1} grating, blazed at 500 nm is used, offering a wavelength coverage of 540 nm over the full wavelength range extending from 250 to 900 nm. Single wavelength absorption changes were monitored using a PMT LP detector (Hamamatsu R928) which covers the spectral range from 185 to 870 nm. The probe was a 150 W ozone-free xenon short arc lamp (OSRAM XBO

150W/CR OFR) that was pulsed at the same frequency of the laser. The excitation wavelength depended on the photosensitizers but in all cases the concentration at the excitation wavelength was adjusted to reach absorbance values between 0.3 and 0.5. All measurements were performed in argon purged solvents at room temperature. An average of 30 to 90 scans per measurements was used.

Photolysis experiments (Chapter III). Ir(III) solutions with an absorbance of ~ 0.5 around 420-440 nm were prepared in acetonitrile. BIH was added to reach a concentration of 1 mM. The solutions were purged with argon for 15 minutes in the dark prior to being irradiated with a blue LED commercial strip for up to 15 minutes. The blue LED irradiation that was selected for this study emits between 420 and 490 nm, with a maximum around 460 nm. The LED stripes are pasted in three circles into a crystallizing dish and the sample is positioned at the middle (roughly 5 cm away from the side of the crystallizing dish) UV-Vis spectra were recorded every 5 minutes. Reversibility of the excited-state reduction was assessed by adding an excess of sacrificial electron acceptor, $K_2S_2O_8$.

Theoretical studies. Our computational methodology is based on Density Functional Theory (DFT) and time dependent DFT (TD-DFT) methods. All calculations were performed using the Gaussian 16 computational chemistry package[475] while applying default procedures integrations grids, algorithms and parameters. As first step, the equilibrium geometries of the singlet states of the investigated photosensitizers were optimized in acetonitrile using the integral equation formalism model (IEFPCM)[476]. These calculations were performed using the hybrid B3LYP exchange-correlation functional.[328, 477, 478] The 6-31G(d,p) basis set[479, 480] was used for the C, N and H atoms while SBKJC-VDZ relativistic effective core potential and associated basis set[481] was employed to describe the Ir atom and the def2-SVP relativistic effective core potential and associated basis set was employed to describe the Ru atoms.[482, 483] The harmonic vibrational frequencies of each complex have been calculated with the same level of calculation, and it has been checked

that all structures correspond to true minima of the potential energy surface. Cartesian coordinates for all atoms in optimized structures of the complexes are provided in the experimental section of each chapter.

TD-DFT method was employed to investigate the excited state electronic structure of each of the two complexes. The first 150 lowest-lying singlet excited states of the two complexes at their ground-state singlet geometry have been evaluated within the vertical TD-DFT approximation, using the level of theory B3LYP/6-31G(d,p)/SBKJC-VDZ. The modelling of solvents effects (in this case acetonitrile) has been included through the IEF-PCM model. To be able to discuss the excited states characters, the natural transition orbitals (NTO's)[484] adapted to the excited state of interest have been used.

Set-up for Gas Chromatography (GC). Monitoring of hydrogen evolution was performed with a PerkinElmer Clarus-480 gas chromatograph with a thermal conductivity detector, Ar as the carrier and eluent gases, a 7 ft. HayeSep N 60/80 precolumn, a 9 ft. molecular sieve 13 × 45/60 column, and a 2 mL injection loop. Three distinct solutions for the PS, catalyst and sacrificial donor and acid source were mixed together to obtain 5 mL of sample solutions in standard 20 mL headspace vials. Those vials were placed in a 20°C thermostatic photoreactor that was illuminated by a 10W LED set at the desired irradiation. An analog power-meter PM100A (THORLABS) associated with a compact photodiode power head with silicon detector S120C was used to evaluate the power of the photon flux. Photo-diode detector was placed at the same distance from the LED surface than the bottom of the illuminated vial. The vials are continuously stirred and bubbled in a controlled way by use of Mass Flow Controllers (Alicat 0-20 SCCM) which were set to deliver a stable flow rate of argon of 10 mL/min or 5 mL/min. The vial was sealed with a rubber septum pierced by two stainless-steel cannulas. The upstream stainless-steel cannula joined a pre-loaded vial containing 5 mL of acetonitrile (to saturate the gas with solvent before it enters the reaction vial). The downstream stainless-steel cannula was connected to a 2 mL empty vial (to protect the GC from any accidental droplet of acetonitrile) which was connected to an 8-port

stream select valve (VICCI). The selected valve allowed the gas stream from the reaction vial to fill the sample loop of the GC. A digital flowmeter (Perkin Elmer FlowMark) was used to check the flow. The solutions were degassed for 30 min under argon flow before turning on the light. A microprocessor (Arduino Uno) coupled with a custom PC interface controls the intervals (defined times) at which gas injections were taken from the reaction vial into the GC sample loop.

A calibration curve, to establish the relationship (**Equation 10.2**) between the integration of the H_2 signal in the TCD trace (y) and the concentration of H_2 in the gas sample (x), was determined by following different, accurately known, concentrations of standard H_2 gas mixtures (balance of mixture is argon) into the sample loop and integrating the observed area under the H2 peak in the TCD trace.

$$\boldsymbol{y = ax + b}$$

Equation 10.2

x = concentration of H_2, in $\mu L\ L^{-1}$

y = H_2 TCD area, in $\mu V\ s$

a = slope

b = noise of H_2 TCD area without hydrogen present, in in $\mu V\ s$

Calibration established the values of a (the constant of proportionality, or slope) and b (noise correction) in **Equation 10.2**. With these values in hand, when a catalyst was tested, the area of the observed H_2 peak in the TCD trace was converted, using **Equation 10.2**, into the concentration of H_2 in $\mu L\ L^{-1}$. The flow rate of the argon vector gas was known, so the rate of H_2 generation was readily calculated using **Equation 10.3**.

$$H_2 \text{ production rate } (mL_{H2}\ min^{-1}) = [H_2 \text{ standard}]\ (mL_{H2}\ L^{-1}) \text{ x Ar flow rate } (L\ min^{-1})$$

Equation 10.3

The ideal gas law (**Equation 10.4**) allowed the conversion of volume of H_2 in L to the amount of substance in mol.

$$\boldsymbol{n = \frac{PV}{RT}}$$

Equation 10.4

P = pressure = 1 atm

T = temperature = 298 K

R = ideal gas constant = 0.082 L atm K^{-1} mol^{-1}

V = hydrogen volume in L

n = amount of hydrogen in mol

Extended X-ray Absorption Fine Structure (EXAFS). Athena software[485] was used for data processing. The energy scale for each scan was normalized using cobalt and iridium metal standard. Data in energy space were pre-edge corrected, normalized, deglitched (if necessary), and background corrected. The processed data were next converted to the photoelectron wave vector (k) space and weighted by k^2. The electron wave number is defined as $k = [2m(E - E_0)/\hbar^2]^{1/2}$, E_0 is the energy origin or the threshold energy. K-space data were truncated near the zero crossings k = 2 to 11 $Å^{-1}$ for the Co and Iridium complexes´ ground states Co/Ir EXAFS Fourier transformation. The k-space data were transferred into the Artemis Software for curve fitting. In order to fit the data, the Fourier peaks were isolated separately, grouped together, or the entire (unfiltered) spectrum was used. The individual Fourier peaks were isolated by applying a Hanning window to the first and last 15% of the chosen range, leaving the middle 70% untouched. Curve fitting was performed using *ab initio*-calculated phases and amplitudes from the FEFF8[486] program from

the University of Washington. *Ab initio*-calculated phases and amplitudes were used in the EXAFS equation (**Equation 10.5**).

$$\chi(k) = S_0^2 \sum_j \frac{N_j}{kR_j^2} f_{eff_j}(\pi, k, R_j) e^{-2\sigma_j^2 k^2} e^{\frac{-2R_j}{\lambda_j(k)}} \sin(2kR_j + \phi_{ij}(k))$$

Equation 10.5

where N_j is the number of atoms in the j^{th} shell; R_j the mean distance between the absorbing atom and the atoms in the j^{th} shell; $f_{eff_j}(\pi, k, R_j)$ is the *ab initio* amplitude function for shell *j*, and the Debye-Waller term $e^{-2\sigma_j^2 k^2}$ accounts for damping due to static and thermal disorder in absorber-backscatterer distances. The mean free path term $e^{\frac{-2R_j}{\lambda_j(k)}}$ reflects losses due to inelastic scattering, where $\lambda_j(k)$, is the electron mean free path. The oscillations in the EXAFS spectrum are reflected in the sinusoidal term $\sin(2kR_j + \phi_{ij}(k))$, where $\phi_{ij}(k)$ is the *ab initio* phase function for shell *j*. This sinusoidal term shows the direct relation between the frequency of the EXAFS oscillations in k-space and the absorber-backscatterer distance. S_0^2 is an amplitude reduction factor.

The EXAFS equation[4] (**Equation 10.5**) was used to fit the experimental Fourier isolated data (q-space) as well as unfiltered data (k-space) and Fourier transformed data (R-space) using *N*, S_0^2, E_0, *R,* and σ^2 as variable parameters (**Table S5.1**). *N* refers to the number of coordination atoms surrounding Co/Ir for each shell. The quality of fit was evaluated by R-factor and the reduced Chi^2 value. The deviation in E_0 ought to be less than or equal to 10 eV. R-factor less than 2% denotes that the fit is good enough. R-factor between 2 and 5% denotes that the fit is correct within a consistently broad model. The reduced Chi^2 value is used to compare fits as more absorber-backscatter shells are included to fit the data. A smaller reduced Chi^2 value implies a better fit. Similar results were obtained from fits done in k, q, and R-spaces.

Steady-state and time-resolved XAS measurements. Steady-state and time-resolved X-ray absorption spectra were collected at 11 ID-D[487] beamlines at the Advanced Photon Source using undulator radiation at electron energy 7.71 KeV (Co K-edge) and 11.22 KeV (Ir L_3-edge) in solvent grade acetonitrile. The samples were circulated through a stainless-steel nozzle into a free-flowing cylindrical jet inside an airtight aluminum chamber, and continuously degassed with nitrogen. This sample handling technique ensures proper sample recovery such that the subsequent laser pulse can hit a "fresh" sample position. Cooled running water from a chiller was additionally circulated around the jacketed sample flask to prevent heating damage of the complexes by radiation. The X-ray fluorescence signals were collected with two avalanche photodiodes (APDs) positioned at 90° on both sides of the liquid jet, and a combination of Z-1 filters and soller slits with conical geometry were used to reduce the background from elastically scattered X-rays.

The experiments were carried out using the 24-bunch timing mode of APS (in top up mode with a constant 102 mA ring current) which consists of a train of X-rays separated by 153 ns. This mode easily allows for gateable detectors that selects X-ray pulses. This timing mode was suitable for this type of experiments in which the separation between adjacent X-ray pulses was long enough for the Avalanche Photodiode (APD) detector to resolve individual X-ray pulses.

The time-resolved experiments were carried out by pumping the samples at 400 nm wavelength using a regenerative amplified laser with 10 kHz repetition rate 5 ps-FWHM pulse length and laser power of 630 mW at the sample. The X-ray and laser beam were spatially overlapped with an X-ray spot size of 100 µm(V) x 450 µm(H) and laser spot size of 170 µm(V) x 550 µm. With a liquid flow speed of around 4.5 m/s, the pumped laser volume was calculated to move out of the FWHM laser pulse region in around 20 µs. This temporal range ensured that the excited state volume was probed more at the centre and less at the edges where the excitation fraction would be less, due to movement of the sample. Beamline 11 ID-D has an automated data

digitization system which allows for all X-ray pulses after laser excitation to be collected. Such a system, together with the larger X-ray beam spot size, was very useful for our experiments, as multiple X-ray pulses after laser excitation were averaged to monitor the dynamics for the formation and decay of the Co(II) transient signal in the nano-microsecond time regime.

The UV-vis measurements of the dyads before and after X-ray and laser exposure were checked after each run to ensure lack of X-ray and laser damage of the complexes. The laser-on XAS of the dyads at both Co K-edge and Ir L-edge energies were further checked scan by scan at every 20 min interval to ensure lack of X-ray radiation and laser-induced damage (**Figure S5.6**). The "laser-off" X-ray measurements of the **dyads I** and **II** collected over one batch of experiments after laser exposure and over the course of 2.7 hours at Co K-edge and Ir L-edge energies are shown in **Figure S5.6**. No decomposition of the dyads was hereby observed, thus ensuring the samples' integrity. The delay between the pump and X-ray pulses was adjusted by a programmable delay line (PDL-100A-20NS, Colby Instruments). A Co/Ir metal foil was placed between two ionization chambers downstream to the X-ray beam, and its transmission recorded with each scan for energy calibration.

Transient Absorption Measurements (Chapter V). Ultrafast transient absorption spectroscopy was carried out at the Centre for Nanoscale materials at Argonne National Laboratory with an amplified Ti-sapphire laser (Spectra Physics, Spitfire Pro) at 1 KHz repetition rate and an automated data acquisition system (Ultrafast Systems, Helios). The Ir dyads and Ir complexes were pumped with 405 nm excitation and typical pulse energy of 300 nJ per pulse, and probed with a super-continuum (Ultrafast systems, Helios) light source. The transient absorption data included a set of two-dimensional data together with kinetics spectra for a probe wavelength of 450 to 750 nm. The temporal chirp in the optical transient absorption data of the probe beam were corrected using the non-resonant response of blank water, and acetonitrile solvent, the latter of which gave an IRF of 400 fs. The samples were degassed with N_2 gas and continuously magnetically stirred in a 2 mm cuvette.

DFT Calculations (Chapter V). The DFT optimization calculations were performed using the ORCA (Version 5.0) program package developed by Neese[488] and co-workers. The geometry optimizations were carried out using the solid-state (XRD) as a starting point. The calculations were carried out using the BP86 exchange-correlation functional[328] in combination with the triple zeta valance polarization functions (def2-TZVP)[482] , and the atom-pairwise dispersion correction with the Becke-Johnson damping scheme (D3BJ)[329, 489]. The RI[490] approximation were used to accelerate Coulomb and exchange integrals for the ground and excited state calculations respectively. The default GRID settings were further used for the self-consistent field iterations and for the final energy evaluation. The calculated structures were confirmed to be minima based on a check of the energies and the absence of imaginary frequencies from frequency calculations carried out on the optimized geometries.

Time-dependent (TD)-DFT XANES Calculations. Time-dependent DFT (TD)-DFT calculations for the XANES spectra of the Cu complexes were carried out using the hybrid-DFT functional B3LYP due to its preferred use in predicting spectroscopic features.[491] The TD-DFT XANES simulations were in this case performed with the B3LYP[492, 493] as functional with the def2-TZVP triple-zeta[492, 493] basis sets together with the ZORA approximation and D3BJ dispersion correction effects with dense integration grids. The def2-TZVP/J auxiliary basis set was also employed. The XANES absorption spectra from the TD-DFT calculations were shifted in energy, by -5 eV relative to the experimental data as previously demonstrated[78, 494, 495], and a broadening of 2.0 eV was applied to all calculated spectra. Up to 150 roots were calculated. The calculated XANES spectrum contains contributions from electric quadrupole, electric dipole and magnetic dipole transitions. All spectra were broadened with a Gaussian line shape of 2.0 eV (FWHM).

Cage escape yields measurements. The protocol to determine cage escape yields was previously reported in detail.[406] Briefly, a solution of $[Ru(bpy)_3]^{2+}$ with an absorbance around 0.5 at 470 nm was prepared in acetonitrile. The

solution was purged with argon for 30 minutes. This solution served as actinometer. The absorbance (Abs_{ref}) at the excitation wavelength (λ_{exc}) was recorded on an Agilent Cary 60 spectrophotometer. The sample was then irradiated using pulsed light attenuation while monitoring the bleach at 450 nm (ΔA_{ESref}). The laser power was attenuated to ensure good signal/noise ratio while also avoiding saturation of the ΔAbs signal at 450nm with increasing laser power. A $\Delta\varepsilon$ value of –11000 $M^{-1}cm^{-1}$ was used for the actinometer at 450 nm.[130-132] A sample of the iron (III) complex was then prepared with an absorbance between 0.4 and 0.7 at the same excitation wavelength as the actinometer (λ_{exc}). The absorbance (Abs_{PS}) at the excitation wavelength (λ_{exc}) was also recorded on an Agilent Cary 60 spectrophotometer. The solution was purged with argon for 30 minutes. Increasing concentration of halides were then added. These halides solutions were prepared in stock solution of the photosensitizers to ensure constant absorption, but the absorbance value was still recorded after any given addition. The steady-state photoluminescence with added halide was recorded, which enable to determine the % of quenching (%PL Quenched) after any given addition of halide. The signal of the mono-reduced Fe (III) photosensitizer (ΔA_{PS-}) was recorded at 385 nm. A $\Delta\varepsilon$ value $\Delta\varepsilon_{385nm}$ = 7200 $M^{-1}cm^{-1}$ was used from literature.[99] The signal of the mono-reduced Ir(III) photosensitizer (ΔA_{PS-}) was recorded at 600 nm ($\Delta\varepsilon$ = 9500 $M^{-1}cm^{-1}$) for Ir_2-TPPHZ, at 620 nm ($\Delta\varepsilon$ = 6500 $M^{-1}cm^{-1}$) for Ir_2-TAPHAT, at 550 nm ($\Delta\varepsilon$ = 2700 M^{-1} cm^{-1}) for Ir-TAP and at 430 nm ($\Delta\varepsilon$ = 4500 M^{-1} cm^{-1}) for Ir-HATPHE. For Ir-TPPHZ and Ir-PHEHAT, a detection wavelength of 590 nm ($\Delta\varepsilon_{TPPHZ}$ = 5200 M^{-1} cm^{-1} and $\Delta\varepsilon_{PHEHAT}$ = 7800 M^{-1} cm^{-1}) was used in acetonitrile, whereas absorption changes were monitored at 420 nm ($\Delta\varepsilon_{TPPHZ}$ = 12750 M^{-1} cm^{-1} and $\Delta\varepsilon_{PHEHAT}$ = 10800 M^{-1} cm^{-1}) in acetonitrile/water 50:50 in order to improve measurement quality. All the $\Delta\varepsilon$ for the Ir(III) photosensitizers were determined by nsTAS using tri-*p*-tolylamine With these experimentally determined values and **Equation 1.28** and **1.29**, the relative yield of mono-reduced PS produced at any given concentration of halide (Φ) was plotted against the percentage of quenched PL (%PL) and final cage escape yields (Φ_{CE}) values were obtained from the slope of the linear fit.

References

1. Hassan, Q.; Algburi, S.; Sameen, A. Z.; Al-Musawi, T. J.; Al-Jiboory, A. K.; Salman, H. M.; Ali, B. M.; Jaszczur, M., A comprehensive review of international renewable energy growth. *Energy and Built Environment* **2024**.
2. Joselin Herbert, G. M.; Iniyan, S.; Sreevalsan, E.; Rajapandian, S., A review of wind energy technologies. *Renewable and Sustainable Energy Reviews* **2007,** *11* (6), 1117-1145.
3. Roga, S.; Bardhan, S.; Kumar, Y.; Dubey, S. K., Recent technology and challenges of wind energy generation: A review. *Sustainable Energy Technologies and Assessments* **2022,** *52*, 102239.
4. Berga, L., The Role of Hydropower in Climate Change Mitigation and Adaptation: A Review. *Engineering-London* **2016,** *2* (3), 313-318.
5. Kaunda, C. S.; Kimambo, C. Z.; Nielsen, T. K., Hydropower in the Context of Sustainable Energy Supply: A Review of Technologies and Challenges. *ISRN Renewable Energy* **2012,** *2012*, 730631.
6. Barbier, E., Geothermal energy technology and current status: an overview. *Renewable and Sustainable Energy Reviews* **2002,** *6* (1), 3-65.
7. Rosillo-Calle, F., A review of biomass energy – shortcomings and concerns. *J. Chem. Technol. Biotechnol.* **2016,** *91* (7), 1933-1945.
8. Khan, N.; Kalair, A.; Abas, N.; Haider, A., Review of ocean tidal, wave and thermal energy technologies. *Renewable and Sustainable Energy Reviews* **2017,** *72*, 590-604.
9. Iglesias, G.; Tercero, J. A.; Simas, T.; Machado, I.; Cruz, E., Environmental Effects. In *Wave and Tidal Energy*, 2018; pp 364-454.
10. Iglesias, G.; Astariz, S.; Vazquez, A., The Economics of Wave and Tidal Energy. In *Wave and Tidal Energy*, 2018; pp 513-532.
11. Lewis, N. S.; Nocera, D. G., Powering the planet: Chemical challenges in solar energy utilization. *Proceedings of the National Academy of Sciences* **2006,** *103* (43), 15729-15735.
12. Ritchie, H.; Rosado, P.; Max, R., Energy Production and Consumption. *Our World in Data* **2020**.
13. Chapin, D. M.; Fuller, C. S.; Pearson, G. L., A New Silicon p-n Junction Photocell for Converting Solar Radiation into Electrical Power. *J. Appl. Phys.* **1954,** *25* (5), 676-677.
14. Segev, G.; Kibsgaard, J.; Hahn, C.; Xu, Z. J.; Cheng, W.-H.; Deutsch, T. G.; Xiang, C.; Zhang, J. Z.; Hammarström, L.; Nocera, D. G.; Weber, A. Z.; Agbo, P.; Hisatomi, T.; Osterloh, F. E.; Domen, K.; Abdi, F. F.; Haussener, S.; Miller, D. J.; Ardo, S.; McIntyre, P. C.; Hannappel, T.; Hu, S.; Atwater, H.; Gregoire, J. M.; Ertem, M. Z.; Sharp, I. D.; Choi, K.-S.; Lee, J. S.; Ishitani, O.; Ager, J. W.; Prabhakar, R. R.; Bell, A. T.; Boettcher, S. W.; Vincent, K.; Takanabe, K.; Artero, V.; Napier, R.; Cuenya, B. R.; Koper, M. T. M.; Van De Krol, R.; Houle, F., The 2022 solar fuels roadmap. *J. Phys. D Appl. Phys.* **2022,** *55* (32), 323003.
15. Wang, Q.; Pornrungroj, C.; Linley, S.; Reisner, E., Strategies to improve light utilization in solar fuel synthesis. *Nat. Energy* **2022,** *7* (1), 13-24.
16. Bolton, J. R., Solar photoproduction of hydrogen: A review. *Sol. Energy* **1996,** *57* (1), 37-50.
17. Rahaman, M.; Andrei, V.; Wright, D.; Lam, E.; Pornrungroj, C.; Bhattacharjee, S.; Pichler, C. M.; Greer, H. F.; Baumberg, J. J.; Reisner, E., Solar-driven liquid multi-carbon fuel production using a standalone perovskite–BiVO4 artificial leaf. *Nat. Energy* **2023,** *8* (6), 629-638.
18. Shang, B.; Rooney, C. L.; Gallagher, D. J.; Wang, B. T.; Krayev, A.; Shema, H.; Leitner, O.; Harmon, N. J.; Xiao, L.; Sheehan, C.; Bottum, S. R.; Gross, E.; Cahoon, J. F.; Mallouk, T. E.; Wang, H., Aqueous Photoelectrochemical CO(2) Reduction to CO and Methanol over a Silicon Photocathode Functionalized with a Cobalt Phthalocyanine Molecular Catalyst. *Angew. Chem. Int. Edit.* **2023,** *62* (4), e202215213.
19. Müller, A. V.; Ahmad, S.; Sirlin, J. T.; Ertem, M. Z.; Polyansky, D. E.; Grills, D. C.; Meyer, G. J.; Sampaio, R. N.; Concepcion, J. J., Reduction of CO to Methanol with Recyclable Organic Hydrides. *J. Am. Chem. Soc.* **2024,** *146* (15), 10524-10536.
20. Brady, M. D.; Sampaio, R. N.; Wang, D.; Meyer, T. J.; Meyer, G. J., Dye-Sensitized Hydrobromic Acid Splitting for Hydrogen Solar Fuel Production. *J. Am. Chem. Soc.* **2017,** *139* (44), 15612-15615.
21. Brady, M. D.; Troian-Gautier, L.; Sampaio, R. N.; Motley, T. C.; Meyer, G. J., Optimization of Photocatalyst Excited- and Ground-State Reduction Potentials for Dye-Sensitized HBr Splitting. *ACS Appl. Mater. Inter.* **2018,** *10* (37), 31312-31323.
22. Nocera, D. G., The Artificial Leaf. *Acc. Chem. Res.* **2012,** *45* (5), 767-776.
23. Balzani, V.; Credi, A.; Raymo, F. M.; Stoddart, J. F., Artificial Molecular Machines. *Angew. Chem. Int. Edit.* **2000,** *39* (19), 3348-3391.
24. Ciamician, G.; Silber, P., Chemische Lichtwirkungen. *Ber. Dtsch. Chem. Ges.* **1908,** *41* (1), 1071-1080.

25. How Hydrogen Empowers the Energy Transition. *Hydrogen Council* **2017**.
26. Koroneos, C.; Dompros, A.; Roumbas, G.; Moussiopoulos, N., Life cycle assessment of hydrogen fuel production processes. *Int. J. Hydrogen Energ.* **2004,** *29* (14), 1443-1450.
27. Balzani, V.; Moggi, L.; Manfrin, M. F.; Bolletta, F.; Gleria, M., Solar Energy Conversion by Water Photodissociation: Transition metal complexes can provide low-energy cyclic systems for catalytic photodissociation of water. *Science* **1975,** *189* (4206), 852-6.
28. Nong, G.; Li, Y.; Yin, Y., Energy analysis on the water cycle consisting of photo catalyzing water splitting and hydrogen reacting with oxygen in a hydrogen fuel cell. *Chem. Phys. Lett.* **2019,** *737*, 100033.
29. Dau, H.; Limberg, C.; Reier, T.; Risch, M.; Roggan, S.; Strasser, P., The Mechanism of Water Oxidation: From Electrolysis via Homogeneous to Biological Catalysis. *ChemCatChem* **2010,** *2* (7), 724-761.
30. Barber, J.; Tran, P. D., From natural to artificial photosynthesis. *J. Roy. Soc. Interface* **2013,** *10* (81), 20120984.
31. Nguyen, D. N.; Chenevier, P.; Artero, V.; Tran, P. D., Engineering of a Viable Artificial Leaf for Solar Hydrogen Production. **2020**.
32. Balzani, V.; Credi, A.; Venturi, M., Photoprocesses. *Curr. Opin. Chem. Biol.* **1997,** *1* (4), 506-513.
33. Schulz, M.; Karnahl, M.; Schwalbe, M.; Vos, J. G., The role of the bridging ligand in photocatalytic supramolecular assemblies for the reduction of protons and carbon dioxide. *Coordin. Chem. Rev.* **2012,** *256* (15), 1682-1705.
34. Ozawa, H.; Sakai, K., Photo-hydrogen-evolving molecular devices driving visible-light-induced water reduction into molecular hydrogen: structure–activity relationship and reaction mechanism. *Chem. Commun.* **2011,** *47* (8), 2227-2242.
35. Pellegrin, Y.; Odobel, F., Sacrificial electron donor reagents for solar fuel production. *C. R. Chim.* **2017,** *20* (3), 283-295.
36. Whang, D. R.; Sakai, K.; Park, S. Y., Highly Efficient Photocatalytic Water Reduction with Robust Iridium(III) Photosensitizers Containing Arylsilyl Substituents. *Angew. Chem. Int. Edit.* **2013,** *52* (44), 11612-11615.
37. Yang, M.; Yarnell, J. E.; El Roz, K.; Castellano, F. N., A Robust Visible-Light-Harvesting Cyclometalated Ir(III) Diimine Sensitizer for Homogeneous Photocatalytic Hydrogen Production. *ACS Appl. Energy Mater.* **2020,** *3* (2), 1842-1853.
38. Guo, S.; Chen, K.-K.; Dong, R.; Zhang, Z.-M.; Zhao, J.; Lu, T.-B., Robust and Long-Lived Excited State Ru(II) Polyimine Photosensitizers Boost Hydrogen Production. *ACS Catal.* **2018,** *8* (9), 8659-8670.
39. Neta, P.; Huie, R. E.; Ross, A., Rate Constants for Reactions of Inorganic Radicals in Aqueous Solution. *J. Phys. Chem. Ref. Data* **1979,** *17*, 1027-1284.
40. Thomas, J. K., Pulse radiolysis of aqueous solutions of methyl iodide and methyl bromide. The reactions of iodine atoms and methyl radicals in water. *J. Phys. Chem.* **1967,** *71* (6), 1919-1925.
41. Troian-Gautier, L.; Turlington, M. D.; Wehlin, S. A. M.; Maurer, A. B.; Brady, M. D.; Swords, W. B.; Meyer, G. J., Halide Photoredox Chemistry. *Chem. Rev.* **2019,** *119* (7), 4628-4683.
42. Bevernaegie, R.; Wehlin, S. A. M.; Piechota, E. J.; Abraham, M.; Philouze, C.; Meyer, G. J.; Elias, B.; Troian-Gautier, L., Improved Visible Light Absorption of Potent Iridium(III) Photo-oxidants for Excited-State Electron Transfer Chemistry. *J. Am. Chem. Soc.* **2020,** *142* (6), 2732-2737.
43. Deetz, A. M.; Troian-Gautier, L.; Wehlin, S. A. M.; Piechota, E. J.; Meyer, G. J., On the Determination of Halogen Atom Reduction Potentials with Photoredox Catalysts. *J. Phys. Chem. A* **2021,** *125* (42), 9355-9367.
44. Balzani, V.; Ceroni, P.; Juris, A., *Photochemistry and Photophysics: Concepts, Research, Applications*. Wiley-VCH: 2014.
45. Kasha, M., Characterization of electronic transitions in complex molecules. *Discuss. Faraday Soc.* **1950,** *9* (0), 14-19.
46. Jablonski, A., Efficiency of Anti-Stokes Fluorescence in Dyes. *Nature* **1933,** *131* (3319), 839-840.
47. Evans, R. C.; Douglas, P.; Burrow, H. D., *Applied Photochemistry*. Springer Dordrecht: 2013.
48. Valeur, B.; Berberan-Santos, M. N., Characteristics of Fluorescence Emission. In *Molecular Fluorescence*, 2012; pp 53-74.
49. Valeur, B.; Berberan-Santos, M. N., Time-Resolved Fluorescence Techniques. In *Molecular Fluorescence*, 2012; pp 285-325.
50. Brouwer, A. M., Standards for photoluminescence quantum yield measurements in solution (IUPAC Technical Report). *Pure Appl. Chem.* **2011,** *83* (12), 2213-2228.
51. Stern, O.; Volmer, M., *Physik Z.* **1919,** *20*, 183-188.

52. Arias-Rotondo, D. M.; McCusker, J. K., The photophysics of photoredox catalysis: a roadmap for catalyst design. *Chem. Soc. Rev.* **2016,** *45* (21), 5803-5820.
53. Weber, G., The quenching of fluorescence in liquids by complex formation. Determination of the mean life of the complex. *Trans. Faraday Soc.* **1948,** *44* (0), 185-189.
54. Marton, A.; Clark, C. C.; Srinivasan, R.; Freundlich, R. E.; Narducci Sarjeant, A. A.; Meyer, G. J., Static and Dynamic Quenching of Ru(II) Polypyridyl Excited States by Iodide. *Inorg. Chem.* **2006,** *45* (1), 362-369.
55. Clark, C. C.; Marton, A.; Meyer, G. J., Evidence for Static Quenching of MLCT Excited States by Iodide. *Inorg. Chem.* **2005,** *44* (10), 3383-3385.
56. Farnum, B. H.; Gardner, J. M.; Marton, A.; Narducci-Sarjeant, A. A.; Meyer, G. J., Influence of ion pairing on the oxidation of iodide by MLCT excited states. *Dalton Trans.* **2011,** *40* (15), 3830-3838.
57. Boaz, H.; Rollefson, G. K., The Quenching of Fluorescence. Deviations from the Stern-Volmer Law. *J. Am. Chem. Soc.* **1950,** *72* (8), 3435-3443.
58. De Kreijger, S.; Gillard, M.; Elias, B.; Troian-Gautier, L., Spectroscopic Techniques to Unravel Mechanistic Details in Light-Induced Transformations and Photoredox Catalysis. *ChemCatChem* **2024,** *16* (1), e202301100.
59. Valeur, B.; Berberan-Santos, M. N., Excitation Energy Transfer. In *Molecular Fluorescence*, 2012; pp 213-261.
60. van der Meer, B. W., Förster Theory. In *FRET – Förster Resonance Energy Transfer*, 2013; pp 23-62.
61. Dexter, D. L., A Theory of Sensitized Luminescence in Solids. *J. Chem. Phys.* **1953,** *21* (5), 836-850.
62. Naimovičius, L.; Bharmoria, P.; Moth-Poulsen, K., Triplet–triplet annihilation mediated photon upconversion solar energy systems. *Materials Chemistry Frontiers* **2023,** *7* (12), 2297-2315.
63. Bossanyi, D. G.; Sasaki, Y.; Wang, S.; Chekulaev, D.; Kimizuka, N.; Yanai, N.; Clark, J., Spin Statistics for Triplet–Triplet Annihilation Upconversion: Exchange Coupling, Intermolecular Orientation, and Reverse Intersystem Crossing. *JACS Au* **2021,** *1* (12), 2188-2201.
64. Neveselý, T.; Wienhold, M.; Molloy, J. J.; Gilmour, R., Advances in the E → Z Isomerization of Alkenes Using Small Molecule Photocatalysts. *Chem. Rev.* **2022,** *122* (2), 2650-2694.
65. Chatterjee, A.; König, B., Birch-Type Photoreduction of Arenes and Heteroarenes by Sensitized Electron Transfer. *Angew. Chem. Int. Edit.* **2019,** *58* (40), 14289-14294.
66. Rehm, D.; Weller, A., Kinetik und Mechanismus der Elektronübertragung bei der Fluoreszenzlöschung in Acetonitril. *Berichte der Bunsengesellschaft für physikalische Chemie* **1969,** *73* (8-9), 834-839.
67. Rehm, D.; Weller, A., Kinetics of fluorescence quenching by electron and H-atom transfer. *Israel Journal of Chemistry* **1970,** *8* (2), 259-271.
68. Kalyanasundaram, K., Photophysics, photochemistry and solar energy conversion with tris(bipyridyl)ruthenium(II) and its analogues. *Coordin. Chem. Rev.* **1982,** *46*, 159-244.
69. Gibbs energy of photoinduced electron transfer. 3.0.1 ed.; International Union of Pure and Applied Chemistry (IUPAC): 2019.
70. Turro, N. J.; Ramamurthy, V.; Scaiano, J. C., *Principles of molecular photochemistry : an introduction*. University Science Books: Sausalito, Calif., 2009.
71. Sinha, N.; Wegeberg, C.; Häussinger, D.; Prescimone, A.; Wenger, O. S., Photoredox-active Cr(0) luminophores featuring photophysical properties competitive with Ru(II) and Os(II) complexes. *Nat. Chem.* **2023,** *15* (12), 1730-1736.
72. Glaser, F.; Schmitz, M.; Kerzig, C., Coulomb interactions for mediator-enhanced sensitized triplet–triplet annihilation upconversion in solution. *Nanoscale* **2024,** *16* (1), 123-137.
73. Tian, L.; Till, N. A.; Kudisch, B.; MacMillan, D. W. C.; Scholes, G. D., Transient Absorption Spectroscopy Offers Mechanistic Insights for an Iridium/Nickel-Catalyzed C–O Coupling. *J. Am. Chem. Soc.* **2020,** *142* (10), 4555-4559.
74. Aydogan, A.; Bangle, R. E.; De Kreijger, S.; Dickenson, J. C.; Singleton, M. L.; Cauët, E.; Cadranel, A.; Meyer, G. J.; Elias, B.; Sampaio, R. N.; Troian-Gautier, L., Mechanistic investigation of a visible light mediated dehalogenation/cyclisation reaction using iron(iii), iridium(iii) and ruthenium(ii) photosensitizers. *Catal. Sci. Technol.* **2021,** *11* (24), 8037-8051.
75. Aydogan, A.; Bangle, R. E.; Cadranel, A.; Turlington, M. D.; Conroy, D. T.; Cauët, E.; Singleton, M. L.; Meyer, G. J.; Sampaio, R. N.; Elias, B.; Troian-Gautier, L., Accessing Photoredox Transformations with an Iron(III) Photosensitizer and Green Light. *J. Am. Chem. Soc.* **2021,** *143* (38), 15661-15673.
76. Chen, L. X.; Zhang, X.; Shelby, M. L., Recent advances on ultrafast X-ray spectroscopy in the chemical sciences. *Chem. Sci.* **2014,** *5* (11), 4136-4152.

77. Zhao, J.; De Kreijger, S.; Troian-Gautier, L.; Yu, J.; Hu, W.; Zhang, X.; Elias, B.; Moonshiram, D., Deciphering the photophysical kinetics, electronic configurations and structural conformations of iridium–cobalt hydrogen evolution photocatalysts. *Chem. Commun.* **2022,** *58* (58), 8057-8060.
78. Moonshiram, D.; Gimbert-Suriñach, C.; Guda, A.; Picon, A.; Lehmann, C. S.; Zhang, X.; Doumy, G.; March, A. M.; Benet-Buchholz, J.; Soldatov, A.; Llobet, A.; Southworth, S. H., Tracking the Structural and Electronic Configurations of a Cobalt Proton Reduction Catalyst in Water. *J. Am. Chem. Soc.* **2016,** *138* (33), 10586-10596.
79. Till, N. A.; Oh, S.; MacMillan, D. W. C.; Bird, M. J., The Application of Pulse Radiolysis to the Study of Ni(I) Intermediates in Ni-Catalyzed Cross-Coupling Reactions. *J. Am. Chem. Soc.* **2021,** *143* (25), 9332-9337.
80. Troian-Gautier, L.; Mugeniwabagara, E.; Fusaro, L.; Cauët, E.; Kirsch-De Mesmaeker, A.; Luhmer, M., Photo-CIDNP Reveals Different Protonation Sites Depending on the Primary Step of the Photoinduced Electron-/Proton-Transfer Process with Ru(II) Polyazaaromatic Complexes. *J. Am. Chem. Soc.* **2017,** *139* (42), 14909-14912.
81. Ma, J.; Zhang, X.; Phillips, D. L., Time-Resolved Spectroscopic Observation and Characterization of Water-Assisted Photoredox Reactions of Selected Aromatic Carbonyl Compounds. *Acc. Chem. Res.* **2019,** *52* (3), 726-737.
82. Earley, J. D.; Zieleniewska, A.; Ripberger, H. H.; Shin, N. Y.; Lazorski, M. S.; Mast, Z. J.; Sayre, H. J.; McCusker, J. K.; Scholes, G. D.; Knowles, R. R.; Reid, O. G.; Rumbles, G., Ion-pair reorganization regulates reactivity in photoredox catalysts. *Nat. Chem.* **2022,** *14* (7), 746-753.
83. Swords, W. B.; Yoon, T. P., Transient absorption spectroscopy in visible-light photocatalysis. In *Photochemistry: Volume 50*, Crespi, S.; Protti, S., Eds. The Royal Society of Chemistry: 2022; Vol. 50, p 0.
84. Norrish, R. G. W.; Porter, G., Chemical Reactions Produced by Very High Light Intensities. *Nature* **1949,** *164* (4172), 658-658.
85. Porter, G.-N.; Norrish, R. G. W., Flash photolysis and spectroscopy. A new method for the study of free radical reactions. *Proceedings of the Royal Society of London. Series A. Mathematical and Physical Sciences* **1950,** *200* (1061), 284-300.
86. Porter, G., Flash Photolysis and Some of Its Applications. *Science* **1968,** *160* (3834), 1299-1307.
87. Eigen, M.; Kurtze, G.; Tamm, K., Zum Reaktionsmechanismus der Ultraschallabsorption in wäßrigen Elektrolytlösungen. *Zeitschrift für Elektrochemie, Berichte der Bunsengesellschaft für physikalische Chemie* **1953,** *57* (2), 103-118.
88. Eigen, M., Über die Kinetik sehr schnell verlaufender Ionenreaktionen in wässeriger Lösung.*. *Z. Phys. Chem.* **1954,** *1* (3_4), 176-200.
89. Glaser, F.; Kerzig, C.; Wenger, O. S., Multi-Photon Excitation in Photoredox Catalysis: Concepts, Applications, Methods. *Angew. Chem. Int. Edit.* **2020,** *59* (26), 10266-10284.
90. Ripak, A.; De Kreijger, S.; Sampaio, R. N.; Vincent, C. A.; Cauët, É.; Jabin, I.; Tambar, U. K.; Elias, B.; Troian-Gautier, L., Photosensitized activation of diazonium derivatives for C–B bond formation. *Chem Catalysis* **2023,** *3* (2), 100490.
91. Cadranel, A.; Pieslinger, G. E.; Tongying, P.; Kuno, M. K.; Baraldo, L. M.; Hodak, J. H., Spectroscopic signatures of ligand field states in {RuII(imine)} complexes. *Dalton Trans.* **2016,** *45* (13), 5464-5475.
92. Cadranel, A.; Hodak, J. H., Four chromophores in one building block: synthesis, structure and characterization of trans-[Ru(MQ)4Cl2]4+ and trans-[Ru(4,4'-bpy)4Cl2] (MQ+ = N-methyl-4,4'-bipyridinium, bpy = bipyridine). *Journal of Coordination Chemistry* **2015,** *68* (8), 1452-1464.
93. Cotic, A.; Cerfontaine, S.; Slep, L. D.; Elias, B.; Troian-Gautier, L.; Cadranel, A., Anti-Dissipative Strategies toward More Efficient Solar Energy Conversion. *J. Am. Chem. Soc.* **2023,** *145* (9), 5163-5173.
94. Cotic, A.; Cerfontaine, S.; Slep, L. D.; Elias, B.; Troian-Gautier, L.; Cadranel, A., A photoinduced mixed valence photoswitch. *Phys. Chem. Chem. Phys.* **2022,** *24* (24), 15121-15128.
95. Suntrup, L.; Stein, F.; Hermann, G.; Kleoff, M.; Kuss-Petermann, M.; Klein, J.; Wenger, O. S.; Tremblay, J. C.; Sarkar, B., Influence of Mesoionic Carbenes on Electro- and Photoactive Ru and Os Complexes: A Combined (Spectro-)Electrochemical, Photochemical, and Computational Study. *Inorg. Chem.* **2018,** *57* (21), 13973-13984.
96. Bürgin, T. H.; Glaser, F.; Wenger, O. S., Shedding Light on the Oxidizing Properties of Spin-Flip Excited States in a CrIII Polypyridine Complex and Their Use in Photoredox Catalysis. *J. Am. Chem. Soc.* **2022,** *144* (31), 14181-14194.
97. Glaser, F.; Kerzig, C.; Wenger, O. S., Sensitization-initiated electron transfer via upconversion: mechanism and photocatalytic applications. *Chem. Sci.* **2021,** *12* (29), 9922-9933.

98. Chábera, P.; Liu, Y.; Prakash, O.; Thyrhaug, E.; Nahhas, A. E.; Honarfar, A.; Essén, S.; Fredin, L. A.; Harlang, T. C. B.; Kjær, K. S.; Handrup, K.; Ericson, F.; Tatsuno, H.; Morgan, K.; Schnadt, J.; Häggström, L.; Ericsson, T.; Sobkowiak, A.; Lidin, S.; Huang, P.; Styring, S.; Uhlig, J.; Bendix, J.; Lomoth, R.; Sundström, V.; Persson, P.; Wärnmark, K., A low-spin Fe(iii) complex with 100-ps ligand-to-metal charge transfer photoluminescence. *Nature* **2017,** *543* (7647), 695-699.
99. Kjær, K. S.; Kaul, N.; Prakash, O.; Chábera, P.; Rosemann, N. W.; Honarfar, A.; Gordivska, O.; Fredin, L. A.; Bergquist, K.-E.; Häggström, L.; Ericsson, T.; Lindh, L.; Yartsev, A.; Styring, S.; Huang, P.; Uhlig, J.; Bendix, J.; Strand, D.; Sundström, V.; Persson, P.; Lomoth, R.; Wärnmark, K., Luminescence and reactivity of a charge-transfer excited iron complex with nanosecond lifetime. *Science* **2019,** *363* (6424), 249-253.
100. Prakash, O.; Lindh, L.; Kaul, N.; Rosemann, N. W.; Losada, I. B.; Johnson, C.; Chábera, P.; Ilic, A.; Schwarz, J.; Gupta, A. K.; Uhlig, J.; Ericsson, T.; Häggström, L.; Huang, P.; Bendix, J.; Strand, D.; Yartsev, A.; Lomoth, R.; Persson, P.; Wärnmark, K., Photophysical Integrity of the Iron(III) Scorpionate Framework in Iron(III)–NHC Complexes with Long-Lived 2LMCT Excited States. *Inorg. Chem.* **2022,** *61* (44), 17515-17526.
101. Sampaio, R. N.; Piechota, E. J.; Troian-Gautier, L.; Maurer, A. B.; Hu, K.; Schauer, P. A.; Blair, A. D.; Berlinguette, C. P.; Meyer, G. J., Kinetics teach that electronic coupling lowers the free-energy change that accompanies electron transfer. *Proceedings of the National Academy of Sciences* **2018,** *115* (28), 7248-7253.
102. Sampaio, R. N.; Troian-Gautier, L.; Meyer, G. J., A Charge-Separated State that Lives for Almost a Second at a Conductive Metal Oxide Interface. *Angewandte Chemie* **2018,** *130* (47), 15616-15620.
103. Piechota, E. J.; Sampaio, R. N.; Troian-Gautier, L.; Maurer, A. B.; Berlinguette, C. P.; Meyer, G. J., Entropic Barriers Determine Adiabatic Electron Transfer Equilibrium. *The Journal of Physical Chemistry C* **2019,** *123* (6), 3416-3425.
104. Wang, D.; Sampaio, R. N.; Troian-Gautier, L.; Marquard, S. L.; Farnum, B. H.; Sherman, B. D.; Sheridan, M. V.; Dares, C. J.; Meyer, G. J.; Meyer, T. J., Molecular Photoelectrode for Water Oxidation Inspired by Photosystem II. *J. Am. Chem. Soc.* **2019,** *141* (19), 7926-7933.
105. Holze, R., Fundamentals and applications of near infrared spectroscopy in spectroelectrochemistry. *Journal of Solid State Electrochemistry* **2004,** *8* (12), 982-997.
106. Kaim, W.; Sarkar, B.; Kumar Lahiri, G., Mixed-Valence Intermediates as Ideal Targets for Spectroelectrochemistry (SEC). In *Spectroelectrochemistry*, Kaim, W.; Klein, A., Eds. The Royal Society of Chemistry: 2008; p 0.
107. Dhungana, S.; Crumbliss, A. L., UV-Vis Spectroelectrochemistry of Selected Iron-Containing Proteins. In *Spectroelectrochemistry*, Kaim, W.; Klein, A., Eds. The Royal Society of Chemistry: 2008; p 0.
108. Best, S. P.; Borg, S. J.; Vincent, K. A., Infrared Spectroelectrochemistry. In *Spectroelectrochemistry*, Kaim, W.; Klein, A., Eds. The Royal Society of Chemistry: 2008; p 0.
109. Catherine Salsman, J.; Kubiak, C. P., Infrared Spectroelectrochemical Investigations of Ultrafast Electron Transfer in Mixed-Valence Complexes. In *Spectroelectrochemistry*, Kaim, W.; Klein, A., Eds. The Royal Society of Chemistry: 2008; p 0.
110. Murray, P. R.; Yellowlees, L. J., EPR Spectroelectrochemistry. In *Spectroelectrochemistry*, Kaim, W.; Klein, A., Eds. The Royal Society of Chemistry: 2008; p 0.
111. Kornfeld, G.; Farkas, L.; Rabinowitsch, E., General discussion. *Trans. Faraday Soc.* **1934,** *30* (0), 130-131.
112. Franck, J.; Rabinowitsch, E., Some remarks about free radicals and the photochemistry of solutions. *Trans. Faraday Soc.* **1934,** *30* (0), 120-130.
113. Lyon, R. K.; Levy, D. H., Demonstration of the "Cage" Effect. *J. Am. Chem. Soc.* **1961,** *83* (20), 4290-4290.
114. Jayanthi, S.; Ramamurthy, P., Photoinduced electron transfer reactions of 2,4,6 triphenylpyrylium: solvent effect and charge-shift type of systems. *Phys. Chem. Chem. Phys.* **1999,** *1*, 4751-4757.
115. Aydogan, A.; Bangle, R. E.; Cadranel, A.; Turlington, M. D.; Conroy, D. T.; Cauët, E.; Singleton, M. L.; Meyer, G. J.; Sampaio, R. N.; Elias, B.; Troian-Gautier, L., Accessing Photoredox Transformations with an Iron(III) Photosensitizer and Green Light. *J. Am. Chem. Soc.* **2021,** *143* (38), 15661-15673.
116. Wolff, H.-J.; Bürßner, D.; Steiner, U. E., Spin-orbit coupling controlled spin chemistry of $Ru(bpy)_3^{2+}$ photooxidation: Detection of strong viscosity dependence of in-cage backward electron transfer rate. *Pure Appl. Chem.* **1995,** *67*, 167-174.

117. Meidlar, K.; Das, P. K., Tris(2,2'-bipyridine)ruthenium(II)-Sensitized Photooxidation of Phenols. Environmental Effects on Electron Transfer Yields and Kinetics. *J. Am. Chem. Soc.* **1982,** *104*, 7462-7469.
118. Ohno, T.; Lichtin, N. N., Electron Transfer in the Quenching of Triplet Methylene Blue by Complexes of Iron(II). *J. Am. Chem. Soc.* **1980,** *102*, 4636-4643.
119. Sun, H.; Neshvad, G.; Hoffman, M. Z., Energy Gap Dependence of the Efficiency of Charge Separation upon the Sacrificial Reductive Quenching of the Excited States of Ru(II)-Diimine Photosensitizers in Aqueous Solution. *Mol. Cryst. Liq. Cryst.* **2006,** *194* (1), 141-150.
120. DiLuzio, S.; Connell, T. U.; Mdluli, V.; Kowalewski, J. F.; Bernhard, S., Understanding Ir(III) Photocatalyst Structure-Activity Relationships: A Highly Parallelized Study of Light-Driven Metal Reduction Processes. *J. Am. Chem. Soc.* **2022,** *144*, 1431-1444.
121. Hoffman, M. Z., Cage Escape Yields from the Quenching of $*Ru(bpy)_3^{2+}$ by Methylviologen in Aqueous Solution. *J. Phys. Chem.* **1988,** *92*, 3458–3464.
122. Gibbons, D. J.; Farawar, A.; Mazzella, P.; Leroy-Lhez, S.; Williams, R. M., Making triplets from photo-generated charges: observations, mechanisms and theory. *Photochem. Photobiol. Sci.* **2020,** *19*, 136-158.
123. Kikuchi, K.; Hoshi, M.; Niwa, T.; Takahashi, Y.; Miyashi, T., Heavy-atom effects on the excited singlet-state electron-transfer reaction. *J. Phys. Chem.* **1991,** *95*, 38–42.
124. Olmsted, J.; Meyer, T. J., Factors affecting cage escape yields following electron-transfer quenching. *J. Phys. Chem.* **1987,** *91* (6), 1649-1655.
125. Kalyanasundaram, K.; Neumann-Spallart, M., Influence of added salts on the cage escape yields in the photoredox quenching of $Ru(bpy)_2^{+3}$ excited states. *Chem. Phys. Lett.* **1982,** *88*, 7-12
126. Goodwin, M. J.; Dickenson, J. C.; Ripak, A.; Deetz, A. M.; McCarthy, J. S.; Meyer, G. J.; Troian-Gautier, L., Factors that Impact Photochemical Cage Escape Yields. *Chem. Rev.* **2024**.
127. Wang, C.; Li, H.; Bürgin, T. H.; Wenger, O. S., Cage escape governs photoredox reaction rates and quantum yields. *Nat. Chem.* **2024,** *16* (7), 1151-1159.
128. Sreenath, K.; Thomas, T. G.; Gopidas, K. R., Cu(II) Mediated Generation and Spectroscopic Study of the Tris(4-anisyl)amine Radical Cation and Dication. Unusually Shielded Chemical Shifts in the Dication. *Organic Letters* **2011,** *13* (5), 1134-1137.
129. DiMarco, B. N.; Troian-Gautier, L.; Sampaio, R. N.; Meyer, G. J., Dye-sensitized electron transfer from TiO2 to oxidized triphenylamines that follows first-order kinetics. *Chem. Sci.* **2018,** *9* (4), 940-949.
130. Yoshimura, A.; Hoffman, M. Z.; Sun, H., An evaluation of the excited state absorption spectrum of Ru(bpy)32+ in aqueous and acetonitrile solutions. *J. Photoch. Photobio. A* **1993,** *70* (1), 29-33.
131. Goez, M.; von Ramin-Marro, D.; Othman Musa, M. H.; Schiewek, M., Photoionization of [Ru(bpy)3]2+: A Catalytic Cycle with Water as Sacrificial Donor. *J. Phys. Chem. A* **2004,** *108* (6), 1090-1100.
132. Müller, P.; Brettel, K., [Ru(bpy)3]2+ as a reference in transient absorption spectroscopy: differential absorption coefficients for formation of the long-lived 3MLCT excited state. *Photochem. Photobio. Sci.* **2012,** *11* (4), 632-636.
133. Kurtz, D. A.; Dempsey, J. L., Proton-Coupled Electron Transfer Kinetics for the Photoinduced Generation of a Cobalt(III)-Hydride Complex. *Inorg. Chem.* **2019,** *58* (24), 16510-16517.
134. DiMarco, B. N.; O'Donnell, R. M.; Meyer, G. J., Cation-Dependent Charge Recombination to Organic Mediators in Dye-Sensitized Solar Cells. *The Journal of Physical Chemistry C* **2015,** *119* (37), 21599-21604.
135. Wehlin, S. A. M.; Troian-Gautier, L.; Li, G.; Meyer, G. J., Chloride Oxidation by Ruthenium Excited-States in Solution. *J. Am. Chem. Soc.* **2017,** *139* (37), 12903-12906.
136. De Kreijger, S.; Elias, B.; Troian-Gautier, L., Chloride, Bromide, and Iodide Photooxidation in Acetonitrile/Water Mixtures Using Binuclear Iridium(III) Photosensitizers. *Inorg. Chem.* **2023,** *62* (39), 16196-16202.
137. Dwyer, F. P.; Gyarfas, E. C., A Reaction for the Study of the Kinetics of Electron Transfer. *Nature* **1950,** *166* (4220), 481-481.
138. Brandt, W. W.; Dwyer, F. P.; Gyarfas, E. D., Chelate Complexes of 1,10-Phenanthroline and Related Compounds. *Chem. Rev.* **1954,** *54* (6), 959-1017.
139. Lytle, F. E.; Hercules, D. M., Luminescence of tris(2,2'-bipyridine)ruthenium(II) dichloride. *J. Am. Chem. Soc.* **1969,** *91* (2), 253-257.
140. Burstall, F. H., 34. Optical activity dependent on co-ordinated bivalent ruthenium. *J. Chem. Soc.* **1936,** (0), 173-175.
141. van der Westhuizen, D.; von Eschwege, K. G.; Conradie, J., Electrochemical data of polypyridine complexes of Ru(II). *Data in Brief* **2019,** *27*, 104759.

142. Goldschmid, S. L.; Bednářová, E.; Beck, L. R.; Xie, K.; Tay, N. E. S.; Ravetz, B. D.; Li, J.; Joe, C. L.; Rovis, T., Tuning the Electrochemical and Photophysical Properties of Osmium-Based Photoredox Catalysts. *Synlett* **2022,** *33* (03), 247-258.
143. Sauvage, J. P.; Collin, J. P.; Chambron, J. C.; Guillerez, S.; Coudret, C.; Balzani, V.; Barigelletti, F.; De Cola, L.; Flamigni, L., Ruthenium(II) and Osmium(II) Bis(terpyridine) Complexes in Covalently-Linked Multicomponent Systems: Synthesis, Electrochemical Behavior, Absorption Spectra, and Photochemical and Photophysical Properties. *Chem. Rev.* **1994,** *94* (4), 993-1019.
144. Pandya, C.; Sivaramakrishna, A., Organoruthenium-bipyridyl complexes – A platform for diverse chemistry and applications. *Coordin. Chem. Rev.* **2024,** *504*, 215655.
145. Cesana, P. T.; Li, B. X.; Shepard, S. G.; Ting, S. I.; Hart, S. M.; Olson, C. M.; Martinez Alvarado, J. I.; Son, M.; Steiman, T. J.; Castellano, F. N.; Doyle, A. G.; MacMillan, D. W. C.; Schlau-Cohen, G. S., A biohybrid strategy for enabling photoredox catalysis with low-energy light. *Chem* **2022,** *8* (1), 174-185.
146. Kerzig, C.; Wenger, O. S., Sensitized triplet–triplet annihilation upconversion in water and its application to photochemical transformations. *Chem. Sci.* **2018,** *9* (32), 6670-6678.
147. Coles, M. S.; Quach, G.; Beves, J. E.; Moore, E. G., A Photophysical Study of Sensitization-Initiated Electron Transfer: Insights into the Mechanism of Photoredox Activity. *Angew. Chem. Int. Edit.* **2020,** *59* (24), 9522-9526.
148. Tomar, N.; Agrawal, A.; Dhaka, V. S.; Surolia, P. K., Ruthenium complexes based dye sensitized solar cells: Fundamentals and research trends. *Sol. Energy* **2020,** *207*, 59-76.
149. Rilak Simović, A.; Masnikosa, R.; Bratsos, I.; Alessio, E., Chemistry and reactivity of ruthenium(II) complexes: DNA/protein binding mode and anticancer activity are related to the complex structure. *Coordin. Chem. Rev.* **2019,** *398*, 113011.
150. Puttaswamy, N. Y.; Mahanta, P.; Sarma, P.; Medhi, C.; Kaid, S. M. A.; Kullaiah, B.; Basumatary, D.; Manjasetty, B. A., Structure-based biological investigations on ruthenium complexes containing 2,2′-bipyridine ligands and their applications in photodynamic therapy as a potential photosensitizer. *Chem. Biol. Drug. Des.* **2023,** *102* (6), 1506-1520.
151. Wei, Y.; Li, Y.; Zheng, M.; Zhou, X.; Zou, Y.; Yang, C., Simultaneously High Upconversion Efficiency and Large Anti-Stokes Shift by Using Os(II) Complex Dyad as Triplet Photosensitizer. *Adv. Opt. Mater.* **2020,** *8* (9), 1902157.
152. Haruki, R.; Sasaki, Y.; Masutani, K.; Yanai, N.; Kimizuka, N., Leaping across the visible range: near-infrared-to-violet photon upconversion employing a silyl-substituted anthracene. *Chem. Commun.* **2020,** *56* (51), 7017-7020.
153. Ravetz, B. D.; Tay, N. E. S.; Joe, C. L.; Sezen-Edmonds, M.; Schmidt, M. A.; Tan, Y.; Janey, J. M.; Eastgate, M. D.; Rovis, T., Development of a Platform for Near-Infrared Photoredox Catalysis. *ACS Cent. Sci.* **2020,** *6* (11), 2053-2059.
154. Goldschmid, S. L.; Soon Tay, N. E.; Joe, C. L.; Lainhart, B. C.; Sherwood, T. C.; Simmons, E. M.; Sezen-Edmonds, M.; Rovis, T., Overcoming Photochemical Limitations in Metallaphotoredox Catalysis: Red-Light-Driven C–N Cross-Coupling. *J. Am. Chem. Soc.* **2022,** *144* (49), 22409-22415.
155. Glaser, F.; Wenger, O. S., Sensitizer-controlled photochemical reactivity via upconversion of red light. *Chem. Sci.* **2023,** *14* (1), 149-161.
156. Han, G.; Li, G.; Huang, J.; Han, C.; Turro, C.; Sun, Y., Two-photon-absorbing ruthenium complexes enable near infrared light-driven photocatalysis. *Nat. Commun.* **2022,** *13* (1), 2288.
157. Kinoshita, T.; Fujisawa, J.-i.; Nakazaki, J.; Uchida, S.; Kubo, T.; Segawa, H., Enhancement of Near-IR Photoelectric Conversion in Dye-Sensitized Solar Cells Using an Osmium Sensitizer with Strong Spin-Forbidden Transition. *J. Phys. Chem. Lett.* **2012,** *3* (3), 394-398.
158. Wehlin, S. A. M.; Troian-Gautier, L.; Maurer, A. B.; Brennaman, M. K.; Meyer, G. J., Photophysical characterization of new osmium (II) photocatalysts for hydrohalic acid splitting. *J. Chem. Phys.* **2020,** *153* (5).
159. Lazic, S.; Kaspler, P.; Shi, G.; Monro, S.; Sainuddin, T.; Forward, S.; Kasimova, K.; Hennigar, R.; Mandel, A.; McFarland, S.; Lilge, L., Novel Osmium-based Coordination Complexes as Photosensitizers for Panchromatic Photodynamic Therapy. *Photochem. Photobio. Sci*. **2017,** *93* (5), 1248-1258.
160. Roque, J. A.; Barrett, P. C.; Cole, H. D.; Lifshits, Liubov M.; Shi, G.; Monro, S.; von Dohlen, D.; Kim, S.; Russo, N.; Deep, G.; Cameron, C. G.; Alberto, M. E.; McFarland, S. A., Breaking the barrier: an osmium photosensitizer with unprecedented hypoxic phototoxicity for real world photodynamic therapy. *Chem. Sci.* **2020,** *11* (36), 9784-9806.
161. Cerfontaine, S.; Wehlin, S. A. M.; Elias, B.; Troian-Gautier, L., Photostable Polynuclear Ruthenium(II) Photosensitizers Competent for Dehalogenation Photoredox Catalysis at 590 nm. *J. Am. Chem. Soc.* **2020,** *142* (12), 5549-5555.

162. Schmid, L.; Kerzig, C.; Prescimone, A.; Wenger, O. S., Photostable Ruthenium(II) Isocyanoborato Luminophores and Their Use in Energy Transfer and Photoredox Catalysis. *JACS Au* **2021,** *1* (6), 819-832.
163. Glaser, F.; De Kreijger, S.; Achilleos, K.; Narayan Satheesh, L.; Ripak, A.; Chantry, N.; Bourgois, C.; Quiquempoix, S.; Scriven, J.; Rubens, J.; Vander Wee-Léonard, M.; Daenen, M.; Gillard, M.; Elias, B.; Troian-Gautier, L., A Compendium of Methodically Determined Ground- and Excited-State Properties of Homoleptic Ruthenium(II) and Osmium(II) Photosensitizers *ChemPhotoChem* **2024**.
164. Kumaresan, D.; Shankar, K.; Vaidya, S.; Schmehl, R. H., Photochemistry and Photophysics of Coordination Compounds: Osmium. In *Photochemistry and Photophysics of Coordination Compounds II*, Balzani, V.; Campagna, S., Eds. Springer Berlin Heidelberg: Berlin, Heidelberg, 2007; pp 101-142.
165. Lecomte, J.-P.; Kirsch-De Mesmaeker, A.; Orellana, G., Photophysics of Polyazaaromatic Ruthenium(II) Complexes Interacting with DNA. *J. Phys. Chem.* **1994,** *98* (20), 5382-5388.
166. Content, S.; Kirsch-De Mesmaeker, A., A novel metallic complex as photoreagent for the DNA guanine bases: Osmium(II) tris(tetraazaphenanthrene). *J. Chem. Soc. Faraday T.* **1997,** *93* (6), 1089-1094.
167. Fuller, Z. J.; Bare, W. D.; Kneas, K. A.; Xu, W. Y.; Demas, J. N.; DeGraff, B. A., Photostability of Luminescent Ruthenium(II) Complexes in Polymers and in Solution. *Anal. Chem.* **2003,** *75* (11), 2670-2677.
168. Kim, D.; Teets, T. S., Strategies for accessing photosensitizers with extreme redox potentials. *Chem. Phys. Rev.* **2022,** *3* (2).
169. Henwood, A. F.; Zysman-Colman, E., A Comprehensive Review of Luminescent Iridium Complexes Used in Light-Emitting Electrochemical Cells (LEECs). In *Iridium(III) in Optoelectronic and Photonics Applications*, 2017; pp 275-357.
170. Lamansky, S.; Djurovich, P.; Murphy, D.; Abdel-Razzaq, F.; Lee, H.-E.; Adachi, C.; Burrows, P. E.; Forrest, S. R.; Thompson, M. E., Highly Phosphorescent Bis-Cyclometalated Iridium Complexes: Synthesis, Photophysical Characterization, and Use in Organic Light Emitting Diodes. *J. Am. Chem. Soc.* **2001,** *123* (18), 4304-4312.
171. Caporale, C.; Massi, M., Cyclometalated iridium(III) complexes for life science. *Coordin. Chem. Rev.* **2018,** *363*, 71-91.
172. Bevernaegie, R.; Doix, B.; Bastien, E.; Diman, A.; Decottignies, A.; Feron, O.; Elias, B., Exploring the Phototoxicity of Hypoxic Active Iridium(III)-Based Sensitizers in 3D Tumor Spheroids. *J. Am. Chem. Soc.* **2019,** *141* (46), 18486-18491.
173. Ho, P.-Y.; Ho, C.-L.; Wong, W.-Y., Recent advances of iridium(III) metallophosphors for health-related applications. *Coordin. Chem. Rev.* **2020,** *413*, 213267.
174. Shaw, M. H.; Twilton, J.; MacMillan, D. W. C., Photoredox Catalysis in Organic Chemistry. *J. Org. Chem.* **2016,** *81* (16), 6898-6926.
175. Prier, C. K.; Rankic, D. A.; MacMillan, D. W. C., Visible Light Photoredox Catalysis with Transition Metal Complexes: Applications in Organic Synthesis. *Chem. Rev.* **2013,** *113* (7), 5322-5363.
176. Kelly, C. B.; Patel, N. R.; Primer, D. N.; Jouffroy, M.; Tellis, J. C.; Molander, G. A., Preparation of visible-light-activated metal complexes and their use in photoredox/nickel dual catalysis. *Nat. Protoc.* **2017,** *12* (3), 472-492.
177. Xu, B.; Troian-Gautier, L.; Dykstra, R.; Martin, R. T.; Gutierrez, O.; Tambar, U. K., Photocatalyzed Diastereoselective Isomerization of Cinnamyl Chlorides to Cyclopropanes. *J. Am. Chem. Soc.* **2020,** *142* (13), 6206-6215.
178. Pfund, B.; Steffen, D. M.; Schreier, M. R.; Bertrams, M.-S.; Ye, C.; Börjesson, K.; Wenger, O. S.; Kerzig, C., UV Light Generation and Challenging Photoreactions Enabled by Upconversion in Water. *J. Am. Chem. Soc.* **2020,** *142* (23), 10468-10476.
179. Deetz, A. M.; Goodwin, M. J.; Kober, E. A.; Meyer, G. J., Nanosecond Intra-Ionic Chloride Photo-Oxidation. *Inorg. Chem.* **2023,** *62* (29), 11414-11425.
180. Kuramochi, Y.; Ishitani, O., Iridium(III) 1-Phenylisoquinoline Complexes as a Photosensitizer for Photocatalytic CO2 Reduction: A Mixed System with a Re(I) Catalyst and a Supramolecular Photocatalyst. *Inorg. Chem.* **2016,** *55* (11), 5702-5709.
181. Kuramochi, Y.; Ishitani, O., An Ir(III) Complex Photosensitizer With Strong Visible Light Absorption for Photocatalytic CO2 Reduction. *Front. Chem.* **2019,** *7*.
182. Wee-Léonard, M. V.; Elias, B.; Troian-Gautier, L., Photoinduced One-Electron Chloride Oxidation in Water Using a Pentacationic Ir(III) Photosensitizer. *J. Am. Chem. Soc.* **2024,** *146* (16), 11031-11035.
183. Lentz, C.; Schott, O.; Auvray, T.; Hanan, G.; Elias, B., Photocatalytic Hydrogen Production Using a Red-Absorbing Ir(III)–Co(III) Dyad. *Inorg. Chem.* **2017,** *56* (18), 10875-10881.
184. Lentz, C.; Marcélis, L.; Troian-Gautier, L.; Robeyns, K.; Cauët, E.; Elias, B., Excited-state behavior and photoinduced electron transfer of pH-sensitive Ir(III) complexes with cyclometallation (C/N–) ratios between 0/6 and 3/3. *J. Photoch. Photobio. A* **2021,** *405*, 112957.

185. King, K. A.; Spellane, P. J.; Watts, R. J., Excited-state properties of a triply ortho-metalated iridium(III) complex. *J. Am. Chem. Soc.* **1985,** *107* (5), 1431-1432.
186. King, K. A.; Watts, R. J., Dual emission from an ortho-metalated iridium(III) complex. *J. Am. Chem. Soc.* **1987,** *109* (5), 1589-1590.
187. Flynn, C. M., Jr.; Demas, J. N., Synthesis and luminescence of the tris(2,2'-bipyridine)iridium(III) ion. *J. Am. Chem. Soc.* **1974,** *96* (6), 1959-1960.
188. Fan, S.; Zong, X.; Shaw, P. E.; Wang, X.; Geng, Y.; Smith, A. R. G.; Burn, P. L.; Wang, L.; Lo, S.-C., Energetic requirements of iridium(iii) complex based photosensitisers in photocatalytic hydrogen generation. *Phys. Chem. Chem. Phys.* **2014,** *16* (39), 21577-21585.
189. Kim, P. S.; Choi, S.; Kim, S.-Y.; Jo, J. H.; Lee, Y. S.; Kim, B.; Kim, W.; Choi, W.; Kim, C. H.; Son, H.-J.; Pac, C.; Kang, S. O., Organometallic Iridium(III) Complex Sensitized Ternary Hybrid Photocatalyst for CO2 to CO Conversion. *Chem. Eur. J.* **2019,** *25* (59), 13609-13623.
190. Sinopoli, A.; Wood, C. J.; Gibson, E. A.; Elliott, P. I. P., Hybrid Cyclometalated Iridium Coumarin Complex as a Sensitiser of Both n- and p-Type DSSCs. *Eur. J. Inorg. Chem.* **2016,** *2016* (18), 2887-2890.
191. Li, C.; Lu, W.; Zhou, X.; Pang, M.; Luo, X., Visible-Light Driven Photoelectrochemical Platform Based on the Cyclometalated Iridium(III) Complex with Coumarin 6 for Detection of MicroRNA. *Anal. Chem.* **2018,** *90* (24), 14239-14246.
192. Flamigni, L.; Barbieri, A.; Sabatini, C.; Ventura, B.; Barigelletti, F., Photochemistry and Photophysics of Coordination Compounds: Iridium. In *Photochemistry and Photophysics of Coordination Compounds II*, Balzani, V.; Campagna, S., Eds. Springer Berlin Heidelberg: Berlin, Heidelberg, 2007; pp 143-203.
193. Meyer, T. J., Photochemistry of metal coordination complexes: metal to ligand charge transfer excited states. *Pure Appl. Chem.* **1986,** *58* (9), 1193-1206.
194. Razavet, M.; Artero, V.; Fontecave, M., Proton Electroreduction Catalyzed by Cobaloximes: Functional Models for Hydrogenases. *Inorg. Chem.* **2005,** *44* (13), 4786-4795.
195. Matheu, R.; Ertem, M. Z.; Benet-Buchholz, J.; Coronado, E.; Batista, V. S.; Sala, X.; Llobet, A., Intramolecular Proton Transfer Boosts Water Oxidation Catalyzed by a Ru Complex. *J. Am. Chem. Soc.* **2015,** *137* (33), 10786-10795.
196. Hawecker, J.; Lehn, J.-M.; Ziessel, R., Electrocatalytic reduction of carbon dioxide mediated by Re(bipy)(CO)3Cl (bipy = 2,2′-bipyridine). *Journal of the Chemical Society, Chemical Communications* **1984,** (6), 328-330.
197. Troian-Gautier, L.; Mugeniwabagara, E.; Fusaro, L.; Moucheron, C.; Kirsch-De Mesmaeker, A.; Luhmer, M., pH Dependence of Photoinduced Electron Transfer with [Ru(TAP)3]2+. *Inorg. Chem.* **2017,** *56* (4), 1794-1803.
198. Hall, J. P.; Poynton, F. E.; Keane, P. M.; Gurung, S. P.; Brazier, J. A.; Cardin, D. J.; Winter, G.; Gunnlaugsson, T.; Sazanovich, I. V.; Towrie, M.; Cardin, C. J.; Kelly, J. M.; Quinn, S. J., Monitoring one-electron photo-oxidation of guanine in DNA crystals using ultrafast infrared spectroscopy. *Nat. Chem.* **2015,** *7* (12), 961-967.
199. Keane, P. M.; Poynton, F. E.; Hall, J. P.; Sazanovich, I. V.; Towrie, M.; Gunnlaugsson, T.; Quinn, S. J.; Cardin, C. J.; Kelly, J. M., Reversal of a Single Base-Pair Step Controls Guanine Photo-Oxidation by an Intercalating Ruthenium(II) Dipyridophenazine Complex. *Angew. Chem. Int. Edit.* **2015,** *54* (29), 8364-8368.
200. Keane, P. M.; O'Sullivan, K.; Poynton, F. E.; Poulsen, B. C.; Sazanovich, I. V.; Towrie, M.; Cardin, C. J.; Sun, X.-Z.; George, M. W.; Gunnlaugsson, T.; Quinn, S. J.; Kelly, J. M., Understanding the factors controlling the photo-oxidation of natural DNA by enantiomerically pure intercalating ruthenium polypyridyl complexes through TA/TRIR studies with polydeoxynucleotides and mixed sequence oligodeoxynucleotides. *Chem. Sci.* **2020,** *11* (32), 8600-8609.
201. Moucheron, C.; Kirsch-De Mesmaeker, A.; Kelly, J. M., Photoreactions of ruthenium (II) and osmium (II) complexes with deoxyribonucleic acid (DNA). *Journal of Photochemistry and Photobiology B: Biology* **1997,** *40* (2), 91-106.
202. Elias, B.; Kirsch-De Mesmaeker, A., Photo-reduction of polyazaaromatic Ru(II) complexes by biomolecules and possible applications. *Coordin. Chem. Rev.* **2006,** *250* (13), 1627-1641.
203. Liska, A.; Triskova, I.; Ludvik, J.; Trnkova, L., Oxidation potentials of guanine, guanosine and guanosine-5′-monophosphate: Theory and experiment. *Electrochimica Acta* **2019,** *318*, 108-119.
204. Castano, A. P.; Demidova, T. N.; Hamblin, M. R., Mechanisms in photodynamic therapy: part one—photosensitizers, photochemistry and cellular localization. *Photodiagnosis and Photodynamic Therapy* **2004,** *1* (4), 279-293.
205. Tamayo, A. B.; Alleyne, B. D.; Djurovich, P. I.; Lamansky, S.; Tsyba, I.; Ho, N. N.; Bau, R.; Thompson, M. E., Synthesis and Characterization of Facial and Meridional Tris-cyclometalated Iridium(III) Complexes. *J. Am. Chem. Soc.* **2003,** *125* (24), 7377-7387.

206. Collin, J.-P.; Dixon, I. M.; Sauvage, J.-P.; Williams, J. A. G.; Barigelletti, F.; Flamigni, L., Synthesis and Photophysical Properties of Iridium(III) Bisterpyridine and Its Homologues: a Family of Complexes with a Long-Lived Excited State. *J. Am. Chem. Soc.* **1999,** *121* (21), 5009-5016.
207. Jacques, A.; Kirsch-De Mesmaeker, A.; Elias, B., Selective DNA Purine Base Photooxidation by Bis-terdentate Iridium(III) Polypyridyl and Cyclometalated Complexes. *Inorg. Chem.* **2014,** *53* (3), 1507-1512.
208. Leslie, W.; Poole, R. A.; Murray, P. R.; Yellowlees, L. J.; Beeby, A.; Williams, J. A. G., Near infra-red luminescence from bis-terpyridyl iridium(III) complexes incorporating electron-rich pendants. *Polyhedron* **2004,** *23* (17), 2769-2777.
209. Radwan, Y. K.; Maity, A.; Teets, T. S., Manipulating the Excited States of Cyclometalated Iridium Complexes with β-Ketoiminate and β-Diketiminate Ligands. *Inorg. Chem.* **2015,** *54* (14), 7122-7131.
210. Shon, J.-H.; Sittel, S.; Teets, T. S., Synthesis and Characterization of Strong Cyclometalated Iridium Photoreductants for Application in Photocatalytic Aryl Bromide Hydrodebromination. *ACS Catal.* **2019,** *9* (9), 8646-8658.
211. Goldsmith, J. I.; Hudson, W. R.; Lowry, M. S.; Anderson, T. H.; Bernhard, S., Discovery and High-Throughput Screening of Heteroleptic Iridium Complexes for Photoinduced Hydrogen Production. *J. Am. Chem. Soc.* **2005,** *127* (20), 7502-7510.
212. Lowry, M. S.; Hudson, W. R.; Pascal, R. A.; Bernhard, S., Accelerated Luminophore Discovery through Combinatorial Synthesis. *J. Am. Chem. Soc.* **2004,** *126* (43), 14129-14135.
213. Till, N. A.; Tian, L.; Dong, Z.; Scholes, G. D.; MacMillan, D. W. C., Mechanistic Analysis of Metallaphotoredox C–N Coupling: Photocatalysis Initiates and Perpetuates Ni(I)/Ni(III) Coupling Activity. *J. Am. Chem. Soc.* **2020,** *142* (37), 15830-15841.
214. Lowry, M. S.; Goldsmith, J. I.; Slinker, J. D.; Rohl, R.; Pascal, R. A.; Malliaras, G. G.; Bernhard, S., Single-Layer Electroluminescent Devices and Photoinduced Hydrogen Production from an Ionic Iridium(III) Complex. *Chem. Mater.* **2005,** *17* (23), 5712-5719.
215. Takizawa, S.-y.; Shimada, K.; Sato, Y.; Murata, S., Controlling the Excited State and Photosensitizing Property of a 2-(2-Pyridyl)benzo[b]thiophene-Based Cationic Iridium Complex through Simple Chemical Modification. *Inorg. Chem.* **2014,** *53* (6), 2983-2995.
216. Graetz, J., New approaches to hydrogen storage. *Chem. Soc. Rev.* **2009,** *38* (1), 73-82.
217. Jacques, A.; Schott, O.; Robeyns, K.; Hanan, G. S.; Elias, B., Hydrogen Photoevolution from a Green-Absorbing Iridium(III)–Cobalt-(III) Dyad. *Eur. J. Inorg. Chem.* **2016,** *2016* (12), 1779-1783.
218. Losse, S.; Vos, J. G.; Rau, S., Catalytic hydrogen production at cobalt centres. *Coordin. Chem. Rev.* **2010,** *254* (21), 2492-2504.
219. Artero, V.; Chavarot-Kerlidou, M.; Fontecave, M., Splitting Water with Cobalt. *Angew. Chem. Int. Edit.* **2011,** *50* (32), 7238-7266.
220. Ozawa, H.; Haga, M.-a.; Sakai, K., A Photo-Hydrogen-Evolving Molecular Device Driving Visible-Light-Induced EDTA-Reduction of Water into Molecular Hydrogen. *J. Am. Chem. Soc.* **2006,** *128* (15), 4926-4927.
221. Pfeffer, M. G.; Schäfer, B.; Smolentsev, G.; Uhlig, J.; Nazarenko, E.; Guthmuller, J.; Kuhnt, C.; Wächtler, M.; Dietzek, B.; Sundström, V.; Rau, S., Palladium versus Platinum: The Metal in the Catalytic Center of a Molecular Photocatalyst Determines the Mechanism of the Hydrogen Production with Visible Light. *Angew. Chem. Int. Edit.* **2015,** *54* (17), 5044-5048.
222. Pfeffer, M. G.; Müller, C.; Kastl, E. T. E.; Mengele, A. K.; Bagemihl, B.; Fauth, S. S.; Habermehl, J.; Petermann, L.; Wächtler, M.; Schulz, M.; Chartrand, D.; Laverdière, F.; Seeber, P.; Kupfer, S.; Gräfe, S.; Hanan, G. S.; Vos, J. G.; Dietzek-Ivanšić, B.; Rau, S., Active repair of a dinuclear photocatalyst for visible-light-driven hydrogen production. *Nat. Chem.* **2022,** *14* (5), 500-506.
223. Rau, S.; Schäfer, B.; Gleich, D.; Anders, E.; Rudolph, M.; Friedrich, M.; Görls, H.; Henry, W.; Vos, J. G., A Supramolecular Photocatalyst for the Production of Hydrogen and the Selective Hydrogenation of Tolane. *Angew. Chem. Int. Edit.* **2006,** *45* (37), 6215-6218.
224. Tschierlei, S.; Karnahl, M.; Presselt, M.; Dietzek, B.; Guthmuller, J.; González, L.; Schmitt, M.; Rau, S.; Popp, J., Photochemical Fate: The First Step Determines Efficiency of H2 Formation with a Supramolecular Photocatalyst. *Angew. Chem. Int. Edit.* **2010,** *49* (23), 3981-3984.
225. Fihri, A.; Artero, V.; Razavet, M.; Baffert, C.; Leibl, W.; Fontecave, M., Cobaloxime-Based Photocatalytic Devices for Hydrogen Production. *Angew. Chem. Int. Edit.* **2008,** *47* (3), 564-567.
226. Bevernaegie, R.; Wehlin, S. A. M.; Elias, B.; Troian-Gautier, L., A Roadmap Towards Visible Light Mediated Electron Transfer Chemistry with Iridium(III) Complexes. *ChemPhotoChem* **2021,** *5* (3), 217-234.
227. Yuan, Y.-J.; Yu, Z.-T.; Chen, D.-Q.; Zou, Z.-G., Metal-complex chromophores for solar hydrogen generation. *Chem. Soc. Rev.* **2017,** *46* (3), 603-631.

228. O'Regan, B.; Grätzel, M., A low-cost, high-efficiency solar cell based on dye-sensitized colloidal TiO2 films. *Nature* **1991,** *353* (6346), 737-740.
229. Heyduk, A. F.; Nocera, D. G., Hydrogen Produced from Hydrohalic Acid Solutions by a Two-Electron Mixed-Valence Photocatalyst. *Science* **2001,** *293* (5535), 1639-1641.
230. Gardner, J. M.; Giaimuccio, J. M.; Meyer, G. J., Evidence for Iodine Atoms as Intermediates in the Dye Sensitized Formation of I−I Bonds. *J. Am. Chem. Soc.* **2008,** *130* (51), 17252-17253.
231. Gardner, J. M.; Abrahamsson, M.; Farnum, B. H.; Meyer, G. J., Visible Light Generation of Iodine Atoms and I−I Bonds: Sensitized I− Oxidation and I3− Photodissociation. *J. Am. Chem. Soc.* **2009,** *131* (44), 16206-16214.
232. Powers, D. C.; Hwang, S. J.; Zheng, S.-L.; Nocera, D. G., Halide-Bridged Binuclear HX-Splitting Catalysts. *Inorg. Chem.* **2014,** *53* (17), 9122-9128.
233. Hwang, S. J.; Powers, D. C.; Maher, A. G.; Anderson, B. L.; Hadt, R. G.; Zheng, S.-L.; Chen, Y.-S.; Nocera, D. G., Trap-Free Halogen Photoelimination from Mononuclear Ni(III) Complexes. *J. Am. Chem. Soc.* **2015,** *137* (20), 6472-6475.
234. Hwang, S. J.; Anderson, B. L.; Powers, D. C.; Maher, A. G.; Hadt, R. G.; Nocera, D. G., Halogen Photoelimination from Monomeric Nickel(III) Complexes Enabled by the Secondary Coordination Sphere. *Organometallics* **2015,** *34* (19), 4766-4774.
235. Gonzalez, M. I.; Gygi, D.; Qin, Y.; Zhu, Q.; Johnson, E. J.; Chen, Y.-S.; Nocera, D. G., Taming the Chlorine Radical: Enforcing Steric Control over Chlorine-Radical-Mediated C–H Activation. *J. Am. Chem. Soc.* **2022,** *144* (3), 1464-1472.
236. Tsai, K. Y.-D.; Chang, I. J., Oxidation of Bromide to Bromine by Ruthenium(II) Bipyridine-Type Complexes Using the Flash-Quench Technique. *Inorg. Chem.* **2017,** *56* (14), 8497-8503.
237. Li, G.; Brady, M. D.; Meyer, G. J., Visible Light Driven Bromide Oxidation and Ligand Substitution Photochemistry of a Ru Diimine Complex. *J. Am. Chem. Soc.* **2018,** *140* (16), 5447-5456.
238. Li, G.; Ward, W. M.; Meyer, G. J., Visible Light Driven Nanosecond Bromide Oxidation by a Ru Complex with Subsequent Br–Br Bond Formation. *J. Am. Chem. Soc.* **2015,** *137* (26), 8321-8323.
239. Li, G.; Swords, W. B.; Meyer, G. J., Bromide Photo-oxidation Sensitized to Visible Light in Consecutive Ion Pairs. *J. Am. Chem. Soc.* **2017,** *139* (42), 14983-14991.
240. Ward, W. M.; Farnum, B. H.; Siegler, M.; Meyer, G. J., Chloride Ion-Pairing with Ru(II) Polypyridyl Compounds in Dichloromethane. *J. Phys. Chem. A* **2013,** *117* (36), 8883-8894.
241. Troian-Gautier, L.; Swords, W. B.; Meyer, G. J., Iodide Photoredox and Bond Formation Chemistry. *Acc. Chem. Res.* **2019,** *52* (1), 170-179.
242. Swords, W. B.; Li, G.; Meyer, G. J., Iodide Ion Pairing with Highly Charged Ruthenium Polypyridyl Cations in CH3CN. *Inorg. Chem.* **2015,** *54* (9), 4512-4519.
243. Troian-Gautier, L.; Beauvilliers, E. E.; Swords, W. B.; Meyer, G. J., Redox Active Ion-Paired Excited States Undergo Dynamic Electron Transfer. *J. Am. Chem. Soc.* **2016,** *138* (51), 16815-16826.
244. Ripak, A.; Vega Salgado, A. K.; Valverde, D.; Cristofaro, S.; de Gary, A.; Olivier, Y.; Elias, B.; Troian-Gautier, L., Factors Controlling Cage Escape Yields of Closed- and Open-Shell Metal Complexes in Bimolecular Photoinduced Electron Transfer. *J. Am. Chem. Soc.* **2024**.
245. Bühler, R. E.; Ebert, M., Transient Charge-transfer Complexes with Chlorine Atoms by Pulse Radiolysis of Carbon Tetrachloride Solutions. *Nature* **1967,** *214*, 1220-1221.
246. Li, P.; Deetz, A. M.; Hu, J.; Meyer, G. J.; Hu, K., Chloride Oxidation by One- or Two-Photon Excitation of N-Phenylphenothiazine. *J. Am. Chem. Soc.* **2022,** *144* (38), 17604-17610.
247. Meyer, T. J., Chemical Approaches to Artificial Photosynthesis. *Acc. Chem. Res.* **1989,** *22* (5), 163-170.
248. Hammarström, L.; Styring, S., Proton-Coupled Electron Transfer of Tyrosines in Photosystem II and Model Systems for Artificial Photosynthesis: the Role of a Redox-Active Link Between Catalyst and Photosensitizer. *Energy & Environmental Science* **2011,** *4* (7), 2379-2388.
249. Gust, D.; Moore, T. A.; Moore, A. L., Artificial photosynthesis. *Theoretical and Experimental Plant Physiology* **2013,** *25*, 182-185.
250. Eberhart, M. S.; Bowers, L. M. R.; Shan, B.; Troian-Gautier, L.; Brennaman, M. K.; Papanikolas, J. M.; Meyer, T. J., Completing a Charge Transport Chain for Artificial Photosynthesis. *J. Am. Chem. Soc.* **2018,** *140* (31), 9823-9826.
251. Concepcion, J. J.; House, R. L.; Papanikolas, J. M.; Meyer, T. J., Chemical Approaches to Artificial Photosynthesis. *Proceedings of the National Academy of Sciences* **2012,** *109* (39), 15560-15564.
252. Shan, B.; Vanka, S.; Li, T.-T.; Troian-Gautier, L.; Brennaman, M. K.; Mi, Z.; Meyer, T. J., Binary molecular-semiconductor p–n junctions for photoelectrocatalytic CO2 reduction. *Nat. Energy* **2019,** *4* (4), 290-299.
253. Cancelliere, A. M.; Puntoriero, F.; Serroni, S.; Campagna, S.; Tamaki, Y.; Saito, D.; Ishitani, O., Efficient trinuclear Ru(ii)–Re(i) supramolecular photocatalysts for CO2 reduction based on a new tris-chelating bridging ligand built around a central aromatic ring. *Chem. Sci.* **2020,** *11* (6), 1556-1563.

254. Sampaio, R. N.; Grills, D. C.; Polyansky, D. E.; Szalda, D. J.; Fujita, E., Unexpected Roles of Triethanolamine in the Photochemical Reduction of CO2 to Formate by Ruthenium Complexes. *J. Am. Chem. Soc.* **2020,** *142* (5), 2413-2428.
255. Morris, A. J.; Meyer, G. J.; Fujita, E., Molecular Approaches to the Photocatalytic Reduction of Carbon Dioxide for Solar Fuels. *Acc. Chem. Res.* **2009,** *42* (12), 1983-1994.
256. Dempsey, J. L.; Brunschwig, B. S.; Winkler, J. R.; Gray, H. B., Hydrogen Evolution Catalyzed by Cobaloximes. *Acc. Chem. Res.* **2009,** *42* (12), 1995-2004.
257. Teets, T. S.; Nocera, D. G., Photocatalytic hydrogen production. *Chem. Commun.* **2011,** *47* (33), 9268-9274.
258. Esswein, A. J.; Nocera, D. G., Hydrogen Production by Molecular Photocatalysis. *Chem. Rev.* **2007,** *107* (10), 4022-4047.
259. Fihri, A.; Artero, V.; Pereira, A.; Fontecave, M., Efficient H2-producing photocatalytic systems based on cyclometalated iridium- and tricarbonylrhenium-diimine photosensitizers and cobaloxime catalysts. *Dalton Trans.* **2008,** (41), 5567-5569.
260. Sullivan, B. P.; Bolinger, C. M.; Conrad, D.; Vining, W. J.; Meyer, T. J., One- and two-electron pathways in the electrocatalytic reduction of CO2 by fac-Re(bpy)(CO)3Cl (bpy = 2,2′-bipyridine). *Journal of the Chemical Society, Chemical Communications* **1985,** (20), 1414-1416.
261. Deaton, J. C.; Castellano, F. N., Archetypal Iridium(III) Compounds for Optoelectronic and Photonic Applications. In *Iridium(III) in Optoelectronic and Photonics Applications*, Zysman-Colman, E., Ed. John Wiley & Sons Ltc.: Chichester, West Sussex, 2017; pp 1-69.
262. Nonoyama, M., Benzo[h]quinolin-10-yl-N Iridium(III) Complexes. *Bulletin of the Chemical Society of Japan* **1974,** *47* (3), 767-768.
263. Bevernaegie, R.; Marcélis, L.; Moreno-Betancourt, A.; Laramée-Milette, B.; Hanan, G. S.; Loiseau, F.; Sliwa, M.; Elias, B., Ultrafast charge transfer excited state dynamics in trifluoromethyl-substituted iridium(iii) complexes. *Phys. Chem. Chem. Phys.* **2018,** *20* (43), 27256-27260.
264. Bevernaegie, R.; Marcélis, L.; Laramée-Milette, B.; De Winter, J.; Robeyns, K.; Gerbaux, P.; Hanan, G. S.; Elias, B., Trifluoromethyl-Substituted Iridium(III) Complexes: From Photophysics to Photooxidation of a Biological Target. *Inorg. Chem.* **2018,** *57* (3), 1356-1367.
265. Franco, C.; Olmsted, J., Photochemical determination of the solubility of oxygen in various media. *Talanta* **1990,** *37* (9), 905-909.
266. Juris, A.; Balzani, V.; Barigelletti, F.; Campagna, S.; Belser, P.; von Zelewsky, A., Ru(II) polypyridine complexes: photophysics, photochemistry, eletrochemistry, and chemiluminescence. *Coordin. Chem. Rev.* **1988,** *84*, 85-277.
267. Campagna, S.; Puntoriero, F.; Nastasi, F.; Bergamini, G.; Balzani, V., Photochemistry and Photophysics of Coordination Compounds: Ruthenium. In *Photochemistry and Photophysics of Coordination Compounds I*, Balzani, V.; Campagna, S., Eds. Springer Berlin Heidelberg: Berlin, Heidelberg, 2007; pp 117-214.
268. Giereth, R.; Obermeier, M.; Forschner, L.; Karnahl, M.; Schwalbe, M.; Tschierlei, S., Exploring the Full Potential of Photocatalytic Carbon Dioxide Reduction Using a Dinuclear Re2Cl2 Complex Assisted by Various Photosensitizers. *ChemPhotoChem* **2021,** *5* (7), 644-653.
269. Takeda, N.; Miller, J. R., Inverted Region in Bimolecular Electron Transfer in Solution Enabled by Delocalization. *J. Am. Chem. Soc.* **2020,** *142* (42), 17997-18004.
270. Piechota, E. J.; Meyer, G. J., Introduction to Electron Transfer: Theoretical Foundations and Pedagogical Examples. *Journal of Chemical Education* **2019,** *96* (11), 2450-2466.
271. Closs, G. L.; Miller, J. R., Intramolecular Long-Distance Electron Transfer in Organic Molecules. *Science* **1988,** *240* (4851), 440-447.
272. Connell, T. U.; Fraser, C. L.; Czyz, M. L.; Smith, Z. M.; Hayne, D. J.; Doeven, E. H.; Agugiaro, J.; Wilson, D. J. D.; Adcock, J. L.; Scully, A. D.; Gómez, D. E.; Barnett, N. W.; Polyzos, A.; Francis, P. S., The Tandem Photoredox Catalysis Mechanism of [Ir(ppy)2(dtb-bpy)]+ Enabling Access to Energy Demanding Organic Substrates. *J. Am. Chem. Soc.* **2019,** *141* (44), 17646-17658.
273. Morton, C. M.; Zhu, Q.; Ripberger, H.; Troian-Gautier, L.; Toa, Z. S. D.; Knowles, R. R.; Alexanian, E. J., C–H Alkylation via Multisite-Proton-Coupled Electron Transfer of an Aliphatic C–H Bond. *J. Am. Chem. Soc.* **2019,** *141* (33), 13253-13260.
274. Hankache, J.; Niemi, M.; Lemmetyinen, H.; Wenger, O. S., Photoinduced Electron Transfer in Linear Triarylamine–Photosensitizer–Anthraquinone Triads with Ruthenium(II), Osmium(II), and Iridium(III). *Inorg. Chem.* **2012,** *51* (11), 6333-6344.
275. Sauvageot, E.; Lafite, P.; Duverger, E.; Marion, R.; Hamel, M.; Gaillard, S.; Renaud, J.-L.; Daniellou, R., Iridium complexes inhibit tumor necrosis factor-α by utilizing light and mixed ligands. *Journal of Organometallic Chemistry* **2016,** *808*, 122-127.

276. Lin, S.; Gao, W.; Tian, Z.; Yang, C.; Lu, L.; Mergny, J.-L.; Leung, C.-H.; Ma, D.-L., Luminescence switch-on detection of protein tyrosine kinase-7 using a G-quadruplex-selective probe. *Chem. Sci.* **2015,** *6* (7), 4284-4290.
277. Lu, L.; Shiu-Hin Chan, D.; Kwong, D. W. J.; He, H.-Z.; Leung, C.-H.; Ma, D.-L., Detection of nicking endonuclease activity using a G-quadruplex-selective luminescent switch-on probe. *Chem. Sci.* **2014,** *5* (12), 4561-4568.
278. Lin, S.; He, B.; Yang, C.; Leung, C.-H.; Mergny, J.-L.; Ma, D.-L., Luminescence switch-on assay of interferon-gamma using a G-quadruplex-selective iridium(iii) complex. *Chem. Commun.* **2015,** *51* (89), 16033-16036.
279. Liu, L.-J.; Lu, L.; Zhong, H.-J.; He, B.; Kwong, D. W. J.; Ma, D.-L.; Leung, C.-H., An Iridium(III) Complex Inhibits JMJD2 Activities and Acts as a Potential Epigenetic Modulator. *Journal of Medicinal Chemistry* **2015,** *58* (16), 6697-6703.
280. Zhao, Q.; Liu, S.; Shi, M.; Wang, C.; Yu, M.; Li, L.; Li, F.; Yi, T.; Huang, C., Series of New Cationic Iridium(III) Complexes with Tunable Emission Wavelength and Excited State Properties: Structures, Theoretical Calculations, and Photophysical and Electrochemical Properties. *Inorg. Chem.* **2006,** *45* (16), 6152-6160.
281. Nocera, D. G., Chemistry of Personalized Solar Energy. *Inorg. Chem.* **2009,** *48* (21), 10001-10017.
282. Armaroli, N.; Balzani, V., Solar Electricity and Solar Fuels: Status and Perspectives in the Context of the Energy Transition. *Chem. Eur. J.* **2016,** *22* (1), 32-57.
283. Yatsuzuka, K.; Yamauchi, K.; Sakai, K., Redox tuning in Pt(bpy)-viologen catalyst-acceptor dyads enabling photocatalytic hydrogen evolution from water. *Chem. Commun.* **2021,** *57* (42), 5183-5186.
284. Yatsuzuka, K.; Yamauchi, K.; Kawano, K.; Ozawa, H.; Sakai, K., Improving the overall performance of photochemical H2 evolution catalyzed by the Co-NHC complex via the redox tuning of electron relays. *Sustainable Energy & Fuels* **2021,** *5* (3), 740-749.
285. Lang, P.; Habermehl, J.; Troyanov, S. I.; Rau, S.; Schwalbe, M., Photocatalytic Generation of Hydrogen Using Dinuclear π-Extended Porphyrin–Platinum Compounds. *Chem. Eur. J.* **2018,** *24* (13), 3225-3233.
286. Habermehl, J.; Nauroozi, D.; Martynow, M.; Vilk, Y. E.; Beranek, R.; Guthmuller, J.; Rau, S., Synthesis and hydrogen evolving catalysis of a panchromatic photochemical molecular device. *Sustainable Energy & Fuels* **2020,** *4* (2), 619-624.
287. Connolly, P.; Espenson, J. H., Cobalt-catalyzed evolution of molecular hydrogen. *Inorg. Chem.* **1986,** *25* (16), 2684-2688.
288. Lazarides, T.; Delor, M.; Sazanovich, I. V.; McCormick, T. M.; Georgakaki, I.; Charalambidis, G.; Weinstein, J. A.; Coutsolelos, A. G., Photocatalytic hydrogen production from a noble metal free system based on a water soluble porphyrin derivative and a cobaloxime catalyst. *Chem. Commun.* **2014,** *50* (5), 521-523.
289. Du, P.; Schneider, J.; Jarosz, P.; Zhang, J.; Brennessel, W. W.; Eisenberg, R., Photoinduced Electron Transfer in Platinum(II) Terpyridyl Acetylide Chromophores: Reductive and Oxidative Quenching and Hydrogen Production. *The Journal of Physical Chemistry B* **2007,** *111* (24), 6887-6894.
290. Wang, X.; Goeb, S.; Ji, Z.; Pogulaichenko, N. A.; Castellano, F. N., Homogeneous Photocatalytic Hydrogen Production Using π-Conjugated Platinum(II) Arylacetylide Sensitizers. *Inorg. Chem.* **2011,** *50* (3), 705-707.
291. Li, C.; Wang, M.; Pan, J.; Zhang, P.; Zhang, R.; Sun, L., Photochemical hydrogen production catalyzed by polypyridyl ruthenium–cobaloxime heterobinuclear complexes with different bridges. *Journal of Organometallic Chemistry* **2009,** *694* (17), 2814-2819.
292. Rupp, M.; Auvray, T.; Rousset, E.; Mercier, G. M.; Marvaud, V.; Kurth, D. G.; Hanan, G. S., Photocatalytic Hydrogen Evolution Driven by a Heteroleptic Ruthenium(II) Bis(terpyridine) Complex. *Inorg. Chem.* **2019,** *58* (14), 9127-9134.
293. Probst, B.; Rodenberg, A.; Guttentag, M.; Hamm, P.; Alberto, R., A Highly Stable Rhenium−Cobalt System for Photocatalytic H2 Production: Unraveling the Performance-Limiting Steps. *Inorg. Chem.* **2010,** *49* (14), 6453-6460.
294. Probst, B.; Guttentag, M.; Rodenberg, A.; Hamm, P.; Alberto, R., Photocatalytic H2 Production from Water with Rhenium and Cobalt Complexes. *Inorg. Chem.* **2011,** *50* (8), 3404-3412.
295. Takizawa, S.-y.; Katoh, S.; Okazawa, A.; Ikuta, N.; Matsushima, S.; Zeng, F.; Murata, S., Triplet Excited States Modulated by Push–Pull Substituents in Monocyclometalated Iridium(III) Photosensitizers. *Inorg. Chem.* **2021,** *60* (7), 4891-4903.
296. Tsuboyama, A.; Iwawaki, H.; Furugori, M.; Mukaide, T.; Kamatani, J.; Igawa, S.; Moriyama, T.; Miura, S.; Takiguchi, T.; Okada, S.; Hoshino, M.; Ueno, K., Homoleptic Cyclometalated Iridium Complexes with Highly Efficient Red Phosphorescence and Application to Organic Light-Emitting Diode. *J. Am. Chem. Soc.* **2003,** *125* (42), 12971-12979.

297. Lentz, C.; Schott, O.; Auvray, T.; Hanan, G. S.; Elias, B., Design and photophysical studies of iridium(iii)–cobalt(iii) dyads and their application for dihydrogen photo-evolution. *Dalton Trans.* **2019,** *48* (41), 15567-15576.
298. Lowry, M. S.; Bernhard, S., Synthetically Tailored Excited States: Phosphorescent, Cyclometalated Iridium(III) Complexes and Their Applications. *Chem. Eur. J.* **2006,** *12* (31), 7970-7977.
299. Elgrishi, N.; Rountree, K. J.; McCarthy, B. D.; Rountree, E. S.; Eisenhart, T. T.; Dempsey, J. L., A Practical Beginner's Guide to Cyclic Voltammetry. *Journal of Chemical Education* **2018,** *95* (2), 197-206.
300. Brouwer, A., Standards for photoluminescence quantum yield measurements in solution (IUPAC Technical Report)*. *Pure and Applied Chemistry* **2011,** *83*.
301. Lakowicz, J. R., *Principles of Fluorescence Spectroscopy*. Springer US, New York: 2006.
302. Rupp, M. T.; Auvray, T.; Shevchenko, N.; Swoboda, L.; Hanan, G. S.; Kurth, D. G., Substituted 2,4-Di(pyridin-2-yl)pyrimidine-Based Ruthenium Photosensitizers for Hydrogen Photoevolution under Red Light. *Inorg. Chem.* **2021,** *60* (1), 292-302.
303. Four, P.; Guibe, F., Palladium-catalyzed reaction of tributyltin hydride with acyl chlorides. A mild, selective, and general route to aldehydes. *J. Org. Chem.* **1981,** *46* (22), 4439-4445.
304. Kober, E. M.; Caspar, J. V.; Lumpkin, R. S.; Meyer, T. J., Application of the energy gap law to excited-state decay of osmium(II)-polypyridine complexes: calculation of relative nonradiative decay rates from emission spectral profiles. *J. Phys. Chem.* **1986,** *90* (16), 3722-3734.
305. *Bruker SADABS and TWINABS,*. Bruker AXS Inc.: Madison, Wisconsin, USA.,: 2001.
306. Sheldrick, G. M., A short history of SHELX. *Acta Crystallogr A* **2008,** *64* (Pt 1), 112-22.
307. Sheldrick, G. M., SHELXT - integrated space-group and crystal-structure determination. *Acta Crystallogr A Found Adv* **2015,** *71* (Pt 1), 3-8.
308. Spek, A. L., Structure validation in chemical crystallography. *Acta Crystallogr D Biol Crystallogr* **2009,** *65* (Pt 2), 148-55.
309. *CCDC Mercury 3.1 - 3.3.* **2001-2003**.
310. Costa, R. n. D.; OrtÃ-, E.; Bolink, H. J.; Graber, S.; Schaffner, S.; Neuburger, M.; Housecroft, C. E.; Constable, E. C., Archetype Cationic Iridium Complexes and Their Use in Solid-State Light-Emitting Electrochemical Cells. *Advanced Functional Materials* **2009,** *19* (21), 3456-3463.
311. Liu, S.-J.; Zhao, Q.; Fan, Q.-L.; Huang, W., A Series of Red-Light-Emitting Ionic Iridium Complexes: Structures, Excited State Properties, and Application in Electroluminescent Devices. *Eur. J. Inorg. Chem.* **2008,** *2008* (13), 2177-2185.
312. Chen, L. X., X-Ray Transient Absorption Spectroscopy. In *X-Ray Absorption and X-Ray Emission Spectroscopy*, 2016; pp 213-249.
313. Iglesias-Juez, A.; Chiarello, G. L.; Patience, G. S.; Guerrero-Pérez, M. O., Experimental methods in chemical engineering: X-ray absorption spectroscopy—XAS, XANES, EXAFS. *The Canadian Journal of Chemical Engineering* **2022,** *100* (1), 3-22.
314. Zhang, X.; Canton, S. E.; Smolentsev, G.; Wallentin, C.-J.; Liu, Y.; Kong, Q.; Attenkofer, K.; Stickrath, A. B.; Mara, M. W.; Chen, L. X.; Wärnmark, K.; Sundström, V., Highly Accurate Excited-State Structure of [Os(bpy)2dcbpy]2+ Determined by X-ray Transient Absorption Spectroscopy. *J. Am. Chem. Soc.* **2014,** *136* (24), 8804-8809.
315. Chen, L. X.; Zhang, X.; Wasinger, E. C.; Attenkofer, K.; Jennings, G.; Muresan, A. Z.; Lindsey, J. S., Tracking Electrons and Atoms in a Photoexcited Metalloporphyrin by X-ray Transient Absorption Spectroscopy. *J. Am. Chem. Soc.* **2007,** *129* (31), 9616-9618.
316. Wang, J.-W.; Zhang, X.; Velasco, L.; Karnahl, M.; Li, Z.; Luo, Z.-M.; Huang, Y.; Yu, J.; Hu, W.; Zhang, X.; Yamauchi, K.; Sakai, K.; Moonshiram, D.; Ouyang, G., Precious-Metal-Free CO2 Photoreduction Boosted by Dynamic Coordinative Interaction between Pyridine-Tethered Cu(I) Sensitizers and a Co(II) Catalyst. *JACS Au* **2023,** *3* (7), 1984-1997.
317. Pushkar, Y.; Moonshiram, D.; Purohit, V.; Yan, L.; Alperovich, I., Spectroscopic Analysis of Catalytic Water Oxidation by [RuII(bpy)(tpy)H2O]2+ Suggests That RuV═O Is Not a Rate-Limiting Intermediate. *J. Am. Chem. Soc.* **2014,** *136* (34), 11938-11945.
318. Gimbert-Suriñach, C.; Moonshiram, D.; Francàs, L.; Planas, N.; Bernales, V.; Bozoglian, F.; Guda, A.; Mognon, L.; López, I.; Hoque, M. A.; Gagliardi, L.; Cramer, C. J.; Llobet, A., Structural and Spectroscopic Characterization of Reaction Intermediates Involved in a Dinuclear Co–Hbpp Water Oxidation Catalyst. *J. Am. Chem. Soc.* **2016,** *138* (47), 15291-15294.
319. Velasco, L.; Liu, C.; Zhang, X.; Grau, S.; Gil-Sepulcre, M.; Gimbert-Suriñach, C.; Picón, A.; Llobet, A.; DeBeer, S.; Moonshiram, D., Mapping the Ultrafast Mechanistic Pathways of Co Photocatalysts in Pure Water through Time-resolved X-ray Spectroscopy. *ChemSusChem* **2023,** *n/a* (n/a), e202300719.
320. Li, Z.-J.; Zhan, F.; Xiao, H.; Zhang, X.; Kong, Q.-Y.; Fan, X.-B.; Liu, W.-Q.; Huang, M.-Y.; Huang, C.; Gao, Y.-J.; Li, X.-B.; Meng, Q.-Y.; Feng, K.; Chen, B.; Tung, C.-H.; Zhao, H.-F.; Tao,

Y.; Wu, L.-Z., Tracking Co(I) Intermediate in Operando in Photocatalytic Hydrogen Evolution by X-ray Transient Absorption Spectroscopy and DFT Calculation. *J. Phys. Chem. Lett.* **2016,** *7* (24), 5253-5258.
321. Jayasekara, G. K.; Antolini, C.; Smith, M. A.; Jacoby, D. J.; Escolastico, J.; Girard, N.; Young, B. T.; Hayes, D., Mechanisms of the Cu(I)-Catalyzed Intermolecular Photocycloaddition Reaction Revealed by Optical and X-ray Transient Absorption Spectroscopies. *J. Am. Chem. Soc.* **2021,** *143* (46), 19356-19364.
322. Westre, T. E.; Kennepohl, P.; DeWitt, J. G.; Hedman, B.; Hodgson, K. O.; Solomon, E. I., A Multiplet Analysis of Fe K-Edge 1s → 3d Pre-Edge Features of Iron Complexes. *J. Am. Chem. Soc.* **1997,** *119* (27), 6297-6314.
323. Smolentsev, G.; van Vliet, K. M.; Azzaroli, N.; van Bokhoven, J. A.; Brouwer, A. M.; de Bruin, B.; Nachtegaal, M.; Tromp, M., Pump–probe XAS investigation of the triplet state of an Ir photosensitizer with chromenopyridinone ligands. *Photochem. Photobio. Sci.* **2018,** *17* (7), 896-902.
324. Du, P.; Schneider, J.; Luo, G.; Brennessel, W. W.; Eisenberg, R., Visible Light-Driven Hydrogen Production from Aqueous Protons Catalyzed by Molecular Cobaloxime Catalysts. *Inorg. Chem.* **2009,** *48* (11), 4952-4962.
325. Du, P.; Schneider, J.; Luo, G.; Brennessel, W. W.; Eisenberg, R., Correction to Visible Light-Driven Hydrogen Production from Aqueous Protons Catalyzed by Molecular Cobaloxime Catalysts. *Inorg. Chem.* **2009,** *48* (17), 8646-8646.
326. Kirch, M.; Lehn, J.-M.; Sauvage, J.-P., Hydrogen Generation by Visible Light Irradiation of Aqueous Solutions of Metal Complexes. An approach to the photochemical conversion and storage of solar energy. *Helvetica Chimica Acta* **1979,** *62* (4), 1345-1384.
327. Chan, S. F.; Chou, M.; Creutz, C.; Matsubara, T.; Sutin, N., Mechanism of the formation of dihydrogen from the photoinduced reactions of poly(pyridine)ruthenium(II) and poly(pyridine)rhodium(III) complexes. *J. Am. Chem. Soc.* **1981,** *103* (2), 369-379.
328. Becke, A. D., Density-functional exchange-energy approximation with correct asymptotic behavior. *Physical Review A* **1988,** *38* (6), 3098-3100.
329. Grimme, S.; Antony, J.; Ehrlich, S.; Krieg, H., A consistent and accurate ab initio parametrization of density functional dispersion correction (DFT-D) for the 94 elements H-Pu. *J. Chem. Phys.* **2010,** *132* (15), 154104.
330. Chan, A. Y.; Perry, I. B.; Bissonnette, N. B.; Buksh, B. F.; Edwards, G. A.; Frye, L. I.; Garry, O. L.; Lavagnino, M. N.; Li, B. X.; Liang, Y.; Mao, E.; Millet, A.; Oakley, J. V.; Reed, N. L.; Sakai, H. A.; Seath, C. P.; MacMillan, D. W. C., Metallaphotoredox: The Merger of Photoredox and Transition Metal Catalysis. *Chem. Rev.* **2022,** *122* (2), 1485-1542.
331. Tay, N. E. S.; Lehnherr, D.; Rovis, T., Photons or Electrons? A Critical Comparison of Electrochemistry and Photoredox Catalysis for Organic Synthesis. *Chem. Rev.* **2022,** *122* (2), 2487-2649.
332. Archer, S. A.; Raza, A.; Dröge, F.; Robertson, C.; Auty, A. J.; Chekulaev, D.; Weinstein, J. A.; Keane, T.; Meijer, A. J. H. M.; Haycock, J. W.; MacNeil, S.; Thomas, J. A., A dinuclear ruthenium(ii) phototherapeutic that targets duplex and quadruplex DNA. *Chem. Sci.* **2019,** *10* (12), 3502-3513.
333. Gill, M. R.; Thomas, J. A., Ruthenium(ii) polypyridyl complexes and DNA—from structural probes to cellular imaging and therapeutics. *Chem. Soc. Rev.* **2012,** *41* (8), 3179-3192.
334. Raza, A.; Archer, S. A.; Fairbanks, S. D.; Smitten, K. L.; Botchway, S. W.; Thomas, J. A.; MacNeil, S.; Haycock, J. W., A Dinuclear Ruthenium(II) Complex Excited by Near-Infrared Light through Two-Photon Absorption Induces Phototoxicity Deep within Hypoxic Regions of Melanoma Cancer Spheroids. *J. Am. Chem. Soc.* **2020,** *142* (10), 4639-4647.
335. Gillard, M.; Bonnet, H.; Lartia, R.; Yacoub, H.; Dejeu, J.; Defrancq, E.; Elias, B., Luminescent Ruthenium(II) Complexes Used for the Detection of 8-Oxoguanine in the Human Telomeric Sequence. *Bioconjugate Chemistry* **2023,** *34* (2), 414-421.
336. Gillard, M.; Piraux, G.; Daenen, M.; Abraham, M.; Troian-Gautier, L.; Bar, L.; Bonnet, H.; Loiseau, F.; Jamet, H.; Dejeu, J.; Defrancq, E.; Elias, B., Photo-Oxidizing Ruthenium(II) Complexes with Enhanced Visible-Light Absorption and G-quadruplex DNA Binding Abilities. *Chem. Eur. J.* **2022,** *28* (66), e202202251.
337. Gillard, M.; Troian-Gautier, L.; Decottignies, A.; Elias, B., pH-Activatable Ruthenium(II) Fluorescein Salphen Schiff Base Photosensitizers for Theranostic Applications. *Journal of Medicinal Chemistry* **2024,** *67* (4), 2549-2558.
338. Huang, H.; Yu, B.; Zhang, P.; Huang, J.; Chen, Y.; Gasser, G.; Ji, L.; Chao, H., Highly Charged Ruthenium(II) Polypyridyl Complexes as Lysosome-Localized Photosensitizers for Two-Photon Photodynamic Therapy. *Angew. Chem. Int. Edit.* **2015,** *54* (47), 14049-14052.
339. Mani, A.; Feng, T.; Gandioso, A.; Vinck, R.; Notaro, A.; Gourdon, L.; Burckel, P.; Saubaméa, B.; Blacque, O.; Cariou, K.; Belgaied, J.-E.; Chao, H.; Gasser, G., Structurally Simple Osmium(II) Polypyridyl Complexes as Photosensitizers for Photodynamic Therapy in the Near Infrared**. *Angew. Chem. Int. Edit.* **2023,** *62* (20), e202218347.

340. Pozza, M. D.; Mesdom, P.; Abdullrahman, A.; Prieto Otoya, T. D.; Arnoux, P.; Frochot, C.; Niogret, G.; Saubaméa, B.; Burckel, P.; Hall, J. P.; Hollenstein, M.; Cardin, C. J.; Gasser, G., Increasing the π-Expansive Ligands in Ruthenium(II) Polypyridyl Complexes: Synthesis, Characterization, and Biological Evaluation for Photodynamic Therapy Applications. *Inorg. Chem.* **2023,** *62* (45), 18510-18523.
341. Andreiadis, E. S.; Chavarot-Kerlidou, M.; Fontecave, M.; Artero, V., Artificial Photosynthesis: From Molecular Catalysts for Light-driven Water Splitting to Photoelectrochemical Cells. *Photochem. Photobio. Sci.* **2011,** *87* (5), 946-964.
342. Brennaman, M. K.; Dillon, R. J.; Alibabaei, L.; Gish, M. K.; Dares, C. J.; Ashford, D. L.; House, R. L.; Meyer, G. J.; Papanikolas, J. M.; Meyer, T. J., Finding the Way to Solar Fuels with Dye-Sensitized Photoelectrosynthesis Cells. *J. Am. Chem. Soc.* **2016,** *138* (40), 13085-13102.
343. Alibabaei, L.; Brennaman, M. K.; Norris, M. R.; Kalanyan, B.; Song, W.; Losego, M. D.; Concepcion, J. J.; Binstead, R. A.; Parsons, G. N.; Meyer, T. J., Solar water splitting in a molecular photoelectrochemical cell. *Proceedings of the National Academy of Sciences* **2013,** *110* (50), 20008-20013.
344. Hu, K.; Sampaio, R. N.; Schneider, J.; Troian-Gautier, L.; Meyer, G. J., Perspectives on Dye Sensitization of Nanocrystalline Mesoporous Thin Films. *J. Am. Chem. Soc.* **2020,** *142* (38), 16099-16116.
345. Troian-Gautier, L.; Moucheron, C., Ruthenium(II) Complexes bearing Fused Polycyclic Ligands: From Fundamental Aspects to Potential Applications. *Molecules* **2014,** *19* (4), 5028-5087.
346. Troian-Gautier, L.; Marcelis, L.; De Winter, J.; Gerbaux, P.; Moucheron, C., Two ruthenium complexes capable of storing multiple electrons on a single ligand - photophysical, photochemical and electrochemical properties of [Ru(phen)2(TAPHAT)]2+ and [Ru(phen)2(TAPHAT)Ru(phen)2]4+. *Dalton Trans.* **2017,** *46* (44), 15287-15300.
347. Bolger, J.; Gourdon, A.; Ishow, E.; Launay, J.-P., Mononuclear and Binuclear Tetrapyrido[3,2-a:2‘,3‘-c:3‘‘,2‘‘-h:2‘‘‘,3‘‘‘-j]phenazine (tpphz) Ruthenium and Osmium Complexes. *Inorg. Chem.* **1996,** *35* (10), 2937-2944.
348. Servaty, K.; Moucheron, C.; Kirsch-De Mesmaeker, A., Trinuclear ruthenium dendrons based on bridging PHEHAT and TPAC ligands. *Dalton Trans.* **2011,** *40* (44), 11704-11711.
349. Boisdenghien, A.; Moucheron, C.; Kirsch-De Mesmaeker, A., [Ru(phen)2(PHEHAT)]2+ and [Ru(phen)2(HATPHE)]2+: Two Ruthenium(II) Complexes with the Same Ligands but Different Photophysics and Spectroelectrochemistry. *Inorg. Chem.* **2005,** *44* (21), 7678-7685.
350. Leveque, J.; Elias, B.; Moucheron, C.; Kirsch-De Mesmaeker, A., Dendritic Tetranuclear Ru(II) Complexes Based on the Nonsymmetrical PHEHAT Bridging Ligand and Their Building Blocks: Synthesis, Characterization, and Electrochemical and Photophysical Properties. *Inorg. Chem.* **2005,** *44* (2), 393-400.
351. Elias, B.; Herman, L.; Moucheron, C.; Kirsch-De Mesmaeker, A., Dinuclear RuIIPHEHAT and -TPAC Complexes: Effects of the Second RuII Center on Their Spectroelectrochemical Properties. *Inorg. Chem.* **2007,** *46* (12), 4979-4988.
352. Tisaun, J.; Laramée-Milette, B.; Beckwith, J. S.; Bierwagen, J.; Hanan, G. S.; Reber, C.; Hauser, A.; Moucheron, C., Two RuII Linkage Isomers with Distinctly Different Charge Transfer Photophysics. *Inorg. Chem.* **2021,** *60* (6), 3677-3689.
353. Klingler, S.; Bagemihl, B.; Mengele, A. K.; Kaufhold, S.; Myllyperkiö, P.; Ahokas, J.; Pettersson, M.; Rau, S.; Mizaikoff, B., Rationalizing In Situ Active Repair in Hydrogen Evolution Photocatalysis via Non-Invasive Raman Spectroscopy. *Angew. Chem. Int. Edit.* **2023,** *62* (44), e202306287.
354. Ryland, E. S.; Liu, X.; Kumar, G.; Raj, S. L.; Xie, Z.-L.; Mengele, A. K.; Fauth, S. S.; Siewerth, K.; Dietzek-Ivanšić, B.; Rau, S.; Mulfort, K. L.; Li, X.; Cordones, A. A., Site-specific electronic structure of covalently linked bimetallic dyads from nitrogen K-edge x-ray absorption spectroscopy. *J. Chem. Phys.* **2024,** *160* (8).
355. De Kreijger, S.; Schott, O.; Troian-Gautier, L.; Cauët, E.; Hanan, G. S.; Elias, B., Red Absorbing Cyclometalated Ir(III) Diimine Photosensitizers Competent for Hydrogen Photocatalysis. *Inorg. Chem.* **2022,** *61* (13), 5245-5254.
356. Holden, L.; Gkika, K. S.; Burke, C. S.; Long, C.; Keyes, T. E., Selective, Disruptive Luminescent Ru(II) Polypyridyl Probes of G-Quadruplex. *Inorg. Chem.* **2023,** *62* (5), 2213-2227.
357. Moucheron, C.; Kirsch-De Mesmaeker, A.; Choua, S., Photophysics of Ru(phen)2(PHEHAT)2+: A Novel “Light Switch” for DNA and Photo-oxidant for Mononucleotides. *Inorg. Chem.* **1997,** *36* (4), 584-592.
358. Moucheron, C.; Kirsch-De Mesmaeker, A., New DNA-binding ruthenium(II) complexes as photo-reagents for mononucleotides and DNA. *Journal of Physical Organic Chemistry* **1998,** *11* (8-9), 577-583.
359. Vanderlinden, W.; Blunt, M.; David, C. C.; Moucheron, C.; Kirsch-De Mesmaeker, A.; De Feyter, S., Mesoscale DNA Structural Changes on Binding and Photoreaction with Ru[(TAP)2PHEHAT]2+. *J. Am. Chem. Soc.* **2012,** *134* (24), 10214-10221.

360. Poynton, F. E.; Bright, S. A.; Blasco, S.; Williams, D. C.; Kelly, J. M.; Gunnlaugsson, T., The development of ruthenium(ii) polypyridyl complexes and conjugates for in vitro cellular and in vivo applications. *Chem. Soc. Rev.* **2017,** *46* (24), 7706-7756.
361. Denti, G.; Campagna, S.; Sabatino, L.; Serroni, S.; Ciano, M.; Balzani, V., Luminescent and redox-reactive building blocks for the design of photochemical molecular devices: mono-, di-, tri-, and tetranuclear ruthenium(II) polypyridine complexes. *Inorg. Chem.* **1990,** *29* (23), 4750-4758.
362. Serroni, S.; Juris, A.; Campagna, S.; Venturi, M.; Denti, G.; Balzani, V., Tetranuclear Bimetallic Complexes of Ruthenium, Osmium, Rhodium, and Iridium. Synthesis, Absorption Spectra, Luminescence, and Electrochemical Properties. *J. Am. Chem. Soc.* **1994,** *116* (20), 9086-9091.
363. Campagna, S.; Denti, G.; Serroni, S.; Ciano, M.; Juris, A.; Balzani, V., A tridecanuclear ruthenium(II)-polypyridine supramolecular species: synthesis, absorption and luminescence properties and electrochemical oxidation. *Inorg. Chem.* **1992,** *31* (13), 2982-2984.
364. Balzani, V.; Juris, A.; Venturi, M.; Campagna, S.; Serroni, S., Luminescent and Redox-Active Polynuclear Transition Metal Complexes. *Chem. Rev.* **1996,** *96* (2), 759-834.
365. Chiorboli, C.; Rodgers, M. A. J.; Scandola, F., Ultrafast Processes in Bimetallic Dyads with Extended Aromatic Bridges. Energy and Electron Transfer Pathways in Tetrapyridophenazine-Bridged Complexes. *J. Am. Chem. Soc.* **2003,** *125* (2), 483-491.
366. Chiorboli, C.; Bignozzi, C. A.; Scandola, F.; Ishow, E.; Gourdon, A.; Launay, J.-P., Photophysics of Dinuclear Ru(II) and Os(II) Complexes Based on the Tetrapyrido[3,2-a:2‘,3‘-c:3‘ ‘,2‘ ‘-h:2‘ ‘‘-3‘ ‘‘-j]phenazine (tpphz) Bridging Ligand. *Inorg. Chem.* **1999,** *38* (10), 2402-2410.
367. Chiorboli, C.; Fracasso, S.; Ravaglia, M.; Scandola, F.; Campagna, S.; Wouters, K. L.; Konduri, R.; MacDonnell, F. M., Primary Photoinduced Processes in Bimetallic Dyads with Extended Aromatic Bridges. Tetraazatetrapyridopentacene Complexes of Ruthenium(II) and Osmium(II). *Inorg. Chem.* **2005,** *44* (23), 8368-8378.
368. Campagna, S.; Serroni, S.; Bodige, S.; MacDonnell, F. M., Absorption Spectra, Photophysical Properties, and Redox Behavior of Stereochemically Pure Dendritic Ruthenium(II) Tetramers and Related Dinuclear and Mononuclear Complexes. *Inorg. Chem.* **1999,** *38* (4), 692-701.
369. Queyriaux, N.; Wahyuono, R. A.; Fize, J.; Gablin, C.; Wächtler, M.; Martinez, E.; Léonard, D.; Dietzek, B.; Artero, V.; Chavarot-Kerlidou, M., Aqueous Photocurrent Measurements Correlated to Ultrafast Electron Transfer Dynamics at Ruthenium Tris Diimine Sensitized NiO Photocathodes. *The Journal of Physical Chemistry C* **2017,** *121* (11), 5891-5904.
370. Windle, C. D.; Kumagai, H.; Higashi, M.; Brisse, R.; Bold, S.; Jousselme, B.; Chavarot-Kerlidou, M.; Maeda, K.; Abe, R.; Ishitani, O.; Artero, V., Earth-Abundant Molecular Z-Scheme Photoelectrochemical Cell for Overall Water-Splitting. *J. Am. Chem. Soc.* **2019,** *141* (24), 9593-9602.
371. Shan, B.; Nayak, A.; N. Sampaio, R.; Eberhart, M. S.; Troian-Gautier, L.; Brennaman, M. K.; Meyer, G. J.; Meyer, T. J., Direct Photoactivation of a Nickel-Based, Water-Reduction Photocathode by a Highly Conjugated Supramolecular Chromophore. *Energy & Environmental Science* **2018,** *11* (2), 447-455.
372. Li, T.-T.; Shan, B.; Meyer, T. J., Stable Molecular Photocathode for Solar-Driven CO2 Reduction in Aqueous Solutions. *ACS Energy Letters* **2019**, 629-636.
373. Bourguignon, C.; Moinel, A.; Huet, A.; Kervella, Y.; Windle, C. D.; Massin, J.; Artero, V.; Chavarot-Kerlidou, M.; Demadrille, R., Photoelectrochemical Hydrogen Production by a Cobalt Tetrapyridyl Catalyst Using Push–Pull Dye-Sensitized NiO Photocathodes. *Advanced Energy and Sustainability Research* **2023,** *4* (12), 2300095.
374. Nguyen, D. N.; Giannoudis, E.; Straistari, T.; Fize, J.; Koepf, M.; Tran, P. D.; Chavarot-Kerlidou, M.; Artero, V., Unassisted Solar Syngas Production by a Molecular Dye-Cobalt Catalyst Assembly in a Tandem Photoelectrochemical Cell. *ACS Energy Letters* **2024,** *9* (3), 829-834.
375. Case, F. H.; Brennan, J. A., Substituted 1,10-Phenanthrolines. XI. Aza Derivatives1. *J. Am. Chem. Soc.* **1959,** *81* (23), 6297-6301.
376. Nasielski-Hinkens, R.; Benedek-Vamos, M.; Maetens, D., Synthesis of 9-substituted-1,4,5,8-tetraazaphenanthrenes. *Journal of Heterocyclic Chemistry* **1980,** *17* (5), 873-876.
377. Nasielski-Hinkens, R.; Benedek-Vamos, M.; Maetens, D.; Nasielski, J., A new heterocyclic ligand for transition metals: 1,4,5,8,9,12-hexaazatriphenylene and its chromium carbonyl complexes. *Journal of Organometallic Chemistry* **1981,** *217* (2), 179-182.
378. Kohne, B.; Praefcke, K., Eine neue und einfache Synthese des Dipyrazino[2,3-f:2′,3′-h]-chinoxalin-Ringsystems. *Liebigs Annalen der Chemie* **1985,** *1985* (3), 522-528.
379. Rogers, D. Z., Improved synthesis of 1,4,5,8,9,12-hexaazatriphenylene. *J. Org. Chem.* **1986,** *51* (20), 3904-3905.
380. Praefcke, K.; Kohne, B.; Korinth, F.; Psaras, P.; Nasielski, J.; Verhoeven, C.; Nasielski-Hinkens, R., Benzenepentamine – Its Easy Accessibility and Use in Syntheses of Pyrazinoquinoxalines. *Liebigs Annalen der Chemie* **1989,** *1989* (7), 617-621.

381. Masui, H.; Lever, A. B. P.; Dodsworth, E. S., Substituent effects and bonding characteristics in (o-benzoquinone diimine)bis(bipyridine)ruthenium(II) complexes. *Inorg. Chem.* **1993,** *32* (3), 258-267.
382. Metcalfe, R. A.; Dodsworth, E. S.; Lever, A. B. P.; Pietro, W. J.; Stufkens, D. J., Effect of donors and acceptors on the twist angle of a ruthenium complex of bis(bipyridine)ruthenium(II) 3,4-diamino-3',4'-diimino-3',4'-dihydrobiphenyl. A bifunctional biphenyl derivative and a potential molecular switch. *Inorg. Chem.* **1993,** *32* (17), 3581-3582.
383. Ebadi, M.; Lever, A. B. P., Ruthenium Complexes of Quinone Related Ligands: A Study of the Electrochemical Properties of 2-Aminothiophenolatobis(2,2'-Bipyridine)Ruthenium(II). *Inorg. Chem.* **1999,** *38* (3), 467-474.
384. Auburn, P. R.; Lever, A. B. P., Synthesis and spectroscopic characterization of bis[bis(bipyridine)ruthenium(II)]-3,3',4,4'-tetraimino-3,3',4,4'-tetrahydrobiphenyl and its redox products. *Inorg. Chem.* **1990,** *29* (14), 2551-2553.
385. Metcalfe, R. A.; Dodsworth, E. S.; Fielder, S. S.; Stufkens, D. J.; Lever, A. B. P.; Pietro, W. J., Influence of Remote Ligand Lone Pairs on the Electronic Structure and Spectrum of Bis(bipyridine)ruthenium(II) 3,4-Diamino-3',4'-diimino-3',4'-dihydrobiphenyl. Tuning by External Donors and Acceptors. *Inorg. Chem.* **1996,** *35* (26), 7741-7750.
386. Ishow, E.; Gourdon, A.; Launay, J.-P.; Chiorboli, C.; Scandola, F., Synthesis, Mass Spectrometry, and Spectroscopic Properties of a Dinuclear Ruthenium Complex Comprising a 20 Å Long Fully Aromatic Bridging Ligand. *Inorg. Chem.* **1999,** *38* (7), 1504-1510.
387. C. Fletcher, N.; C. Robinson, T.; Behrendt, A.; C. Jeffery, J.; R. Reeves, Z.; D. Ward, M., Structural, electrochemical and UV/VIS/NIR spectroelectrochemical properties of diastereomerically pure dinuclear ruthenium complexes based on the bridging ligand phenanthroline-5,6-diimine, and a mononuclear by-product with a peripheral isoimidazole group. *Journal of the Chemical Society, Dalton Transactions* **1999,** (17), 2999-3006.
388. Ghumaan, S.; Sarkar, B.; Patra, S.; van Slageren, J.; Fiedler, J.; Kaim, W.; Lahiri, G. K., Sensitive Oxidation State Ambivalence in Unsymmetrical Three-Center (M/Q/M) Systems [(acac)2Ru(μ-Q)Ru(acac)2]n, Q = 1,10-Phenanthroline-5,6-dione or 1,10-Phenanthroline-5,6-diimine (n = +, 0, −, 2−). *Inorg. Chem.* **2005,** *44* (9), 3210-3214.
389. Sorsche, D.; Pehlken, C.; Baur, C.; Rommel, S.; Kastner, K.; Streb, C.; Rau, S., Novel phenanthroline–diaryldiazadiene ligands with heteroditopic coordination spheres. *Dalton Trans.* **2015,** *44* (35), 15404-15407.
390. Belser, P.; Von Zelewsky, A.; Zehnder, M., Synthesis and properties of ruthenium(II) complexes with o-quinodiimine ligands. Crystal and molecular structure of Ru(bpy)2(C6H4(NH)2)(PF6)2. *Inorg. Chem.* **1981,** *20* (9), 3098-3103.
391. Masschelein, A.; Jacquet, L.; Kirsch-De Mesmaeker, A.; Nasielski, J., Ruthenium complexes with 1,4,5,8-tetraazaphenanthrene. Unusual photophysical behavior of the tris-homoleptic compound. *Inorg. Chem.* **1990,** *29* (4), 855-860.
392. Pyle, A. M.; Barton, J. K., Synthesis and spectroscopic characterization of the purple tris(phenanthrenequinone diimine)ruthenium(II) ion. *Inorg. Chem.* **1987,** *26* (22), 3820-3823.
393. Balzani, V.; Bolletta, F.; Gandolfi, M. T.; Maestri, M., Bimolecular electron transfer reactions of the excited states of transition metal complexes. *Organic Chemistry and Theory* **2006**, 1-64.
394. Englman, R.; Jortner, J., The energy gap law for radiationless transitions in large molecules. *Molecular Physics* **1970,** *18* (2), 145-164.
395. Nasielski-Hinkens, R.; Benedek-Vamos, M., Synthesis of di- and tetra-substituted 1,4,5,8-tetra-azaphenanthrenes (pyrazino[2,3-f]quinoxalines). *Journal of the Chemical Society, Perkin Transactions 1* **1975,** (13), 1229-1229.
396. Oderinde, M. S.; Johannes, J. W., Practical Syntheses of [2,2′-Bipyridine]bis[3,5-Difluoro-2-[5-(Trifluoromethyl)-2-Pyridinyl]phenyl]iridium(III) Hexafluorophosphate, [Ir{dF(CF3)ppy}2(bpy)]PF6 and [4,4′-bis(tert-butyl)-2,2′-bipyridine]bis[3,5-Difluoro-2-[5-(Trifluoromethyl)-2-Pyridinyl]ph. *Organic Syntheses* **2017,** *94*, 77-92.
397. Wachter, E.; Glazer, E. C., Mechanistic Study on the Photochemical "Light Switch" Behavior of [Ru(bpy)2dmdppz]2+. *J. Phys. Chem. A* **2014,** *118* (45), 10474-10486.
398. Shao, F.; Elias, B.; Lu, W.; Barton, J. K., Synthesis and Characterization of Iridium(III) Cyclometalated Complexes with Oligonucleotides: Insights into Redox Reactions with DNA. *Inorg. Chem.* **2007,** *46* (24), 10187-10199.
399. Troian-Gautier, L.; Marcélis, L.; De Winter, J.; Gerbaux, P.; Moucheron, C., Two ruthenium complexes capable of storing multiple electrons on a single ligand – photophysical, photochemical and electrochemical properties of [Ru(phen)2(TAPHAT)]2+ and [Ru(phen)2(TAPHAT)Ru(phen)2]4+. *Dalton Trans.* **2017,** *46* (44), 15287-15300.

400. Curtis, J. C.; Sullivan, B. P.; Meyer, T. J., Hydrogen-bonding-induced solvatochromism in the charge-transfer transitions of ruthenium(II) and ruthenium(III) ammine complexes. *Inorg. Chem.* **1983,** *22* (2), 224-236.
401. Strekas, T. C.; Diamandopoulos, P. S., Surface-enhanced raman spectroscopy of bipyridines and phenylpyridines. *J. Phys. Chem.* **1990,** *94* (5), 1986-1991.
402. Zanoni, K. P. S.; Kariyazaki, B. K.; Ito, A.; Brennaman, M. K.; Meyer, T. J.; Murakami Iha, N. Y., Blue-Green Iridium(III) Emitter and Comprehensive Photophysical Elucidation of Heteroleptic Cyclometalated Iridium(III) Complexes. *Inorg. Chem.* **2014,** *53* (8), 4089-4099.
403. Yarnell, J. E.; McCusker, C. E.; Leeds, A. J.; Breaux, J. M.; Castellano, F. N., Exposing the Excited-State Equilibrium in an IrIII Bichromophore: A Combined Time Resolved Spectroscopy and Computational Study. *Eur. J. Inorg. Chem.* **2016,** *2016* (12), 1808-1818.
404. McCusker, C. E.; Chakraborty, A.; Castellano, F. N., Excited State Equilibrium Induced Lifetime Extension in a Dinuclear Platinum(II) Complex. *J. Phys. Chem. A* **2014,** *118* (45), 10391-10399.
405. Kirsch-De Mesmaeker, A.; Nasielski-Hinkens, R.; Maetens, D.; Pauwels, D.; Nasielski, J., Synthesis and spectroscopic and electrochemical properties of a new ruthenium complex: the tris(1,4,5,8-tetraazaphenanthrene)ruthenium(II) dication. *Inorg. Chem.* **1984,** *23* (3), 377-379.
406. Ripak, A.; De Kreijger, S.; Elias, B.; Troian-Gautier, L., A protocol for determining cage-escape yields using nanosecond transient absorption spectroscopy. *STAR Protocols* **2023,** *4* (2), 102312.
407. Mallouk, T. E.; Krueger, J. S.; Mayer, J. E.; Dymond, C. M. G., Reductive quenching of ruthenium polypyridyl sensitizers by cyanometalate complexes. *Inorg. Chem.* **1989,** *28* (18), 3507-3510.
408. De Kreijger, S.; Ripak, A.; Elias, B.; Troian-Gautier, L., Investigation of the Excited-State Electron Transfer and Cage Escape Yields Between Halides and a Fe(III) Photosensitizer. *J. Am. Chem. Soc.* **2024**.
409. Sun, H.; Hoffman, M. Z., Photo-induced charge separation by ruthenium (II) photosensitizers. *Journal of Chemical Sciences* **1993,** *105* (6), 487-494.
410. Wolff, H.-J.; Burssher, D.; Steiner, U. E., Spin-orbit coupling controlled spin chemistry of Ru(bpy)32+ photooxidation: Detection of strong viscosity dependence of in-cage backward electron transfer rate. *Pure Appl. Chem.* **1995,** *67* (1), 167-174.
411. Steiner, U. E.; Wolff, H. J.; Ulrich, T.; Ohno, T., Spin-orbit coupling and magnetic field effects in photoredox reactions of ruthenium(II) complexes. *J. Phys. Chem.* **1989,** *93* (13), 5147-5154.
412. Senz, A.; Gsponer, H. E., Yield of ions produced in the luminescence quenching of tris (2,2′-bipyridine)ruthenium(II) by dichlorophenolate ions. *Journal of Physical Organic Chemistry* **1995,** *8* (11), 706-712.
413. Jayanthi, S. S.; Ramamurthy, P., Excited Singlet State Reactions of Thiopyrylium with Electron Donors: Electron Transfer, Induction of Triplet by Internal and External Heavy Atom Effect, and Comparison of Pyrylium and Thiopyrylium Reactions. *J. Phys. Chem. A* **1998,** *102* (3), 511-518.
414. Ondersma, J. W.; Hamann, T. W., Measurements and Modeling of Recombination from Nanoparticle TiO2 Electrodes. *J. Am. Chem. Soc.* **2011,** *133* (21), 8264-8271.
415. DeVries, M. J.; Pellin, M. J.; Hupp, J. T., Dye-Sensitized Solar Cells: Driving-Force Effects on Electron Recombination Dynamics with Cobalt-Based Shuttles. *Langmuir* **2010,** *26* (11), 9082-9087.
416. Monos, T. M.; Sun, A. C.; McAtee, R. C.; Devery, J. J., III; Stephenson, C. R. J., Microwave-Assisted Synthesis of Heteroleptic Ir(III)+ Polypyridyl Complexes. *J. Org. Chem.* **2016,** *81* (16), 6988-6994.
417. De Kreijger, S.; Cauët, E.; Elias, B.; Troian-Gautier, L., Synthesis of Ru(ii) and Os(ii) photosensitizers bearing one 9,10-diamino-1,4,5,8-tetraazaphenanthrene scaffold. *Dalton Trans.* **2024,** *53* (24), 10270-10284.
418. Amouyal, E.; Homsi, A.; Chambron, J.-C.; Sauvage, J.-P., Synthesis and study of a mixed-ligand ruthenium(II) complex in its ground and excited states: bis(2,2′-bipyridine)(dipyrido[3,2-a : 2′,3′-c]phenazine-N4N5)ruthenium(II). *Journal of the Chemical Society, Dalton Transactions* **1990,** (6), 1841-1845.
419. Wenger, O. S., Is Iron the New Ruthenium? *Chem. Eur. J.* **2019,** *25* (24), 6043-6052.
420. Fink, D. W.; Ohnesorge, W. E., Temperature effects on charge-transfer luminescence intensity of some transition metal ion chelates. *J. Am. Chem. Soc.* **1969,** *91* (18), 4995-4998.
421. Paris, J. P.; Brandt, W. W., CHARGE TRANSFER LUMINESCENCE OF A RUTHENIUM(II) CHELATE. *J. Am. Chem. Soc.* **1959,** *81* (18), 5001-5002.
422. Hauser, A., Excited-state lifetimes of [Fe (bipy)3]2+ and [Fe(phen)3]2+. *Chem. Phys. Lett.* **1990,** *173* (5), 507-512.
423. Brady, C.; McGarvey, J. J.; McCusker, J. K.; Toftlund, H.; Hendrickson, D. N., Time-Resolved Relaxation Studies of Spin Crossover Systems in Solution. In *Spin Crossover in Transition Metal Compounds III*, Gütlich, P.; Goodwin, H. A., Eds. Springer Berlin Heidelberg: Berlin, Heidelberg, 2004; pp 1-22.

424. McCusker, J. K.; Walda, K. N.; Dunn, R. C.; Simon, J. D.; Magde, D.; Hendrickson, D. N., Sub-picosecond .DELTA.S = 2 intersystem crossing in low-spin ferrous complexes. *J. Am. Chem. Soc.* **1992,** *114* (17), 6919-6920.
425. Smeigh, A. L.; Creelman, M.; Mathies, R. A.; McCusker, J. K., Femtosecond Time-Resolved Optical and Raman Spectroscopy of Photoinduced Spin Crossover: Temporal Resolution of Low-to-High Spin Optical Switching. *J. Am. Chem. Soc.* **2008,** *130* (43), 14105-14107.
426. Chang, H. R.; McCusker, J. K.; Toftlund, H.; Wilson, S. R.; Trautwein, A. X.; Winkler, H.; Hendrickson, D. N., [Tetrakis(2-pyridylmethyl)ethylenediamine]iron(II) perchlorate, the first rapidly interconverting ferrous spin-crossover complex. *J. Am. Chem. Soc.* **1990,** *112* (19), 6814-6827.
427. Creutz, C.; Chou, M.; Netzel, T. L.; Okumura, M.; Sutin, N., Lifetimes, spectra, and quenching of the excited states of polypyridine complexes of iron(II), ruthenium(II), and osmium(II). *J. Am. Chem. Soc.* **1980,** *102* (4), 1309-1319.
428. Juban, E. A.; Smeigh, A. L.; Monat, J. E.; McCusker, J. K., Ultrafast dynamics of ligand-field excited states. *Coordin. Chem. Rev.* **2006,** *250* (13), 1783-1791.
429. Cannizzo, A.; Milne, C. J.; Consani, C.; Gawelda, W.; Bressler, C.; van Mourik, F.; Chergui, M., Light-induced spin crossover in Fe(II)-based complexes: The full photocycle unraveled by ultrafast optical and X-ray spectroscopies. *Coordin. Chem. Rev.* **2010,** *254* (21), 2677-2686.
430. McCusker, J. K., Electronic structure in the transition metal block and its implications for light harvesting. *Science* **2019,** *363* (6426), 484-488.
431. Förster, C.; Heinze, K., Photophysics and photochemistry with Earth-abundant metals – fundamentals and concepts. *Chem. Soc. Rev.* **2020,** *49* (4), 1057-1070.
432. Wenger, O. S., Photoactive Complexes with Earth-Abundant Metals. *J. Am. Chem. Soc.* **2018,** *140* (42), 13522-13533.
433. Sinha, N.; Wenger, O. S., Photoactive Metal-to-Ligand Charge Transfer Excited States in 3d6 Complexes with Cr0, MnI, FeII, and CoIII. *J. Am. Chem. Soc.* **2023,** *145* (9), 4903-4920.
434. Liu, Y.; Persson, P.; Sundström, V.; Wärnmark, K., Fe N-Heterocyclic Carbene Complexes as Promising Photosensitizers. *Acc. Chem. Res.* **2016,** *49* (8), 1477-1485.
435. Chábera, P.; Lindh, L.; Rosemann, N. W.; Prakash, O.; Uhlig, J.; Yartsev, A.; Wärnmark, K.; Sundström, V.; Persson, P., Photofunctionality of iron(III) N-heterocyclic carbenes and related d5 transition metal complexes. *Coordin. Chem. Rev.* **2021,** *426*, 213517.
436. de Groot, L. H. M.; Ilic, A.; Schwarz, J.; Wärnmark, K., Iron Photoredox Catalysis–Past, Present, and Future. *J. Am. Chem. Soc.* **2023,** *145* (17), 9369-9388.
437. Dixon, I. M.; Alary, F.; Boggio-Pasqua, M.; Heully, J.-L., Reversing the relative 3MLCT–3MC order in Fe(ii) complexes using cyclometallating ligands: a computational study aiming at luminescent Fe(ii) complexes. *Dalton Trans.* **2015,** *44* (30), 13498-13503.
438. Liu, Y.; Harlang, T.; Canton, S. E.; Chábera, P.; Suárez-Alcántara, K.; Fleckhaus, A.; Vithanage, D. A.; Göransson, E.; Corani, A.; Lomoth, R.; Sundström, V.; Wärnmark, K., Towards longer-lived metal-to-ligand charge transfer states of iron(ii) complexes: an N-heterocyclic carbene approach. *Chem. Commun.* **2013,** *49* (57), 6412-6414.
439. Chábera, P.; Kjaer, K. S.; Prakash, O.; Honarfar, A.; Liu, Y.; Fredin, L. A.; Harlang, T. C. B.; Lidin, S.; Uhlig, J.; Sundström, V.; Lomoth, R.; Persson, P.; Wärnmark, K., FeII Hexa N-Heterocyclic Carbene Complex with a 528 ps Metal-to-Ligand Charge-Transfer Excited-State Lifetime. *J. Phys. Chem. Lett.* **2018,** *9* (3), 459-463.
440. Leis, W.; Argüello Cordero, M. A.; Lochbrunner, S.; Schubert, H.; Berkefeld, A., A Photoreactive Iron(II) Complex Luminophore. *J. Am. Chem. Soc.* **2022,** *144* (3), 1169-1173.
441. Malme, J. T.; Clendening, R. A.; Ash, R.; Curry, T.; Ren, T.; Vura-Weis, J., Nanosecond Metal-to-Ligand Charge-Transfer State in an Fe(II) Chromophore: Lifetime Enhancement via Nested Potentials. *J. Am. Chem. Soc.* **2023,** *145* (11), 6029-6034.
442. Glaser, F.; Aydogan, A.; Elias, B.; Troian-Gautier, L., The great strides of iron photosensitizers for contemporary organic photoredox catalysis: On our way to the holy grail? *Coordin. Chem. Rev.* **2024,** *500*, 215522.
443. Rosemann, N. W.; Lindh, L.; Bolaño Losada, I.; Kaufhold, S.; Prakash, O.; Ilic, A.; Schwarz, J.; Wärnmark, K.; Chábera, P.; Yartsev, A.; Persson, P., Competing dynamics of intramolecular deactivation and bimolecular charge transfer processes in luminescent Fe(iii) N-heterocyclic carbene complexes. *Chem. Sci.* **2023,** *14* (13), 3569-3579.
444. Thorarinsdottir, A. E.; Veroneau, S. S.; Nocera, D. G., Self-healing oxygen evolution catalysts. *Nat. Commun.* **2022,** *13* (1), 1243.
445. Feng, C.; Wang, F.; Liu, Z.; Nakabayashi, M.; Xiao, Y.; Zeng, Q.; Fu, J.; Wu, Q.; Cui, C.; Han, Y.; Shibata, N.; Domen, K.; Sharp, I. D.; Li, Y., A self-healing catalyst for electrocatalytic and photoelectrochemical oxygen evolution in highly alkaline conditions. *Nat. Commun.* **2021,** *12* (1), 5980.

446. Maeda, K.; Teramura, K.; Lu, D.; Takata, T.; Saito, N.; Inoue, Y.; Domen, K., Photocatalyst releasing hydrogen from water. *Nature* **2006,** *440* (7082), 295-295.
447. Wang, Q.; Domen, K., Particulate Photocatalysts for Light-Driven Water Splitting: Mechanisms, Challenges, and Design Strategies. *Chem. Rev.* **2020,** *120* (2), 919-985.
448. Pornrungroj, C.; Mohamad Annuar, A. B.; Wang, Q.; Rahaman, M.; Bhattacharjee, S.; Andrei, V.; Reisner, E., Hybrid photothermal–photocatalyst sheets for solar-driven overall water splitting coupled to water purification. *Nature Water* **2023,** *1* (11), 952-960.
449. Andrei, V.; Wang, Q.; Uekert, T.; Bhattacharjee, S.; Reisner, E., Solar Panel Technologies for Light-to-Chemical Conversion. *Acc. Chem. Res.* **2022,** *55* (23), 3376-3386.
450. Andrei, V.; Ucoski, G. M.; Pornrungroj, C.; Uswachoke, C.; Wang, Q.; Achilleos, D. S.; Kasap, H.; Sokol, K. P.; Jagt, R. A.; Lu, H.; Lawson, T.; Wagner, A.; Pike, S. D.; Wright, D. S.; Hoye, R. L. Z.; MacManus-Driscoll, J. L.; Joyce, H. J.; Friend, R. H.; Reisner, E., Floating perovskite-BiVO4 devices for scalable solar fuel production. *Nature* **2022,** *608* (7923), 518-522.
451. Shan, B.; Brennaman, M. K.; Troian-Gautier, L.; Liu, Y.; Nayak, A.; Klug, C. M.; Li, T.-T.; Bullock, R. M.; Meyer, T. J., A Silicon-Based Heterojunction Integrated with a Molecular Excited State in a Water-Splitting Tandem Cell. *J. Am. Chem. Soc.* **2019,** *141* (26), 10390-10398.
452. Spitler, M. T.; Modestino, M. A.; Deutsch, T. G.; Xiang, C. X.; Durrant, J. R.; Esposito, D. V.; Haussener, S.; Maldonado, S.; Sharp, I. D.; Parkinson, B. A.; Ginley, D. S.; Houle, F. A.; Hannappel, T.; Neale, N. R.; Nocera, D. G.; McIntyre, P. C., Practical challenges in the development of photoelectrochemical solar fuels production. *Sustainable Energy & Fuels* **2020,** *4* (3), 985-995.
453. Dogutan, D. K.; Nocera, D. G., Artificial Photosynthesis at Efficiencies Greatly Exceeding That of Natural Photosynthesis. *Acc. Chem. Res.* **2019,** *52* (11), 3143-3148.
454. Bold, S.; Massin, J.; Giannoudis, E.; Koepf, M.; Artero, V.; Dietzek, B.; Chavarot-Kerlidou, M., Spectroscopic Investigations Provide a Rationale for the Hydrogen-Evolving Activity of Dye-Sensitized Photocathodes Based on a Cobalt Tetraazamacrocyclic Catalyst. *ACS Catal.* **2021,** *11* (6), 3662-3678.
455. Shang, B.; Rooney, C. L.; Gallagher, D. J.; Wang, B. T.; Krayev, A.; Shema, H.; Leitner, O.; Harmon, N. J.; Xiao, L.; Sheehan, C.; Bottum, S. R.; Gross, E.; Cahoon, J. F.; Mallouk, T. E.; Wang, H., Aqueous Photoelectrochemical CO2 Reduction to CO and Methanol over a Silicon Photocathode Functionalized with a Cobalt Phthalocyanine Molecular Catalyst. *Angew. Chem. Int. Ed.* **2023,** *62* (4), e202215213.
456. Müller, A. V.; Ahmad, S.; Sirlin, J. T.; Ertem, M. Z.; Polyansky, D. E.; Grills, D. C.; Meyer, G. J.; Sampaio, R. N.; Concepcion, J. J., Reduction of CO to Methanol with Recyclable Organic Hydrides. *J. Am. Chem. Soc.* **2024**.
457. Schwarz, J.; Ilic, A.; Johnson, C.; Lomoth, R.; Wärnmark, K., High turnover photocatalytic hydrogen formation with an Fe(iii) N-heterocyclic carbene photosensitiser. *Chem. Commun.* **2022,** *58* (35), 5351-5354.
458. Rosemann, N. W.; Chábera, P.; Prakash, O.; Kaufhold, S.; Wärnmark, K.; Yartsev, A.; Persson, P., Tracing the Full Bimolecular Photocycle of Iron(III)–Carbene Light Harvesters in Electron-Donating Solvents. *J. Am. Chem. Soc.* **2020,** *142* (19), 8565-8569.
459. Kaul, N.; Lomoth, R., The Carbene Cannibal: Photoinduced Symmetry-Breaking Charge Separation in an Fe(III) N-Heterocyclic Carbene. *J. Am. Chem. Soc.* **2021,** *143* (29), 10816-10821.
460. Note that the slope determined from the steady-state photoluminescence data (PLI0/PLI) was systematically slightly larger than the one determined from the time-resolved data (□0/□). This could be indicative of a small static quenching contribution. Static constant of 2.32, 1.78 and 0.55 M–1 were determined for iodide, bromide and chloride, respectively, in dichloromethane containing 0.5M TBAPF6.
461. Verity, B.; Bigger, S. W., The dependence of quinine fluorescence quenching on ionic strength. *International Journal of Chemical Kinetics* **1996,** *28* (12), 919-923.
462. Bronsted, J. N.; Teeter, C. E., On Kinetic Salt Effect. *J. Phys. Chem.* **1924,** *28* (6), 579-587.
463. Jonnalagadda, S. B.; Gollapalli, N. R., Kinetics of Reduction of Toluidine Blue with Sulfite—Kinetic Salt Effect in Elucidation of Mechanism. *Journal of Chemical Education* **2000,** *77* (4), 506.
464. Indelli, A., KINETIC SALT EFFECTS BY THE TETRAALKYLAMMONIUM IONS. *J. Phys. Chem.* **1961,** *65* (6), 972-974.
465. McTigue, P. T., Theory of kinetic salt effects. *Trans. Faraday Soc.* **1964,** *60* (0), 127-136.
466. Armarego, W. L. F., Chapter 4 - Purification of Inorganic and Metal-Organic Chemicals. In *Purification of Laboratory Chemicals (Eighth Edition)*, Armarego, W. L. F., Ed. Butterworth-Heinemann: 2017; pp 635-770.
467. Wang, C.; Li, H.; Bürgin, T. H.; Wenger, O. S., Cage escape governs photoredox reaction rates and quantum yields. *Nat. Chem.* **2024**.

468. Ohno, T.; Yoshimura, A.; Mataga, N., Bell-shaped energy-gap dependence of backward electron transfer occurring within geminate radical pairs produced by quenching of ruthenium(II) polypyridine complexes by aromatic amines. *J. Phys. Chem.* **1990,** *94* (12), 4871-4876.
469. Gould, I. R.; Ege, D.; Moser, J. E.; Farid, S., Efficiencies of photoinduced electron-transfer reactions: role of the Marcus inverted region in return electron transfer within geminate radical-ion pairs. *J. Am. Chem. Soc.* **1990,** *112* (11), 4290-4301.
470. Burget, D.; Jacques, P.; Vauthey, E.; Suppan, P.; Haselbach, E., Marcus inverted region: nature of donor–acceptor pairs and free ion yields. *J. Chem. Soc. Faraday T.* **1994,** *90* (17), 2481-2487.
471. Niwa, T.; Kikuchi, K.; Matsusita, N.; Hayashi, M.; Katagiri, T.; Takahashi, Y.; Miyashi, T., Solvent effects on photoinduced electron-transfer reactions. *J. Phys. Chem.* **1993,** *97* (46), 11960-11964.
472. Kikuchi, K.; Niwa, T.; Takahashi, Y.; Ikeda, H.; Miyashi, T., Quenching mechanism in a highly exothermic region of the Rehm-Weller relationship for electron-transfer fluorescence quenching. *J. Phys. Chem.* **1993,** *97* (19), 5070-5073.
473. Hino, T.; Akazawa, H.; Masuhara, H.; Mataga, N., Ionic photodissociation of excited electron donor-acceptor systems. II. Importance of the chemical property of donor-acceptor pairs. *J. Phys. Chem.* **1976,** *80* (1), 33-37.
474. Zanini, G. P.; Montejano, H. A.; Previtali, C. M., Photoinduced electron-transfer quenching of excited singlet states of polycyclic aromatic hydrocarbons by organic acceptors. *J. Chem. Soc. Faraday T.* **1995,** *91* (8), 1197-1202.
475. Frisch, M. J.; Trucks, G. W.; Schlegel, H. B.; Scuseria, G. E.; Robb, M. A.; Cheeseman, J. R.; Scalmani, G.; Barone, V.; Petersson, G. A.; Nakatsuji, H.; Li, X.; Caricato, M.; Marenich, A. V.; Bloino, J.; Janesko, B. G.; Gomperts, R.; Mennucci, B.; Hratchian, H. P.; Ortiz, J. V.; Izmaylov, A. F.; Sonnenberg, J. L.; Williams; Ding, F.; Lipparini, F.; Egidi, F.; Goings, J.; Peng, B.; Petrone, A.; Henderson, T.; Ranasinghe, D.; Zakrzewski, V. G.; Gao, J.; Rega, N.; Zheng, G.; Liang, W.; Hada, M.; Ehara, M.; Toyota, K.; Fukuda, R.; Hasegawa, J.; Ishida, M.; Nakajima, T.; Honda, Y.; Kitao, O.; Nakai, H.; Vreven, T.; Throssell, K.; Montgomery Jr., J. A.; Peralta, J. E.; Ogliaro, F.; Bearpark, M. J.; Heyd, J. J.; Brothers, E. N.; Kudin, K. N.; Staroverov, V. N.; Keith, T. A.; Kobayashi, R.; Normand, J.; Raghavachari, K.; Rendell, A. P.; Burant, J. C.; Iyengar, S. S.; Tomasi, J.; Cossi, M.; Millam, J. M.; Klene, M.; Adamo, C.; Cammi, R.; Ochterski, J. W.; Martin, R. L.; Morokuma, K.; Farkas, O.; Foresman, J. B.; Fox, D. J. *Gaussian 16 Rev. C.01*, Wallingford, CT, 2016.
476. Tomasi, J.; Mennucci, B.; Cancès, E., The IEF version of the PCM solvation method: an overview of a new method addressed to study molecular solutes at the QM ab initio level. *Journal of Molecular Structure: THEOCHEM* **1999,** *464* (1), 211-226.
477. Lee, C.; Yang, W.; Parr, R. G., Development of the Colle-Salvetti correlation-energy formula into a functional of the electron density. *Physical Review B* **1988,** *37* (2), 785-789.
478. Miehlich, B.; Savin, A.; Stoll, H.; Preuss, H., Results obtained with the correlation energy density functionals of becke and Lee, Yang and Parr. *Chem. Phys. Lett.* **1989,** *157* (3), 200-206.
479. Hariharan, P. C.; Pople, J. A., The influence of polarization functions on molecular orbital hydrogenation energies. *Theoretica chimica acta* **1973,** *28* (3), 213-222.
480. Hehre, W. J.; Ditchfield, R.; Pople, J. A., Self—Consistent Molecular Orbital Methods. XII. Further Extensions of Gaussian—Type Basis Sets for Use in Molecular Orbital Studies of Organic Molecules. *J. Chem. Phys.* **1972,** *56* (5), 2257-2261.
481. Stevens, W. J.; Krauss, M.; Basch, H.; Jasien, P. G., Relativistic compact effective potentials and efficient, shared-exponent basis sets for the third-, fourth-, and fifth-row atoms. *Canadian Journal of Chemistry* **1992,** *70* (2), 612-630.
482. Weigend, F.; Ahlrichs, R., Balanced basis sets of split valence, triple zeta valence and quadruple zeta valence quality for H to Rn: Design and assessment of accuracy. *Phys. Chem. Chem. Phys.* **2005,** *7* (18), 3297-3305.
483. Andrae, D.; Häußermann, U.; Dolg, M.; Stoll, H.; Preuß, H., Energy-adjustedab initio pseudopotentials for the second and third row transition elements. *Theoretica chimica acta* **1990,** *77* (2), 123-141.
484. Martin, R. L., Natural transition orbitals. *J. Chem. Phys.* **2003,** *118* (11), 4775-4777.
485. Ravel, B.; Newville, M., ATHENA, ARTEMIS, HEPHAESTUS: data analysis for X-ray absorption spectroscopy using IFEFFIT. *J. Synchrot. Radiat.* **2005,** *12*, 537-541.
486. Rehr, J. J.; Albers, R. C., Theoretical approaches to x-ray absorption fine structure. *Rev. Mod. Phys.* **2000,** *72* (3), 621-654.
487. Chen, L. X.; Zhang, X., Photochemical Processes Revealed by X-ray Transient Absorption Spectroscopy. *J. Phys. Chem. Lett.* **2013,** *4* (22), 4000-4013.
488. Neese, F., The ORCA program system. *Wiley Interdisciplinary Reviews: Computational Molecular Science* **2012,** *2* (1), 73-78.

489. Grimme, S.; Ehrlich, S.; Goerigk, L., Effect of the damping function in dispersion corrected density functional theory. *Journal of Computational Chemistry* **2011,** *32* (7), 1456-1465.
490. Kossmann, S.; Neese, F., Efficient Structure Optimization with Second-Order Many-Body Perturbation Theory: The RIJCOSX-MP2 Method. *Journal of Chemical Theory and Computation* **2010,** *6* (8), 2325-2338.
491. Tomson, N. C.; Williams, K. D.; Dai, X.; Sproules, S.; DeBeer, S.; Warren, T. H.; Wieghardt, K., Re-evaluating the Cu K pre-edge XAS transition in complexes with covalent metal-ligand interactions. *Chem. Sci.* **2015,** *6* (4), 2474-2487.
492. Becke, A. D., Density-functional thermochemistry. III. The role of exact exchange. *J. Chem. Phys.* **1993,** *98* (7), 5648-5652.
493. Stephens, P. J.; Devlin, F. J.; Chabalowski, C. F.; Frisch, M. J., Ab Initio Calculation of Vibrational Absorption and Circular Dichroism Spectra Using Density Functional Force Fields. *J. Phys. Chem.* **1994,** *98* (45), 11623-11627.
494. Roemelt, M.; Beckwith, M. A.; Duboc, C.; Collomb, M.-N.; Neese, F.; DeBeer, S., Manganese K-Edge X-Ray Absorption Spectroscopy as a Probe of the Metal–Ligand Interactions in Coordination Compounds. *Inorg. Chem.* **2012,** *51* (1), 680-687.
495. Moonshiram, D.; Guda, A.; Kohler, L.; Picon, A.; Guda, S.; Lehmann, C. S.; Zhang, X.; Southworth, S. H.; Mulfort, K. L., Mechanistic Evaluation of a Nickel Proton Reduction Catalyst Using Time-Resolved X-ray Absorption Spectroscopy. *The Journal of Physical Chemistry C* **2016,** *120* (36), 20049-20057.